XIV Reunión del Comité de Optoelectrónica

2-4 julio 2025, Terrassa

- LIBRO DE ACTAS -

optoel 2025

Center for Sensors, Instruments and System Development - UPC

COMITÉ EDITORIAL

Francisco Javier Burgos Fernández
Sara Giménez Aragón
Maite Valentino Herrera
Santiago Royo Royo

© De los textos e imágenes, los autores, 2025.

ISBN: 979-13-87613-54-9
DOI: 10.5821/ebook-9791387613549

PROGRAMA

ÍNDICE

BIENVENIDA 5

COMITÉS 7

SEDE Y LOGÍSTICA 9

LOCALIZACIÓN DE PATROCINADORES, EXPOSITORES Y COLABORADORES 13

PREMIOS A ESTUDIANTES 14

PONENTES INVITADOS 24

PROGRAMA 25

DATOS GENERALES 43

COMUNICACIONES 44

- Comunicaciones ópticas 54
- Sensores ópticos 88
- Dispositivos fotónicos 287
- Fotónica integrada 334
- Biofotónica 384
- Inteligencia artificial y fotónica 390
- Optoelectrónica en energía renovable 414
- Fotónica cuántica y no lineal 445

BIENVENIDA

Estimado participante,

En primer lugar, ¡gracias por tu asistencia a OPTOEL y bienvenidos a Terrassa! En un momento en que todo se acelera cada vez a mayor velocidad, es especialmente valioso poder parar un par de días entre amigos para actualizar conocimientos, charlar con conocidos y amigos del campo de la Optoelectrónica, y conocer a las nuevas generaciones de científicos y tecnólogos que darán forma al campo en España en los años que vienen.

Si es año es impar, toca OPTOEL... ¡hace ya 26 años!. Nuestro hábito de encontrarnos cada dos años desde Teruel 1999 nos impide celebrar en el congreso el vigesimoquinto aniversario de OPTOEL por un puro tema logístico, lo que no deja de hacerlo un hito relevante. Desde el Comité Organizador nos hemos esforzado por darle a esta decimocuarta edición el tono de celebración que la ocasión se merece, y, para ello, modificar ligeramente el programa para intentar mejorar los contenidos adaptándolos a los nuevos tiempos. Como sabéis, desde el CD6 siempre hemos hecho bandera de la innovación... no iba a ser menos cuando organizamos un OPTOEL.

Así, este año inauguramos el OPTOEL Joven, organizado por el Student Chapter PhotoniCAT de la UPC y el Área Joven de SEDOPTICA. Se trata de un espacio especialmente diseñado para el encuentro entre jóvenes investigadores en un entorno relajado. La jornada contará con un taller práctico para reflexionar sobre las presiones del entorno académico y trabajar herramientas para la gestión emocional. Abierto a todos, celebraremos el Pint of Optoelectronics, un formato distendido donde los participantes compartirán sus experiencias y anécdotas científicas en monólogos breves.

Os proponemos, también, añadir por primera vez al programa una mesa redonda en el ámbito de la conciliación familiar y laboral, organizada con el soporte del Área de Mujer, Óptica y Fotónica de SEDOPTICA. Hay también algunos ajustes en los espacios del Foro de Talento y del Foro de Innovación, que tan bien funcionaron en el OPTOEL de Sevilla. Todo ello, por supuesto, conservando los espacios tradicionales de intercambio científico que siguen siendo el corazón del congreso, y unas ponencias invitadas que nos han parecido especialmente relevantes.

No puedo acabar esta introducción sin agradecer sinceramente su apoyo para este OPTOEL a algunos agentes clave. En primer lugar, por supuesto a nuestro patrocinador especial Fibercom EXFO, pero con igual intensidad al resto de los doce expositores que han completado la totalidad de los espacios disponibles para presentaciones comerciales, así como a nuestros tres colaboradores. Otro agradecimiento muy especial va para las empresas e instituciones que nos han permitido ofrecer seis premios orientados a diferentes temáticas para los jóvenes investigadores que presenten los mejores trabajos de este decimocuarto OPTOEL.

Como sabéis, con esto de los agradecimientos uno no acaba nunca... gracias al soporte organizativo del Ayuntamiento de Terrassa; desde la ESEIAAT y la FOOT; y también a los que os habéis dejado convencer (tan fácilmente!) para actuar como tribunales de los premios... Muy especialmente, quiero cerrar con un agradecimiento al comité organizador de este OPTOEL. Ha sido muy estimulante trabajar con todos vosotros, y conoceros en un entorno diferente. Se ha hecho muy fácil organizar todo esto.

Voy acabando. Esperamos que disfrutéis de lo que os hemos preparado con nuestro mejor criterio. Entre todos haremos que sean unos días inolvidables tanto científica como personalmente.
Saludos cordiales y... adelante con el decimocuarto OPTOEL!!

Santiago ROYO ROYO

Meritxell VILASECA RICART

Comité Organizador de la OPTOEL 2025

ORGANIZADO POR

CD6 Center for Sensors, Instruments and Systems Development - UPC

Comité de Optoelectrónica

SEDOPTICA
SOCIEDAD ESPAÑOLA DE ÓPTICA

CON LA COLABORACIÓN DE

secpho

fotónica21
Plataforma Tecnológica Española de Fotónica

UPC UNIVERSITAT POLITÈCNICA DE CATALUNYA BARCELONATECH

Ajuntament de Terrassa

COMITÉS

COMITÉ ORGANIZADOR

Presidente:

SANTIAGO ROYO ROYO – Universitat Politècnica de Catalunya

Vicepresidenta:

MERITXELL VILASECA RICART – Universitat Politècnica de Catalunya

Vocales:

FRANCISCO JAVIER BURGOS FERNÁNDEZ – Universitat Politècnica de Catalunya
GERARD DE MAS GIMÉNEZ – Universitat Politècnica de Catalunya
MARIA BALLESTA GARCIA – Universitat Politècnica de Catalunya
CLARA MESTRE FERRER – Universitat Politècnica de Catalunya
AINA TURULL MALLOFRÉ – Universitat Politècnica de Catalunya
MAITE VALENTINO HERRERA – Universitat Politècnica de Catalunya
JOAN GOSET MALDONADO – Universitat Politècnica de Catalunya
ALEIX RAMÓN BOBI OLMO– Universitat Politècnica de Catalunya
SARA GIMÉNEZ ARAGÓN – Universitat Politècnica de Catalunya
ALEJANDRO CARBALLAR RINCÓN – Universidad de Sevilla
MARTINA DELGADO PINAR – Universitat de València
JOSÉ ANTONIO LÁZARO VILLA – Universitat Politècnica de Catalunya
SERGIO SÁEZ – SECPHO

COMITÉ CIENTÍFICO

Presidente:

ALEJANDRO CARBALLAR RINCÓN – Universidad de Sevilla

Vicepresidente:

SANTIAGO ROYO ROYO – Universitat Politècnica de Catalunya

Secretaria:

SONIA MARTÍN LÓPEZ – Universidad de Alcalá

COMITÉS

COMITÉ CIENTÍFICO

Vocales:

ALEJANDRO CARBALLAR RINCÓN – Universidad de Sevilla
ANA ISABEL GÓMEZ VARELA – Universidade de Santiago de Compostela
ANTONIO DÍEZ CREMADES – Universitat de València
ANTONIO PUERTA NOTARIO – Universidad de Málaga
AUGUSTO BELÉNDEZ VÁZQUEZ – Universitat d'Alacant
BEATRIZ SANTAMARÍA FERNÁNDEZ – Universidad Politécnica de Madrid
CARMEN VÁZQUEZ GARCÍA – Universidad Carlos III de Madrid
ENRIQUE CARRETERO CHAMARRO – Universidad de Zaragoza
FRANCISCO JAVIER BURGOS FERNÁNDEZ – Universitat Politècnica de Catalunya
FRANCISCO JAVIER FRAILE PELÁEZ – Universidade de Vigo
GABRIEL JUNYENT GIRALT – Universitat Politècnica de Catalunya
IGNACIO ESQUIVIAS MOSCARDÓ – Universidad Politécnica de Madrid
IGNACIO MORENO SORIANO – Universidad Miguel Hernández de Elche
IÑIGO MOLINA FERNÁNDEZ – Universidad de Málaga
JOSÉ ANTONIO LÁZARO VILLA – Universitat Politècnica de Catalunya
JOSÉ MANUEL SÁNCHEZ PENA – Universidad Carlos III de Madrid
JOSEBA ZUBIA ZABALLA – Universidad del País Vasco / Euskal Herriko Unibertsitatea
JUAN DIEGO ANIA CASTAÑÓN – Instituto de Óptica, CSIC
JUAN IGNACIO GARCÉS GREGORIO – Universidad de Zaragoza
LAURA REY BARROSO – Universitat Politècnica de Catalunya
MANUEL JOAQUIM BASTOS MARQUÉS – Universidade do Porto, Portugal
MANUEL LÓPEZ-AMO – Universidad Pública de Navarra
MARIA BALLESTA GARCIA – Universitat Politècnica de Catalunya
MARÍA DEL CARMEN BAO VARELA – Universidade de Santiago de Compostela
MARÍA TERESA FLORES ARIAS – Universidade de Santiago de Compostela
MARTINA DELGADO PINAR – Universitat de València
MIGUEL GONZÁLEZ HERRÁEZ – Universidad de Alcalá de Henares
MIGUEL VICENTE ANDRÉS BOU – Universitat de València
OSCAR ESTEBAN MARTÍNEZ – Universidad de Alcalá de Henares
PABLO GARCÍA GÓMEZ – Beamagine S.L.
PEDRO CORREDERA GUILLÉN – Instituto de Óptica, CSIC
RAFAEL PÉREZ JIMÉNEZ – Universidad de Las Palmas de Gran Canaria
ROSA ANA PÉREZ HERRERA – Universidad Pública de Navarra
SALVADOR SALES MAICAS – Universitat Politècnica de València
SANTIAGO MIGUEL OLAIZOLA – CEIT Universidad de Navarra
XABIER QUINTANA ARREGUI – Universidad Politécnica de Madrid

SEDE Y LOGÍSTICA

El OPTOEL 2025 se celebrará en el **Auditorio Municipal de Terrassa**, un espacio emblemático y referente cultural y musical de la ciudad, que acogerá las charlas y conferencias del congreso.
Su ubicación privilegiada, junto al Parc de Vallparadís, permite un acceso cómodo en transporte público. La estación Vallparadís Universitat de los Ferrocarrils de la Generalitat de Catalunya (FGC) se encuentra a tan solo 200 metros.

Audiorio Municipal de Terrassa
Passeig d'Ernest Lluch, 1, 08222 Terrassa, Barcelona

Auditorio municipal de Terrassa

Salón de actos – Conferencias Plenarias

Hall central – Zona de exposición de empresas y catering

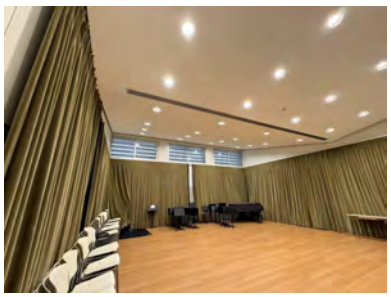

Sala de pósteres

Acceso a la red wifi SenseFils del Ayuntamiento de Terrassa

Para conectarte, sigue estos dos sencillos pasos:

1. Conéctate a la red sensefils.terrassa.cat y registra tu número de móvil. Recibirás la contraseña por SMS.

1. Usa la contraseña para conectarte a la red sensefils2.terrassa.cat y ya estarás listo para navegar.

SEDE Y LOGÍSTICA

Los Foros de Talento e Innovación (jueves 3 de julio de 16h a 18h) tendrán lugar en el **Edificio GAIA (TR14) de la UPC**, situado a apenas 50 metros del Auditorio.

Edificio GAIA TR14 UPC
Rambla de Sant Nebridi, 22, 08222 Terrassa, Barcelona

Hall GAIA TR14 UPC – Foro Talento

Sala Showroom GAIA TR14 UPC – Foro Innovación

SEDE Y LOGÍSTICA

CENAS DEL CONGRESO

Miércoles 2 de julio de 2025

Recepción de Bienvenida

***Ubicación**: Jardines de la Casa Alegre de Sagrera (Calle Cardaire, 19)*

Un elegante palacete modernista del siglo XIX convertido en museo, que conserva su decoración original y ofrece un entorno único para dar la bienvenida a los asistentes al congreso.

Jueves 3 de julio de 2025

Cena de Networking

***Ubicación**: El Vapor de Prodis (Calle del Bruc, 24)*

Ubicado en un antiguo edificio de la industria textil, este restaurante combina historia, compromiso social y un ambiente acogedor para el networking.

Disfrutaremos de una experiencia gastronómica de alta calidad en un espacio inclusivo que brinda oportunidades laborales a personas con discapacidad intelectual y trastornos de salud mental.

EMPRESAS PARTICIPANTES

Patrocinador Especial

fibercom

EXFO | Platinum PARTNER

Expositores Plus

secpho

amsTECHNOLOGIES

ZEPREN Solutions

mtb TECNOLOGÍA DE PRECISIÓN

[L*] ProCareLight Light, Laser and Safety Solutions

PRO-LITE TECHNOLOGY

iberOptics sistemas ópticos

HAMAMATSU PHOTON IS OUR BUSINESS

monocrom

UPV fAB

PIC-UPV PERTE CHIP CHAIR

LASING

Colaboradores

fotónica21 Plataforma Tecnológica Española de Fotónica

ARAGÓN PHOTONICS

WOOPTIX

Patrocinadores de Premios a Estudiantes

fibercom

ARAGÓN PHOTONICS

RADIANTIS

SPIE. SEDOPTICA SOCIEDAD ESPAÑOLA DE ÓPTICA

OPTICA

VLC PHOTONICS A Hitachi Group Company

LOCALIZACIÓN DE PATROCINADORES, EXPOSITORES Y COLABORADORES:

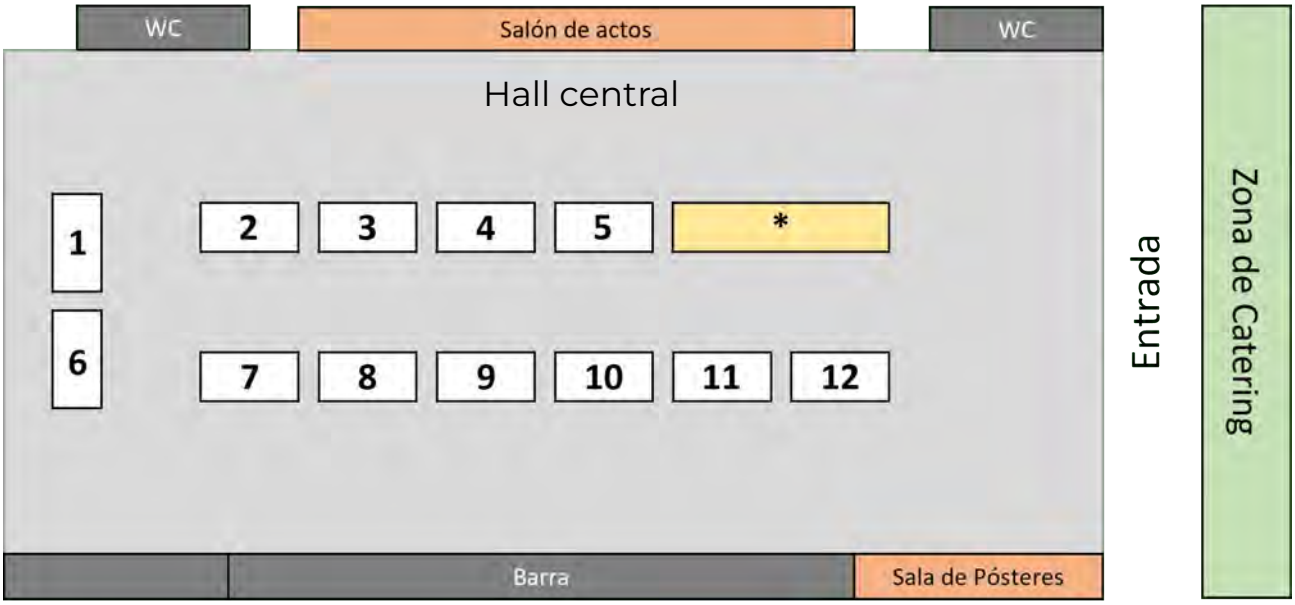

Planta baja del Auditorio municipal de Terrassa

* Patrocinador Especial

fibercom

EXFO | Platinum PARTNER

Expositor Plus

1. HAMAMATSU PHOTON IS OUR BUSINESS
2. iberOptics sistemas ópticos
3. monocrom
4. ZEPREN Solutions
5. UPV fAB
6. ProCareLight Light, Laser and Safety Solutions
7. mtb TECNOLOGÍA DE PRECISIÓN
8. ams TECHNOLOGIES
9. PRO-LITE TECHNOLOGY
10. LASING
11. PIC-UPV PERTE CHIP CHAIR
12. secpho

PREMIOS A ESTUDIANTES

Con el objetivo de promover la investigación de calidad entre los más jóvenes y reconocerla a través de sus resultados, el Comité de Optoelectrónica ofrece seis premios a los mejores trabajos:

PREMIO CARLOS GÓMEZ-REINO
Categoría: Tecnología Láser
patrocinado por Radiantis

PREMIO MARÍA VICTORIA (MARIVÍ) PÉREZ MARTÍN
Categoría: Abierta a todas las temáticas
patrocinado por OPTICA

PREMIO MARÍA JOSEFA (MARIFÍ) YZUEL
Categoría: Abierta a todas las temáticas
patrocinado por SPIE-SEDOPTICA

PREMIO JAVIER PELAYO
Categoría: Fibra Óptica – Fundamentos y Teoría
patrocinado por Aragón Photonics Labs

PREMIO FRANCISCO VILLUENDAS
Categoría: Fibra Óptica – Experimental y Aplicada
patrocinado por Fibercom

PREMIO VLC PHOTONICS
Categoría: Fotónica Integrada (PIC)
patrocinado por VLC-Photonics

Para conceder estos premios, el Comité Científico de OPTOEL 2025 valorará todas las contribuciones cuyo autor principal sea un estudiante. Los premios consistirán en una aportación económica bruta de **750 €** y un diploma acreditativo. Los requisitos para poder participar en los anteriores premios son los siguientes:

- Estar inscrito en el OPTOEL 2025, ser estudiante de grado, máster o doctorado o haber leído la tesis durante el curso 2024-2025 y haber aportado un documento que acredite dicha condición.
- Ser autor principal de la comunicación aceptada en OPTOEL 2025.

PREMIOS A ESTUDIANTES

Carlos Gómez-Reino

PREMIO CARLOS GÓMEZ-REINO

Categoría: Tecnología Láser

patrocinado por Radiantis

Carlos Gómez-Reino fue Catedrático de Óptica en la Universidad de Santiago de Compostela (USC), donde creó el primer laboratorio de óptica para estudiantes y cofundó, junto a María Victoria Pérez Martín, el grupo de investigación GRIN Optics (Gradient-Index Optics). Inició su carrera docente en la Universidad Complutense de Madrid, donde también obtuvo el Doctorado en Física con premio extraordinario. Fue pionero en óptica GRIN, holografía e interferometría, y autor del libro Gradient Index Optics: Fundamentals and Applications (Springer, 2002).

Con más de 150 publicaciones y seis sexenios de investigación, recibió el Premio de Investigación de la Xunta de Galicia (1992) y fue nombrado OSA Fellow en 1998. Miembro activo de la Real Sociedad Española de Física (RSEF) y de la Sociedad Española de Óptica (SEDOPTICA), ejercía como vicepresidente del Comité de Optoelectrónica en el momento de su fallecimiento.

PREMIO MARÍA VICTORIA (MARIVÍ) PÉREZ MARTÍN

Categoría: Abierta a todas las temáticas

patrocinado por OPTICA

María Victoria (Mariví) Pérez Martín

María Victoria Pérez Martín fue profesora titular en la Universidad de Santiago de Compostela (USC) y una destacada física experimental, pionera en óptica física, interferometría y metrología óptica desde sus inicios en la Universidad Complutense de Madrid (UCM). En 1979 se trasladó a Santiago, donde cofundó con Carlos Gómez-Reino el grupo GRIN Optics y lideró la creación del primer laboratorio de óptica para estudiantes.

Sus principales líneas de investigación incluyen la óptica GRIN, óptica fisiológica y óptica espacial y temporal. Con seis sexenios de investigación, fue autora de más de 90 publicaciones, y del volumen Gradient-Index Optics: Fundamentals and Applications (Springer, 2002).

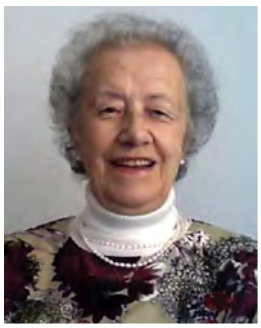

María Josefa (Marifí) Yzuel

PREMIO MARÍA JOSEFA (MARIFÍ) YZUEL

Categoría: Abierta a todas las temáticas

patrocinado por SPIE-SEDOPTICA

María Josefa Yzuel es Catedrática Emérita y Profesora Honoraria de la Universitat Autònoma de Barcelona (UAB), con una destacada trayectoria en imagen difractiva y moduladores espaciales de luz. Ha impartido docencia en óptica en las universidades de Zaragoza, Granada y la UAB. Fue presidenta de la Sociedad Española de Óptica (SEDOPTICA) entre 1993 y 1996, y de la International Society for Optics and Photonics (SPIE) en 2009. Ha recibido distinciones como el Doctorado Honoris Causa por las universidades de Elche y Granada, la Medalla de Física de la RSEF y la Encomienda de Alfonso X el Sabio.

PREMIOS A ESTUDIANTES

PREMIO JAVIER PELAYO

Categoría: Fibra Óptica – Fundamentos y Teoría
patrocinado por Aragón Photonics Labs

Javier Pelayo fue profesor e investigador en la Universidad de Zaragoza y figura clave en la creación del Grupo de Tecnologías Fotónicas (GTF). Pionero en la caracterización de dispersión cromática (CD) y por polarización (PMD) en fibras ópticas, participó en campañas europeas como COST 217 y 241. Su trayectoria abarcó desde el modelado teórico hasta el diseño experimental de dispositivos, destacando el desarrollo del BOSA (Brillouin Optical Spectrum Analyzer), un instrumento de resolución subpicométrica comercializado por Aragón Photonics Labs y adoptado internacionalmente.

Javier Pelayo a la izquierda y Francisco Villuendas a la derecha

En su última etapa investigó la caracterización espectral del estado de polarización y parámetros como OSNR (Optical Signal to Noise Ratio) y DGD (Differential Group Delay) en sistemas de telecomunicaciones. Su legado trasciende las aportaciones técnicas: dejó una forma de hacer ciencia y una actitud ante la universidad que siguen siendo referente.

PREMIO FRANCISCO VILLUENDAS

Categoría: Fibra Óptica – Experimental y Aplicada
patrocinado por Fibercom

Francisco Villuendas fue Catedrático de Física Aplicada en la Universidad de Zaragoza y figura clave en la creación del Grupo de Tecnologías Fotónicas (GTF), del que han surgido importantes contribuciones científicas y profesionales destacados. Comprometido con el impacto social de la ciencia, impulsó en 1991 la fundación de Fibercom, una de las primeras spin-offs surgidas del entorno universitario en España, centrada en redes ópticas de telecomunicación. Su visión emprendedora y su preocupación por la transferencia de conocimiento dieron lugar al actual Grupo Fibercom, en cuyo seno se encuentran empresas como Aragón Photonics Labs, nacida en 2004 como división industrial y de I+D de la empresa original. Quienes le conocieron destacan su trato directo, su carisma y su firme convicción de que la investigación debía estar al servicio de la sociedad.

PREMIO VLC PHOTONICS

Categoría: Fotónica Integrada (PIC)
patrocinado por VLC-Photonics

VLC Photonics es una empresa que ofrece servicios de ingeniería para clientes interesados en desarrollar productos con fotónica integrada. Se especializa en diseño, test y caracterización de circuitos fotónicos integrados (PIC) y fue fundada en julio de 2011 como spin-off de la Universidad Politécnica de Valencia. Desde sus inicios, VLC Photonics mantiene un firme compromiso con la innovación y excelencia técnica. En un sector dinámico como la fotónica integrada, la formación continua es esencial para mantenerse a la vanguardia. Por ello, valoramos profundamente la educación y el desarrollo de nuevos talentos que contribuyan al avance de esta tecnología clave. Esta iniciativa busca reconocer y fomentar el talento emergente, asegurando profesionales capacitados para enfrentar retos de un mercado en constante evolución.
En VLC Photonics, creemos que invertir en formación y apoyar a futuros expertos es fundamental para liderar el desarrollo de soluciones fotónicas avanzadas que impactan positivamente en diversas industrias y en la sociedad en general.

PREMIOS A ESTUDIANTES

JURADO:

ALEJANDRO CARBALLAR RINCÓN – Universidad de Sevilla

MARTINA DELGADO PINAR – Universitat de València

JOSÉ ANTONIO LÁZARO VILLA – Universitat Politècnica de Catalunya

SONIA MARTÍN LÓPEZ – Universidad Complutense de Madrid

JOSÉ MANUEL GARCÍA TIJERO – Universidad Politécnica de Madrid

CARMEN VÁZQUEZ GARCÍA – Universidad Carlos III de Madrid

PREMIO CARLOS GÓMEZ-REINO

Categoría: Tecnología Láser

Patrocinado por Radiantis

RADIANTIS

Premiado: Alejandro Casillas Rubio.

Contribución: Upconversion Nanoparticles Luminescence Lifetime Dependence on Excitation Parameters.

PREMIOS A ESTUDIANTES

PREMIO MARÍA VICTORIA (MARIVÍ) PÉREZ MARTÍN

Categoría: Abierta a todas las temáticas

Patrocinado por OPTICA

Premiado: Javier Pereiro García.

Contribución: Orbital Angular Momentum Multiplexing employing Liquid Crystal Reconfigurable Devices.

PREMIOS A ESTUDIANTES

PREMIO MARÍA JOSEFA (MARIFÍ) YZUEL

Categoría: Abierta a todas las temáticas

Patrocinado por SPIE-SEDOPTICA

Premiada: Sara Giménez Aragón.

Contribución: Optical Characterization of a Novel Concept of Deformable Primary Mirror for CubeSat Telescopes.

PREMIOS A ESTUDIANTES

PREMIO JAVIER PELAYO

Categoría: Fibra Óptica – Fundamentos y Teoría

Patrocinado por Aragón Photonics

Premiada: Anna I. Garrigues Navarro.

Contribución: Multipoint strain sensing based on optomechanical interaction in optical fibers.

PREMIOS A ESTUDIANTES

PREMIO FRANCISCO VILLUENDAS

Categoría: Fibra Óptica – Experimental y Aplicada

Patrocinado por Fibercom

Premiado: Javier Barco.

Contribución: Monitoring Technique Based on Tilted Fiber Bragg Gratings for Power over Fiber in Multicore Fibers.

PREMIOS A ESTUDIANTES

PREMIO VLC-PHOTONICS

Categoría: Fotónica Integrada (PIC)

Patrocinado por VLC-Photonics

Premiado: José Lozano.

Contribución: Large-scale Silicon Photonics antenna for next-generation integrated FSO transceivers.

PREMIOS A ESTUDIANTES

¡ENHORABUENA!
¡ENHORABUENA!
¡ENHORABUENA!

¡ENHORABUENA!
¡ENHORABUENA!
¡ENHORABUENA!

PONENTES INVITADOS

El OPTOEL2025 contará con la participación de 5 profesionales de dilatada trayectoria en optoelectrónica y fotónica, con trayectoria en investigación, industria y gestión tecnológica dentro y fuera de España.
Sus ponencias ofrecerán un espacio para compartir experiencias, conocimientos y líneas de trabajo en diversas áreas del congreso, fomentando el diálogo y la generación de nuevas oportunidades.

Aude Martin
Thales Group, France
Título Ponencia: ***Architectures and Demonstrations of Sensing Systems and Free-Space Optical Communication at Thales Research and Technology: From the Short to the Mid-Infrared Regions.***

Joan Manel Ramírez
III-VLab, France
Título Ponencia: ***Heterogeneous integration of III-V materials on silicon photonics: the quest for optical gain and high-speed modulation on-a-chip.***

Małgorzata Szczerska
Gdańsk University of Technology, Poland
Título Ponencia: ***Fiber optic temperature sensor.***

Jessica Ramella-Roman
Florida International University, USA
Título Ponencia: ***Advancing Polarization-Sensitive Imaging for Biomedical Diagnostics***

Christophe Caucheteur
University of Mons, Belgium
Título Ponencia: ***Plasmonic optical fiber grating biosensors: from their discovery to their possible industrialization.***

PROGRAMA

	Martes 01 JULIO	Miércoles 02 JULIO	Jueves 03 JULIO	Viernes 04 JULIO
08:30-09:00		Acreditaciones		
09:00-09:30		Sesión Apertura	Conferencia Invitada Małgorzata Szczerska *Gdańsk University of Technology (Polonia)*	Sesión Pósteres 4
09:30-10:00		Conferencia Invitada Aude Martín *Thales Group (Francia)*		
10:00-10:30			Charla Técnica *Hamamatsu, Iberoptics, Monocrom*	
10:30-11:00		Charla Técnica *Fibercom-EXFO*	Pausa Café	Charla Técnica *MTB, AMS Technologies, Pro-Lite*
11:00-11:30		Pausa Café	Sesión Pósteres 3	Pausa Café
11:30-12:00		Sesión Pósteres 1		Conferencia Invitada Christophe Caucheteur *University of Mons (Bélgica)*
12:00-12:30				
12:30-13:00			Charla Técnica *ZEPREN Solutions, UPVfab, ProCareLight*	Charla Técnica *LASING, PIC-UPV Chip Chair, SECPHO*
13:00-13:30		Conferencia Invitada Joan Manel Ramírez *III-VLab (Francia)*	Conferencia Invitada Jessica Ramella-Roman *Florida International University (USA)*	Entrega de Premios Clausura
13:30-14:00				
14:00-14:30		Pausa Comida	Pausa Comida	Cocktail Despedida
14:30-15:00				
15:00-15:30		Ponencia y Mesa Redonda organizada por el Área MOF *Conciliación laboral y familiar – Un reto compartido*	Asamblea Comité Optoelectrónica	
15:30-16:00	I OPTOEL Joven			
16:00-16:30		Sesión Pósteres 2	Foro de Talento Foro de Innovación	
16:30-17:00				
17:00-17:30				
17:30-18:00				
18:00-19:00				
19:00-20:30		Ruta Cultural	Ruta Cultural	
20:30-23:00		Recepción de Bienvenida	Cena de Networking	

MARTES, 01 DE JULIO – I OPTOEL JOVEN

*Organizado por **PhotoniCAT** (UPC Student Chapter) y el **Área Joven de SEDOPTICA***

*Patrocinado por **OPTICA** y **SPIE***

¡Llega la primera edición de OPTOEL Joven!
Un espacio pensado para los investigadores más jóvenes, con formación, networking y un toque de humor.

15:30 - 16:00 **Bienvenida y Apertura de puertas**
***Ubicación**: Aula 2.0, Edificio TR5 UPC (Calle de Colom, 15)*

16:00 - 18:00 **Ponencia y Workshop con Montserrat Lucena: "El poder de la mirada"**

Montserrat Lucena
Directora y formadora en SPELLARTS, S.L.
Experta en Programación Neurolingüística, Comunicación y Negociación.
Profesora asociada en UPC, Departamento de Óptica y Optometría.

Objetivo: Adquirir herramientas personales para el desempeño del trabajo de investigación, de forma saludable y con bienestar emocional.

Tema: Habilidades de comunicación intra e inter personales en los primeros años de investigación que favorecen la salud mental, la motivación y el rendimiento.

En el workshop observaremos juntos temas como la gestión emocional, la autoconfianza, y la relación entre la gestión del tiempo y el estrés en el campo de la investigación.

18:00 - 19:00 **Pausa**

19:00 – 23:00 **Pint of Optoelectronics**
***Ubicación**: Sala Showroom, Edificio GAIA TR14 UPC (Rambla Sant Nebridi, 22)*

Un espacio informal donde los jóvenes investigadores podrán compartir, en un monólogo corto (3-5 min), su trayectoria, su campo de investigación o anécdotas del mundo académico, sin necesidad de tecnicismos. Puedes hablar de tus logros, de los desafíos que has encontrado en el camino o de esos experimentos que no salieron como esperabas.

Un ambiente relajado, abierto a todos los asistentes de OPTOEL, con piscolabis y sorpresas.

MIÉRCOLES, 02 DE JULIO

08:30 - 09:00 **Recogida de Acreditaciones y Documentación**
Hall central

09:00 - 09:30 **Sesión de Apertura**
Salón de actos

09:30 - 10:30 **Conferencia invitada 1**
Salón de actos

Aude Martín
Thales Group, France

Architectures and Demonstrations of Sensing Systems and Free-Space Optical Communication at Thales Research and Technology: From the Short to the Mid-Infrared Regions

Thales Research and Technology (TRT) is dedicated to advancing sensing and free-space optical (FSO) communication technologies, focusing on the infrared spectrum for defense, aerospace, and telecommunications. This talk will present innovations in LiDAR and FSO systems, beginning with a Frequency Modulated Continuous Wave (FMCW) LiDAR at 1550 nm for 3D imaging and long-range detection. It will then explore SWIR free-space optical communication, addressing challenges like atmospheric turbulence with adaptive optics and coherent beam combining. The discussion will extend to MWIR/LWIR applications, including quantum cascade laser (QCL)-based FMCW LiDAR, before concluding with an active polarimetric imager in the SWIR domain, enhancing material detection for defense and civilian applications.

10:30 - 11:00 **Charlas Técnicas 1:**
Salón de actos

Charla impartida por

fibercom
EXFO | Platinum PARTNER

11:00 - 11:30 **Pausa Café**
Hall central

MIÉRCOLES, 02 DE JULIO

11:30 - 13:00 **Sesión de Pósteres 1**
Sala de pósteres

COMUNICACIONES ÓPTICAS

1.1	Numerical characterization of a 2x2 matrix of sub-wavelength radiant emitters for beam steering Francisco José Torcal-Milla, Carlos Sanchez-Azqueta and Luis Miguel Sánchez-Brea
1.2	Propagador Electromagnético 3D para Antenas Ópticas Integradas José Luis Vega García, Laureano Moreno Pozas, Miguel Barona Ruiz, Alejandro Sánchez Sánchez, Alejandro Ortega Moñux, Íñigo Molina Fernández, Robert Halir and J. Gonzalo Wangüemert Pérez
1.3	Monitoring Technique Based on Tilted Fiber Bragg Gratings for Power over Fiber in Multicore Fibers Javier Barco, Rubén Altuna, David Sánchez, David Barrera, Salvador Sales and Carmen Vázquez
1.4	Descomposición Modal en Fibras Ópticas mediante Aprendizaje Supervisado basado en MobileNetV2 Lucía Méndez, Juan Carlos Martín and Ana María López-Torres
1.5	Impact of Received Optical Power on the Transmission Performance of Standalone NB-IoT over PMMA GI-POF Muhammad Waseem, Alicia López, Pedro Luis Carro and Mª Ángeles Losada
1.6	Machine Learning based Non-Linear Model of Radio over large-core SI-POF in 5G/ NB-IoT scenarios Pedro Luis Carro, Maria Ángeles Losada, Muhammad Waseem, Alicia Lopez, Paloma García-Dúcar, Jesús de Mingo, Antonio Valdovinos and Javier Mateo

SENSORES ÓPTICOS

1.7	Portable pressure and gait sensing system with plastic optical fibers Aurélia Marchand, Javier Barco, Rubén Sánchez-Gómez and Carmen Vázquez
1.8	Sensor láser de fibra óptica para medir torsión utilizando una fibra de tres núcleos y un reflector basado en nanocristales Angel Ignacio Correa Serrano, José R. Vento Alvarez, Marko Galarza, Arturo Sanchez-Gonzalez, Romain Dauliat, Raphael Jamier, Philippe Roy, Georges Humbert, Rosa A. Perez-Herrera and Manuel Lopez-Amo
1.9	Sensor de deformación de alta sensibilidad basado en dos fibras especiales diferentes y con efecto Vernier Angel I. Correa, Jose R. Vento Alvarez, Marko Galarza, Romain Dauliat, R. Jamier, Philippe Roy, Rosa Ana Perez-Herrera and Manuel Lopez-Amo

MIÉRCOLES, 02 DE JULIO

11:30 - 13:00 **Sesión de Pósteres 1**
Sala de pósteres

SENSORES ÓPTICOS

1.10	Enhancing optical feedback interferometry with an integrated variable optical attenuator Ayesha Arshad, Usman Zabit, Olivier Bernal, Clement Deleau and Robert Halir
1.11	Distributed Acoustic Sensing for High-Speed Train Monitoring on Concrete Viaduct Felipe Muñoz, Jose María Perez Casas, Pedro Perez, Diego Gaston and Marco Jimenez-Rodriguez
1.12	Self-referenced carrier frequency offset interferogram correction for dual-comb systems Alonso Romero Barrueco, Camino Escobar-Vera, Clara Quevedo-Galán, Alejandro Rosado, Júlia Mateu-Comas, Sonia Martin-Lopez, Miguel Gonzalez-Herraez, Ignacio Esquivias and Maria del Rosario Fernández-Ruiz
1.13	Phase-sensitive common-path dual frequency comb spectroscopy Júlia Mateu Comas, Alonso Romero Barrueco, Miguel Gonzalez Herraez, Sonia Martin Lopez and María del Rosario Fernández Ruiz
1.14	An experimental study of forward-stimulated Brillouin scattering in optical fibers under hydrostatic pressure Carlos Andrés Álvarez Ocampo, Aleksander S Paterno, Martina Delgado Pinar, Antonio Díez Cremades, José Luis Cruz and Miguel Vicente Andrés Bou
1.15	Nanophotonic Interferometric Immunosensor for Label-Free and Real-Time Monitoring of Pollutants in Drinking Water Andrés Alonso Fernández, Patricia Ramírez Priego, Mari Carmen Estevez, Adrián Fernández Gavela and Laura M. Lechuga
1.16	Nano-precision metrology of X-ray mirrors with multifiber interferometers Albert Van Eeckhout, Igors Sics, Dominique Heinis and Josep Nicolas
1.17	Laser heterodyne radiometry for greenhouse gases monitorization Adela Collado-Rodríguez, Aldo Moreno-Oyervides, Oscar Elías Bonilla-Manrique, Omaira García and Pedro Martín-Mateos
1.18	Propuesta de solución óptica para medida de temperatura de recipiente y señalización en cocinas de inducción con encimera opaca Cristina Pelayo, Pilar Blasco, Enrique Carretero, Rafael Alonso and Sergio Llorente
1.19	Evaluación de FBGs como sensores de alta temperatura en aplicaciones de energía solar concentrada Manuel Jerez, Alejandro Carballar and Joaquín Granado

MIÉRCOLES, 02 DE JULIO

11:30 - 13:00 **Sesión de Pósteres 1**
Sala de pósteres

SENSORES ÓPTICOS

1.20 Integrated Optical Biosensors and Microfluidics for Real-Time Optical Sensing in Lab-on-a-Chip Systems
Beatriz Santamaría Fernández, Rafael Casquel del Campo, Haizea Apellaniz, Jorge Martinez de la Mata Gaitan, María Fe Laguna Heras, Andrés Otero, Airan Frances and Miguel Holgado Bolaños

1.21 Hemoglobin Level Determination with a Fiber Optic Sensor Using Boron-Doped Diamond Film
Monika Kosowska

13:00 - 14:00 **Conferencia invitada 2**
Salón de actos

Joan Manel Ramírez
III-VLab, France

Heterogeneous integration of III-V materials on silicon photonics: the quest for optical gain and high-speed modulation on-a-chip.
The integration of active components such as lasers and modulators into silicon photonics platforms is essential for advancing high-speed optical communication. Heterogeneous integration of III-V materials has emerged as a promising solution, enabling optical gain and efficient modulation directly on silicon chips. These advances leverage the scalability and CMOS compatibility of silicon, making them attractive for compact, co-packaged photonic systems.
This talk will review key developments in high-speed silicon photonic transceivers, focusing on the co-integration of III-V lasers and electro-absorption modulators. Recent demonstrations have shown excellent bandwidth and record-high modulation amplitudes. However, challenges remain, including thermal management, electrical cross-talk, and large-scale integration. We will present recent results and discuss future directions toward fully integrated, high-performance optical transmitters.

14:00 - 15:00 **Pausa Comida**
Hall central

MIÉRCOLES, 02 DE JULIO

15:00 - 16:00 **Ponencia y Mesa Redonda:**
Conciliación laboral y familiar – Un reto compartido
Organizado por el Área de Mujer, Óptica y Fotónica
Salón de actos

El evento comenzará con una **ponencia de Virginia Carrera Garrosa**, experta en relaciones laborales con perspectiva feminista y profesora en la Universidad de Salamanca, con más de 20 años de experiencia en igualdad y conciliación en CCOO Castilla y León

A continuación, se celebrará una **mesa redonda** moderada por **Beatriz Santamaría Fernández** (Vicepresidenta del Área de Mujeres en Óptica y Fotónica de SEDOPTICA) para compartir ideas y experiencias entre perfiles diversos. Acompañarán a Virginia Carrera:

- **Carmen Vázquez**, Catedrática de Tecnología Electrónica en la Universidad Carlos III de Madrid, referente internacional en el ámbito de la fotónica y comprometida con la promoción de la diversidad en las disciplinas STEM.
- **Mikel Aldaba**, profesor agregado del Departamento de Óptica y Optometría de la Universidad Politécnica de Cataluña y presidente del comité de ciencias de la visión de Sedoptica. Con experiencia investigadora internacional y un fuerte compromiso con la ciencia aplicada.

Este evento pretende ser un foro de **debate abierto y plural**, donde se visibilicen los obstáculos y oportunidades para una conciliación real y corresponsable, poniendo en el centro la experiencia de quienes, desde distintos ámbitos profesionales, enfrentan este desafío cada día.

Beatriz Santamaría

Virginia Carrera

Mikel Aldaba

Mª Carmen Vázquez

16:00 - 17:30 **Sesión de Pósteres 2**
Sala de pósteres

SENSORES ÓPTICOS	
2.1	Polarimetría Mueller Full Poincaré usando diversas fuentes de luz para caracterizar medios con actividad óptica natural Gemma Piquero, Juan Carlos González de Sande, Juan Carlos Suárez Bermejo and Massimo Santarsiero
2.2	Interferometría de Ruido Ambiente mediante DAS con pulsos chirpados Jorge Canudo, Javier Preciado-Garbayo, Pascual Sevillano, Jesús Subías, Miguel Gonzalez-Herraez, Hugo F. Martins, Beatriz Gaite-Castrillo, Jose Benito Bravo-Monge, Irene De Maria and Miguel Rodriguez-Plaza

MIÉRCOLES, 02 DE JULIO

16:00 - 17:30 **Sesión de Pósteres 2**
Sala de pósteres

SENSORES ÓPTICOS

2.3	Development and Validation of a Spectral Albedometer (200-2500 nm): Cuasi-Simultaneous Measurement of Solar and Snow Cover Reflected Radiation. Adrián Subías Martín, Pascual Navarro, Jorge Ciudad-Real, Víctor Herráiz-López, Iñigo Salinas and Rafael Alonso
2.4	Upconversion Nanoparticles Luminescence Lifetime Dependence on Excitation Parameters Alejandro Casillas-Rubio, Khouloud Hamraoui, Diego Mendez-Gonzalez, Marco Laurenti, Jorge Rubio-Retama, Oscar G. Calderón and Sonia Melle
2.5	Multipoint strain sensing based on optomechanical interaction in optical fibers Anna I. Garrigues-Navarro, Martina Delgado-Pinar, Antonio Díez and Miguel V. Andrés
2.6	Modelling an inversion layer photodiode in COMSOL Multiphysics Rubén Gómez Cornejo, Sucheta Sharma, Trinh Tran, Erkki Ikonen, Pedro Corredera and Joaquín Campos
2.7	Study of bandwidth and response saturation on PQED photodiode Rubén Gómez Cornejo, Noelia Castrejón, Juan Galindo-Santos, Joaquín Campos and Pedro Corredera
2.8	Detección de fugas en tuberías mediante redes de Bragg y algoritmos de Inteligencia Artificial Javier Madrigal, Victor Javier Ruiz, Beatriz Defez, Jorge Gosálvez and Salvador Sales
2.9	Dual-comb ranging using densified gain-switched optical frequency combs Clara Quevedo-Galán, Antonio Pérez-Serrano, José Manuel G. Tijero and Ignacio Esquivias
2.10	Forward Stimulated Brillouin Scattering in Optical Fibers under Hydrogen Diffusion Aleksander Paterno, Carlos Alvarez, Antonio Díez-Cremades, José Luis Cruz, Martina Delgado-Pinar and Miguel Andrés
2.11	Microwave Frequency OTDR for High Strain-rate Sensing Yan Ren, Pedro J. Vidal-Moreno, María R. Fernández-Ruiz, Sonia Martín-López, Luis Costa, Zhongwen Zhan and Miguel González-Herráez
2.12	Exploration of Optical Fiber Based Sensor Phenomena, Use Cases and Potential Calibration Method for Vibrations Ángel Redondo and José Antonio Lázaro
2.13	A Monte Carlo model of the propagation of polarized pulses in turbid media for modelling polarized lidar in fog Maria Ballesta-Garcia, Aleix R. Bobi Olmo and Santiago Royo
2.14	Development of a LiDAR-integrated multimodal system for underwater sensing Aleix.R Bobi-Olmo, Eduardo Bernal, Pablo García-Gomez, Maria Ballesta-Garcia and Santiago Royo

MIÉRCOLES, 02 DE JULIO

16:00 - 17:30 **Sesión de Pósteres 2**
Sala de pósteres

SENSORES ÓPTICOS

2.15	Optical Characterization of a Novel Concept of Deformable Primary Mirror for CubeSat Telescopes Sara Giménez-Aragón, Toni Ruiz-Valverde, Alejandro Santillán, Armengol Torres, Eduardo Ferrer and Santiago Royo
2.16	Phi-OTDR de pulso chirpeado largo para medidas en fibra de nanodeformaciónes de kHz a 24h con alto rango dinámico Hugo F. Martins
2.17	Autocorrección de referencias en MFDD-DAS: Hacia medidas absolutas en condiciones reales Pedro J. Vidal-Moreno, Marcos G. Barriopedro, Alejandro Rosado, Laura Hernández-Martín, Sonia Martin-Lopez and Hugo F. Martins
2.18	Phi-OTDR de pulso chirpeado largo asistido por Raman para termometría de fibra distribuida en milikelvin de largo alcance Laura Hernández-Martín, Javier Preciado-Garbayo, Jorge Canudo, Juan D. Ania-Castañón and Hugo F. Martins
2.19	High-Finesse Fiber-Optic Fabry-Perot Interferometer for Gas Pressure Sensing with Minimal Temperature Influence Elena Lorente, Luis Alberto Sánchez, Bryan Sanipatin, Daniel Maldonado-Hurtado and Salvador Sales
2.20	Development and Experimental Validation of a Fiber Bragg Grating-Based Hydrogen Sensor Using Pt-Doped WO_3 Pablo Sancho-Villach, Bryan Sanipatin, Rubén Martín-Cabezuelo, Laurent Sauvanaud, Luis Alberto Sánchez and Salvador Sales
2.21	Análisis exhaustivo y modelo simplificado de un sensor de fibra óptica para desplazamiento angular Gorka Zubia-Garea, Joseba Zubia Zaballa, Josu Amorebieta, Gotzon Aldabaldetreku and Gaizka Durana

19:00 - 20:30 **Rutas Culturales**

Ruta Medieval
***Ubicación**: La Seu d'Ègara (Plaça del Rector Homs)*

Ruta Modernista
***Ubicación**: Ajuntament de Terrassa (Raval de Montserrat, 14)*

20:30 - 23:00 **Recepción de Bienvenida**
***Ubicación**: Jardines Casa Alegre de Sagrera (Calle Cardaire, 19)*

JUEVES, 03 DE JULIO

09:00 - 10:00 **Conferencia invitada 3**
Salón de actos

Małgorzata Szczerska
Gdańsk University of Technology, Poland

Fiber optic temperature sensor.
Temperature is a key control marker in many technological processes, yet its measurement often relies on indirect observations of related physical properties. Traditional contact-based sensors can be impractical in extreme conditions, moving objects, or hazardous environments. Fiber optic sensors offer a reliable alternative, enabling real-time temperature monitoring in remote or challenging locations while remaining immune to electromagnetic interference and resistant to harsh conditions. Their integration with interferometry allows for precise measurements, making them increasingly valuable in industrial automation and control systems. This talk will present a critical analysis of recent advancements in fiber optic temperature sensing, highlighting their benefits, applications, and future potential.

10:00 - 10:30 **Charlas Técnicas 2**
Salón de actos

Charlas impartidas por:

HAMAMATSU PHOTON IS OUR BUSINESS
iber optics sistemas ópticos
monocrom

10:30 - 11:00 **Pausa Café**
Hall central

JUEVES, 03 DE JULIO

11:00 - 12:30 **Sesión de Pósteres 3**
Sala de pósteres

DISPOSITIVOS FOTÓNICOS

3.1	Improving the Efficiency of Blazed gratings in Vertical Aligned LCoS device Guillem Najar, Fco. Javier Martínez Guardiola, Andres Marquez, Adrián Moya, Emilio José Mena Ruiz, Jorge Francés Monllor, Sergi Gallego Rico, Inmaculada Pascual and Augusto Beléndez
3.2	Fabrication and characterization of photoaligned MR-based liquid crystal cells Adrián Moya Aliaga, Eva María Calzado, Emilio José Mena, Guillem Najar, Andrés Márquez, Augusto Beléndez and Inmaculada Pascual
3.3	Effects of addition of terminal emitter on device performance in hyperfluorescent OLEDs Thomas Sayner, Arvydas Ruseckas and Ifor Samuel
3.4	Optical generation, measurement and tuning of optomechanical spheroidal resonances in a silica microsphere Juan Julian-Barriel, Martina Delgado-Pinar, Antonio Díez and Miguel V. Andrés
3.5	Performance of gravity-compensated focus-tunable lens Fátima Cuéllar, Elisabet Pérez-Cabré, Laura Clavé and María Sagrario Millán
3.6	Desarrollo de películas delgadas de AlN amorfo sobre ITO-vidrio e ITO-PET a baja temperatura mediante rf-sputtering Miriam Cadenas, Michael Sun, Susana Fernández, Sirona Valdueza-Felip and Fernando Bernabé Naranjo
3.7	Orbital Angular Momentum Multiplexing employing Liquid Crystal Reconfigurable Devices Javier Pereiro García, Byron Ganazhapa, José Jaraba, Pablo De la Rosa, Xabier Quintana and Morten Geday
3.8	Low cost optical device to measure blood plasma coagulation Gemma García-Mandayo, Lucía Ruiz Fernández de Bobadilla, María Guijo, Oihane Beldarrain, Aitor Larrañaga-Jaio, Javier Gallego, Patricia Blanco, Carles Pizarro and Santiago M. Olaizola
3.9	Caracterización robusta de retardadores mediante el uso de un interferómetro de doble rendija de Young Inés Meili Diaz García, Jesus del Hoyo, Armando Gonzalez García, Joaquín Andrés Porras, Ángela Soria García, Isabel González-Martínez, Karen Priscila Soto González, Javier Alda and Luis Miguel Sánchez Brea

JUEVES, 03 DE JULIO

11:00 - 12:30 **Sesión de Pósteres 3**
Sala de pósteres

FOTÓNICA INTEGRADA

3.10	IMB-CNM Silicon Nitride Platform for Integrated Photonics Marçal Blasco-Solvas, Joaquín Hernández-Betanzos, Jad Sabek, Carlos Domínguez-Horna and Joaquín Faneca
3.11	Simulador eficiente de antenas ópticas integradas con radiación en ángulos arbitrarios Elio Godoy Lorite, Laureano Moreno Pozas, Robert Halir, Alejandro Ortega Moñux, Gonzalo Wangüemert Pérez and Iñigo Molina Fernández
3.12	Next-generation photonic devices enabled by functional materials in silicon photonics Jorge Parra, Iñigo López-Mulet, Jorge Caso, Juan Francisco Morcillo and Pablo Sanchis
3.13	Prototyping of microstructures for photonic devices and glass interposers using powerful femtosecond laser source Bogusz Stepak, Katarzyna Pietrusińska, Natalia Grudzien, Yuriy Stepanenko, Michal Nejbauer and Juan Luis Vadillo
3.14	Simplified Polarization Independent Integrated Coherent Receiver for Passive Optical Networks Natalia Herguedas, Jorge Ciudad-Real, David Izquierdo, Pascual Sevillano and Ignacio Garcés
3.15	Dual-comb generator based on a monolithically integrated InP Photonic Integrated Circuit Pablo López-Querol, Clara Quevedo-Galán, José Manuel G. Tijero, Ignacio Esquivias and Antonio Pérez-Serrano
3.16	Design of a Monolithically Integrated Photonic RF Phase Shifter Gonzalo Soldevilla Gómez, Pablo López Querol, José Manuel García Tijero, Ignacio Esquivias Moscardo and Antonio Pérez Serrano
3.17	Development of Silicon Nitride Photonic Integrated Circuits: Fully in-house Fabrication and Optical Characterization Giuseppe Libero Bufi, Christian Camilo Cano Vasquez, Louw Roel van der Zon, Adrián Fernández, Rubén Alemany, César Alminyana, Isabelle Rodriguez, Gloria Micó, Pascual Muñoz and Daniel Pastor
3.18	Large-scale Silicon Photonics antenna for next-generation integrated FSO transceivers José Lozano, Pablo Ginel and Alejandro Ortega

JUEVES, 03 DE JULIO

12:30 - 13:00 **Charlas Técnicas 3**
Salón de actos

Charlas impartidas por:

ZEPREN Solutions

UPV fAB

ProCareLight
Light, Laser and Safety Solutions

13:00 - 14:00 **Conferencia invitada 4**
Salón de actos

Jessica Ramella-Roman
Florida International University, USA

Advancing Polarization-Sensitive Imaging for Biomedical Diagnostics
Polarization-sensitive imaging is emerging as a powerful tool in biomedical diagnostics, offering enhanced contrast and structural insight beyond conventional intensity-based methods. By analyzing parameters such as depolarization, retardance, and diattenuation, it enables improved detection and characterization of pathological changes in tissue.
This talk will present recent advances in polarization-sensitive modalities developed in our lab, including Mueller polarimetry and Polarization-Resolved Second Harmonic Generation (P-SHG). These techniques have shown promising results in diagnosing diseases affecting collagen in the extracellular matrix, with applications in cervical cancer, preterm labor, and glaucoma. We will discuss how decomposition of the Mueller matrix and collagen-specific imaging with P-SHG provide clinically relevant information. Finally, we address key challenges such as interpreting complex optical signals and standardizing methodologies, highlighting the path toward clinical adoption of polarization imaging in healthcare.

14:00 - 15:00 **Pausa Comida**
Hall central

15:00 - 16:00 **Asamblea Comité Optoelectrónica**
Salón de actos

JUEVES, 03 DE JULIO

16:00 - 18:00 **Foro de Innovación**
***Ubicación**: Sala Showroom, Edificio GAIA TR14 UPC (Rambla Sant Nebridi, 22)*

El objetivo de este Foro es generar proyectos de innovación colaborativos entre las empresas asistentes del sector industrial, proyectos en los que las tecnologías Deep Tech suponen un potente foco de innovación.
Para ello, estaremos abordando varios retos y la dinámica estará enfocada en generar debates útiles y centrada en problemáticas concretas, de manera que se impulse la colaboración entre los asistentes.

Coordinadores:
Sergio Sáez, *Clúster Manager de SECPHO.*
Rosa Sánchez, *Innovation Manager de SECPHO.*

Foro de Talento
***Ubicación**: Hall del Edificio GAIA TR14 UPC (Rambla Sant Nebridi, 22)*

El Foro de Talento se presenta como una feria de empleo dinámica que conecta las oportunidades de la industria con candidaturas de talento emergente procedente de las universidades. Su objetivo es fomentar que el talento fotónico español desarrolle su carrera investigadora o profesional dentro del país, ya sea en centros de investigación o en empresas del sector.
El equipo de SECPHO y Fotónica21 coordina esta iniciativa, recopilando previamente las ofertas y candidaturas, y diseñando las dinámicas de conexión que tienen lugar durante OPTOEL.

19:00 - 20:30 **Rutas Culturales**
Ruta Medieval
***Ubicación**: La Seu d'Ègara (Plaça del Rector Homs)*

Ruta Modernista
***Ubicación**: Ajuntament de Terrassa (Raval de Montserrat, 14)*

20:30 - 23:00 **Cena de Networking**
***Ubicación**: El Vapor de Prodis (Calle del Bruc, 24)*

VIERNES, 04 DE JULIO

09:00 - 10:30 **Sesión de Pósteres 4**
Sala de pósteres

BIOFOTÓNICA

4.1	Portable multispectral fundus camera: a pilot study Marina Bou Marin, Meritxell Vilaseca Ricart and Francisco J. Burgos Fernández

INTELIGENCIA ARTIFICIAL Y FOTÓNICA

4.2	Machine Learning Approach to Find the Optimal Window for LIPSS Formation in Femtosecond Laser Processing Aitor Larrañaga-Jaio, Iñigo Ramon-Conde, Aldara Pan Cabo, Isabel Ayerdi Olaizola, Santiago M Olaizola and Ainara Rodríguez
4.3	Addressing ROS 2 Limitations for Dependable Multimodal Sensing Applications Jokin Arozamena-Rodríguez, Santiago Royo, Jorge Parra and Maider Zamalloa
4.4	Multimodal data acquisition prototype for autonomous driving in adverse weather conditions Gerard DeMas-Giménez, Adrià Subirana, Pablo García-Gómez, Eduardo Bernal, Jordi Riu, Josep Ramon Casas and Santiago Royo
4.5	Plastics Sorting Using Terahertz Frequencies and Machine Learning Daniel Moreno París, Oscar Elías Bonilla Manrique, David Hernandez Guerrero, Pedro Martín Mateos and Aldo Moreno Oyervides

OPTOELECTRÓNICA EN ENERGÍA RENOVABLE

4.6	Capa antirreflejante en el rango visible basada en nanopartículas metálicas embebidas en un fotopolímero. Aplicación a células solares de película delgada Óscar Esteban, Sirona Valdueza-Felip and Fernando B. Naranjo
4.7	Comparación teórica de concentradores solares luminiscentes con distintas geometrías Jagoba Barata, Jon Arrue, Joseba Zubia and María Asunción Illarramendi
4.8	Impacto del espesor de la capa de nitruro en la eficiencia fotovoltaica de heterouniones AlInN/a-Si/Si(100) Sirona Valdueza-Felip, Michael Sun, Miriam Cadenas, Sofía Figueroa and Fernando B. Naranjo
4.9	Medida de Flujo Solar Concentrado en Simulador Solar basado en fibra óptica y fotodiodo Manuel Jerez, Alejandro Carballar, Ricardo Conceição, José González-Aguilar, Xabier Rández and Olaia Itoiz
4.10	Using Semiconductor Photodiodes as Detector Element for Solar Radiation Measurements Manuel Jerez, Alejandro Carballar and Joaquín Granado

VIERNES, 04 DE JULIO

09:00 - 10:30 **Sesión de Pósteres 4**
Sala de pósteres

FOTÓNICA CUÁNTICA Y NO LINEAL

4.11	Efficient frequency down-conversion of quantum-dot-compatible single photons enabled by molecular modulation Arturo Mena, Pau Arcos, Joseba Zubia and David Novoa
4.12	Deep ultraviolet source via cooperative Raman combs in gas-filled hollow-core fibres Pau Arcos, David Novoa and Joseba Zubia
4.13	Ultrafast Bright Squeezed Vacuum Light Source María Sánchez-Hernández, Miriam Lazo, Arturo Mena, Tasio Gonzalez-Raya, Mikel Sanz, Joseba Zubia and David Novoa
4.14	Towards a broadband measurement of waveguide dispersion curves Marc P. Safont, Enrique Silvestre, Antonio Díez, Martina Delgado-Pinar, Miguel V. Andrés and David Castelló-Lurbe
4.15	Intracavity upconversion of images in the SWIR pumped by a passively V3+:YAG Q-Switched Nd3+:YVO4 laser at 1342 nm Adrián J. Torregrosa, María Luisa Rico, Haroldo Maestre, Miguel Cuenca and Juan Capmany
4.16	Towards improved performance of an Yb:KGW laser-based intracavity image upconverter Adrián J. Torregrosa, María Luisa Rico, Juan Capmany, Miguel Cuenca, Angela E. Ortega, Carlos R. Fernández-Pousa and Haroldo Maestre
4.17	Impact of nonlinearity multifrequency dispersion on instabilities cancelation Miguel A. Bosch, Enrique Silvestre, Martina Delgado-Pinar, Antonio Díez, Miguel V. Andrés and David Castelló-Lurbe

10:30 - 11:00 **Charlas Técnicas 4**
Salón de actos

Charlas impartidas por:

mtb TECNOLOGÍA DE PRECISIÓN
ams TECHNOLOGIES
PRO-LITE TECHNOLOGY

VIERNES, 04 DE JULIO

11:00 - 11:30 **Pausa Café**
Hall central

11:30 - 12:30 **Conferencia invitada 5**
Salón de actos

Christophe Caucheteur
University of Mons, Belgium

Plasmonic optical fiber grating biosensors: from their discovery to their possible industrialization.

Plasmonic optical fiber grating biosensors combine the advantages of tilted fiber Bragg gratings (TFBGs) with the sensitivity of plasmonic resonances, enabling real-time, label-free detection of biochemical interactions. These sensors exploit the coupling between core and cladding modes, made possible by the tilted structure of TFBGs, to achieve high sensitivity to changes in the surrounding refractive index. Since their initial development, these devices have evolved significantly, with improvements in sensitivity, surface functionalization, and miniaturization.
This talk will provide an overview of the progress made in the field, from the early stages of research to recent technological innovations. It will also address the current challenges in scaling up for industrial use, including reproducibility, robustness, and manufacturing costs. Finally, potential applications in healthcare, environmental monitoring, and food safety will be discussed, along with strategies for overcoming the remaining barriers to real-world deployment.

12:30 - 13:00 **Charlas Técnicas 5**
Salón de actos

Charlas impartidas por:

LASING PIC-UPV PERTE CHIP CHAIR secpho

13:00 - 14:00 **Entrega de Premios | Clausura**
Salón de actos

14:00 - 15:00 **Cocktail Despedida**
Hall central

MAPA OPTOEL 2025

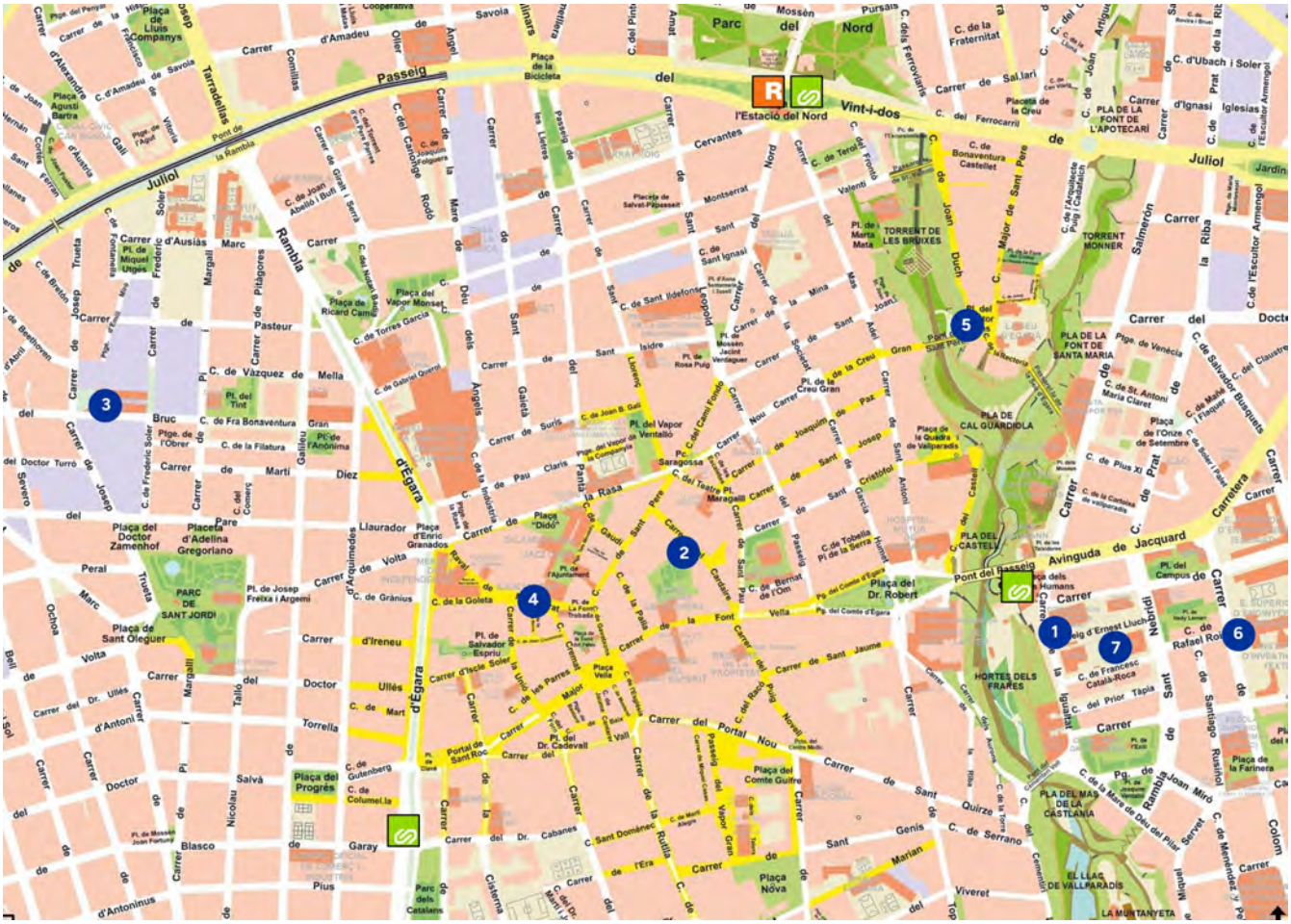

1. Auditorio de Terrassa
2. Casa Alegre de Sagrera
3. El Vapor de Prodis
4. Punto salida ruta modernista (Ayuntamiento)
5. Punto salida ruta medieval (Seu d'Ègara)
6. OPTOEL Joven
7. Pint of optoelectronics
   Foro de talento
   Foro de innovación

Ferrocarriles de la Generalitat

R Cercanías Renfe

DATOS GENERALES

Evento:
OPTOEL2025

Fechas:
2 al 4 de julio de 2025

Sede:
Auditorio Municipal de Terrassa
Passeig d'Ernest Lluch, 1
08222 Terrassa, Barcelona

Web del Congreso:
www.optoel.es

Email de contacto:
info2025@optoel.es

Organiza:

CD6 Center for Sensors, Instruments and Systems Development - UPC

Comité de Optoelectrónica

SEDOPTICA SOCIEDAD ESPAÑOLA DE ÓPTICA

Con la colaboración de:

secpho

fotónica21 Plataforma Tecnológica Española de Fotónica

UPC UNIVERSITAT POLITÈCNICA DE CATALUNYA BARCELONATECH

Ajuntament de Terrassa

COMUNICACIONES

ÍNDICE

COMUNICACIONES ÓPTICAS

1.1	Numerical characterization of a 2x2 matrix of sub-wavelength radiant emitters for beam steering Francisco José Torcal-Milla, Carlos Sanchez-Azqueta and Luis Miguel Sánchez-Brea	55
1.2	Propagador Electromagnético 3D para Antenas Ópticas Integradas José Luis Vega García, Laureano Moreno Pozas, Miguel Barona Ruiz, Alejandro Sánchez Sánchez, Alejandro Ortega Moñux, Íñigo Molina Fernández, Robert Halir and J. Gonzalo Wangüemert Pérez	59
1.3	Monitoring Technique Based on Tilted Fiber Bragg Gratings for Power over Fiber in Multicore Fibers Javier Barco, Rubén Altuna, David Sánchez, David Barrera, Salvador Sales and Carmen Vázquez	65
1.4	Descomposición Modal en Fibras Ópticas mediante Aprendizaje Supervisado basado en MobileNetV2 Lucía Méndez, Juan Carlos Martín and Ana María López-Torres	71
1.5	Impact of Received Optical Power on the Transmission Performance of Standalone NB-IoT over PMMA GI-POF Muhammad Waseem, Alicia López, Pedro Luis Carro and Mª Ángeles Losada	77
1.6	Machine Learning based Non-Linear Model of Radio over large-core SI-POF in 5G/ NB-IoT scenarios Pedro Luis Carro, Maria Ángeles Losada, Muhammad Waseem, Alicia Lopez, Paloma García-Dúcar, Jesús de Mingo, Antonio Valdovinos and Javier Mateo	83

SENSORES ÓPTICOS

1.7	Portable pressure and gait sensing system with plastic optical fibers Aurélia Marchand, Javier Barco, Rubén Sánchez-Gómez and Carmen Vázquez	89
1.8	Sensor láser de fibra óptica para medir torsión utilizando una fibra de tres núcleos y un reflector basado en nanocristales Angel Ignacio Correa Serrano, José R. Vento Alvarez, Marko Galarza, Arturo Sanchez-Gonzalez, Romain Dauliat, Raphael Jamier, Philippe Roy, Georges Humbert, Rosa A. Perez-Herrera and Manuel Lopez-Amo	95

SENSORES ÓPTICOS

1.9	Sensor de deformación de alta sensibilidad basado en dos fibras especiales diferentes y con efecto Vernier Angel I. Correa, Jose R. Vento Alvarez, Marko Galarza, Romain Dauliat, R. Jamier, Philippe Roy, Rosa Ana Perez-Herrera and Manuel Lopez-Amo	101
1.10	Enhancing optical feedback interferometry with an integrated variable optical attenuator Ayesha Arshad, Usman Zabit, Olivier Bernal, Clement Deleau and Robert Halir	107
1.11	Distributed Acoustic Sensing for High-Speed Train Monitoring on Concrete Viaduct Felipe Muñoz, Jose María Perez Casas, Pedro Perez, Diego Gaston and Marco Jimenez-Rodriguez	113
1.12	Self-referenced carrier frequency offset interferogram correction for dual-comb systems Alonso Romero Barrueco, Camino Escobar-Vera, Clara Quevedo-Galán, Alejandro Rosado, Júlia Mateu-Comas, Sonia Martin-Lopez, Miguel Gonzalez-Herraez, Ignacio Esquivias and Maria del Rosario Fernández-Ruiz	119
1.13	Phase-sensitive common-path dual frequency comb spectroscopy Júlia Mateu Comas, Alonso Romero Barrueco, Miguel Gonzalez Herraez, Sonia Martin Lopez and María del Rosario Fernández Ruiz	125
1.14	An experimental study of forward-stimulated Brillouin scattering in optical fibers under hydrostatic pressure Carlos Andrés Álvarez Ocampo, Aleksander S Paterno, Martina Delgado Pinar, Antonio Díez Cremades, José Luis Cruz and Miguel Vicente Andrés Bou	131
1.15	Nanophotonic Interferometric Immunosensor for Label-Free and Real-Time Monitoring of Pollutants in Drinking Water Andrés Alonso Fernández, Patricia Ramírez Priego, Mari Carmen Estevez, Adrián Fernández Gavela and Laura M. Lechuga	135
1.16	Nano-precision metrology of X-ray mirrors with multifiber interferometers Albert Van Eeckhout, Igors Sics, Dominique Heinis and Josep Nicolas	141
1.17	Laser heterodyne radiometry for greenhouse gases monitorization Adela Collado-Rodríguez, Aldo Moreno-Oyervides, Oscar Elías Bonilla-Manrique, Omaira García and Pedro Martín-Mateos	145

SENSORES ÓPTICOS

1.18	Propuesta de solución óptica para medida de temperatura de recipiente y señalización en cocinas de inducción con encimera opaca Cristina Pelayo, Pilar Blasco, Enrique Carretero, Rafael Alonso and Sergio Llorente	151
1.19	Evaluación de FBGs como sensores de alta temperatura en aplicaciones de energía solar concentrada Manuel Jerez, Alejandro Carballar and Joaquín Granado	157
1.20	Integrated Optical Biosensors and Microfluidics for Real-Time Optical Sensing in Lab-on-a-Chip Systems Beatriz Santamaría Fernández, Rafael Casquel del Campo, Haizea Apellaniz, Jorge Martinez de la Mata Gaitan, María Fe Laguna Heras, Andrés Otero, Airan Frances and Miguel Holgado Bolaños	162
1.21	Hemoglobin Level Determination with a Fiber Optic Sensor Using Boron-Doped Diamond Film Monika Kosowska	167
2.1	Polarimetría Mueller Full Poincaré usando diversas fuentes de luz para caracterizar medios con actividad óptica natural Gemma Piquero, Juan Carlos González de Sande, Juan Carlos Suárez Bermejo and Massimo Santarsiero	172
2.2	Interferometría de Ruido Ambiente mediante DAS con pulsos chirpados Jorge Canudo, Javier Preciado-Garbayo, Pascual Sevillano, Jesús Subías, Miguel Gonzalez-Herraez, Hugo F. Martins, Beatriz Gaite-Castrillo, Jose Benito Bravo-Monge, Irene De Maria and Miguel Rodriguez-Plaza	177
2.3	Development and Validation of a Spectral Albedometer (200-2500 nm): Cuasi-Simultaneous Measurement of Solar and Snow Cover Reflected Radiation. Adrián Subías Martín, Pascual Navarro, Jorge Ciudad-Real, Víctor Herráiz-López, Iñigo Salinas and Rafael Alonso	182
2.4	Upconversion Nanoparticles Luminescence Lifetime Dependence on Excitation Parameters Alejandro Casillas-Rubio, Khouloud Hamraoui, Diego Mendez-Gonzalez, Marco Laurenti, Jorge Rubio-Retama, Oscar G. Calderón and Sonia Melle	188
2.5	Multipoint strain sensing based on optomechanical interaction in optical fibers Anna I. Garrigues-Navarro, Martina Delgado-Pinar, Antonio Díez and Miguel V. Andrés	193

SENSORES ÓPTICOS

2.6	Modelling an inversion layer photodiode in COMSOL Multiphysics Rubén Gómez Cornejo, Sucheta Sharma, Trinh Tran, Erkki Ikonen, Pedro Corredera and Joaquín Campos	198
2.7	Study of bandwidth and response saturation on PQED photodiode Rubén Gómez Cornejo, Noelia Castrejón, Juan Galindo-Santos, Joaquín Campos and Pedro Corredera	203
2.8	Detección de fugas en tuberías mediante redes de Bragg y algoritmos de Inteligencia Artificial Javier Madrigal, Victor Javier Ruiz, Beatriz Defez, Jorge Gosálvez and Salvador Sales	209
2.9	Dual-comb ranging using densified gain-switched optical frequency combs Clara Quevedo-Galán, Antonio Pérez-Serrano, José Manuel G. Tijero and Ignacio Esquivias	215
2.10	Forward Stimulated Brillouin Scattering in Optical Fibers under Hydrogen Diffusion Aleksander Paterno, Carlos Alvarez, Antonio Díez-Cremades, José Luis Cruz, Martina Delgado-Pinar and Miguel Andrés	220
2.11	Microwave Frequency OTDR for High Strain-rate Sensing Yan Ren, Pedro J. Vidal-Moreno, María R. Fernández-Ruiz, Sonia Martín-López, Luis Costa, Zhongwen Zhan and Miguel González-Herráez	226
2.12	Exploration of Optical Fiber Based Sensor Phenomena, Use Cases and Potential Calibration Method for Vibrations Ángel Redondo and José Antonio Lázaro	232
2.13	A Monte Carlo model of the propagation of polarized pulses in turbid media for modelling polarized lidar in fog Maria Ballesta-Garcia, Aleix R. Bobi Olmo and Santiago Royo	236
2.14	Development of a LiDAR-integrated multimodal system for underwater sensing Aleix. R. Bobi-Olmo, Eduardo Bernal, Pablo García-Gomez, Maria Ballesta-Garcia and Santiago Royo	242
2.15	Optical Characterization of a Novel Concept of Deformable Primary Mirror for CubeSat Telescopes Sara Giménez-Aragón, Toni Ruiz-Valverde, Alejandro Santillán, Armengol Torres, Eduardo Ferrer and Santiago Royo	248

SENSORES ÓPTICOS

2.16	Phi-OTDR de pulso chirpeado largo para medidas en fibra de nanodeformaciónes de kHz a 24h con alto rango dinámico Hugo F. Martins	254
2.17	Autocorrección de referencias en MFDD-DAS: Hacia medidas absolutas en condiciones reales Pedro J. Vidal-Moreno, Marcos G. Barriopedro, Alejandro Rosado, Laura Hernández-Martín, Sonia Martin-Lopez and Hugo F. Martins	260
2.18	Phi-OTDR con pulsos chirpados de gran tamaño asistido por Raman para termometría de fibra distribuida en milikelvin de largo alcance Laura Hernández-Martín, Javier Preciado-Garbayo, Jorge Canudo, Juan D. Ania-Castañón and Hugo F. Martins	266
2.19	High-Finesse Fiber-Optic Fabry-Perot Interferometer for Gas Pressure Sensing with Minimal Temperature Influence Elena Lorente, Luis Alberto Sánchez, Bryan Sanipatin, Daniel Maldonado-Hurtado and Salvador Sales	271
2.20	Development and Experimental Validation of a Fiber Bragg Grating-Based Hydrogen Sensor Using Pt-Doped WO_3 Pablo Sancho-Villach, Bryan Sanipatin, Rubén Martín-Cabezuelo, Laurent Sauvanaud, Luis Alberto Sánchez and Salvador Sales	276
2.21	Análisis exhaustivo y modelo simplificado de un sensor de fibra óptica para desplazamiento angular Gorka Zubia-Garea, Joseba Zubia Zaballa, Josu Amorebieta, Gotzon Aldabaldetreku and Gaizka Durana	281

DISPOSITIVOS FOTÓNICOS

3.1	Improving the Efficiency of Blazed gratings in Vertical Aligned LCoS device Guillem Najar, Fco. Javier Martínez Guardiola, Andres Marquez, Adrián Moya, Emilio José Mena Ruiz, Jorge Francés Monllor, Sergi Gallego Rico, Inmaculada Pascual and Augusto Beléndez	288
3.2	Fabrication and characterization of photoaligned MR-based liquid crystal cells Adrián Moya Aliaga, Eva María Calzado, Emilio José Mena, Guillem Najar, Andrés Márquez, Augusto Beléndez and Inmaculada Pascual	292
3.3	Effects of addition of terminal emitter on device performance in hyperfluorescent OLEDs Thomas Sayner, Arvydas Ruseckas and Ifor Samuel	297

DISPOSITIVOS FOTÓNICOS

3.4	Optical generation, measurement and tuning of optomechanical spheroidal resonances in a silica microsphere Juan Julian-Barriel, Martina Delgado-Pinar, Antonio Díez and Miguel V. Andrés	302
3.5	Performance of gravity-compensated focus-tunable lens Fátima Cuéllar, Elisabet Pérez-Cabré, Laura Clavé and María Sagrario Millán	308
3.6	Desarrollo de películas delgadas de AlN amorfo sobre ITO-vidrio e ITO-PET a baja temperatura mediante rf-sputtering Miriam Cadenas, Michael Sun, Susana Fernández, Sirona Valdueza-Felip and Fernando Bernabé Naranjo	314
3.7	Orbital Angular Momentum Multiplexing employing Liquid Crystal Reconfigurable Devices Javier Pereiro García, Byron Ganazhapa, José Jaraba, Pablo De la Rosa, Xabier Quintana and Morten Geday	320
3.8	Low cost optical device to measure blood plasma coagulation Gemma García-Mandayo, Lucía Ruiz Fernández de Bobadilla, María Guijo, Oihane Beldarrain, Aitor Larrañaga-Jaio, Javier Gallego, Patricia Blanco, Carles Pizarro and Santiago M. Olaizola	324
3.9	Caracterización robusta de retardadores mediante el uso de un interferómetro de doble rendija de Young Inés Meili Diaz García, Jesus del Hoyo, Armando Gonzalez García, Joaquín Andrés Porras, Ángela Soria García, Isabel González-Martínez, Karen Priscila Soto González, Javier Alda and Luis Miguel Sánchez Brea	330

FOTÓNICA INTEGRADA

3.10	IMB-CNM Silicon Nitride Platform for Integrated Photonics Marçal Blasco-Solvas, Joaquín Hernández-Betanzos, Jad Sabek, Carlos Domínguez-Horna and Joaquín Faneca	335
3.11	Simulador eficiente de antenas ópticas integradas con radiación en ángulos arbitrarios Elio Godoy Lorite, Laureano Moreno Pozas, Robert Halir, Alejandro Ortega Moñux, Gonzalo Wangüemert Pérez and Iñigo Molina Fernández	341

FOTÓNICA INTEGRADA

3.12	Next-generation photonic devices enabled by functional materials in silicon photonics Jorge Parra, Iñigo López-Mulet, Jorge Caso, Juan Francisco Morcillo and Pablo Sanchis	347
3.13	Prototyping of microstructures for photonic devices and glass interposers using powerful femtosecond laser source Bogusz Stepak, Katarzyna Pietrusińska, Natalia Grudzien, Yuriy Stepanenko, Michal Nejbauer and Juan Luis Vadillo	352
3.14	Simplified Polarization Independent Integrated Coherent Receiver for Passive Optical Networks Natalia Herguedas, Jorge Ciudad-Real, David Izquierdo, Pascual Sevillano and Ignacio Garcés	356
3.15	Dual-comb generator based on a monolithically integrated InP Photonic Integrated Circuit Pablo López-Querol, Clara Quevedo-Galán, José Manuel G. Tijero, Ignacio Esquivias and Antonio Pérez-Serrano	362
3.16	Design of a Monolithically Integrated Photonic RF Phase Shifter Gonzalo Soldevilla Gómez, Pablo López Querol, José Manuel García Tijero, Ignacio Esquivias Moscardo and Antonio Pérez Serrano	366
3.17	Development of Silicon Nitride Photonic Integrated Circuits: Fully in-house Fabrication and Optical Characterization Giuseppe Libero Bufi, Christian Camilo Cano Vasquez, Louw Roel van der Zon, Adrián Fernández, Rubén Alemany, César Alminyana, Isabelle Rodriguez, Gloria Micó, Pascual Muñoz and Daniel Pastor	372
3.18	Large-scale Silicon Photonics antenna for next-generation integrated FSO transceivers José Lozano, Pablo Ginel and Alejandro Ortega	378

BIOFOTÓNICA

4.1	Portable multispectral fundus camera: a pilot study Marina Bou Marin, Meritxell Vilaseca Ricart and Francisco J. Burgos Fernández	385

INTELIGENCIA ARTIFICIAL Y FOTÓNICA

4.2	Machine Learning Approach to Find the Optimal Window for LIPSS Formation in Femtosecond Laser Processing Aitor Larrañaga-Jaio, Iñigo Ramon-Conde, Aldara Pan Cabo, Isabel Ayerdi Olaizola, Santiago M Olaizola and Ainara Rodríguez	391
4.3	Addressing ROS 2 Limitations for Dependable Multimodal Sensing Applications Jokin Arozamena-Rodríguez, Santiago Royo, Jorge Parra and Maider Zamalloa	397
4.4	Multimodal data acquisition prototype for autonomous driving in adverse weather conditions Gerard De Mas-Giménez, Adrià Subirana, Pablo García-Gómez, Eduardo Bernal, Jordi Riu, Josep Ramon Casas and Santiago Royo	403
4.5	Plastics Sorting Using Terahertz Frequencies and Machine Learning Daniel Moreno París, Oscar Elías Bonilla Manrique, David Hernandez Guerrero, Pedro Martín Mateos and Aldo Moreno Oyervides	409

OPTOELECTRÓNICA EN ENERGÍA RENOVABLE

4.6	Capa antirreflejante en el rango visible basada en nanopartículas metálicas embebidas en un fotopolímero. Aplicación a células solares de película delgada Óscar Esteban, Sirona Valdueza-Felip and Fernando B. Naranjo	415
4.7	Comparación teórica de concentradores solares luminiscentes con distintas geometrías Jagoba Barata, Jon Arrue, Joseba Zubia and María Asunción Illarramendi	421
4.8	Impacto del espesor de la capa de nitruro en la eficiencia fotovoltaica de heterouniones AlInN/a-Si/Si(100) Sirona Valdueza-Felip, Michael Sun, Miriam Cadenas, Sofía Figueroa and Fernando B. Naranjo	427
4.9	Medida de Flujo Solar Concentrado en Simulador Solar basado en fibra óptica y fotodiodo Manuel Jerez, Alejandro Carballar, Ricardo Conceição, José González-Aguilar, Xabier Rández and Olaia Itoiz	433
4.10	Using Semiconductor Photodiodes as Detector Element for Solar Radiation Measurements Manuel Jerez, Alejandro Carballar and Joaquín Granado	439

FOTÓNICA CUÁNTICA Y NO LINEAL

4.11	Efficient frequency down-conversion of quantum-dot-compatible single photons enabled by molecular modulation Arturo Mena, Pau Arcos, Joseba Zubia and David Novoa	446
4.12	Deep ultraviolet source via cooperative Raman combs in gas-filled hollow-core fibres Pau Arcos, David Novoa and Joseba Zubia	451
4.13	Ultrafast Bright Squeezed Vacuum Light Source María Sánchez-Hernández, Miriam Lazo, Arturo Mena, Tasio Gonzalez-Raya, Mikel Sanz, Joseba Zubia and David Novoa	455
4.14	Towards a broadband measurement of waveguide dispersion curves Marc P. Safont, Enrique Silvestre, Antonio Díez, Martina Delgado-Pinar, Miguel V. Andrés and David Castelló-Lurbe	460
4.15	Intracavity upconversion of images in the SWIR pumped by a passively V3+:YAG Q-Switched Nd3+:YVO4 laser at 1342 nm Adrián J. Torregrosa, María Luisa Rico, Haroldo Maestre, Miguel Cuenca and Juan Capmany	465
4.16	Towards improved performance of an Yb:KGW laser-based intracavity image upconverter Adrián J. Torregrosa, María Luisa Rico, Juan Capmany, Miguel Cuenca, Angela E. Ortega, Carlos R. Fernández-Pousa and Haroldo Maestre	471
4.17	Impact of nonlinearity multifrequency dispersion on instabilities cancelation Miguel A. Bosch, Enrique Silvestre, Martina Delgado-Pinar, Antonio Díez, Miguel V. Andrés and David Castelló-Lurbe	477

Comunicaciones ópticas

Numerical characterization of a 2x2 matrix of sub-wavelength radiant emitters for beam steering

Francisco José TORCAL-MILLA[1,2,3], Carlos SÁNCHEZ-AZQUETA[1,2], and Luis Miguel SANCHEZ-BREA[3]

1. Applied Physics Department, EINA, University of Zaragoza, C/ María de Luna 3, 50018, Zaragoza (Spain).
2. Aragon Institute for Engineering Research (I3A), C/ Mariano Esquillor S/N, 50018, Zaragoza (Spain).
3. Applied Optics Complutense Group, Facultad de Ciencias Físicas, UCM, Plaza de las Ciencias 1, 28080, Madrid (Spain).

Contact: Francisco José TORCAL-MILLA (fjtorcal@unizar.es).

ABSTRACT:

In this work, we present a partial characterization of a 2×2 array of subwavelength-scale radiant emitters, focusing on the phase delay introduced by each element and its impact on beam deflection angles. We also examine the influence of individual emitter size and inter-element spacing, finding negligible variation in performance as long as both dimensions remain subwavelength. These arrays, known as Optical Phased Arrays (OPAs), hold promising potential for applications in nanophotonics, beam shaping, and dynamic light control, despite current technological limitations that hinder their full realization. To perform our analysis, we used the Python-based simulation package Diffractio, which enables numerical modeling of optical fields and the implementation of custom phase masks. For the configuration studied, diffractive effects are absent, which facilitates efficient beam steering by concentrating the radiated energy into a single, directed beam.

Key words: Beam steering, Optical Phased Arrays

1.- Introduction

Optical Phased Arrays (OPAs) have emerged as a powerful tool for beam steering and wavefront shaping in modern photonic applications, including free-space optical communications, LiDAR, optical sensing, and holography [1,2]. By precisely controlling the phase of individual emitters within an array, OPAs enable dynamic, reconfigurable beamforming without the need for mechanical components [3,4]. In this numerical study, phase control is applied externally and ideally to each emitter; however, we acknowledge that achieving such control experimentally remains a major challenge and is an active area of research in integrated photonics. This capability makes them attractive for applications requiring fast and precise control over optical emission patterns. Recent advancements in nanophotonics have facilitated the development of sub-wavelength radiant emitters, enabling highly compact and efficient OPAs [5]. A fundamental challenge in designing these arrays is achieving accurate numerical characterization of their emission properties, including far-field beam profiles, phase coherence, and interference effects [6]. While extensive studies have explored large-scale OPAs [7], the behavior of small-scale arrays, such as a 2×2 matrix of sub-wavelength emitters, remains less investigated. These miniaturized arrays are of particular interest for integrated photonics, where compact and efficient beam-steering devices are essential. In this work, we present a numerical characterization of a 2×2 matrix of sub-

wavelength radiant emitters operating as an Optical Phased Array. Using the Diffractio python library for optical simulations [8], we analyze the impact of the emitter spacing, the phase modulation, and the size of the single emitter on the far field intensity. The Diffractio Python library was selected due to its flexibility for modeling phase masks and simulating scalar optical fields, providing a suitable framework for analyzing beam profiles and phase variations in compact emitter arrays.

2.- Numerical approach

In this section, the numerical characterization of the 2x2 matrix is carried on by varying some of the characteristics of the matrix, such as the emitter spacing or the emitter size, among others. To start, we fix the single emitter size, *w*, to 0.25λ, that is set to λ= 632.8 nm, and the emitter spacing, *d*, to 0.55λ. An example of emitter matrix is shown in Figure 1, where the phase is shown in the colorbar (degrees).

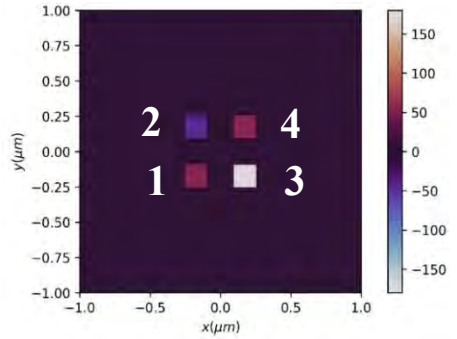

Fig. 1: Example of matrix of emitters. The colorbar represents the phase delay applied to each emitter in degrees.

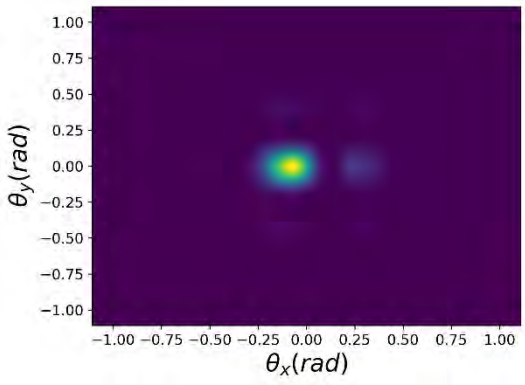

Fig. 2: Far field intensity obtained with $\phi_L = \pi$ rad and $\phi_R = \pi/2$ rad.

2.1.- Lateral beam steering

The first set of simulations consists of fixing the phase of the left column, ϕ_L, and modify the phase of the right column, ϕ_R. This way, we are able to deflect the beam to one or other side of the x axis. Figure 2 shows an example of the far field intensity obtained with $\phi_L = \pi$ rad and $\phi_R = \pi/2$ rad.

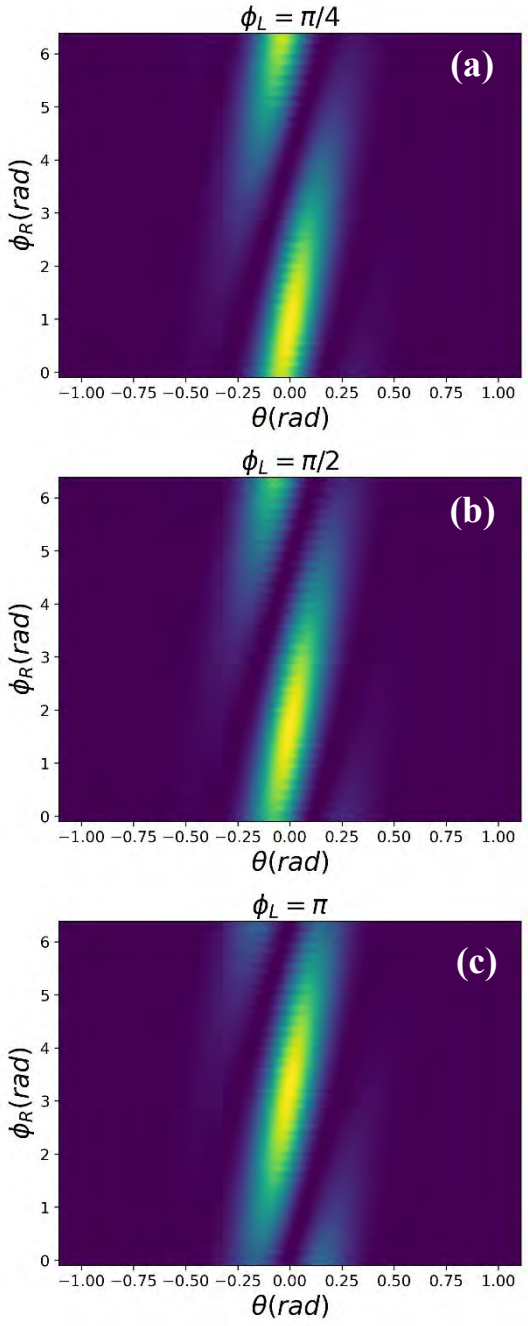

Fig. 3: Deflection angle in terms of the phase applied to the right column of the matrix. (a) $\phi_L = \pi/4$ rad, (b) $\phi_L = \pi/2$ rad, and (c) $\phi_L = \pi$ rad.

For completeness, Figure 3 shows the deflection angle, θ, along the x-axis for several examples in which the phase of the right column emitters was set to π/4 rad, π/2 rad, and π rad, shown in Figures 3a, 3b, and 3c, respectively. As it can be observed, the case with $\phi_L = \pi$ rad (Figure 3c) produces a symmetric deflection angle with respect to the center.

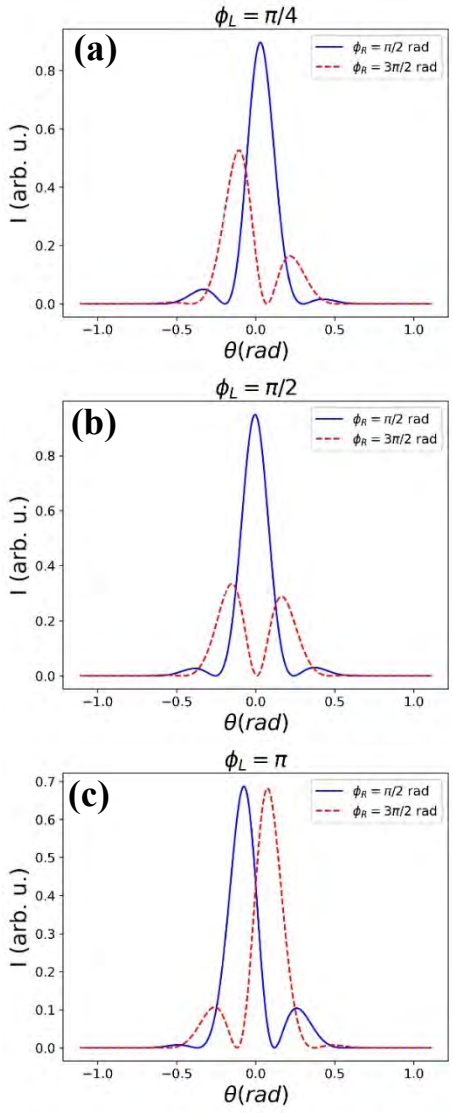

Fig. 4: Beam profile for the cases depicted in Figure 3 and two phases of the right column emitters (π/2 rad and 3π/2 rad). (a) $\phi_L = \pi/4$ rad, (b) $\phi_L = \pi/2$ rad, and (c) $\phi_L = \pi$ rad.

In addition, Figure 4 shows the beam profile for $\phi_R = \pi/2$ rad and $3\pi/2$ rad. We have chosen these two angles since the beam presents almost only one lobe. Secondary lobes appear for higher deflection angle, as can be observed also in Figures 3 and 4. Figure 4c shows the best option since the behavior is symmetric.

2.1.1.- Effect of the distance between emitters

In this section, let us modify the distance between emitters, *d*, to evaluate its effect on the deflection angle and/or far field intensity distribution. As it can be observed in Figure 5a, the deflection angle does not change but the width of the main lobe increases by reducing the distance between emitters.

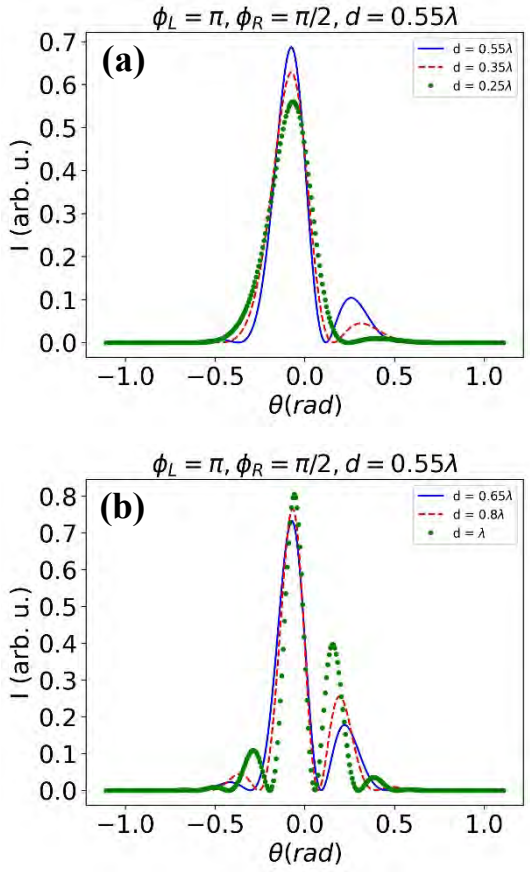

Fig. 5: Beam profile for the case depicted in Figure 4c and $\phi_R = \pi/2$ rad. The plots correspond to different distances between emitters (see legends). (a) decreasing distance and (b) increasing distance.

In addition, Figure 5b shows the same lobe as in Figure 5a but increasing the distance between emitters until reaching the wavelength. It is shown that when *d* approaches the wavelength, diffractive effects appear and the beam is divided in several beams, Figure 6. Although a

detailed analysis of mutual coupling or crosstalk between emitters is beyond the scope of this work, the configuration used ensures subwavelength spacing, minimizing such effects and preserving the intended far-field behavior.

2.1.2.- Effect of the size of the emitters

In this section, let us change the size of each individual emitter but maintaining the distance between them, Figure 7. As it can be observed, the position of the main lobe does not change but the intensity is higher, as it is expected. The greater the emitter, the higher the amount of light that emits.

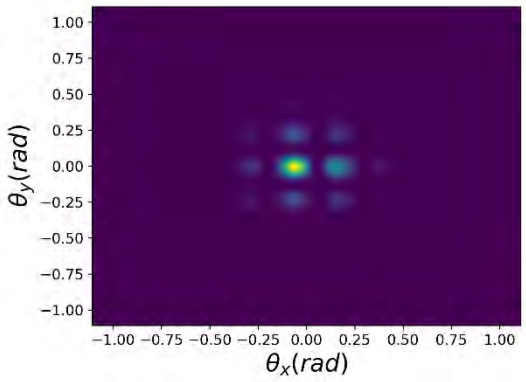

Fig. 6: Far field intensity obtained with $\phi_L = \pi$ rad, $\phi_R = \pi/2$ rad, and $d = \lambda$.

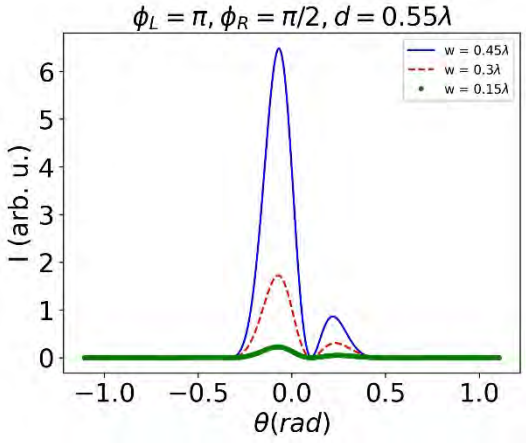

Fig. 7: Beam intensity for three different emitter sizes, w.

4.- Conclusion

In this work, a preliminary partial characterization of the emitting properties of a 2x2 matrix of subwavelength emitters has been carried out. The size of the single emitters and the spacing between them have been tested, and the deflected angle has been obtained. This kind of optical elements, called Optical Phased Arrays, has great interests in photonics applications and, therefore, the obtained results could be of interest for the optical community.

Acknowledgements: This work has been sponsored by the project "Desarrollo de un sistema opto-electrónico optimizado de matriz de antenas activas para redes de comunicaciones 5G", funded by the program IMPULSO of the Aragon Research and Engineering Institute, 2024 call, the Tecnologías Ópticas Láser group (E44_23R), and the Group of Electronic Design (T26_23R), both belonging to the Gobierno de Aragón.

References

[1] Y. LIU, *"The integrated optical phased array on silicon photonics"*, (Technical University of Denmark,2021).

[2] Z. Ma, *et al.*, *"Photonic integrated optical phased arrays and their applications"*, Chinese Optics Letters, *22*(2), 020041, 2024.

[3] S. LIN, Y. CHEN, and Z. J. WONG, "*High-performance optical beam steering with nanophotonics*", Nanophotonics, 11(11), 2617-2638, 2022.

[4] Y. LI, *et al.*, *"Wide-steering-angle high-resolution optical phased array"*, Photonics research, 9(12), 2511-2518, 2021.

[5] Z. LI, *et al.*, *"A sub-wavelength Si LED integrated in a CMOS platform"*, Nature Communications, 14(1), 882, 2023.

[6] J. HUE, *et al.*, *"Modular and versatile characterization test bench for optical phased arrays"*, in *Photonic Instrumentation Engineering IX,* 157-169, 2022.

[7] K. KOMATSU, *et al.*, *"Large-scale monolithic InP-based optical phased array"*, IEEE Photonics Technology Letters, *33*(20), 1123-1126, 2021.

[8] L.M. SANCHEZ-BREA, *et al.* "Diffractio: an open-source library for diffraction and interference calculations, 2024, in SPIE Vol. 12997, 236-243.

Propagador Electromagnético 3D para Antenas Ópticas Integradas

José Luis VEGA-GARCÍA[(1)], Laureano MORENO-POZAS[(1)], Miguel BARONA-RUIZ[(1)], Alejandro SÁNCHEZ-SÁNCHEZ[(1)], Alejandro ORTEGA-MOÑUX[(1)], Robert HALIR[(1)], Íñigo MOLINA-FERNÁNDEZ[(1)], J. Gonzalo WANGÜEMERT-PÉREZ[(1)].

1. Telecommunication Research Institute (TELMA), Universidad de Málaga, Louis Pasteur 35, 29010, Málaga, España.

Contact: José Luis VEGA-GARCÍA (jose_vegagarcia@uma.es).

ABSTRACT:

Accurate modeling of electromagnetic propagation is crucial for the design and optimization of integrated optical antennas, with applications in chip-to-fiber coupling, beam shaping, and free-space optical (FSO) communications. This work presents a 3D electromagnetic propagator based on the angular spectrum method, capable of computing the field evolution over both near-field and far-field regimes without paraxial approximations.

The proposed approach enables precise long-distance propagation, maintaining a 99.99% integral overlap with the analytical solution for Gaussian beams over distances up to tens of kilometers. Additionally, we provide simple analytical expressions to configure simulation parameters, ensuring numerical accuracy and computational efficiency. The tool is validated through two case studies: (i) long-distance Gaussian beam propagation in free space and (ii) near-field characterization of an integrated optical antenna for fiber coupling. The results confirm the versatility and accuracy of the proposed propagator for photonic applications.

Key words: Silicon photonics, integrated optical antennas, angular spectrum, near field, far field, diffraction, Gaussian beam.

1.- Introducción

La fotónica de silicio ha surgido como una tecnología clave para el desarrollo de circuitos ópticos integrados, con aplicaciones en comunicaciones ópticas de muy alta velocidad, sensado, computación óptica y procesamiento de señales fotónicas, entre otras [1]. Su compatibilidad con la tecnología CMOS permite la fabricación en masa con un bajo coste, facilitando además la integración con sistemas electrónicos convencionales.

Dentro de esta tecnología, un área de especial interés es el diseño de antenas ópticas integradas, dispositivos capaces de radiar luz fuera del chip de manera controlada. El espectro de aplicaciones donde son necesarias es muy amplio, como en la interfaz chip-fibra mediante rejillas de difracción (*grating couplers*) convencionales y autoenfocantes, o en las antenas de ancho de haz muy estrecho (décimas de grado o incluso menos), necesarias para las comunicaciones en espacio libre (FSO, *Free Space Optics*) [2]. Resulta por tanto fundamental poder caracterizar con precisión la propagación del campo radiado por el dispositivo, tanto en la zona de campo cercano como en la de campo lejano, según la aplicación específica.

En este trabajo, se presenta una herramienta capaz de simular la propagación eficiente y

precisa de perfiles arbitrarios de campo electromagnético. La herramienta se basa en la descomposición y propagación de ondas planas en medios homogéneos (espectro angular), la cual funciona para ondas electromagnéticas con cualquier longitud de onda. Se derivan expresiones analíticas sencillas que permiten conocer *a priori* los parámetros de simulación necesarios, como el tamaño de ventana, el mallado, o si se deben emplear absorbentes laterales si la distancia de propagación supera cierto valor.

Para demostrar su versatilidad, se presentan dos casos de interés que operan a distancias de propagación muy diferentes: i) la propagación de haces Gaussianos en espacio libre a distancias muy largas (decenas de km), ii) y el análisis del campo generado por una rejilla de difracción autoenfocante que enfoca toda la luz radiada por un chip en una fibra situada a 1 mm de distancia de su superficie.

2.- Propagación electromagnética basada en el espectro angular

El estudio de la propagación electromagnética se centra en determinar el campo que existe en cualquier punto del espacio, conocida la distribución en amplitud y fase que existe en todos los puntos del plano de la fuente. En general, cuando se desea propagar grandes distancias, es común emplear aproximaciones paraxiales de la ecuación de ondas [3]. No obstante, dado que el objetivo de este trabajo es desarrollar una herramienta versátil aplicable tanto a problemas de campo cercano como de campo lejano, no se van a emplear aproximaciones paraxiales.

El método del espectro angular se basa en descomponer el campo en una superposición de ondas planas mediante la transformada directa de Fourier. Como la propagación de una onda plana es analítica, se propaga cada una de estas ondas por separado y luego se recombinan en el punto de observación, mediante la transformada inversa de Fourier.

Matemáticamente, el espectro angular de la excitación en $z = 0$ puede expresarse mediante su transformada de Fourier 2D espacial como [4]:

$$\hat{E}(k_x, k_y) = \iint_{-\infty}^{\infty} E(x, y, 0) \cdot e^{j(k_x x + k_y y)} dx dy, \quad (1)$$

donde k_x y k_y son las frecuencias angulares en las direcciones transversales x e y, e indican las diferentes direcciones angulares de cada onda plana que compone el espectro de la excitación. Cada componente espectral $\hat{E}(k_x, k_y)$ está asociada a una onda plana con vector de onda $\vec{k} = (k_x, k_y, k_z)$, donde:

$$|\vec{k}| = \sqrt{k_x^2 + k_y^2 + k_z^2} = 2\pi/\lambda = \\ = 2\pi/(\lambda_o/n) = k_o n, \quad (2)$$

siendo λ la longitud de onda en el medio, λ_o la longitud de onda en el vacío y n el índice de refracción en el medio. Los ángulos de elevación θ y de azimut ϕ, característicos del sistema de coordenadas esféricas, pueden determinarse como:

$$\theta = \sin^{-1}\left(\frac{\sqrt{k_x^2 + k_y^2}}{k_o n}\right), \quad (3)$$

$$\phi = \tan^{-1}\left(\frac{k_y}{k_x}\right). \quad (4)$$

Una vez obtenida la descomposición de ondas planas, es posible hallar el campo eléctrico en cualquier punto del espacio (x, y, z), propagando primero cada onda plana en el eje z con su correspondiente frecuencia espacial k_z, y posteriormente regresar al dominio espacial por medio de la transformada inversa de Fourier [4]:

$$E(x, y, z) = \iint_{-\infty}^{\infty} \left(\hat{E}(k_x, k_y) \cdot e^{-jk_z z}\right) \cdot \\ e^{-j(k_x x + k_y y)} \frac{dk_x dk_y}{(2\pi)^2}. \quad (5)$$

Si la fuente tuviera componentes espectrales que cayeran fuera del círculo de radio $k_o n$:

$$k_x^2 + k_y^2 > k_o^2 n^2, \quad (6)$$

las k_z asociadas serían imaginarias puras. Son lo que se conoce como ondas evanescentes, y serán filtradas de manera natural por el medio. Estas componentes tienen repercusión en la zona de campo cercano. En este trabajo, las componentes de campo evanescente también se van a tener en

cuenta en la propagación, con el objetivo de que el modelo contemple todas las situaciones posibles, desde la propagación en condiciones de campo cercano hasta en condiciones de campo lejano.

Cabe destacar que la propagación basada en el espectro angular es completamente equivalente a evaluar la integral de difracción de Rayleigh-Sommerfeld [5], por lo que se obtiene una solución exacta (no aproximada como la integral de Fresnel) del campo propagado en cualquier punto del espacio.

3.- Consideraciones numéricas

El cálculo del espectro angular de la excitación se realiza en este trabajo mediante la transformada rápida de Fourier de dos dimensiones (FFT2), una técnica optimizada para el cálculo eficiente de transformadas de Fourier discretas. La elección adecuada del tamaño de la ventana y la separación entre muestras en los dominios espacial y frecuencial es fundamental para evitar posibles problemas de evaluación del campo propagado. El estudio se centrará en el caso 2D ($E = E(x,z)$) para simplificar las expresiones, aunque el propagador también se ha desarrollado para el caso general 3D ($E = E(x,y,z)$).

La distancia entre muestras en el dominio del espacio (Δx), debe elegirse de manera que se evite el solapamiento (*aliasing*) de las réplicas de los espectros angulares que provoca el hecho de muestrear. Es lo que se conoce como criterio de Nyquist [6]:

$$f_s = \frac{1}{\Delta x} \geq 2 \cdot f_{\max}, \qquad (7)$$

donde f_s es la frecuencia de muestreo espacial y $f_{\max}$ es la frecuencia máxima del espectro angular de la excitación inicial. Dado que $f_{\max} = k_{x,\max}/2\pi$ está relacionado con el ángulo $\theta_{\max}$ mediante la ecuación (3), la separación entre muestras debe cumplir:

$$\Delta x \leq \Delta x_{\max} = \lambda_o/(2n \cdot \sin\theta_{\max}). \qquad (8)$$

Es recomendable adoptar $\Delta x = \Delta x_{\max}/2$ para asegurar un margen adicional.

Otro parámetro de simulación es el tamaño X_o de la ventana espacial. Un criterio razonable consiste en elegir el tamaño de ventana de forma que, a la distancia de propagación z_p deseada, el campo no alcance los bordes de la ventana de simulación, evitando así el solapamiento espacial debido a la periodicidad que impone la FFT2. De esta forma, el tamaño de la ventana debe ser:

$$X_o = 2 \cdot z_p \cdot \tan\theta_{\max}. \qquad (9)$$

Este criterio implica que se requerirán tamaños de ventana tanto mayores cuanto mayor sea el ancho de banda angular y la distancia de propagación deseada. En este punto, es interesante determinar una expresión que relacione la máxima distancia de propagación con el número de puntos de muestreo, N_p, y el ancho de banda angular de la excitación ($\theta_{\max}$). Teniendo en cuenta $X_o = \Delta x \cdot N_p$, la distancia de propagación máxima con un solo paso es:

$$z_{p,\max} = \frac{N_p}{8n \cdot \sin^2\theta_{\max}} \cdot \cos\theta_{\max}. \qquad (10)$$

Aunque las ecuaciones han sido planteadas para el caso 2D, son directamente aplicables al caso 3D, considerando que existen dos perfiles, cada uno con su ancho de banda angular correspondiente ($\theta_{\max,x}, \theta_{\max,y}$). La particularización de la ecuación (10) al caso de excitación Gaussiana, da como resultado:

$$z_{p,\max} = \frac{0.137}{(\lambda_o/n)} N_p \cdot \mathrm{MFD}^2, \qquad (11)$$

donde el MFD (*Mode Field Diameter*) se define como el ancho efectivo donde la intensidad del campo cae a $1/e^2$ de su valor máximo. Se ha usado la expresión propuesta en [4] que relaciona el MFD de una Gaussiana con su ancho de banda angular ($\theta_{\max}$) que contiene el 99% de la potencia:

$$\mathrm{MFD} = 3\lambda_o/(n \cdot \pi \cdot \theta_{\max}). \qquad (12)$$

La Figura 1 muestra la distancia máxima de propagación en un solo paso para una excitación Gaussiana 3D en función del diámetro del campo (MFD). Se observa que, a medida que el tamaño espacial de la excitación aumenta, la distancia máxima

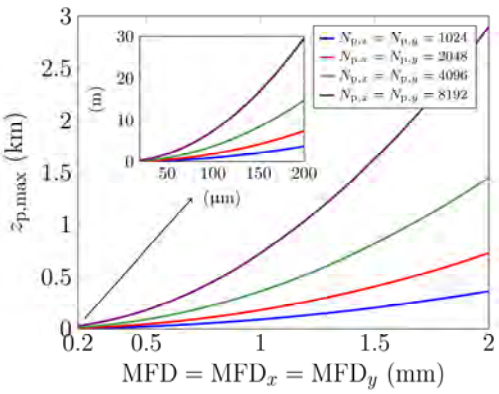

Fig. 1: Distancia máxima de propagación $z_{p,max}$ para una excitación Gaussiana 3D en función del MFD y número de puntos en los ejes x e y, en el vacío y para $\lambda_o = 1.55\ \mu m$.

alcanzable también se incrementa. Este comportamiento se debe a que excitaciones de mayor tamaño presentan anchos de banda angulares ($\theta_{\max}$) más reducidos, lo que relaja las restricciones de muestreo (Δx) y además disminuye la divergencia del haz.

Para extender la propagación a distancias mayores sin aumentar el número de puntos (o, de manera equivalente, el tamaño de ventana), se puede dividir la distancia total en distancias menores que la distancia máxima. Si se multiplica el campo que resulta tras propagarse dichas distancias por una función plana en la zona de interés (D) y evanescente en el resto de la ventana de cómputo, el efecto resultante es equivalente a colocar un absorbente (ABC, Absorbing Boundary Conditions). En este caso se ha escogido un filtro de tipo super-Gaussiano de orden 8 [3]. Este procedimiento se ilustra esquemáticamente en la Figura 2 y se validará mediante un ejemplo en la sección 4.

4.- Ejemplos de aplicación

En esta sección se va a aplicar la herramienta de propagación a diversos casos.

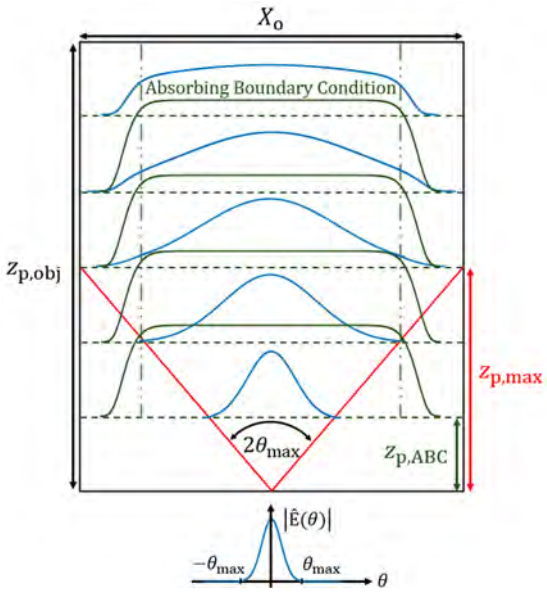

Fig. 2: Esquema de la propagación mediante el espectro angular para una excitación Gaussiana en varios pasos con filtrado para un tamaño fijo de ventana X_o, un ángulo máximo θ_{max} y una distancia de propagación parcial $z_{p,ABC}$.

4.1.- Validación del método de propagación a largas distancias

Para validar el método de propagación a largas distancias, se ha propagado una excitación Gaussiana con un diámetro del campo $\mathrm{MFD} = 2$ mm en el vacío, con una longitud de onda $\lambda_o = 1.55$ µm, un número de puntos en cada dirección (x, y) $N_p = 2048$, y una región de interés $D = 80$ cm. Según se vio en la Figura 1, la distancia máxima sin usar absorbentes para este caso era de 750 m. Sin embargo, la utilización de absorbentes ha permitido propagar una distancia de 5 km en un solo minuto de simulación y 21 MB de memoria.

En la Figura 3 a) se muestra un mapa de la propagación obtenido a partir de la solución analítica del haz Gaussiano [4] para una distancia de 5 km. En la Figura 3 b) se presenta el resultado de la propagación numérica utilizando la herramienta desarrollada en este trabajo, considerando $N_p = 2048$. Como se puede observar, en la zona común de ambos mapas de contorno los campos obtenidos con el método

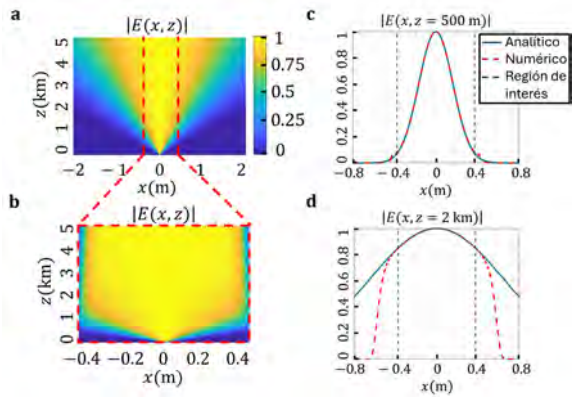

Fig. 3: Propagación de una excitación Gaussiana en el vacío con $\lambda_o = 1.55\ \mu m$ y $MFD = 2\ mm$. a) Propagación analítica. b) Propagación numérica con $N_p = 2048$, empleando absorbente y ventana de 80 cm. En ambos casos se ha normalizado el campo para una mejor visualización. c) y d) Comparación de los campos analítico y numérico a las distancias de propagación $z_p = 500\ m$ y $z_p = 2\ km$, respectivamente.

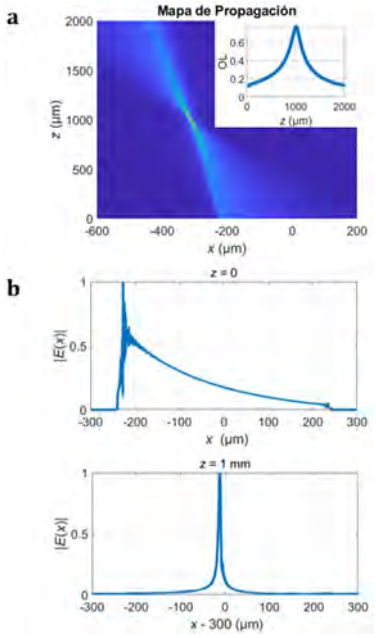

Fig. 4: a) Mapa del campo generado por una rejilla de difracción enfocante y su integral de solapamiento en el eje z. b) Módulo del campo eléctrico en la apertura de la rejilla de difracción y tras propagar 1 mm.

desarrollado coinciden con los analíticos. Para cuantificar mejor la exactitud de los resultados, se han representado en la Figura 3 c) y 3 d) los módulos del campo propagado a las distancias de 500 m y 2 km, respectivamente.

La validación se llevó a cabo mediante el cálculo de la conocida integral de solapamiento entre el campo obtenido por el simulador y la solución analítica en una región de interés de 80 cm, obteniendo un valor de 99.99%. Se han logrado propagaciones de hasta 100 km, manteniendo el número de puntos $N_p = 2048$, con un valor de la integral de solapamiento del 99.9%.

4.2.- Aplicación a un problema real en óptica integrada

En óptica integrada, las antenas que enfocan luz en un punto concreto con una determinada anchura de haz, tienen aplicaciones como facilitar el acoplo de luz a una fibra. En la Figura 4 a) se muestra el campo radiado por una antena enfocante diseñada para maximizar el acoplo a una fibra óptica estándar SMF-28 [7] a una distancia de 1 mm.

En la Figura 4 b) se muestran en detalle los campos que se tienen al comienzo, en $z = 0$, y en el punto de enfoque, $z = 1$ mm, respectivamente. Como se puede observar, el campo se concentra a la distancia de diseño. Si se calcula la eficiencia de acoplo, esta antena logra un acoplamiento a la fibra del 76.7 %.

5.- Conclusión

Se ha desarrollado un propagador electromagnético 3D capaz de calcular la evolución del campo tanto en el régimen de campo cercano como en el de campo lejano, permitiendo simulaciones a distancias de hasta varias decenas de kilómetros.

Para ello, se han obtenido expresiones analíticas simples que facilitan la configuración de los parámetros de simulación, como el mallado y el tamaño de la ventana. La validación del simulador se ha realizado en dos casos de uso: la propagación de un haz Gaussiano en espacio libre hasta 100 km, con tiempos de cómputo de solo unos minutos, y la propagación de un

campo radiado por una antena óptica integrada. Para el primer caso, si se sigue la configuración propuesta en este trabajo, se logra una integral de solapamiento del 99.99% con respecto a la solución analítica Gaussiana.

Agradecimientos:

Este trabajo ha sido financiado por el Ministerio de Universidades, Ciencia e Innovación bajo el proyecto PID2023-151178OB-I00, el proyecto PDC2023-145833-I00, Beca de Colaboración del Ministerio de Educación, Formación Profesional y Deportes del Gobierno de España, convocatoria 2024 y la Universidad de Málaga.

Referencias

[1] S. SHEKHAR, et al., *Roadmapping the next generation of silicon photonics.* Nat Commun 15, 751, 2024.

[2] Pablo GINEL-MORENO, et al., *On-Chip Metamaterial Antenna Array with Distributed Bragg Deflector for Generation of Collimated Steerable Beams.* Laser & Photonics Reviews vol. 16, no 9, p. 2200164, 2022.

[3] Jason D. SCHMIDT, *Numerical simulation of optical wave propagation with examples in MATLAB.* 2010.

[4] Bahaa EA. SALEH, Malvin Carl TEICH, *Fundamentals of photonics, 2 volume set*. John Wiley & Sons, 2019.

[5] Sophocles J. ORFANIDIS, *Electromagnetic waves and antennas,* 2002.

[6] Alan V. OPPENHEIM, et al., *Signals & systems*. Pearson Educación, 1997.

[7] Fiber SMF-28-100, https://www.thorlabs.com/thorproduct.cfm?partnumber=smf-28-100

Monitoring Technique Based on Tilted Fiber Bragg Gratings for Power over Fiber in Multicore Fibers.

Javier Barco [(1)], Rubén Altuna [(1)], David Sánchez Montero [(1)], David Barrera [(2)], Salvador Sales [(2)] and Carmen Vázquez [(1)]

1. Electronics Technology Department, Universidad Carlos III de Madrid, Av. De la Universidad 30, CP-28911 Leganés, Madrid, Spain.
2. Photonics Research Labs, ITEAM Research Institute, Universidad Politécnica de Valencia, Camino de Vera, s/n, 46022, Valencia, Spain.

Contact: Javier Barco (jbarco@ing.uc3m.es).

ABSTRACT:

We present a novel power over fiber (PoF) monitoring technique using tilted fiber Bragg gratings (TFBGs) inscribed in multicore fibers (MCFs). Experimental tests were conducted on 400 m long, 4-core MCFs, achieving average optical power errors of 0.57 dB and 0.27 dB for different configurations. Simultaneously, 5G New Radio signals and the PoF signal delivering up to 2 W of optical power were transmitted to analyze the Error Vector Magnitude at different power levels.

Key words: Power over fiber, multicore fibers, tilted fiber Bragg gratings, 5G NR, Power monitoring.

1.- Introduction

The evolution of mobile networks from the fifth generation (5G) to the upcoming sixth generation (6G) requires enhanced capacity and performance. With anticipated data rates of 1 Tbps and ultra-low latency [1], 6G poses a significant challenge for the existing transport infrastructure, particularly in dense cell deployments. In this context, optical access networks emerge as a crucial supporting technology [2].

The centralized or cloud-based radio access network (C-RAN) architecture plays a crucial role in 5G networks, serving as an optical fronthaul solution that enhances performance through the strategic distribution of remote radio units (RU) and the relocation of baseband units (BBU) to a central office (CO) [3]. Typically, C-RANs operate using digital radio over fiber (DRoF), which transmits high-speed digital signals over fiber. However, this approach requires a large bandwidth and high sampling frequencies.

An alternative is using analog radio over fiber (ARoF), where analog signals are transmitted, increasing spectral efficiency by eliminating the need for digitization [4]. This results in improved energy consumption and scalability.

Furthermore, advancements in power over fiber (PoF) enable centralized power delivery to specific network segments, improving compatibility with C-RAN architectures while enhancing overall efficiency [5]. Various PoF configurations applied to radio over fiber (RoF) in convergence with passive optical networks are discussed in [6]. Fig. 1 depicts an example of C-RAN architecture integrating PoF and data links.

Spatial division multiplexing (SDM) with multicore fibers (MCF) enhances both transmission capacity and space efficiency. Studies on 4- and 7-core MCF have demonstrated the feasibility of simultaneous data and power transmission without significant Bit Error Rate penalties [7].

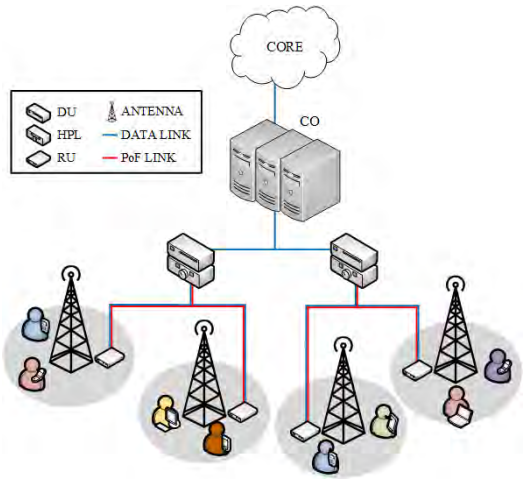

Fig. 1: C-RAN architecture schematic including data and PoF links.

For long-distance applications, a 10 km 7-core MCF PoF link with 5G New Radio (5G-NR) signals was implemented, featuring remote sleep control for RU management and energy savings [8]. Additionally, up to 1 W of electrical power was delivered over 11 km in a 4-core MCF, though without simultaneous ARoF data transmission [9]. Successful PoF and 5G-NR ARoF transmissions were provided in 4-core MCF of 10 km [10] along with throughputs up to 39.5 Gbps over 250 m of 7-core MCF, as reported in [11]. MCFs enables innovative functionalities such as network sensing and monitoring of PoF power delivery to RUs. Given the potential risks of high-power optical signals damaging infrastructure in case of link failure, implementing a monitoring solution is crucial for network protection.

Innovative sensing techniques in MCF using passive elements include backscattering detection and crosstalk measurement. One approach monitors backscattering in the core carrying the high-power laser (HPL), requiring a high-power circulator at the system's input [12]. Another technique measures crosstalk in an adjacent core through which the HPL is launched. This method utilizes a wavelength division multiplexing (WDM) filter at the end of the MCF, centered at the HPL wavelength, to inject the detected crosstalk at 1480 nm into another core for analysis at the system's input [13] [14].

In this work, we analyze in detail the proposed novel monitoring technique for PoF systems shown in [15] inscribing tilted fiber Bragg gratings (TFBGs) on specific MCF cores, close to the RU site. This technique reduces the costs associated with adding input circulators or output WDM filters and involves only one core of the MCF for the monitoring system. We demonstrate the technique on a 4-core MCF, with lengths of 400 m, transmitting 5G NR signals and a PoF signal delivering up to 2 W of optical power to the RU.

2.- Operational principle

The slight tilt of the gratings in TFBGs induces coupling between the core mode and the cladding modes, resulting in pronounced resonant dips in the TFBG transmission spectrum [16]. The inscription angle determines the number and properties of the excited cladding modes. In MCF, cladding modes can couple with a guided mode in the same or opposite core, depending on the grating angle. This coupling is more efficient when another diffraction grating is present in the second core.

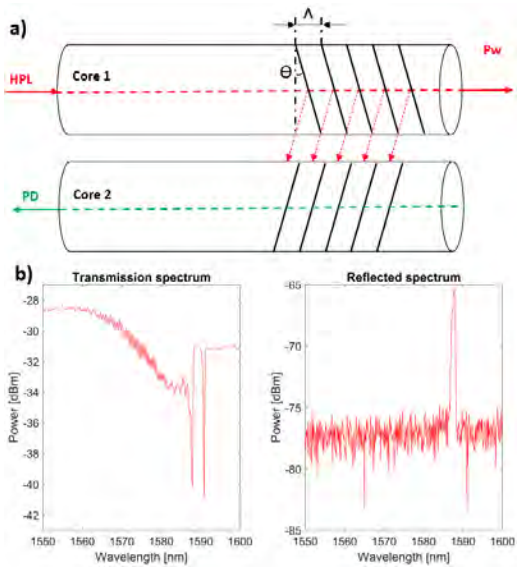

Fig. 2: a) Effects of including TFBGs in core 1 and core 2 in an adjacent core within MCF. b) Transmission and reflected spectrum measured.

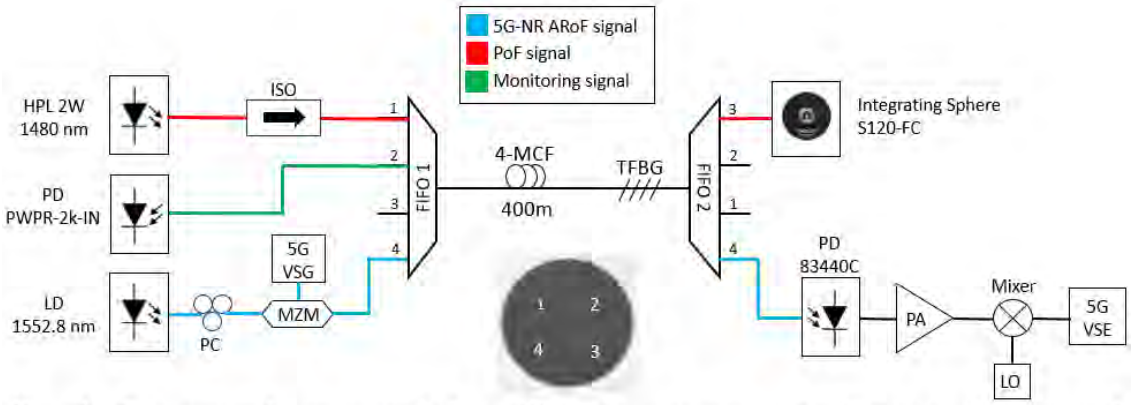

Fig. 3: Experimental set-up including ARoF transmission, optical energy delivery and monitoring.

Fig. 2.a illustrates two MCF cores with inscribed TFBGs, highlighting the energy exchange between the core delivering HPL power and the monitoring core.

Fig. 2.b shows the transmitted spectrum at the end of core 1 and the reflected spectrum in core 2, centered at the desired wavelength.

The Bragg wavelength λ_{bragg} in tilted gratings and the cladding modes λ_{cla} wavelength are given by:

$$\lambda_{bragg} = \frac{2 \cdot \eta_{eff,core} \cdot \Lambda}{\cos(\theta)} \quad (1)$$

$$\lambda_{cla} = \frac{(\eta_{eff,core} + \eta_{eff,cla}) \cdot \Lambda}{\cos(\theta)} \quad (2)$$

where $\eta_{eff,core}$ is the core effective refractive index, Λ is the grating period, θ is the tilt angle and $\eta_{eff,cla}$ is the cladding mode effective refractive index.

Stimulated Raman scattering occurs when the laser power exceeds a specific threshold, generating two main frequency components: the lower-frequency Stokes and the higher-frequency Antistokes. In silica-based optical fibers, a laser centered at 1480 nm, as HPL used in PoF systems, induces stimulated Raman scattering, producing signals at longer wavelengths, typically around 1550-1600 nm. [17]. To optimize the monitoring process of this HPL in PoF systems, a wavelength of around 1587 nm was selected, ensuring maximum available power within this range without compromising the optically delivered power.

3.- Experimental set-up

The experimental set-up, depicted in Fig. 3, involves transmitting the PoF signal through core 1, which includes a HPL to generate the PoF signal up to 2 W, along with an isolator (ISO) for laser protection.

The core 2 is dedicated to monitoring, using a highly sensitive InGaAs photodetector (PD) to accurately measure the received power.

The core 4 is used for testing data transmission, where a laser diode (LD) operating at 1552.8 nm generates the optical carrier for the 5G NR ARoF signal. This signal passes through a polarization controller (PC) to avoid polarization losses. A Mach-Zehnder modulator (MZM) modulates the optical carrier with an electrical signal generated by an SMW200A Vector Signal Generator (VSG) and the 5G NR baseband signal. At reception, a Vector Signal Explorer (VSE) processes the signal quality. To overcome the oscilloscope's 2 GHz bandwidth limitation, a mixer with a local oscillator (LO) is used, along with a power amplifier (PA) to enhance the received RF signal.

Additionally, two fan-in/fan-out (FIFO) devices are employed, and an integrating sphere is used for power control at the RU.

4.- Monitoring system resolution

The monitoring technique is tested using 4-core MCFs with a length of 400 m.

We analyze the behavior of the monitoring technique by sweeping the HPL power range from 23 to 33 dBm in 0.1 dBm steps over time. The data obtained can be observed in Fig. 4. Additional measurements are performed with a filter placed before the photodetector, which removes the 1480 nm component reflected due to backscattering, allowing only the TFBG effect to be considered.

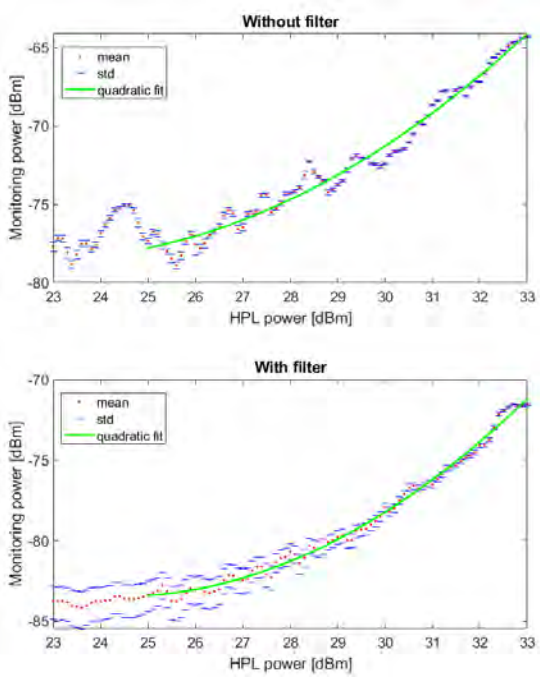

Fig. 4: Monitoring power of the signal from TFBG and backscattering crosstalk vs. HPL power.

By analyzing the obtained results, a more stable behavior is observed across the different power levels swept when the filter is used. This is due to the energy at 1480 nm, which comes from MCF crosstalk Rayleigh backscattering and, as a result, introduces instability in the monitored signal at 1587 nm. By using the filter, the 1480 nm component is reduced (by 20 dB), allowing the energy from the TFBG at 1587 nm to dominate, which leads to greater stability.

It is important to note that in the proposed set-up an additional filter needs to be added, which reduces the received power levels.

Depending on the resolution requirements and the analyzed distances, employing one of the techniques presented may be advisable.

The average received power at the CO versus the HPL power (P_{HPL}) were fitted to the quadratic equations (3) and (4) for the cases of the monitoring power without a filter (P_{m_NF}) and with a filter (P_{m_F}), respectively. The quadratic fitting is applied for a range from 25 to 33 dBm of configured HPL power. This is because, when using the filter, the monitoring process detects almost no power at lower HPL power levels. Similarly, without the filter, the lower power levels result in significant noise fluctuations.

$$P_{m_NF} = 0.135 \cdot P_{HPL}^2 - 6.15 \cdot P_{HPL} - 8.71 \quad (3)$$

$$P_{m_F} = 0.163 \cdot P_{HPL}^2 - 7.95 \cdot P_{HPL} - 13.2 \quad (4)$$

The maximum absolute error for each HPL power level was calculated by comparing the data obtained to the quadratic fit in the range from 25 to 33 dBm, and the resulting error distribution histogram is shown in Fig. 5. Without a filter, the maximum error reached was 1.84 dB, with an average error of all absolute values of approximately 0.57 dB. With the filter, the maximum error was reduced to 0.67 dB, while the average error decreased to around 0.27 dB.

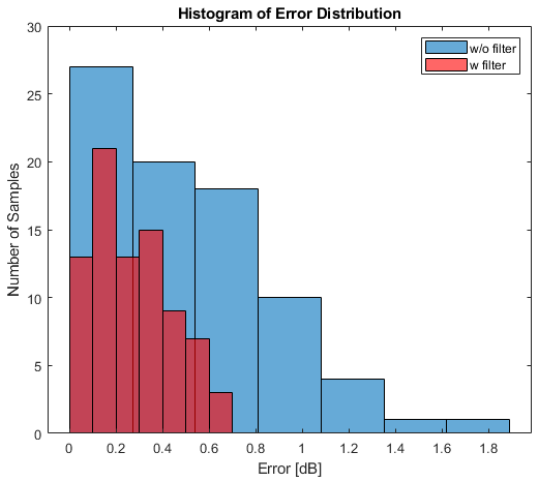

Fig. 5: Histogram of Monitoring technique Error Distribution with (w) and without (w/o) Filter.

5.- Evaluation of 5G-NR ARoF signals

Analyzing the constellation measured at the RU from data transmitted in the link at each HPL power level allows for the determination of the Error Vector Magnitude (EVM). The transmitted 5G NR signal was the test model TM3.1a, configured with a 100 MHz bandwidth, 30 kHz subcarrier spacing, 256-QAM modulation format, and a carrier frequency centered at 20 GHz within the FR3 range. The data rate obtained for the 5G NR signal used in this work is around 800 Mbps with signaling and 606.4 Mbps pure data. According to the standard, the maximum allowable error is set at 4.5%, and as illustrated in Fig. 6, this requirement is met across all power levels.

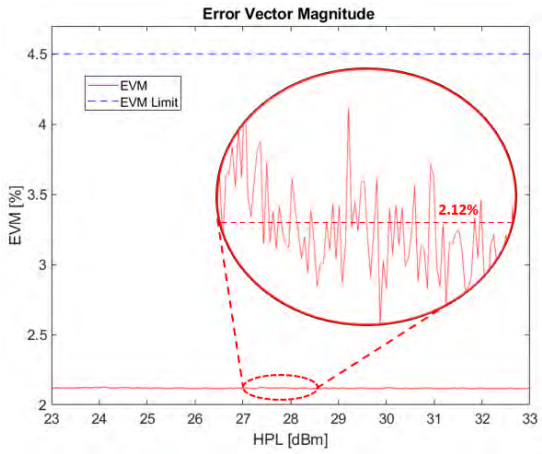

Fig. 6: EVM measured for every HPL power.

6.- Conclusions

An analysis of a detection system for monitoring the power supplied to the RU through a PoF system in MCF has been conducted. The scalability of this technique for different scenarios stands out, as well as its ability to operate without additional power consumption at the remote node, given that it relies on passive components. The test was carried out on a 4-core MCF with a length of 400 m, transmitting 5G NR signals using the TM3.1a standard. An EVM of around 2.1% significantly lower than the maximum allowed by the standard (4.5%) was achieved.

The monitoring technique is based on the insertion of TFBGs in both the PoF and monitoring cores, enabling the measurement of optical power supplied to the RUs near end without significantly affecting the optically delivered power.

The system offers different resolutions depending on whether a filter is used to remove the 1480 nm component. A resolution of 0.57 dB is achieved without the filter, while 0.27 dB is reached when the filter is applied, both for HPL power levels ranges from 25 to 33 dBm.

Acknowledgements: This work was supported in part by UNICO-5G I+D Ministerio de Asuntos Económicos y Transformación Digital and NextGenerationEU underGrant TSI-063000- 2021-135 (6GXtreme I), in part by Spanish Research Agency under Grant PID2021-122505OB-C32 and by PIPF-2023/TEC-30589.

References

[1] N. Chen and M. Okada, “Toward 6G Internet of Things and the Convergence With RoF System,” *IEEE Internet Things J.*, vol. 8, no. 11, pp. 8719–8733, Jun. 2021, doi: 10.1109/JIOT.2020.3047613.

[2] C. Ranaweera, J. Kua, I. Dias, E. Wong, C. Lim, and A. Nirmalathas, “4G to 6G: disruptions and drivers for optical access [Invited],” *J. Opt. Commun. Netw.*, vol. 14, no. 2, pp. A143–A153, Feb. 2022, doi: 10.1364/JOCN.440798.

[3] S. Rommel *et al.*, “Towards a Scaleable 5G Fronthaul: Analog Radio-over-Fiber and Space Division Multiplexing,” *J. Light. Technol.*, vol. 38, no. 19, pp. 5412–5422, Oct. 2020, doi: 10.1109/JLT.2020.3004416.

[4] P. Chanclou, L. Anet Neto, K. Grzybowski, Z. Tayq, F. Saliou, and N. Genay, “Mobile Fronthaul Architecture and Technologies: A RAN Equipment Assessment [Invited],” *J. Opt. Commun. Netw.*, vol. 10, no. 1, p. A1, Jan. 2018, doi: 10.1364/JOCN.10.0000A1.

[5] C. Vázquez, G. Otero, R. Altuna, J. D. López-Cardona, and D. Larrabeiti, “Power over Fiber Pooling as part of 6G optical fronthaul,” *J. Light. Technol.*, pp. 1–8, 2024, doi: 10.1109/JLT.2024.3375972.

[6] C. Vázquez, D. S. Montero, F. M. A. Al-Zubaidi, and J. D. López-Cardona, "Experiments on Shared- and Dedicated-Power over Fiber Scenarios in Multi-core Fibers," in *2019 European Conference on Networks and Communications (EuCNC)*, Jun. 2019, pp. 412–415. doi: 10.1109/EuCNC.2019.8802042.

[7] C. Vázquez *et al.*, "Multicore Fiber Scenarios Supporting Power Over Fiber in Radio Over Fiber Systems," *IEEE Access*, vol. 7, pp. 158409–158418, 2019, doi: 10.1109/ACCESS.2019.2950599.

[8] J. D. López-Cardona *et al.*, "Power-over-fiber in a 10 km long multicore fiber link within a 5G fronthaul scenario," *Opt. Lett.*, vol. 46, no. 21, pp. 5348–5351, Nov. 2021, doi: 10.1364/OL.439105.

[9] M. Wada, K. Kurokawa, T. Matsui, H. Iida, and K. Nakajima, "High-Efficiency and Long-Distance Power-over-Fibre Transmission using a 125-µm Cladding Diameter 4-Core Fibre," in *49th European Conference on Optical Communications*, Oct. 2023.

[10] R. Altuna, Y. Jung, P. Petropoulos, and C. Vázquez, "Power Over Fiber and Analog Radio Over Fiber Simultaneous Transmission Over Long Distance in Single Mode, Multicore, and Hollow Core Fibers," *Laser Photonics Rev.*, vol. 18, no. 8, p. 2400157, Aug. 2024, doi: 10.1002/lpor.202400157.

[11] R. Altuna, J. Barco-Alvárez, and C. Vázquez, "Power Over Fiber Co-Transmission With 39.5 Gpbs Mixing 5 G NR Analog Radio Over Fiber and NRZ Signals Over Multicore Fiber," *J. Light. Technol.*, pp. 1–7, 2025, doi: 10.1109/JLT.2025.3534921.

[12] R. Altuna, J. Barco-Álvarez, and C. Vázquez, "Backscattering-Based and Crosstalk-Based Monitoring Techniques for Power over Fiber Signals in Spatial Division Multiplexed Links," in *6th Optical Wireless and Fiber Power Transmission Conference (OWPT)*, Apr. 2024.

[13] R. Altuna, J. D. López-Cardona, and C. Vázquez, "Monitoring of Power Over Fiber Signals Using Intercore Crosstalk in ARoF 5G NR Transmission," *J. Light. Technol.*, vol. 41, no. 23, pp. 7155–7161, Dec. 2023, doi: 10.1109/JLT.2023.3300184.

[14] R. Altuna, J. D. López-Cardona, and C. Vázquez, "Crosstalk-Based Remote Monitoring Technique for Power over Fiber Signals in Spatial Division Multiplexing Links," in *2022 IEEE International Topical Meeting on Microwave Photonics (MWP)*, Oct. 2022, pp. 1–4. doi: 10.1109/MWP54208.2022.9997712.

[15] J. Barco, R. Altuna, D. Sánchez, D. Barrera, S. Sales, and C. Vázquez, "Analog Radio and Power over Fiber Monitored via Bragg Gratings in Multicore Fiber Links," 2025.

[16] T. Erdogan and J. E. Sipe, "Tilted fiber phase gratings," *J. Opt. Soc. Am. A*, vol. 13, pp. 296–313, 1996, doi: 10.1364/JOSAA.13.000296.

[17] R. Ramaswami and K. Sivarajan, "Optical Networks: A Practical Perspective (3nd Edition)," *Elsevier Sci. Technol.*, pp. 165–167, 2010, doi: 10.1016/C2009-0-17339-7.

Descomposición Modal en Fibras Ópticas mediante Aprendizaje Supervisado basado en MobileNetV2

Lucía MÉNDEZ [(1)], Juan Carlos MARTÍN [(1,3)], Ana María LÓPEZ-TORRES [(2,3)]

1. Departamento de Física Aplicada, Facultad de Ciencias, Universidad de Zaragoza, c/ Pedro Cerbuna 12, 50009, Zaragoza (España).
2. Departamento de Ingeniería Electrónica y Comunicaciones. Escuela Universitaria Politécnica de Teruel, Universidad de Zaragoza, c/ Pedro Cerbuna 12, 50009, Zaragoza (España).
3. Instituto de Investigación en Ingeniería de Aragón (I3A).

Contacto: Juan Carlos MARTÍN (jcmartin@unizar.es).

ABSTRACT:

An AI-based procedure to find the modal composition of the intensity distribution of a multimode optical fiber has been implemented. For the case under study, with three propagation modes, a convolutional neural network has been trained in order to receive an intensity distribution image and provide the mode weights and phases information necessary to reproduce the given image by means of mode field superposition.

A training database has been synthesized to cover all possible combinations of modes but avoiding, as far as possible, introducing ambiguous information into the system due to the loss of phase information associated with working with intensity distributions. The proposed method allows real-time mode decomposition implementation with a tolerable error for most applications.

Key words: Few-mode fibers, mode decomposition, space division multiplexing, machine learning, convolutional neural network, transfer learning.

1.- Introducción

Los procedimientos de descomposición modal (DM), que permiten determinar la distribución modal en la salida de una fibra multimodo, resultan imprescindibles para el análisis y puesta a punto de cualquier sistema en que se requiera un control preciso de su composición modal. Por tanto, estas técnicas resultan esenciales para el desarrollo de sistemas de multiplexado espacial (*space division multiplexing,* SDM), propuestos como posible solución para responder a la escalada en el volumen de datos intercambiados a través de las redes de fibra óptica [1, 2], que hoy día parece lejos de detenerse [3, 4]. Además, estas técnicas constituyen herramientas muy interesantes para el estudio de fenómenos de competición modal [5] o de efectos no lineales asociados a la interacción de varios modos [6].

Los métodos de DM pueden clasificarse en directos o indirectos: los primeros requieren montajes experimentales relativamente complejos, pero proporcionan información en tiempo real sobre el peso de los diferentes modos presentes en la salida del sistema; los segundos son sencillos experimentalmente, pues no requieren más que el registro de la distribución de intensidad a la salida del sistema, pero conllevan un tratamiento numérico posterior, por lo que la DM no se efectúa en tiempo real. Entre los métodos directos, destacan los de la evaluación de la interferencia multimodo, conocidos como S^2 (*spatially and spectrally resolved imaging)* [7] y C^2 (*frequency domain cross-correlated imaging*) [8] y los basados en filtros de

correlación [9, 10]. Entre los métodos indirectos, cabe citar diferentes algoritmos: SPGD [11], genético [12] y el propuesto en [13].

Los avances recientes en cuanto a disponibilidad de herramientas basadas en inteligencia artificial (IA) han permitido abordar el problema de DM desde otra perspectiva [14-16], combinando la sencillez de los montajes experimentales, que no requieren más que el registro de la distribución de intensidad a la salida de la fibra, con una gran rapidez en el análisis (el método implementado en [16] llega a analizar 910 imágenes por segundo). En estos trabajos, el entrenamiento del algoritmo se lleva a cabo con una estrategia de aprendizaje automático supervisado aplicado a un problema de regresión múltiple. Al sistema se le suministran como entrada diferentes distribuciones de intensidad conocidas junto con información de la combinación de modos que ha dado lugar a dicha distribución. Esta información se presenta como un vector de coeficientes correspondientes a las amplitudes normalizadas de cada modo y a los cosenos de las diferencias de fase entre ellos. Con estos datos se entrena una red neuronal convolucional que, a partir de la distribución de intensidad de salida de la fibra, proporciona los valores de amplitudes y fases relativas entre modos para que su superposición reproduzca dicha distribución. Aunque en algunos de los trabajos se diseñan redes neuronales específicas para este problema, en [14-15] se parte de modelos conocidos usados en el reconocimiento de imágenes que se modifican añadiendo capas a la salida (transfer learning) cuyos coeficientes son entrenados con el dataset descrito. De esta manera se aprovecha el conocimiento asociado a modelos robustos, entrenados con gran cantidad de muestras, a la misma vez que se personaliza al problema a resolver mediante el entrenamiento de sus últimas capas con los datos específicos.

En este trabajo se utiliza una estrategia similar, pero a diferencia de [15,16] en donde se parte de la red VGG-16 para obtener el modelo de predicción, se parte de redes MobileNetV2 [17]. Esta arquitectura está especialmente diseñada para su uso en sistemas con capacidad de cálculo reducida (móviles u ordenadores monoplaca tipo Raspberry Pi) lo que permitiría la implementación de detectores de descomposición modal en dispositivos independientes dotados de una cámara con calidad suficiente.

2.- Metodología

Para poner a prueba el método se ha elegido una fibra óptica teórica de salto de índice con los siguientes parámetros: radio del núcleo, 8mm, índice de refracción del núcleo, 1.46 y apertura numérica, 0.10. La longitud de onda de trabajo es 1550 nm, para la cual esta fibra presenta tres modos de propagación en la aproximación de guiado débil: LP_{01}, LP^{E}_{11} y LP^{O}_{11} (los superíndices E y O hacen referencia a *even* y *odd*, respectivamente). En lo sucesivo nos referiremos a ellos como modos 1, 2 y 3.

2.1.-Dataset

Para llevar a cabo las fases de entrenamiento, validación y test del algoritmo, se han generado imágenes de 128 x 128 píxeles resultado de la superposición de los campos de los tres modos con diferentes combinaciones de sus pesos (C_i) y fases (ϕ_i) (i=1, 2 o 3). Asumimos polarización lineal y denotamos por $E_i(x,y)$ a la distribución normalizada de campo eléctrico del modo i, de manera que la superposición se calcula mediante la expresión siguiente, en donde $\phi_{ik} = \phi_k - \phi_i$:

$$|E(x,y)|^2 = \sum_{i=1}^{3} C_i |E_i(x,y)|^2 + 2\sum_{i=2}^{3}\sum_{k=1}^{i-1} C_i C_k E_i(x,y)\, E_k(x,y)\cos(\phi_{ik}). \quad (1)$$

Para cada una de estas imágenes se genera una etiqueta formada por un vector de 5 coeficientes: el porcentaje de amplitud asociado a cada uno de los modos, y los cosenos $\cos\phi_{12}$ y $\cos\phi_{23}$. Se considera el coseno y no el valor de la fase para evitar la

incertidumbre asociada a que dos ondas con la misma amplitud compleja dan lugar a la misma distribución de intensidad [14]. Como contrapartida, en general se obtienen dos posibles valores de $\cos\phi_{13}$. Determinar cuál de ellos es el correcto requiere una operación adicional, que se explicará en el apartado de resultados.

Se han combinado 15 valores posibles para las amplitudes normalizadas (valores entre 0 y 1) y también 15 valores para las diferencias de fase (entre 0 y 2π). La suma de los coeficientes con información sobre la amplitud de los modos debe ser 1. El rango de valores [-1,1] propio del coseno de las diferencias de fase se hace corresponder linealmente con el rango [0,1] para facilitar el entrenamiento de la red.

Se generan un total de 20868 tras eliminar combinaciones que dan lugar a una misma distribución de intensidad. De este conjunto un 64% se utiliza en el entrenamiento de la red y un 16% en el proceso de validación. Se reserva un 20% de las distribuciones de intensidad simuladas para probar el funcionamiento del modelo.

2.2.-Estructura de la red neuronal convolucional

Como ya se ha mencionado en el apartado de introducción, utilizando técnicas de transfer learning se parte del modelo MobileNetV2 con los coeficientes obtenidos al ser entrenado con la base de imágenes Imagenet. Su capa de salida es sustituida por una capa MaxPooling con el objetivo de reducir el tamaño de la red, seguida por dos capas completamente conectadas, la primera de ellas formada por 224 neuronas y la segunda, que es la capa de salida, con 5 neuronas, tantas como variables de salida. La función de activación de esta última capa es la función lineal, apropiada para salidas de tipo continuo (regresión) como es este caso. En la figura 1 se muestra el esquema completo del modelo de red neuronal utilizado.

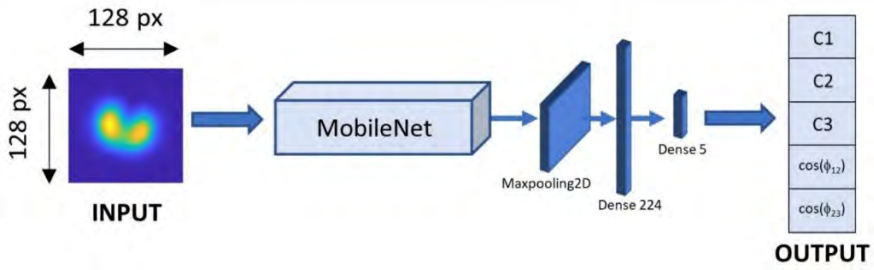

Fig. 1: Esquema de la red neuronal empleada

2.3.-Entrenamiento

Este modelo se entrena congelando los coeficientes correspondientes a la red MobileNetV2. Para este entrenamiento se utiliza la librería de aprendizaje automático TensorFlow desarrollada por Google. Una vez definido el modelo este se entrena con las imágenes generadas. Se utiliza el algoritmo de optimización Adam y el error cuadrático medio como función de pérdidas. Este error se visualiza en la figura 2 para el caso de un entrenamiento durante 28 épocas con un tamaño de lote igual a 32 y una tasa de aprendizaje de 0.001. El entrenamiento se detiene cuando la pérdida en el conjunto de validación no mejora durante cinco épocas (*early stopping*), para evitar sobreajuste.

La figura 2 muestra la esperada disminución del error cuadrático medio a lo largo de las épocas, tanto para el entrenamiento como para la validación. El valor de la función de pérdidas de la última época resulta ser $9.2\ 10^{-4}$ para entrenamiento y $1.3\ 10^{-3}$ para validación.

Para comprobar el funcionamiento del modelo se utiliza el conjunto test. En la figura 3 aparece el histograma del valor absoluto medio (Mean Absolute Error MAE) cometido en la predicción de las etiquetas de 5 coeficientes. Se observa un valor medio de 0.0208 con una varianza de 0.000721.

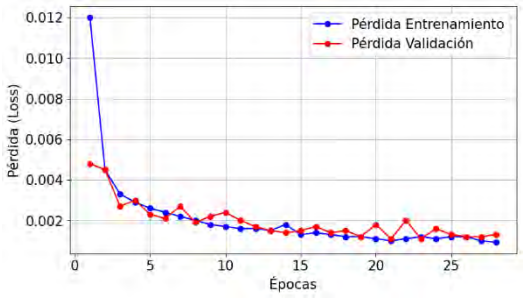

Fig. 2: Evolución del error cuadrático medio a lo largo de las épocas, en las fases de entrenamiento y validación

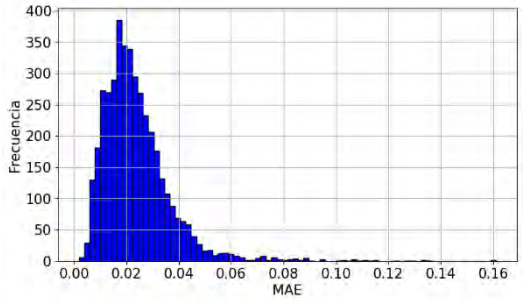

Fig. 3: Distribución del MAE en las predicciones realizadas con el conjunto test.

3.- Resultados

En la figura 4 se muestra un caso como ejemplo de funcionamiento del modelo que, además, emplearemos para mostrar cómo elegir el valor correcto de $\cos\phi_{13}$, de entre los dos valores compatibles con los parámetros de salida de la red.

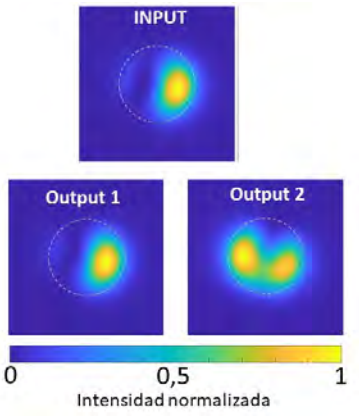

Fig. 4: Distribución de intensidad a analizar (input) y dos distribuciones obtenidas al superponer los tres modos permitidos con los dos conjuntos de fases compatibles con las etiquetas de salida proporcionadas por la red neuronal. En línea discontinua, la frontera núcleo-recubrimiento de la fibra óptica.

La distribución "input" de la figura 4 tiene como parámetros: $C_1 = C_2 = 0{,}125$; $C_3 = 0{,}75$; $\phi_1 = \phi_3 = 0$; $\phi_2 = 2\pi/3$. La red neuronal otorga a esta figura parámetros $C_1 = 0{,}1428$; $C_2 = 0{,}0999$; $C_3 = 0{,}7526$; $\cos\phi_{12} = -0{,}6948$ y $\cos\phi_{23} = -0{,}6240$. Con ellos, los dos posibles valores de $\cos\phi_{13}$ son 0,9956 (*opción 1*) y -0,1284 (*opción 2*). En este caso, la comparación visual de las dos posibles distribuciones de salida con la de entrada indica claramente que la opción 1 es la correcta. En general, la comparación se automatiza mediante el cálculo de los coeficientes de correlación 2D (en adelante, Γ) entre la entrada y las dos posibles opciones de salida [15]. En concreto, para el caso de la figura 4 se obtienen, respectivamente para las opciones 1 y 2, $\Gamma = 0{,}9991$ y $\Gamma = 0{,}6501$.

La tabla 1 presenta una comparación entre los pesos y fases de varias imágenes "input" con sus correspondientes "output", incluyendo el caso mostrado en la figura 4 y otros casos representativos de otros rangos de MAE. En cada caso se incluye la información del mejor coeficiente Γ obtenido, de entre la pareja de coeficientes asociados a los dos posibles valores de $\cos\phi_{13}$. Es de destacar la correlación superior a 0,95 en todos los casos, lo que indica el buen funcionamiento del método. La figura 5 muestra el aspecto de las imágenes "input" y "output" de todos los casos mostrados en la tabla 1, y corrobora la utilidad del procedimiento que proponemos.

Del análisis conjunto de la tabla 1 y la figura 5, concluimos que para evaluar el acierto de la red neuronal en cada caso es preferible fijarse en Γ más que en el MAE y que la correlación entre ambos parámetros no es elevada.

Esta falta de correlación tiene que ver con situaciones en que los valores de algunas etiquetas resultan irrelevantes. Un ejemplo de ello es el caso 6, con $C_3 = 0$. En tal situación, el parámetro $\cos\phi_{23}$ es irrelevante para la reconstrucción de la imagen mediante superposición, pero la diferencia entre sus valores input y output sí repercute en un aumento del MAE. En otras palabras, este resultado es mejor que lo que podría pensarse

atendiendo exclusivamente a su MAE y, de hecho, es el que presenta mejor coeficiente de correlación.

No obstante, el cálculo de un error asociado a los coeficientes es mucho más rápido que el de Γ de las imágenes y por ello el proceso de entrenamiento de la red se ha basado en este primero, con buenos resultados como se ha visto. En resumen, ambos tipos de errores ofrecen información de interés: uno resulta más adecuado para la fase de entrenamiento y otro evalúa mejor el grado de acierto de cada predicción.

Tabla 1: Comparación de las etiquetas de diferentes inputs (filas en negrita) con sus correspondientes outputs, para diferentes casos. En todos ellos se indica su MAE y su coeficiente de correlación 2D (Γ).

CASO	C_1	C_2	C_3	$\cos\phi_{12}$	$\cos\phi_{23}$	*MAE*	*Γ*
1	**0**	**0,25**	**0,75**	**1**	**-0,5**		
	0,0078	0,2504	0,7500	0,9955	-0,4896	0,0031	0,9747
2	**0,5**	**0,12**	**0,38**	**0,7661**	**0,1737**		
	0,5071	0,1178	0,3735	0,9955	-0,4896	0,0035	0,9954
3	**0**	**0,38**	**0,62**	**1**	**1**		
	0,0097	0,3871	0,6265	0,9400	0,8813	0,0225	0,9557
4	**0,75**	**0,125**	**0,125**	**0,7661**	**0,7660**		
	0,7477	0,1294	0,1226	0,7865	0,9536	0,0237	0.9929
5	**0,125**	**0,125**	**0,75**	**-0,5**	**-0,5**		
(Fig. 4)	0,1428	0,0999	0,7526	-0,6948	-0,6240	0,0409	0,9991
6	**0,88**	**0,12**	**0**	**0,7661**	**0,7661**		
	0,8537	0,1163	0,0279	0,8408	0,6934	0,0497	0,9993

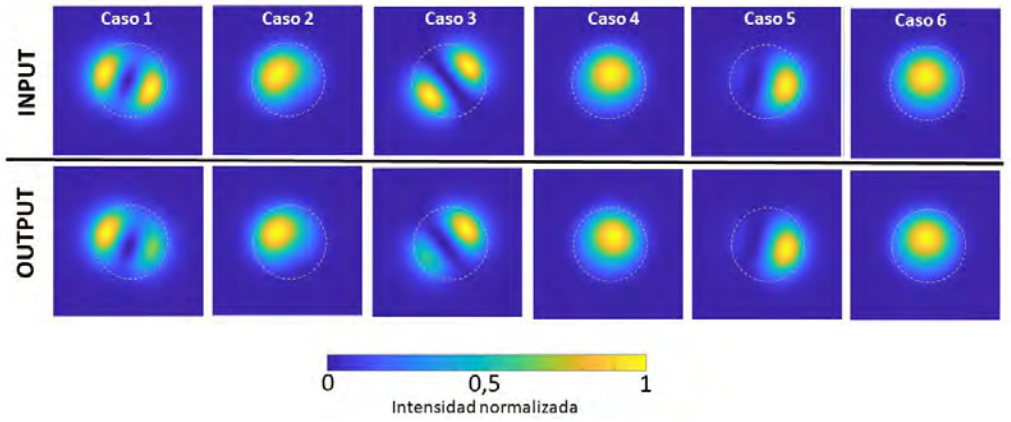

Fig. 5: Varias distribuciones de intensidad a analizar (input) y sus correspondientes distribuciones output. En los casos con dos conjuntos de fases compatibles con las etiquetas de salida proporcionadas por la red neuronal, se ha seleccionado la solución con mayor correlación con su imagen input. En línea discontinua, la frontera núcleo-recubrimiento de la fibra óptica.

4.- Conclusión

En este trabajo se ha implementado un sistema de Descomposición Modal para fibras multimodo utilizando una red neuronal convolucional basada en la estructura MobileNetV2. A partir de la distribución de intensidad a la salida de la fibra, el sistema proporciona el porcentaje de amplitud correspondiente a cada modo y la diferencia de fase entre ellos.

Este modelo ha sido entrenado con un conjunto de imágenes propio especialmente diseñado para evitar introducir en el sistema la ambigüedad asociada a la perdida de parte de

la información de fase en la salida de intensidad. De esa manera se consigue errores de entrenamiento y validación muy bajos que se traducen en un buen comportamiento del error de predicción del valor de los coeficientes en las muestras test. Hemos comprobado como la reducción de la incertidumbre asociada a las fases en el dataset de entrenamiento ha sido un factor clave a la hora de reducir estos errores.

La comparación de las distribuciones de intensidad construidas con esos coeficientes y las de entrada al modelo, permiten eliminar la ambigüedad de fase y muestran un alto grado de correlación.

El trabajo con un modelo ligero como MobileNet permitirá en un futuro implementar dispositivos de bajo coste que permitan obtener esta descomposición a tiempo real.

Agradecimientos: Este trabajo ha sido financiado por el departamento de Ciencia, Universidad y Sociedad del Conocimiento del Gobierno de Aragón mediante el proyecto E44-23R.

References

[1] Li G, Bai N, Zhao N, Xia C, *"Space-division multiplexing: The next frontier in optical communication"*. Adv. Opt. Photonics, 6, 413–487, 2014.

[2] Trichili A, Park KH, Zghal M, Ooi BS, Alouini MS, *"Communicating using spatial mode multiplexing: Potentials, challenges, and perspectives"*. IEEE Commun. Surv. Tutor., 21, 3175–3203, 2019.

[3] Winzer PJ, Neilson DT, *"From Scaling Disparities to Integrated Parallelism: A Decathlon for a Decade". J. Lightw. Tech.*, 35, 1099-1115, 2017.

[4] Cisco annual internet report, https://www.cisco.com/c/en/us/solutions/collateral/executive-perspectives/annual-internet-report/white-paper-c11-741490.html

[5] Jollivet C, Mafi A, Flamm D, Duparré M, Schuster K, Grimm S, Schülzgen A, *"Mode-resolved gain analysis and lasing in multi-supermode multi-core fiber laser"*. Opt. Express, 22, 30377–30386, 2014.

[6] Mohammadzahery Z, Jandaghi M, Aghayari E, Nabavi H, *"Observation of spatial nonlinear self-cleaning in a few-modestep-index fiber for special distributions of initial excited modes"*. Sci. Rep., 11, 1–7, 2021.

[7] Nicholson JW, Yablon AD, Ramachandran S, Ghalmi S, *"Spatially and spectrally resolved imaging of modal content in large-mode-area fibers"*, Opt. Express, 16, 7233–7243, 2008.

[8] Schimpf D.N, Barankov, RA, Ramachandran S, *"Cross-correlated (C2) imaging of fiber and waveguide modes"*, Opt. Express, 19, 13008–13019, 2011.

[9] Kaiser T, Flamm D, Schröter S, Duparré M, *"Complete modal decomposition for optical fibers using CGH-based correlation filters"*, Opt. Express, 17, 9347–9356, 2009.

[10] Flamm D, Naidoo D, Schulze C, Forbes A, Duparré M, *"Mode analysis with a spatial light modulator as a correlation filter"*, Opt. Lett., 37, 2478–2480, 2012.

[11] Lü H, Zhou P, Wang X, Jiang Z, *"Fast and accurate modal decomposition of multimode fiber based on stochastic parallel gradient descent algorithm"*, Appl. Opt., 52, 2905–2908, 2013.

[12] Li L, Leng J, Zhou P, Chen J, *"Multimode fiber modal decomposition based on hybrid genetic global optimization algorithm"*, Opt. Express, 25, 19680–19690, 2017.

[13] Manuylovich ES, Dvoyrin VV, Turytsin SK, *"Fast mode decomposition in few-mode fibers"*, Nature Comm., 11, 5507, 2020.

[14] An Y, Huang L, Li J, Leng J, Yang L, Zhou P, *"Learning to decompose the modes in few-mode fibers with deep convolutional neural network"*, Opt. Express, 27, 10127–10137, 2019.

[15] Rothe S., Zhang Q., Koukourakis N., & Czarske J, Deep learning for computational mode decomposition in optical fibers. Applied Sciences 2020;10(4):1367. https://doi.org/10.3390/app10041367

[16] Zhang Q, Rothe S, Koukourakis N, Czarske J, *"Learning the matrix of few-mode fibers for high-fidelity spatial mode transmission"*. APL Photonics, 7, 066104, 2022.

[17] Howard, A.G., Zhu, M., Chen, B., Kalenichenko, D., Wang, W., Weyand, T., Andreetto, M., & Adam, H. *MobileNets: Efficient Convolutional Neural Networks for Mobile Vision Applications*. 2017 ArXiv, abs/1704.04861.

Impact of Received Optical Power on the Transmission Performance of Standalone NB-IoT over PMMA GI-POF

Muhammad WASEEM [(1)], Alicia LÓPEZ [(1,2)], Pedro Luis CARRO [(1,3)], Mª Ángeles LOSADA [(1,2)]

1: Electronics Engineering and Communications Dept., EINA, University of Zaragoza, Zaragoza, Spain
2: GTF, Aragón Institute of Engineering Research (i3A), University of Zaragoza, Zaragoza, Spain
3: CeNIT, Aragón Institute of Engineering Research (i3A), University of Zaragoza, Zaragoza, Spain

Contact: Muhammad WASEEM (mwaseem@unizar.es)

ABSTRACT:

In this work, we have evaluated the impact of the received optical power on the performance of a Radio over Plastic Optical Fiber (RoPOF) system. More specifically, we have transmitted signals according to an Internet of Things (IoT) standard NB-IoT (Narrowband IoT) over PMMA Graded Index POF. The analysis has been performed using a custom POF-specific optical attenuator based on an Optical Neutral Density Filter (ONDF) that allowed for a continuous variation of the received optical power. Results show that the transmission performance is affected not only by RF input power, but also by received optical power, although excellent transmission performance can be obtained for a wide range of both parameters.

Key words: Standalone NB-IoT, RoPOF transmission, PMMA GI-POF

1.- Introduction

In recent years, a dramatic proliferation has been observed in the Internet of Things (IoT) devices, which has brought about a significant rise in the connectivity demands, being most of the data traffic generated from homes, offices, hospitals, etc. [1]. In this context, short-range communication networks have gained a huge significance, which has driven a seamless development of the associated technologies [2]. Short-range coverage with enhanced service quality can efficiently be achieved by exploiting the paradigm of Distributed Antenna System (DAS) [3], [4]. In fact, the use of fiber optics as the wired backbone of the DAS system provides high capacity with low attenuation and has been researched thoroughly [5]. The convergence of radio and fiber optic technologies, gives rise to the Radio over Fiber (RoF) systems which can enable broadband wireless services that can support extremely high data traffic rates [5]. In this regard, RoF networks for long-haul scenarios have been proposed using mainly Silica Single Mode Fiber (SMF) [7], [8]. Nevertheless, regarding the short-range scenarios, Multimode Glass Fibers (MMF) and Plastic Optical Fibers (POF) are also considered as the most effective solutions [8], [9], [10], [11], [12]. Especially, in the short-range applications having moderate bandwidth requirements, Plastic Optical Fibers show even a superior performance than the Glass Optical Fibers [13]. In this context, POFs have many advantages over GOFs, as effortless handling, flexibility, mechanical resistance, and easier and simpler deployment due to its large core [14], which leads to cost-effective solutions. Nonetheless, they have higher attenuation and exhibit large modal dispersion due to which they have moderate

low bandwidth [15], [16]. These drawbacks limit the applications of the POFs to short-range networks with moderate bandwidth requirements [17], [18]. In this respect, we formerly performed characterization of the transmission performance of LTE and NB-IoT signals through 75-meter PMMA graded index Plastic optical Fiber (GI-POF) and we obtained an excellent performance for an ample range of input RF power values [19]. Besides the RF input power, the operating point of the transmitter, set by its laser bias current, may also substantially affect the transmission quality of the signals [20].

In this context, in one of our previously published works [21], we analysed how RoPOF non-linear effects can impact the transmission performance of LTE and NB-IoT signals through the measurement of both Error Vector Magnitude (EVM) and Adjacent Channel Power Ratio (ACPR). Our results showed that the minimum EVM and ACPR were obtained nearly at the same input RF power which revealed that the optimum operating conditions of the transmitter could be estimated by measuring and analyzing the ACPR [22].

In this paper, we analyze the impact of the received optical power on the transmission performance of 925 and 960-MHz NB-IoT in standalone operation mode. For this purpose, we have set an optical back-to-back RoPOF link using short fiber of 1-meter length whose received optical power was changed by a POF-specific optical attenuator. The rest of the paper is organized as follows: In Section 2, the experimental setup and the experimental procedure are described. Experimental results are provided in Section 3. Finally, the conclusions have been drawn in Section 4.

2.- Experimental Setup

Figure 2 shows the experimental setup used in this work. We carried out a downlink transmission of standalone Narrowband IoT (NB-IoT) over a large-core PMMA Graded Index Plastic Optical Fiber (GI-POF).

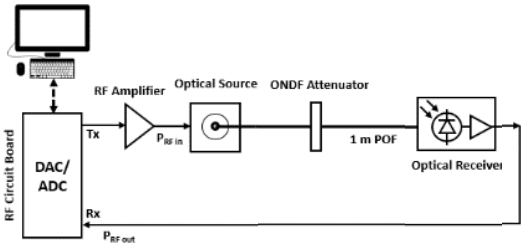

Fig. 1: Experimental setup

The NB-IoT signal according to the standalone operation mode over the two carrier frequencies considered (925 MHz and 960 MHz) was generated offline using Matlab. After generation, the signal was passed through an RF Circuit Board that performed the necessary DAC conversion and then it was amplified in order to set the desired input RF power ($P_{RF\,in}$ in the schematic). This input RF signal was used to directly modulate the optical source, which was a 55-mA biased 658-nm laser diode (LD L658P040) with measured threshold current of 32 mA and nominal emission power of 40 mW, mounted on the LDM9T laser mount. The optical signal at the output of the laser source was passed to a custom POF-specific optical attenuator based on an Optical Neutral Density Filter (ONDF) NDC-50C-4M-A that allowed us to change the optical power with only small disturbance of the angular power distribution [5]. The ONDF was installed on a special mount with drive belt linked to a bipolar motor that can remotely be controlled with an Arduino board. A short fiber segment (30 cm) was connected to the laser mount, while its other end faces one side of the ONDF. The input end of a 70-cm fiber was placed on the other side of the ONDF and its output end joined to the receiver (SPD2). At the receiver side, we used the SPD-2-650 optical receiver. Finally, the output signal was received by the electronic RF board that further delivered it to the computer for required demodulation and analysis.

In order to analyze the impact of the received optical power, i.e., the impact of the link loss, on the downlink transmission of standalone NB-IoT, signals with that format at 925 and 960 MHz were generated and transmitted using the setup described before. The fiber

considered was a 1-meter segment POF, that presumably didn't introduce any attenuation or dispersion. Received optical power was varied through the described optical attenuator in a range from -4.54 dBm down to -19.4 dBm with 1-dB step. The results obtained from this setup will give us information about the transmission performance of the system when using different GI-POF lengths, since the main impairment introduced by this type of fiber is attenuation, being modal dispersion very low thanks to its index profile.

3.- Experimental Results

The transmission performance of the RoPOF link was obtained by the estimation of the EVM. In addition, we also calculated the ACPR, as this parameter shows the spectral regrowth when non-linear effects are present in the system. In fact, these effects are responsible of the performance degradation at high input RF power values.

Figures 2 and 3 show the results obtained when transmitting signals at 925-MHz and at 960-MHz carrier frequencies, respectively. In the left plots, EVM versus RF input power is represented for the different values of received optical power considered, which are shown in different colors. In the same way, the right plots show ACPR versus RF input power.

Regarding the EVM, results show excellent transmission performance for both carrier frequencies for a wide range of RF input power, for which EVM values are well below the standard limit of 17.5% defined by 3GPP for the QPSK NB-IoT. In fact, only when RF input power is higher than -6 dBm, that threshold is reached. We also observe that the curves for the different received optical powers rise at similar RF input power values, so that the non-linear behaviour doesn't depend on received optical power but on RF input power and therefore can be attributed to the transmitter side, that plays a major role except for the higher received optical powers (-5.47 and -4.54 dBm) as shown by the blue and red curves which rise at lower RF input power values.

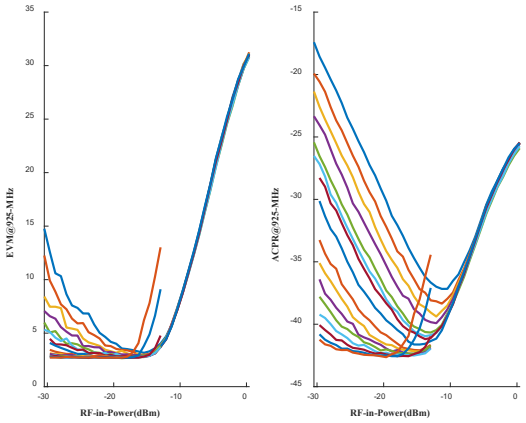

Fig 2. 925-MHz carrier frequency results: EVM (left) and ACPR (right) as a function of RF input power for different received optical power values (colors).

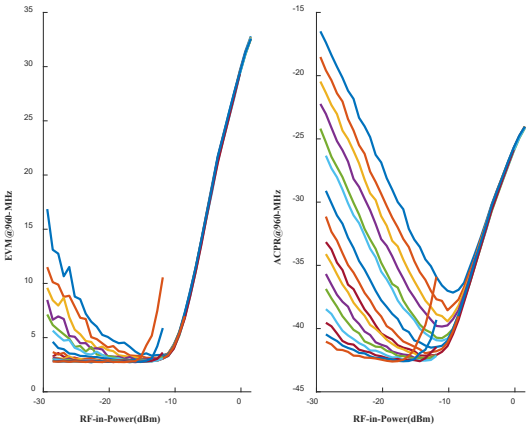

Fig 3. 960-MHz carrier frequency results: EVM (left) and ACPR (right) as a function of RF input power for different received optical power values (colors).

Regarding the ACPR, results show a similar behaviour in terms of the RF input power at which the system non-linear behaviour is predominant and spectral regrowth occurs. As for the minimum ACPR value obtained for each of the received optical power values considered, we observe significantly higher ACPR at lower values of the received optical power and a gradual reduction of this parameter as the optical power increases.

If we compare the results at the different carrier frequencies, they show similar behaviour, although both EVM and ACPR are slightly shifted to the right in the case of 960 MHz as compared to the 925-MHz case. This is consistent with the system frequency

response that introduces a slightly higher attenuation at the higher carrier frequency, so that the system allows slightly higher input RF power values.

In general, we conclude that both figures of merit, EVM and ACPR, show similar behaviour, although a detailed analysis of the RF input power at which the minimum values are found, which represent the operating point for optimum performance, would be desirable. From these measurements, we have extracted the minimum values of EVM and ACPR as a function of the received optical power. Results are shown in Figs. 4 and 5 for signal transmission at 925-MHz carrier frequency and at 960-MHz carrier frequency, respectively.

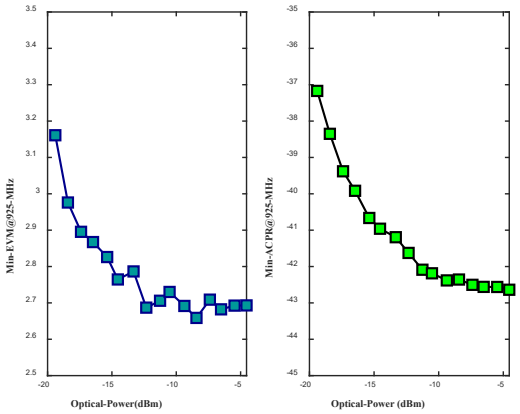

Fig 4. Minimum EVM (left) and minimum ACPR (right) as a function of received optical power at 925-MHz.

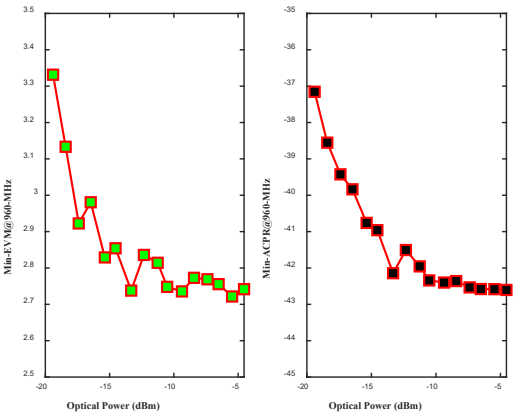

Fig 5. Minimum EVM (left) and minimum ACPR (right) as a function of received optical power at 960-MHz.

As can be observed, the highest values of minimum EVM and minimum ACPR are obtained with the lower received optical power, while the best minimum EVM and ACPR are obtained by increasing the optical power. In fact, we observe a gradual exponential-like decrease in both the minimum EVM and the minimum ACPR at both carrier frequencies when increasing the optical power.

When comparing 925 and 960-MHz results, we can conclude that there are practically no differences in the ACPR behaviour. Comparison in terms of EVM shows only small differences so that transmission quality is slightly better at 925 MHz than at 960 MHz Nevertheless, all minimum EVM results meet the standard quality limit set by 3GPP.

Finally, Figs. 6 and 7 show the results in terms of the RF input power necessary for minimum EVM (left plots) and for minimum ACPR (right plots) as a function of received optical power for 925 and 960-MHz carrier frequencies, respectively. As explained before in Figs. 1 and 2, when comparing results at both carrier frequencies we observe that less RF input power is required to get the minimum EVM and ACPR at 925 MHz than at 960 MHz. Also, it can be observed that both plots for both carrier frequencies show that RF input power values for minimum EVM and for minimum ACPR decrease approximately linearly when increasing the received optical power.

Moreover, it can be observed that the best RF input power value for minimum EVM in both carrier frequencies is lower than the RF input power for minimum ACPR for all the received optical power values and this difference varies from 1 dB to 3 – 4 dB. In any case, the EVM curves obtained in the standalone NB-IoT transmission are quite flat in an ample range of input RF power values, so that the choice of a suboptimal value for the input RF power of the system will probably lead to acceptable penalties, that should in any case be quantified.

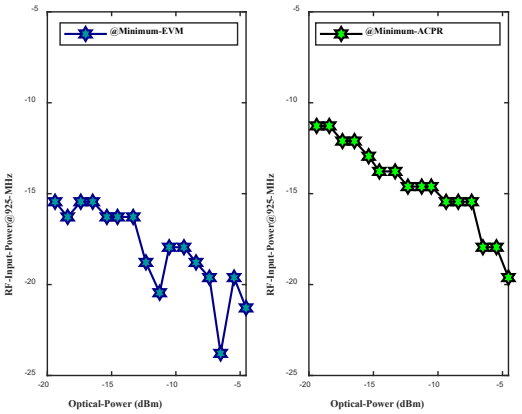

Fig 6. RF input power for minimum EVM (left) and for minimum ACPR (right) at 925-MHz carrier frequency.

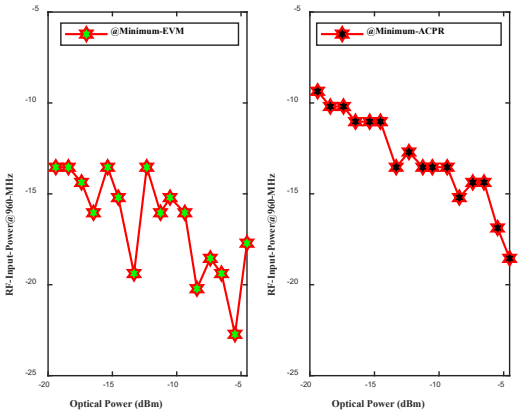

Fig 7. RF input power for minimum EVM (left) and for minimum ACPR (right) at 960-MHz carrier frequency.

4.- Conclusion

In this work, we have performed an analysis of the transmission performance of downlink standalone NB-IoT as a function of received optical power at carrier frequencies of 925 and 960-MHz. Results show that the optical power affects in a similar way the behaviour of EVM and ACPR as a function of input RF power. In any case, RF input power values at which minimum EVM and minimum ACPR are obtained present significant differences. This effect should be further analyzed in order to gain insight of the RoPOF link behaviour in terms of EVM and ACPR and to explore the feasibility of our previous proposal for complexity-reduced configuration of the link transmitter.

Acknowledgements: This research was funded by the Spanish Ministry of Science and Innovation (MIMICINN/FEDER), grant PID2021-122505OB-C33, and by the Aragón Government (DGA), grants T20-23R and T31-23R.

Reference

[1] Muhammad WASEEM, Alicia LOPEZ, Pedro LUIS CARRO, Ma ÁNGELES LOSADA, “Radio Over Plastic Optical Fiber Transmission for Short-Range Future Networks”, in *Proceedings of the 2022 Global Conference on Wireless and Optical Technologies (GCWOT)*, pp. 1–4, 2022.

[2] Julio CESAR MOLINA RAMIREZ, *Digital Signal Processing on FPGA for Short-Range Optical Communications Systems over Plastic Optical Fiber* (Politecnico di Torino, 2012).

[3] Muhammad WASEEM, Alicia LOPEZ, Pedro LUIS CARRO CEBALLOS, María ÁNGELES LOSADA BINUE, et al., “Evaluation of Radio over Plastic Optical Fiber Communications”, *Jornada de Jóvenes Investigadores del I3A*, vol. 10, 2022.

[4] Tetsuya KAWANISHI, *Handbook of Radio and Optical Networks Convergence* (Springer Nature, 2024).

[5] Christina LIM, Ampalavanapillai NIRMALATHAS “Radio-over-fiber technology: Present and future”, *Journal of Lightwave Technology*, vol. 39, no. 4, pp. 881–888, 2020.

[6] Gaurav PANDEY, Amol CHOUDHARY, Abhishek DIXIT, “Wavelength Division Multiplexed Radio Over Fiber Links for 5G Fronthaul Networks”, *IEEE Journal on Selected Areas in Communications*, vol. 39, no. 9, pp. 2789–2803, 2021.

[7] Jun SHAN WEY, Junwen ZHANG, “Passive Optical Networks for 5G Evolution”, in *Proceedings of Broadband Access Communication Technologies XII*, pp. 127–132, 2018.

[8] C. VAZQUEZ, D. S. MONTER, W. Ponce, P. C. LALLANA, D. LARRABEIT, J. MONTALVO, A. TAPETADO, P. J. PINZON, “Multimode Fibers in Millimeter-Wave Evolution for 5G Cellular Networks”, in *Proceedings of Broadband Access Communication Technologies X*, pp. 93–98, 2016.

[9] Aadil RAZA, Salman GHAFOOR, Muhammad FASIH UDDIN BUTT, "MIMO-enabled Integrated MGDM–WDM Distributed Antenna System Architecture Based on Plastic Optical Fibers for Millimeter-Wave Communication", *Photonic Network Communications*, vol. 35, pp. 265–273, 2018.

[10] T. AIBA et al., "28 GHz Band 5G Mobile Radio Signal Transmission Employing Graded-Index Plastic Optical Fibers", in *Proceedings of the 28th International Conference on Plastic Optical Fibers*, pp. 43–44, 2019.

[11] Azusa INOUE, Yasuhiro KOIKE, "Low-Noise Radio Over Graded-Index Plastic Optical Fiber", *Optics Letters*, vol. 45, no. 12, pp. 3192–3195, 2020.

[12] Diego F. PAREDES-PALIZ, Guillermo ROYO, Francisco AZNARz, Concepción ALDEA, Santiago CELMA, "Radio over fiber: An alternative broadband network technology for IoT", *Electronics*, vol. 9, no. 11, p. 1785, 2020.

[13] Kenta MURAMOTO, Azusa INOUE, Yasuhiro KOIKE, "Noise and Distortion Reduction in OFDM Radio-over-Fiber Link by Graded-Index Plastic Optical Fiber", *IEEE Photonics Technology Letters*, vol. 32, no. 13, pp. 835–838, 2020.

[14] Marcelo M. WERNECK, Regina CELIA S. B. ALLIL, *Plastic Optical Fiber Sensors: Science, Technology and Applications* (CRC Press, 2019).

[15] F. FORNI, "Indoor Optical Network Technologies for Multiple Services Provisioning", 2018.

[16] Mohamed ATEF, Horst ZIMMERMAN, *Optical Communication Over Plastic Optical Fibers: Integrated Optical Receiver Technology* (Springer, 2012).

[17] Kenta MURAMOTO, Azusa INOUE, Yasuhiro KOIKE, "Nonlinear Distortion Reduction Effect of Graded-Index Plastic Optical Fiber", *IEEE Photonics Technology Letters*, vol. 31, no. 10, pp. 791–794, 2019.

[18] Federico FORNI, Yipeng SHI, Nguyen Cac TRAN, HP A van den BOOM, Eduward TANGDIONGGA, AMJ KOONEN, "Multiformat Wired and Wireless Signals Over Large-Core Plastic Fibers for In-Home Network", *Journal of Lightwave Technology*, vol. 36, no. 16, pp. 3444–3452, 2018.

[19] Muhammad WASEEM, Alicia LÓPEZ, Pedro LUIS CARRO, María ÁNGELES LOSADA, "Cellular Guardband NB-IoT Performance Over PMMA Plastic Optical Fibers", *Journal of Lightwave Technology*, vol. 41, no. 23, pp. 7302–7308, 2023.

[20] Wai Pang NG, Thavamaran KANESAN, Zabih GHASSEMLOOY, Chao LU, "Theoretical and Experimental Optimum System Design for LTE-RoF Over Varying Transmission Span and Identification of System Nonlinear Limit", *IEEE Photonics Journal*, vol. 4, no. 5, pp. 1560–1571, 2012.

[21] Muhammad WASEEM, Alicia LÓPEZ, Pedro LUIS CARRO, María ÁNGELES LOSADA, "Evaluation of Transmission Performance in LTE+ NB-IoT Radio over Large-Core Plastic Optical Fiber Systems", in *Proceedings of the 30th International Conference on Plastic Optical Fibers*, 2022.

[22] Muhammad WASEEM, Alicia LÓPEZ, Pedro LUIS CARRO, María ÁNGELES LOSADA, "Complexity-Reduced Estimation of the Transmitter Parameters in Radio Over PMMA Graded-Index POF", in *Proceedings of the 24th International Conference on Transparent Optical Networks (ICTON)*, pp. 1–4, 2024.

Machine Learning based Non-Linear Model of Radio over large-core SI-POF in 5G/ NB-IoT scenarios

Pedro L. CARRO, María Ángeles LOSADA, Muhammad WASEEM, Alicia LÓPEZ, Paloma GARCÍA-DÚCAR, Jesús DE MINGO, Antonio VALDOVINOS, Javier MATEO.

Departamento de Ingeniería Electrónica y Comunicaciones, Instituto de Investigación en Ingeniería de Aragón (I3A), Universidad de Zaragoza, Zaragoza, 50018, España.

Contact Person: Pedro L. Carro (plcarro@unizar.es).

ABSTRACT:

In this work, we introduce a Matching Learning based model (MLP) of the non-linear behavior of a Radio over Plastic Optical Fiber (RoPOF) link adapted to Orthogonal Frequency Division Multiplexing (OFDM) signals and validated by the transmission of 5G / Narrow-Band Internet of Things (NB-IoT) of Poly(methyl methacrylate) (PMMA) Step-Index (SI) large-core POFs.

Key words: Large-core PMMA SI-POF, Radio over Fiber, modeling, non-linearities, NB-IoT, Matching Learning

1.- Introduction

The In short-reach environments with moderate bandwidth requirements, transmission of radio signals through Plastic Optical Fibers (POFs) is a potential solution to implement the wired backbone in fast deployments of Internet of Things (IoT) services at low cost and with the added advantage of ruggedness and resistance [1]. In fact, POFs are easily coupled to cost effective sources, such as visible-light laser diodes, that can be directly modulated with analogue signals to avoid the use of expensive external modulators. However, Narrow-Band IoT (NB-IoT) signals are transmitted using Orthogonal Frequency Division Multiplexing (OFDM) with a high Peak to Average Power Ratio (PAPR) that, combined with direct laser modulation, is a source of non-linear distortion [2]. In this work, we present a behavioral model [3] of a Plastic Optical Fiber (POF) link, based on the improved Machine Learning model whose parameters are empirically obtained, and revised to accommodate OFDM signals. Our approach provides a simple way to assess the impact of the component non-linearities over the Radio over POF (RoPOF) link performance at high RF powers, and to determine the limits of the usable range of Radio-Frequency (RF) powers.

The paper is organized as follows. First, we introduce our approach, which is based on the Multi-layer Perceptron model and adapted to model Radio-over-Fiber (RoF) links. Second, we describe our experimental set-up to implement a RoPOF link using a laser diode directly modulated by the RF signals, and explain the procedure applied to obtain the free model parameters from the results of the one-tone and the two-tone intermodulation tests. Our analysis included a PMMA 1mm-core SI-POF and one frequency band of the NB-IoT standard: 925 MHz. Then, we apply the model to simulate the RoPOF link, and to calculate the Error Vector Magnitude (EVM). Model predictions are compared to the experimental results of the transmission of standalone NB-IoT to validate the model. Finally, we summarize our results and present our conclusions.

2.- Machine Learning based MLP Model

ML algorithms have been in recent years considered as an interesting solution for

practical modeling of nonlinear systems such as wireless transmitters or Radio over Fiber architectures. An artificial Neural Network (ANN) can be used for predicting the distortion suffered by the transmitted signals based on regression operation. In this case, a supervised ANN can learn a behavioral model given its input and output samples. In this work, we have we have chosen a Multi-Layer Perceptron (MLP) for developing the ANN-based model, since it can be successfully deployed to represent continuous variables with nonlinear behavior. Despite its simplicity, the MLP can be efficiently used for modeling the RoF system under different excitations and in contrast to other works may be augmented to include some memory effects without the need of using other topologies such as Recurrent Neural Networks.

Other differences with previous works [4], [5] stem from the fact that Plastic Optical Fiber based Radio over Fiber architectures have not been considered until now with this kind of models and with direct laser modulation, as it is usual in these systems. Furthermore, ML algorithms can be viewed as a reliable and versatile complex solution with modeling performance similar to the classic Volterra models and can even outperform classic models since they have remarkable nonlinear representation and generalization capacity.

2.1.- Multi-layer Perceptron Model

A generic MLP model is composed of L+1 layers containing K_l neurons per layer. The ANN is fed by a data set containing not only the real and imaginary parts of the considered waveform sample, but also from previous samples to include memory up to certain specified memory depth. The target labels are the instantaneous real and imaginary parts from the distorted 5G/ NB-IoT signal [6] at the photodiode output. Thus, the output signal will contain distortion effects due to the laser, the POF frequency response and detector which lead to a performance degradation in terms of EVM and BER due to linear and nonlinear phenomena and noise. The neural network carries out nonlinear transformations on the 5G/ NB-IoT signals to model the RoPOF system distortions. Given an input vector **y**, which in this case contains also the delayed signal samples computes

$$\mathbf{x} = f\left(\mathbf{W}\times\mathbf{y}+\mathbf{b}\right) \quad (1)$$

and minimizes an averaged loss function $L(.)$ according to the training sample size N

$$L\left(\mathbf{W},\mathbf{b}\right)=\frac{1}{N}\sum_{n=0}^{N-1}\ell\left[s\left(n\right),\hat{s}\left(n,\mathbf{W},\mathbf{b}\right)\right], \quad (2)$$

where **W** is a matrix containing the MLP weights, **b** is a bias vector and $f(.)$ and $l(.)$ are called activation and loss function respectively.

In order to fit the model every parameter must be carefully chosen so that a good modeling performance can be achieved. In this work, we will focus on the classical Minimum Square Error (MSE) and the remaining features will be chosen according to the measured signals.

3.- Experimental Setup

Figure 1 shows the experimental setup designed for downlink 5G/NB-IoT transmission over PMMA large-core SI-POFs. After generation, the signal was passed through an ADALM Pluto platform that performed the analogical to digital conversion. This signal was then amplified using the ZHL-4240 amplifer to reach the desired input RF power (P_{RFin} in the schematic) to directly modulate the optical source through the LDM9T laser mount. As the required RF powers for the longest fibers tested were very high, the amplifier was enclosed in a shielding box to avoid wireless signal direct transmission to the platform. In any case, the RF power was limited to guarantee that the amplifier was working well below its linear range. The optical source was a laser diode (L515A1) with a measured threshold current of 28 mA, nominal emission power of 10 mW, and a maximum recomended bias current of 120 mA. Thus, the L515A1 offers an ample operating range that permits modulation with high RF powers without exceeding its limits which could trigger non-linear behavior. Its peak wavelength is at 515-nm where PMMA SI-POFs have lower attenuation than at the conventional red light .

The optical signal at the output of the laser source was transmitted through different SI-POFs. The analyzed SI-POFs were all manufactured by Mitsubishi: MH4001 (MH), termed ESKA-MEGA, is a fiber with a NA of 0.3, achieved by a double-cladding design and is recommended for broadband transmission; In the experiments, available reels of different lengths were directly used, but other fiber lengths were achieved by connecting two reels with ST connectors. Finally, at the receiver side, we used the SPD-2-520 optical receiver, optimized for green light and with a 3-dB bandwidth of 1.2 GHz. The SPD output signal (P_{RFout}) was fed to the electronic board that further delivered it to the computer for processing.

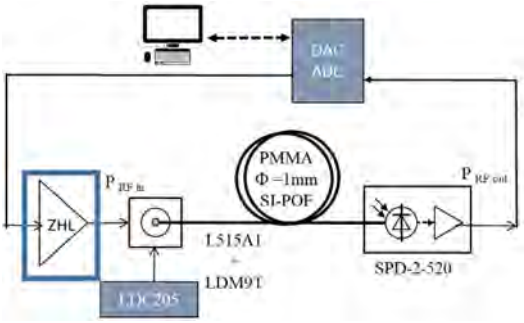

Figure 1. Experimental setup for transmission of downlink Standalone NB-IoT through SI-POFs.

We tested the transmission of downlink Standalone NB-IoT with two carriers, 925 MHz and 960 MHz through the three different fibers and several lengths, optimizing the laser operation current for each case. We found that a bias current of 110 mA produced the best results except for the 50-m MH fiber. In this case, we used 90 mA to avoid saturation. For each condition, we obtained Adjacent Channel Power Ration (ACPR) and Error Vector Magnitude (EVM). In addition, the received optical power and the frequency response were measured just before transmission. In the next section, we present and discuss the results.

4.- Results and Discussion

4.1.- Nonlinear operation evaluation

Figure 2. shows the EVM results with 60 m, 65 and 70 m of the MH fiber as a function of RF-input power for 925 MHz. The straight black lines mark the limits stablished by the standard: 8% for the 16-QAM 5G and 17.5% for the NB-IoT signals, respectively. As expected, the performance in terms of EVM is achieved when shorter fiber lengths are considered. In addition, the suitability of the Radio over SI-POF link under these distances is confirmed because for certain power ranges the EVM is well below the maximum allowed specified required standard value.

Moreover, the power ranges within nonlinear operation are clearly identified. This allows to set up the input power considered for modelling purposes in this work, which is around 17 dBm.

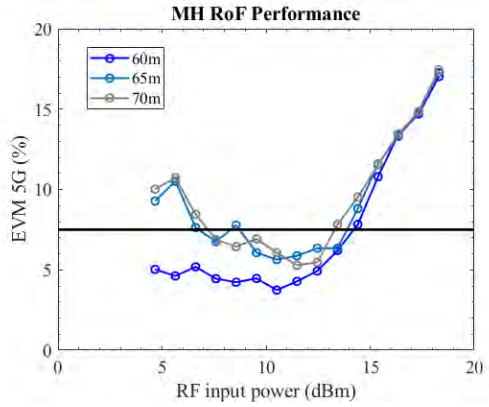

Fig. 2: EVM performance for 5 MHz 5G (LTE compatible) waveform.

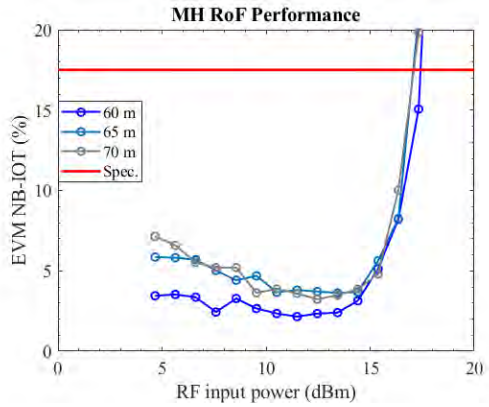

Fig. 3: EVM performance for 6 dB boost NB-IoT waveform.

4.2.- Modeling parameters and Performance

Fig. 4 shows the evaluated MLP ANN architecture implemented in this paper. It actually comprises two different MLPs with one single hidden layer, one for the real part

of the output and the other for the imaginary part. Although it is possible to use just one single MLP with more hidden layers with two outputs, authors have chosen two different ANNs as a first approach to identify possible source of errors and provide more flexibility. In addition, to improve accuracy and without loss of generality, input and output waveforms have been normalized to their maximum envelope values.

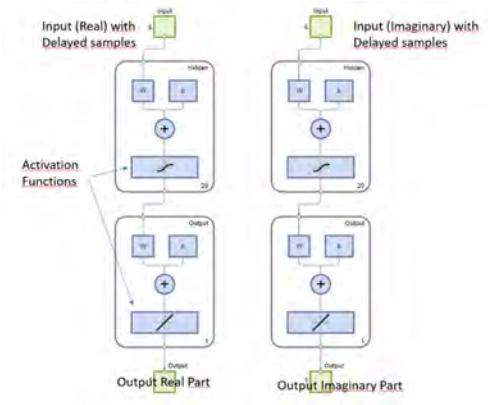

Fig. 4: ANN MLP architecture

Firstly, the impact of the hidden layer size (i.e number of neurons per layer and per feature) and memory depth with a tanh(.) activation function are investigated applied to the output with a Radio over POF system length about 60 m due to its performance.

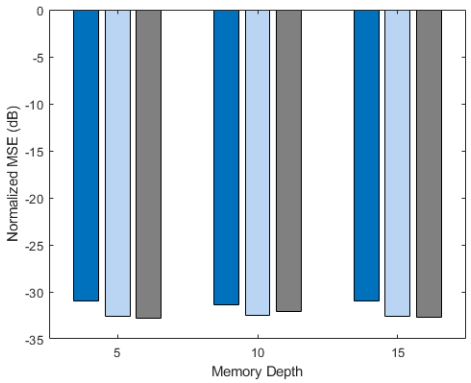

Fig. 5: Hidden Layer Size and Memory Depth Analysis

The NMSE error reveals that, as expected the number of neurons can improve the identification process. However, there is not a significative difference between 20 and 30 neurons, and thus, taking into account the complexity, the remaining experiments will be carried out with a hidden layer size of 20. As far as the memory depth is concerned, a value of 5 is high enough to include memory effects in the model.

Furthermore, Table I and II shows the identification errors (NMSE) and the loss function (MSE) value achieved when the algorithm is performed with two different activation functions and different lengths. In addition to test the effectivity of the memory depth, Table I provides results memoryless results.

Length	Error (dB) f=tanh		Error (dB) f=satsig	
	MSE	NMSE	MSE	NMSE.
60	-33.09	-23.16	-32.91	-22.99
65	-27.56	-17.56	-27.51	-17.49
70	-29.16	-19.36	-28.99	-19.19

Table I: Memoryless MLP identification results.

Length	Error (dB) f=tanh		Error (dB) f=satsig	
	MSE	NMSE	MSE	NMSE.
60	-42.5	-32.56	-38.42	-28.49
65	-37.35	-27.34	-35.91	-25.9
70	-37.36	-27.56	-34.46	-24.66

Table II: MLP identification results with a memory depth of value 5.

As conclusion, the inclusion of the memory in the model improves around 10 dB the identification for every tested length. In addition, we see a performance degradation in the identification the longer the fiber is. A reason for that may be that the waveform signal to noise is worse when greater fiber lengths are considered.

Finally, it is important to pay attention not only to the time domain results quantified by means of the NMSE, but also to frequency domain results. Fig. 6 and Fig.7 show the power spectral densities corresponding to the measured and modeled signals. Results confirm that the model can model the signal in the frequency domain at least in the adjacent channel and the main channel as well. However, a performance degradation is seen when farther channels are considered due to increase in fiber length and worst quality

output signal. Nonetheless, results seems to be enough accurate to predict the nonlinear behavior.

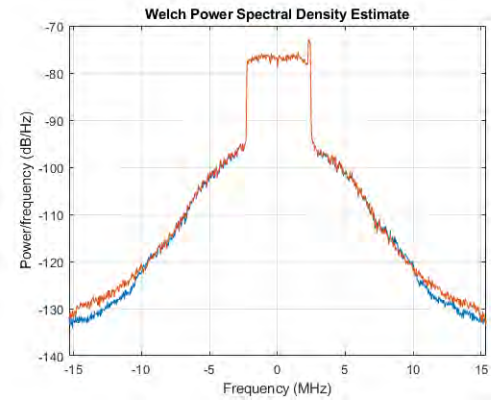

Fig. 6: Meas. (Orange) vs Model (blue) PSD for SI-POF with 60 m in length.

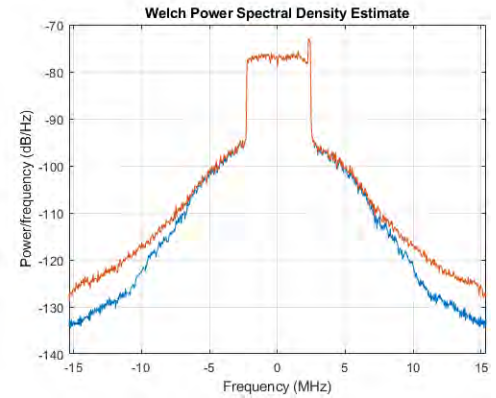

Fig. 7: Meas. (Orange) vs Model (blue) PSD for SI-POF with 65 m in length.

5.- Conclusion

In this work, we introduce a model of the non-linear behavior of a Radio over Plastic Optical Fiber (RoPOF) link adapted to Orthogonal Frequency Division Multiplexing (OFDM) signals and validated by the transmission of 5G / Narrow-Band Internet of Things (NB-IoT) of Poly(methyl methacrylate) (PMMA) Step-Index (SI) large-core POFs. Results show that a MLP Neural Network can model the system with enough accuracy so that the model can serve to predict performances. In addition, the suitability of the Radio over POF system for NB-IoT in the considered scenario is confirm with fibers around 70 m in length.

Acknowledgements: This research was funded by the Spanish Ministry of Science and Innovation (MIMICINN/FEDER), grant PID2021-122505OB-C33, and by the Aragón Government (DGA), grants T20-23R and T31-23R.

References

[1] [1] K. Muramoto, A. Inoue and Y. Koike, "Noise and Distortion Reduction in OFDM Radio-Over-Fiber Link by Graded-Index Plastic Optical Fiber," IEEE Photonics Technol. Lett., vol. 32, no. 13, pp. 835-838, July 2020.

[2] Y. Koike and K. Muramoto, "Proposal of Error-Free GI POF for Beyond 5G Society," 2024 Conference on Lasers and Electro-Optics Pacific Rim (CLEO-PR), Incheon (Korea), pp.1-2, 2024.

[3] L. C. Vieira, and F. van Dijk, “Behavioral Modeling of Radio-over-Fiber Links Using Memory Polynomials,” IEEE International Topical Meeting on Microwave Photonics, Oct. 2010.

[4] L. A. M. Pereira, L. L. Mendes, C. J. A. Bastos-Filho and A. C. S. Jr, "Machine Learning-Based Linearization Schemes for Radio Over Fiber Systems," in IEEE Photonics Journal, vol. 14, no. 6, pp. 1-10, Dec. 2022.

[5] D. Wang, M. Aziz, M. Helaoui and F. M. Ghannouchi, "Augmented Real-Valued Time-Delay Neural Network for Compensation of Distortions and Impairments in Wireless Transmitters," in IEEE Transactions on Neural Networks and Learning Systems, vol. 30, no. 1, pp. 242-254, Jan. 2019.

[6] F. Forni, *et al.*: Multiformat Wired and Wireless Signals Over Large-Core Plastic Fibers for In-Home Network, *J. Lightw. Technol.*, vol. 36, no. 16, pp. 3444-3452, 2018.

Sensores ópticos

Portable pressure and gait sensing system with plastic optical fibers

Aurélia Marchand [(1)], Javier Barco[(1)], Rubén Sánchez-Gómez[(2)], Carmen Vázquez[(1)]

1. Electronics Technology Department, University Carlos III, Av. De la Universidad 30, CP-28911 Leganés, Madrid, Spain
2. Nursing Department, Universidad Complutense de Madrid, 28040, Madrid, Spain; rusanc02@ucm.es

Contact: Carmen Vázquez cvazquez@ing.uc3m.es.

ABSTRACT:

The way the pressure is distributed on the foot has a huge impact on the patients' health. Therefore, it is necessary to be able to measure it with precision and accuracy. So far, several possibilities exist but measuring remains expensive, lacks portability, inclusiveness or efficiency. This paper presents a new in-shoe device using the macro-bend propriety of plastic optical fiber in a way that makes it possible to adapt the position of each sensor on the insole. The system was tested to verify the ability of using it to measure the plantar pressure in movement and characterize its main properties.

The results shows that even though it is very customizable, it does not lose its ability to be used to monitor the plantar pressure in a large variety of situations.

Key words: plastic optical fiber, gait, macro-bend sensor, pressure, portable, insole, in-shoe system, portable, IoT, Bluetooth Low Energy.

1.- Introduction

The plantar pressure is defined as the strength exerted by the foot on the ground at a moment of contact. It can happen while standing, walking, running or jumping and the way it is distributed on the foot can be both a cause and a consequence of illness. Thus, checking it can enlighten foot pathologies or abnormalities in the walking style, prevent the patient from getting hurt the way he/she walks or runs, it can also improve sport performance, and prevent the development of ulcers in diabetic patients [1].

With the purpose of monitoring it, different systems have been developed that can be separated into two main categories: platforms and in-shoe systems. Platforms are flat and stationary devices stuck to the floor. The patient can either stand on it or walk through it, passing by the centre to ensure the best accuracy possible. Anyway, to get representative values, some space around it is necessary so that the patient can walk normally [2]. Those constraints have led to the development of another kind of system: the in-shoe device. It is a flexible device that can be put in the shoe of the patient enabling a real dynamic study of the gait. To measure the pressure, different sensing principles can be used: resistive, capacitive or piezoelectric among others [3]. Nevertheless, studying the gait or the plantar pressure remains expensive, restricted to a narrow patient weight range and sometimes lacks accuracy.

Using plastic optical fibre (POF) sensor can be an alternative thanks to its characteristics. It has a low price, is flexible, compact and it is as easy to implement as it is to process the output signals. For those reasons, several devices have already been developed [4] mainly using the Fibre Bragg Grating (FBG). However, few uses the fact that the fibre loses optical power when being macro-bended. It has been proven that the output tension resulting from the bending is linked proportionally to the applied pressure [5] and some preliminary tests on gait measurements were reported. Yet the system is focused on measuring the average value of the normal force resulting from the applied pressure, it has poor portability and a limited insole ergonomics.

In this work we proposed a new portable pressure and gait instrumentation system based on adaptable POF macro-bend sensor with wide measuring force range and bandwidth allowing dynamic pressure and gait measurements.

2.- The system mechanism and design

2.1.- The sensing system

The system, see Fig.1, uses the POF fiber transmitting the light, coming from a polarised LED emitting at 650 nm. Two conditioning circuits, on the emission and receptions sides respectively generate the right voltage to forward bias the LED while flowing a constant current and amplify the photogenerated current at the photodiode through a transimpedance amplifier. In a first configuration, the fibre sensor has a loop shape as in [5], placed where the pressure is to be measured and fixed on an insole that can be put in a shoe, see Fig.2.

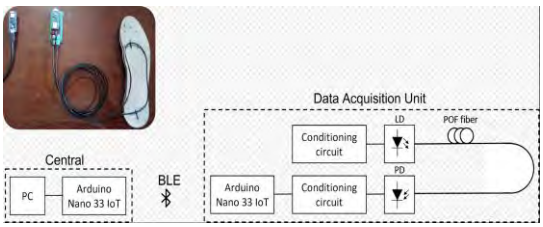

Figure 1: Schematic (down) and photo (top left) of the sensing system.

The other side of the fibre is connected to a photodiode that converts the light received into an electrical current. After being conditioned, the voltage signal is acquired by an Arduino Nano 33 IoT acquisition card and sent using Bluetooth Low Energy (BLE) to the PC where the signal is processed. The signal can be sent up to a distance of 100 m [7]. The data is acquired at a frequency of 1 kHz. However, to reduce the noise linked to both cards, it is necessary to average the values which decreases the period between averaged measurements down to 0.1 s.

The conditioning circuits, on the protoboard back side, adapt the voltages to obtain the widest output signal span following equation (1) where V_{offset} and α are parameters related to the electronic circuit, I the photocurrent generated by the photodiode at the output of the fibre and V_{out}, the output voltage connected to the acquisition card.

$$V_{out} = V_{offset} - \alpha * I \qquad (1)$$

The portable parts including sensing, detection, acquisition and wireless transmission are powered by a 2000 mAh external battery.

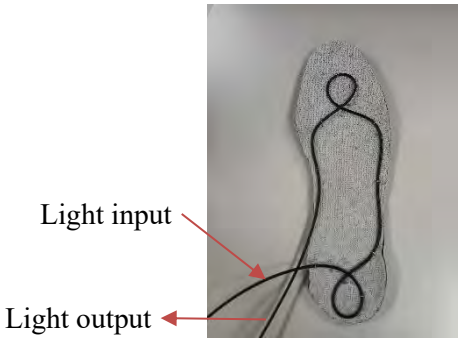

Figure 2: Photo of the loop sensor placed on the sensitive areas on the insole.

2.2.- Comparison of expected POF sensor characteristics with commercial devices

To evaluate the competitiveness of the proposed system and consider possible improvements we first compare its performance with current commercial systems, see Table I.

In the positive side, our POF system has a lower price and larger measuring range and

Table I: Comparison of gait commercial sensing systems and our proposal.

	This work	***Teckscan*** [8]	***Pedar*** [9]	***GIMA*** [10]
Measure type	*Pression*	*Pression*	*Pression*	*Footprint*
Sensing technology	*POF*	*Resistive*	*Resistive*	*N/A*
Number of sensors	*>2*	*966*	*84-99*	*N/A*
Acquisition Frequency (Hz)	*1000*	*Up to 500*	*50 to 100*	*N/A*
Maximum weight (kg)	*>400*	*No data*	*No data*	*135*
Measuring Range (kPa)	*>20000**	*345-862*	*15-600*	*N/A*
Technology for portability	*BLE*	*Micro-SD card*	*Wi-Fi*	*Non portable*
Weight of the electronic system(g)	*101*	*133* [11]	*54*	*N/A*
Price (€) [12]**	*<150*	*~15400*	*~17000*	*530*

*SD =Secure Digital. *Calculated by approximatively overrating the surface area of the sensing node (as the pressure amounts to the force of gravity divided by the surface area of the sensor)*

***The prices displayed come from the conversion in euro from pound given the value of the euro in 2016, as used in [10]. Only indicative as the commercial systems include specific software capabilities*

sensitivity. This means that the system could be used in a lot of different applications (sports for example) and with any patient without weight limit. On the other hand, the main issue is the number of sensors.

However, although there are not as many sensors on the insole, the average value is good enough and the system has a high adaptability: sensors can be added or removed depending on the needs of the podiatrist.

2.3.- Normalization and calibration

To calibrate foot pressure sensors, two main methods exist: either to put the sole under a bladder full of air at a known pressure [13] or the user of the sole stands on one foot to put all the weight on the sensor. The downside of the second method is that it can lack precision and repeatability given that the way the participant stands can change slightly between each measurement and not be natural. However, it gives fast results and a first order of magnitude of the output. Thus, it is the process used for this work.

The participant putting weight on one sensor will return a reference. Additionally, when the system is at rest, the output is a constant non-zero value as can be observed in Fig.3. The difference between those two measured values, named dV or reference, is used to compare the future measurements and represent them as a percentage of the body weight as illustrated by equation (2). This normalization is done by looking for the minimum of the set, V_{min} and then dividing the difference between each value and this minimum by the reference.

$$V_{normalized} = \frac{V_{out} - V_{min}}{dV} \quad (2)$$

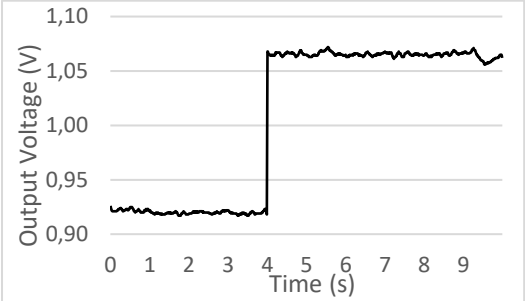

Figure 3: Output voltage during the calibration process, corresponding to voltage without any weight (0-4 s) and with body weight (4-9 s).

2.4.- Experimental procedures

The sensor loop shape of Fig.2 has shown good results and accuracy [5]. However, it requires a lot of space and lacks adaptability. To tackle this, another shape is considered. It is based on the same principle and measurement method but reduces the amount of fiber and area needed by making the fiber curb around a little piece of hard material and not around itself. However, although it is more practical because it makes it easier to change the location of the sensors if needed or wanted for the experiments, it is necessary to verify that it does not undermine results compared to the loop shape. In that view, a comparative study can determine the effect of the change on the average output voltage. To this end, a load test is performed five times using the body weight.

In another experiment, the shape of the curve is to be validated. To do so, four sensors are positioned on the sole at the heel, the midfoot, the second metatarsal and the toe. The participant takes a step, very slowly.
Lastly, dynamic tests are performed using two sensitive areas. The participant walks for forty seconds with a steady rhythm and step length to study the repeatability of the sensor.

2.5.- Participants

One healthy control participant (age 23, Body Mass Index (BMI): 21.6) performs the test.

3.- Results

3.1.- Effect of the sensor's shape

As previously discussed, two different sensor shapes are going to be analyzed. With a loop shape named type A sensor, the sensitive area is a loop where the change of intensity is generated mostly by the flexion of the fiber at the crossing. Although it delivers consistent results, its size and the difficulty to increase the number of sensors on the sole make it interesting to consider another shape.
The straight shape is named type B, and is based on a piece of hard and thin material that makes the fiber curb around when pressure is applied. A tiny piece of POF works.
The experiments are conducted for two sensitive areas, at the heel and the third metatarsal at the fore foot: first with B shape and then with A shape, using the same fiber and without disconnecting it to proceed with the exact same experimental conditions. Values are normalized with the reference obtained with the calibration of the B shape.
Two tests are performed. First, the participant stands and does not move for several seconds. Then, the participant walks slowly taking five steps. Each test is repeated five times.
Table II illustrates the results showing the average normalized value, the average of the standard deviation within each set (σ) and the coefficient of variation (CV, defined as the ratio of the standard deviation to the average) for each kind of sensor. According to the results, for the same load, the output voltage for the straight shape is worth only 74% of the loop result. It means that the shape A is more sensitive to very low weights but that shape B can be used with heavier participants. What's more, the coefficient of variation and the average of the standard deviation for each experiment are lower for the shape B. This means that the values of the latter vary less and, thus, that it has better stability.

Figure 4: Photo of the insole with the B sensor's shape.

Table II: Comparison of different sensor shapes

	A (loop)	*B (straight)*
Normalized value	*1.45*	*1.08*
Average σ	*0.004*	*0.003*
CV	*0.013*	*0.004*

Therefore, for its stability, tininess and practicality given that it can be put wherever the fiber passes in the insole, it is more advantageous to use a straight sensor.

3.2.- Validation of the shape of the gait response with four sensing areas

Various studies have proven that the gait follows a pattern, having the shape of an M [14].

The gait cycle can be divided into two mains phases: the stance and the swing. The stance occurs when the heel strikes the ground with an acceleration, then the foot gets full contact with the floor and finally the toes is the last part touching the ground, coming off accelerating. The output magnitude, that is proportional to the input pressure, should reach a peak when the heel gets in contact with the ground, then decrease down to a local minimum when the whole shoe touches the surface and finally reach a second peak when the foot takes off and enters the stance phase.

In the previous work [5], the pattern had been validated for two sensors, placed at the heel and at the toe of the foot. However, to be fully able to confirm the shape, this M should also be obtained when more sensors are used.

To verify this, four sensors are placed on the sole: at the heel, the midfoot, the second metatarsal and the toe, see Fig.5, and the insole was placed in the shoe. The participant is asked to take a step very slowly.

Figure 5: Picture of the insole and sensor location for the validation of the M- shape response.

The results, shown in Fig.6, underline that the M-shape remains even though the number of sensors increases, which validates the use of this technology to monitor the gait.

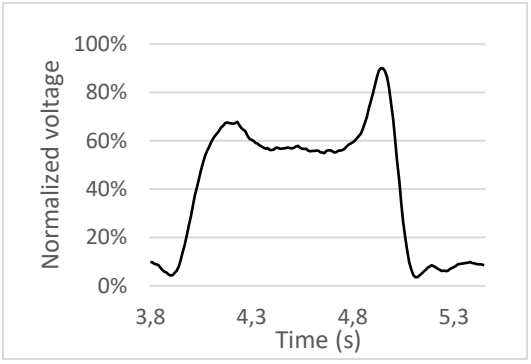

Figure 6: Evolution of the normalized voltage over time when the participant takes a 60 cm step.

3.3.- Dynamic analysis

For the device to be efficient and clinically usable, it must return the same value each time the same experiment is performed. To verify it, the participant is asked to walk for forty seconds at a 3 km/h speed on a training mill. The insole was put in the right shoe with four sensors on it, at the heel and at the first, third and fifth metatarsal.

About twenty-five seconds of the normalized output voltage are shown in Fig.7 below. Again, the curve follows the known pattern and the coefficient of deviations of the peak's values, shown in Table III, emphasize the repeatability of the system, being 3.5% and 6.1% respectively.

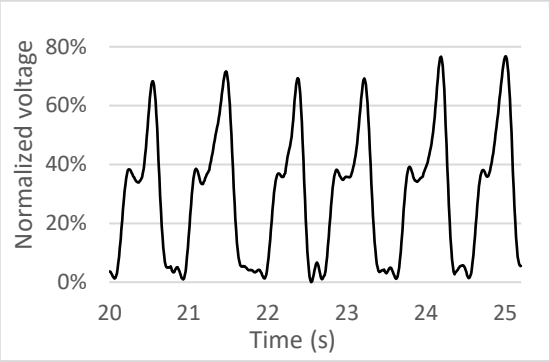

Figure 7: Evolution of the voltage over time when the participant walks for one minute.

Table III: Average and coefficient of variation of the peak value of each walking period

	First peak	Second peak
Average	0.38	0.73
CV	0.035	0.061

5.- Conclusions

The developed POF system is very portable, can operate for several hours in a row and is easy to adapt thanks to the shape of the sensing areas. Its accuracy and portability have been tested and show good results which make it suitable for long-lasting and dynamic measurements.
The way to calibrate as well as the stability of the results might still need further investigation.

References

[1] R. Gary Sibbald and K. Y. Woo, 'The biology of chronic foot ulcers in persons with diabetes', *Diabetes Metab. Res. Rev.*, vol. 24, no. S1, pp. S25–S30, 2008, doi: 10.1002/dmrr.847.

[2] A. H. Abdul Razak, A. Zayegh, R. K. Begg, and Y. Wahab, 'Foot Plantar Pressure Measurement System: A Review', *Sensors*, vol. 12, no. 7, Art. no. 7, Jul. 2012, doi: 10.3390/s120709884.

[3] P. Castro-Martins, A. Marques, L. Coelho, M. Vaz, and J. S. Baptista, 'In-shoe plantar pressure measurement technologies for the diabetic foot: A systematic review', *Heliyon*, vol. 10, no. 9, p. e29672, May 2024, doi: 10.1016/j.heliyon.2024.e29672.

[4] M. F. Domingues *et al.*, 'Insole optical fiber Bragg grating sensors network for dynamic vertical force monitoring', *J. Biomed. Opt.*, vol. 22, no. 9, p. 091507, Feb. 2017, doi: 10.1117/1.JBO.22.9.091507.

[5] S. Safarloo, A. Núñez-Cascajero, R. Sanchez-Gomez, and C. Vázquez, 'Polymer Optical Fiber Plantar Pressure Sensors: Design and Validation', *Sensors*, vol. 22, no. 10, Art. no. 10, Jan. 2022, doi: 10.3390/s22103883.

[6] S. Savović, A. Djordjevich, and I. Savović, 'Theoretical investigation of bending loss in step-index plastic optical fibers', *Opt. Commun.*, vol. 475, p. 126200, Nov. 2020, doi: 10.1016/j.optcom.2020.126200.

[7] 'Maximizing BLE Range'. Accessed: Feb. 03, 2025. [Online]. Available: https://www.argenox.com/

[8] 'F-Scan GO System | In-Shoe Pressure Measurement Foot Function Gait Analysis System | Tekscan'. Accessed: Jan. 24, 2025. [Online]. Available: https://www.tekscan.com/products-solutions/systems/f-scan-system

[9] 'pedar insole details', novel.de. Accessed: Jan. 24, 2025. [Online]. Available: https://novel.de/products/pedar/pedar-insole-details/

[10] Accessed: Jan. 24, 2025. [Online]. Available: https://www.gimaitaly.com/prodotti.asp?sku=27363&dept_selected=28&dept_id=291

[11] 'F-Scan™ GO - Système à semelles haute résolution sans fil', Mescan. Accessed: Feb. 03, 2025. [Online]. Available: https://www.mescan.com/f-scan-go?srsltid=AfmBOoqcsHzdMPNjSLNxWQjEUD7QumGOmawrmdmo8hEL1hGF046oyOpu

[12] C. Price, D. Parker, and C. Nester, 'Validity and repeatability of three in-shoe pressure measurement systems', *Gait Posture*, vol. 46, pp. 69–74, May 2016, doi: 10.1016/j.gaitpost.2016.01.026.

[13] M. N. Orlin and T. G. McPoil, 'Plantar pressure assessment', *Phys. Ther.*, vol. 80, no. 4, pp. 399–409, Apr. 2000, doi: 10.1093/ptj/80.4.399.

[14] C. Kirtley, *Clinical gait analysis*. Edinburgh New York: Elsevier, 2006.

Sensor láser de fibra óptica para medir torsión utilizando una fibra de tres núcleos y un reflector basado en nanocristales

Angel I. CORREA [1,2], José R. VENTO ALVAREZ [1,4], Marko GALARZA [1,2], Arturo SANCHEZ-GONZALEZ [1,2], Romain DAULIAT [3], Raphael JAMIER [3], Philippe ROY [3], Georges HUMBERT [3], Rosa A. PEREZ-HERRERA [1,2], and Manuel LOPEZ-AMO [1,2]

1.Departamento de Ingeniería Eléctrica, Electrónica y Comunicación, Universidad Pública de Navarra, 31006 Pamplona, España.

2.Instituto de "Smart cities" (ISC), Universidad Pública de Navarra, 31006 Pamplona, España.

3.XLIM, UMR CNRS/7252. Universidad de Limoges 87060 Limoges, Francia.

4.Departamento de Ingeniería de Telecomunicaciones y Electrónica, Universidad de Pinar del Río, Cuba.

Persona de contacto: Angel I. CORREA (angelignacio.correa@unavarra.es).

RESUMEN

Este estudio presenta un nuevo sensor de torsión altamente sensible basado en una fibra multinúcleo (MCF) dentro de un interferómetro Sagnac. El interferómetro actúa a la vez como espejo y cabezal sensor de un láser de anillo de fibra. Esta configuración de sensor láser también incorpora un reflector distribuido, consistente en un segmento de fibra óptica dopado con nanocristales de $ZnGa_2O_4$, lo que mejora el rendimiento global. El sensor demuestra una alta sensibilidad a la torsión; en un rango de 0° a 150°. El análisis de fase en el rango 0°-50° alcanza una sensibilidad de 0,08 rad/º. La aplicación de aprendizaje automático, con una red neuronal de ajuste de funciones, muestra un límite de detección de 0,06°.

Palabras clave: interferómetro Sagnac, fibra óptica multinúcleo, sensor de torsión, nanocristales, red neuronal.

ABSTRACT

This study presents a novel and highly sensitive torsion sensor based on a multicore fiber (MCF) inside a Sagnac interferometer, which acts both as a mirror and a sensor head of a fiber ring laser. This laser sensor configuration also incorporates a distributed reflector consisting of an optical fiber segment doped with $ZnGa_2O_4$ nanocrystals, enhancing the overall performance. The sensor demonstrates high sensitivity to torsion across a range of 0° to 150°. The phase analysis in the 0°-50° range achieves a sensitivity of 0.08 rad/º. The Machine Learning application, with a function-fitting neural network, shows a detection limit of 0.06°.

Keywords: Sagnac interferometer, multicore optical fiber, torsion sensor, nanocrystals, neural network.

1.- Introducción

Entre los diversos tipos de sensores de fibra óptica que más han progresado en los últimos años se encuentran los sensores de torsión [1]. Los primeros estudios introdujeron diversos enfoques para este tipo de sensores, pero el interés general surgió a partir de la década de los 2000. Desde entonces, se han empleado diversos principios, como la modulación de la

birrefringencia [2]. Entre ellos, los interferómetros de Sagnac son una estructura óptica de alta sensibilidad [3]. A menudo, mediante la inserción en ella de fibras de alta birrefringencia cuyos cambios axiales modifican el patrón de interferencia.

La incorporación de sensores de fibra óptica en sistemas láser potencia significativamente la relación señal/ruido y facilita la monitorización remota de parámetros [4]. Aprovechando estas ventajas, en este estudio, se presenta una configuración de láser de anillo que incorpora una fibra de tres núcleos dentro de un interferómetro Sagnac (IS). Se consigue una sensibilidad a la torsión de 0,13 nm/° en longitud de onda, y una sensibilidad de 0,5 dBm/° medida en amplitud. Estos resultados pretenden contribuir al campo de la medida de la torsión, proporcionando mejoras respecto a los sensores de torsión de fibra óptica publicados anteriormente (véase, por ejemplo [5]).

2.- Configuración y principio de funcionamiento

Proponemos una nueva estructura para la medición de torsión, que combina un segmento de fibra de tres núcleos insertado en un IS. Este interferómetro actúa como espejo y, también como cabeza sensora dentro de un láser en anillo. Dicho láser también dispone de un reflector distribuido consistente en un segmento de fibra dopado con nanocristales (NC).

El transductor de torsión para el sensor se fabricó fusionando un segmento de 1,2 cm de una MCF entre dos segmentos de 30 cm de una SMF. Después, esta estructura de detección se introdujo en un interferómetro tipo Sagnac. Este interferómetro se basa en la interferencia de luz que viaja en direcciones opuestas, en nuestro caso en una conexión de fibras. Cuando los haces se recombinan, cualquier diferencia de fase causada por perturbaciones externas (como rotación o deformación) da lugar a un patrón de interferencia que puede medirse. La intensidad de salida de un IS viene dada por:

$$I = I_o \cdot [1 + \cos(\Delta\varphi)] \qquad (1)$$

donde I_o es la intensidad de entrada y $\Delta\varphi$ es la diferencia de fase entre los haces contra propagados. Esta diferencia de fase es sensible a influencias externas, lo que facilita una alta sensibilidad del interferómetro. Cuando se incluye dentro del interferómetro una fibra birrefringente, $\Delta\varphi$ puede definirse además como:

$$\Delta\varphi = \left(\frac{2\pi L}{\lambda}\right) \cdot (n_f - n_s) \qquad (2)$$

donde L es la longitud de la fibra, λ es la longitud de onda y n_f y n_s son los índices de refracción de los ejes rápido y lento de la fibra respectivamente. La diferencia, $(n_f - n_s)$ representa la birrefringencia de la fibra [6].

Cuando se aplica torsión a la fibra, la birrefringencia cambia, lo que da lugar a una modificación de $\Delta\varphi$ y, en consecuencia, a un cambio en la intensidad de salida I. Este principio fundamental permite utilizar el sistema como sensor de torsión. La caracterización del IS se realizó utilizando una fuente de banda ancha, y la respuesta espectral normalizada resultante se muestra en la Fig. 1.

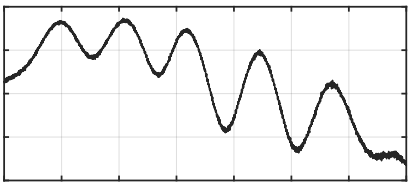

Fig. 1 Respuesta espectral normalizada de la caracterización del interferómetro Sagnac, obtenida utilizando una fuente óptica de banda ancha.

Las estructuras de láser de fibra óptica son valiosas para realizar mediciones precisas en sistemas de sensores de fibra óptica. Además de su coherencia y estrecho ancho de línea, se consigue una reducción significativa del ruido en la medición, lo que las hace adecuadas para mediciones en aplicaciones de detección avanzadas [7].

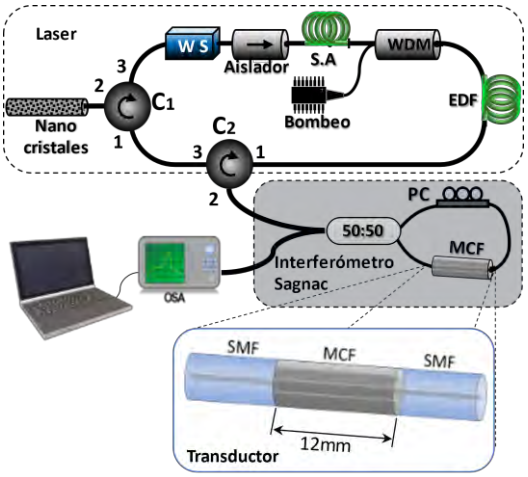

Fig. 2 Montaje experimental del láser de fibra en anillo, diseñado para medir torsión utilizando un IS con un segmento de fibra multinúcleo (MCF) como transductor de torsión. (WS) filtro sintonizable (Waveshaper 1000S), (SA) absorbente saturable, (WDM) multiplexor por división en longitud de onda, (EDF) fibra dopada con erbio, (C_1) y (C_2) circuladores ópticos, (PC) controlador de polarización, (OSA) analizador de espectros óptico.

Como se ha señalado anteriormente, esta estructura de detección se introdujo en un interferómetro Sagnac, como se muestra en la Fig. 2. La estructura consiste en una fibra dopada con erbio (EDF) M12 de 3.4 m conectada al puerto común del (WDM) y bombeada a una longitud de onda de 976 nm con una potencia de bombeo de 175 mW. El extremo opuesto de la EDF se conectó al puerto 1 del circulador óptico C_2. El puerto 2 de C_2 se conectó a un IS, que actúa como espejo sensor. El puerto 3 de este circulador óptico se conectó al puerto 1 del circulador óptico C_1, en cuyo puerto 2 se conectó una sección de 80 cm de fibra dopada con nanocristales, que actúa como reflector. Por último, el puerto 3 del C_1 se conectó a la entrada de un filtro óptico programable (WS) centrado en λc = 1558,37 nm con un ancho de banda de 0,08 nm. La salida del filtro alimenta un aislador óptico, seguido de 3 m de un EDF que actúa como absorbente saturable (SA), y conectado al puerto de 1550 nm del WDM, completando así la configuración del anillo de fibra. La señal para la monitorización de la torsión se extrajo conectando un analizador de espectros ópticos (OSA) (Anritsu MS97040A) al puerto de salida del IS con una resolución de 0,03 nm. Sin embargo, la emisión de esta configuración láser presenta algunas deficiencias como su inestabilidad, que puede alcanzar más de 2 dB [8]. Para reducir las inestabilidades, en los láseres de fibra se suelen utilizar reflectores que introducen retrodispersión de forma distribuida. En nuestro caso el rendimiento del láser se mejoró al incorporar una fibra dopada con nanocristales (NC) [9] como reflector en nuestra configuración de láser de fibra con cavidad en anillo. La fibra dopada con NC tiene un núcleo de $ZnGa_2O_4$ (SiO_2-ZnO-Ga_2O_3-Na_2O) incrustado en el vidrio de sílice. Las fibras compuestas por nanocristales embebidos en una matriz de sílice, son una nueva clase de fibras ópticas que dan lugar a luz de dispersión Rayleigh más intensa debido a la composición de los nanocristales. El proceso de fabricación permite altas concentraciones de dopaje (>10%) [10] sin aglomeración, proporcionando un mayor control sobre las propiedades ópticas de la fibra. Los NC de $ZnGa_2O_4$ (tamaño ~60 nm) actúan como centros de dispersión, proporcionando una retroalimentación distribuida a lo largo de la longitud de la fibra, lo que mejora la selección y la estabilidad del modo. Esto da lugar a un ancho de línea más estrecho y a una reducción de los saltos de modo [11].

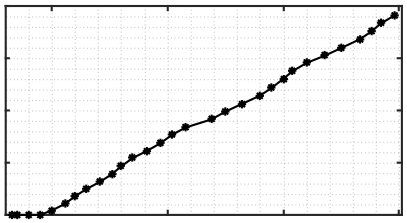

Fig. 3 Nivel de potencia de salida en función la potencia de bombeo para el láser de fibra de cavidad en anillo.

Se evaluaron las características de salida del láser en función de la corriente de bombeo y su estabilidad a largo plazo. El nivel de potencia de salida en función de la corriente de bombeo mostró un umbral de bombeo de 85 mW y una eficiencia del 0,86%, como puede verse en la Fig. 3.

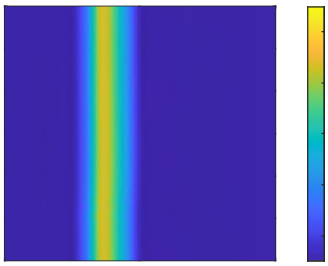

Fig. 4 Fluctuaciones de la potencia medida durante un periodo de 120 minutos.

El láser obtenido emite a una longitud de onda de 1558,37 nm con un nivel de potencia de salida de -22,5 dBm, una anchura a mitad del máximo (FWHM) de 46 pm y una relación señal/ruido óptico (OSNR) de 43,5 dB para una potencia de bombeo de 175 mW. La evaluación de la estabilidad del nivel de potencia de salida a lo largo del tiempo se realizó a temperatura ambiente durante un periodo de 120 minutos, con intervalos de medida de 9,8 segundos (Fig. 4). Utilizando un nivel de confianza del 95%, la variación máxima de la potencia de salida fue de 0,4 dB, lo que indica una buena estabilidad del sistema. Cuando se retiró el reflector de fibra dopada con NC, la inestabilidad de la potencia aumentó a 1,5 dB.

3.- Resultados

Se utilizó un sistema mecánico de precisión para aplicar una torsión controlada al segmento MCF, indicado en la Fig. 2 como sección del transductor. Una pinza fija sujetó un extremo del MCF, proporcionando una referencia estable, mientras que una pinza giratoria en el extremo opuesto permitió controlar la torsión. La respuesta espectral de 1520 nm a 1565 nm, para ángulos de torsión entre 0° y 150°, se presenta en la Fig. 5 (a). Se observó un comportamiento sin histéresis tanto para ángulos crecientes como decrecientes. Además, cuando el ángulo de torsión era superior a 88°, se observó un aumento del nivel de potencia de salida medido hasta 150°, seguido de una disminución en correspondencia con la reducción de la torsión. Fig. 5 (b) muestra la respuesta espectral cuando el sensor de torsión basado en IS se insertó en la cavidad láser en anillo representada en la Fig. 2.

Este comportamiento se prestó a un análisis

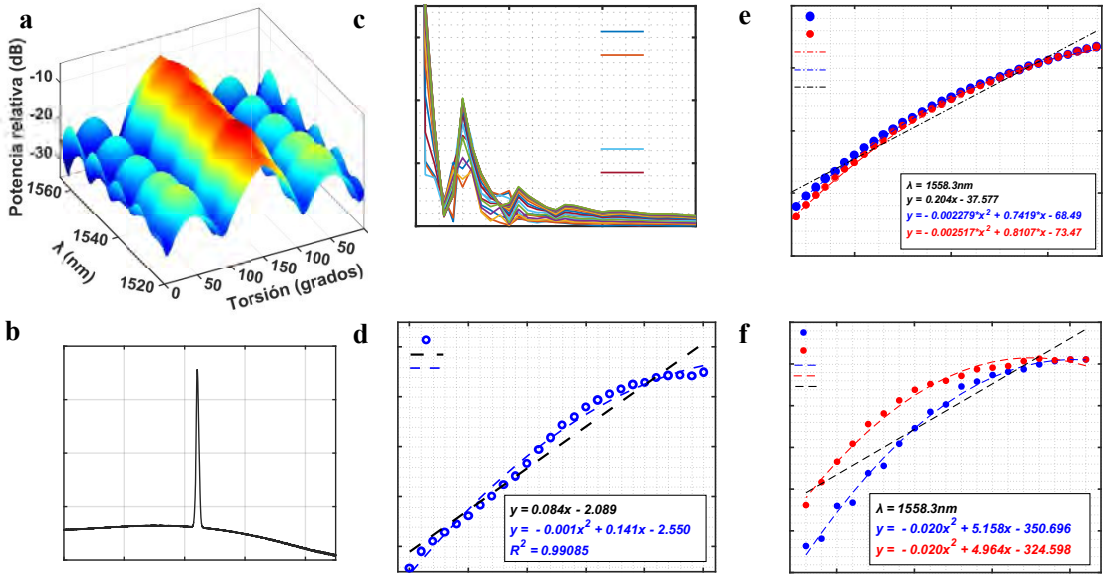

Fig. 5. (a) Comportamiento espectral para torsiones de 0° a 150° a la salida del interferómetro Sagnac excitado con una fuente ancha. (b) Medida espectral de la emisión láser para 100° de torsión. (c) Caracterización del comportamiento de las componentes espaciales de la FFT del espectro óptico a la salida. (d) Comportamiento de la fase en el pico con una frecuencia espacial de 0,1 nm^{-1}. (e) Potencia de salida del Sagnac utilizando una fuente de banda ancha y (f) insertada en un láser de cavidad en anillo a una longitud de onda constante de 1558,3 nm.

posterior en amplitud y fase, ajustando en consecuencia el rango de medida. La Fig. 5 (c) ilustra la transformada rápida de Fourier (FFT) de la señal óptica para ángulos de torsión de 0° a 50°, revelando un patrón de interferencia con un ciclo de 0,1 nm^{-1}. El análisis de fase de este pico, como se muestra en la Fig. 5 (d) confirmó su información sobre el ángulo de torsión. El desplazamiento de fase (en radianes) frente al ángulo de torsión (en grados) arrojó una sensibilidad lineal de 0,08 rad/º, con R^2 de 0,9582, y un ajuste cuadrático superior de R^2 de 0,991. Entre 50° y 88°, ni la fase ni la potencia mostraron una tendencia clara o monótona que pudiera modelarse mediante una función simple, creando un intervalo en el que ninguno de los métodos por sí solo podía recuperar con precisión el ángulo de torsión. Por lo tanto, se empleó un modelo de aprendizaje automático para mejorar el sistema. A partir de 88 ° la fase pierde linealidad y los valores se repiten; en consecuencia, se emplea la medición en potencia para garantizar una respuesta continua del sensor. Como resultado, el análisis se dividió en dos subrangos: 0°-50° (basado en la fase) y 88°-150° (basado en la potencia), mientras que el aprendizaje automático garantizó la continuidad de 50° a 88°, unificando la medición en todo el rango de 0°-150°. Fig. 5 (e) muestra el análisis basado en la potencia realizado de 88° a 150°. Para este análisis, se seleccionó una longitud de onda y se examinó su variación de potencia en relación con el ángulo de torsión aplicado. La potencia aumentó de -22 dBm a 88° a un máximo de -8,3 dBm a 150°, lo que dio lugar a una excursión de amplitud de 13,7 dBm a lo largo de 62° de torsión. Un ajuste lineal indicó 0,2 dBm/° con un R^2 de 0,964, mientras que un ajuste cuadrático alcanzó un R^2 de 0,9992. La incorporación del sensor dentro del láser en anillo, que tiene una fibra dopada con NC como reflector, mejoró aún más el rendimiento del sistema. Como se muestra en la Fig. 5 (f), la sensibilidad aumentó a 0,5 dBm por grado, lo que representa un factor de mejora de 2,5. El sistema demostró potencias de salida de -36,8 dBm a 95° y -14,5 dBm a 132°, una excursión de amplitud de 22,4 dBm sobre 37° de torsión. Un ajuste cuadrático R^2 de 0,995 confirmó que esta configuración basada en láser proporciona una respuesta superior a los ángulos de torsión.

La integración del sensor en una cavidad láser mejora significativamente la metodología de interrogación y la resolución del sistema. Teniendo en cuenta la resolución de los instrumentos utilizados para la caracterización, la configuración láser mostró una resolución de 0,8°, lo que supone una mejora de 2,5 veces con respecto a la configuración sin láser. El método de detección basado en láser no sólo aumentó la sensibilidad, sino que también proporcionó una técnica de medición más robusta y resistente al ruido.

Como ya se mencionó; para cubrir el rango de 50° a 88°, los espectros obtenidos durante los experimentos se emplearon para entrenar un modelo de aprendizaje automático basado en una red neuronal de ajuste de funciones. La red neuronal utilizada en este estudio tiene una arquitectura formada por cuatro capas ocultas. Cada capa contenía 3, 1000, 1000 y 3 neuronas respectivamente. La red se entrenó utilizando el algoritmo de entrenamiento de gradiente conjugado escalado. Los datos se dividieron aleatoriamente en tres conjuntos: entrenamiento (70%), validación (15%) y prueba (15%). El entrenamiento se detuvo tras un máximo de 5.000 épocas o si el error de validación no mejoraba tras 10 épocas consecutivas. Tras el entrenamiento del modelo de aprendizaje automático, el error cuadrático medio mínimo obtenido fue de $3{,}05 \cdot 10^{-3}$. Esto significa que el error cuadrático medio alcanzado fue de 0,06, lo que indica que el sensor tiene un límite de detección de 0,06°. Los resultados demuestran un rendimiento de R^2 0,99998.

4.- Conclusiones

Este trabajo presenta un nuevo sensor de torsión altamente sensible basado en un interferómetro Sagnac de fibra multinúcleo integrado en una cavidad láser. El láser incorpora un reflector distribuido formado por un segmento de fibra dopado con nanocristales de $ZnGa_2O_4$, que mejoró el rendimiento global del sistema. El sensor

demostró una alta sensibilidad a la torsión en un rango de 0° a 150°. El análisis de fase en el rango de 0°-50°, consiguió una sensibilidad de 0,08 rad/º de torsión. El análisis de amplitud en el rango 88°-150° obtuvo una sensibilidad de 0,2 dBm/º. Empleando la configuración de láser en anillo, esta sensibilidad mejoró hasta 0,5 dBm/º, lo que supone una mejora de 2,5 veces. Finalmente, se usó la integración con aprendizaje automático, con una red neuronal de ajuste de funciones, para la medición continua en todo el rango 0°-150°, indicando un límite de detección de 0,06°.

Agradecimientos: Este trabajo ha sido financiado en parte por los proyectos PID2022-137269OB, financiado por MCIN/AEI/10.13039/501100011033 y FEDER "A way to make Europe", y TED2021-130378B financiado por MCIN/AEI/10.13039/501100011033 y la Unión Europea "Next generation EU"/PRTR.

Referencias

[1] Vedran BUDINSKI, Denis DONLAGIC, "*Fiber-Optic Sensors for Measurements of Torsion, Twist and Rotation: A Review*", Sensors, 17, 3, 443, 2017.

[2] A. GALTAROSSA, L. PALMIERI, "*Measure of twist-induced circular birefringence in long single-mode fibers: theory and experiments*", Journal of Lightwave Technology, 20, 7, 1149–1159, 2002.

[3] Qiang LIU, Liang XING, Zhaoxia WU, Yongqing FU, Shuguang LI, Pingsheng XUE, Wai Pang NG, Qiang WU, Richard BINNS, "*Cascaded Sagnac Loops Embedded With Two Polarization Maintaining Photonic Crystal Fibers for Highly Sensitive Strain Measurement*", IEEE Transactions on Instrumentation and Measurement, 70, 1–9, 2021.

[4] V. DEMIGUEL-SOTO, D. LEANDRO, M. LOPEZ-AMO, "*Ultra-long (290 km) remote interrogation sensor network based on a random distributed feedback fiber laser*", Optics Express, 26, 21, 27189–27200, 2018.

[5] Jiaqi CAO, Xin WANG, Bingsen HUANG, Shuqin LOU, Paul K. CHU, Zhufeng SHENG, "*Using machine learning to enlarge the measurement range and promote the compactness of the optical fiber torsion sensor based on the Sagnac interferometer*", Optics Express, 32, 5, 6929, 2024.

[6] Daniel LEANDRO, Mikel BRAVO, Amaia ORTIGOSA, Manuel LOPEZ-AMO, "*Real-Time FFT Analysis for Interferometric Sensors Multiplexing*", Journal of Lightwave Technology, 33, 2, 354–360, 2015.

[7] Galina NEMOVA, "*Brief Review of Recent Developments in Fiber Lasers*", Applied Sciences, 14, 6, 2323, 2024.

[8] L. TALAVERANO, S. ABAD, S. JARABO, M. LOPEZ-AMO, "*Multiwavelength fiber laser sources with Bragg-grating sensor multiplexing capability*", Journal of Lightwave Technology, 19, 4, 553–558, 2001.

[9] Victor FUERTES, Nicolas GRÉGOIRE, Philippe LABRANCHE, Stéphane GAGNON, Ruohui WANG, Yannick LEDEMI, Sophie LAROCHELLE, Younès MESSADDEQ, "*Engineering nanoparticle features to tune Rayleigh scattering in nanoparticles-doped optical fibers*", Scientific Reports, 11, 1, 9116, 2021.

[10] Damien POMAREDE, Jean-Louis AUGUSTE, Georges HUMBERT, Mathieu ALLIX, Cécile GENEVOIS, Emmanuel VERON, Sébastien CHENU, Gaëlle DELAIZIR, "*Optical element and associated manufacturing method*", US11880063B2, 2024.

[11] Rosa Ana PEREZ-HERRERA, Pablo ROLDAN-VARONA, Luis Rodriguez COBO, Jose Miguel LOPEZ-HIGUERA, Manuel LOPEZ-AMO, "*Single Longitudinal Mode Lasers by Using Artificially Controlled Backscattering Erbium Doped Fibers*", IEEE Access, 9, 27428–27433, 2021.

Sensor de deformación de alta sensibilidad basado en dos fibras especiales diferentes y con efecto Vernier

Angel I. CORREA[1,2], Jose R. VENTO ALVAREZ[1,4], Marko GALARZA[1,2], Romain DAULIAT[3], Raphael JAMIER[3], Philippe ROY[3], Rosa A. PEREZ-HERRERA[1,2] y Manuel LOPEZ-AMO[1,2]

1. Departamento de Ingeniería Eléctrica, Electrónica y de Comunicación, Universidad Pública de Navarra, 31006 Pamplona, España.
2. Instituto de "Smart cities" (ISC), Universidad Pública de Navarra, 31006 Pamplona, España.
3. XLIM, UMR CNRS/Universidad de Limoges 87060 Limoges, Francia.
4. Departamento de Ingeniería Electrónica y Telecomunicaciones de la Universidad de Pinar del Río, Cuba.

Persona de contacto: Angel I. CORREA (angelignacio.correa@unavarra.es).

RESUMEN:

En este estudio, se desarrolla y caracteriza un nuevo sensor de deformación basado en el efecto Vernier, que ofrece un amplio rango dinámico y alta sensibilidad a la deformación; el sensor combina un interferómetro Fabry-Perot (FPI) formado por una fibra de núcleo hueco (HCF) y un interferómetro de supermodos (SMI) compuesto por una fibra multinúcleo (MCF). Combinando estos dos interferómetros en una configuración Michelson, la envolvente Vernier amplifica la respuesta del sistema, logrando una mayor sensibilidad a la deformación en comparación con los enfoques convencionales. El sensor demuestra una respuesta lineal, con sensibilidades de 1,9 pm/με a 5 pm/με para un segmento de fibra de 30 mm, y de hasta 22,2 pm/με cuando la longitud del segmento se ha incrementado hasta 85 mm; permitiendo una deformación de hasta 6280 με sin ruptura de la fibra. Además, la caracterización en temperatura validó una sensibilidad de 766,5 pm/°C, confirmando así la robustez del diseño propuesto.

Palabras clave: sensor de deformación, interferometría óptica, fibra multinúcleo, fibra de núcleo hueco, configuración Michelson, efecto Vernier.

ABSTRACT:

In this study, a new strain sensor based on the Vernier effect was developed and characterized, offering a wide dynamic range and high sensitivity to strain, with temperature compensation. The sensor combined a Fabry-Perot interferometer (FPI) formed by a hollow-core fiber (HCF) and a super-mode interferometer (SMI) composed of a multicore fiber (MCF). By combining these two interferometers in a Michelson configuration, the Vernier envelope amplifies the system response, achieving higher strain sensitivity in comparison with conventional approaches. The sensor demonstrated a linear response, with sensitivities of 1.9 pm/με to 5 pm/με for a fiber segment of 30 mm, and up to 22.2 pm/με when the segment length was increased to 85 mm, allowing a strain of up to 6280 με without fiber rupture. Additionally, temperature characterization validated a sensitivity of 766.5 pm/°C, thus confirming the robustness of the proposed design.

Keywords: strain sensor, optical interferometry, multicore fiber, hollow-core fiber, Michelson configuration, Vernier effect.

1.- Introducción

La creciente demanda de sistemas de detección con alta sensibilidad y resolución ha impulsado el desarrollo de nuevas estrategias en el campo de los sensores basados en fibra óptica. En este contexto, el efecto Vernier -originalmente inspirado en instrumentos de medición tradicionales como el calibre Vernier- se ha convertido en una herramienta prometedora para mejorar las respuestas espectrales de los sensores [1,2]. En concreto, la aplicación del efecto Vernier a los sensores de deformación permite detectar deformaciones mínimas con mayor precisión que los sensores convencionales [3]. Al combinar una parte de la estructura sensora afectada por la deformación con una referencia estable, la señal resultante se amplifica, lo que facilita la identificación de pequeñas variaciones en la longitud de la fibra. Además, la incorporación de estructuras innovadoras como las fibras multinúcleo altamente acopladas [3] ofrecen una versatilidad que abre nuevas posibilidades para aplicaciones de monitorización en las que una detección precisa resulta crucial.

La ventaja de este desarrollo sobre otros reportados en la literatura [3,4],es que nuestro sensor tiene una capacidad de respuesta a la deformación 10 veces superior sin romperse. En este trabajo se ha medido un límite superior de 6280 με soportados sin romperse, y una sensibilidad de 22,2 pm/με. Dichos valores presentan una mejora competitiva respecto a los sensores de deformación más avanzados.

2.- Consideraciones Teóricas

Como ya se ha mencionado, el efecto Vernier óptico se basa en la combinación de dos funciones de transferencia interferométricas con rangos espectrales libres (*FSR*) ligeramente diferentes, que generan un patrón de batido caracterizado por una envolvente de baja frecuencia capaz de magnificar cualquier desplazamiento inducido en el espectro por una perturbación externa [4].

Al aplicar el efecto Vernier óptico, es necesario controlar el desajuste entre las frecuencias de señal de ambos interferómetros. Esto se logra modificando la longitud del camino óptico *(OPL*), ya sea alterando el índice de refracción efectivo o cambiando la longitud física del interferómetro. Por lo tanto, dados dos interferómetros, I_1 e I_2 (que sirven como primera y segunda escalas Vernier, respectivamente), se puede optimizar el interferómetro I_2 para maximizar la mejora proporcionada por el efecto Vernier. Este trabajo se centra en una disposición en paralelo que emplea una configuración Michelson. En concreto, combina un interferómetro FPI construido a partir de una HCF y un interferómetro de super-modos diseñado a partir de una fibra de tres núcleos en forma de V (3MCF-V).

El interferómetro basado en la estructura SMS-HCF-SMF ha sido ampliamente estudiado [5]. Sus dimensiones se han acotado para que sea insensible a la temperatura, lo que requiere que la longitud de la HCF no supere un valor crítico L_c.

La estructura del segundo interferómetro (SMF-3MCF-V), consiste en un segmento de fibra 3MCF-V de longitud $L_{3MCF\text{-}V}$ que se fusiona a una fibra SMF convencional, cuyo extremo se ha impregnado con una pintura a base de plata, generando un espejo con una reflectividad de aproximadamente el 95%. Este proceso se describe detalladamente en [6]. En esta estructura, el núcleo de la fibra SMF y el núcleo central de la fibra 3MCF-V se alinearon de modo que sólo el modo fundamental de la SMF excitara la fibra 3MCF-V. Esta suposición es válida para un rango de longitudes de onda de aproximadamente 1260 nm a 1650 nm, en el que tanto el núcleo de la fibra SMF como el de la MCF operan en régimen monomodo. En estas condiciones de excitación, en la fibra 3MCF-V sólo se excitan dos supermodos; hecho demostrado por otros autores en [7]. Los supermodos viajan dos veces a lo largo del segmento 3MCF-V, además, la reflexión de la estructura SMF-3MCF-V se puede encontrar en [8].

Para el interferómetro de Michelson en el que se combinaron los dos interferómetros descritos anteriormente (FPI-HCF y SMI-MCF), la intensidad de salida en función de las OPL viene dada por [4,9].

El *FSR* de la envolvente Vernier puede expresarse en función de la desafinación o los *FSRs* de cada interferómetro como:

$$FSR_{envolvente} = \left|\frac{\lambda_2\lambda_1}{\delta}\right| = \left|\frac{FSR_1 FSR_2}{FSR_1 - FSR_2}\right| \quad (1)$$

donde, λ_1 y λ_2 son las longitudes de onda de dos máximos (o mínimos) consecutivos de la envolvente, δ es la desafinación, FSR_1 y FSR_2 son los *FSR* de los dos interferómetros, respectivamente.

Un término importante es el factor de ampliación *M*, que puede definirse como la relación entre la *FSR* de la envolvente y la *FSR* del interferómetro sensor que se define como [1]:

$$M = \frac{FSR_{envolvente}}{FSR_1} \quad (2)$$

3.- Montaje experimental

Teniendo en cuenta las consideraciones teóricas mencionadas, se han fabricado los interferómetros. El interferómetro de referencia se ha realizado fusionando un segmento de fibra HCF (con L_{HCF} de 320 µm de longitud), entre dos segmentos de fibra SMF, Fig.2 (Ref.). La HCF se cortó utilizando una cortadora de fibra comercial acoplada a un microposicionador, y la fusión se llevó a cabo aplicando una descarga de arco desplazada, mediante una fusionadora Fujikura FSM100P, para evitar que la estructura de la *HCF* se colapsara. La respuesta espectral de este interferómetro, mostrada en Fig.1 (a) y (b), (espectro de reflexión y análisis FFT, respectivamente) muestra un pico alrededor de 0,2 nm^{-1} que corresponde a una FSR_{HCF} de 4,2 nm.

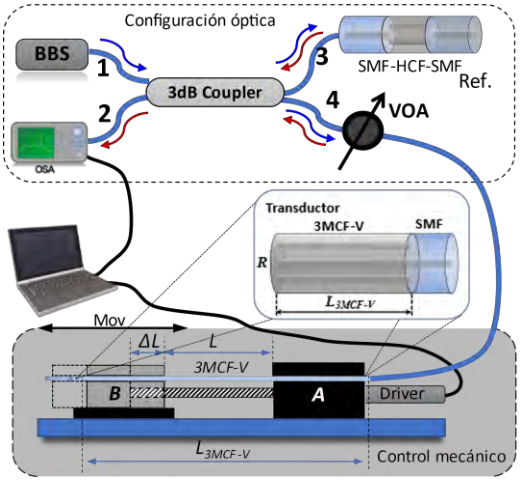

Fig.2 Montaje experimental del sensor de deformación basado en el efecto Vernier. La configuración óptica consiste en: Fuente de banda ancha (BBS), analizador de espectro óptico (OSA), estructura interferométrica de referencia (Ref), atenuador óptico variable (VOA). Transductor: Transductor y cabezal sensor; Control mecánico: Esquema de configuración automática utilizado para caracterizar la respuesta del sensor a la deformación.

El segundo interferómetro se ha construido fusionando 230 mm de la fibra *MCF* con 3 núcleos en forma de V; con una fibra SMF convencional Fig.2 (Transductor). El núcleo central de la *MCF* se ha alineado con el de la SMF. El extremo de la *MCF* se ha cortado perpendicularmente, y se ha aplicado un espejo de pintura como ya se ha mencionado. Tras la aplicación de este espejo, se ha

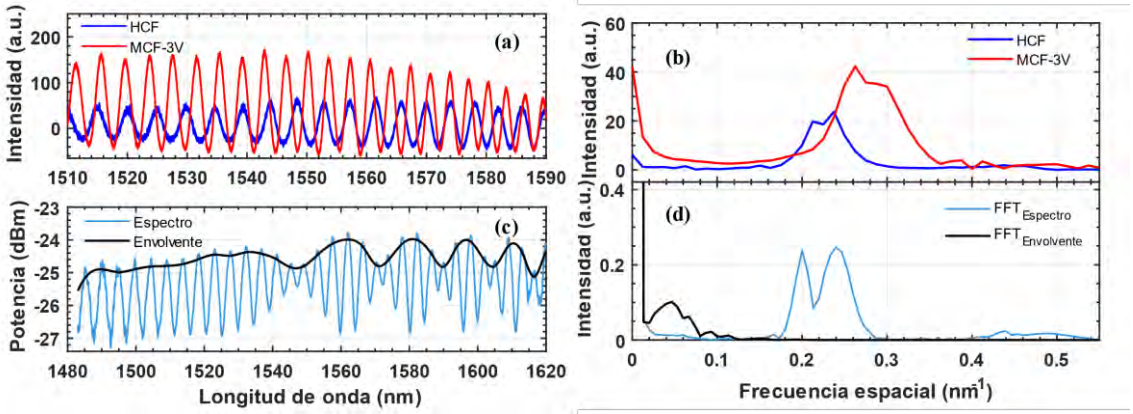

Fig.1 (a) y (b) respuesta espectral de los dos interferómetros de la estructura y respuesta en frecuencias espaciales calculadas a partir de la FFT de ambas funciones de transferencia, (c) respuesta espectral al combinar ambos interferómetros, (d) FFT del espectro y de la envolvente.

conseguido una interferencia con un $FCR_{3MCF\text{-}V}$ predominante de 3,8 nm, como se muestra en Fig.1 (a) y (b). Una vez fabricados y caracterizados, los interferómetros se conectaron a través de un acoplador de 3 dB.

Para caracterizar el sensor, se ha conectado una fuente de banda ancha (BBS) al puerto 1 del acoplador y un analizador de espectros ópticos (Anritsu MS9740A) al puerto 2. La luz se divide entre los puertos de salida 3 y 4, se refleja en cada interferómetro y se recombina en el acoplador. La Fig.1 (c), muestra la respuesta espectral resultante de la interferencia de ambos interferómetros, donde se puede observar la aparición de una envolvente de baja frecuencia, causada por la diferencia de fase derivada de la diferencia espectral entre ambos interferómetros. El atenuador óptico variable (VOA) permite igualar las amplitudes de la señal óptica de los dos interferómetros, consiguiendo así un mejor índice de modulación de la envolvente Vernier. La Fig.1 (d) presenta el análisis de frecuencia espacial, revelando los picos asociados con cada interferómetro en la señal combinada, junto con un componente de frecuencia más baja correspondiente a la envolvente lenta del Vernier.

4.- Resultados y discusión de los mismos.

Las medidas de deformación se realizaron fijando el segmento 3MCF-V de 230 mm de longitud en la configuración mecánica que se muestra en Fig.2 (control mecánico). Este diagrama ilustra cómo la fibra (de longitud total $L_{3MCF\text{-}V}$) se sujetó entre dos soportes: el soporte A, que ha permanecido fijo y está unido al servocontrol, y el soporte B, que se ha movido mediante un tornillo roscado, proporcionando un desplazamiento ΔL controlado. Este sistema automatizado se ha aplicado una deformación sobre 30 mm del 3MCF-V (L), con una resolución de paso de 17 nm. Durante este proceso, se ha monitorizado la temperatura mediante un sensor electrónico y una red de difracción de Bragg de fibra (FBG) para su posterior evaluación y compensación. Se han realizado tres ciclos de medidas, aplicando deformación y volviendo al punto de partida.

La Fig.3 (a) muestra el desplazamiento espectral bajo deformación, donde los valles de la derecha muestran una mayor sensibilidad. Fig.3 (b), (c), y (d) presentan los ciclos de deformación en el tiempo y el desplazamiento de la longitud de onda en función de la deformación aplicada para cada valle V_1, V_2, y V_3 respectivamente. La línea discontinua indica el desplazamiento antes de aplicar la compensación de temperatura.

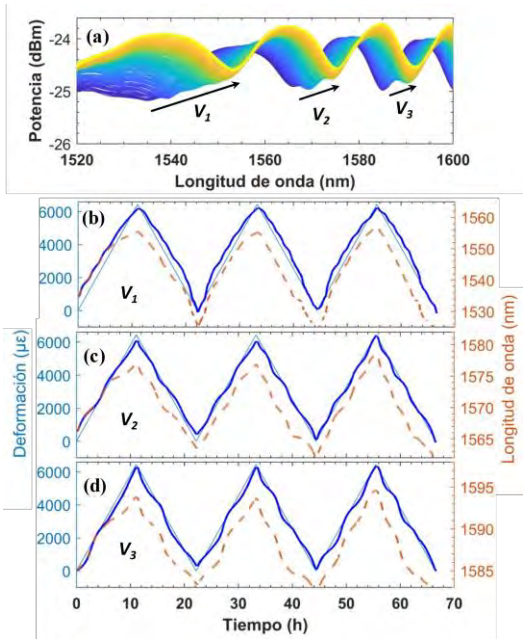

Fig.3 (a) Desplazamiento espectral de la envolvente del espectro, (b), (c) y (d) muestran los ciclos de deformación en función del tiempo y el desplazamiento de la longitud de onda de cada valle en función de la deformación aplicada y su repetibilidad en el tiempo.

La Fig.4 muestra el comportamiento de cada valle bajo la deformación aplicada, donde puede observarse que el sensor no presenta histéresis. También se ha obtenido excelentes coeficientes de determinación para un ajuste lineal, y la sensibilidad para cada valle es de 5 pm/με, 2,4 pm/με y 1,9 pm/με, respectivamente.

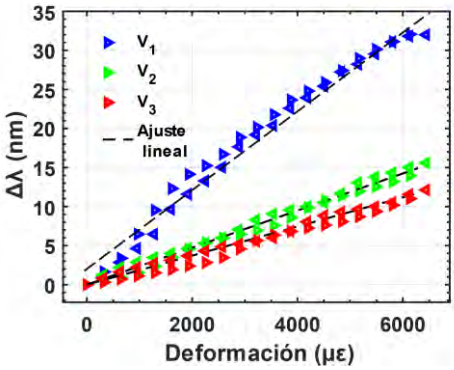

Fig.4 Desplazamiento de la longitud de onda de tres valles de la envolvente en función de la deformación aplicada.

En un segundo experimento, se ha sometido a tensión un segmento de fibra más largo, de aproximadamente 85 mm. Esta mayor longitud mejoró el rendimiento del sensor bajo la tensión aplicada y dio lugar a una nueva sensibilidad de 22,2 pm/με. Sólo se ha caracterizado el valle 1, ya que anteriormente había mostrado la mayor sensibilidad. Los resultados se presentan en Fig.5 (a), que muestra el desplazamiento del valle, y en Fig.5 (b), que muestra la curva de calibración.

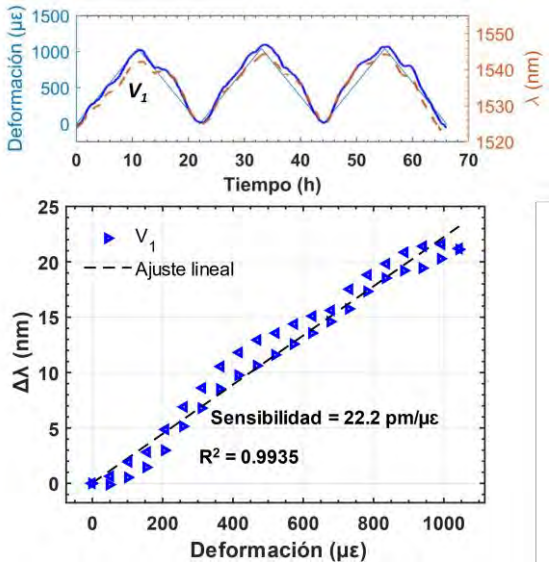

Fig.5 (a) Evolución temporal de la deformación, desplazamiento de la longitud de onda del valle V_1, ilustrando tres ciclos de deformación y la compensación de temperatura; (b) Desplazamiento de la longitud de onda frente a la deformación aplicada y curva de ajuste lineal.

Por último, la *Tabla I* presenta un resumen de los resultados de sensibilidad y coeficiente de determinación R^2 obtenidos aplicando tensión a segmentos de 30 mm y 85 mm de la 3MCF-V. Se observa un marcado aumento de la sensibilidad cuando la longitud de la fibra se amplía hasta 85 mm (valle V_1), alcanzando 22,2 pm/με y manteniendo al mismo tiempo un alto valor de R^2. Esto confirma la respuesta lineal en las condiciones evaluadas.

Tabla I: Sensibilidad y coeficiente de determinación para diferentes longitudes de segmento 3MCF-V en mediciones de deformación.

Longitud	*Valle*	*Sensibilidad*	*R^2*
30 mm	*V_1*	*5 pm/με*	*0,9972*
	V_2	*2,4 pm/με*	*0,9972*
	V_3	*1,9 pm/με*	*0,9903*
85 mm	*V_1*	*22,2 pm/με*	*0,9935*

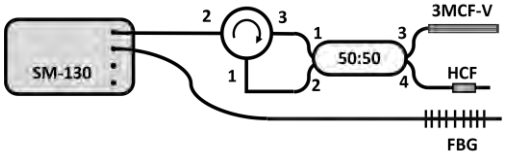

Fig.6 Montaje experimental para la caracterización de la temperatura.

La caracterización en temperatura del sensor se ha llevado a cabo usando un interrogador de sensores ópticos (Micron Optics SM-130), como se muestra en Fig.6. El canal 1 del interrogador se ha conectado al puerto 2 de un circulador óptico, y la señal se dirige desde el puerto 3 del circulador al puerto 1 de un acoplador de 3 dB. En el acoplador, la luz se divide en dos ramas a través de sus puertos 3 y 4, donde se refleja en cada estructura y se combina en el acoplador. Los haces combinados se dirigen a través del puerto 2 del acoplador al puerto 1 del circulador, generando así la interferencia ya mostrada en Fig.1 (c). Simultáneamente, el canal 2 del interrogador se utilizó para leer un sensor de temperatura basado en una FBG.

Durante la caracterización, se ha variado de forma controlada la temperatura de 25 °C a 75 °C y se ha registrado la respuesta espectral tanto de la configuración Vernier (756 pm/°C) como de la FBG (9,6 pm/°C) (véase Fig. 7).

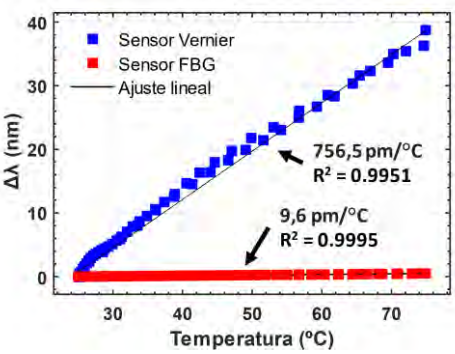

Fig. 7 Desplazamiento de la longitud de onda en función de la temperatura.

4.- Conclusión

En este trabajo, presentamos un novedoso sensor de deformación que emplea una fibra multinúcleo (3MCF-V) en una configuración Vernier, que ha demostrado un rango dinámico ampliado y una sensibilidad mejorada en comparación con los sensores de fibra óptica convencionales y otros sensores interferométricos [10]. Se ha alcanzado una sensibilidad de 22,2 pm/με utilizando un segmento 3MCF-V de 85 mm de longitud, que ha permitido deformaciones de hasta 6280 με sin fallo estructural. Además, el diseño del sistema del sensor incorpora una compensación de temperatura integrada, lo que permite un rendimiento fiable en condiciones ambientales variables. Estos resultados confirman la robustez y precisión de la configuración propuesta para aplicaciones que exigen una monitorización de la deformación de alta resolución y amplio rango dinámico.

Agradecimientos: Este trabajo ha sido financiado en parte por los proyectos PID2022-137269OB, financiado por MCIN/AEI/10.13039/501100011033 y FEDER "A way to make Europe", y TED2021-130378B financiado por MCIN/AEI/10.13039/501100011033 y la Unión Europea "Next generation EU"/PRTR

Referencias

[1] André D. GOMES, Hartmut BARTELT, Orlando FRAZÃO, "*Optical Vernier Effect: Recent Advances and Developments*", Laser & Photonics Reviews, 15, 7, 2000588, 2021.

[2] Yunhao CHEN, Li ZHAO, Shuai HAO, Jianing TANG, "*Advanced Fiber Sensors Based on the Vernier Effect*", Sensors, 22, 7, 2694, 2022.

[3] Paulo ROBALINHO, André GOMES, Orlando FRAZÃO, "*Colossal Enhancement of Strain Sensitivity Using the Push-Pull Deformation Method*", IEEE Sensors Journal, 21, 4, 4623–4627, 2021.

[4] André D. GOMES, Marta S. FERREIRA, Jörg BIERLICH, Jens KOBELKE, Manfred ROTHHARDT, Hartmut BARTELT, Orlando FRAZÃO, "*Optical Harmonic Vernier Effect: A New Tool for High Performance Interferometric Fiber Sensors*", Sensors, 19, 24, 5431, 2019.

[5] Rosa Ana PEREZ-HERRERA, Mikel BRAVO, Daniel LEANDRO, Susana NOVAIS, Javier PRADAS, Manuel LOPEZ-AMO, "*Multiparameter Sensor Based on a Multi-Interferometric Serial Configuration For Temperature and Strain Measurements*", IEEE Journal of Selected Topics in Quantum Electronics, 27, 6, 1–4, 2021.

[6] Angel I. CORREA, Marko GALARZA, Romain DAULIAT, Raphael JAMIER, Philippe ROY, Manuel LOPEZ-AMO, Rosa Ana PEREZ-HERRERA, "*High frequency vibration sensor using a fiber laser with a multicore fiber interferometer*", IEEE Sensors Journal, 1–1, 2024.

[7] N. KISHI, E. YAMASHITA, K. ATSUKI, "*Modal and coupling field analysis of optical fibers with circularly distributed multiple cores and a central core*", Journal of Lightwave Technology, 4, 8, 991–996, 1986.

[8] Jose A. FLORES-BRAVO, Ruben FERNÁNDEZ, Enrique ANTONIO LOPEZ, Joseba ZUBIA, Axel SCHÜLZGEN, Rodrigo AMEZCUA CORREA, Joel VILLATORO, "*Simultaneous Sensing of Refractive Index and Temperature With Supermode Interference*", Journal of Lightwave Technology, 39, 22, 7351–7357, 2021.

[9] Byeong Ha LEE, Young Ho KIM, Kwan Seob PARK, Joo Beom EOM, Myoung Jin KIM, Byung Sup RHO, Hae Young CHOI, "*Interferometric Fiber Optic Sensors*", Sensors, 12, 3, 2467–2486, 2012.

[10] Zhiqi LU, Changning LIU, Chi LI, Jie REN, Lun YANG, "*Ultra-High Sensitivity and Temperature-Insensitive Optical Fiber Strain Sensor Based on Dual Air Cavities*", Materials, 16, 8, 3165, 2023.

Enhancing optical feedback interferometry with an integrated variable optical attenuator

Ayesha Arshad [1,2], Usman Zabit [2], Olivier Bernal [3], Clement Deleau [4], and Robert Halir [1,5]

1. Telecommunication Research Institute (TELMA), University of Málaga, Louis Pasteur 35, Málaga, 29010, Spain.
2. Department of Electrical Engineering, National University of Sciences and Technology (NUST), Islamabad, Pakistan.
3. LAAS-CNRS, Université de Toulouse, INP, Toulouse, 31400, France.
4. Nanoscale Quantum Photonics Laboratory, RIKEN Cluster for Pioneering Research, Saitama, 351-0198, Japan.
5. IBIMA Plataforma BIONAND, Parque Tecnológico de Andalucía, Málaga, 29010, Spain.

Contact: Ayesha Arshad (aarshad@uma.es)

ABSTRACT:

Optical feedback interferometry is a promising technique for displacement sensing. Maintaining stable and precise optical feedback requires effective control of reflected light intensity. In this study, we propose an integrated on-chip OFI system featuring a variable optical attenuator (VOA) for dynamic feedback regulation. We develop a novel analytical model and, through a realistic attenuator design, demonstrate the system's capability to achieve high-precision displacement measurements over a wide optical feedback parameter range ($2 < C < 100$) for target distances up to a few centimeters. These results highlight the potential of this approach for short-range applications with variable reflection conditions, such as MEMS characterisation.

Key words: Self-mixing interferometry, Laser Sensor, Displacement Sensing, Integrated Optics, Silicon-on-Insulator

1.- Introduction

Optical feedback interferometry (OFI) is a widely recognized and effective technique for displacement sensing because of its inherent self-alignment and low cost [1]. It is based on feeding light reflected from a target back into a laser cavity and photodetection of the output power [see Fig. 1]. The displacement, $D(t)$ of the target can then be recovered from the output power, $P(t)$, using signal processing [2].

OFI is very sensitive because of its coherent nature [3]. For robust operation, the amount of optical feedback in an OFI system

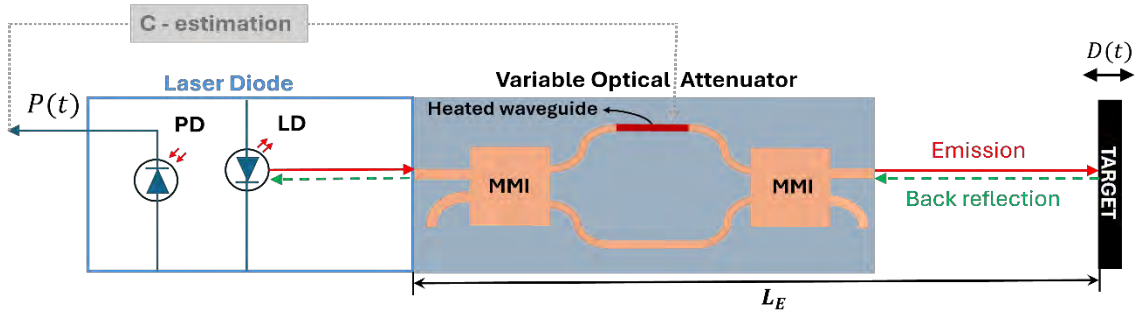

Fig. 1: Schematic of the proposed optical feedback interferometry system with an integrated variable optical attenuator based on a Mach-Zehnder interferometer.

needs to be controlled to keep in within the moderate optical feedback regime [1,4]. Different techniques involving piezo-electric transducers or external attenuators have been used to achieve this [5,6].

However, these solutions are vibration sensitive and difficult to integrate into embedded systems. Integrated Photonics is emerging as an attractive technology to implement devices due to its high transparency in the NIR region, high refractive index contrast leading to very compact systems, as well as compatibility with CMOS processes [7].

In this work, we present and analyse an on-chip OFI system with an integrated photonic variable optical attenuator. We present a novel model that establishes a direct relationship between the performance of the VOA and the overall OFI system. We show that this approach enables precise control of optical feedback, ensuring high displacement measurement accuracy even under significant variations in optical feedback. Furthermore, we investigate the effect of fabrication constraints in the integrated VOA on range of optical feedback that can be controlled.

2.- A typical OFI system and its integration with a VOA

2.1.- OFI system without VOA

Referring to Fig. 1, in OFI systems a laser beam, with a wavelength λ_0, is directed at a remote target moving with a displacement $D(t)$, typically on the order of a few micrometers. The target backscatters the beam back into the laser cavity resulting in interference between the back-reflected field with the field within the active laser cavity. This interference affects the operating state of the laser and varies the output power which is measured with a photodetector [1]. The modulated output power $P(t)$ is,

$$P(t) = P_0[1 + m\cos(\phi_F(t))] \quad (1)$$

where P_0 is the average emitted optical power, $\phi_F(t)$ is the laser phase with optical feedback and m is the modulation index. The phase under optical feedback $\phi_F(t)$ is related to the phase without feedback $\phi_0(t)$ by the transcendental Lang-Kobayashi excess phase equation [9]:

$$\phi_F(t) + C\sin(\phi_F(t) + \theta) = \phi_0(t) = \frac{4\pi}{\lambda_0}D(t) \quad (2)$$

Where C is the optical feedback coupling factor [10, 11], $\theta = \arctan(\alpha)$ and α is the linewidth enhancement factor [12]. This equation allows calculating $D(t)$ using the detected $P(t)$ signal. Since there is no closed-form expression that relates $D(t)$ to $P(t)$ (because equation (2) is transcendental), numerical algorithms are needed to solve for $D(t)$, and these numerical algorithms work best in for certain values of C, under optical feedback. Laser diode operation depends on the value of C, which depends on the reflection coefficient of the target and its distance from the front mirror of the laser cavity.

Depending on the value of C, specific operating regimes have been identified. For displacement measurements, the moderate feedback regime ($1 < C < 4.6$) is preferred because in this regime the displacement $D(t)$ can be recovered with relatively simple algorithms from the measured power $P(t)$. One of the most widely used algorithms for measurement precision in region II is consecutive-samples based unwrapping (CSU) algorithm [13], providing a measurement precision of the order of $\lambda_0/30$ when $1.5 \leq C \leq 2$ [14].

2.2.- OFI system with VOA

The OFI system with VOA is modelled according to the schematic shown in Fig. 2 with the VOA between the laser cavity (formed by the mirrors M_1 and M_2) and the target (M_3). As discussed in the previous subsection, the laser diode operation is affected by the C parameter [11], which is defined as, without considering the presence of VOA,

$$C = \frac{\epsilon r_{ext}(1-r_2^2)}{r_2}\frac{L_T}{L_{LD}n_{LD}}\sqrt{1+\alpha^2} \quad (3)$$

where ϵ is a coefficient that takes into account for possible mode mismatch between the lasing mode and the reflected light, r_{ext} is the reflection coefficient of the

target, r_2 is the reflection coefficient of the laser front mirror (M_2) that emits the light, L_T is the distance between the target and laser and L_{LD} and n_{LD} are the length and the refractive index of laser cavity respectively. The objective of introducing the VOA is to control r_{ext} and hence the value of C as seen in equation (3).

In this work, we consider a lossless VOA with negligible reflections. It introduces a transmission coefficient t_{VOA} where $|t_{VOA}| \in [0,1]$. The equivalent reflection coefficient r_{eq} of the target can be modelled as

$$r_{eq} \approx \epsilon r_{ext} |t_{VOA}|^2 e^{j\beta L_E}. \quad (4)$$

The square in $|t_{VOA}|$ arises because light travels through the VOA twice.

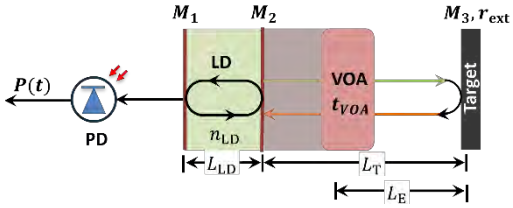

Fig. 2: Schematic of an OFI system using a VOA placed between the laser cavity and the remote target.

With that the equivalent optical feedback parameter $C_{eq}$is,

$$C_{eq} \approx C|t_{VOA}|^2 \quad (5)$$

Equation (5) indicates that with adequate values of t_{VOA} even large C values can be adjusted into the range $1.5 < C < 2$, making them suitable for the CSU algorithm.

3.- Design of a VOA on SOI

3.1.- Working principle of the VOA

We have established that an ideal VOA enables precise control of C values, ensuring optimal feedback control. The next step is to assess how closely an integrated VOA can approximate this ideal behavior. In this section, we briefly describe the design of the VOA which could be integrated into an OFI system and the impact of fabrication tolerances on the overall system. Fig. 3(a) shows the layer structure used for this design. The design is based on thermal modulation using the structure of a Mach-Zehnder interferometer (MZI) which consists of two multi-mode interference couplers (MMIs) acting as 3-dB splitters and combiners (Fig. 3(b)). By controlling the phase shift between the arms, this interference can be tuned from a constructive to a destructive state, thus achieving the desired variable attenuation. The transmission parameter is, as given in [15],

$$|t_{VOA}|^2 = |S_{31}|^2 = \frac{1}{2}(1 - \cos\varphi_T) \quad (6)$$

and

$$\angle t_{VOA} = \angle S_{31} = \frac{\pi}{2} - \frac{\varphi_T}{2}, \quad (7)$$

where

$$\varphi_T = \frac{2\pi}{\lambda_0}\frac{dn_{\text{eff}}}{dT}\Delta T L_{VOA}. \quad (8)$$

Here, dn_{eff}/dT is the effective thermo-optic coefficient of the heated arm, ΔT is the increase in temperature and L_{VOA} is the length of the heated arm. According to equation (6), the output power of the VOA varies sinusoidally with the temperature increase of one of the MZI arms with a linear change in phase as per equation (7).

3.2.- Components of the VOA and fabrication tolerances.

The main components of the VOA are multimode interference couplers for splitting and combining light waves, S-bends to separate the interferometer arms, and a waveguide heater to change the temperature in one of the arms. The optimized dimensions are summarized in Table 1. We investigate the impact of fabrication tolerances of the most critical dimension, MMI width, $W_{\text{MMI}} \pm \Delta$. As seen in Fig. 4(a), for small deviations $|\Delta| \leq 40$ nm, the dynamic range of the device is more than 24 dB. However, for larger deviations, the performance gradually deteriorates.

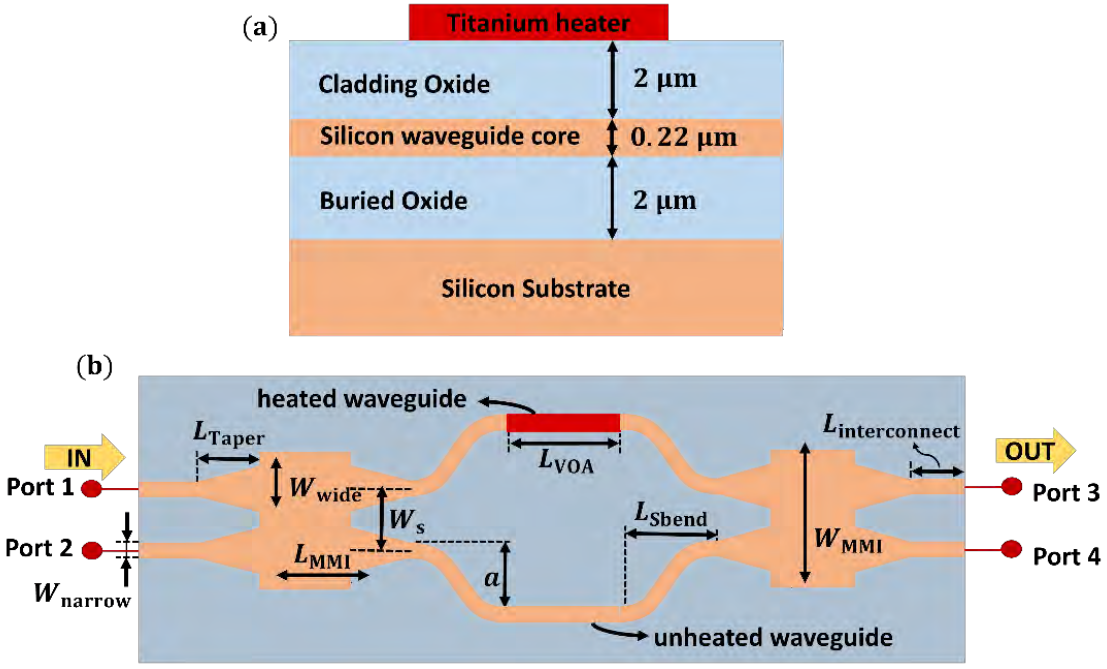

Fig. 3: (a) The layer structure of a waveguide-heater system on SOI. (b) Schematic of a variable optical attenuator based on a Mach-Zehnder interferometer consisting of two MMIs; one of which acts as a 3 dB splitter and the other as a combiner of light waves.

Table 1: Dimensions of the VOA

Dimension	W_{narrow}	W_{wide}	W_s	L_{taper}	L_{MMI}	W_{MMI}	a	L_{sbend}	L_{VOA}
Si Design (µm)	*0.5*	*1.3*	*1.85*	*12*	*33.1*	*3*	*8*	*12*	*100.81*

4.- OFI performance with a realistic VOA

In this section, we analyse the performance of the OFI system that can be achieved considering realistic fabrication tolerances of the integrated VOA based on equation (5). Fig. 4(b) shows the range of *C*-values that can be compensated by the VOA with fabrication constraints.

It is observed that *C*-values between ~ 2 and larger than 100 can be compensated by the VOA in a wide range of fabrication tolerances (-40 nm $< \Delta <$ 50nm). Beyond this range, the increasing imbalance of the MMIs hinders the effective cancellation of the VOA output power. However, it has been noted that reflections from the VOA also limit this range: the greater the target distance, the smaller the VOA reflections need to be [15]. If we restrict target distances a few centimeters the effect of these reflections on the measurement accuracy is negligible.

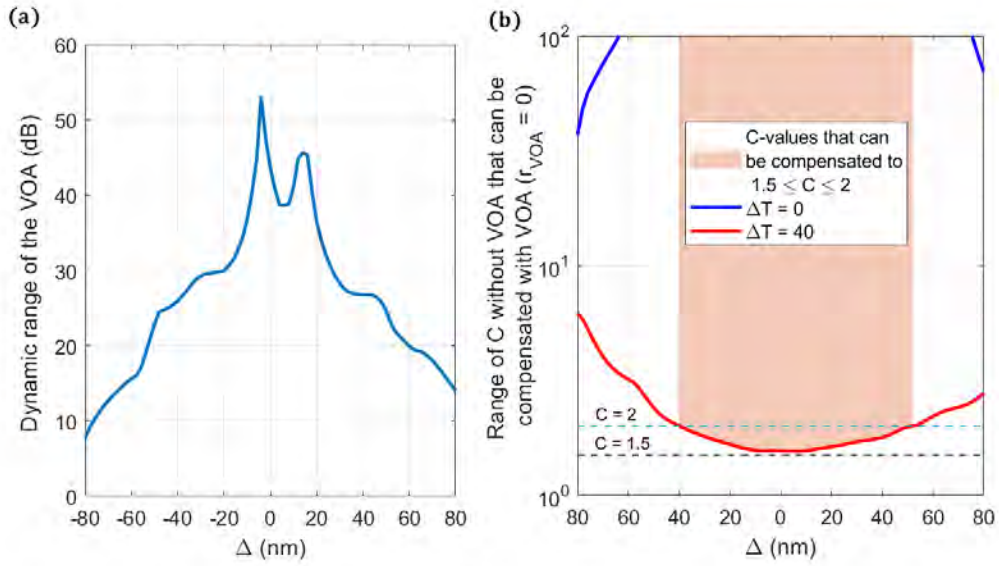

Fig. 4: (a) Dynamic range of the VOA. (b) C compensation range for the realistic VOA with fabrication constraints considering reflections from the VOA negligible.

5.- Conclusion

In this work, we have demonstrated that the performance of an OFI system can be improved significantly with the use of an integrated variable optical attenuator. We establish the conditions required for optimal displacement sensing performance by modelling the OFI system analytically and considering the fabrication constraints in the VOA concluding that their range should be below ± 40 nm.

Acknowledgements: This work has been sponsored by project TED2021-130400B-I00 / AEI / 10.13039 / 501100011033 Union Europea NextGenerationEU/PRTR and project ANR-20-CE42-0010 PICSONDE.

References

[1] T. Taimre, M. Nikolić, K. Bertling, *et al.*, "Laser feedback interferometry: a tutorial on the self-mixing effect for coherent sensing," Adv. Opt. Photonics **7**, 570–631 (2015).

[2] N. Ali, U. Zabit, and O. D. Bernal, "Nanometric vibration sensing using spectral processing of laser self-mixing feedback phase," IEEE Sensors J. 21, 17766–17774 (2021).

[3] R. Li, Z. Hu, H. Li, et al., "All-fiber laser-self-mixing interferometer with adjustable injection intensity for remote sensing of 40 km," J. Light. Technol. 40, 4863–4870 (2022).

[4] J. Schundelmeier, Q. Yang, and S. Hugger, "Hysteresis behavior of external cavity quantum cascade lasers in the strong feedback regime," IEEE J. Quantum Electron. 60, 1–10 (2024).

[5] M. Norgia, S. Donati, and D. D'Alessandro, "Interferometric measurements of displacement on a diffusing target by a speckle tracking technique," IEEE J. Quantum Electron. 37, 800–806 (2001).

[6] M. Norgia and S. Donati, "A displacement measuring instrument utilizing self-mixing interferometry," IEEE Trans. on Instrum. Meas. 52, 1765–1770 (2003).

[7] X. Chen, M. M. Milosevic, S. Stanković, et al., "The emergence of silicon photonics as a flexible technology platform," Proc. IEEE 106, 2101–2116 (2018).351

[8] C. Deleau, H. C. Seat, F. Surre, et al., "Optical feedback fm-to-am conversion with photonic integrated circuits for displacement sensing applications," J. Light. Technol. 42, 3446–3453 (2024).

[9] R. Lang and K. Kobayashi, "External optical feedback effects on semiconductor injection laser properties," IEEE J. Quantum Electron. 16, 347–355 (1980).

[10] T. Taimre and A. D. Rakić, "On the nature of acket's characteristic parameter c in semiconductor lasers," Appl. Opt. 53, 1001–1006 (2014).

[11] G. Acket, D. Lenstra, A. Den Boef, and B. Verbeek, "The influence of feedback intensity on longitudinal mode properties and optical noise in index-guided semiconductor lasers," IEEE J. Quantum Electron. 20, 1163–1169 (1984).

[12] C. Henry, "Theory of the linewidth of semiconductor lasers," IEEE J. Quantum Electron. 18, 259–264 (1982).

[13] A. Ehtesham, U. Zabit, O. D. Bernal, et al., "Analysis and implementation of a direct phase unwrapping method for displacement measurement using self-mixing interferometry," IEEE Sensors J. 17, 7425–7432 (2017).

[14] Zabit, U., Bernal, O. D., Amin, S., Qureshi, M. F., Khawaja, A. H., & Bosch, T, "Spectral processing of self-mixing interferometric signal phase for improved vibration sensing under weak-and moderate-feedback regime," IEEE Sensors Journal, 19.23, 11151-11158 (2019).

[15] A. Arshad, U. Zabit, O. Bernal, C. Deleau and R. Halir, "Robust integrated optical feedback interferometry via variable optical attenuation," *under review*

Distributed Acoustic Sensing for High-Speed Train Monitoring on Concrete Viaduct

Felipe Muñoz [1,2], José María Pérez Casas [3], Pedro Marín Pérez Martínez [4], Diego Gastón [1], Marco Jimenez-Rodriguez [1].

1. Uptech Sensing SL, 31192 Mutilva baja, Spain.
2. Department of Electronic Engineering, Universidad Técnica Federico Santa María, 2390123 Valparaíso, Chile.
3. SENER Mobility c\ Severo Ochoa 4, Tres Cantos. Madrid.
4. Ingeniero de Caminos, Canales y Puertos. Técnico de Ingeniería Civil en Proyectos de I+D+i en ADIF.

Contact: Felipe Muñoz (felipe.munoz@upetech-sensing.com)

ABSTRACT:

This study explores the application of distributed acoustic sensing (DAS) technology for railway monitoring, utilizing an optical fiber embedded within a concrete viaduct supporting high-speed train tracks. The system enables a range of functionalities, including train detection, track identification, classification of train models, precise speed estimation, and real-time monitoring of rolling stock condition. These capabilities contribute to improved safety, operational efficiency, and predictive maintenance strategies, fostering a more intelligent and resilient railway infrastructure.

Key words: Distributed Acoustic Sensing, Railway Monitoring, High-Speed Trains, Train Detection, Predictive Maintenance, Rolling Stock Assessment

1.- Introduction

Distributed Acoustic Sensing (DAS) technology has emerged as a transformative solution for railway and train monitoring, offering real-time insights into the condition of tracks and trains while enhancing safety and operational efficiency. By continuously monitoring the acoustic signals generated by trains, DAS can provide valuable data on track integrity, train movements, and even detect events such as trespassing or equipment failures. Railway operators can gain unprecedented visibility into track conditions and train performance, enabling them to identify potential issues before they escalate into serious problems. The ability to analyze these acoustic signals in real-time not only helps in reducing downtime and maintenance costs but also significantly improves the overall safety of rail operations. This innovative technology utilizes optical fiber cables to detect mechanical vibrations along the railway infrastructure. This is achieved by transmitting short pulses of highly coherent light to the optical fiber and analyzing the Rayleigh backscattered signal. Remarkably, this is accomplished without physical sensors, as the entire fiber itself functions as a distributed sensing element. Furthermore, DAS technology can leverage existing optical fiber networks, converting them into large-scale, high-resolution sensor arrays [1]. This capability makes DAS a cost-effective and scalable solution for extensive monitoring applications.

Recent studies have demonstrated its effectiveness in train detection, speed estimation, axle counting, and condition

monitoring of both tracks and rolling stock [2-5]. While dedicated fiber installations provide consistent sensitivity [6], the use of existing telecom fibers presents challenges due to variable coupling conditions [7]. Advances in signal processing and machine learning are improving the reliability of DAS-based railway monitoring [2]. These efforts aim to enhance the accuracy and applicability of DAS in railway monitoring, further contributing to the optimization of railway infrastructure and operations.

This paper presents an overview of monitoring techniques applied in a railway environment, using a DAS sensor to interrogate an optical fiber coupled within the structure of a concrete viaduct supporting high-speed train tracks. We explore a range of applications, including the detection of train passage, train track identification, identification of different train models, accurate speed calculation, and monitoring of rolling stock condition. These advancements offer significant potential for proactive maintenance and optimization, paving the way for smarter, more resilient transportation networks.

2.- Optical fiber cable installation and experimental conditions

The monitored concrete viaduct is 471 m long and has eleven spans. The DAS interrogator is located in span 1 at the north end of the viaduct. The sensing optical fiber is coupled to the structure with epoxy resin, forming two complete round trips to monitor its internal walls. The installation follows a structured path (Fig. 1a), starting from the interrogator, it runs along the upper right side (UR), returns via the upper left (UL), continues along the lower left (LL), and completes the loop on the lower right (LR). This configuration results in approximately 2 km of fiber and four complete passes through the viaduct.

The optical fiber is interrogated by a UTS-AS1000 DAS system from Uptech Sensing [10]. It is configured with 1kHz sampling rate, a pulse width of 50 ns, a gauge length of 5 m and a spatial sampling interval of 5 m, resulting in 400 fiber monitoring locations along the optical fiber.

Fig. 1b shows a waterfall diagram of a 15-second measurement window in which a train passage is detected by the DAS system. The waterfall plot reveals four distinct linear patterns with opposite slopes, each corresponding to the acoustic signal recorded as the train interacts with each of the four optical fiber sections coupled to the viaduct. At the top of the figure, the four fiber segments are labeled, mapping each position in the waterfall diagram to its respective fiber section. The color scale represents signal amplitude; darker colors correspond to higher signal levels. For each fiber section, ten distinct zones without vibrations are noticeable, which align with the viaduct the transitions between viaduct spans.

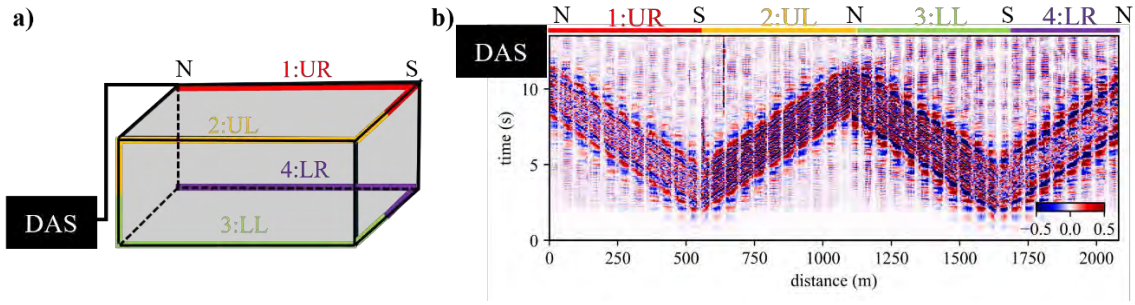

Fig. 1: (a) Fiber installation schematic. The DAS sensor located at north end (N) is shown connected to the fiber from the upper right side (1: UR, red) to the south end (S), then is connected to the upper left side (2: UL, yellow), lower left side (3: LL, green) and lower right side (4: LR, purple). (b) Waterfall diagram and optical fiber layout. A waterfall diagram of 15 seconds measurements is shown. The upper section of the figure illustrates the corresponding optical fiber segments, mapping each position in the waterfall diagram to its respective fiber section.

The train's northbound direction is inferred from any of the fiber segments, since vibrations first appear far from the interrogator at the south end (S) and progress toward the north end (N). The train is on the left track, as amplitudes in the UL and LL sections are higher than in the UR and LR sections. Comparing amplitudes enables clear identification of both the train track and direction of travel.

3.- Train detection

For automated train detection, an activity detector based on energy and spatial density is employed. DAS measurements are analyzed using a circular buffer that continuously processes data to identify significant changes in acoustic energy. An initial calibration establishes the noise level of the installation, defining a threshold for detecting anomalous activity. Since a passing train generates strong vibrations in the viaduct, the resulting acoustic energy is significantly higher than the baseline noise level. Moreover, because trains are hundreds of meters long, these vibrations are simultaneously detected at multiple spatial locations. This serves as a key criterion for train detection. The system robustness is further enhanced by leveraging the redundancy of the four fiber segments monitoring the same structure, effectively reducing the false positives to zero. A train is detected when the acoustic energy from DAS measurements exceeds the activity threshold at multiple fiber locations simultaneously across the four fiber segments.

4.- Train model identification

Train model identification is achieved using the following procedure: First, trains are automatically detected over a trial period to build a training dataset. Second, a clustering algorithm groups similar waveforms, which are subsequently matched with available train model information to create a labeled database. This process establishes a representative waveform for each train model. Third, when a new train is detected, its waveform is compared to the reference waveforms. A similarity score is then computed using the mean squared error between waveforms after temporal alignment. Finally, the train model is assigned based on the highest similarity score.

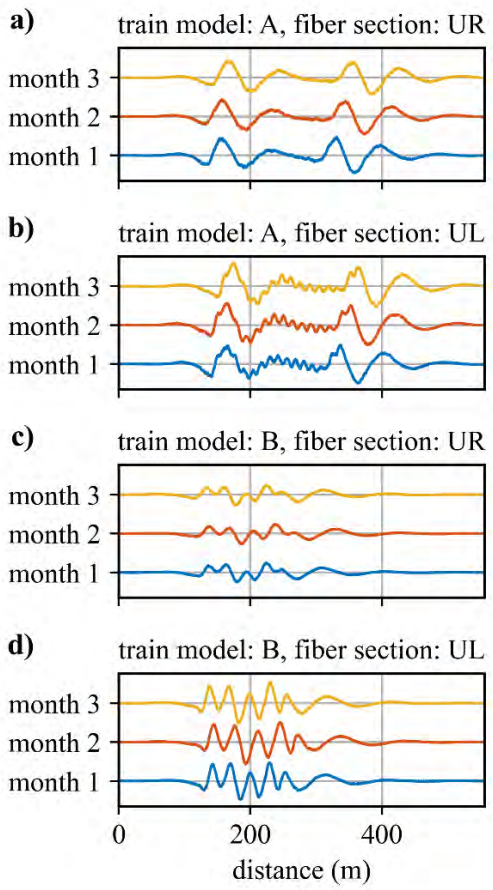

Fig. 2: Waveforms of train models A and B in the upper left (UL) and upper right fiber (UR) sections. The figure presents five waveforms recorded on different months for the same train machine (a) train A-UR section. (b) train A-UL section. (c) train B-UR section, and (d) train B-UL section.

Figure 2 displays the waveforms generated by two different train models (referred to as train A and B) as they pass through the UR and UL fiber sections. Trains following a northbound trajectory are selected. Each color represents a waveform recorded from a train crossing the viaduct at one-month intervals. The waveforms were recorded at a fixed spatial location, with the time axis converted to distance based on the estimated speed of the trains.

A comparison between waveforms of train A on the UR and UL sections (Figs. 2a and 2b) reveals that while the low-frequency components are similar, the high-frequency content is significantly attenuated in the UR section. This attenuation suggests that train vibrations undergo progressive filtering as they propagate along the viaduct. A similar trend is observed for train B, (Figs. 2c and 2d) where the UR section shows an additional reduction in amplitude. A comparison of the waveforms generated by train A and train B reveals distinct differences between the two models. Train A, with a length of approximately 200 meters, produces a waveform that differs significantly from that of Train B, which is approximately 100 meters long. Additionally, the peak configuration in their waveforms is distinct, providing a unique signature for each train. The waveforms within each subplot show high consistency across months, enabling the identification of a characteristic signature for each train model. This phenomenon will be further explored in a later section.

5.- Train velocity estimation

By taking advantage of prior knowledge of the geometry of the trains crossing the viaduct, the expected spectral signature of the waveform generated by the train can be calculated as a function of its speed, as following the method described in [11]. Once the train model is identified, its geometry is used to construct the expected spectral response as a function of train speed. Then, the actual signals measured by the DAS sensor are analyzed to extract its temporal spectra. After a peak detection stage, an optimization algorithm is applied to determine the speed that best aligns the theoretical and the experimental spectra. Figure 3a shows the Fourier transform applied to the temporal signals generated by the passage of a train for each fiber location. Color scale represents normalized spectral magnitude. Multiple spectral lines between 20 and 60 Hz are noticeable (as shown on Fig. 3b), as well as isolated lines around 120 Hz (as shown on Fig. 3c). These spectral lines are observed consistently across all spatial locations. A symmetry around the 420-meter mark is noticeable, consistent with the symmetry observed in the waterfall diagrams and reflective of the installation's geometric configuration. The sensor's ability to precisely capture the frequency content associated with the train's passage enables the application of spectral methods such as [11] to estimate the train's speed. Notably, this approach allows for the detection of speed variations along the viaduct. This is demonstrated by the slight frequency variations observed in the spectral lines across different fiber positions (Fig. 3c), indicating changes in the train's velocity as it traverses the structure.

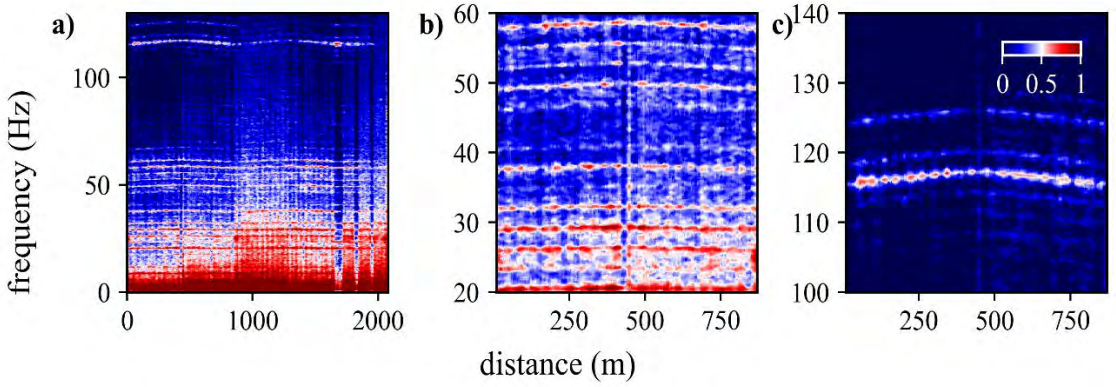

Fig. 4: Fourier transform analysis of the temporal signals generated by a train's passage, obtained for all fiber locations in the first two fiber segments (UR and UL). (a) Zoomed-in view of the frequency range 20–60 Hz. (b) Zoomed-in view of the frequency range 100–140 Hz. Color scale represents normalized spectral magnitude.

6.- Rolling stock condition monitoring

The rolling stock condition monitoring process follows a systematic workflow. It begins with the detection of an approaching train. Once detected, the system identifies the train model and estimates its speed, as outlined in previous sections. Using this speed estimate, the acoustic waveforms recorded at various positions along the optical fiber are temporally synchronized to compensate for time delays between spatial locations. This synchronization process transforms the diagonal pattern typical of a moving train into a horizontal aligned signal, ensuring that peaks and troughs in the waveform are temporally matched across all fiber locations. From these time-aligned waveforms, an acoustic fingerprint is extracted at each spatial point, representing the recorded energy levels as the train passes. These fingerprints are then associated with the train's unique identification number, creating a historical database that enables tracking and analysis of changes over time. Importantly, because the same train is monitored simultaneously by multiple fiber segments, independent fingerprints can be obtained for each segment. This redundancy enhances the reliability of anomaly detection and provides cross-validation between segments.

Figure 5 illustrates the evolution of the acoustic fingerprint of a specific train over several days, recorded from two fiber segments: the upper-right (UR) and upper-left (UL) segments, shown in Figs. 5a and 5b respectively. In both figures, the color scale represents the normalized acoustic energy. During the first 15 days, the fingerprint remains consistent, with no significant variation in energy levels. However, starting around day 15, a progressive increase in acoustic energy is observed at a specific spatial location near the 200-meter mark. This is indicated by a red arrow labeled "anomaly" in Fig. 5b and suggests increased vibration, likely caused by a mechanical issue in a specific component of the train.

Between days 30 and 35, the train is temporarily removed from service, as shown by the black horizontal lines, where no data is available for that train. Upon its return on day 35, the elevated acoustic energy is no longer present (orange arrow labeled "no anomaly"), suggesting that maintenance was performed to address the issue. However, by day 61, the anomaly reappears at the same spatial location (red arrow labeled "anomaly"), indicating a recurring problem. The train is then taken out of service again (blue arrow labeled "no train"), and following this second interruption, the anomaly once again disappears (orange arrow labeled "no anomaly").

Comparing the two fiber segments reveals that anomalies are consistently detected in both. However, the UL segment (Fig. 5b) provides greater spatial resolution and detail, which can be attributed to the fact that this specific train model travels on the left-hand track, closer to the UL fiber. This observation aligns with the variability in waveform characteristics between different fiber sections, as previously shown in Fig. 2.

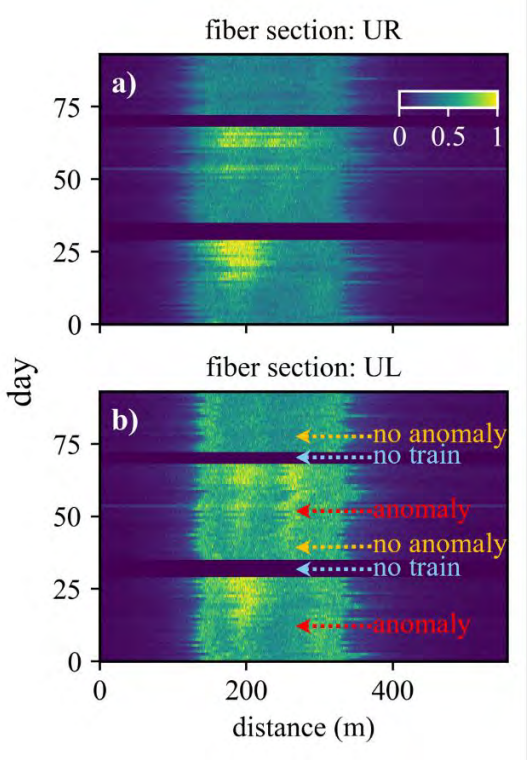

Fig. 5: Temporal signature of Train A over different days. (a) UR fiber section. (b) UL fiber section. Both fiber sections show a recurrent anomaly around the 200-meter mark.

7.- Conclusion

The results demonstrate the feasibility of monitoring high-speed trains using a distributed acoustic sensor system interrogating a fiber coupled to a concrete viaduct. The system successfully detects train passages, identifies tracks, classifies train models, estimates speed accurately, and monitors the condition of rolling stock. This study highlights the potential of collaboration between different institutions to enhance processing techniques by leveraging detailed information about trains, including their dimensions, plans, and engine numbers. Such collaborations between sensor technology and railway engineering are essential for advancing these capabilities. These findings position DAS technology as a valuable tool in the railway sector, offering real-time insights that contribute to safer and more efficient transportation infrastructure. Looking ahead, this work lays the foundation for further research and development of advanced techniques to provide even more detailed information on track conditions and anomalies, ultimately improving diagnostic capabilities, enhancing safety, and optimizing transport systems.

Acknowledgements: Se agradece al Centro para el Desarrollo Tecnológico Industrial (CDTI), e.p.e., por el contrato de servicios de I+D con SENER-UPTECH (CPP 03/2021 AB UTE) para el desarrollo de soluciones innovadoras en inspección y mantenimiento predictivo de puentes, viaductos y aparatos de desvío (lote 1, expediente CPP 03/2021 AB), en el marco del programa de Compra Pública Precomercial del CDTI. El desarrollo se ha realizado en el Viaducto de Guadalmazán (LAV Córdoba-Málaga, subtramo Guadalcázar–Fuente Palmera) por la UTE Sener Ingeniería y Sistemas – UPTECH SENSING.

Funding: Trabajo parcialmente financiado por: PTQ2021-011958 (Torres Quevedo, Ministerio de Ciencia), 0011-1408-2022-000020 y 0011-1408-2023-000026 (Doctorados Industriales, Gobierno de Navarra), y PNA-020100-2023-30 (PERTE-ECOFOSS, Ministerio de Industria).

References

[1] A.H. HARTOG, An Introduction to Distributed Optical Fibre Sensors (CRC Press, 2017).

[2] M.A. RAHMAN, S. JAMAL, H. TAHERI, "Remote condition monitoring of rail tracks using distributed acoustic sensing (DAS): A deep CNN-LSTM-SW based model," Green Energy and Intelligent Transportation, vol. 3, no. 5, 2024.

[3] C. WIESMEYR, et al., "Real-time train tracking from distributed acoustic sensing data," Applied Sciences, vol. 10, no. 2, 2020.

[4] F. PENG, N. DUAN, Y.J. RAO, J. LI, "Real-time position and speed monitoring of trains using phase-sensitive OTDR," IEEE Photonics Technology Letters, vol. 26, no. 20, pp. 2055–2057, 2014.

[5] G. CEDILNIK, R. HUNT, G. LEES, "Advances in Train and Rail Monitoring with DAS," in Proceedings of the 26th International Conference on Optical Fiber Sensors, paper ThE35, 2018.

[6] G. ZHANG, Z. SONG, A.G. OSOTUYI, R. LIN, B. CHI, "Railway traffic monitoring with trackside fiber-optic cable by distributed acoustic sensing Technology," Frontiers in Earth Science, vol. 10, 2022.

[7] F. MUÑOZ, J. URRICELQUI, M.A. SOTO, M. JIMENEZ-RODRIGUEZ, "Finding Well-Coupled Optical Fiber Locations for Railway Monitoring Using Distributed Acoustic Sensing," Sensors, vol. 23, no. 14, 2023.

[8] L. GAO, C. ZHOU, H. XIAO, Z. CHEN, "Continuous vertical Wheel-rail force Reconstruction method based on the distributed Acoustic sensing technology," Measurement, vol. 197, 2022.

[9] D. MILNE, A. MASOUDI, E. FERRO, G. WATSON, L. LE PEN, "An analysis of railway track behaviour based on distributed optical fibre acoustic sensing," Mechanical Systems and Signal Processing, vol. 142, 2020.

[10] Uptech Sensing, UTS-AS1000: High-resolution Distributed Acoustic Sensing Unit, http://uptech-sensing.com/producto-ampliado-uts-as1000.html.

[11] G. KOUROUSSIS, D.P. CONNOLLY, M.C. FORDE, O. VERLINDEN, "Train speed calculation using ground vibrations," Proceedings of the Institution of Mechanical Engineers, Part F: Journal of Rail and Rapid Transit, vol. 229, no. 5, pp. 466–483, 2015.

Self-referenced carrier frequency offset interferogram correction for dual-comb systems

A. ROMERO-BARRUECO*[(1)], C. ESCOBAR-VERA [(1)], C. QUEVEDO-GALÁN [(2)], A. ROSADO [(3,4)], J. MATEU-COMAS [(1)], S. MARTIN-LOPEZ [(1)], M. GONZALEZ-HERRAEZ [(1)], I. ESQUIVIAS [(2)], M. R. FERNÁNDEZ-RUIZ [(1)]

1. GRIFO - Sensors and Photonic Technologies, Universidad de Alcalá (UAH), Associate Unit to CSIC by Institute of Optics, 28805 Alcalá de Henares, Spain.
2. CEMDATIC - E.T.S.I. Telecomunicación, Universidad Politécnica de Madrid, 28040 Madrid, Spain.
3. Photonics Systems and Sensing Lab, School of Electronic Engineering, Dublin City University, Glasnevin, Dublin 9, Ireland.
4. CONNECT Research Centre, Dunlop Oriel House, Trinity College Dublin, Dublin, Ireland.

Contact: Alonso ROMERO-BARRUECO (alonso.romero@uah.es).

ABSTRACT:

Dual optical frequency comb (DOFC) has been unveiled as a prevailing tool for an increasing range of applications, such as molecular spectroscopy, ranging, imaging, and distributed sensing. Maintaining a high degree of temporal stability between the two mutually coherent interfering combs composing the DOFC is essential in emerging applications such as ranging and distributed sensing, where the amplitude and/or the phase profiles of subsequent interferograms are compared to extract time-varying information. In this work, we present a simple and efficient self-referencing correcting technique aimed at estimating and compensating for carrier frequency offset of time-domain interferograms. We validate our algorithm through a proof-of-concept spectroscopy experiment based on DOFC generated using optically injected gain-switched semiconductor lasers. Our experiments validate proper interferogram alignment with an SNR improvement of 38 dB along an interrogation time of nearly 0.2 s.

Key words: Carrier offset error correction, dual comb interferometry, molecular spectroscopy, optical fiber sensing

1.- INTRODUCCIÓN

La interferometría de doble peine se ha consolidado como una técnica altamente efectiva para caracterizar la respuesta compleja (amplitud y fase) de una muestra o sistema en un amplio ancho de banda, con alta resolución espectral y gran precisión, sin necesidad de componentes mecánicos móviles [1]. Su principio de funcionamiento se basa en el uso de dos peines de frecuencia óptica (OFC, por sus siglas en inglés) mutuamente coherentes, que comparten características similares excepto por una pequeña diferencia en su espaciamiento entre líneas, en una configuración conocida como peine de frecuencia óptica dual. Desde su propuesta, el uso de la interferometría de doble peine ha crecido de manera significativa, trascendiendo los límites de la espectroscopía y aplicándose en áreas como medición de distancias, formación de imágenes y detección distribuida en fibra óptica [2]. Algunas de estas aplicaciones innovadoras requieren OFCs con espaciado entre líneas muy estrechos, en el rango de los

MHz, ya que están diseñadas para operar en grandes distancias.

Dada la relación entre el ancho de banda óptico BW_o, el espaciamiento entre líneas f_R y el desplazamiento δf ($\delta f < f_R^2/(2 \cdot BW_o)$), impuesta para la conversión del dominio óptico al de radiofrecuencia (RF), el uso de espaciamientos entre líneas reducidos da lugar a interferogramas extremadamente largos (cuya duración es proporcional a $\propto 1/\delta f$). En este tipo de aplicaciones, es fundamental mantener la coherencia temporal de los interferogramas a lo largo de distancias extensas, ya que la información de interés suele extraerse a partir de la comparación en amplitud y/o fase de interferogramas que varían en el tiempo.

Uno de los principales obstáculos en estos sistemas es la desviación de la frecuencia de la portadora (CFO, por sus siglas en inglés), que se refiere a un desajuste en la frecuencia de la envolvente de la portadora entre los dos trenes de pulsos interferentes, e.g, por variaciones en la frecuencia del láser durante la medición. La presencia de CFO introduce ruido de fase y desplazamientos de frecuencia en los interferogramas generados por el sistema [3,4], lo que disminuye la precisión de la medición y degrada la resolución tanto en el dominio de la frecuencia como en el tiempo. Por ello, la corrección del CFO es un aspecto clave para garantizar la integridad y fiabilidad de los datos adquiridos.

En la literatura, se han propuesto diversos métodos para compensar las desviaciones en los interferogramas. Los enfoques tradicionales para la corrección del CFO suelen basarse en soluciones a nivel de hardware, como la mejora en la estabilidad de los osciladores, el uso de componentes con compensación térmica, referenciar con un sistema f-2f, la modulación electroóptica y técnicas de realimentación, entre otras [1]. Si bien estos métodos pueden ser efectivos en ciertos contextos, en general presentan altos costes económicos y reducen la portabilidad del sistema.

Por otro lado, los algoritmos de corrección digital aplicados en el postprocesado ofrecen una alternativa más flexible y económica [3,4]. Sin embargo, la mayoría de estos algoritmos se basan en el ajuste temporal de los interferogramas mediante correlaciones. En consecuencia, su eficacia se ve limitada en aquellas aplicaciones donde no se presenta un perfil bien definido para dichas correlaciones. Este es el caso de técnicas de detección distribuida como la reflectometría óptica en el dominio del tiempo con sensibilidad de fase y expansión temporal (TE-ΦOTDR), donde los interferogramas exhiben un perfil tipo speckle [2], o en experimentos en los que los peines de interrogación han sido modulados para mejorar la relación señal-ruido (SNR) de la medición [5].

En este trabajo, presentamos un algoritmo de postprocesado para sistemas interferométricos de doble peine, diseñado específicamente para aplicaciones que dependen de la comparación entre interferogramas variables en el tiempo. El método se basa en un análisis de correlación cruzada espectral entre conjuntos adecuados de interferogramas, aprovechando la alta resolución temporal y espectral de los sistemas de fibra óptica para lograr una alineación precisa de los componentes de frecuencia y mitigar los efectos de la desviación del CFO. Se valida el método mediante una medición espectroscópica basada en una configuración dual maestro-esclavo de láseres semiconductores conmutados en ganancia por inyección óptica [6]. La espectroscopía se ha utilizado como prueba de concepto del algoritmo, ya que permite ilustrar de manera clara su principio de funcionamiento.

2.- ALGORITMO DE CORRECCIÓN DE CFO

2.1. Descripción del algoritmo

Para la medición de información con parte compleja, se emplea una configuración asimétrica en la interferometría de doble peine. En este esquema, uno de los OFC del sistema de doble peine óptico (DOFC) se propaga a través de la muestra, mientras que el segundo OFC actúa como oscilador local (LO). Es necesario adquirir dos conjuntos de datos: el primero, obtenido con la muestra en

prueba (SUT) ubicada en el brazo de interrogación del sistema interferométrico, y un segundo conjunto de referencia, obtenido sin la SUT. Dependiendo de la aplicación, la SUT puede corresponder a una muestra de gas o líquido en una medición espectroscópica, a la distancia a un objetivo específico en un sistema de medición de distancias, o a una fibra sensora en un método de detección distribuida, como en TE-ΦOTDR.

El método de corrección se basa en tres etapas principales. En primer lugar, cada interferograma se completa con ceros (zero-padding) para mejorar la resolución espectral. Luego, se aplica la transformada rápida de Fourier (FFT), y se conserva únicamente la primera zona de Nyquist mediante un filtro de paso banda (BPF) adecuado. En la segunda etapa, cada interferograma con zero-padding se correlaciona de manera cruzada con el primero, que se usa como referencia, y se corrige la desviación del CFO. El ajuste de frecuencia a nivel submuestral se logra mediante un ajuste parabólico del pico de correlación cruzada.

Finalmente, en la tercera etapa, se compensa el desfase residual generado por la corrección de frecuencia entre interferogramas. Esto se realiza restando la fase de una línea de referencia a la fase de todo el espectro. La línea de referencia puede ser cualquier línea con una alta relación portadora-ruido (CNR). Estas tres etapas deben aplicarse tanto a los datos como a la medición de referencia. Una vez corregidas ambas adquisiciones, la respuesta espectral de la SUT se obtiene dividiendo el espectro de la muestra entre el espectro de referencia. Los interferogramas corregidos, que corresponden a la respuesta impulsional de la SUT, se obtienen aplicando la transformada inversa de Fourier (IFFT) a la respuesta espectral de la SUT.

2.2. Resultados experimentales y discusión

Para validar el algoritmo propuesto de corrección del CFO, hemos llevado a cabo un experimento de prueba de concepto basado en una medición de espectroscopía molecular. Un sistema DOFC fue generado mediante la técnica de bloqueo por inyección en láseres semiconductores conmutados en ganancia, bajo excitación eléctrica pulsada, como se ilustra en la Fig. 1 [6]. Para ello, se utilizaron dos láseres de modo discreto (DMLs) como láseres esclavos. El primer láser esclavo (SL1), que actuó como peine de interrogación, fue excitado con la superposición de una corriente de polarización I_{bias} = 1mA y un tren de pulsos eléctricos con una amplitud de voltaje V_{RF} = 6.5 V. El segundo DML (SL2), encargado de generar el oscilador local (LO), fue alimentado con I_{bias} = 4.8 mA y pulsos eléctricos de V_{RF} = 7 V. En ambos casos, los pulsos eléctricos, de corta duración (τ_{elec} = 200ps), fueron generados por generadores de patrones de pulsos (PPGs) y posteriormente amplificados para obtener amplitudes de modulación elevadas. Como láser maestro (ML), se empleó un láser sintonizable con un ancho de línea medido de ~60 kHz. La inyección óptica se realizó a 1549.5 nm, asegurando la generación de dos peines mutuamente coherentes y con un perfil espectral de tipo flat-top.

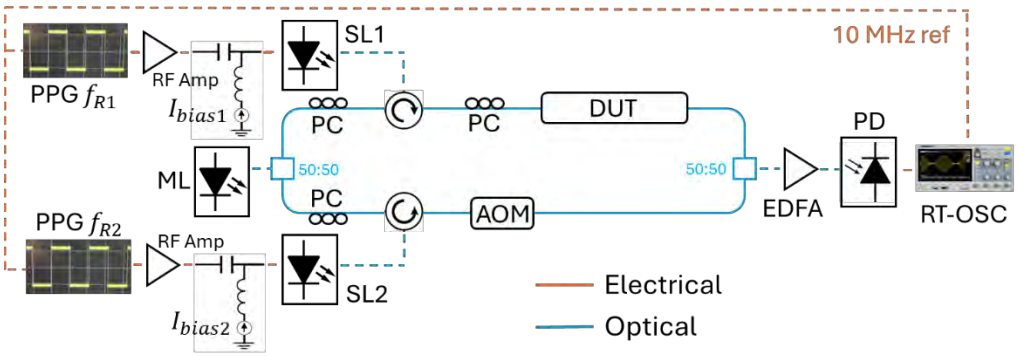

Fig. 1: Montaje experimental. ML: laser maestro, SL: laser esclavo, PC: controlador de polarización, DUT: muestra en evaluación, EDFA: filtro amplificador de erbio dopado, PD: fotodetector.

Bajo estas condiciones, se generaron dos peines de frecuencia óptica con un ancho de banda óptico de 100 GHz. El peine de interrogación tenía un espaciamiento entre líneas de f_R = 100 MHz mientras que el peine del oscilador local (LO) presentaba un

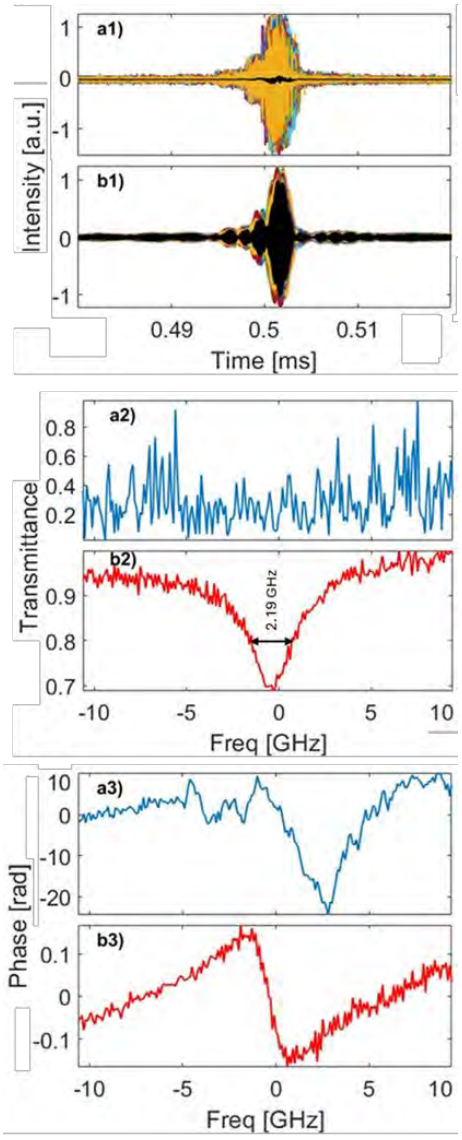

Fig. 2: 1) Corte central de la superposición de 200 interferogramas de 1ms, donde la línea negra representa la media del set completo; (a1) antes de la corrección; (b1) después de la corrección. 2) Respuesta espectral medida en el pico de absorción del HCN; (a2) Espectrograma normalizado antes de la corrección; (b2) Espectrograma normalizado después de la corrección. 3) Perfil de fase espectral en el pico de absorción; (a3) antes de la corrección; (b3) después de la corrección.

espaciamiento de $f_R + \delta f$ = 100 MHz + 1kHz. Para aprovechar al máximo el ancho de banda óptico disponible, se insertó un modulador acusto-óptico (AOM) en la rama LO, introduciendo un desplazamiento de frecuencia de 80 MHz en el peine LO. El peine de interrogación atravesó la muestra y la señal resultante se combinó con LO mediante un acoplador óptico 50:50. Para la adquisición de datos, la tasa de muestreo del osciloscopio se configuró en 200 MSa/s. Se capturaron interferogramas durante un período de 0.2 s, lo que equivale a 200 interferogramas independientes, con una duración de 1 ms cada uno (1/δf1/\delta f1/δf). La muestra utilizada fue una celda de HCN acoplada a fibra (25 Torr, 2 GHz), con un pico de absorción localizado en 1549.73 nm. El tiempo de procesado del algoritmo para la muestra empleada es de aproximadamente un minuto.

Los resultados de la medición espectroscópica se presentan en la Fig. 2. Debido al uso del AOM, la región espectral de interés en los interferogramas se desplaza hacia frecuencias más altas, alcanzando los 80 MHz. Estos interferogramas desplazados en frecuencia se han utilizado como datos de referencia, ya que presentan múltiples picos en el dominio temporal, lo que los convierte en un excelente ejemplo de los patrones no convencionales abordados en este trabajo. La fila superior de la Fig. 2 muestra los resultados obtenidos sin aplicar ninguna corrección, mientras que en la fila inferior se presentan los datos tras la aplicación del algoritmo descrito anteriormente. La columna de la izquierda muestra la superposición de las 200 mustras temporales detectadas. En negro, se representa el promedio temporal de todos ellos. Como se observa, la baja correlación entre los interferogramas impide obtener un promedio representativo a lo largo de los 0.2 s cuando no se aplica corrección (Fig. 2.a1). Si se obtiene el espectro de la señal promedio mediante FFT, las características de absorción y fase del HCN no pueden ser recuperadas (Figs. 2.a2 y 2.a3). Tras la aplicación del algoritmo de corrección, la coherencia entre interferogramas mejora significativamente, hasta el punto en que el promedio de los 200

períodos representa fielmente la tendencia general del conjunto (Fig. 2.b1). En el dominio de la frecuencia, el pico de absorción del HCN se vuelve claramente visible tanto en amplitud como en fase (Figs. 2.b2 y 2.b3, respectivamente). En particular, la profundidad de absorción y el ancho de línea medidos a partir del pico de absorción obtenido son T= 0.67 and FWHM= 2.19 GHz, respectivamente. Estos valores muestran una buena concordancia con los datos de transmisión proporcionados por el NIST (T= 0.5592) [7] y con la especificación de ancho de línea indicada por el fabricante de la celda de gas (~2 GHz).

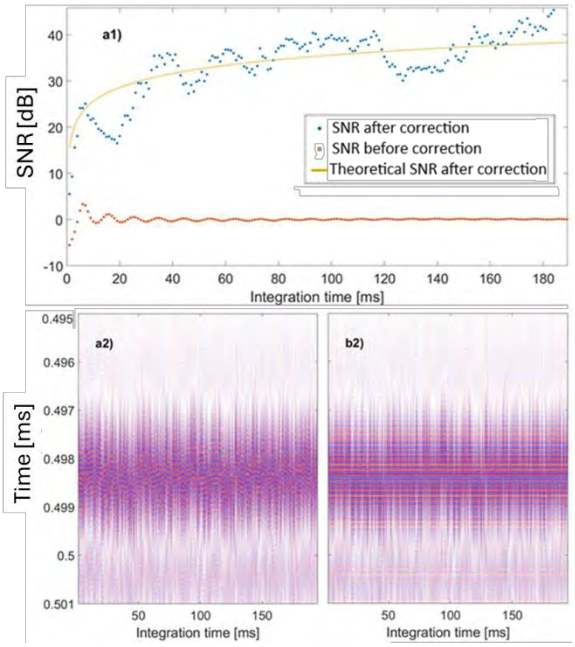

Fig. 3: 1) SNR después (azul) y antes (naranja) de la corrección, y estimación teórica (amarillo). 2) Todos los interferogramas concatenados antes (a2) y después (b2) de la corrección, evidenciando el alineamiento final.

El rendimiento del sistema puede evaluarse analizando la evolución de la relación señal-ruido (SNR) en función del tiempo de integración, como se ilustra en la Fig. 3. La SNR se calcula como la potencia de la señal (considerada como la media de la curva corregida, en negro en la Fig. 1.b1) dividida por la varianza del ruido (σ^2_{noise}), donde el ruido se obtiene restando la señal a cada interferograma. La SNR se determina antes y después de aplicar la corrección y se representa en la Figura 3.a. Para ilustrar mejor el comportamiento del sistema, se ha incluido una curva de referencia (SNR_0/n^2), donde SNR_0 es la SNR de cada uno de los n interferogramas. Se observa una buena concordancia con los datos experimentales, alcanzando una mejora de hasta 38 dB en la SNR a lo largo de aproximadamente 0.2 s. Adicionalmente, la Figura 3 resalta la mejora en la calidad de los datos obtenida gracias a la alineación de los interferogramas mediante el algoritmo propuesto.

4.- Conclusión

En este trabajo, hemos presentado un nuevo método de corrección del desplazamiento de frecuencia de la portadora (CFO) para sistemas interferométricos de doble peine, especialmente adecuado para aplicaciones en las que los interferogramas no están bien condicionados para una corrección en el dominio temporal mediante correlaciones. Esto incluye casos en los que los peines de interrogación requieren modulación para mejorar la relación señal-ruido (SNR) de la medición, así como métodos de sensado distribuido, como en TE-ΦOTDR. Nuestro enfoque se basa en la estimación y compensación del CFO en el dominio espectral mediante la correlación cruzada de los espectros de los interferogramas. Adicionalmente, se corrige la fase de los espectros para evitar discontinuidades entre las trazas corregidas en frecuencia.

Hemos demostrado la eficacia del método mediante una prueba de concepto en la que se detectó el pico de absorción de una muestra de HCN a partir de un conjunto de interferogramas desplazados a 80 MHz. Los resultados confirman la capacidad del algoritmo para compensar el ruido en frecuencia y fase, recuperando una señal de alta calidad a lo largo de 0.2 segundos y logrando una mejora en la SNR de 38 dB.

Acknowledgements: The work of M.R.F-R. was supported by MCIN/AEI/10.13039/501100011033 and European Union «NextGenerationEU»/PRTR under grant RYC2021-032167-I. This work was supported in part by the Spanish MCIN/AEI/10.13039/501100011033 and the European Union NextGenerationEU/PRTR Program under Grants PSI: ref. PLEC2021-007875 and REMO ref. CPP2021-008869, in part by the Spanish MCIN/AEI/10.13039/501100011033, and FEDER Una manera de hacer Europa under Grants PRECISION: ref. PID2021-128000OB-C21, MOTION: ref. PID2022-140963OA-I00, ref. PID2021-1234590B-C21, and ref. TED2021-131957B-100; in part by the European Innovation Council under Grants SAFE: ref. 101098992 and SUBMERSE: ref.101095055, and in part by the MCIN/AEI/10.13039/501100011033 under Grant SEASNAKE+, ref. PCI2023-145978-2 of the CETPartnership 2022 joint call. A. R. also acknowledges the financial support of Taighde Éireann – Research Ireland under Grant number 13/RC/2077_P2 at CONNECT: the Research Ireland Centre for Future Networks.by…

References

[1] I. Coddington, N. Newbury, Swann W. Dual-comb spectroscopy. Optica. 2016;3(4):10.1364/optica.3.000414.

[2] Soriano-Amat, M., Martins, H. F., Durán, V., Costa, L., Martin-Lopez, S., Gonzalez-Herraez, M., & Fernández-Ruiz, M. R. (2021). Time-expanded phase-sensitive optical time-domain reflectometry. Light Science & Applications, 10(1).

[3] H. Yu, K. Ni, Q. Zhou, X. Li, X. Wang, and G. Wu, "Digital error correction of dual-comb interferometer without external optical referencing information," Vol. 27, Opt. Express, 29425–29438 (2019).

[4] N. B. Hébert, V. Michaud-Belleau, J. -D. Deschênes and J. Genest, "Self-Correction Limits in Dual-Comb Interferometry," Vol. 55, IEEE Journal of Quantum Electronics, Article 8700311 (August 2019).

[5] M. Tapiador et al., "Definition of a FPGA-Based SoC Architecture for PRBS Transmission in Optical Spectroscopy," in IEEE Transactions on Instrumentation and Measurement, vol. 72, pp. 1-9, 2023, Art no. 2007109.

[6] C. Quevedo-Galán, V. Durán, A. Rosado, A. Pérez-Serrano, J. M. G. Tijero, and I. Esquivias, "Gain-switched semiconductor lasers with pulsed excitation and optical injection for dual-comb spectroscopy," Opt. Express 28, 33307-33317 (2020).

[7] S. Gilbert, W. Swann, and C. Wang, 2519a, Hydrogen cyanide H13C14N absorption reference for 1530 nm to 1565 nm wavelength calibration - SRM, (2005).

Phase-sensitive common-path dual frequency comb spectroscopy

Júlia MATEU-COMAS [(1)], Alonso ROMERO-BARRUECO [(1)], Miguel GONZALEZ-HERRAEZ [(1)], Sonia MARTIN-LOPEZ [(1)], María R. FERNÁNDEZ-RUIZ [(1)]

1. GRIFO – Sensors and Photonic Technologies, Universidad de Alcalá (UAH), Associate Unit to CSIC by Institute of Optics, 28805 Alcalá de Henares, Spain

Contact: Júlia MATEU-COMAS (julia.mateu@uah.es).

ABSTRACT:

Common-path dual comb spectroscopy using a single electro-optic modulator has been reported as a flexible, simple and low-cost symmetric dual comb configuration capable of measuring fine spectral signatures in the MHz regime with an extraordinarily high stability over acquisition times of seconds. However, the main drawback of symmetric dual comb configurations is that only the amplitude spectral response of the sample is obtained, losing any information from the phase spectral profile. In this work, we formulate and demonstrate, for the first time to our knowledge, an algorithm capable of extracting spectral phase information from a symmetric dual comb configuration. A phase reconstruction strategy based on the analysis of the spectral phase profile of high order Nyquist zones is performed. Our proposed algorithm is validated by extracting the transmission and phase profiles of a lossy fiber-based ring resonator.

Key words: Dual comb spectroscopy, ring resonator, symmetric dual comb configuration, electro-optic frequency combs, complex-valued spectral characterization.

1.- Introducción

En los últimos años, la espectroscopía de doble peine (DCS) ha llamado la atención gracias a sus interesantes propiedades como, por ejemplo, la alta tasa de adquisición, su excelente resolución espectral y simplicidad, ya que un ancho rango de espectro óptico puede ser interrogado con fotodetectores que presenten un ancho de banda relativamente estrecho. DCS se basa en usar un doble peine en frecuencias (DFC), es decir, un par de peines ópticos en frecuencias con características espectrales muy similares en términos de magnitud, perfil de fases y ancho de banda, pero con un pequeño desplazamiento, δf, en su tasa de repetición (conocida como, f_R y $f_R + \delta f$, respectivamente, con $\delta f \ll f_R$) [1]. Existen dos principales configuraciones DCS. En la configuración asimétrica, uno de los dos peines se usa como señal sonda y se propaga a través de la muestra sometida a ensayo (SUT). Por lo tanto, la amplitud espectral y el perfil de fases de la SUT estarán codificados en las frecuencias del peine sonda. El segundo peine se usa como referencia u oscilador local (LO). La interferencia entre los dos peines es fotodetectada. Entonces, una versión comprimida y reducida en frecuencias de la sonda modulada por la SUT se obtiene en el dominio de la radio frecuencia (RF). Por el contrario, en la configuración simétrica, los dos peines que comprenden el DFC se combinan, por ejemplo, usando un acoplador óptico, y seguidamente se propagan por la SUT. Consecuentemente la información de la SUT esta codificada en los dos peines. La señal de salida es fotodetectada y, en el dominio de la RF, el peine comprimido sólo

conserva la información sobre el perfil de magnitud de la SUT con variaciones de intensidad, mientras que la información de fase se pierde. Esta última configuración se prefiere típicamente cuando la interacción con la muestra es relativamente débil, y únicamente se necesitan cambios en la amplitud para su posterior caracterización [1].

En la mayoría de las configuraciones de doble peine, los dos peines en frecuencia se propagan por distintas ramas antes de interferir. Esto impone un límite en la coherencia de los dos peines durante la interferencia, ya que cualquier fluctuación o variación en el camino óptico causada por diferencias de temperatura, longitud del camino óptico o tensión entre los dos brazos afecta directamente a su coherencia mutua. Hace unos años se propuso un espectrómetro electroóptico de doble peine con una sola rama [2]. Implementaba una configuración simétrica en la que el peine dual se generaba con un único modulador Mach-Zehnder accionado por una señal eléctrica adaptada que consistía en la superposición de dos trenes de pulsos con velocidades de repetición ligeramente diferentes. Por lo tanto, el espectro óptico estaba compuesto por dos peines de frecuencias intercalados cuyo espaciado entre líneas difería en un pequeño desplazamiento. Dado que los dos peines interferentes comparten el camino óptico, el DCS implementado permitió realizar mediciones autorreferenciadas con estabilidad a lo largo de tiempos de integración de 1 segundo (como se demostró en [2]) sin necesidad de métodos de corrección en tiempo real ni bucles de realimentación. De todas formas, esta configuración simétrica no era capaz de medir la información de fase de la SUT. En este trabajo, proponemos un algoritmo para recuperar la fase espectral óptica de una SUT a partir de un sistema espectroscópico de doble peine de trayecto común. Demostramos que, analizando los perfiles espectrales de fase de la primera y tercera zona de Nyquist, es posible reconstruir la fase óptica de la SUT, permitiendo una caracterización completa. Nuestra propuesta se valida midiendo los perfiles de transmisión en amplitud y fase de un anillo de fibra resonador con pérdidas en dos regímenes de funcionamiento diferentes, conocidos como, subacoplado y sobreacoplado (con retardos de grupo positivos y negativos, respectivamente) [3].

2.- Reconstrucción de fase en configuración de doble peine simétrica

En esta sección, se describe el procedimiento propuesto seguido para la reconstrucción de la fase espectral de la SUT en la configuración simétrica de doble peine. Para aplicar este procedimiento necesitamos dos medidas. En una, los dos peines de frecuencia que componen el DFC se propagan a través de la muestra y la señal de la interferencia se fotodetecta. En este conjunto de datos, la información de fase y de amplitud de la SUT (con respuesta espectral $H(f) = |H(f)|e^{j\phi(f)}$) se codifica en las líneas espectrales de los dos peines. El siguiente conjunto de datos consiste en una medida de referencia, donde los dos peines interfieren en el fotodetector sin pasar por la SUT. Una vez se tienen los datos, con tal de reconstruir la fase primero se obtiene la transformada rápida de Fourier (FFT) de los dos conjuntos de datos y seguidamente se divide el espectro con la información de la SUT entre la referencia (solo en las frecuencias que estén presentes las líneas de batido). Este paso permite restar cualquier modulación de fase espectral inicial de los peines ópticos en el dominio de RF, de manera que las fases de las líneas de batido solo incluyan la contribución de la fase $H(f)$ evaluada en las correspondientes frecuencias ópticas ($\phi^{opt}(f)$). La amplitud de las líneas del peine en la primera zona de Nyquist se puede aproximar como la raíz de la respuesta en amplitud de la muestra. La fase de la n^{th} línea del peine en la primera zona de Nyquist es $\phi_n^{1NZ} = \phi_{n'}^{opt} - \phi_n^{opt}$, donde n' y n se refieren a los índices de los dos peines, siendo el representado con el primo el peine con un mayor desplazamiento de envolvente de portadora, como se muestra en la Fig. 1.a). En la tercera zona de Nyquist, la fase de la n^{th} línea de peine es $\phi_n^{3NZ} = \phi_{(n+1)'}^{opt} - \phi_n^{opt}$ (mirar Fig.1.b)). El perfil de fase de cada línea

de la primera zona de Nyquist se resta del perfil de fase de la tercera zona de Nyquist. Por lo tanto, $\phi_n^{\Delta} = \phi_{(n+1)'}^{opt} - \phi_{n'}^{opt}$. Nótese que, en este punto, ϕ_n^{Δ} es directamente proporcional al retardo de grupo de la SUT con signo opuesto, dado que $\tau_g = -(1/2\pi) \cdot d\phi(f)/df$. En particular, el perfil de fase recuperado ϕ_n^{Δ} es proporcional al diferencial de la fase óptica evaluada en la tasa de repetición del peine de sondeo, es decir $\tau_g = \phi_n^{\Delta}/(2\pi f_R)$. Finalmente, el perfil de fase resultante obtenido en las frecuencias de batido se integra a lo largo del eje de frecuencia, convirtiéndose este último al dominio óptico escalado con el factor de compresión ($CF = f_R/\delta f$). La curva resultante corresponde al perfil de fase óptica de la SUT muestreado por uno de los dos peines ópticos.

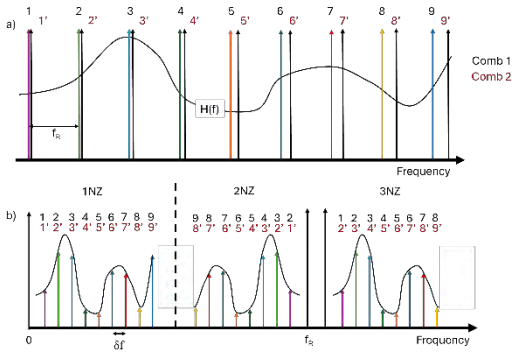

Fig. 1: (a) Representación de una configuración de peine de frecuencia dual de trayectoria común, donde los dos peines ópticos se propagan a través de la muestra, cuya respuesta espectral es $H(f)$. (b) Espectro de RF de la señal de batido y disposición de las líneas convertidas a baja frecuencia en diferentes zonas de Nyquist (NZ). Los índices en negro y rojo se refieren a las frecuencias de cada uno de los dos peines, respectivamente.

Este algoritmo funciona correctamente siempre que la respuesta al impulso de la SUT (es decir, la transformada inversa de Fourier de $H(f)$) sea mucho más corta que el período de los peines de interrogación ($T \approx 1/f_R$). Esto significa que el muestreo espectral de $H(f)$ realizado por los peines de interrogación es lo suficientemente alto como para reconstruir la información espectral de la SUT sin ambigüedades.

3.- Demostración experimental

La validez del algoritmo propuesto se demuestra mediante la caracterización espectral completa de un resonador de anillo de fibra con pérdidas [3,4]. El montaje experimental se corresponde con el esquema presente en la Fig. 2. La fuente de luz es un láser CW (NKT Koheras Basik X15) operando a una longitud de onda central, λ_0, de 1550.12 nm, y con un ancho de línea de aproximadamente 100 Hz. La salida del láser se modula mediante un modulador de Mach-Zender (MZM) accionado por una señal diseñada con las características convenientes mediante un generador formas de onda arbitrarias (AWG, Keysight M8195A). La señal consiste en la parte real de una señal analítica correspondiente a la suma de dos peines de frecuencia en el dominio del tiempo, abarcando un ancho de banda de 7GHz con un espaciado entre líneas de f_R= 3.5 MHz. El desplazamiento entre los dos peines es δf= 800 Hz. La señal resultante se amplifica con un amplificador de fibra dopada con erbio (EDFA) con el objetivo de aumentar la potencia óptica a la salida de los peines de frecuencia generados y, posteriormente, se filtra con un filtro óptico de banda ajustable (TBPF). La función del TBPF es doble: reduce el ruido fuera de banda que genera el EDFA debido a emisión espontánea y mantiene una única banda de la modulación de doble banda lateral realizada por el MZM [2]. La señal filtrada entra en un acoplador óptico 70/30, donde el 70% de la señal entra al anillo resonador. El anillo consta de un controlador de la polarización (PC) y un atenuador óptico manual ajustable (VOA). Finalmente, la salida del anillo resonador se fotodetecta (PD) y se adquiere con un osciloscopio de alta velocidad.

En el anillo resonador, el PC asegura que la polarización se mantiene constante a lo largo de cada vuelta. El retardo de grupo variará entre dos regímenes dependiendo de la tasa de acoplo, κ, y de las pérdidas en el resonador, a, tal y como se describe en [3]. En el régimen sobreacoplado, $\kappa \gg a$ y el retardo de grupo será negativo. Por el contrario, en el régimen

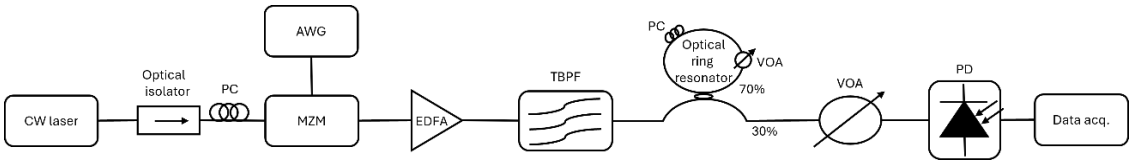

Fig. 2: Configuración experimental del camino común propuesto para la caracterización espectral de un anillo resonador óptico. Las siglas se definen en el texto principal.

subacoplado, $\kappa \ll a$, y el retardo de grupo inducido por el anillo es positivo. Por lo tanto, cada régimen nos da una respuesta en fase distinta y bien definida, permitiéndonos así validar el método espectroscópico propuesto. Para obtener más información sobre el comportamiento del resonador de anillo, se remite al lector interesado a la referencia [3]. La amplitud del espectro consistirá en picos de resonancia con una periodicidad de c/nL donde c se corresponde con la velocidad de la luz en el vacío, n con el índice de refracción efectivo de la fibra y L la longitud del anillo. En nuestro caso, L, tendrá un valor estimado de 5.5 m, generando una periodicidad espectral de aproximadamente 36 MHz. Esto respalda la elección de una tasa de muestreo de 3.5 MHz, lo que permite alrededor de 10 puntos de muestreo por pico de resonancia. Se han realizado múltiples medidas con diferentes niveles de atenuación para así tener un barrido por los distintos regímenes del sistema. La medida de referencia se ha obtenido eludiendo la estructura del anillo.

En la Fig. 3, se muestran los resultados del algoritmo diseñado para la reconstrucción de la fase espectral de la SUT, en nuestro caso, el anillo resonador óptico. Tal y como se ha mencionado antes, el anillo resonador presenta dos regímenes distintos en su característica espectral, dependiendo de la relación entre los valores κ y a. En la Fig. 3.a) se muestran los resultados obtenidos en el régimen sobreacoplado ($\kappa \gg a$), mientras que en la Fig. 3.b) los resultados se muestran en el régimen subacoplado ($\kappa \ll a$). En las dos figuras superiores, se observa la transmisión espectral recuperada, obtenida directamente a partir de la amplitud espectral de la primera zona de Nyquist, como se menciona en la Sección 2. En azul, podemos observar los resultados experimentales obtenidos, que son comparados con los valores teóricos obtenidos a partir de la función de transferencia analítica del anillo resonador óptico, en rojo [3,4]. Para obtener la curva teórica se ha considerado $L = 5.645\ m$ y $A = -8.1498 \times 10^{-8}\ s$, siendo respectivamente la longitud del anillo resonador y el offset del retardo de grupo. Para el caso (a), los valores de a y k son 0.384 y 0.548, respectivamente. En el caso (b), los valores de A, a y k son $1.0102 \times 10^{-7}\ s$, 0.935 y 0.548, respectivamente. En ambos regímenes, observamos una perfecta coincidencia con los resultados teóricamente esperados.

La segunda fila de la Fig. 3 presenta el retardo de grupo dentro de una región específica del ancho de banda. Finalmente, la fila inferior muestra las fases ópticas. En todos los casos, las mediciones experimentales están representadas en azul, mientras que los valores teóricos de estos datos se muestran en rojo. Las curvas experimentales obtenidas de retardo de grupo y fase han sido reconstruidas siguiendo el procedimiento descrito en la sección anterior. En nuestros resultados, observamos, como era de esperar, una clara distinción entre los dos regímenes de acoplamiento. Para el régimen de sobreacoplamiento, el retardo de grupo es negativo, mientras que para el subacoplamiento es positivo. En cuanto a las fases, en el caso (a), obtenemos un perfil similar a un diente de sierra con picos de $1.5\ rad$ (azul). Estos resultados concuerdan correctamente con los teóricos (rojo), predichos mediante la integral del retardo de grupo previamente calculado. Las diferencias con respecto al perfil de fase típico de un resonador de anillo en un régimen de sobreacoplamiento se atribuyen a la resolución espectral disponible en nuestro sistema (3.5 MHz). En el caso (b), obtenemos el perfil de fase escalonado descendente esperado según la teoría [4]. Nuevamente, los

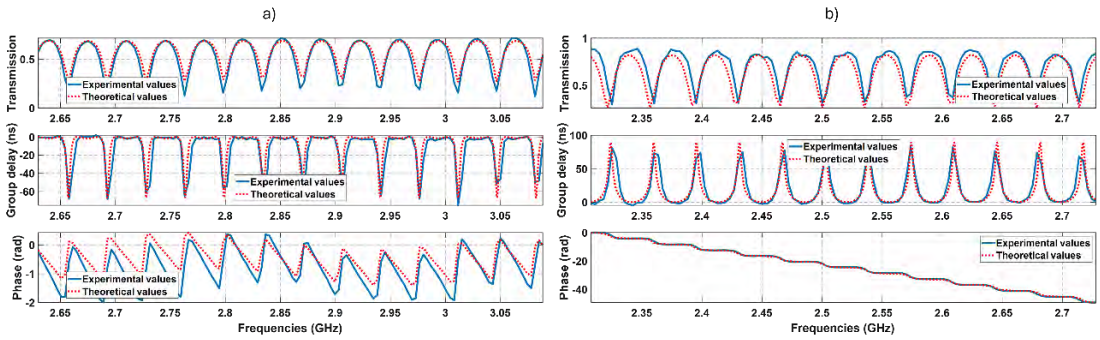

Fig. 3: Respuesta de fase, módulo y retardo de grupo en función de la frecuencia en un lazo de fibra de L metros en los dos diferentes regímenes de atenuación: (a) sobreacoplamiento y (b) subacoplamiento.

resultados teóricos y experimentales coinciden perfectamente. Esto corrobora la validez de nuestro algoritmo para el cálculo de la fase de una SUT a partir de las fases espectrales experimentales obtenidas en la primera y la tercera zona de Nyquist.

4.- Conclusiones

En este trabajo, hemos formulado y demostrado, por primera vez según nuestro conocimiento, un método sencillo para obtener información espectral de fase de una SUT bajo una configuración simétrica de doble peine de frecuencias.

Para la demostración experimental, hemos empleado adicionalmente una configuración de camino común, en la cual los dos peines interferentes se generan en la misma modulación óptica, comparten el mismo camino óptico y, por lo tanto, se compensa cualquier perturbación relacionada con la longitud del trayecto en el proceso de batido.

Como prueba de concepto, hemos caracterizado completamente, tanto en magnitud como en fase, la respuesta espectral de un resonador de anillo de fibra con pérdidas en sus dos modos de operación, obteniendo una excelente coincidencia con las curvas teóricas esperadas.

Esperamos que este trabajo allane el camino hacia esquemas de espectroscopía de doble peine más estables y simples, así como en otras aplicaciones basadas en peines de frecuencia duales, como, por ejemplo, imagen, medición de distancias o la detección distribuida por fibra óptica.

Acknowledgements: The work of M.R.F-R. was supported by MCIN/AEI/10.13039/501100011033 and European Union «NextGenerationEU»/PRTR under grant RYC2021-032167-I. This work was supported in part by the Spanish MCIN/AEI/10.13039/501100011033 and the European Union NextGenerationEU/PRTR Program under Grants PSI: ref. PLEC2021-007875 and REMO ref. CPP2021-008869, in part by the Spanish MCIN/AEI/10.13039/501100011033, and FEDER Una manera de hacer Europa under Grants PRECISION: ref. PID2021-128000OB-C21 and MOTION: ref. PID2022-140963OA-I00; in part by the European Innovation Council under Grants SAFE: ref. 101098992 and SUBMERSE: ref.101095055, and in part by the MCIN/AEI/10.13039/501100011033 under Grant SEASNAKE+, ref: PCI2023-145978-2 of the CETPartnership 2022 joint call.

References

[1] Ian CODDINGTON, Nathan NEWBURY, William SWANN, "Dual-comb spectroscopy", *Optica*, 3(4), 414-426, 2016. https://doi.org/10.1364/OPTICA.3.000414

[2] Vicente DURÁN, Camilo ESCOBAR-VERA, Miguel SORIANO-AMAT, Hugo F. MARTINS, Sonia MARTIN-LOPEZ, Miguel GONZALEZ-HERRAEZ, María R. FERNÁNDEZ-RUIZ, "Dual electro-optic comb spectroscopy using a single pseudo-randomly driven modulator", *Optics Express*,

30(15), 25103-25110, 2022. https://doi.org/10.1364/OE.463604

[3] Mikel BRAVO, Xabier ANGULO-VINUESA, Sonia MARTIN-LOPEZ, Manuel LÓPEZ-AMO, Miguel GONZÁLEZ-HERRÁEZ, "Slow-Light and Enhanced Sensitivity in a Displacement Sensor Using a Lossy Fiber-Based Ring Resonator", *Journal of Lightwave Technology*, 31(23), 3752-3757, 2013. https://doi.org/10.1109/JLT.2013.2288455

[4] John E. HEEBNER, Vincent WONG, Aaron SCHWEINSBERG, Robert W. BOYD, Deborah J. JACKSON, "Optical Transmission Characteristics of Fiber Ring Resonators", *IEEE Journal of Quantum Electronics*, 40(6), 726-730, 2004. https://doi.org/10.1109/JQE.2004.828232

An experimental study of forward-stimulated Brillouin scattering in optical fibers under hydrostatic pressure

Carlos Andrés ÁLVAREZ-OCAMPO[(1)], Aleksander S. PATERNO[(1,3)], Martina DELGADO-PINAR[(1,2)], Antonio DÍEZ[(1,2)], José Luis CRUZ[(1,2)], Miguel V. ANDRÉS[(1,2)]

1. Laboratory of Fiber Optics, ICMUV, Dr Moliner 50, Burjassot, Spain
2. Departament de Física Aplicada y Electromagnetisme, Universitat de València, Dr Moliner 50, Burjassot, Spain
3. Santa Catarina State University, Rua Paulo Malshitzky, 200, Joinville, Brazil

Contact: Carlos Andrés ÁLVAREZ-OCAMPO (carlos.alvarez@uv.es).

ABSTRACT:

We present a proposal to measure hydrostatic pressure with optical fibers based on the nonlinear phenomenon of forward-stimulated Brillouin scattering (FSBS). The method is based on the pressure sensitivity of the cutoff frequency of acoustic modes stimulated by FSBS. The results indicate that this technique successfully measures the pressure in the low/mid range.

Key words: Forward-stimulated Brillouin scattering, optomechanics, hydrostatic pressure, optical fiber sensing.

1.- Introduction

In the field of sensing of environmental variables such as pressure, fiber optic-based techniques have gained great interest due to their small size, light weight and immunity to electromagnetic fields [1]. The need for accurate pressure measurements in various fields such as oil and gas exploration, underwater environment and vessel monitoring, structural health in aerospace engineering and monitoring of pressurized gas containers, has prompted research into more efficient and accurate sensing methods [1-3].

One promising physical mechanism for pressure measurement is forward-stimulated Brillouin scattering (FSBS). FSBS is an optomechanical interaction that involves two co-propagating optical waves and nearly transverse acoustic modes resonances (TAMR's) of the optical fiber. Frequency shift analysis of the FSBS spectrum allows the determination of environmental parameters [4-6].

Previous investigations have revealed that torsional-radial acoustic modes ($TR_{2,m}$) which modulate the polarization of the optical field in the fiber, show a linear relationship between the frequency shift and the hydrostatic pressure applied to the fiber. In addition, pressure sensitivity has been found to differ between radial and torsional-radial acoustic modes [2-3]. The resolution, i.e. the smallest pressure change detectable is largely determined by the linewidth of the acoustic modes. The narrower the resonances, the better the resolution. In previous works, the reported resolution is relatively poor since they are based on spontaneous forward Brillouin scattering. Since the gain of the spontaneous process is very low, tens of meters of fiber were used. Additionally, the requirement of a long fiber length forces to maintain the fiber polymer coating. As a consequence of both, the linewidth of the resonant acoustic modes is of several MHz (Q-factor ~150).

Recently, we showed that acoustic mode resonances stimulated by FSBS in sub-cm fiber length can be probed optically with good efficiency [7]. Linewidth of the acoustic resonances measured in a bare optical fiber of a few cm in length is in the order of a few tens of kHz. Here, we report our experimental results regarding hydrostatic pressure measurement with FSBS, using a short telecom optical fiber.

2.- Theoretical background

FSBS is a nonlinear optomechanical interaction involving two copropagating optical waves and an acoustic wave propagating together in an optical waveguide. The stimulation of the acoustic mode relies on electrostriction. The acoustic waves that enable phase-matching are acoustic modes very close to their cutoff with almost zero axial wavevector. These are nearly transverse acoustic mode (TAMRs) of the optical fiber. The interaction is highly dependent on the geometry of the optical fiber and its elastic properties. In single-mode optical fibers, because of the symmetry of the optical and the acoustic fields, the fundamental optical fiber mode can only stimulate two types of acoustic modes, that is pure radial modes $R_{0,m}$ and torsional-radial modes with angular order 2, $TR_{2,m}$. In this work, we focused on $TR_{2,m}$ acoustic modes. It can be distinguished two different subtypes. The first, named as $TR^{(1)}_{2,m}$, behaves as torsional-like modes with a nearly azimuthal displacement vector, and the second subtype, named $TR^{(2)}_{2,m}$ are radial-like modes with displacement vector almost radial. The cutoff frequency of both subtype of torsional-radial modes can be approximated by [4]:

$$f^{(1)}_{2,m} \approx \frac{V_S}{2\pi a}\left(c_{m+1} - \frac{15}{8c_{m+1}}\right), \quad (1)$$

$$f^{(2)}_{2,m} \approx \frac{V_L}{2\pi a}\left(c_{m+1} - \frac{15}{8c_{m+1}}\right), \quad (2)$$

where a is the radius of the fiber, V_S and V_L are shear and longitudinal acoustic velocity, respectively, and $c_{m+1} = \left((m+1)\pi - \pi/4\right)$ being m ($m = 1, 2, 3 \ldots$) an integer denoting the mode order. The dependence of the acoustic velocities with pressure [8], leads to the frequency shift of the FSBS spectrum.

3.- Experimental methodology

Figure 1 shows the experimental setup. Stimulation of torsional-radial acoustic modes was archived through short optical pulses generated by a pump source. The pump laser was a Q-switched microchip laser emitting linearly polarized pulses of 700 ps duration at a repetition rate of 20 kHz, with an average power of 150 mW at 1064 nm. The polarization of the pump beam was controlled by a set of waveplates. Oscillation of the acoustic modes was probed optically. For the optical probe, we used a linearly polarized continuous wave diode laser emitting in the telecom C-band. The polarization of the probe beam was adjusted with a fiber polarization controller. The pump and probe beams were delivered into the fiber under test (FUT) by means of a 30× aspheric lens and a 3-axis stage.

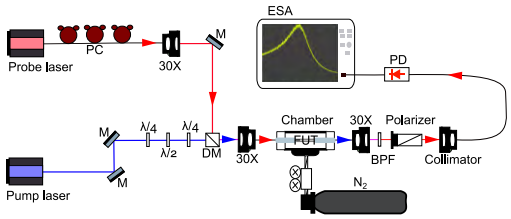

Fig. 1: Experimental arrangement. BPF: band-pass filter; M: mirror; PD: fast photodiode; DM: dichroic mirror; PC: optical fiber polarization controller; FUT: fiber under test (bare SMF-28); ESA: electric spectrum analyzer.

The torsional-radial modes were detected by polarization analysis of the probe beam after propagating through the FUT. The birefringence modulation of the FUT due to the oscillation of $TR_{2,m}$ acoustic modes resulted in the polarization modulation of the probe beam, which was converted into an intensity-modulated signal by the linear polarizer. A band pass filter was used to remove the pump wave. The probe signal was detected by a fast photodetector and recorded with an electrical spectrum analyzer (ESA).

Experiments were done with a bare optical fiber segment of 30 cm in length, in which the

polymer cladding was removed. To investigate the effect of hydrostatic pressure on the acoustic modes, the FUT was inserted into a sealed chamber and pressure was applied by connecting the chamber to a pressurized tank of N_2. Measurements were performed between 1 to 51 bar with a step of 5 bar.

4.- Results

Figures 2 (a) and (b) shows the peaks in the radio-frequency spectrum caused by the oscillation of acoustic modes $TR_{2,4}^{(1)}$ and $TR_{2,4}^{(2)}$, respectively. Two effect can be noticed when pressure was applied. First, the peaks shift to shorter frequency as the pressure was increased. As mentioned before, the origin of such a frequency shift is the reduction of both acoustic velocities with pressure [8]. Figure 2 (c) shows the frequency shift for the two acoustic modes. The shift rate $\Delta f/\Delta P$ for these two acoustic modes are 0.47 kHz/bar and 0.83 kHz/bar, respectively. Second, a clear increase in linewidth is observed for the two peaks. Figure 2 (d) shows the Q factor of the two resonances as a function of pressure. This effect has not been previously reported. Two contributions might be at the origin of linewidth increase with pressure. The impedance of the medium surrounding the fiber increases with pressure, thus acoustic surface dumping also does it. Additionally, the viscosity of glass is expected to increase as well. Both contribution increase the attenuation of the acoustic mode resonances leading to the line broadening.

5.- Conclusions

An experimental study of the effect of hydrostatic pressure on the acoustic mode resonances of an optical fiber is reported. Acoustic modes were stimulated by FSBS and detected optically using a pump and probe scheme. Torsional-radial modes of the two type were investigated. A double effect was found, a shift of the resonance frequency and a decrease of the Q-factor. In the range of our measurements, both the resonance frequency and Q-factor of the acoustic modes decreases linearly with pressure. The results shown support different schemes for the development of optical fiber pressure sensors based on FSBS for measuring pressure in a wide range.

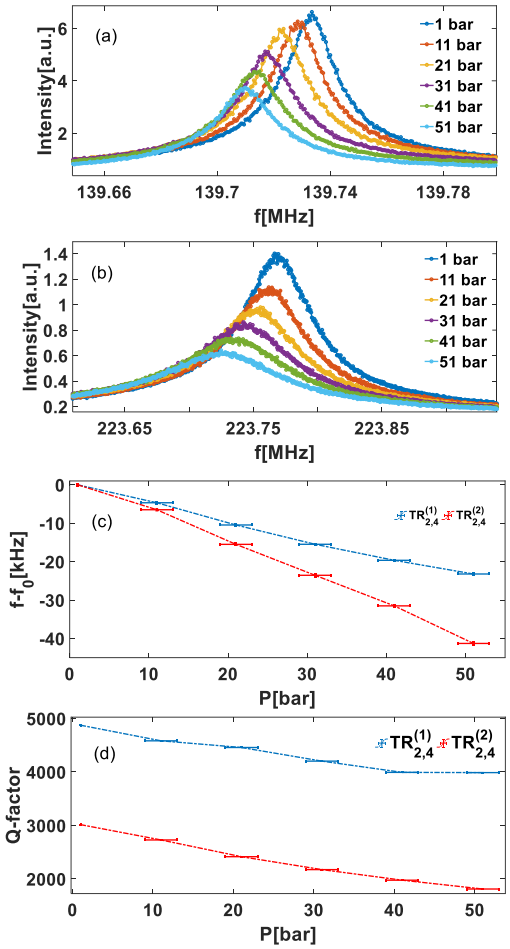

Fig. 2: Radio-frequency spectrum of the probe signal for different pressure showing (a) $TR_{2,4}^{(1)}$, and (b) $TR_{2,4}^{(2)}$ acoustic modes. (c) Frequency shift as a function of pressure. (d) Q-factor as a function of pressure.

Acknowledgements: This work has been partially funded by Horizon 2020 Framework Programme (H2020-MSCA-RISE-2019-872049); Generalitat Valenciana (CIPROM/2022/30); Ministerio de Ciencia, Innovación y Universidades (CNS2023-145717, PID2023-146725OB-I00).

References

[1] Vorathin, E., Hafizi, Z. M., Ismail, N., Loman, M., *"Review of high sensitivity fibre-optic pressure sensors for low pressure sensing,"*

Opt. & Laser Technol., 121, art. 105841, 2019.

[2] Li, X., Lu, Y. Zhang, Z., "*Simultaneous Measurement of Temperature and Pressure Based on Forward Brillouin Scattering in Double-Coated Optical Fiber*," J. Lightwave Technol. 41(15), 5130-5137, 2023.

[3] Zhu, M., Lu, Y., Zhang, Z., Liu, P., Zhang, W., *"High accuracy pressure and temperature simultaneous measurement based on forward Brillouin scattering in highly nonlinear fiber,"* Opt. & Fiber Technol., 84, art. 103741, 2024.

[4] Sánchez, L. A., Díez, A., Cruz, J. L., Andrés, M. V., *"High accuracy measurement of Poisson's ratio of optical fibers and its temperature dependence using forward-stimulated Brillouin scattering,"* Opt. Express 30(1), 42–52 (2022).

[5] Sánchez, L. A., Díez, A., Cruz, J. L., Andrés, M. V., *"Strain and temperature measurement discrimination with forward Brillouin scattering in optical fibers,"* Opt. Express 30 (9), 14384–14392 (2022).

[6] Bernstein, A., Zehavi, E., London, Y., Hen, M., Suna, R., Ben-Ami, S., Zadok A., *"Tensor characteristics of forward Brillouin sensors in bare and coated fibers,"* APL Photon. 8, art. 126105, 2023.

[7] Álvarez-Ocampo, C. A., Delgado-Pinar, M., Díez, A., Cruz, J. L., Andrés, M. V., *"Experimental study towards the development of highly sensitive opto-mechanical sensors based on FSBS in telecom optical fibers"* Opt. Express. 32 (23), 41984–41992, 2024.

[8] Yokoyama, A., Matsui, M., Higo, Y., Kono, Y., Irifune, T., Funakoshi, K., *"Elastic wave velocities of silica glass at high temperatures and high pressures"*, J. Appl. Phys. 107, art. 123530, 2010.

Nanophotonic Interferometric Immunosensor for Label-Free and Real-Time Monitoring of Pollutants in Drinking Water

Andrés ALONSO-FERNÁNDEZ [(1)], Patricia RAMÍREZ-PRIEGO [(1)], M.-Carmen ESTÉVEZ [(1)], Adrián FERNÁNDEZ-GAVELA [(2)], and Laura M. LECHUGA [(1)]

1. Nanobiosensors and Bioanalytical Applications Group, Catalan Institute of Nanoscience and Nanotechnology (ICN2), CSIC, BIST, and CIBER-BBN, 08193 Barcelona, Spain
2. Physics Department, University of Oviedo, 33007 Oviedo, Spain

Contact: Andrés ALONSO-FERNÁNDEZ (andres.alonso@icn2.cat).

ABSTRACT

The chemical pollution of drinking water is a growing concern for both environmental and public health, driven by global factors such as industrialization, agriculture, and urbanization. Recent reports indicate that 60% of surface waters in Europe fail to meet an adequate chemical status, underscoring the scale of the challenge. To address this issue, rapid and reliable detection methods are essential, particularly in drinking water treatment plants, which serve as the last safeguard before water reaches consumers. In this context, biosensors offer an adequate solution due to their high sensitivity, accuracy, selectivity, and point-of-use capabilities.

In the framework of the European H2020 NIAGARA project, we propose a novel nanophotonic point-of-care biosensor based on bimodal waveguide interferometers to be implemented in drinking water plants to detect multiple pollutants in the same water sample.

Keywords: nanophotonic, biosensor, point-of-use, label-free, environmental monitoring, drinking water

1.- Introduction

In recent years, rising pollutants levels in water have posed a significant threat to environmental and public health, driven by human activities such as industrialization, agricultural, large-scale farming, and urbanization. This issue has far-reaching global consequences, with the United Nations reporting that in 2022, 2.2 billion people lacked access to safely managed drinking water [1]. In Europe, the situation is equally concerning, as the 2022 European Water Report found that about 60% of surface waters fails to meet good ecological status [2].

Conventional reference methods such as chromatographic techniques and immunoassays, are constrained by the need for centralized laboratories, trained personnel, costly instrumentation, sample pretreatment and time-consuming processes. Additionally, these laboratory techniques operate in a single-analyte detection configuration (singleplex), which is inadequate for water analysis, where detecting multiple pollutants is essential. These limitations highlight the need for rapid and efficient monitoring methods, particularly in drinking water treatments plants, which serve as the final safeguard before water reaches consumers.

In this context, biosensors offer a promising alternative due to their low limit of detection (LOD), high accuracy, selectivity, and label-free and real-time capabilities. Among them,

optical biosensors based on evanescent field have witnessed impressive progress, benefiting from their label-free and real-time operation, with strong potential for multiplexing and miniaturization [3].

However, integrating a complete point-of-use multiplexed biosensor requires combining different components, including microfluidic subsystems, surface biofunctionalization protocols, electronics, software, hardware, and optical readout technologies. Given the technical challenges involved in integration, the advancement of multiplexed photonic biosensors has progressed at a moderate pace, with a limited number of multiplexed photonic biosensors developed to date [4-8].

In the frame of the European H2020 NIAGARA project, we propose a nanophotonic interferometric biosensor based on bimodal waveguides (BiMW) for the simultaneous detection of multiple pollutants.

This biosensor will be validated for monitoring both chemicals and microbiological contaminants in water, including bisphenol A (BPA), *Helicobacter pylori* (*H. pylori*), imazalil, ibuprofen, and paracetamol. These pollutants were selected based on their prevalent presence in freshwaters environments. Pharmaceuticals, including ibuprofen and paracetamol, are some of the most widespread chemicals in freshwater environments, with traces commonly found in rivers and lakes at concentrations of approximately 8 µg/L and 40 ng/L, respectively. These compounds are primarily sourced from human and veterinary medication residues that enter the water supply through wastewater treatment facilities [9].

In terms of pesticides, imazalil represents a growing concern. While not regulated, it is widely used in fruit plantations, and its presence in surface waters is becoming more noticeable, with levels exceeding 0.072 µg/L. Its persistence and the lack of regulatory oversight raise alarms about potential environmental and human health impacts [10].

BPA, a well-known industrial chemical, is the most concentrated contaminant in European freshwater sources, especially in sewage waters, where concentrations can surpass 700 µg/L (3.02 µM) [11]. This chemical is a significant environmental concern due to its endocrine-disrupting properties, affecting both aquatic organisms and humans.

Lastly, *Helicobacter pylori* (*H. pylori*) is an emerging waterborne pathogen with serious implications for public health. Its ability to survive traditional water disinfection processes makes it a significant concern for drinking water quality. Recent studies have reported the detection of *H. pylori* in 38.7% of drinking water samples from Eastern Spain, signalling the potential risks of waterborne transmission [12].

Together, these contaminants form a complex and concerning mix of chemical and biological threats in freshwater systems, emphasizing the importance of achieving reliable biosensors for their monitoring and control.

2.- Nanophotonic Biosensor

2.1.- Sensor chip

The nanophotonic sensor is based on bimodal waveguide interferometers (BiMW). The sensor chip consists of silicon nitride rib waveguides designed to enhance the evanescent field when excited by monochromatic, polarized laser light in the visible region. As shown in *Fig. 1*, in the initial section of the waveguide, the polarized input light is coupled into a rib waveguide that supports the fundamental electromagnetic mode; after certain distance, the core thickness of the waveguide is increased, acting as a modal splitter that excites the first electromagnetic light mode. Both modes then travel through the sensing region toward the output. These two modes have different velocities and evanescent field penetration depths into the external medium, which results in varying sensitivities to changes in the refractive index. As both modes are differently affected by local changes of the refractive index, an interference pattern is generated at the output of the waveguide,

which is related to local refractive index changes induced by any variation at the sensor surface [13].

The sensor chips are fabricated at wafer-scale at the ICTS Clean Room facilities Micronanofabs at the Microelectronic National Center (IMB-CNM-CSIC) in Barcelona. The fabrication process, based on standard microelectronic technology, including photolithography and etching processes on a silicon wafer substrate, has been previously described in the literature [13].

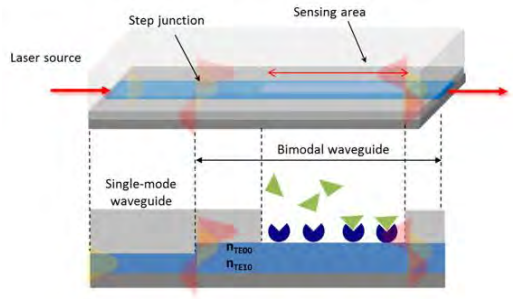

Fig. 1: Schematic representation of the BiMW interferometer characteristics and the working principle. The single mode and bimodal sections are highlighted.

2.2.- Experimental setup

The experimental setup employed for the biosensor evaluation is shown in *Fig. 2*. The sensor chip is placed on a custom holder with a temperature controller and a 3-axis stage to couple the incoming light into the sensor chip. The light source is a laser diode (wavelength of 660 nm) combined with optics that isolate, polarize, and focus the light source for proper chip coupling. The readout system employs conventional photodetectors placed at the chip output, an electronic system, and a custom designed software. The photodetector reads the intensity interference pattern from the output chip, generated by the two propagation modes. This signal is passed through an electronic system, which converts and amplifies the intensity received into a voltage signal, and the software transforms the interferometric signal into a quantitative phase signal and displays the signal for real-time analysis. A novel microfluidic system is also employed to individually flow different samples through each chip waveguide for the evaluations.

To estimate the sensing performance of the nanophotonic chip we have performed a bulk sensitivity evaluation by flowing hydrochloric acid (HCl) solutions of varying concentrations, each with a different refractive index (n_{HCl} = 1.33322-1.33684 RIU) through the sensor chips, using Milli-Q water as a running buffer (n_{H2O} = 1.33302 RIU). The real-time sensograms of the successive injections show that the interferometric behavior of the waveguides remains stable and consistent, achieving a limit of detection (LOD) ~ (5 ± 7) × 10^{-7} RIU for all the waveguides tested.

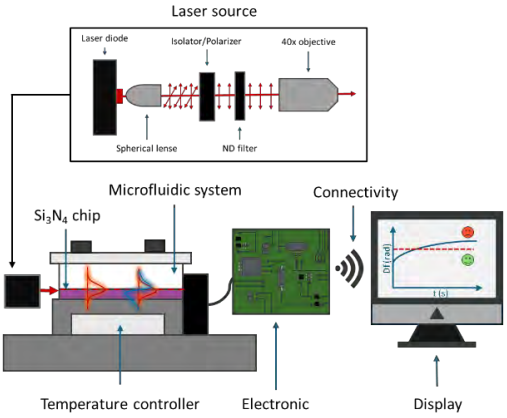

Fig. 2: Schematic diagram illustrating the experimental setup of the sensor device designed for analyte detection.

3.- Biosensor performance

The main objective of this work is to employ the biosensors for the detection of the chemicals BPA, imazalil, ibuprofen, paracetamol, and *H. pylori* bacteria. Besides *H. pylori,* all the chemicals have a low molecular weight (<500 Da), thus, they are not able to induce significant refractive index changes on the sensor surface. Therefore, to reach good sensitivity is advisable to perform a competitive immunoassay approach. For *H. pylori* bacterium, with a molecular weight of approximately 128 kDa, a direct approach can be performed, relying on the direct capture of the bacterium using specific antibodies.

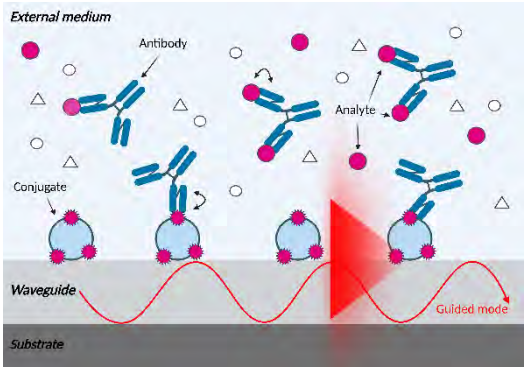

Fig. 3: Schematic representation of a competitive immunoassay performed in evanescent wave-based biosensor.

In the competitive approach (see *Fig. 3*), a protein conjugate containing an anlyte derivative (i.e. BPA-BSA) is immobilized on the sensor surface, and a fixed amount of antibody is incubated with the samples containing the free analyte. When the sample is injected into the biosensor, the analyte competes with the immobilized conjugate for the binding of the antibody, and the refractive index change comes from binding of the remaining free antibody [14].

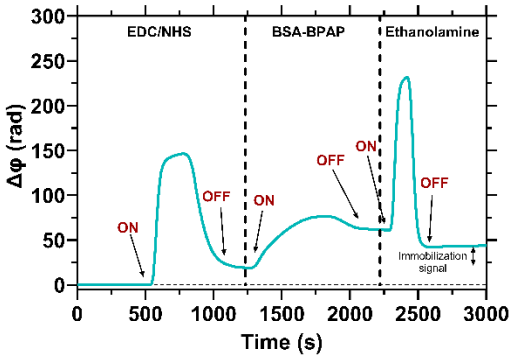

Fig. 4: Real-time sensogram showing the three-step biofunctionalization of the sensor chip with the BPA conjugate (surface activation with EDC/NHS, coupling of BPA conjugate, and deactivation of unreacted activated groups with ethanolamine).

To immobilize the bioreceptor on the sensor chip, a chemical modification of the silicon nitride surface to introduce reactive groups, known as silanization, must be first performed. This silanization process enables the generation of carboxyl (COOH) functional groups on the surface, which facilitate the subsequent covalent binding with the protein conjugate.

Among the previously described analytes, the first results obtained for Bisphenol A are presented. *Fig. 4* shows the immobilization process of the BPAP-BSA conjugate over the silicon nitride sensor surface. Firstly, COOH groups, incubated in the sensor surface after the silanization process, are activated with a solution of 1-ethyl-3-(3-dimethylaminopropyl) carbodiimide (EDC) and N-hydroxysulfosuccinimide (NHS), followed by the injection of the conjugate at 20 µg/mL. Finally, an ethanolamine solution was passed over the sensor surface to block any unreacted active groups.

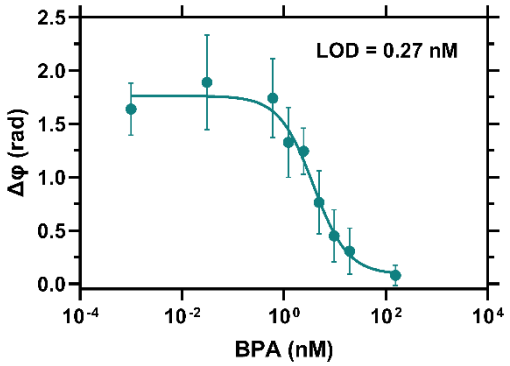

Fig. 5: Competitive immunoassay for BPA detection. These results correspond to the sensor response of seven waveguides with duplicates, plotted versus the logarithmic scale of the analyte concentration of each sample measured.

Once the conjugate has been immobilized, several BPA concentrations were analyzed under buffer conditions, using PBST 0.05% as running buffer, after a 10-minute incubation with a BPA antibody solution at a fixed optimal concentration (i.e., 1 µg/mL). Various parameters, including detection buffer, antibody and conjugate concentrations, incubation time, and flow rate, were optimized to obtain an optimal calibration curve, shown in *Fig. 5*. The competitive immunoassay for BPA reports a LOD of 0.27 nM, a half-maximal inhibitory concentration (IC_{50}) of 3.81 nM, and a working range between 0.93 and 10.66 nM. The LOD value is below 10.95 nM, the minimum concentration allowed in drinking water as

established by the European Union to ensure it is wholesome and clean [15].

Currently, we are optimizing the assay parameters for the BPA detection directly in drinking water. Additionally, we are evaluating the best conditions for the analysis of the remaining analytes of the project to ensure optimal results across all target substances.

4.- Conclusion

A nanophotonic point-of-use biosensor has been developed for multiple detection in real-time. The sensor chip performance and the different setup subsystems have been implemented. The sensor demonstrates stable and consistent interferometric behavior, achieving a limit of detection (LOD) for the bulk sensitivity evaluation of ~ $(5 \pm 7) \times 10^{-7}$ RIU for all the waveguides sensors tested.

The biosensor has been demonstrated for rapid (<20 min) detection of BPA by using a competitive immunoassay. The biosensor has reached an excellent limit of detection (0.27 nM), which is within the analytical values required by the European Union, with remarkable reproducibility among the different waveguides sensors, and with a dynamic working range of 0.93 -10.66 nM.

Acknowledgements:

We acknowledge EU financial support (project NIAGARA 101093166). ICN2 is supported by the Severo Ochoa Centres of Excellence programme, Grant CEX2021-001214-S, funded by MCIN/AEI/10.13039.501100011033. The Nanob2A group is a consolidated research group (Grup de Recerca) from Generalitat de Catalunya and has support from the Department de Recerca i Universitats de la Generalitat de Catalunya (Expedient: 2021 SGR 00456).

References

[1] UN Water, Ed., *Water for prosperity and peace*. in The United Nations World Water Development Report, no. 2024. Paris: UNESCO, 2024.

[2] European Environment Agency., *European waters: assessment of status and pressures 2018.* https://data.europa.eu/doi/10.2800/303664

[3] Adrián FERNÁNDEZ-GAVELA, Daniel GRAJALES GARCIA, Jhonattan RAMIREZ, and Laura M. LECHUGA, *"Last Advances in Silicon-Based Optical Biosensors,"* Sensors, vol. 16, no. 3, p. 285, Feb. 2016.

[4] John S. COGNETTI and Benjamin L. MILLER, *"Monitoring Serum Spike Protein with Disposable Photonic Biosensors Following SARS-CoV-2 Vaccination,"* Sensors, vol. 21, no. 17, p. 5857, Aug. 2021.

[5] Konstantinos MISIAKOS, Eleni MAKARONA, Marcel HOEKMAN, Romanos FYROGENIS, Kari TUKKINIEMI, Gerhard JOBST, Panagiota S. PETROU, Sotirios E. KAKABAKOS, Alexandros SALAPATAS, Dimitrios GOUSTOURIDIS, Mikko HARJANNE, Paivi HEIMALA, and Ioannis RAPTIS, *"All-Silicon Spectrally Resolved Interferometric Circuit for Multiplexed Diagnostics: A Monolithic Lab-on-a-Chip Integrating All Active and Passive Components,"* ACS Photonics, vol. 6, no. 7, pp. 1694–1705, Jul. 2019.

[6] Michael R. BRYAN, Jordan N. BUTT, Zhong DING, Natalya TAKRANOVA, Nathaniel CADY, Brian PIOREK, Carl MEINHART, Joshua TICE, and Benjamin L. MILLER, *"A Multiplex 'Disposable Photonics' Biosensor Platform and Its Application to Antibody Profiling in Upper Respiratory Disease,"* ACS Sens., vol. 9, no. 4, pp. 1799–1808, Apr. 2024.

[7] Maribel GÓMEZ-GÓMEZ, Carles SÁNCHEZ, Sergio PERANSI, David ZURITA, Laurent BELLIERES, Sara RECUERO, Manuel RODRIGO, Santiago SIMÓN, Alessandra CAMARCA, Alessandro CAPO, Maria STAIANO, Antonio VARRIALE, Sabato D'AURIA, Georgios MANESSIS, Athnasios I. GELASAKIS, Ioannis BOSSIS, Gyula BALKA, Lilla DÉNES, Maciej FRANT,

Lapo NANNUCCI, Matteo BONASSO, Alessandro GIUSTI, and Amadeu GRIOL, *"Photonic Label-Free Biosensors for Fast and Multiplex Detection of Swine Viral Diseases,"* Sensors, vol. 22, no. 3, p. 708, Jan. 2022.

[8] Jhonattan C. RAMIREZ, Daniel GRAJALES, Jesús MALDONADO, Adrián FERNÁNDEZ-GAVELA, *"Current Trends in Photonic Biosensors: Advances towards Multiplexed Integration,"* Chemosensors, vol. 10, no. 10, p. 398, Sep. 2022.

[9] Samuel FEKADU, Esayas ALEMAYEHU, Raf DEWIL, and Bart VAN DER BRUGGEN, *"Pharmaceuticals in freshwater aquatic environments: A comparison of the African and European challenge,"* Sci. Total Environ., vol. 654, pp. 324–337, Mar. 2019.

[10] European Food Safety Authority (EFSA) *et al.*, *"Modification of the existing maximum residue levels for imazalil in various commodities," EFSA J.*, vol. 16, no. 6, Jun. 2018.

[11] Francisco G. CALVO-FLORES, Joaquín ISAC-GARCÉA, and José A. DOBADO, *"Detection and Analysis of Chemical Pollutants,"* in Emerging Pollutants, 1st ed., Wiley, 2018.

[12] Laura MORENO-MESONERO, Yolanda MORENO, José L. ALONSO, and M. Antonia FERRÚS, *"Detection of viable Helicobacter pylori inside free-living amoebae in wastewater and drinking water samples from Eastern Spain,"* Environ. Microbiol., vol. 19, no. 10, pp. 4103–4112, Oct. 2017.

[13] Kirill E. ZINOVIEV, Ana B. GONZÁLEZ-GUERRERO, Carlos DOMINGUEZ, and Laura M. LECHUGA, *"Integrated Bimodal Waveguide Interferometric Biosensor for Label-Free Analysis,"* J. Light. Technol., vol. 29, no. 13, pp. 1926–1930, Jul. 2011.

[14] Patricia RAMIREZ-PRIEGO, M.-Carmen ESTÉVEZ, Heriberto J. DÍAZ-LUISRAVELO, Juan J MANCLÚS, Ángel MONTOYA, and Laura M. LECHUGA, *"Real-time monitoring of fenitrothion in water samples using a silicon nanophotonic biosensor,"* Anal. Chim. *Acta*, vol. 1152, p. 338276, Apr. 2021.

[15] European Commission, Ed., *Analysis of pressures and impacts: Guidance document No 3*. Luxembourg: Office for Official Publications of the European Communities, 2003.

Nano-precision metrology of X-ray mirrors with multifiber interferometers

Albert VAN EECKHOUT [(1)], Igors SICS [(1)], Dominique HEINIS [(1)], Josep NICOLAS [(1)]

1. ALBA Synchrotron Light Source, Carrer de la Llum 2-26, 08290 Cerdanyola del Vallès, Barcelona, Spain

Contact: Albert VAN EECKHOUT (aveeckhout@cells.es).

ABSTRACT:

We present a new metrology system based on multiple fiber interferometers with the potential of measuring strongly curved X-ray mirrors (total slope ≥10) with nanometer and sub-nanometer figure errors. The system comprises three fiber interferometers mounted on a linear scanning stage and an external autocollimator to track their orientation. With this architecture, the profile of X-ray mirrors can be measured independently of any guidance error. The system is experimentally tested by measuring a flat reflecting surface with a radius of curvature of 75 km. The obtained figure profile is compared with those acquired using other state-of-the-art techniques reaching a sub-nanometric agreement with differences of 0.5 nm root mean square.

Key words: Optics, Metrology, Optical Fibers, Interferometry, Stitching, X-ray.

1.- Introduction

Advancements in Diffraction-Limited Storage Rings (DLSRs) and Free-Electron Laser (FEL) sources demand X-ray mirrors with total slope ranges exceeding 10 mrad and shape tolerances at the nanometer or sub-nanometer scale [1], [2]. These stringent specifications introduce significant challenges in X-ray mirror metrology with state-of-the-art techniques: Long Trace Profilometers (LTP) [3], Nanometer Optical component measuring Machine (NOM) [4], Nano-accuracy Surface Profiler (NSP) [5], and Stitching interferometry systems (SYS) [6]. With a total slope > 10 mrad, measured mirrors cannot be treated as flat surfaces [7], and certain measurement errors take a more substantial role [8].

To deal with these issues some authors proposed adding retrace errors to the existing stitching models [9], or considering angle-dependent measurement errors in the LTP, NOM, and NSP systems [10]. Alternatively, other studies explore the implementation of new techniques based on a Shack-Hartmann wavefront sensor [11], the analysis of laser speckle [12], or the use of a zero-method scanning-probe profilometer (ZSP) [13].

This work presents a new alternative metrology system based on multiple fiber interferometers. The employed architecture is based on the scheme proposed in ref. [14], which should be suitable for measuring strongly curved mirrors by focusing each fiber on the surface.

In the following sections, we describe the operational principle of the system, show the prototype we built, and test the performance of that prototype by experimentally measuring a flat reflecting surface (75 km radius of curvature). Finally, the results are compared with the NOM and the SIS techniques.

2.- Multifiber interferometers stitching principle

The system we propose comprises a set of optical fiber interferometers mounted on a linear stage to scan the surface of an X-ray mirror (see the scheme of Fig. 1). As stated in ref. [14], stage displacements introduce guiding errors which can be classified into:

transverse position errors, R(x), and platform orientation errors, U(x) (see Fig. 1). With this in mind, each fiber measurement, $m_p(x)$, can be modeled as:

$$m_p(x) = s(x + x_p) + R(x) + U(x)x_p + T_p \quad (1)$$

where x_p is the meridional position of the fiber on the stage and T_p is a fiber offset value for non-absolute fiber measurements.

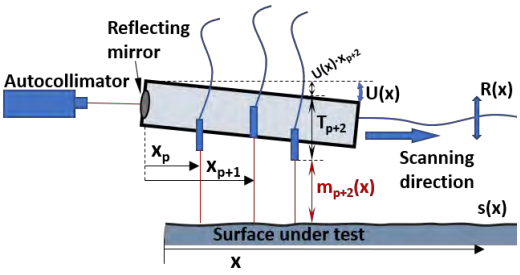

Fig. 1: Scheme of the multifiber interferometer stitching system.

In the Fig. 1 scheme, we consider using an external autocollimator to track the orientation errors of the platform, U(x). With this architecture, the measured U(x) is used to correct each fiber measurement in the following way:

$$M_p(x) = m_p(x) - U(x)x_p = s(x + x_p) + R(x) + T_p \quad (2)$$

Then, by evaluating the difference between fiber measurements we obtain the next expression independent of the R(x) guidance errors:

$$M_{p+1}(x) - M_p(x) = s(x + x_{p+1}) - s(x + x_p) + T_{p+1} - T_p \quad (3)$$

Equation (3) is very similar to stitching interferometry expressions [15], being able to reconstruct the measured surface. However, this model has the next set of ambiguities:

i. Like in the 1D stitching interferometry case [15], periodic distances between pairs of fiber positions end with periodic errors in the reconstruction. At least two pairs of fiber positions must be incommensurable to avoid them. That is, the least common multiple of the inverse of both distances must be larger than the sampling frequency.

ii. The orientation of the measured surface will be completely unknown because it is coupled with fiber offset values.

Once the periodic error condition is fulfilled, the system should be able to measure the 1D profile of the mirror independently of guidance errors.

3.- Multifiber interferometer stitching system

The experimental implementation of a multifiber interferometer stitching system is shown in Figure 2. It is based on three quDIS fiber interferometers, distributed by qutools Gmbh, with a signal stability < 0.05 nm and a 25kHz acquisition bandwidth.

The three fibers are mounted on the ALBA-NOM linear stage [16] (see Fig.2). The linear stage leads to displacing fibers with an accuracy of 3.5 µm in the scanning direction and with a straightness accuracy of 2.2 µm [16]. Note that the straightness accuracy is in the order of micrometers while X-ray figure errors should be sub-nanometric. This highlights the necessity of using multiple fibers to compensate for guiding errors.

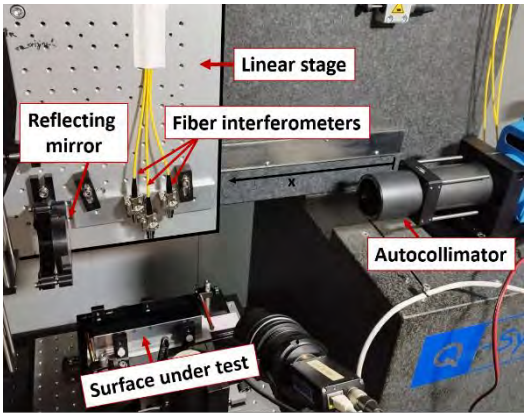

Fig. 2: Image of the ALBA's multifiber interferometer stitching system.

The optical fibers are collimated to the Surface Under Test (SUT) at a working distance of 200 mm.

During the scan of the SUT, the orientation of the fibers changes jointly with the stage orientation. These angular variations are tracked with an autocollimator ELCOMAT 5000/10 which measures the orientation of a

2-inch flat reflecting mirror attached to the linear stage. At our laboratory, the autocollimator takes measurements with repeatability below 0.05 µrad in a 250 Hz bandwidth.

The whole system is contained in the thermally isolated enclosure of the ALBA-NOM [16], which is installed in the class 10,000 clean room of the Optics Laboratory of ALBA. The 10,000 clean room is stabilized in temperature within 0.2˚C by the air conditioning system. By contrast, the temperature of the ALBA-NOM enclosure is not actively stabilized and relies on the huge heat capacity of a granite bench and minimal power dissipation [16]. With this configuration, the environment stabilizes around 50 milliKelvins within a week [16].

4.- Experimental results

In order to evaluate the performance of the multifiber system we measured the profile of the SUT imaged in Fig. 2. The SUT has a meridional radius of curvature of 75 km and the results are shown in Figure 3 (blue line). A complete scan of the 150 mm SUT takes 20 seconds with the multifiber system, with a spatial resolution of 0.2 mm. For the sake of comparison, the same SUT profile was measured with the consolidated ALBA-NOM [16] (red line of Fig. 3) and ALBA-SIS [17] (green line of Fig. 3).

Fig. 3 (a) shows the reconstructed profile dominated by the SUT curvature. Each measurement was repeated 10 times and the repeatability is shown using a shaded area around each reconstructed profile. The curvature of the SUT is 72 km, 80 km, and 68 km, according to the multifiber, NOM, and SIS measurements. These three values are consistent considering the accuracy of the techniques. It is worth mentioning that curvature measurements are conditioned by many parameters, such as pixel error calibration, system positioning errors, reference curvature miscalibration, etc., all compromising the final accuracy of the curvature standardization.

By detrending the curvature, we highlight the figure errors of the SUT in Fig. 3 (b). The figure error profile obtained with multifiber measurements agrees with the other techniques. Multifiber profiles have a difference of 0.49 nm and 0.48 nm root mean square (rms) with the NOM and the SIS acquisitions, respectively. Therefore, we consider multifiber interferometer stitching as a new method with results comparable to state-of-the-art surface metrology techniques.

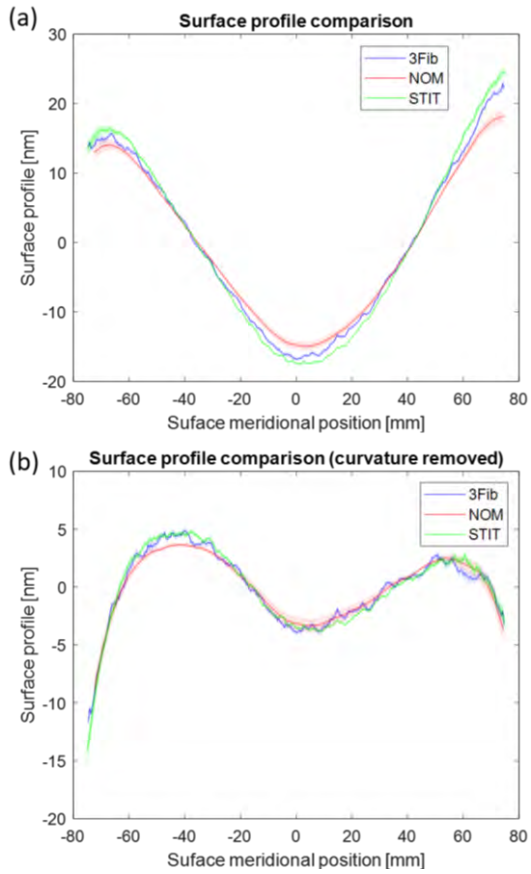

Fig. 3: (a) Height profile of the SUT measured with the three fibers (blue line), the NOM (red line), and the stitching system (green line). (b) Figure errors of the SUT after removing the curvature.

5.- Conclusion

We have presented the first version of a multifiber interferometer stitching system. The system is based on three fibers and an autocollimator. We have discussed a set of conditions that must be satisfied to measure the profile of a reflecting surface independent of the guidance errors (distance between fibers must be incommensurable to avoid periodic errors in the reconstruction).

In addition, we have proved that the multifiber system can measure the profile of a surface with a 75 km radius of curvature with an agreement of 0.5 nm rms compared to the NOM and the SYS results. These multifiber measurements take a similar time compared with the NOM, but with better spatial resolution.

This work opens the door to developing new systems based on multiple focused fiber interferometers for the metrology of strongly curved profiles (total slope > 10 mrad).

Acknowledgments: This work has been sponsored by LEAPS-INNOV, and the Spanish MINECO (PID2021-562 126509OB-C21).

References

[1] H. Yumoto *et al.*, "Ellipsoidal mirror for two-dimensional 100-nm focusing in hard X-ray region," *Sci Rep*, vol. 7, no. 1, p. 16408, 2017.

[2] T. Shimamura *et al.*, "Soft-X-ray nanobeams formed by aberration-reduced elliptical mirrors with large numerical aperture," *Opt. Express*, vol. 31, no. 23, pp. 38132–38145, Nov. 2023.

[3] P. Z. Takacs, S. Qian, and J. Colbert, "Design Of A Long Trace Surface Profiler," in *Proc.SPIE*, Apr. 1987, pp. 59–64.

[4] F. Siewert, T. Noll, T. Schlegel, T. Zeschke, and H. Lammert, "The Nanometer Optical Component Measuring Machine: a new Sub-nm Topography Measuring Device for X-ray Optics at BESSY," *AIP Conf Proc*, vol. 705, no. 1, pp. 847–850, May 2004.

[5] S. Qian and M. Idir, "Innovative nano-accuracy surface profiler for sub-50 nrad rms mirror test," in *Proc.SPIE*, Oct. 2016, p. 96870D.

[6] L. Assoufid, M. Bray, and D. Shu, "Development of a Linear Stitching Interferometric System for Evaluation of Very Large X-ray Synchrotron Radiation Substrates and Mirrors," *AIP Conf Proc*, vol. 705, no. 1, pp. 851–854, May 2004.

[7] L. Huang, T. Wang, F. Polack, J. Nicolas, K. Nakhoda, and M. Idir, "Measurement Uncertainty of Highly Asymmetrically Curved Elliptical Mirrors Using Multi-Pitch Slope Stitching Technique," *Front Phys*, vol. 10, 2022.

[8] Z. Shi *et al.*, "Effect of pixel size and lateral distortion on the accuracy of stitching interferometry for high-precision x-ray mirrors," *Opt. Express*, vol. 33, no. 1, pp. 355–368, Jan. 2025.

[9] L. Huang, T. Wang, C. Austin, D. Kim, and M. Idir, "Two-step retrace error calibration removing tilt ambiguity in coherence scanning interferometry," *Opt. Lett.*, vol. 49, no. 3, pp. 590–593, Feb. 2024.

[10] L. Huang *et al.*, "Multi-pitch nano-accuracy surface profiler for strongly curved X-ray mirror metrology," *Opt Lasers Eng*, vol. 162, p. 107428, 2023.

[11] B. R. Adapa, G. Dovillaire, A. Vivo, F. Perrin, R. Mayer, and R. Barrett, "Measurement techniques to improve the accuracy of x-ray mirror metrology using stitching Shack–Hartmann wavefront sensors," *Review of Scientific Instruments*, vol. 92, no. 11, p. 113103, Nov. 2021.

[12] H. Wang, S. Moriconi, and K. Sawhney, "Nano-precision metrology of X-ray mirrors with laser speckle angular measurement," *Light Sci Appl*, vol. 10, no. 1, p. 195, 2021.

[13] H. Yumoto *et al.*, "High-fluence and high-gain multilayer focusing optics to enhance spatial resolution in femtosecond X-ray laser imaging," *Nat Commun*, vol. 13, no. 1, p. 5300, 2022.

[14] C. Elster, I. Weingärtner, and M. Schulz, "Coupled distance sensor systems for high-accuracy topography measurement: Accounting for scanning stage and systematic sensor errors," *Precis Eng*, vol. 30, no. 1, pp. 32–38, 2006.

[15] J. Nicolas, M. L. Ng, P. Pedreira, J. Campos, and D. Cocco, "Completeness condition for unambiguous profile reconstruction by sub-aperture stitching," *Opt. Express*, vol. 26, no. 21, pp. 27212–27220, Oct. 2018.

[16] J. Nicolas and J. C. Martínez, "Characterization of the error budget of Alba-NOM," *Nucl Instrum Methods Phys Res A*, vol. 710, pp. 24–30, 2013.

[17] A. Van Eeckhout, I. Sics, L. Ribó, C. Colldelram, and J. Nicolas, "The stitching interferometry system of ALBA," in *EUV and X-ray Optics: Synergy between Laboratory and Space VIII*, R. Hudec and L. Pina, Eds., SPIE, Jun. 2023, p. 15.

Laser heterodyne radiometry for greenhouse gases monitorization

Adela COLLADO-RODRÍGUEZ [(1)], Aldo MORENO-OYERVIDES [(1)], Oscar Elías BONILLA-MANRIQUE [(1)], Omaira GARCÍA [(2)], Pedro MARTÍN-MATEOS [(1)]

1. Electronics Technology Department, Universidad Carlos III de Madrid, Leganes, 28911 Madrid, Spain.
2. Izaña Atmospheric Research Center (IARC), State Meteorological Agency of Spain (AEMet), Santa Cruz de Tenerife, 38002, Canarias, Spain.

Contact: Adela COLLADO-RODRÍGUEZ (adcollad@pa.uc3m.es).

ABSTRACT:

In recent decades, there has been a significant increase in the interest of greenhouse gases monitoring. In this regard, novel systems have been examined to supplement Fourier Transform Infrared (FTIR) spectrometers, commonly used for atmospheric gas measurements. In this context, laser heterodyne radiometers are particularly noteworthy due to their portability, high resolution, and cost-effectiveness, making them well-suited for measuring multiple gases simultaneously. However, the scanning range of these systems is limited by the local laser oscillator, which restricts their effectiveness. To address this limitation, the use of widely tunable lasers has been proposed.

This work presents the various studies and advancements made in the field of heterodyne laser radiometry systems for atmospheric gas monitoring.

Key words: Laser heterodyne radiometry, frequency comb, optical spectroscopy, tunable lasers, greenhouse gases, optical atmospheric sounding.

1.- Introduction

The accurate monitoring of greenhouse gases (GHGs), particularly carbon dioxide (CO_2), is critical in addressing global climate change. The atmospheric concentration of GHGs, primarily influenced by human activities, is a key driver of global warming. As the demand for accurate emissions accounting intensifies, the need for improved observation networks has become paramount. Current ground-based monitoring systems, such as Fourier Transform Infrared (FTIR) spectrometers, are widely employed for measuring multiple trace gases with high precision. However, these systems are often large and expensive, limiting their applicability for characterizing localized "hot spot" sources of GHG emissions.

In response to these challenges, Laser Heterodyne Radiometry (LHR) has emerged as a promising alternative [1]. LHR offers several advantages, including high optical resolution, operational flexibility, and the potential for compact, portable instrument designs. These characteristics make LHR an ideal candidate to complement and enhance existing GHG monitoring systems. LHR works by analyzing the solar spectrum through spectroscopic techniques, enabling the measurement of various atmospheric gases. However, the primary limitation of LHR systems lies in the optical span, which is restricted by the tuning range of the local oscillator laser, typically a distributed-feedback (DFB) laser due to its excellent performance characteristics. This limitation restricts the number of absorption lines that can be analyzed, which directly impacts the

effectiveness of gas concentration retrieval algorithms. So far, to overcome this, more than one local operates simultaneously [2], leading to an increase in both the cost and the complexity of the systems, nevertheless, covering a large number of absorption lines remains technically unfeasible. Widely tunable lasers seem like the best approach for enabling these spectral measurements over very wide ranges. A study to evaluate the applicability of these sources has been conducted.

In this context, an initial system allowing the measurement of atmospheric CO_2 and a second version adding a channel for O_2 measurement have been designed and tested with great results. Both systems implement frequency comb calibration.

2.- Laser Heterodyne Radiometry and frequency comb

LHR is a technique that enables the retrieval of an optical signal's spectrum with very high optical resolution. In LHR systems, the incoming optical signal is combined with the emission of a local oscillator laser, and the resulting combined signal is directed to a photodetector. The photodetector produces a downshifted radio frequency (RF) signal, which is a lower-frequency copy of the optical signal's spectrum. This RF signal is then amplified and filtered to set the optical resolution of the radiometer. The RF power is subsequently detected by a power meter, from which the spectrum of the original optical signal can be retrieved when the laser emission frequency is swept. Figure 1 shows a simplified diagram of a LHR system.

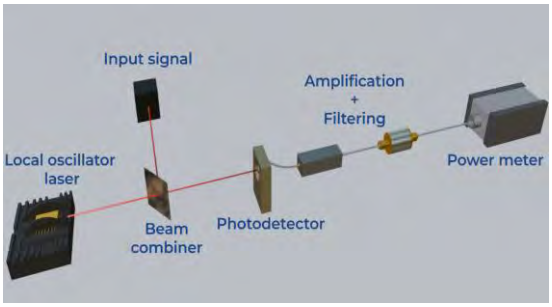

Fig. 1: Simplified diagram of LHR systems.

The main aspect that must be considered for an adequate line characterization is the frequency axis characterization. For this, a frequency comb is implemented. The position of all the teeth of the comb are identified and stored. After the proper processing, an accurate frequency axis determination is achieved.

2.1.- Initial system

The detailed diagram of the implemented LHR is shown in Figure 2. The system was designed to switch automatically (electronically) from the conventional mode of operation (measurement of the absorption profile of the absorption lines) to WM-LHR, a mode analogous to Wavelength Modulation Spectroscopy, in which derivatives of the absorption profile are obtained. This functionality is achieved through the use of a data acquisition system that controls both the electro-optical modulator and the laser diode current source.

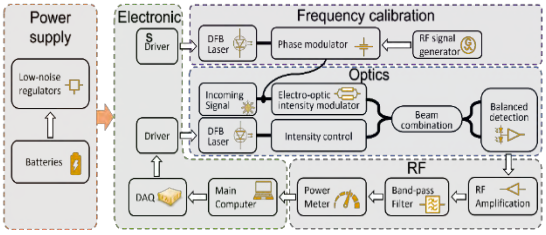

Fig. 2: LHR system implementation.

The resulting heterodyne signal is filtered with a 20 MHz bandpass filter at a configurable frequency ranging from 100 MHz to 300 MHz, providing dual-band optical resolutions ranging from 0.0066 cm^{-1} to 0.02 cm^{-1}. After filtering, the RF signal is amplified by a low-noise RF amplifier and recorded with a USB power sensor, which directly provides a digitized readout of the signal power averaged over a configurable integration time in 20 ms steps. This approach simplifies the physical implementation of the system, allowing high portability of the entire instrument. It should be noted that a second optical input was integrated into the system to allow the injection of the frequency comb into the instrument for calibration.

Finally, for the measurement of the solar absorption spectra, a specially developed solar tracker was used, implemented by two motorized rotating axes, whose positions were

corrected by the measurements of a four-quadrant sensor. A C80APC-C large beam fiber optic collimator (Thorlabs) was used to capture the solar beam. For more details, see [3].

2.1.1.- Results

In addition to a complete and detailed laboratory characterization [3], the LHR system was tested at different locations in the Madrid metropolitan area and at the Izaña Atmospheric Observatory (IZO, Tenerife, Spain). The observations, acquired under different atmospheric and observing conditions, were focused on the spectral characterization of the three CO_2 absorption lines located at wavelengths around 1570.28 nm, 1570.54 nm and 1570.82 nm. An optical resolution of 600 MHz (0.02 cm^{-1}), standard for GHG monitoring networks, was used for all measurements [4].

Figure 3 shows the measurements of a solar transmittance spectrum in the conventional 3-line LHR mode of operation made in July 2023 at IZO, where the agreement with the coincident measurements of the high resolution (HR)-FTIR spectrometer documents the potential of the new system for atmospheric composition monitoring.

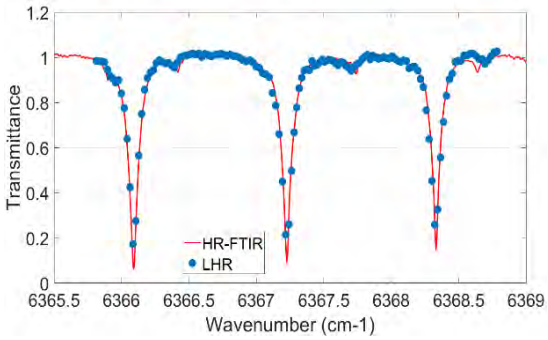

Fig. 3: Example of measurements acquired with the HR-FTIR spectrometer (red) and the LHR (blue) for July 11, 2023 (solar zenith angle of 65° and surface CO_2 concentration of 421.1 ppm) at IZO.

As mentioned above, the system is able to operate in WM-LHR mode. Figures 4(a) and (b) present a typical characterization result using the LHR mode of operation. Figures 4(c) and (d) show the signals obtained with the instrument operating in WM-LHR mode for the same configuration as in the conventional LHR case. The line measured corresponds with the first derivative of the absorption line. This information will be complementary to that obtained in LHR mode, improving the evaluation of the observed spectra.

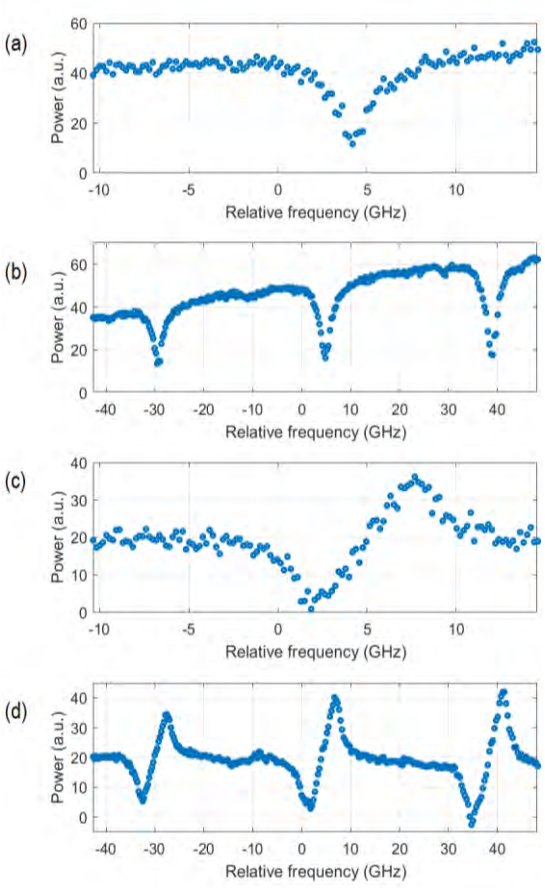

Fig. 4: Example of measurements for October 17, 2022 (60° solar zenith angle) in Madrid: (a) a single absorption line centered at 1570.54 nm and (b) three absorption lines at 1570.28 nm, 1570.54 nm and 1570.82 nm, acquired in conventional mode of operation. (c) and (d) similar to (a) and (b), but in WM-LHR mode of operation.

2.2.- Applicability of widely tunable lasers

As mentioned above, the main limitation of LHR system is the number of lines analyzable, limited to 3 or 4 by the tuning range of the local oscillator. Widely tunable lasers, such sources could become the best to overcome this issue. On the other hand, these sources are extremely sensitive to disturbances and impose constraints when transporting and operating the equipment in open environments.

A high performance widely tunable laser (CTL 1550 Toptica) and a DFB laser, which is very commonly employed in current LHR implementations (EPI1570-DM, Eblana Photonics) have been compared [5]. The original system was simply modified to work with the tunable laser and the attenuation of both sources has been adjusted so that the average power is equalized, ensuring a fair comparison. For more details [5].

2.2.1.- Results

In the initial tests, the power characteristics of the lasers and raw measurements were analyzed within a 1 nm spectral window. A total of 5 full sweeps of 370 points taken with an integration time of 400 ms per point were analyzed. To analyze the variability between scans, the average standard deviation of the difference of each scan with respect to the average spectrum was calculated. This resulted in an average difference of 7.16×10^{-7} for the DFB laser and 8.32×10^{-7} for the widely tunable laser. In addition, to study the extent of the variability, we used the coefficient of variability. In no instance did the proportion exceed 1.25%, and an average of approximately 0.5% was ascertained, thereby evidencing the minimal variation between each sweep.

The results show that both laser sources clearly identify the three CO_2 absorption lines. However, significant differences in the measurement baseline were observed, influenced by the power profile of each laser. The DFB laser exhibited a relatively flat power profile, while the widely tunable laser showed strong power ripples, making baseline characterization more complex. External power measurements confirmed these findings. To compensate for these baseline fluctuations, an eighth-order sum of sines fitting was necessary for the widely tunable laser (see Figure 5(b)). On the other hand, a simple third-order linear fit can be used to accurately fit and remove the baseline for the DFB laser measurement (see Figure 5(a)).

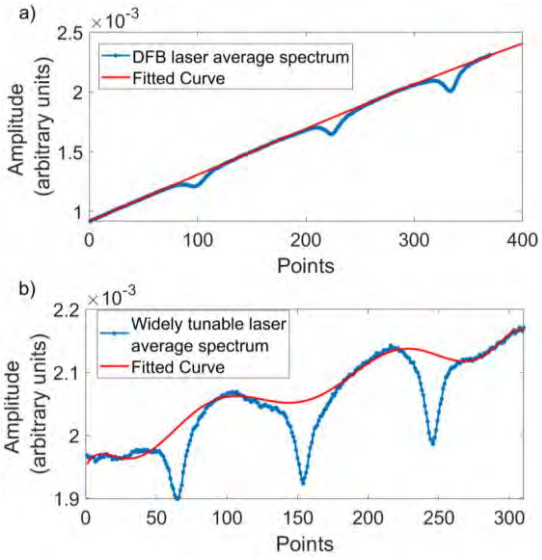

Fig. 5:(a) Averaged raw spectrum measured with DFB laser (blue) and fitter curve for its baseline adjustment. (b) Averaged raw spectrum measured with widely tunable laser (blue) and fitter curve for its baseline adjustment.

Figures 6 and 7 show both the results obtained with both sources after baseline adjustments and axis calibration together with HITRAN [6] spectrum simulation. Both sources show great potential for future implementation, despite the widely tunable laser's disadvantages, such as higher intensity fluctuations and less precise wavelength sweep control. However, it offers notable advantages beyond its broader tuning range, including improved wavelength accuracy.

The main challenge identified in this study is the power variability of widely tunable lasers during the sweep, which complicates baseline compensation. A key limitation for practical implementation lies in the size and cost of widely tunable lasers, which are significantly larger and an order of magnitude more expensive than DFB lasers. While DFB lasers remain a more convenient option for field applications, widely tunable lasers offer up to 100 times greater spectral coverage, albeit with increased complexity due to mechanical components requiring precise alignment [7]. Despite current challenges, widely tunable lasers have enormous potential to expand the measurement range and enhance the capabilities of future LHR systems.

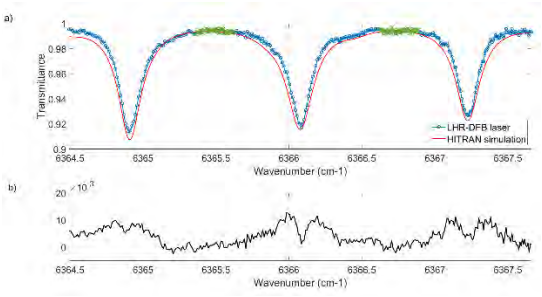

Fig. 6:(a) Comparison of average spectrum measured with DFB laser after baseline compensation and axis correction (blue) and HITRAN simulation (red). (b) Residual error (measurement - simulation).

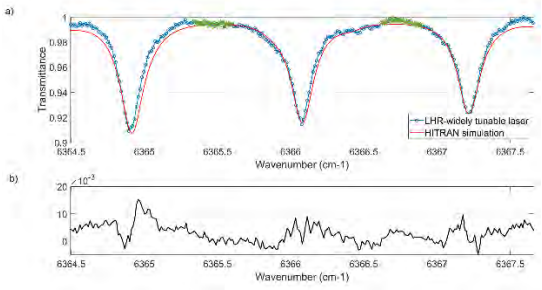

Fig. 7:(a) Comparison of average spectrum measured with the widely tunable laser after baseline compensation and axis correction (blue) and HITRAN simulation (red). (b) Residual error (measurement - simulation).

2.3.- New implementation

After the promising results obtained with the first system, we developed an upgraded version of the LHR system. This contribution will present the development of a novel, high-performance LHR, with optical frequency comb calibration, which allows the measurement of CO_2 and O_2 atmospheric concentrations in the field. The results of a measurement campaign, in which the developed system has been compared in detail with the FTIR spectrometer of the TCCON network at IZO [8], will be presented and discussed. We believe that the results obtained provide a clear and promising outlook on the future possibilities of using LHR systems for atmospheric composition monitoring.

4.- Conclusion

These studies indicate that heterodyne laser radiometry is a highly promising technique for greenhouse gas monitoring, complementing existing measurement systems.

The system tested shows that it is possible to obtain results comparable to those of FTIR systems, while allowing a reduction in size and cost. Although they have a reduced scanning range, the study with the tunable laser demonstrates that, despite various challenges, widely tunable have enormous potential for extending the measurement range, and thus multiplying the capabilities, of the LHR systems of the future.

The scope of measurements will be expanded to include O_2 characterization, in addition to the previously evaluated CO_2 characterization, using an enhanced system.

Acknowledgements: This work was supported by the European Union's Horizon Europe programme under grant agreement No. 101189654 – Project GASPOF-Pervasive gas sensing using optical fibers, as part of the communication network of the future

References

[1] Damien WEIDMANN, Tracy TSAI, Neil A. MACLEOD, Gerard WYSOCKI, *"Atmospheric observations of multiple molecular species using ultra-high-resolution external cavity quantum cascade laser heterodyne radiometry*", Optics Letters, 36:1951-1953, 2011.

[2] Wang GAOXUAN, Yuqi ZHU, Tie ZHANG, Mingxuan DU, Jingli WANG, Shengnan WU, Sailing HE, "*Simultaneous remote sensing of multiple atmospheric gases (CO_2, CH_4, and H_2O) based on an all-fiber laser heterodyne spectroradiometer"*Applied Physics B, 129(8), 2023.

[3] Aldo MORENO-OYERVIDES, Oscar E. BONILLA-MANRIQUE, Omaira. E GARCÍA, Pedro MARTÍN-MATEOS, *"Design and evaluation of a portable frequency comb-referenced laser heterodyne* radiometer", Optics and Lasers in Engineering. 171:107801, 2023.

[4] Bradley MATTHEWS, Omaira E. GARCÍA, Emilio CUEVAS, Wolfgang SPANGL, María P. CASTO, *"Report on how EIONET*

and EEA can contribute to the urban in situ requirements of a future Copernicus anthropogenic CO_2 observing system", European Environment Agency (EEA), 2020.

[5] Adela COLLADO-RODRÍGUEZ, Aldo MORENO-OYERVIDES, Omaira GARCÍA, Pedro MARTÍN-MATEOS, *"Investigating the applicability of modern widely tunable lasers to laser heterodyne radiometry for atmospheric composition monitoring"*, IEEE Transactions on Instrumentation and Measurement, 2025.

[6] Iouli GORDON et al, "*The HITRAN2020 molecular spectroscopic database,"* Journal of Quantitative Spectroscopy & Radiative Transfer, vol. 277, p. 107949, 2022.

[7] Vicent WELDON, David MCINERNEY, Richard PHELAN, Michael LYNCH, John DONEGAN, *"Characteristics of several NIR tunable diode lasers for spectroscopic based gas sensing: a comparison",* Spectrochimica acta. Part A: Molecular and biomolecular spectroscopy, 63(5), 1013–1020, 2006.

[8] Emilio CUEVAS et al., *"Izaña Atmospheric Research Center Activity Report 2019-2020*", State Meteorological Agency (AEMET), Madrid, Spain and World Meteorological Organization, Geneva, Switzerland, NIPO: 666-22-014-0, WMO/GAW Report No. 276, 2022.

Propuesta de solución óptica para medida de temperatura de recipiente y señalización en cocinas de inducción con encimera opaca

Cristina PELAYO [(1)], Pilar BLASCO [(1)], Enrique CARRETERO [(2)], Rafael ALONSO [(1)], Sergio LLORENTE [(3)]

1. Departamento de Física Aplicada, Grupo de Tecnologías Fotónicas (GTF), Instituto de Investigación en Ingeniería de Aragón (I3A), Universidad de Zaragoza, C/ María de Luna 3, 50018 Zaragoza, España.
2. Departamento de Física Aplicada, Grupo de Tecnologías Fotónicas (GTF), Facultad de Ciencias, Universidad de Zaragoza, C/ Pedro Cerbuna 12, 50009 Zaragoza, España.
3. BSH Electrodomésticos España, Avenida de la Industria, 49, Santa Isabel, 50016 Zaragoza, España.

Contacto: Cristina PELAYO (c.pelayo@unizar.es).

ABSTRACT:

This work describes the design and development of a prototype comprising two functionalities required for induction cooking devices. The innovation resides in the fact that it must work properly inside a new concept of cooking device hidden under an opaque cooktop. The prototype includes a light signaling system for the user to see which cooking zones are active or have residual heat, and an IR sensor to control that the temperature of the cookware remains within a safe range of operation. The document also presents the experimental validation of the temperature sensor functionality.

Key words: induction cooking, IR thermometry, optical sensors, light signaling, electro-optical devices, safe cooking, optical simulation.

1.- Introducción

Actualmente, los nuevos diseños de cocinas de inducción permiten al usuario cocinar directamente sobre la encimera, resultando así un nuevo concepto de cocina altamente atractiva tanto desde el punto de vista estético como práctico. Esta nueva cocina, como ilustra la figura 1 [1], contiene todos los componentes activos bajo una encimera opaca y continua, lo que obliga a replantear los diseños de las funcionalidades auxiliares incluidas en la cocina.

Este artículo presenta una solución que integra en un mismo dispositivo óptico dos de estas funcionalidades, adaptadas para su inclusión en las novedosas cocinas bajo la encimera. Las dos funciones incluidas son la señalización luminosa de las distintas zonas de cocción, así como la estimación sin contacto de la temperatura del recipiente de cocinado, ambas necesarias principalmente por razones de seguridad.

Fig. 1: Imagen publicitaria de un modelo comercial de los nuevos diseños de cocina oculta.

El Grupo de Tecnologías Fotónicas (GTF) ha participado en los últimos años en numerosos proyectos de investigación y transferencia en colaboración con la empresa BSH Electrodomésticos España, enfocados, entre otros temas, al desarrollo de innovadores sistemas luminosos de señalización [2, 3] y de sensores infrarrojos (IR) para estimación sin contacto de temperatura de recipiente [4, 5] en cocinas de inducción vitrocerámicas convencionales. La solución aquí presentada se ha desarrollado igualmente en estrecha colaboración con BSH y ha sido objeto de solicitud de varias patentes por parte de la empresa [6, 7].

2.- Diseño del prototipo

El prototipo aquí propuesto incluye en un mismo dispositivo, colocado en el interior de la cocina de inducción bajo la encimera, un sistema de iluminación para indicar visualmente al usuario las zonas de cocción, y otro que permita estimar la temperatura a la que se encuentra el recipiente de cocinado a partir de su emisión térmica IR. Al ser la encimera de un material opaco tanto en el rango visible como en el IR del espectro, ninguna de las dos funciones puede implementarse directamente a través de la misma. Se hace necesario abrir un orificio en la encimera para permitir el paso tanto de la luz visible desde el dispositivo hacia el exterior, como de la emisión IR del recipiente hacia el dispositivo sensor. Para mantener la estanqueidad de la cocina, dicho orificio debe quedar sellado con un material que transmita las longitudes de onda requeridas, al cual nos referiremos como guía.

Las dimensiones del prototipo, así como otros requerimientos de carácter técnico especificados por BSH, quedan definidas por su ubicación en el centro de cada elemento inductor de la cocina, como muestra esquemáticamente la figura 2.

Fig. 2: Esquema de la ubicación del prototipo en una cocina de inducción bajo la encimera.

A continuación, se describen los dos sistemas que componen el prototipo en su configuración final, así como la guía que transmite la radiación entre el dispositivo y el exterior de la encimera.

2.1.- Sistema de señalización luminosa

El dispositivo cuenta con dos fuentes luminosas de tipo LED de tamaño reducido y potencia adecuada para la aplicación, una en color blanco para señalizar las zonas de cocción que están activas en cada momento, que además sirve como indicador visual para la colocación de los recipientes centrados en cada inductor, y otra de color naranja que advierte del calor residual en zonas inactivas, para asegurar la seguridad del usuario. Se escogieron los modelos más adecuados de fuentes LED teniendo en cuenta todos los requerimientos de diseño, tales como rango de longitud de onda, tamaño, coste, estabilidad, eficacia de emisión, etc. La selección del LED activo en cada momento y la regulación de corriente para establecer la intensidad de emisión del LED se realiza externamente al prototipo aquí presentado, y se desarrolló en BSH, que cuenta con gran experiencia en desarrollo de sistemas de señalización luminosa.

En la sección 2.3 de este documento se detalla la optimización del nivel luminoso emitido por los LEDs en combinación con la guía luminosa cuya parte superior será lo que observe el usuario de la cocina.

2.2.- Sensor IR de temperatura de recipiente

El fundamento de la termografía IR en la que se basa este sensor es la emisión térmica en infrarrojo de cualquier cuerpo caliente, proporcional a su temperatura como indica la ley de Planck, aplicable a un cuerpo negro [8]. En la aplicación que nos ocupa, el fondo del recipiente de cocinado se comporta como un cuerpo gris que emitirá radiación térmica en función de la temperatura a la que se encuentre y de la emisividad de su superficie inferior. Esta radiación será recogida por la guía que se encuentra bajo el recipiente, en el centro de su base, y dirigida hacia un elemento detector.

La selección del sub-rango espectral del IR más adecuado para esta aplicación se estableció atendiendo a criterios que combinan una tecnología de detección eficaz, estable a las temperaturas elevadas de trabajo presentes en el interior de la cocina, y el espectro de transmisión de la guía, que además debe ser de un material adecuado mecánicamente para la estanqueidad del orificio en la encimera.

El detector escogido es por tanto un fotodiodo de InGaAs de Hamamatsu Photonics, con rango espectral de respuesta entre 0,9 y 1,7 µm. Se trata de un modelo de reducido tamaño en formato de montaje superficial, y con el área sensible adecuada para las intensidades de radiación que se espera detectar durante procesos tanto de cocción como de fritura. Se seleccionó un fotodiodo que incluye una pequeña lente para estrechar el campo de visión del detector y así mejorar la relación señal a fondo del sensor, puesto que al detector no llega solo radiación de interés procedente del recipiente de cocinado, sino también radiación térmica de otros elementos calientes presentes sobre el detector, principalmente de la encimera y la guía.

La radiación detectada por el fotodiodo se convierte en señal útil de voltaje mediante un amplificador de transimpedancia diseñado específicamente para esta aplicación, cuyo esquema se muestra en la figura 3. Su principal característica distintiva es la cancelación de las tensiones de offset generadas por el operacional a las elevadas temperaturas de trabajo (hasta 100-120°C) gracias a una correcta selección de componentes (fotodiodo con alta responsividad y baja resistencia *shunt*) y a una topología diferencial con dos ramas de alta simetría.

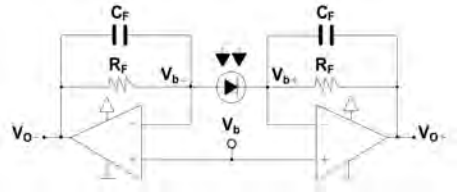

Fig. 3: Topología diferencial de la etapa amplificadora utilizada para la señal del fotodiodo.

El diseño final de la placa electrónica que contiene tanto el sistema de señalización como el sensor IR en el prototipo desarrollado se muestra en la figura 4, donde se puede observar que los elementos activos están en la cara del circuito que se dirigirá hacia arriba, hacia la encimera, y el resto de los componentes del circuito están en la cara inferior.

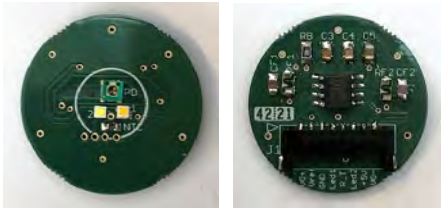

Fig. 4: Imágenes de la cara superior de la placa electrónica con dos LEDs y fotodiodo (izda.) y cara inferior con componentes electrónicos (dcha.).

2.3.- Guía

La guía visible e IR, cuya necesidad se ha justificado en el apartado 1 correspondiente al diseño del prototipo, debe ser dividida en dos partes por razones prácticas de montaje durante la fabricación industrial de la cocina. La parte superior de la guía será la que esté incrustada en el orificio abierto a través de la encimera, de manera que asegure la estanqueidad de la cocina, y la parte inferior (concéntrica con la primera) será la más cercana a la placa electrónica del dispositivo.

El prototipo final desarrollado cuenta por tanto con una guía superior consistente en un cilindro macizo de cuarzo (con transmisión en el rango IR de trabajo) de 14 mm de diámetro y 10 mm de altura, insertado en la encimera; y una guía inferior consistente en una pieza hueca troncocónica con paredes de un material polimérico de alta reflectancia difusa en el rango de trabajo, colocada entre el cilindro de cuarzo y la placa electrónica. En la figura 6 se muestran unas imágenes de esta guía y su colocación en el centro del inductor.

El diseño de ambas partes de la guía se optimizó con la ayuda de dos herramientas de simulación diferentes: el programa Zemax OpticStudio® [9] para simular la propagación de rayos en el rango visible implicados en el sistema de señalización; y el programa de elementos finitos COMSOL Multiphysics®

[10] para simular la transferencia de calor por radiación entre superficies implicada en el sensor IR de temperatura.

El modelo construido en Zemax para la señalización permitió calcular la emisión necesaria para cada modelo de LED que rindiese una irradiancia objetivo en la superficie visible por el usuario. Además, optimizó el diseño de la guía superior de cuarzo, determinando que al menos su cara superior debe estar pulida de manera que resulte difusora. De este modo, la señalización se visualiza como un círculo homogéneo de luz, independientemente de si está encendido el LED blanco o el naranja. La figura 5 ilustra dos resultados parciales de esta simulación.

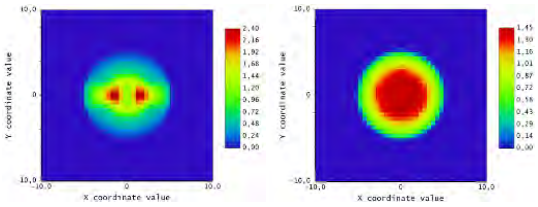

Fig. 5: Imágenes de irradiancia calculada en la cara visible de la guía: con caras especulares (izda.) y con caras difusoras (dcha.)

La modelización del prototipo en COMSOL, incluyendo tanto la guía como elementos pertinentes de su entorno, que emiten radiación térmica de fondo, permitió optimizar el diseño de ambas partes de la guía. Así se determinó que la relación señal a fondo del sensor IR se hacía mucho más favorable para la estimación de temperatura del recipiente cuando a las paredes del cilindro de cuarzo se le aplicaba un recubrimiento reflectante, y cuando la guía inferior se construía en un material con propiedades alta reflectancia difusa tanto en visible como en IR cercano, tal como el Spectralon® [11].

3.- Validación del prototipo

Este apartado se centrará exclusivamente en la validación experimental del sensor IR en el rango de temperaturas del recipiente que se requiere cubrir, puesto que el sistema de señalización fue validado por BSH.

3.1.- Montaje experimental

Para evaluar el funcionamiento del sensor IR en la determinación de la temperatura del fondo del recipiente de cocinado desde el interior de la cocina de inducción bajo la encimera, se preparó en el laboratorio un montaje experimental que reprodujese las condiciones de operación del sensor en la cocina. Este montaje, mostrado en la figura 6, consiste en una encimera del material cerámico utilizado por BSH para las cocinas de nuevo concepto, con un inductor bajo ella para calentar un disco metálico negro que simula el fondo del recipiente. La encimera tiene un orificio circular cuyo eje se coloca coincidente con el eje central del inductor. El prototipo final de la solución presentada se coloca también centrado en ese mismo eje, con la guía superior de cuarzo insertada en el orificio de la encimera, la placa electrónica colocada en el hueco central del inductor y la guía inferior fijada sobre dicha placa.

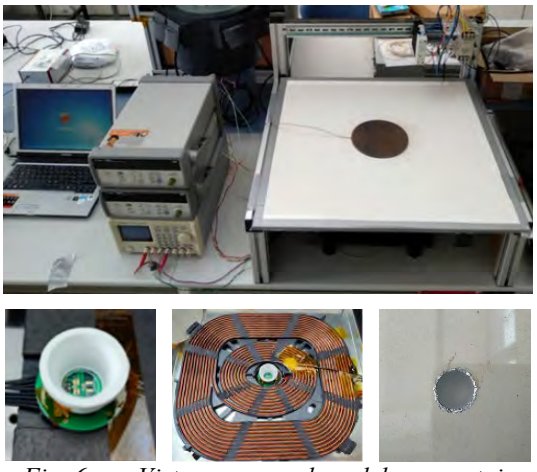

Fig. 6: Vista general del montaje experimental (arriba). Detalle de la guía inferior (izda.), de su colocación (centro) y de la guía de cuarzo (dcha.).

Los experimentos realizados consisten en aplicar potencia al inductor para calentar el disco metálico sucesivamente a ciertas temperaturas fijas (controladas con un termopar colocado en su superficie inferior) y medir el voltaje detectado por el sensor IR a cada temperatura de disco. Para aplicar y estabilizar las temperaturas del disco se utiliza un controlador PID. Después se realiza un calibrado que permite obtener la relación entre

nuestra señal experimental y la temperatura a determinar.

El sensor IR captura, además de la señal de interés, que es la señal procedente del disco, una señal térmica de fondo procedente del entorno y que es necesario sustraer a la señal medida para relacionar la señal del disco con su temperatura. Esta señal de fondo se determina experimentalmente en el mismo montaje, para cada temperatura ensayada de disco, sustituyendo momentáneamente el disco caliente por una lámina bajo emisiva a temperatura ambiente, de modo que llega al sensor la radiación de fondo proveniente principalmente de la encimera y la guía calientes. La relación entre la temperatura del disco T_d (en grados Kelvin, medida por el termopar) y la señal corregida S_c (la medida por el sensor IR menos el fondo correspondiente, en voltios) muestra una tendencia exponencial, característica de la emisión térmica, en la forma:

$$S_c = a \cdot e^{b \cdot T_d} \qquad (1)$$

donde *a* y *b* son dos constantes determinadas experimentalmente por calibración en las condiciones de ensayo descritas.

3.2.- Resultados experimentales

Los datos obtenidos del ensayo a distintas temperaturas del disco negro, entre 90 y 240°C (a temperaturas fijas cada 30°C), en las condiciones descritas en el apartado anterior, se presentan en la figura 7.

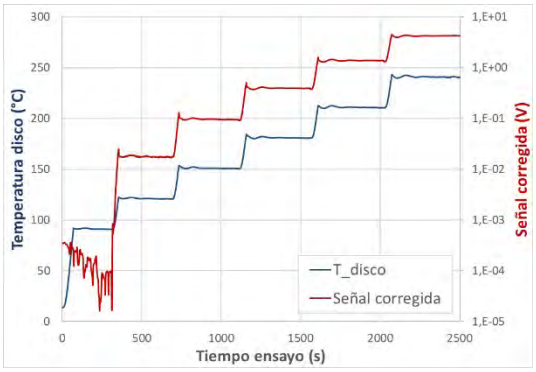

Fig. 7: Evolución temporal de la temperatura de disco medida con termopar de control, T_d, y de la señal IR corregida, S_c.

Como se puede observar en la figura 7, la señal a 90°C de disco es tan pequeña (con la ganancia fija del preamplificador que tiene el prototipo final) que es prácticamente solo ruido eléctrico, y se descarta para el calibrado. Por tanto, la ecuación de calibrado para la estimación de temperatura de disco con el sensor IR del prototipo final se obtiene a partir de los resultados experimentales de ensayo entre 120 y 240°C, mediante un ajuste ilustrado en la figura 8, y tiene la forma mostrada por la ecuación (1).

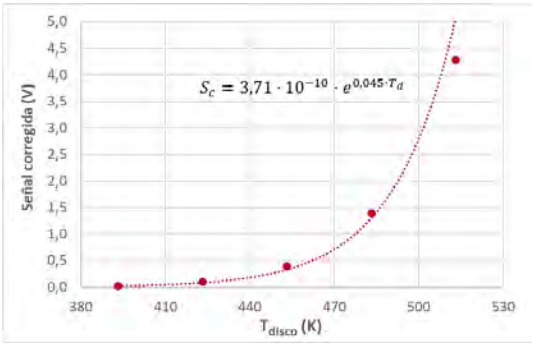

Fig. 8: Calibración: relación entre la señal corregida y la temperatura del disco.

Para evaluar la calidad de este calibrado, válido solamente para las condiciones experimentales concretas de este ensayo, se estiman las temperaturas de disco en cada fase del experimento, calculándolas a partir de la señal corregida y de los coeficientes de calibración *a* y *b* según la ecuación (1).

La comparación de las temperaturas de disco así estimadas con las medidas durante el experimento con el termopar de control se muestra en la siguiente tabla, así como el error cometido en la estimación.

Tabla 1: Temperatura de disco medida, estimada con el sensor IR y error cometido.

T_d	T_d estimada	Error
120	115	-4%
150	153	2%
180	184	2%
210	211	1%
240	236	-2%

A la vista de estos resultados, podemos afirmar que queda validado el funcionamiento del sensor IR para estimar temperaturas de disco negro en las condiciones experimentales de ensayo, en un rango entre 120 y 240°C de

disco, con un error en la determinación menor al 5%.

La calibración del sensor para su aplicación final se realizará en BSH con la solución comercial ya integrada en una cocina completa. Se prevé la inclusión de una ganancia ajustable para poder medir también en el rango bajo de temperaturas, que de este modo cubriría procesos de cocinado tanto de ebullición como de fritura. Además, se considerará la emisividad de los distintos tipos de recipientes de cocinado, cuya emisión térmica es diferente a la del disco negro utilizado en este trabajo.

4.- Conclusiones

El nuevo concepto de cocina de inducción bajo encimera opaca requiere un nuevo diseño tanto para la señalización lumínica de las zonas de cocción como para el control de temperatura de recipiente de cocinado. Este trabajo propone un prototipo de solución que integra ambas funcionalidades. Se describe el diseño y desarrollo de ambas partes del prototipo, considerando todas las restricciones tanto prácticas como de funcionamiento. Se presentan también las medidas experimentales realizadas en el laboratorio para validación del sensor IR incluido en el prototipo final.

A partir de este prototipo, BSH Electrodomésticos España ha desarrollado un producto comercial que ha incluido en sus cocinas de nuevo concepto comercializadas bajo la marca Gaggenau *Essential Induction*® [1], incluyendo tanto la función de señalización como la de control de temperatura, ambas indispensables para la seguridad de los procesos de cocinado.

Agradecimientos: Este trabajo se desarrolló dentro del Proyecto RTC-2017-5965-6, financiado en parte por MCIN/AEI /10.13039/501100011033 y por FEDER, y en parte por el Proyecto T20-20R DGA-FSE. Los autores agradecen también a BSH Electrodomésticos España su financiación y colaboración aportada.

Referencias

[1] GAGGENAU, https://www.gaggenau.com/global/appliances/cooktops/the-essential-induction

[2] E. CARRETERO, R. ALONSO, C. PELAYO, "*Compensation filters for visualization of White LEDs through ceramic glass induction cooktops",* Proceedings of the 5th PHOTOPTICS International Conference on (2017).

[3] *Hob device*. Patent reference number: WO2021151665A1.

[4] E. IMAZ, R. ALONSO, C. HERAS, I. SALINAS, E. CARRETERO, "*Infrared Thermometry System for Temperature Measurement in Induction Heating Appliances",* IEE Transaction on Industrial Electronics, vol.61, no.5, May 2014.

[5] J. LASOBRAS, R. ALONSO, C. CARRETERO, E. IMAZ. "*Infrared Sensor-Based Temperature Control for Domestic Induction Cooktops",* Sensors 2014, 14, 5278-5295, 2014.

[6] Cooking system. Patent reference number: WO2023/117505A1.

[7] Cooking system. Patent reference number: WO2022058226A3.

[8] HOWELL, J.R.; SIEGEL, R.; MENGUC, M.P. Thermal Radiation Heat Transfer, 5th ed.; Taylor and Francis: New 478 York, NY, USA, 2010.

[9] Ansys Zemax optical design software, https://www.ansys.com/products/optics/ansys-zemax-opticstudio

[10] COMSOL software for multiphysics simulation, https://www.comsol.com/heat-transfer-module

[11] Labsphere photonics solutions, https://www.labsphere.com/product/spectralon-diffuse-reflectance-standards/

Evaluación de FBGs como sensores de alta temperatura en aplicaciones de energía solar concentrada

Manuel JEREZ [(1)], Alejandro CARBALLAR [(2)], Joaquín GRANADO

1. Departamento de Ingeniería Electrónica, Universidad de Sevilla (E.T.S. de Ingeniería), C/Camino de los Descubrimientos s/n, 41092 – Sevilla, Spain

Contact: Manuel JEREZ (mjerez@us.es).

ABSTRACT:

The utilization of femtosecond-laser inscribed and regenerated Fiber Bragg Gratings (FBGs) is proposed, and an experimental comparison of both technologies is conducted to assess their potential as temperature sensors in Concentrated Solar Power (CSP) applications, where temperatures exceeding 1000°C are prevalent. Such environments demand not only high precision but also long-term measurement stability. The results indicate that femtosecond-laser inscribed FBGs exhibit superior accuracy and demonstrate enhanced reliability under extreme conditions. However, recalibration is required to optimize their performance and robustness at the higher temperature ranges encountered in these applications.

Key words: Fiber Bragg Gratings, FBG, Temperature Sensors, Concentrating Solar Power, CSP

1.- Introduction

El desarrollo de sensores ópticos en los últimos años ha estado intrínsecamente ligado a los avances en las redes de Bragg en fibra (FBGs), las cuales se han consolidado como una de las tecnologías más extendidas para la medición de temperatura en entornos extremos [1]. En este contexto, su posible aplicación como sensores de temperatura en los receptores de plantas de energía solar de concentración (CSP) surge como una opción viable para afrontar las condiciones extremas, con temperaturas superiores a 1000°C y niveles de radiación extremadamente altos, presentes en estos sistemas de generación de energía renovable [2]. En este contexto, el uso de termopares, el instrumento tradicional para realizar medidas de temperatura se hace difícil, debido a que los altos niveles de radiación adulteran las medidas, además de favorecer la pérdida progresiva de la calibración, que impide el funcionamiento del sensor durante períodos largos de tiempo [3].

Aunque las FBGs de zafiro están cobrando protagonismo en aplicaciones de altas temperaturas [4], existen dos técnicas ampliamente adoptadas en la industria para la fabricación de FBGs en fibras ópticas de alta temperatura: las FBGs inscritas con láser de femtosegundo (fs-FBGs) [5,6] y las FBGs regeneradas (rFBGs) [5,7]. Este trabajo presenta una comparación entre estas dos tecnologías y evalúa su rendimiento en un horno tubular alcanzando temperaturas de hasta 1000°C, analizando su idoneidad para aplicaciones en CSP.

2.- Metodología

El diseño realizado y solicitado a los fabricantes de los dos tipos de FBGs se hizo teniendo en cuenta las características de funcionamiento de estas y los supuestos desplazamientos espectrales, observados anteriormente en [2] y contemplados en la literatura [5-7]. De esta forma, se encargaron 3 FBGs de cada tecnología de fabricación, de forma que las longitudes de onda base (a

temperatura ambiente) de los sensores estuvieran intercaladas y repartidas de manera equiespacial, permitiendo el funcionamiento de estas por separado o las 6 a la vez, utilizando un *splitter* óptico. Con el diseño propuesto, que se adjunta en la Tabla 1, los sensores podían alcanzar más de 950ºC funcionando a la vez.

Tabla 1: Longitudes de onda solicitadas y recibidas para cada uno de los sensores FBG.

Sensor	***Solicitada [nm]***	***Recibida [nm]***	***Diff. [nm]***
fsFBG1	*1501*	*1503.9*	*2.9*
rFBG1	*1517.6*	*-*	*-*
fsFBG2	*1534.3*	*1537.3*	*3*
rFBG2	*1550.9*	*1539.3*	*11.6*
fsFBG3	*1567.6*	*1570.6*	*3*
rFBG3	*1584.2*	*1553.8*	*30.4*

A pesar de este diseño, los sensores recibidos no cumplieron con las especificaciones propuestas, produciéndose un solape entre las 2 FBGs regeneradas y la fs-FBG2. Observando la Tabla 1, resulta fácil de identificar que las rFBGs tienen mucha menor precisión en la fabricación que las fs-FBG, que, aunque también tienen una distancia respecto de la longitud de onda solicitada, es menor, además de mantener el espaciado entre las 3 longitudes de onda base.

Las fs-FBGs fueron fabricadas por Engionic (https://engionic.de/), y en este artículo se ensayan dos de ellas, integradas en una fibra dentro de un capilar de acero con una tercera FBG. Estos sensores fueron calibrados hasta 700°C mediante un polinomio de quinto grado. Los dos sensores regenerados fueron fabricados por la empresa CalSens (https://www.calsens.es/). De estos, uno estaba integrado en un capilar de acero, mientras que el otro se encontraba en un capilar de alúmina; estando calibrados hasta 1050°C utilizando un polinomio de cuarto grado. En la Fig. 1 se muestran las curvas de calibración de los 4 sensores puestos a prueba en este trabajo, donde resulta evidente el solape prácticamente total entre la fs-FBG2 y la rFBG de acero, así como entre la parte más alta del rango de funcionamiento de la rFBG de alúmina y la fsFBG3.

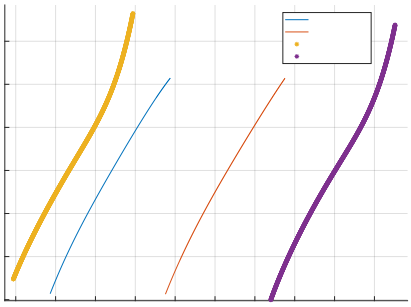

Figura 1. Desplazamiento espectral teórico, según las curvas de calibración, de los 4 sensores puestos a prueba.

Para los experimentos, cada sensor fs-FBG se colocó junto a uno de los rFBG en un horno tubular THHR/60/250/1300, acompañado de un termopar tipo K (TC K 003) utilizado como referencia de temperatura; uniendo los tres sensores con un hilo de platino para garantizar la coherencia espacial entre las medidas en el interior del horno. En la Figura 2 se pueden observar los 3 dispositivos introducidos en el horno. Los experimentos se llevaron a cabo en el Centro de Investigación, Tecnología e Innovación de la Universidad de Sevilla (CITIUS).

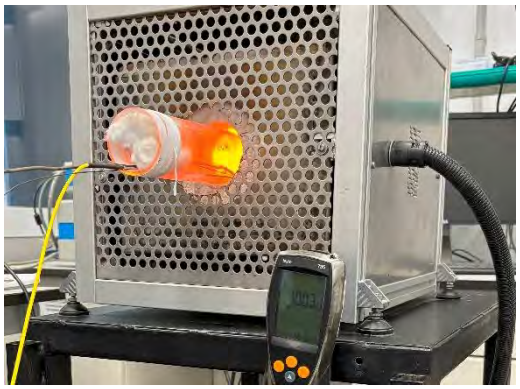

Figura 2. Montaje experimental en el horno tubular.

El procedimiento en el horno consistió en incrementar progresivamente la temperatura hasta 1000°C, realizando distintas paradas en temperaturas intermedias donde tomar medidas. Una vez alcanzados los 1000°C, la

temperatura se redujo a 750°C, seguida de un nuevo incremento hasta 1000°C. Además, se realizó una caracterización de los sensores a temperatura ambiente para analizar sus propiedades ópticas.

3.- Resultados

Antes de discutir los resultados relacionados con los experimentos realizados en el horno, es pertinente analizar los niveles y las formas de la potencia reflejada de los diferentes tipos de sensores. En la Fig. 3, se presenta la traza de potencia resultante de combinar una fibra inscrita con tres fs-FBGs con la r-FBG inscrita en acero utilizando un divisor óptico. Resulta evidente observando la imagen comprobar que la potencia reflejada por los sensores inscritos con láser de femtosegundo es de aproximadamente 15dB mayor que la del sensor regenerado. Además, la Fig. 4 ofrece una vista detallada de la forma de la potencia reflejada para cada sensor, destacando que la fs-FBG presenta una respuesta significativamente más uniforme en comparación con la rFBG. Esta mayor regularidad permite que la robustez de la medición sea mayor, al proporcionar un punto de referencia bien definido para la detección del desplazamiento espectral.

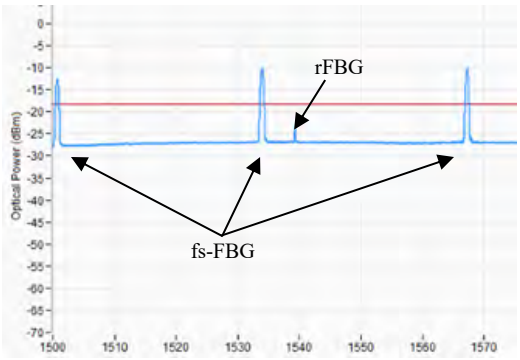

Figura 3. Traza de potencia de 3 fs-FBGs y una rFBG combinados con un divisor óptico.

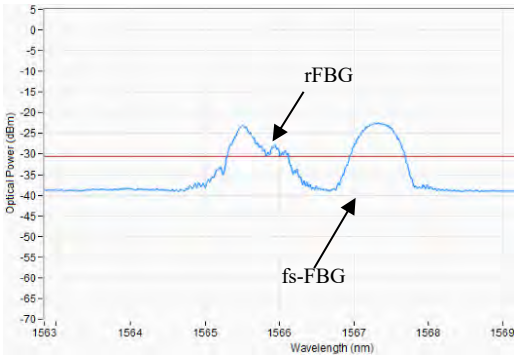

Figura 4. Detalle de la curva de potencia reflejada de una fs-FBG y una rFBG.

En cuanto a los resultados obtenidos en el horno, estos se presentan en la Fig. 5. En primer lugar, se analiza el desplazamiento espectral en la Fig. 5a, comparando el de una de las fs-FBGs con el de la rFBG de acero. En este caso, la rFBG muestra un desplazamiento espectral ligeramente menor, específicamente 0.3nm menos en la temperatura más alta evaluada de 985°C. Un desplazamiento espectral más bajo permitiría conectar un mayor número de sensores al mismo interrogador, dada su gama espectral fija. Sin embargo, esta diferencia no es lo suficientemente significativa como para considerarse una ventaja decisiva, en tanto que el ahorro que se produce al usar rFBGs no es suficiente a lo largo de todo el intervalo espectral del interrogador para incorporar un sensor más. Las Fig. 5b y 5c muestran la precisión en las mediciones proporcionadas por los sensores ópticos frente a la temperatura de referencia, definida como el error relativo entre la temperatura medida por los diferentes FBGs y el termopar.

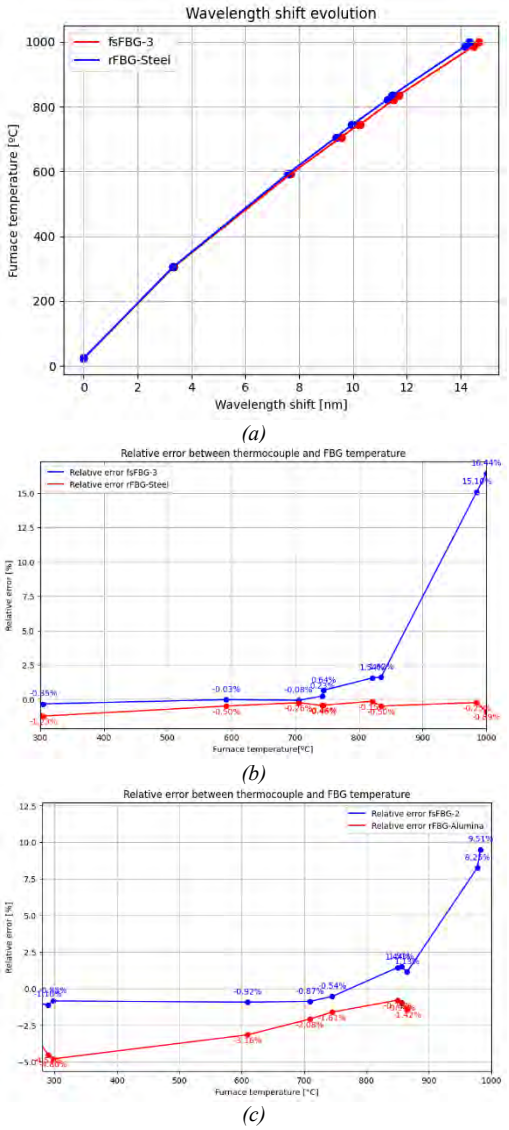

Figura. 5. (a) Desplazamiento espectral de las diferentes FBGs durante los experimentos, (b) error relativo entre fs-FBG y rFBG de acero frente al termopar y (c) error relativo entre fs-FBG y rFBG de alúmina frente al termopar.

La primera conclusión que se puede obtener observando las Figuras 5b y 5c es que todos los sensores muestran un desempeño adecuado en relación con la precisión de sus medidas, destacando las fs-FBGs y la rFBG embebida en el capilar de acero, mostrando errores relativos por debajo del 2% con respecto del termopar de referencia. Entre ellas, las FBGs inscritas con láser de femtosegundos presentan errores más bajos para temperaturas por debajo de 700°C, que es el rango de funcionamiento para el cual estaban calibrados, probablemente gracias al tener un polinomio de calibración de un grado mayor, que hace que la curva de comportamiento se adapte mejor al funcionamiento del propio sensor. Los resultados correspondientes a la FBG regenerada del capilar de alúmina son llamativos en tanto que, a pesar de utilizar la misma tecnología de fabricación que la rFBG de acero, muestra errores significativamente más altos, probablemente debido a la fragilidad del material y los posibles daños físicos sufridos no sólo por la temperatura, sino también durante la propia mecanización y montaje del experimento. Finalmente, resulta evidente comentar que para que las fs-FBGs funcionen correctamente en el rango de temperaturas más alto, sería necesaria una recalibración, adaptando el polinomio de grado cinco que permite mayor fiabilidad hasta los 1000ºC a los que ha sido sometido.

4.- Conclusiones

El estudio realizado ha demostrado que es posible obtener mediciones de temperatura consistentes y precisas hasta 1000°C utilizando tanto FBGs inscritas con láser de femtosegundo como FBGs regeneradas. Sin embargo, las fs-FBGs requerirían una recalibración para ampliar su rango operativo y garantizar la precisión de las mediciones. Dentro del rango de temperatura en el que ambos tipos de sensores se superponen, las dos fs-FBGs proporcionaron mejores resultados que las rFBGs en comparación con el termopar de referencia. Esta mejora podría atribuirse al uso de un polinomio de grado superior, que se ajusta mejor al comportamiento físico del sensor.

Entre las dos FBGs regeneradas, la integrada en el capilar de acero presentó mediciones más cercanas a las del termopar. En cuanto a su posible aplicación en sistemas de energía solar de concentración (CSP), las fs-FBGs parecen ser la opción más adecuada debido a la precisión en la fabricación y la capacidad de multiplexación que nos provee el fabricante, reduciendo los requisitos de equipamiento, disminuyendo los costos y ofreciendo mucho mayor control sobre los sensores, siendo su fabricación más cercana al diseño original. Además, su potencia reflejada

significativamente mayor y su perfil de potencia en comparación con las FBGs regeneradas permitirían una operación prolongada en condiciones extremas, ya que requerirían una degradación más avanzada antes de alcanzar el fallo.

Acknowledgements: Este trabajo se ha desarrollado en el marco de los proyectos de investigación del Ministerio de Ciencia e Innovación, CHLOE con referencia PID2021-125786OB-C22, y CATION con referencia TED2021-132190B-C22; así como del proyecto ASTERIx-CAESar, que ha recibido financiación del programa de investigación e innovación Horizon Europe de la Unión Europea bajo el acuerdo de subvención Nº 101122231.

References

[1] Y. Deng et al., "Optical fiber sensors in extreme temperature and radiation environments: A review", IEEE Sensors Journal 22 (2022), pp. 13811-13834.

[2] R. Rodríguez-Garrido et al., "High-Temperature Monitoring in Central Receiver Concentrating Solar Power Plants with Femtosecond-Laser Inscribed FBG", Sensors 21 (2021), 3762[3].

[3] Z. Kou et al., "Heat transfer error analysis of high-temperature wall temperature measurement using thermocouple", Case Studies in Thermal Engineering 59 (2024), pp. 104518.

[4] B. Wang et al., "Review of high temperature measurement technology based on sapphire optical fiber", Measurement 184 (2021), 109868.

[5] S. J. Mihailov, "Fiber Bragg Grating Sensors for Harsh Environments," Sensors 12 (2012), pp. 1898-1918.

[6] A. Lerner et al., "An intrinsic sensitivity calibration scheme for high temperature measurements using femtosecond point-by-point written fiber Bragg gratings", Optics & Laser technology 170 (2024), 110278.

[7] D. Barrera et al., "Packaged Optical Sensors Based on Regenerated Fiber Bragg Gratings for High Temperature Applications", IEEE Sensors Journal 12 (2012), pp. 107-112

Integrated Optical Biosensors and Microfluidics for Real-Time Optical Sensing in Lab-on-a-Chip Systems

Beatriz SANTAMARÍA[1,2,3], Rafael CASQUEL[1,2,4], Haizea APELLANIZ[1], Jorge MARTINEZ DE LA MATA[5,6], María Fe LAGUNA[1,2,4], Andrés OTERO[5,6], Airan FRANCES[5,6], Miguel HOLGADO[1,2,4]

1. Group of Optics, Photonics, and Biophotonics. Center for Biomedical Technology (CTB). Universidad Politécnica de Madrid. Campus de Montegancedo, M-40 km38, 28223 Pozuelo de Alarcón, Madrid, Spain
2. Group of Organ and Tissue on-a-chip and In-Vitro Detection. Health Research Institute of the Hospital Clínico San Carlos, IdISSC. C/ Profesor Martín Lagos s/n, 4ª Planta Sur 28040, Madrid, Spain
3. Department of Mechanics, Chemistry and Industrial Design Engineering. Escuela Superior de Ingeniería y Diseño Industrial. Universidad Politécnica de Madrid. Ronda de Valencia 3, 28012, Madrid, Spain
4. Department of Applied Physics and Materials Engineering, Escuela Técnica Superior de Ingenieros Industriales, Universidad Politécnica de Madrid, C/José Gutiérrez Abascal, 2, 28006 Madrid, Spain
5. Department of Automatics, Electrical and Electronic Engineering, and Computer Engineering. Escuela Técnica Superior de Ingenieros Industriales, Universidad Politécnica de Madrid, C/José Gutiérrez Abascal, 2, 28006 Madrid, Spain
6. Centro de Electrónica Industrial, Universidad Politécnica de Madrid, C/ José Gutiérrez Abascal 2, 28006 Madrid, Spain

Contact: Beatriz SANTAMARIA (betxu.santamaria@upm.es).

ABSTRACT:

This paper presents the design, fabrication, and preliminary characterization of an integrated microfluidic platform with Resonant Nano Pillar (RNP) optical biosensors, developed within the TALES project (national project under the Spanish State Plan for Scientific, Technical and Innovation Research). The device combines polymer-based microfluidics with silicon-based nanophotonic biosensors for real-time detection of refractive index variations in a continuous flow system. RNPs were fabricated using Nanoimprint Lithography (NIL) on a Si_3N_4-SiO_2 multilayer stack with a central SiO_2 cavity, ensuring high spectral sensitivity. The PDMS-based microfluidic chip was designed for precise flow control and optimized biosensing conditions. Initial experiments confirmed the high-resolution optical response of the RNPs, establishing a baseline for future comparisons with electrical recordings from Microelectrode Arrays (MEAs). The TALES platform aims to enable real-time neurotransmitter detection, providing an innovative tool for studying neural communication and neurotechnology applications. These findings validate its potential for biosensing, photonic integration, and optofluidics.

Key words: Optofluidics, Photonic Biosensors, Integrated Sensing Platform, Microfluidics, Lab-on-a-Chip, Resonant Nano Pillars.

1.- Introduction

The integration of photonic biosensors with microfluidic technologies has emerged as a crucial area of research for developing compact, real-time sensing platforms. Within lab-on-a-chip (LoC) and optofluidic devices, optical biosensors enable label-free, highly sensitive detection of biomolecules by measuring refractive index variations in their surrounding medium [1]. These advances are particularly relevant in neurotechnology, where precise detection of neurotransmitters (such dopamine, octopamine, and histamine) [2] and electrical activity is essential for understanding neural communication [3].

The TALES project aims to develop a multifunctional microfluidic chip that integrates Resonant Nano Pillars (RNPs) as optical biosensors [4] alongside Microelectrode Arrays (MEAs) for electrochemical monitoring [5]. Unlike conventional biosensors, RNPs exhibit high-Q factor resonances, making them particularly well-suited for detecting minimum refractive index variations with high sensitivity [6]. On the other hand, MEAs are devices used to record the electrical activity of cells and tissues. They consist of an array of electrodes that can stimulate and record electrical signals from multiple cells. These electrodes detect changes in electrical potential caused by cellular activity and transmit the signals to contacts, where they are amplified, filtered, and processed [7]. The integration of these biosensors within a microfluidic platform ensures continuous flow operation, controlled diffusion dynamics, and real-time monitoring of target analytes, enabling a robust optofluidic system for biosensing applications.

This study focuses on the fabrication and characterization of two key components within the TALES platform: the microfluidic chip, designed to provide a stable fluidic environment for biosensing while ensuring optimal analyte transport, and the RNP-based optical biosensors, developed to measure refractive index changes under continuous flow conditions.

Preliminary bulk sensing experiments were conducted to evaluate the optical response of the RNP biosensors when exposed to liquids with different refractive indices, confirming their sensitivity and integration capabilities. These initial results will serve as a baseline for future comparisons with electrical sensing data obtained from MEAs, which will be integrated into the final TALES device. Ultimately, the platform aims to enable real-time detection of neurotransmitters released by neuronal networks, providing a powerful tool for studying synaptic activity, neural communication, and advanced neurotechnology applications.

2.- Materials and Methods

2.1.- Fabrication of the Microfluidic Chip

The microfluidic system was designed to ensure controlled laminar flow and maintain stable conditions for optical biosensing. The fabrication process began with the development of a master mold using 3D printing technology, which allowed rapid prototyping and initial validation of the microfluidic design [8]. This approach facilitated adjustments in channel geometry and sensing chamber dimensions before proceeding to more advanced fabrication techniques. Once the preliminary tests confirmed the system's functionality, the mold was refined and manufactured in aluminum using CNC (Computer Numerical Control) machining, ensuring higher precision and durability for reproducible microfluidic chip production.

With the aluminum mold completed, a polydimethylsiloxane (PDMS) layer was cast over it and cured at 80°C for one hour. The cured PDMS structure was then carefully removed and plasma-treated to enhance adhesion before being permanently bonded to a glass substrate. This configuration provided an optically transparent bottom surface, essential for high-precision optical measurements. To facilitate fluid injection

and controlled flow, inlet and outlet ports were precisely created in the PDMS layer.

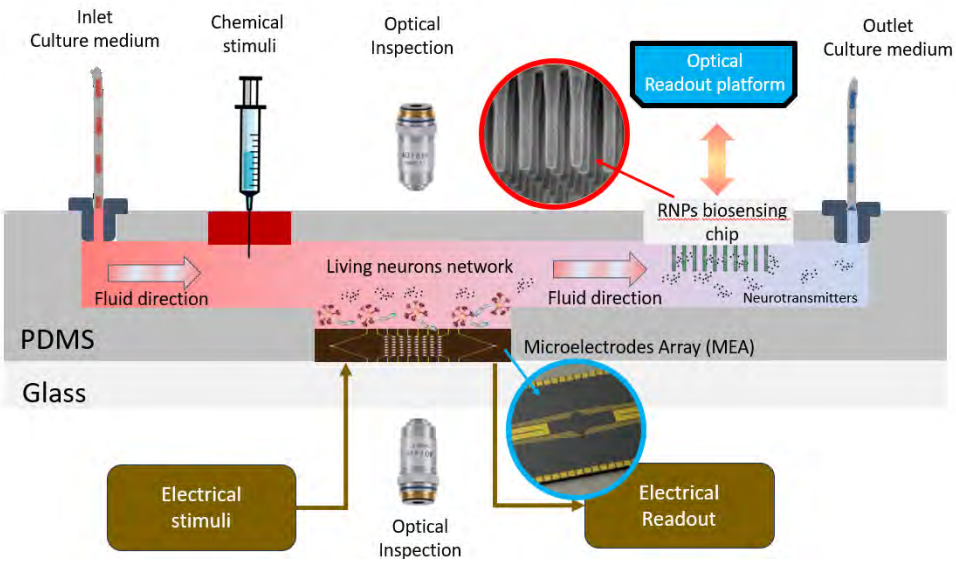

Fig. 1: Schematic cross-sectional diagram of the microfluidic device integrating the mentioned sensors, with the RNP-based optical biosensor highlighted in red and the MEAs highlighted in blue.

2.2.- Fabrication of Resonant Nano Pillars (RNPs) as Optical Biosensors

Resonant Nano Pillars (RNPs) can be fabricated using various nanolithography techniques, such as electron beam lithography (e-beam lithography), laser interference lithography (LIL), or nanoimprint lithography (NIL). Compared to e-beam lithography, LIL and NIL offer advantages such as reduced processing time and lower cost per chip, as e-beam lithography is both time-consuming and expensive.

For the measurements conducted in this study, RNPs were fabricated on a Si_3N_4-SiO_2 multilayer stack designed to enhance Fabry-Pérot resonance and optimize the Q-factor of the optical response [9]. The fabrication process began with Plasma-Enhanced Chemical Vapor Deposition (PECVD) to create a Bragg reflector, consisting of alternating SiO_2 (110 nm) and Si_3N_4 (97 nm) layers, with a central SiO_2 cavity (200 nm). This resulted in a total coating thickness of 2270 nm on a quartz substrate. Following an LIL lithography step, the pattern was transferred into the Si_3N_4-SiO_2 stack using a lift-off process, as described elsewhere [10], producing high-aspect-ratio nanopillars with a diameter of approximately 210 nm, a height of 2.27 µm, and a pitch of 500 nm. The process can also be replicated with NIL instead of LIL by employing PDMS stamps, as recently demonstrated [11].

Finally, structural integrity was assessed using Scanning Electron Microscopy (SEM), while the optical response was characterized using Fourier-transform infrared spectroscopy (FTIR) to measure resonance shifts in different media..

3.- Preliminary Results: Bulk Sensing Evaluation

To evaluate the optical performance of the RNP biosensors, bulk sensing experiments were conducted within the fabricated microfluidic system to assess their sensitivity to refractive index variations under continuous flow conditions. These variations were also reflected in impedance measurements, where a strong correlation was observed between higher saline concentrations and lower impedance, as shown in Figure 2 [12].

The microfluidic chip was connected to a syringe pump to ensure a precise and controlled flow rate of 1 µL/min. Sequential injections of NaCl solutions at different concentrations (300 mg/mL, 225 mg/mL, 75 mg/mL, 0 mg/mL, and an empty reference) were introduced to analyze the biosensors' response. The resonant wavelength shift of the RNPs was monitored in real time using a visual spectrometer (Mightex GH-Resolution High-Stability CCD Spectrometer, 300–1050 nm wavelength range), enabling the detection of refractive index changes.

The results demonstrated a linear correlation between refractive index variations and the optical response of the RNPs, confirming their reliability as optical biosensors. The measured bulk sensitivity, shown in Figure 3, reached 0.047 nm/(mg/mL), aligning with the performance of state-of-the-art photonic biosensors. Furthermore, the experimental data closely matched theoretical predictions, validating the fabrication process and reinforcing the suitability of RNPs for high-sensitivity biosensing applications.

These findings establish a strong foundation for future studies, particularly for integrating RNP biosensors with MEAs to enable simultaneous optical and electrical readout in advanced biosensing platforms.

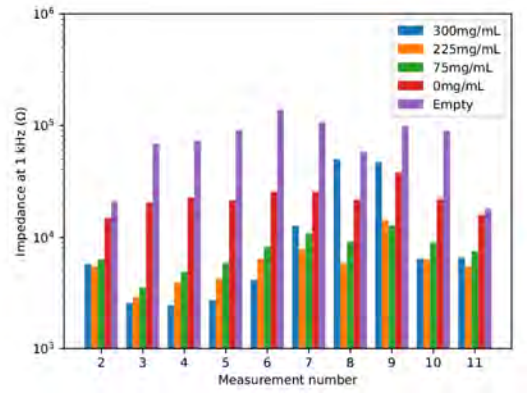

Fig. 2: Impedance measurements performed on the MEAs with different salt solutions.

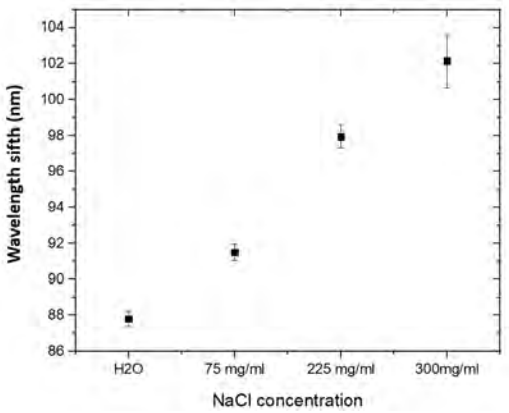

Fig. 3: The optical signal shift (resonance peak shift) of the RNPs in response to varying salt concentrations is displayed.

4.- Conclusion

This study demonstrates the successful fabrication and characterization of an integrated microfluidic system incorporating Resonant Nano Pillar (RNP)-based optical biosensors, highlighting its potential for advanced optofluidic applications. The microfluidic chip was meticulously designed to ensure stable and controlled fluid dynamics, providing a reliable environment for biosensing experiments. The fabricated RNP biosensors exhibited high sensitivity to refractive index variations, validating their suitability for real-time optical detection in continuous flow conditions. Initial bulk sensing experiments confirmed a strong correlation between refractive index changes and spectral shifts, reinforcing the feasibility of integrating these biosensors into lab-on-a-chip (LoC) and optofluidic platforms. These promising results lay the groundwork for further advancements, where upcoming research will focus on functionalizing the RNPs with specific bioreceptors to enable highly selective biomolecular detection. Additionally, efforts will be directed towards optimizing the microfluidic system to enhance long-term stability, minimize nonspecific interactions, and improve overall sensing performance. Future developments will also explore the scalability and reproducibility of the fabrication process, ensuring the robustness of the technology for potential

biomedical and environmental sensing applications.

Acknowledgements: This work has been sponsored by the TALES project, funded by part of the R&D&I project PID2023-149403OB-I00, funded by MICIU, AEI/10.13039/501100011033, and "FEDER: A Way of Making Europe". The authors would like to express their gratitude to Luca Tramarín for his valuable guidance and advice on the sensor fabrication process.

References

[1] P. HERREROS, L. M. BALLESTEROS-ESTEBAN, M. F. LAGUNA, I. LEYVA, I. SENDIÑA-NADAL, and M. HOLGADO, *"Neuronal circuits on a chip for biological network monitoring"*, Biotechnol J, vol. 16, no. 7, p. 2000355, 2021.

[2] U. HOMBERG, *"Neurotransmitters and neuropeptides in the brain of the locust"*, Microsc Res Tech, vol. 56, no. 3, pp. 189–209, 2002.

[3] P. E. M. PHILLIPS, P. J. HANCOCK, and J. A. STAMFORD, *"Time window of autoreceptor-mediated inhibition of limbic and striatal dopamine release"*, Synapse, vol. 44, no. 1, pp. 15–22, 2002.

[4] F. FERNÁNDEZ et al., *"Optical sensor based on periodic array of resonant nanopillars for real time monitoring"*, Sens Actuators B Chem, vol. 244, pp. 323–326, 2017.

[5] S. HWANG, C. N. LAFRATTA, V. AGARWAL, X. YU, D. R. WALT, and S. SONKUSALE, *"CMOS microelectrode array for electrochemical lab-on-a-chip applications"*, IEEE Sens J, vol. 9, no. 6, pp. 609–615, 2009.

[6] R. CASQUEL et al., *"Engineering vertically interrogated interferometric sensors for optical label-free biosensing"*, Anal Bioanal Chem, vol. 412, no. 14, pp. 3285–3297, 2020.

[7] J. PINE, "*A History of MEA Development*," Advances in Network Electrophysiology: Using Multi-Electrode Arrays, pp. 3–23, 2006.

[8] P. HERREROS, A. LÓPEZ-HERNÁNDEZ, M. HOLGADO, and M. F. L. HERAS, *"Melanoma-on-a-chip model for anticancer drug injecting delivery method"*, SLAS Technol, vol. 29, no. 6, p. 100219, 2024.

[9] V. CANALEJAS-TEJERO, A. L. HERNÁNDEZ, R. CASQUEL, S. A. QUINTERO, M. F. LAGUNA, and M. HOLGADO, *"Fabrication of Si_3N_4/SiO_2 tiered resonant nanopillars with nickel caps arrays: application for optochemical sensing"*, Opt Mater Express, vol. 8, no. 4, p. 1082, 2018.

[10] I. CORNAGO, A. L. HERNÁNDEZ, R. CASQUEL, M. HOLGADO, M. F. LAGUNA, F. J. SANZA, AND J. BRAVO, "*Bulk sensing performance comparison between silicon dioxide and resonant high aspect ratio nanopillars arrays fabricated by means of interference lithography*", Opt. Mater. Express **6**, 2264-2272 (2016).

[11] L. TRAMARIN, R. CASQUEL, I. MAÑUECO, and M. HOLGADO, *"High aspect-ratio sub-500 nm UV-PDMS bilayer stamps by means of hybrid thermal-ultraviolet curing for resonant nanopillars fabrication through soft UV-NIL"*, Microelectron Eng, vol. 282, p. 112088, 2023

[12] H. Rodríguez Rodríguez, "*Microelectrode Arrays for In Vitro neural networks and hardware accelerators for their Digital Twins*," MSc thesis, Universidad Politécnica de Madrid, 2024.

Hemoglobin Level Determination with a Fiber Optic Sensor Using Boron-Doped Diamond Film

Monika KOSOWSKA [1]

1. Faculty of Telecommunications, Computer Science and Electrical Engineering, Bydgoszcz University of Science and Technology, Al. Prof. S. Kaliskiego 7, 85-796 Bydgoszcz, Poland

Contact: Monika KOSOWSKA (monika.kosowska@pbs.edu.pl).

ABSTRACT:

This study presents a fiber optic sensor for hemoglobin level determination using boron-doped diamond film as an alternative material for a mirror. Compared to traditional silver mirrors, BDD offers enhanced durability, biocompatibility and longer lifespan. The fiber optic measurement setup was built as a Fabry-Perot interferometer operating in a reflection mode. Series of distance measurements allowed establishment of the optimal cavity length of 80 μm, assuring the signal visibility of 0.994. The measurements were conducted for Hb levels of 2.7 g/dL – 16.1 g/dL. Linear work characteristics was achieved.

Key words: fiber-optic sensor, boron-doped diamond, diamond film, interferometry, hemoglobin, biophotonic sensor, optical measurements

1. Introduction

Current trends focus on developing advanced materials [1], AI-driven analysis [2], [3], and miniaturized sensors to enhance medical diagnostics and personalized healthcare [4]. These advancements result in growing interest in fiber optic sensors, which offer development of simple and rapid diagnostic tools, suitable for point-of-care applications.

Fiber optic sensors have great potential in biomeasurements due to their high sensitivity, small size, and resistance to electromagnetic interference [5]. They enable fast, non-contact, and precise detection of biological parameter changes, which is crucial in medical diagnostics [6]. Additionally, the ability to functionalize the fiber surface allows for selective detection of specific biomarkers [7], [8].

Their capabilities can be further enhanced through advancements in material engineering. For example, boron-doped diamond (BDD) films characterized by remarkable mechanical, chemical, electronic and optical properties [9], [10] can be used to develop elements dedicated for optoelectronic systems [11].

Conventionally, mirrors used in such setups are made from materials with high reflectivity, such as metallic layers (e.g., silver or gold). While these materials offer good optical performance, they are vulnerable to damage.

In this study, hemoglobin level determination with the use of a fiber-optic sensor applying BDD instead of a standard silver mirror is presented. As diamond materials are known for their chemical stability, biocompatibility, and durability, the presented approach addresses limitations of existing standard elements.

2. Experimental

The fiber-optic measurement setup was built as an interferometer. A superluminescent diode Superlum Ltd., Carrigtwohill, Ireland (S-1550-G-I-20: λ = 1550 nm, $\Delta\lambda$FWHM =

45 nm) was applied as a broadband light source. The light was guided through single mode telecommunication fibers (SMF-28, Thorlabs, Newton, MA, USA) and 2 × 1 coupler (Thorlabs, Newton, MA, USA). The interferometric signal was recorded by optical spectrum analyzer (Ando AQ6319, Yokogawa, Japan). The measurement system incorporated micromechanical setup to precisely position the optical fiber probe, stabilize it, and prevent unwanted shifts that could affect measurement accuracy. The schema of the built setup is presented in Figure 1a.

The principle of operation is based on a Fabry-Perot interferometer, with a two-beam approximation [12], as shown in Figure 1b. The incident light is guided through the fiber to the Fabry-Perot cavity formed by two interfaces: fiber/sample and sample/BDD, leading to partial reflections. The reflected beams interfere – introduction of a phase difference between them (i.e. by changing optical path or refractive index of the cavity) will directly impact the measured signal. The light is coupled back to the fiber and recorded by the optical spectrum analyzer (OSA). The signal analysis is performed on a PC.

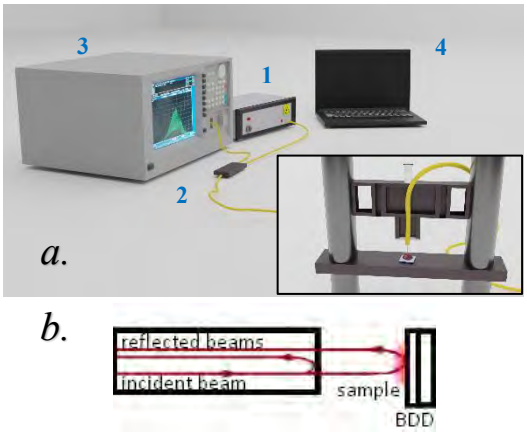

Fig. 1: a. Measurement setup: 1 – light source, 2 – coupler, 3 – OSA, 4 – PC. Inset presents positioning of the probe. b. Work principle.

The boron-doped diamond film was deposited on a silica substrate, the process was described in detail elsewhere [13].

The experimental procedure involved optimizing the Fabry–Perot cavity length, preparing hemoglobin samples across a physiologically relevant concentration range, conducting optical measurements using the fiber-optic interferometric setup with a BDD-based mirror, and analyzing the recorded spectra to correlate interference patterns with Hb levels.

3. Results

The first stage of the research included determination of the optimal cavity length to ensure the highest signal visibility value. Visibility V is a parameter that quantifies the contrast of the optical signal. It is expressed as (1):

$$V = \frac{I_{max} - I_{min}}{I_{max} + I_{min}} \quad (1)$$

where I_{max} is the maximum intensity of the interference fringes, and I_{min} is the minimum intensity.

10 series of distance measurements were performed in a range 40 -200 µm, with a step of 20 ± 2 µm. Slight differences in lengths increments may be due to the scale of the micrometer screw and parallax error. The results are presented in Figure 2 in the form of box plots, where straight lines in the boxes present median values, squares average values, and the whiskers represent standard deviation. Note that the highest visibility (average 0.994) and the most repeatable results were achieved for 80 µm. As such, further measurements are performed with this setting.

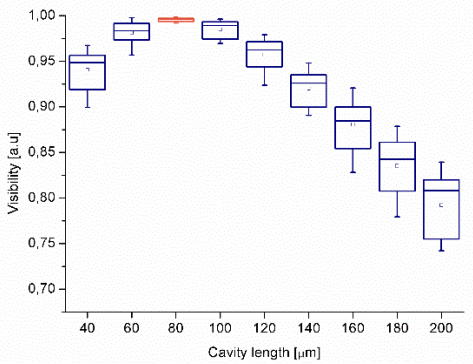

Fig. 2: Visibility values for different cavity lengths calculated for 10 measurement series.

Samples with various hemoglobin (Hb) levels from 2.7 g/dL to 16.1 g/dL were prepared and

subsequently subjected to optical measurements. The investigated range includes hemoglobin levels comparable to those found in the human body [14], ensuring the sensor's applicability for biomedical diagnostics. Representative spectra for 5.9 g/dL and 16.1 g/dL are presented in Figure 3.

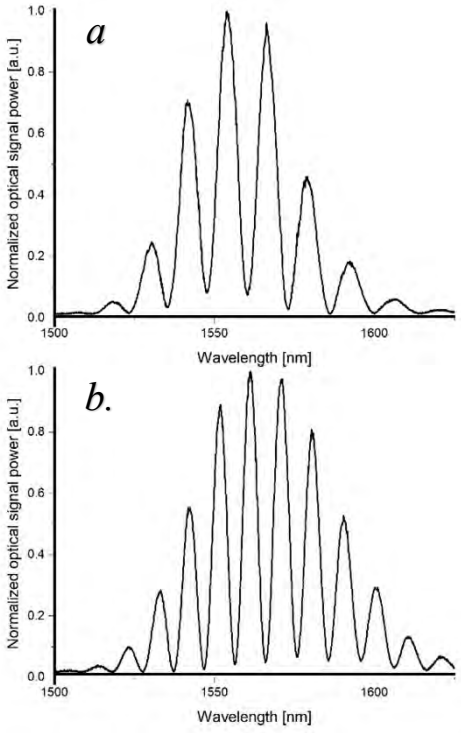

Fig. 3: Recorded optical spectra a) 5.9 g/dL b) 16.1 g/dL.

The observed signal modulation indicates that changes in hemoglobin concentration directly influence the optical path difference, as a result of changing refractive index of the sample. As hemoglobin levels increase, the refractive index of the sample also changes, altering the phase of the propagating light. This affects the interference conditions, leading to changes in the fringe pattern, and a corresponding change in the number of interference fringes observed. Non-ideal results may be attributed to small alterations in the cavity due to the cleaning procedure after each measurement and sample repositioning.

By analyzing the number of interference fringes within the 1520–1620 nm spectral range, a linear relationship was established between the fringe count and hemoglobin concentration, as shown in Figure 4.

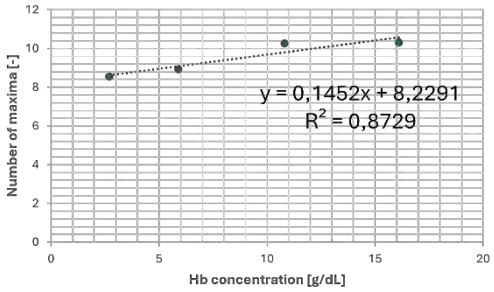

Fig. 4: Sensor work characteristics. Fractions in the Y axis appear, as the number of fringes within a given range is calculated by considering both the full fringe and its partial presence in the range.

The linear dependence simplifies calibration and enhances the sensor's potential for accurate hemoglobin level determination. ensuring consistent and reliable sensor response.

4. Conclusion

A fiber optic sensor incorporating a boron-doped diamond (BDD) film was developed for hemoglobin level determination. The optimal cavity length of 80 µm was established to ensure high signal visibility and measurement repeatability. The measurements were conducted for Hb levels of 2.7 g/dL – 16.1 g/dL. A linear relationship between hemoglobin concentration and number of maxima in the spectra was determined. The use of BDD instead of a traditional silver mirror enhances durability, biocompatibility, and long-term stability. Further perspectives for this solution could focus on system miniaturization and integrating the sensor into portable point-of-care diagnostic systems.

Acknowledgements: This work has been supported by WTIIE DS Funds of the Bydgoszcz University of Science and Technology, and WETI DS Funds of the Gdańsk University of Science and Technology.

The Author acknowledges Mateusz Ficek, PhD EE for providing boron-doped diamond film.

References

[1] P. Wityk *et al.*, "Celebrating biomimicry: bioinspired layers in optical biosensors," *Opt Quant Electron*, vol. 56, no. 8, p. 1303, Jul. 2024, doi: 10.1007/s11082-024-06798-6.

[2] G. S. Pradeep Ghantasala, R. S. R, A. Sungheetha, A. P, S. B, and P. K, "A Review of Advanced Technologies for Intelligent Sensing, Diagnostics, and Personalized Healthcare Solutions," in *2024 4th International Conference on Ubiquitous Computing and Intelligent Information Systems (ICUIS)*, Dec. 2024, pp. 1043–1049. doi: 10.1109/ICUIS64676.2024.10866104.

[3] S. Garcia-Galan *et al.*, "Expert system against machine learning approaches as a virtual sensor for ventricular arrhythmia risk level estimation," *Biomedical Signal Processing and Control*, vol. 102, p. 107255, Apr. 2025, doi: 10.1016/j.bspc.2024.107255.

[4] Y. Zheng *et al.*, "Smart Materials Enabled with Artificial Intelligence for Healthcare Wearables," *Advanced Functional Materials*, vol. 31, no. 51, p. 2105482, 2021, doi: 10.1002/adfm.202105482.

[5] M. Szczerska, "Temperature Sensors Based on Polymer Fiber Optic Interferometer," *Chemosensors*, vol. 10, no. 6, Art. no. 6, Jun. 2022, doi: 10.3390/chemosensors10060228.

[6] K. Cierpiak *et al.*, "C-reactive protein (CRP) evaluation in human urine using optical sensor supported by machine learning," *Sci Rep*, vol. 14, no. 1, p. 18854, Aug. 2024, doi: 10.1038/s41598-024-67821-0.

[7] M. Szczerska, P. Wityk, and P. Listewnik, "The SARS-CoV-2 specific IgG antibodies biophotonic sensor," *Journal of Biophotonics*, vol. 16, no. 1, p. e202200172, 2023, doi: 10.1002/jbio.202200172.

[8] M. Szczerska, M. Kosowska, R. Viter, and P. Wityk, "Photonic sensor to detect rapid changes in CRP levels," *Journal of Biophotonics*, vol. 16, no. 1, p. e202200213, Jan. 2023, doi: 10.1002/jbio.202200213.

[9] D. Majchrowicz, M. Kosowska, P. Struk, and M. Jędrzejewska-Szczerska, "Tailoring the Optical Parameters of Optical Fiber Interferometer With Dedicated Boron-Doped Nanocrystalline Diamond Thin Film," *Physica Status Solidi (a)*, vol. 214, no. 11, p. 1700222, Nov. 2017, doi: 10.1002/pssa.201700222.

[10] R. Bogdanowicz, "Characterization of Optical and Electrical Properties of Transparent Conductive Boron-Doped Diamond thin Films Grown on Fused Silica," *Metrology and Measurement Systems*, vol. 21, pp. 395–408, Dec. 2014, doi: 10.2478/mms-2014-0059.

[11] H. Fei *et al.*, "Research progress of optoelectronic devices based on diamond materials," *Front. Phys.*, vol. 11, Aug. 2023, doi: 10.3389/fphy.2023.1226374.

[12] D. Milewska, K. Karpienko, and M. Jędrzejewska-Szczerska, "Application of thin diamond films in low-coherence fiber-optic Fabry Pérot displacement sensor," *Diamond and*

Related Materials, vol. 64, pp. 169–176, Apr. 2016, doi: 10.1016/j.diamond.2016.02.015.

[13] M. Kosowska, D. Majchrowicz, K. J. Sankaran, M. Ficek, K. Haenen, and M. Szczerska, "Doped Nanocrystalline Diamond Films as Reflective Layers for Fiber-Optic Sensors of Refractive Index of Liquids," *Materials*, vol. 12, no. 13, Art. no. 13, Jan. 2019, doi: 10.3390/ma12132124.

[14] J. El Brihi and S. Pathak, "Normal and Abnormal Complete Blood Count With Differential," in *StatPearls*, Treasure Island (FL): StatPearls Publishing, 2025. Accessed: Mar. 27, 2025. [Online]. Available: http://www.ncbi.nlm.nih.gov/books/NBK604207/

Polarimetría Mueller Full Poincaré usando diversas fuentes de luz para caracterizar medios con actividad óptica natural

Gemma PIQUERO [(1)], J. Carlos G. de SANDE[(2)], Juan Carlos SUÁREZ-BERMEJO[(3)], Massimo SANTARSIERO[(4)]

1. Dpto. de Óptica, U.C.M., Plaza de las Ciencias 1, 28040-Madrid.
2. ETSIS de Telecomunicación, U.P.M., C/ Nikola Tesla, 28031-Madrid.
3. Dpto. de Ciencia de Materiales, U.P.M., Avenida de la Memoria, 28040-Madrid.
4. Dipartimento di Ingegneria Industriale, Elettronica e Meccanica, Università Roma Tre, Via V. Volterra 62, 00146 Rome.

Contacto: Gemma PIQUERO (piquero@ucm.es).

ABSTRACT:

Full Poincaré Mueller Polarimetry is a technique that uses a polarization state generator in parallel, instead of sequentially, as usual. In particular, Full Poincaré beams have been proposed, i.e. those with all possible polarization states across the transverse section of the beam. This technique has already been tested by synthesizing FPBs with laser sources, and for characterizing homogeneous and transparent deterministic media. In this work we present several results obtained with this polarimetric technique, where a LED source is used in addition to a laser to determine the characteristics of retarders and of media with natural optical activity. The treatment of the obtained experimental data is analysed in detail by means of Bayesian inference.

Keywords: Polarimetry, Full Poincaré beams, natural optical activity, structured light, Bayesian inference.

1.- Introducción

La polarimetría Mueller Full Poincaré (FPMP, siglas en inglés) es una propuesta del grupo de investigación "Ingeniería de Haces luminosos" de la UCM, en la cual se sigue investigando [1-3]. El objetivo de la FPMP es determinar la matriz de Mueller de muestras, incidiendo con un haz no uniformemente polarizado en su sección transversal, que presenta todos los estados posibles de luz totalmente polarizada, es decir, un haz Full Poincaré (FPB) [4]. Este haz FPB constituye el generador de estados de polarización (PSG) pero en vez de secuencialmente en el tiempo genera los distintos estados a la misma vez, pero separados espacialmente. Como analizador de estados de polarización (PSA) se puede usar un polarímetro comercial, o un sistema habitual con un polarizador y una lámina de fase. En FPMP se han sintetizados los haces FPB con fuentes de luz láser, en concreto con un láser de He-Ne. En este trabajo se utiliza una fuente LED en vez del láser. Estas fuentes de luz tienen la ventaja de producir menos speckle, son más baratas y permiten seleccionar un amplio rango de longitudes de onda.

Por otro lado, la actividad óptica es una propiedad de algunos medios materiales y se define generalmente como la capacidad de algunas sustancias para rotar el plano de polarización de la luz linealmente polarizada entrante a medida que la atraviesa [5,6]. Midiendo el ángulo girado, se pueden obtener características del medio, por ejemplo, la rotación específica del material, es decir el ángulo girado por unidad de longitud. En particular, se obtiene la birrefringencia circular, es decir, la diferencia de índices de refracción de esa sustancia para las

componentes de la luz polarizada circular a izquierdas (o levógira) y a derechas (o dextrógira).

Generalmente sólo se tiene en cuenta la rotación del plano de polarización de la luz, pero además de la birrefringencia circular, también existe el dicroísmo circular, es decir, la capacidad de la muestra para absorber de forma diferente las componentes circulares a derechas o a izquierdas de la luz.

Por otra parte, para la medida de la birrefringencia se suele utilizar un montaje experimental muy sencillo, sólo un polarizador lineal a la entrada y otro a la salida de la muestra para detectar el ángulo girado. La luz de entrada siempre está polarizada linealmente y la luz o la falta de luz puede observarse a simple vista o con un medidor de potencia. Para caracterizar completamente la muestra es necesario conocer su matriz de Mueller [7-9].

En este trabajo se propone aplicar la FPMP para la caracterización de muestras que presentan actividad óptica natural. Se obtendrá experimentalmente la matriz de Mueller de muestras con actividad óptica natural. Esta propuesta es adecuada para cualquier medio ópticamente activo.

Por último, los resultados experimentales obtenidos con FPMP serán analizados mediante un enfoque nuevo, que es la inferencia Bayesiana [3,10-12].

El trabajo se estructura como sigue. Esta Sección constituye la Introducción, en la Sec. 2 se revisa el formalismo a utilizar. El esquema experimental, junto con algunos de los resultados, se expone en la Sec. 3 de forma breve y finalmente en la Sec. 4 se resumen las principales conclusiones.

2.- Preliminares

2.1.- Polarimetría Mueller Full Poincaré

La polarización de la luz puede describirse adecuadamente mediante cuatro parámetros de Stokes que suelen disponerse en un vector columna [6-8]. El estado de polarización de un haz de luz cambia de forma diferente cuando éste interactúa con una muestra dependiendo de las propiedades de la misma. El cambio del estado de polarización puede describirse mediante la correspondiente matriz de Mueller de la muestra. Si el estado de polarización de los haces de entrada y salida se representan por $\mathbf{S}_{in}$ y $\mathbf{S}_{out}$, respectivamente, están relacionados a través de

$$\mathbf{S}_{out} = M\mathbf{S}_{in} \,. \qquad (1)$$

donde $M=(m_{ij})$, con $i, j=0,1,2,3$ es la matriz de Mueller 4x4 de la muestra. Para un haz polarizado no uniformemente, como es el caso de un FPB, la Ec. (1) se satisface para cada punto de la sección transversal del haz, con diferentes estados de polarización en cada punto. Por lo tanto, analizando estos cambios en un conjunto específico de puntos o en toda la sección transversal del haz, se puede determinar la matriz de Mueller de la muestra.

Para sintetizar el FPB utilizaremos el procedimiento descrito en [4], en donde se ilumina, con un haz divergente cuasi monocromático, un cristal uniáxico de calcita. El haz FPB resultante en cualquier punto (r, θ) de la sección transversal a la salida del cristal tiene un vector de Stokes teórico que puede aproximarse por [4]

$$\vec{S}(r,\theta) = S_0(r,\theta)\begin{bmatrix} 1 \\ -[\cos^2 2\theta + \text{sen}^2 2\theta \cos\delta(r)] \\ -\text{sen}2\theta\cos 2\theta[1-\cos\delta(r)] \\ \text{sen}2\theta\,\text{sen}\delta(r) \end{bmatrix}, \qquad (2)$$

siendo $\delta(r)$ una fase dada por

$$\delta(r) = k(n_e - n_o)\frac{r^2}{l}, \qquad (3)$$

donde k es el número de onda del vacío, l es la longitud del cristal, y n_o y n_e son los índices de refracción ordinario y extraordinario del cristal uniáxico, respectivamente. Se ha demostrado que, para este haz en particular (Ec. (2)), todos los posibles estados de polarización pueden encontrarse en la sección transversal del haz dentro de un semicírculo de radio,

$$r_M = \sqrt{\frac{\pi l}{k|n_e - n_o|}} \,. \qquad (4)$$

Entonces, utilizando un analizador de estados de polarización apropiado y una cámara CCD, los cuatro parámetros de Stokes del haz de

entrada y de salida pueden determinarse al mismo tiempo en toda su sección transversal.

Dado que un FPB contiene todos los posibles estados de polarización (totalmente polarizados) en su sección transversal, analizando los cambios de polarización en N píxeles de la cámara CCD, se puede recuperar la matriz de Mueller de la muestra. Estos datos se procesarán mediante inferencia Bayesiana.

2.2.- Medios con actividad óptica natural

Un medio con actividad óptica natural presentará índices de refracción diferentes para luz circularmente polarizada a derechas o a izquierdas [5-7],

$$\begin{aligned}\tilde{n}_R &= n_R - i\kappa_R,\\ \tilde{n}_L &= n_L - i\kappa_L,\end{aligned} \qquad (5)$$

dónde los índices tienen una parte real, n, y una parte imaginaria, κ, que tiene en cuenta la absorción. La matriz de Mueller, M_{AO}, que representa un medio con actividad óptica natural viene dado por [7]

$$M_{AO}(\lambda,d) = m_{00} \times \begin{bmatrix} \cosh(2\Gamma') & 0 & 0 & -\text{senh}(2\Gamma') \\ 0 & \cos(2\Gamma) & -\text{sen}(2\Gamma) & 0 \\ 0 & \text{sen}(2\Gamma) & \cos(2\Gamma) & 0 \\ -\text{senh}(2\Gamma') & 0 & 0 & \cosh(2\Gamma') \end{bmatrix} \qquad (6)$$

dónde

$$\begin{aligned}\Gamma(\lambda,d) &= \frac{2\pi\Delta n(\lambda)d}{2\lambda},\\ \Gamma'(\lambda,d) &= \frac{2\pi\Delta\kappa(\lambda)d}{2\lambda},\end{aligned} \qquad (7)$$

siendo d el espesor de la muestra y λ la longitud de onda del haz incidente sobre la muestra.

3.- Resultados

3.1.- Esquema experimental de la FPMP

En la Fig. 1 se representa el esquema experimental usado para realizar las medidas [1-4]. La primera parte del esquema consiste en el PSG, en donde como fuente de luz utilizaremos un láser de He-Ne o un LED. Para generar el FPB usaremos un objetivo de microscopio (MO) y un cristal de calcita con el eje óptico en la dirección de propagación y una lente para colimar. A continuación, se coloca la muestra, en nuestro caso un medio que presenta actividad óptica natural o una lámina retardadora. Como PSA usaremos un polarizador, una lámina de fase, que será de cuarto de onda (QWP) para λ=632.8 nm, y una cámara CCD para la medida de las intensidades.

Los parámetros de Stokes tanto del haz de entrada como el de salida se pueden obtener a través de la medida de intensidades con diferentes configuraciones del PSA. En concreto, se han medido (sin la lámina QWP del PSA) la intensidad con el polarizador P a 0 (I_H), a $\pi/4$ (I_{45}), a $\pi/2$ (I_V), y a $-\pi/4$ (I_{135}). Posteriormente, se añade la lámina de fase WP y con ella se orienta el polarizador a $\pi/4$ y a $-\pi/4$ para obtener I_R e I_L, respectivamente. Con esto los parámetros de Stokes se pueden obtener como

$$\begin{aligned}S_0 &= \tfrac{1}{3}(I_H + I_{45} + I_V + I_{135} + I_R + I_L)\\ S_1 &= I_H - I_V\\ S_2 &= I_{45} - I_{135}\\ S_3 &= I_R - I_L\end{aligned} \qquad (8)$$

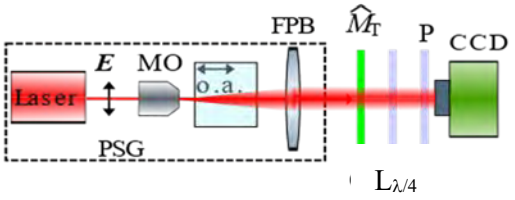

Fig. 1: Esquema experimental utilizado para las medidas con la FPMP [2]

Cuando se utiliza como fuente de luz un LED con λ_{LED}, la lámina de fase a esa longitud de onda presenta un retardo de

$$\gamma = \frac{\pi}{2}\frac{\lambda_{He-Ne}}{\lambda_{LED}}. \qquad (9)$$

En este caso, los parámetros de Stokes S_0, S_1 y S_2 se pueden seguir calculando a partir de los datos experimentales con la Ec. (8) pero el parámetro S_3 se debe obtener como

$$S_3 = \frac{[I_R - I_L - (I_{45} - I_{135})\cos(\gamma)]}{\sin(\gamma)}. \qquad (10)$$

Estos parámetros de Stokes se procesan mediante inferencia bayesiana [3] para obtener la matriz de Mueller de la muestra bajo estudio.

3.2.- Cristal de cuarzo

En primer lugar, analizamos un cristal de cuarzo con su eje óptico orientado en la dirección de propagación del haz FPB. En este caso utilizamos como fuente de luz un láser de He-Ne. A partir de los parámetros de Stokes obtenidos con la Ec. (8) y aplicando el método de inferencia bayesiana descrito en la Ref. [3], se ha obtenido la función densidad de probabilidad para cada uno de los elementos de la matriz de Mueller. Los resultados se muestran en la Fig. 2.

Para una mejor comparación de los resultados obtenidos, se ha utilizado el mismo intervalo horizontal en todas las gráficas. La línea discontinua verde indica la mediana y la barra roja el intervalo de mayor densidad de probabilidad (95% de probabilidad). Se puede observar que todos los elementos de la matriz presentan una distribución muy estrecha. Además, todos los elementos salvo los de la diagonal, son casi nulos indicando que solo se produce birrefringencia circular. A partir de estos datos y ajustando a una matriz de la forma dada por la Ec. (6), se puede obtener los parámetros m_{00} y Γ, cuyos histogramas se muestran en la Fig. 3.

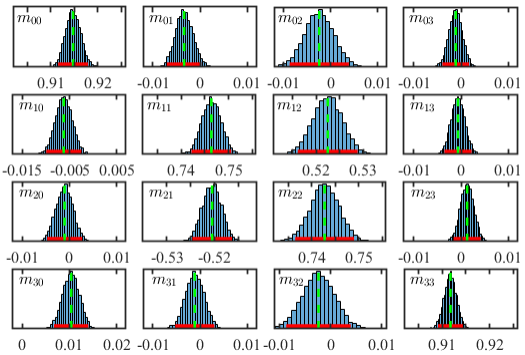

Fig.2: Histogramas obtenidos para los elementos de la matriz de Mueller del cristal de cuarzo.

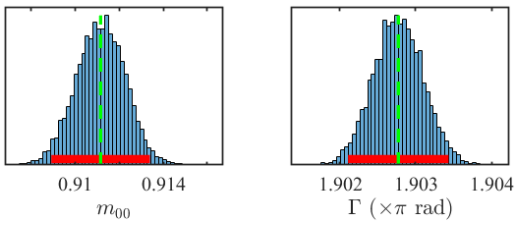

Fig.3: Valores obtenidos para los parámetros de la matriz de Mueller de la muestra analizada.

El valor de m_{00}, distinto de 1, se explica por las pérdidas de la reflexión en incidencia normal en las caras de entrada y salida de la muestra. Por otro lado, a partir de Γ y usando la Ec. (7), se obtiene una birrefringencia circular para el cuarzo de $\Delta n = 6.02 \cdot 10^{-5}$.

3.3.- LED

En esta sección, con el fin de demostrar la validez de la FPMP usando fuentes de luz diferentes a un láser, se ha sustituido el láser del montaje experimental (ver Fig. 1) por un LED. En concreto, se ha utilizado como fuente de luz un LED con $\lambda_{LED} = 595$ nm, con lo cual el retardo de la lámina QWP en la Fig. 1 resulta $\gamma \cong 0.5313\pi$. En este caso, los parámetros de Stokes se obtendrán con la Ecs. (8) excepto el parámetro S_3 que se debe obtener utilizando la Ec. (10). Como muestra se ha utilizado el caso particular de una lámina de fase. La Fig. 4 muestra los histogramas obtenidos mediante inferencia bayesiana [3] para cada uno de los elementos de la matriz de Mueller. Se puede observar que los elementos m_{0j} y m_{j0}, con $j = 1, 2, 3$, son prácticamente nulos como es de esperar para un retardador.

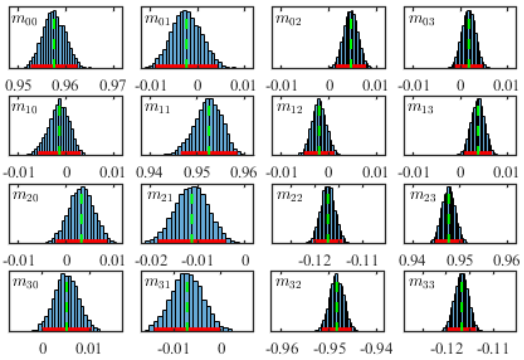

Fig.4: Histogramas obtenidos para los elementos de la matriz de Mueller de una lámina retardadora.

A partir de los valores de los otros 10 elementos de la matriz de Mueller se puede obtener la transmitancia m_{00}, el retardo δ y la orientación θ del retardador. La Fig. 5 muestra los histogramas para estos tres parámetros.

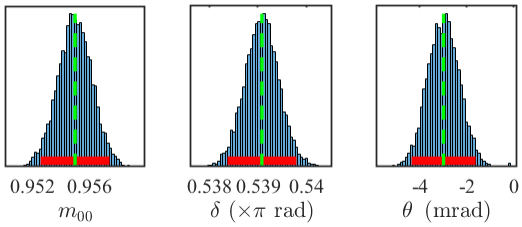

Fig.5: Valores obtenidos para los parámetros de la matriz de Mueller de la muestra analizada.

4.- Conclusión

Los resultados obtenidos demuestran que la técnica FPMP puede adaptarse eficazmente utilizando fuentes LED en lugar de láseres, eliminando el speckle y minimizando efectos de difracción no deseados. Además, mejora su versatilidad al facilitar su aplicación en distintas longitudes de onda. Asimismo, la técnica ha demostrado ser particularmente útil en medios con actividad óptica natural.

Agradecimientos: Este trabajo ha sido financiado por el Ministerio de Economía y Competitividad, proyecto PID2023-148021NB-I00 y FASLIGTH (RED2022-134391-T).

Referencias

[1] Juan Carlos SUÁREZ-BERMEJO, J. Carlos G de SANDE, Massimo SANTARSIERO, Gemma PIQUERO, *"Mueller matrix polarimetry using full Poincaré beams"*, Optics and Lasers in Engineering, 122, 134 – 141, 2019.

[2] Jua Carlos SUÁREZ-BERMEJO, J. Carlos G. de SANDE, Gemma PIQUERO, A.Virgilio FAILLA, Massimo SANTARSIERO, *"Full Poincaré Mueller polarimetry using a CCD camera"*, Photonics, 9, 10, 702, 2022.

[3] Juan Carlos SUÁREZ-BERMEJO, Javier GORGAS, Sergio PASCUAL, Massimo SANTARSIERO, J. Carlos G. de SANDE, Gemma PIQUERO, "*Bayesian inference approach for Full Poincaré Mueller polarimetry,"* Optics and Lasers in Engineering, 168, 109983, 2024.

[4] Gemma PIQUERO, Laura MONROY, Massimo SANTARSIERO, Massimo ALONZO, J. Carlos G. de SANDE, *"Synthesis of full Poincaré beams by means of uniaxial crystals"*, Journal of Optics 20, 6, 065602, 2018.

[5] Grant R. FOWLES *Introduction to Modern Optics* 2nd edn (Dover, 1989).

[6] Russel CHIPMAN, Wai LAM and Garam YOUNG, *Polarized Light and Optical Systems* (CRC Press, 2018).

[7] Pablo CORTÉS, Gemma PIQUERO, J. Carlos G. de SANDE, "*Chiral media and optical rotatory dispersion by means of a simple polarimetric experiment for undergraduate students*," European Journal of Physics. 45, 055303, 2024.

[8] Jose J. GIL, Razvigor OSSIKOVSKI, *"Polarized Light and the Mueller Matrix Approach"* (CRC Press, 2016).

[9] Esther NABADDA, Guadalupe LÓPEZ-MORALES, David MARCO, María del Mar SÁNCHEZ-LÓPEZ, Ignacio MORENO, *"Mueller matrix polarimetric analysis applied to characterize the physical parameters of a twisted-nematic liquid–crystal modulator,"* Optics and Lasers in Engineering, 156, 108567, 2022.

[10] Stephen .E. FIENBERG, *"When did Bayesian inference become 'Bayesian'?"*, Bayesian Analysis 1, 1, 2006.

[11] Rens v.d. SCHOOT, Sarah DEPAOLI, Ruth KING, Bianca KRAMER, Kaspar MÄRTENS, Mahlet .G. TADESSE, Marina VANNUCCI, Andrew GELMAN, Duco VEEN, Joukje WILLEMSEN, Christopher YAU, *"Bayesian statistics and modelling"*, Nature Reviews Methods Primers, 1, 1, 2021.

[12] John. L. QUINN, *"Bayesian analysis of polarization measurements"*, Astronomy & Astrophysics 538, A65, 2011.

Interferometría de ruido ambiente mediante DAS con pulsos chirpados

Jorge CANUDO [1,2], Javier PRECIADO-GARBAYO [1], Pascual SEVILLANO [2], Jesús SUBÍAS [2], Miguel GONZALEZ-HERRAEZ [3], Hugo F. MARTINS [4], Beatriz GAITE-CASTRILLO [5], Jose B. BRAVO-MONGE [5], Irene DE MARIA [6], Miguel RODRIGUEZ-PLAZA [6],

1. Aragón Photonics Labs, C/Prado, 5, 50009, Zaragoza, España.
2. Departamento de Física Aplicada, Universidad de Zaragoza, C/Pedro Cerbuna, 12, 50009, Zaragoza, España.
3. Universidad de Alcalá de Henares, 28805, Madrid, España.
4. Instituto de Óptica, CSIC, C/Serrano, 121, 28006, Madrid, España.
5. Instituto Geográfico Nacional, C/General Fernandez de Ibero, 3, 28003, Madrid, España.
6. Administrador de Infraestructuras Ferroviarias (ADIF), C/Titan 4-6, 28045, Madrid, España.

Contacto: Jorge CANUDO (j.canudo@aragonphotonics.com).

ABSTRACT:

This study demonstrates the potential of Chirped-Pulse Distributed Acoustic Sensing (DAS) technology for subsurface imaging through the application of Ambient Noise Interferometry (ANI). By analyzing strain data, we successfully extracted geological insights without relying on active seismic sources. The low-intensity signals were isolated and enhanced using ANI techniques such as FK filtering, temporal normalization and spectral whitening. Using a custom ANI algorithm, velocity dispersion maps were generated from 24 hours of continuous DAS recordings. These maps revealed dispersion relationships corresponding to different terrain layers. The methodology employed, including Phase-Weighted Stacking and slant-stacking, proved effective for reducing noise and isolating surface wave propagation signals within the frequency range of 0.5–15 Hz. This versatile and cost-effective approach is well-suited for high-resolution, non-invasive subsurface imaging in diverse environments, from submarine cables to urban settings.

Key words: DAS, surface imaging, seismic, ambient noise interferometry, chirped-pulse

1.- Introducción

La exploración del subsuelo es una herramienta esencial en el estudio geológico de un terreno, ya que revela información esencial acerca de la composición del sustrato, así como de los procesos que éste sufre. Además, puede servir como medida preventiva para la detección precoz de problemas en la infraestructura existente en el terreno. Las técnicas tradicionales para la exploración del subsuelo se basan en experimentos con fuentes sísmicas activas y arrays de numerosos detectores [1]. Aunque efectivas, estas técnicas resultan difíciles de implementar en áreas urbanas debido a las restricciones logísticas y normativas existentes en estos contextos. Para superar este problema, se han propuesto técnicas que utilizan fuentes de ruido sísmico pasivas, como puede ser la actividad antropogénica, para extraer información del medio. Este conjunto de técnicas se conoce como Interferometría de Ruido Ambiente (ANI) [2]. Estas técnicas se han aplicado con resultados satisfactorios para obtener información acerca de la velocidad de propagación de las ondas sísmicas superficiales mediante el cálculo de

la función de Green entre dos estaciones de medida [3]. Sin embargo, la tomografía de ruido ambiente de alta resolución requiere de un número elevado y denso de estaciones de detección. En este escenario, la tecnología de Sensado Acústico Distribuido (DAS) se postula como una solución de medida no invasiva con gran resolución espacial y suficiente distancia de medida.

La tecnología DAS hace uso de líneas de fibra óptica estándar como sensor, emitiendo pulsos de luz a través de ellas y recuperando la luz retrodispersada a lo largo de la distancia de medida. La aplicabilidad de los algoritmos de ANI a los datos de medidas DAS ha sido validada en los últimos años con resultados muy positivos en entornos urbanos [4]. En este estudio, se ha monitorizado una fibra óptica tendida a lo largo de una vía de tren y se ha aplicado un algoritmo completo de ANI, para obtener los correspondientes mapas de velocidad de dispersión del terreno. Estos mapas pueden ser empleados posteriormente en combinación con un análisis multicanal de las ondas superficiales para obtener los modelos de velocidades y estructura del terreno subyacente.

2.- Adquisición de datos

2.1.- DAS con pulsos chirpados

La Reflectometría Óptica en Dominio Temporal Sensible a la Fase (ΦOTDR) identifica y localiza perturbaciones externas cercanas a la fibra óptica analizando los cambios en la intensidad de la traza óptica retrodispersada entre pulsos de luz. Esta técnica presenta una serie de desventajas, como la presencia de puntos ciegos de medida o la no-uniformidad de la relación señal-ruido. La técnica de medida conocida como ΦOTDR con pulsos chirpados (CP-ΦOTDR) supera estos retos, permitiendo medir de manera precisa las perturbaciones externas. Estas perturbaciones inducen un cambio de frecuencia en la traza retrodispersada que, gracias a la técnica de medida, se ve reflejado como un retraso temporal de la traza, de acuerdo con la Ecuación (1) [5].

$$-\left(\frac{1}{\nu_0}\right)\left(\frac{\delta\nu}{\tau_p}\right)\Delta t = \frac{\delta\nu}{\nu_0} \approx -0.78\Delta\varepsilon \qquad (1)$$

Donde ν_0 [Hz] representa la frecuencia central del pulso de luz, τ_p [s] representa la anchura temporal de este pulso, $\delta\nu$ representa el contenido espectral del chirp lineal y $\Delta\nu$ corresponde con el cambio de frecuencia del láser que compensa la variación de strain, representado por $\Delta\varepsilon$. La tecnología ΦOTDR con pulso chirpado está disponible comercialmente en el High-Fidelity DAS (HDAS), de Aragón Photonics Labs, equipo que se ha empleado en la toma de datos de este estudio.

2.2.- Instalación experimental

Para el presente trabajo, se ha monitorizado una fibra óptica estándar desplegada en el lateral de una vía de alta velocidad ferroviaria en Granda, España, haciendo uso de una unidad interrogadora HDAS. Este equipo se configuró con una resolución espacial de 10 m y una tasa de muestreo de 100 Hz, ya que las señales objetivo presentan habitualmente frecuencias bajas (<50 Hz). Las medidas fueron tomadas entre julio y agosto de 2022. La Figura 1 muestra el despliegue de la fibra a lo largo de la vía de tren.

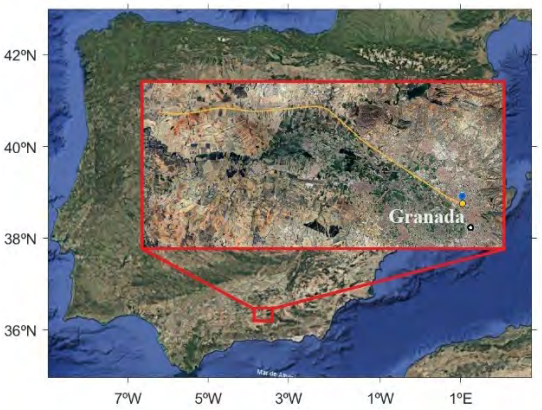

Fig. 1: Localización de la instalación experimental. La línea amarilla corresponde con la fibra óptica monitorizada.

3.- Metodología

La Interferometría de Ruido Ambiente (ANI) es un conjunto de técnicas ampliamente usadas en estudios geológicos para recuperar información acerca de la estructura del terreno haciendo uso de fuentes sísmicas pasivas, como el viento, tráfico o la actividad antropogénica. El principal objetivo de este estudio es la estimación de las relaciones de

dispersión del medio que rodea la fibra monitorizada. Para conseguirlo, se ha desarrollado el siguiente algoritmo, que se ha aplicado a 24 horas de medida continua. En primer lugar, los datos recogidos por el equipo interrogador han sido filtrados en los dominios frecuencial y espacial, restringiendo el rango de frecuencias de interés a [0.5, 15] Hz y la longitud de onda detectada al doble de la distancia evaluada. A continuación, se ha realizado una transformada FK calculando la transformada de Fourier en dimensión espacial y temporal. Gracias a la información obtenida en el dominio FK (Figura 2), es posible filtrar las señales detectadas por velocidad de dispersión, eliminando de esta forma la contribución de fuentes no deseadas, como puede ser el paso de trenes a lo largo de la vía, puesto que presentan velocidades mucho menores a las buscadas. Una vez filtrados, los datos se han normalizado tanto temporal [6] como frecuencialmente [7], de modo que la contribución de las distintas fuentes de ruido sea uniforme. Para el dominio temporal se ha empleado un algoritmo propio, que divide la señal original por su envolvente, renormalizando los valores finales entre -1 y 1. Para la normalización frecuencial, se ha empleado la Transformada de Fourier Rápida (FFT), llevando las amplitudes del rango de interés a 1, mientras que aquellas frecuencias fuera del rango de interés se han apodizado hasta cero haciendo uso de una función coseno cuadrado. Tras ello, se recupera la información en domino temporal con la FFT inversa.

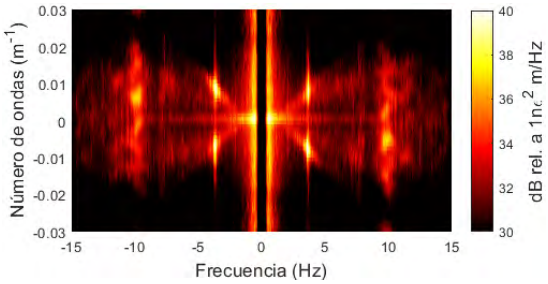

Fig. 2: Transformada FK de los datos medidos en el canal 450 tras el filtrado, con clara presencia de señales sísmicas.

Una vez se ha preprocesado el paquete de datos, de 1 minuto de duración, se selecciona un canal que se empleará como referencia, en adelante, fuente virtual. Para este trabajo, se ha seleccionado el canal 450 como fuente virtual. Se realiza la correlación cruzada entre la fuente virtual y los sucesivos 50 canales, resultando en un mapa de correlación, que puede ser interpretado como si una fuente de ruido se hubiera situado en la posición de la fuente virtual. Esto permite apreciar en el mapa como se propagan las señales presentes por el medio, tanto en tiempo como en espacio [8]. Este proceso se repite para cada minuto del periodo de 24 horas analizado. Los 1440 mapas de correlación resultantes han de ser apilados para minimizar la contribución de señales no deseadas, de modo que el resultado final presente únicamente las señales que se están propagando por el terreno bajo estudio. Para conseguir este objetivo, se ha empleado la técnica de apilado conocida como Phase-Weighted Stack (PWS) [9], que permite asignar a cada mapa de correlación un peso evaluando el nivel de coherencia de la fase instantánea de la traza de correlación, de acuerdo con la Ecuación (2).

$$x_{PWS}(t) = \frac{1}{N}\sum_{j=1}^{N} x_j(t) \left| \frac{1}{N}\sum_{k=1}^{N} exp\{i\Phi_k(t)\} \right|^{\nu} \quad (2)$$

Donde $x_j(t)$ corresponde con la traza de correlación obtenida para el retraso temporal que se está calculando, $\Phi_k(t)$ corresponde con la fase instantánea de la señal analítica de $x_j(t)$ y ν corresponde con un parámetro de pesaje, normalmente en el rango 1-3. Esta técnica de apilado reduce en gran medida el número total de ficheros que hay que apilar para obtener un mapa de correlaciones con buena relación señal-ruido.

Una vez se ha calculado el mapa de correlaciones final, es posible obtener el mapa de velocidades de dispersión con la técnica slant-stacking. Para ello, se recorre un rango de velocidades predefinido de acuerdo con la Ecuación (3), donde $X_{ij}(f)$ corresponde con la FFT de la traza de correlación $x_{ij}(t)$, donde i y j son los correspondientes canales y r_{ij} la distancia entre ellos.

$$B_i(f, c') = \sum_{j=1}^{i+N} X_{ij}(f) exp\left\{\frac{-i2\pi f r_{ij}}{c'}\right\} \quad (3)$$

4.- Resultados

La Figura 3 muestra el mapa de correlaciones obtenido para el canal 450 como fuente virtual, con los datos filtrados en parches de 1 minuto (con 20 segundos de solapado entre archivos), y la correlación cruzada calculada para un intervalo de ± 5 segundos. El retraso de los máximos y mínimos de correlación muestran de manera clara la presencia de señales propagándose a lo largo de la superficie con velocidades entre 100 m/s y 2000 m/s. Estas velocidades son consistentes con los valores típicos de las ondas Rayleigh superficiales. Se observa la presencia de dichas señales en ambas ramas del mapa de correlación, pues el ruido analizado con el algoritmo de ANI puede tener múltiples orígenes que varían de posición en torno a la fuente virtual. Un filtrado FK más detallado permitiría aislar cada una de las ramas para su análisis en profundidad [10].

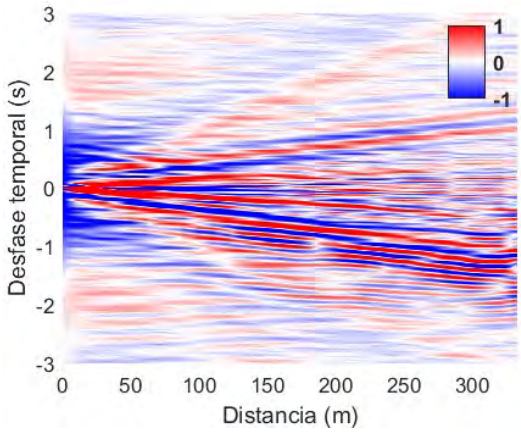

Fig. 3: Mapa de correlación del periodo analizado (Canal 450 como fuente virtual).

Aplicando la técnica slant-stacking al mapa de correlaciones, es posible obtener el mapa de velocidades de dispersión, mostrado en la Figura 4. El máximo de cada frecuencia se muestra como un punto negro, permitiendo apreciar dos relaciones de dispersión asociadas con distintas capas del terreno. El análisis de estos mapas de dispersión permite inferir el perfil vertical de las velocidades de propagación del terreno, que corresponde con la relación entre frecuencia y profundidad gracias a la inversión de las curvas de dispersión. Este parámetro resulta crucial para entender la estructura y composición del subsuelo.

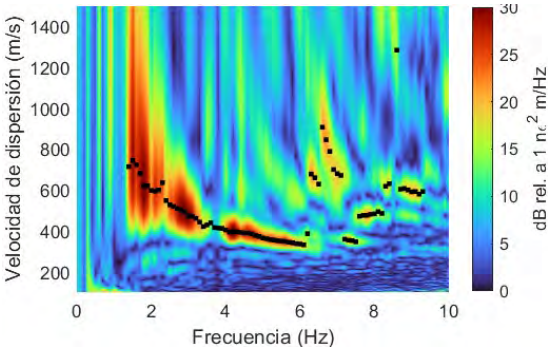

Fig. 4: Mapa de dispersión del periodo analizado (Canal 450 como fuente virtual).

5. Conclusiones

Se ha demostrado que la tecnología DAS con pulsos chirpados permite obtener información geológica del terreno que rodea la fibra monitorizada mediante el análisis de los datos de medida, sin necesidad de fuentes de ruido sísmico activas. A pesar de la baja intensidad de las señales detectadas, es posible un aislamiento y realce de las mismas haciendo uso de técnicas de interferometría de ruido ambiente como el filtrado FK o la normalización temporal y frecuencial. Adicionalmente, se ha desarrollado un algoritmo de integral de ANI cuya aplicabilidad se extiende a numerosos entornos, desde cables de fibra óptica submarina a entornos urbanos. En este trabajo, se ha monitorizado una fibra óptica adyacente a una infraestructura ferroviaria y se ha analizado un periodo de 24 horas de medidas para la obtención de los mapas de dispersión del terreno. Los resultados obtenidos permiten la estimación de perfiles verticales del subsuelo prescindiendo del uso de fuentes sísmicas activas aplicadas directamente sobre el terreno, lo que representa un avance significativo en el ámbito de la monitorización de infraestructuras y la caracterización geológica del medio.

Referencias

[1] C.M. KRAWCZYK, M. STILLER, K. BAUER, B. NORDEN, J. HENNINGES, A. IVANOVA, E. HUENGES, *"3-D seismic exploration across the deep geotermal*

research platform Groß Schönebeck north of Berlin/Germany", Geothermal Energy, 7, 1, 15, 2019.

[2] Z. SONG, X. ZENG, J. XIE, F. BAO, G. ZHANG, *"Sensing Shallow Structure and Traffic Noise with Fiber-optic Internet Cables in an Urban Area"*, Surveys in Geophysics, 42, 6, 1401-1423, 2021.

[3] Y. CHEN, E. SAYGIN, *"Empirical Green's Function Retrieval Using Ambient Noise Source-Receiver Interferometry"*, Journal of Geophysical Research: Solid Earth, 125, 2, 2020.

[4] L. EHSANINEZHAD, C. WOLLIN, V. RODRIGUEZ-TRIBALDOS, B. SCHWARZ, C.M. KRAWCZYK, *"Urban subsurface exploration improved by denoising of virtual shot gathers from distributed acoustic sensing ambient noise"*, Geophysical Journal International, 237, 3, 1751-1764, 2024.

[5] M.R. FERNÁNDEZ-RUIZ, L. COSTA, H.F. MARTINS, *"Distributed Acoustic Sensing Using Chirped-Pulse Phase-Sensitive OTDR Technology"*, Sensors, 19, 20, 4368, 2019.

[6] G.D. BENSEN, M.H. RITZWOLLER, M.P. BARMIN, A.L. LEVSHIN, F. LIN, M.P. MOSCHETTI, N.M. SHAPIRO, Y. YANG, *"Processing seismic ambient noise data to obtain reliable broad-band surface wave dispersion measurements"*, Geophysical Journal International, 169, 3, 1239-1260, 2007.

[7] R.R. MANENTI, W.E. SOUZA, M.J. PORSANI, *"Spectral whitening based on the singular spectral analysis method"*, Journal of Geophysics and Engineering, 15, 4, 1460-1469, 2018.

[8] J. FENG, H. YAO, Y. WANG, P. POLI, Z. MAO, *"Segregated oceanic crust trapped at the bottom mantle transition zone revealed from ambient noise interferometry"*, Nature Communications, 12, 1, 2531, 2021.

[9] M. SCHIMMEL, H. PAULSSEN, *"Noise reduction and detection of weak, coherent signals through phase-weighted stacks"*, Geophysical Journal International, 130, 2, 497-505, 1997.

[10] E.F. WILLIAMS, Z. ZHAN, H.F. MARTINS, M.R. FERNÁNDEZ-RUIZ, S. MARTÍN-LÓPEZ, M. GONZÁLEZ-HERRÁEZ, J. CALLIES, *"Surface Gravity Wave Interferometry and Ocean Current Monitoring with Ocea-Bottom DAS"*, Journal of Geophysical Research: Oceans, 127, 5, 2022.

Development and Validation of a Spectral Albedometer (200-2500 nm): Cuasi-Simultaneous Measurement of Solar and Snow Cover Reflected Radiation.

Adrián SUBÍAS MARTÍN[1], Pascual NAVARRO[2], Jorge CIUDAD-REAL[2], Víctor HERRÁIZ-LÓPEZ[1], Iñigo SALINAS[2] and Rafael ALONSO [1]

1. Departamento de Física Aplicada, Universidad de Zaragoza, Zaragoza 50009, Spain.
2. Departamento de Ingeniería Electrónica y Comunicaciones, Universidad de Zaragoza, Zaragoza 50009, Spain.

Contact: Adrián SUBÍAS MARTÍN (asubia@unizar.es).

ABSTRACT:

This work presents the development and preliminary results of a wide-range spectral albedometer (200-2500 nm), designed to simultaneously measure radiation in the visible and infrared spectrum. The significance of this development lies in its potential to enhance the understanding of reflectance and absorption processes on snow-covered surfaces, with applications in climate studies and energy balance models. These measurements provide information on light absorbing particles (LAPs) and the surface specific surface area (SSA) parameter, and therefore, on surface density. Its main advantage lies in the ability to perform near-simultaneous measurements of incident solar radiation and the radiation reflected by the snowpack. This feature significantly reduces the impact of variations in measurement conditions, allowing for more precise and representative data on snow albedo. The study and validation of the instrument are carried out at the AEMET Formigal-Sarrios test site, located in the Spanish Pyrenees, an optimal environment for analyzing snow-covered surfaces.

Key words: albedo, Pyrenees, snowpack, spectrometer, visible, infrared, LAPs, surface, SSA

1.- Introduction

Albedometers are commonly used in climate and environmental research to measure the reflectivity of different surfaces, including snow, ice, water, soil, and vegetation [1], [2]. In our case, we will use it to measure snow covers (a mixture of three substances: air, ice, and water) in the Spanish Pyrenees. Currently, there are almost no commercial spectral albedometers for remote applications that measure solar radiation in the 350–2500 nm range.

This work focuses on the design, validation, and implementation of a spectral albedometer (200-2500 nm) that simultaneously measures the visible and infrared range [3] of the system and can also measure, almost in the same instant, both incident and reflected radiation. In our case, the incident radiation will be solar radiation, and the reflected radiation will be solar radiation reflected by the snow. The main innovation of this system is the ease of measuring both incident and reflected radiation with minimal changes to the measurement conditions [4]. The snow albedo is closely linked to rapid changes in the atmosphere, so if we measure both radiations at distant time intervals, it could result in significant errors. This system allows the almost simultaneous measurement of both radiations, enabling more precise

measurements of albedo on snow-covered surfaces [5].
The development of this measurement system is driven by the changing climatological conditions of the Aragonese Pyrenees. Snow at this latitude is subject to significant physical changes due to the large temperature differences it undergoes (temperature gradients of more than 20 degrees within the same week), more frequent liquid precipitation and the arrival of dust particles from the Sahara Desert [6]. This last phenomenon is critical because these particles become trapped within the snowpack and create warm zones that melt the snowpack from the inside. These particles are known as light absorbing particles (LAPs) [6], [7], and the best way to measure their presence is through radiation measurement instruments such as an albedometer. Additionally, an albedometer will allow us to measure parameters like the specific surface area (SSA) of the snow surface [2], [8] and therefore, the surface density [2].

2.- Theory on albedo

Albedo is a fundamental parameter in characterizing the radiation reflected by natural surfaces, particularly in snow-covered environments. It is defined as the fraction of incident radiation reflected in all directions of the upper hemisphere[3]. Its determination is crucial for understanding the energy exchange between solar radiation and the surface, as well as for analyzing the composition and structure of the reflective materials.

The reflective behavior of a surface is described by the Bidirectional Reflectance Distribution Function (BRDF) [3] [9], which quantifies the scattering of a collimated beam of incident light as a function of wavelength and the angles of incidence and reflection within the upper hemisphere. From the BRDF, several radiometric quantities are derived, with one of the most relevant being the Spectral Bi-Hemispherical Reflectance (BHR) [9], which represents albedo integrated over the reflected hemisphere and is expressed as:

$$BHR = \rho(\theta_i, \phi_i, 2\pi; 2\pi, \lambda) = \frac{\phi_r(\theta_i,\phi_i,2\pi;2\pi,\lambda)}{\phi_i(\theta_i,\phi_i,2\pi;2\pi,\lambda)} \quad (1)$$

where ϕ_r is the total radiant flux reflected by the surface into the upper hemisphere and ϕ_i is the total radiant flux incident upon the surface, both measured over a 2π steradian angular domain. The incident flux includes both the direct solar irradiance component and the diffuse component, which results from scattering by the atmosphere, surrounding terrain and nearby objects. More specifically, the BHR is expressed in terms of the BRDF using the following equation:

$$\rho_\lambda(\theta_i, \phi_i) = \frac{d\lambda * dA_1 * I_{\lambda,i}(\theta_i, \phi_i) * \cos(\theta_i) * d\Omega_i}{I_{\lambda,i}(\theta_i, \phi_i) * f(\theta_i) * d\lambda} \cdot \cdot \int_\Omega \rho_\lambda(\theta_r, \phi_r, \theta_i, \phi_i) * \mathrm{f}(\theta_r) * d\Omega_r \quad (3)$$

This formulation allows for a representative measurement of albedo without relying on specific angles of incidence or reflection, as it integrates the reflected radiation over the entire hemisphere and uses a cosine-response diffuser to minimize directional effects.

Spectral BHR contains essential information about the radiative energy exchange between solar radiation and the snowpack, as well as insights into the physical structure and composition of surface particles. In ground-based measurements, albedo is typically determined using two pyranometers: one facing upward to measure incoming irradiance and another facing downward to capture reflected irradiance from the surface. Positioned at a fixed height above the ground, these instruments enable a direct estimation of albedo as the ratio of reflected to incident hemispherical irradiance.

3.- Hardware design

Our innovative design consists of using two spectrometers (one for the visible spectrum and another for the infrared) connected to and controlled by a field PC. To measure both types of radiation, two optical fibers, each ending in a Spectralon® diffuser, are used. These fibers are connected to the two spectrometers through a fiber coupler. Additionally, we control the transmission of

radiation using shutters. The schematic of the entire design is shown in Figure 1.

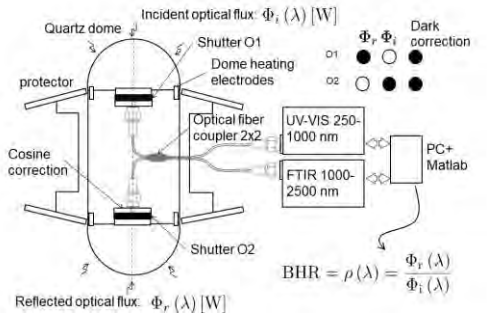

Fig. 1: Diagram of the different components that make up our albedometer.

3.1.- Spectrometers

The measurement system consists of two spectrometers. For the ultraviolet and visible (UV-VIS) range, a Qmini spectrometer (model Qmini AFBR_S20M2WV) [10] is used, featuring a compact design and high robustness. It does not require moving parts within our setup and operates at temperatures as low as -15°C, which is crucial for winter operation at altitudes of 1,800 meters. To measure the near-infrared (NIR) range, we use a Hamamatsu FTIR spectrometer (model C15511) [11], based on Fourier Transform Infrared Spectroscopy, with mechanical and thermal robustness similar to the visible spectrometer. Commercial spectrometers with these specifications have been available for the past five years.

3.2.- Shutters

The control of the incoming radiation is managed by a mechanical shutter (figure 2). Its opening and closing are controlled using the Arduino Leonardo connected to the PC and the commands are sent for execution from MATLAB. This way, we can perfectly coordinate the shutter's opening with the measurement times of the spectrometers. This allows us to avoid introducing any moving elements into our system.

Fig. 2: Detail of the opening and closing mechanism of the shutter used.

Additionally, these shutters will include a Spectralon® diffuser over them, which acts as a cosine corrector. The thickness of these diffusers is around 300 microns to optimize light transmission while maintaining the cosine response. The use of these diffusers is crucial to ensure that the incident and reflected radiation are correctly weighted according to the incidence angle. As a result, Equation (2) will govern our albedo measurements, ensuring the correction of angular effects.

3.3.- Optic fibers

Two optical fibers (Table 1) are used as optical paths for the direct and reflected radiation.

Table 1: Characteristics of the optical fiber used.

Object	Range of wavelength	Core diameter
BFY400MS02	300-1200 nm 400-2200 nm	400±8 um
Cladding diameter	Coating diameter	NA
425±10 um	730±30 um	0.39

3.4.- PC and control system

The system operating in the field is powered and controlled from a Windows PC (Latte Panda Alpha) which includes an Arduino Leonardo in the same board. The software is coded using MATLAB® for versatility and adaptability. From this platform, we can control all the parameters of the spectrometers, connected to the PC via USB, the shutters and the time between measurements.

3.5.- Environmental radomes

The protective components for the entire system, designed to withstand harsh weather conditions, have been manufactured using a filament-based 3D printer. A total of six pieces cover the optical fibers, the measurement entrance, and the heaters used to melt snow during precipitation periods. These

components have undergone multiple priming processes to seal the pores inherent in 3D-printed parts and have been coated with several layers of white paint. The white color was chosen to prevent measurement variations due to temperature in high solar radiation conditions. Additionally, since our measurement is almost instantaneous, temperature variations do not occur between the incident and reflected radiation measurements. The environmental protection system is shown in Figure 3.

Fig. 3: Environmental protection system.

Additionally, the PC and the two spectrometers are housed in an IP66-rated aluminum enclosure, equipped with an external Wi-Fi antenna to enable remote PC access.

4.- Performance evaluation

The first part of the system evaluation test is to verify that it correctly measures the spectra of several commercial LEDs with known wavelengths. This test is conducted in the laboratory, minimizing the entry of natural light and the artificial light present in the lab. The LED wavelengths are distributed across the measurement range of our system. The selected wavelengths are: 351, 525, 940 and 1300 nm.

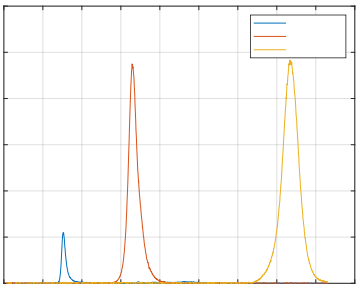

Fig. 4: Measurement of the spectra of the different LEDs used.

The second part of the performance evaluation test consists of measuring the radiation emitted by the sun. This curve is well documented in the literature and can be used for the calibration of our system. The measurement is conducted in a controlled environment at the university. This location is outdoors and is only affected by the shadows cast by the university buildings.

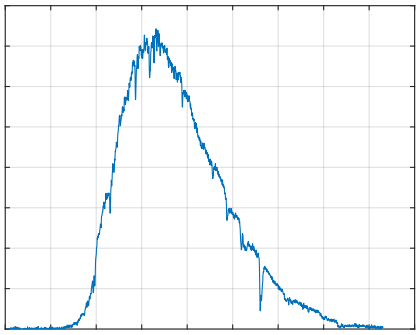

Fig. 5: Measurement of solar radiation in visible range.

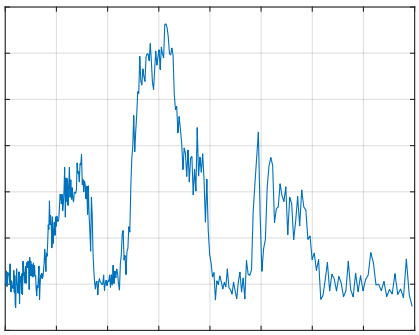

Fig. 6: Measurement of solar radiation in infrared range.

Our field measurement, figures 5 and 6, of the solar spectrum shows the same curve as the solar spectrum indicated by the IEC 60904-3:2016 standard. The two spectrometers with which we work are not calibrated in an absolute manner, so we cannot mix the ranges. The albedo measurement is not affected by this calibration when performing the division between two measurements from the same spectrometer.

5.- Preliminary snow cover measurement

This section presents the preliminary results of the measurement of albedo snow cover. Several albedo measurements are taken without disturbing the surface, with surface disturbance and removing the first few centimeters to reach a layer containing dust particles. For the albedo measurement, an initial calibration is performed to account for losses in both optical paths and to adjust the light intensity using a wavelength-dependent constant. This constant is determined by analyzing the difference in solar radiation between the two optical paths, applying the ratio of the measurement obtained through path 1 to the measurement obtained through path 2.

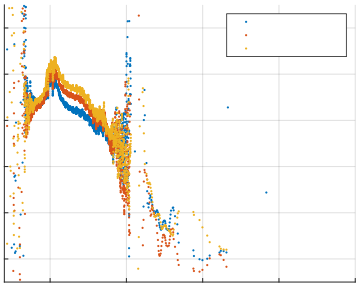

Fig. 7: Measurement of albedo.

Additionally, the snow cover spectrum curve shows that the snow absorbs almost all radiation in the infrared, demonstrating that the snow cover behaves like a black body.

The albedo measurement in Figure 8 shows that, in the visible range, snow barely attenuates and reflects almost all the incident radiation. The literature confirms that the albedo measurement from our system is accurate [2], [3]. In the ultraviolet and 'blue' range, we can find information about light-absorbing particles, as these are located within the snowpack and absorb blue radiation, since blue light is the wavelength that penetrates the most. On the other hand, in the near-infrared range, we obtain information about the internal structure of the snow and the SSA parameter, which characterizes the type of snow and grain size.

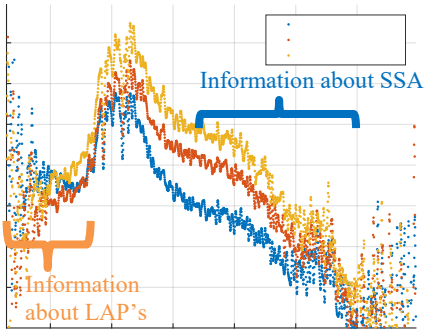

Fig. 8: Measurement of albedo in the visible range and the near-infrared.

The difference between the three lies in the type of snow found on the surface. The blue line represents an undisturbed surface, while the yellow and orange lines correspond to disturbed surfaces. The orange line represents a chaotically disturbed surface, where both undisturbed areas and altered zones exposing deeper snow layers, containing LAPs, can be observed. This explains the significant difference in snow type and the slight variations in LAPs. The orange line also indicates that part of the surface snow was removed to expose a layer containing LAPs. This removal leads to a lower-density snow layer compared to the surface layer, increasing reflection in the infrared region. Additionally, disturbances in the ultraviolet range indicate the presence of LAPs in small quantities.

6.- Conclusion

The device described and evaluated in this study has proven to be an innovative system in both hardware and measurement technique. It allows minimizing differences in the measurements of incident and reflected radiation, which are largely influenced by weather condition changes. Additionally, it enables the integration of radiation measurements from 200 to 2500 nm in a single measurement, covering the entire visible and infrared range. Each spectral range provides different information about the surface being measured. Information about LAPs is found in the visible range, while information about SSA and surface density is located in the infrared range.

Furthermore, the device has demonstrated robustness in withstanding high-mountain weather conditions and has successfully passed operational tests. It has been able to capture the spectra of different LEDs across the entire range and clearly detect the solar spectrum. Therefore, it can be stated that this device is capable of performing continuous measurements during winter field campaigns to characterize the different snow cover types over the season.

Acknowledgements: This work was supported in part by Projects PID2021-124451OB-I00 and TED2021-131180B-I00 co-funded by MICIU/AEI/10.13039/50110001103, by FEDER UE, by the European Union Next Generation EU/PRTR, and in part by the project T20-23R DGA-FSE. The authors would like to thank the Spanish Meteorology Agency (AEMET), especially the observing team from AEMET Aragon Regional Office, for their continuous support on this project and the ski resort Aramón-Formigal.

References:

[1] W. WARREN J. y W. STEPHEN G., «A Model for the Spectral Albedo of Snow. I: Pure Snow». JOURNAL OF THE ATMOSPHERIC SCIENCES, 28 de agosto de 1980.

[2] S. M. Skiles, C. P. Donahue, A. G. Hunsaker, y J. M. Jacobs, «UAV hyperspectral imaging for multiscale assessment of Landsat 9 snow grain size and albedo», *Front. Remote Sens.*, vol. 3, p. 1038287, ene. 2023, doi: 10.3389/frsen.2022.1038287.

[3] M. Dumont, O. Brissaud, G. Picard, y B. Schmitt, «High-accuracy measurements of snow Bidirectional Reflectance Distribution Function at visible and NIR wavelengths – comparison with modelling results», *ACP (Atmospheric Chemistry and Physics)*, n.º 9, pp. 19270-19311, 2009, doi: 10.5194/acp-10-2507-2010.

[4] W. Stephen G. y W. Warren J., «A Model for the Spectral Albedo. II: Snow Containing Atmospheric Aerosols». JOURNAL OF THE ATMOSPHERIC SCIENCES, 28 de agosto de 1980.

[5] K. Kuchiki, T. Aoki, T. Tanikawa, y Y. Kodama, «Retrieval of snow physical parameters using a ground-based spectral radiometer», *Appl. Opt.*, vol. 48, n.º 29, p. 5567, oct. 2009, doi: 10.1364/AO.48.005567.

[6] S. M. Skiles, T. Painter, y G. S. Okin, «A method to retrieve the spectral complex refractive index and single scattering optical properties of dust deposited in mountain snow», *J. Glaciol.*, vol. 63, n.º 237, pp. 133-147, feb. 2017, doi: 10.1017/jog.2016.126.

[7] F. Tuzet *et al.*, «Quantification of the radiative impact of light-absorbing particles during two contrasted snow seasons at Col du Lautaret (2058 m a.s.l., French Alps)», *The Cryosphere*, vol. 14, n.º 12, pp. 4553-4579, dic. 2020, doi: 10.5194/tc-14-4553-2020.

[8] T. H. Painter, N. P. Molotch, M. Cassidy, M. Flanner, y K. Steffen, «Contact spectroscopy for determination of stratigraphy of snow optical grain size», *J. Glaciol.*, vol. 53, n.º 180, pp. 121-127, 2007, doi: 10.3189/172756507781833947.

[9] G. Schaepman-Strub, M. E. Schaepman, T. H. Painter, S. Dangel, y J. V. Martonchik, «Reflectance quantities in optical remote sensing—definitions and case studies», *Remote Sens. Environ.*, vol. 103, n.º 1, pp. 27-42, jul. 2006, doi: 10.1016/j.rse.2006.03.002.

[10] «QMINI». [En línea]. Disponible en: https://www.broadcom.com/products/optical-sensors/spectrometers/spectrometers-qmini/afbr-s20m2wv

[11] «FTIR». [En línea]. Disponible en: https://www.hamamatsu.com/eu/en/product/type/C15511-01/index.html

Upconversion Nanoparticles Luminescence Lifetime Dependence on Excitation Parameters

Alejandro Casillas-Rubio [(1)], Khouloud Hamraoui [(2)], Diego Mendez-Gonzalez [(2)], Marco Laurenti [(2)], Jorge Rubio-Retama [(2)], Oscar G. Calderón [(1)], Sonia Melle [(1)]

1. Department of Optics, Faculty of Optics and Optometry, Complutense University of Madrid, E-28037 Madrid, Spain.
2. Department of Chemistry in Pharmaceutical Sciences, Faculty of Pharmacy, Complutense University of Madrid, E-28040 Madrid, Spain.

Contact: Alejandro Casillas-Rubio (alejcasi@ucm.es).

ABSTRACT:

The upconversion luminescence (UCL) lifetime plays a crucial role in optimizing the performance of upconverting nanoparticles (UCNPs) across various applications. Contrary to common assumptions, UCL lifetime is not solely determined by the intrinsic decay time of the emitting state but is instead influenced by the overall upconversion process dynamics. In this study, we investigate the dependence of the UCL lifetime on the excitation pulse width for β-$NaYF_4$:Yb^{3+}, Er^{3+} nanoparticles. Our results reveal a significant increase in the UCL lifetime with both pulse width and excitation intensity, demonstrating that laser fluence governs the UCL decay dynamics. A rate equation analysis is employed to provide a theoretical framework for these findings. Finally, we discuss the implications of this pulse-width-dependent UCL lifetime for UCNP-based Förster resonance energy transfer (FRET) applications, highlighting potential optimizations for sensing and imaging technologies.

Key words: Upconverting nanoparticles, rare-earth nanoparticles, upconversion luminescence lifetime, excitation pulse width, laser fluence.

1.- Introduction

Luminescent nanomaterials, particularly upconverting nanoparticles (UCNPs) have emerged as key components in advanced applications such as ultrasensitive diagnostics [1], bio-imaging [2], nanothermometry [3], and biosensing based on Förster Resonance Energy Transfer (FRET) [4]. A cornerstone of these technologies is the upconversion luminescence (UCL) lifetime, a parameter traditionally regarded as intrinsic to the nanoparticle and independent of external conditions. It serves not only as a means of characterizing the emission behavior of UCNPs and comparing their performance but also as the gold standard for quantifying FRET efficiency via time-resolved measurements.

However, recent evidence challenges the assumption of excitation-invariant UCL lifetimes. Studies have shown that UCL decay times can be significantly influenced by excitation parameters such as pulse duration [5] and excitation power [6]. This sensitivity undermines the presumed robustness of UCL lifetime as a universal metric and raises concerns about the reliability of lifetime-based FRET measurements. If the UCL lifetime itself varies with excitation conditions, then changes attributed to FRET may be misestimated or confounded by these external factors.

In this work, we investigate the behavior of the green UCL lifetime of β-NaYF4:$Yb_{20\%}$, $Er_{2\%}$ UCNPs under systematically varied excitation conditions. By adjusting pulse width from microseconds to milliseconds, altering excitation power, and modifying the beam spot size, we reveal that UCL lifetime dynamics are governed primarily by the laser fluence. A universal master curve emerges from this analysis, providing a coherent framework for understanding lifetime behavior across different excitation regimes.

We further combine time-resolved UCL measurements with theoretical modeling to demonstrate that lifetime-based FRET quantification is highly susceptible to excitation conditions. This was subsequently confirmed experimentally. Specifically, we show that shorter excitation pulses yield higher apparent FRET efficiencies, while longer pulses or higher excitation powers lead to systematic underestimation. These findings underscore the need for careful control and standardization of excitation parameters in UCNP-based sensing platforms. They also call for a reevaluation of the fundamental interpretation of UCL kinetics, offering new insights into the interplay between excitation dynamics and nonradiative energy transfer processes in complex nanosystems.

2.- Experimental Setup and Methodology

We synthesized β-$NaYF_4$:Yb^{3+}, Er^{3+} UCNPs and characterized their luminescence properties under varying excitation conditions. The laser system emitting at 967 nm enabled precise control of both pulse width and intensity. UCL decay curves were analyzed using a home-built time-resolved photon counting system, ensuring accurate measurement of emission dynamics. The influence of excitation parameters was further explored using a rate equation model, allowing us to separate intrinsic and extrinsic contributions to UCL lifetime modifications.

3.- Results and Discussion

Our findings demonstrate a strong dependence of UCL lifetime on the excitation pulse width, with longer pulses leading to increased lifetimes. A similar trend is observed with laser excitation power (Fig. 1).

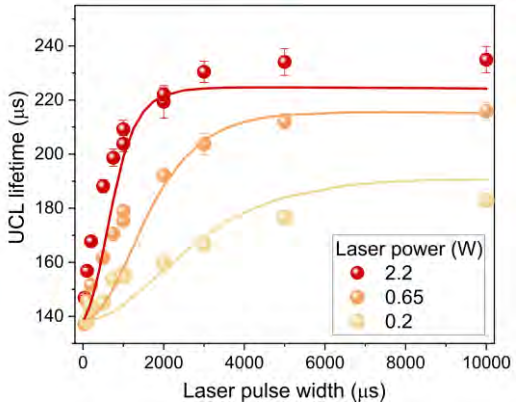

Fig. 1: UCL lifetime at 540 nm as a function of excitation pulse width for three different laser powers. Symbols are experimental data, and solid lines are the simulated results.

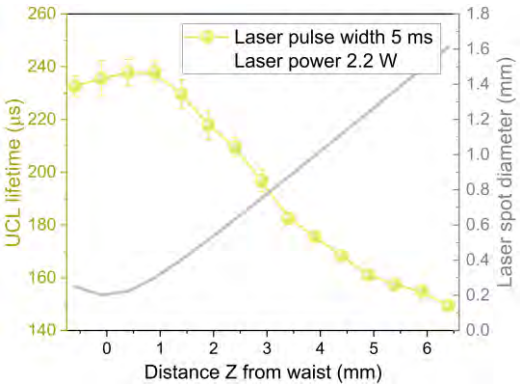

Fig. 2: On the left axis, UCL lifetime as a function of the distance from the excitation beam waist to the cuvette. On the right axis, laser spot size as a function of the cuvette position.

Subsequently, we analyzed the UCL decay curves by positioning the cuvette containing UCNPs at different points along the beam propagation axis while keeping all other excitation parameters constant: a pulse width of 5 ms and a laser power of 2.2 W (Fig. 2). Through this approach, we also observed a similar behavior of UCL lifetime when varying the laser beam size at a fixed pulse width and power.

All these results demonstrate that UCL lifetime is influenced by the optical energy per

unit area, that is laser fluence. This parameter was identified as the key governing factor, as higher fluence led to more pronounced lifetime variations. As shown in Fig. 3, all the data from the previous experiments converge when plotted as a function of their corresponding laser fluence.

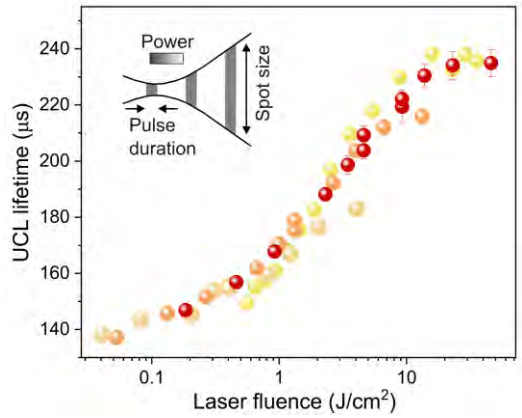

Fig. 3: UCL lifetimes from Fig. 1 and Fig. 2 as a function of the laser fluence.

The theoretical rate equation model successfully reproduced the experimental trends, confirming that the excitation pulse width alters the population distribution of excited states, leading to modified decay dynamics.

Furthermore, we discuss how these findings impact the accuracy of UCL lifetime-based sensing techniques, particularly in Förster resonance energy transfer (FRET)-based applications where precise lifetime measurements are essential.

FRET can be measured through changes in the UCL lifetime caused by the presence of an acceptor, which introduces an additional nonradiative relaxation pathway, using the following expression:

$$\eta_{FRET} = 1 - \frac{\tau_{DA}}{\tau_D} \qquad (1)$$

where τ_D is the lifetime of the UCNP and τ_{DA} is the lifetime of the UCNP close to the acceptor.

Through the theoretical model, we simulated the UCL lifetime dependence with the laser pulse width for UCNPs with and without the presence of the acceptor (Fig. 4, black solid line and black dashed line, respectively). In the case of UCNP with the acceptor, we used a constant FRET rate value representing 25% of the total decay rate (E_{FRET} = 0.25).

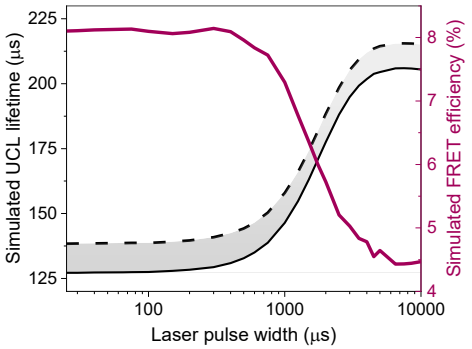

Fig. 4: On the left axis, simulated UCL lifetime in the absence (black dashed line) and in the presence (black solid line) of an acceptor with a FRET efficiency of E_{FRET} = 0.25. On the right axis, using these curves we plotted the simulated FRET efficiency as a function of the laser pulse width (pink solid line).

As anticipated, UCNPs with the acceptor exhibit shorter UCL lifetimes, and both curves show a similar trend with pulse width. Therefore, FRET efficiency is also dependent on excitation pulse width as seen in Fig. 4 (pink solid line). Although the FRET efficiency varies, it never reaches the 25% we have imposed on the rate equation model. This fact can be explained because UCL lifetime of the green level is not exclusively determined by the decay time of the green-emitting level. Instead, it reflects a combination of processes occurring within the complex upconversion system such as energy transfer rates between sensitizer and activator ions, decay rates of intermediate levels, or cross-relaxation rates between Er ions. This underestimation of FRET efficiency has significant implications for the field of FRET sensors based on UCNPs, as it could greatly reduce the achievable detection sensitivity.

These theoretical results were corroborated by experimental measurements. We synthesized β-$NaYF_4$:Yb@$NaYF_4$:Yb,Er UCNPs with and without the Cy3 dye, acting as the FRET acceptor.

To determine FRET efficiency under steady-state conditions, we first measured the emission spectra of both samples (Fig. 5).

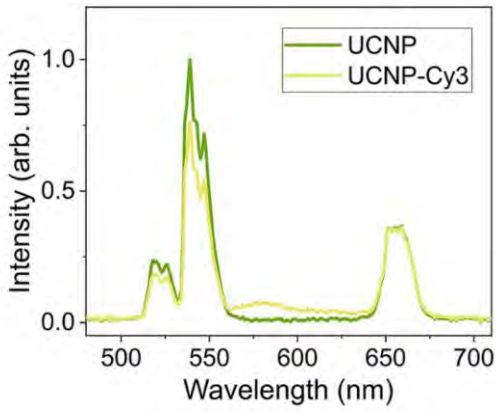

Fig. 5: Green UCL emission spectra for β-NaYF4:Yb@NaYF4:Yb,Er UCNPs with and without Cy3.

Analogous to the lifetime-based approach, FRET efficiency can also be estimated from the emission intensities using the following equation:

$$\eta_{FRET} = 1 - \frac{I_{DA}}{I_D} \quad (1)$$

where I_D and I_{DA} represent the emission intensities of the donor (UCNPs) in the absence and presence of the acceptor, respectively. Based on this data, a FRET efficiency of 29% was obtained.

Next, we measured the UCL lifetime as a function of the laser pulse width for both samples. As expected, the UCL lifetime increased with pulse width (Fig. 6).

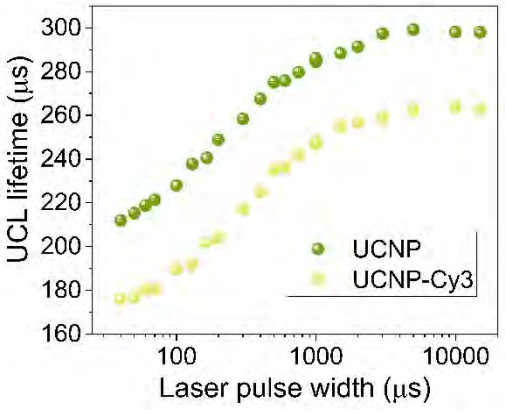

Fig. 6: Green UCL lifetime as a function of the excitation pulse width for UCNPs with and without Cy3.

From these lifetime measurements, the FRET efficiency was calculated, showing a decreasing trend with increasing pulse width, in agreement with the theoretical predictions (Fig. 7).

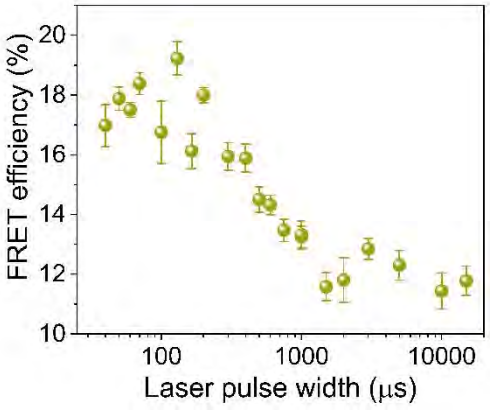

Fig. 7: FRET efficiency calculated from data in Figure 6.

The FRET efficiency ranged from approximately 20% down to 11%, yet it never reached the 29% value obtained under steady-state conditions. These results clearly highlight the critical role of excitation parameters and the necessity for their careful standardization in order to enable meaningful comparisons across different studies.

4.- Conclusion

This work highlights the importance of considering excitation pulse width when analyzing and optimizing UCNP-based applications. The observed UCL lifetime variations have significant implications for FRET-based sensors, where accurate lifetime measurements are crucial for determining energy transfer efficiency. Our results indicate that controlling excitation pulse width could serve as an additional tuning parameter for enhancing the performance of UCNP-based luminescent probes. Future research should explore further refinements to the theoretical model and expand the experimental framework to different host materials and alternative rare-earth dopants.

Acknowledgements: This work was supported by Ministerio de Ciencia e Innovación (PID2021-122806OB-I00, PID2021-

123318OB-I00, TED2021-132317B-I00, PID2023-150645OA-I00), Fundación Alonso (2024/0041), and Comunidad de Madrid (P2022/BMD-7403 RENIM-CM). A.C.R. thanks UCM-Santander for a predoctoral contract (CT15/23).

References

[1] Nina SIRKKA et al., *"Upconverting nanophosphors as reporters in a highly sensitive heterogeneous immunoassay for cardiac troponin I"*, ACS Appl. Mater. Interfaces, 9, 14, 12272-12281, 2017.

[2] Dev K. CHATTERJEE, Abdul J. RUFAIHAH and Yong ZHANG, *"Upconversion fluorescence imaging of cells and small animals using lanthanide doped nanocrystals"*, Biomaterials, 29, 7, 937-943, 2008.

[3] Daniel JAQUE and Fiorenzo VETRONE, *"Luminescence nanothermometry"*, Nanoscale, 4, 15, 4301-4326, 2012.

[4] Shashi BHUCKORY et al., *"Understanding FRET in Upconversion Nanoparticle Nucleic Acid Biosensors"*, Nano Letters, 23, 6, 2253-2261, 2023.

[5] Yuqin GAO et al., *"Excitation pulse width-dependent luminescence decay of lanthanide-doped upconversion nanoparticles"*, Journal of Liminescence, 266, 120325, 2024.

[6] Daniel J. GARGAS et al., *"Engineering bright sub-10-nm upconverting nanocrystals for single-molecule imaging"*, Nature Nanotechnology, 9, 4, 300-305, 2014.

Multipoint strain sensing based on optomechanical interaction in optical fibers

Anna I. GARRIGUES-NAVARRO [(1)], Martina DELGADO-PINAR [(1,2)], Antonio DIEZ [(1,2)], Miguel V. ANDRÉS [(1,2)],

1. Institut Universitari de Ciència dels Materials, Universitat de València, Paterna.
2. Departament de Física Aplicada, Universitat de València, Burjassot.

Contact: Anna I. GARRIGUES-NAVARRO (ana.i.garrigues@uv.es).

ABSTRACT:

In this work, we study the effect of axial strain on forward-stimulated Brillouin scattering (FSBS) optomechanical interaction in single-mode optical fibers. Acoustic mode resonances stimulated by FSBS in the optical fibers were interrogated by a novel and efficient method based on an all-fiber ring resonator capable of probing acoustic oscillations in short (cm-scale) optical fibers. The response of two commercial optical fibers with nominal diameter of 125 μm and 80 μm, respectively, was characterized. Based on the obtained results, a configuration for multiplexed and multi-point strain sensing is demonstrated.

Key words: Optical fibers, forward-stimulated Brillouin scattering, optomechanics, sensing.

1.- Introduction

Research related to sensor applications of forward-stimulated Brillouin scattering (FSBS) in optical fibers have gained increasing attention in the last few years [1-3]. This kind of Brillouin scattering involves the interaction of two copropagating optical tones and an acoustic wave. Its phase-matching condition imposes the acoustic mode to be close to its cut-off frequency, containing most of its energy in the transverse section of the optical fiber. These modes are known as transverse acoustic mode resonances (TAMRs). Its characterization has proven to be useful for sensing outside the cladding boundaries [4], and high precision measurement of fiber elastic properties, [5].

Given the low gain of FSBS, probing of TAMRs usually requires the use of long optical fibers, which makes the development of truly point optical fiber sensors based on FSBS unfeasible. We have recently reported a novel method to excite and interrogate TAMRs in an optical fiber using an all-fiber ring resonator as a phase-to-intensity transducer [6]. This technique is particularly advantageous compared to more conventional interferometric methods as it allows probing FSBS stimulated TAMRS with short fiber lengths (in the order of cm).

In this work, we take advantage of this probing method to investigate the effect of axial strain on the TAMRs of two optical fibers of different diameter. Based on the experimental observations, we propose and demonstrate a multiplexed, multi-point strain sensor using short optical fiber sections.

2.- Theoretical concepts

TAMRs are excited by FSBS when a short optical pulse propagates in an optical fiber [7]. Electrostrictive interaction of the pulse's optical components generates a force field in the transverse section of the fiber that stimulates an acoustic wave packet formed by the superposition of a set of acoustic modes.

In single-mode fibers, owing to the symmetry of the fundamental optical mode, only two families of acoustic modes, i.e. radial ($R_{0,m}$) and torsional-radial ($TR_{2,m}$) modes can be excited [8].

The frequencies of radial mode resonances, $R_{0,m}$, can be approximated by the following expression [1]:

$$\Omega_{0,m} \approx \frac{V_L}{a}\left(c_m - \frac{16\alpha^2 - 1}{8c_m}\right), \qquad (1)$$

where $\alpha = V_S/V_L$, V_L and V_S are the longitudinal and shear acoustic velocities, a is the radius of the fiber and $c_m = m\pi - \frac{\pi}{4}$, where m is the mode order.

Torsional-radial modes can be classified into two different groups, $TR_{2,m}^{(1)}$ and $TR_{2,m}^{(2)}$, based on their characteristics [1]. The former exhibits fields and properties similar to pure torsional modes while modes of the second type show similar properties than dilatational modes. Frequencies of torsional-radial modes can be approximated by:

$$\Omega_{2,m}^{(1)} \approx \frac{V_S}{a}\left(c_{m+1} - \frac{15}{8c_{m+1}}\right), \qquad (2)$$

$$\Omega_{2,m}^{(2)} \approx \frac{V_L}{a}\left(c_{m+1} - \frac{15}{8c_{m+1}}\right) \qquad (3)$$

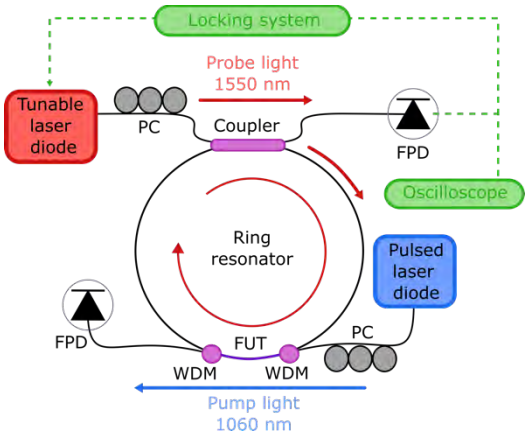

Fig. 1: Experimental setup of the pump and probe system. PC: Polarization controller; WDM: Wave-division multiplexer; FPD: Fast photodiode; FUT: Fiber under test.

3.- Experimental setup

A diagram of the experimental setup is shown in Fig. 1. The all-fiber ring resonator was set up with a commercial optical fiber coupler [6].

TAMRs were stimulated by optical pump pulses from a microchip Nd.YAG laser (700 ps duration at 20 kHz, 1060 nm wavelength) that were delivered to the FUT and extracted from the ring's loop using two WDMs.

The oscillation of a TAMR induced a strain field that modulated in time the refractive index of the fiber via photoelasticity. Such a modulation was probed optically taking advantage of the transfer function of the all-fiber ring. As shown in the left inset of Fig.2, the ring's spectral response comprises a series of transmission notches. By tuning the wavelength of the probe laser to the slope of a notch, the phase modulation induced on the probe light that results from the acoustic vibration is transduced into intensity modulation, as Fig.2 depicts. The probe light is a continuous wave, single-frequency, tunable diode laser (Koheras BASIK, 100 Hz linewidth) centered at 1550 nm.

The intensity modulation of the probe laser was photodetected and recorded in an oscilloscope (1 GHz bandwidth) to obtain the radio-frequency spectrum of TAMRs.

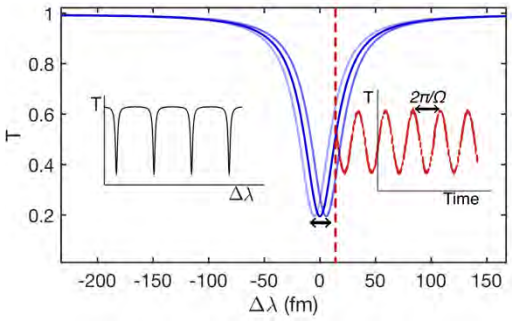

Fig.2: Transmission of an all-fiber ring vs. optical wavelength around a notch, at different instants of time when a single acoustic mode is oscillating at frequency Ω. Vertical line shows the set probe wavelength. Inset: (left) diagram of the all-fiber ring resonator and transmittance vs. wavelength in static conditions; (right) transmittance vs. time at the set point wavelength when an acoustic wave is oscillating.

In our experiments, the fiber under test (FUT) consists of an uncoated section of single-mode fiber that was attached on one end to a linear stage with a micrometer fixed at the other end. The strain resolution of the experimental setup was 0.01 με. We conducted experiments with two fibers, with 125 μm (fiber A) and 80 μm (fiber B) diameter, respectively.

4.- Experimental results and discussion

The radio-frequency spectrum of the probe signal recorded with a standard, 125 μm diameter optical fiber is presented in Fig. 3. Each peak is caused by the oscillation of one TAMRs. Radial and torsional-radial modes are marked in blue and red, respectively.

Measurements were performed by changing the applied strain. The resonant frequencies of TAMRs shifted to higher frequency as the strain was increased. As an example, Fig. 4 shows the response of two TAMRs. For both families of modes, the sensitivity i.e. the frequency shift rate, increased with the mode order. However, the relative frequency-shift, $(\Delta\Omega_m)/\Omega_m$, is the same for all modes of the same family.

Fig. 5 depicts the relative frequency-shift, averaged for at least 5 modes, as a function of strain. Dots and squares show measurements from fiber A and B, respectively.

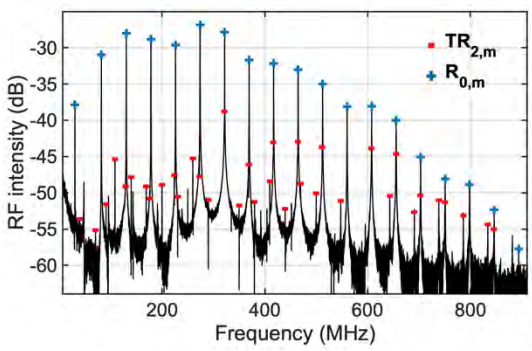

Fig. 3: Radio-frequency spectrum with SMF-28 optical fiber. No strain was applied. Red dots and blue crosses mark the torsional-radial and radial families of TAMRs. Fiber length: 15 cm; average pump power: 60 mW.

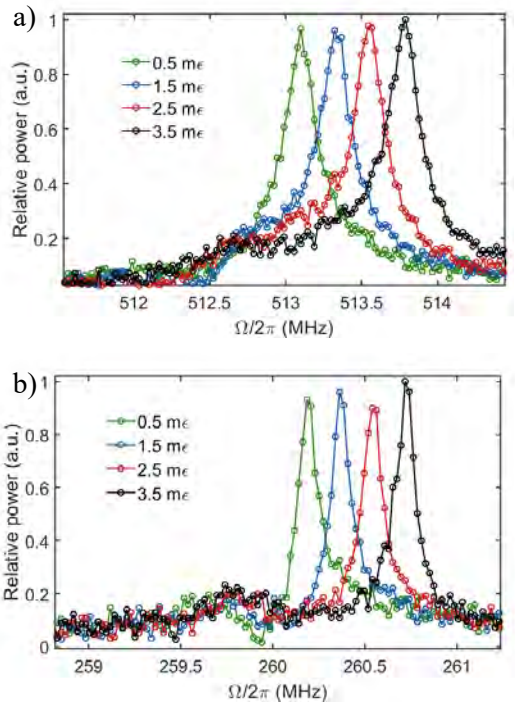

Fig.4: Spectrum of resonances a) $R_{0,11}$ and b) $TR^{(1)}_{2,8}$, for different strain.

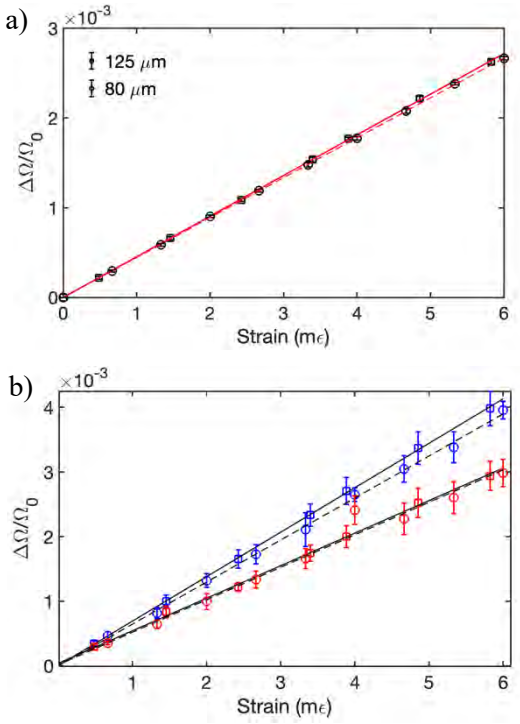

Fig. 5: Relative averaged frequency shift of TAMRs as a function of strain. Dashed and continuous lines show the corresponding linear fits. We plot in a) $R_{0,m}$ and b) $TR_{2,m}$ data. Blue and red markers present $TR^{(1)}_{2,m}$ and $TR^{(1)}_{2,m}$ data.

Thus, the strain dependence can be described by a single, mode-independent parameter for each TAMR family, so that:

$$\frac{\Delta\Omega_{\mathrm{m}}}{\Omega_m} = c_{R,TR} \cdot \epsilon, \qquad (5)$$

where $c_{R,TR}$ is the relative strain coefficient, specific to each family of modes ($R_{0,m}$, $TR^{(1)}_{2,m}$ and $TR^{(2)}_{2,m}$). The obtained relative strain coefficients are summarized in Table 1.

Table 1: Relative strain coefficients for each TAMRs family in strain units.

Fiber	c_R	$c^{(1)}_{TR}$	$c^{(2)}_{TR}$
A	0.453 $\pm$ 0.002	0.687 $\pm$ 0.004	0.50 $\pm$ 0.07
B	0.4451 $\pm$ 0.0012	0.651 $\pm$ 0.008	0.50 $\pm$ 0.02

We find that $TR^{(1)}_{2,m}$ modes, whose resonance frequency depends on the shear acoustic velocity, have a higher dependence on strain while $R_{0,m}$ and $TR^{(2)}_{2,m}$ have similar response. We associate this behavior with the dependence of the resonance frequency with the longitudinal acoustic velocity as stated in Eqs. (1) and (3). Moreover, the values obtained for the relative strain coefficient in both experiments are compatible, as expected since the relative frequency shift does not depend on fiber radius as it can be inferred from Eq. (1)-(3).

5.- Multiplexed sensor: proof of concept

Taking advantage of the results shown in the previous section, we propose a configuration for measuring strain at two different points along a fiber using concatenated sections of both type of fibers. The arrangement is depicted in Fig. 6. A length of ~10 cm of each fiber type was spliced together.

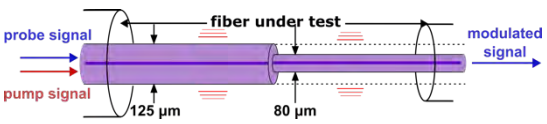

Fig. 6: Schematic of the FUT. Short, red lines represent fiber vibrations.

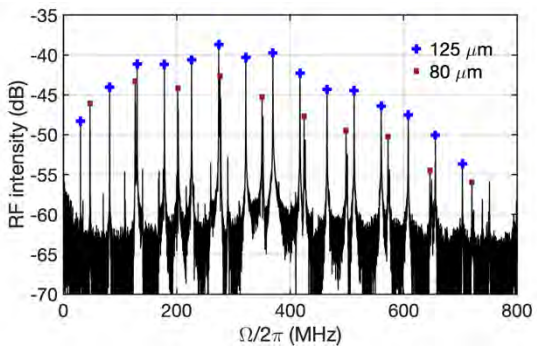

Fig. 7: Radio-frequency spectrum. No strain was applied. Average pump power: 30 mW.

Fig.7 shows the radio-frequency spectrum obtained with this FUT arrangement. The peaks corresponding to the oscillation of TAMRs in each fiber section are identified. Once the resonances corresponding to each fiber have been identified, when strain is applied at some point of the FUT, it is easy to find out which fiber segment is under strain by tracking the displacement of the different peaks. Moreover, the strain value can be obtained using the relative strain coefficients summarized in Table 1.

Measurements of the radio-frequency spectrum were performed as a function of strain. Strain was applied by stretching the FUT comprising both fiber sections. For a certain elongation, the strain induced in each fiber section was estimated considering the different cross-sections.

Figure 8 shows the relative shift of radial resonances of both fibers as a function of strain. The slope, i.e. the strain coefficients, for both fiber sections match.

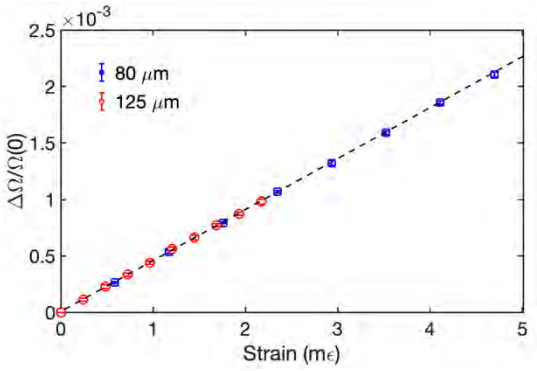

Fig. 8: Relative frequency shift of radial TAMRs as a function of strain for the 125 µm and 80 µm fiber cladding diameter.

5.- Conclusions

In this work, we explore the strain sensing capability of TAMRs in an optical fiber using a fiber ring resonator. We evaluate the performance of two fibers with different cladding diameters and then we proposed a multiplexed configuration for measuring strain at two points along the fiber. The proposed strategy can, in principle, be extended to a larger number of sensing points.

The spatial resolution is directly related to the length of the different fibers sections. The shorter the length, the higher the spatial resolution. In this sense, the technique used here for probing the TAMRS with the all-fiber ring is particularly advantageous since it allows detecting TAMRs with FUT lengths under 2 cm [6].

This study paves the way towards multipoint and multiplexed strain sensors based on interacting optical and acoustic resonators.

Acknowledgements: This work has been partially funded by Horizon 2020 Framework Programme (H2020-MSCA-RISE-2019-872049); Generalitat Valenciana (CIPROM/2022/30, CIACIF/2023/418); Ministerio de Ciencia, Innovación y Universidades (CNS2023-145717, PID2023-146725OB-I00).

References

[1] L.A. Sánchez, A. Díez, J.L. Cruz, M.V. Andrés, *"Recent advances in forward brillouin scattering: sensor applications,"* Sensors, vol. 23, no. 1, Jan. 2023.

[2] A. Zadok, E. Zehavi, and A. Bernstein, *"Opto-mechanical fiber sensing with optical and acoustic cladding modes,"* APL Photonics, vol. 8, no. 7, 2023.

[3] W. Zhang, Y. Lu and C. He, *"Simultaneous measurement of temperature, refractive index, and axial strain based on forward brillouin scattering in polyimide-coated SMF,"* IEEE Sensors Journal, vol. 23, no. 22, pp. 27361-27368, 2023.

[4] Y. Antman, A. Clain, Y. London, et al., *"Optomechanical sensing of liquids outside standard fibers using forward stimulated Brillouin scattering,"* Optica, vol. 3, no. 5, pp. 510–516, 2016.

[5] L. A. Sánchez, A. Díez, J. L. Cruz, and M. V. Andrés, *"High accuracy measurement of Poisson's ratio of optical fibers and its temperature dependence using forward-stimulated Brillouin scattering,"* Opt. Express vol. 30, no. 1, pp. 42-52, 2022.

[6] A. I. Garrigues-Navarro, M. Pinar-Delgado, A. Díez, M. V. Andrés, *"Characterization of FSBS radial acoustic modes in short optical fibers with an all-fiber ring resonator", submitted to J. Lightwave Technol.*

[7] A. Zadok, H. H. Diamandi, Y. London, and G. Bashan, *Forward Brillouin Scattering in Standard Optical Fibers: Single-Mode, Polarization- Maintaining, and Multi-Core,* (Springer Series in Optical Sciences). Springer International Publishing, 2022, vol. 240.

[8] A. S. Biryukov, M. E. Sukharev, and E. M. Dianov, "*Excitation of sound waves upon propagation of laser pulses in optical fibres",* Quantum Electron., vol. 32, no. 9, pp. 765–775, 2002.

Modelling an inversion layer photodiode in COMSOL Multiphysics

Rubén GÓMEZ [1], Sucheta SHARMA [2], Trinh TRAN [3], Erkki IKONEN [2], Pedro CORREDERA [1], Joaquín CAMPOS [1]

1. Instituto de Óptica "Daza de Valdés", Consejo Superior de Investigaciones Científicas (CSIC), C. de Serrano 144, 28006 Madrid, Spain.
2. Metrology Research Institute, Aalto University, 02150 Espoo, Finland.
3. Justervesenet, 2027 Kjeller, Norway.

Contact: Rubén GÓMEZ (ruben.gomez@io.cfmac.csic.es).

ABSTRACT

This paper presents a simulation of an inversion layer silicon photodiode using COMSOL Multiphysics. The device comprises a silicon substrate, and a structured top surface consisting of a silicon nitride layer over a silicon dioxide layer to create inversion layer where light is incident.

The model couples electromagnetic wave propagation with semiconductor physics, including analytic doping profiles, surface charge density effects, trap-assisted surface recombination, and optical transitions. Two stationary studies combined with parametric sweeps allow the extraction of values of photogenerated current, responsivity, dark current and internal quantum deficiency. This simulation framework provides insights into the recombination and charge transport mechanisms that govern device performance.

Key words: inversion layer photodiode, simulation, silicon photodetector, internal quantum deficiency.

1.- Introduction

Accurate optical power measurements require photodetectors with well-characterized quantum efficiency. Inversion layer silicon photodiodes have demonstrated exceptional performance in this regard [1] [2], serving as primary standards for optical radiometry. Modeling such devices is crucial for understanding their operation at a fundamental level and optimizing their design for enhanced accuracy. Numerical simulations allow for a detailed analysis of both optical and electronic processes, providing insights into the impact of material properties and dimensions.

An inversion layer Si photodiode with an Internal Quantum Efficiency that differs from unity by a few p.p.m. and with a low reflectance in the visible spectral range was developed in the framework of the project "Self-calibrating photodiodes for the radiometric linkage to fundamental constants" (EMPIR, 18SIB10 chipS-CALe), thus achieving an absolute radiometer in that spectral range. The follow up project "Self-calibrating photodiodes for UV and exploitation of induced junction technology" (EPM 22IEM06, "S-CALe Up") attempts to extend the validity of this absolute radiometer to the entire Si photodiode response range.

This work aims to transport the aforementioned chipS-CALe inversion layer photodiode into the COMSOL Multiphysics interface, in order to model and simulate its performance, focusing on the analysis of its photogenerated current and its Internal Quantum Deficiency (IQD) due to charge carrier recombination under varying conditions of incident light or bias voltage. Once the simulation results match the measured responsivity for those photodiodes,

this developed model in COMSOL Multiphysics can be used to redesign the photodiode structure to optimize its responsivity in UV spectral range.

2.- Modelling

The model has been initially developed as two-dimensional, to ensure its elements work properly before proceeding to the three-dimensional version of the model, where computational times are much higher. Its geometry consists of a 500 µm-thick and 650 µm-wide bulk silicon substrate, backed by a 1.2 µm-thick aluminum layer. On the top surface, the structure includes a pair of 100 µm-wide metal contacts, with the P-type contact connected to ground and the N-type contact being fed different values of voltage that act as reverse bias. Between the P-contact and the N-contact there is a 200 µm-wide, 6 nm-thick silicon dioxide (SiO_2) layer, which has been proven to help in the insulation of the metal contacts in the real samples of this photodiode. Lastly, the so-called "active region", where the light impinges, is composed of a dual-layer stack: a 6 nm-thick SiO_2 layer underneath a 65 nm-thick silicon nitride (SiNx) layer, both extending 250 µm in width [3]. Fig. 1 shows a layer diagram of the model, where some of the layers have been magnified for better visualization. All the dimension values are listed and collected in a "Parameters" group in the "Global Definitions" section in COMSOL Multiphysics, to make it easier to modify these values at any given time.

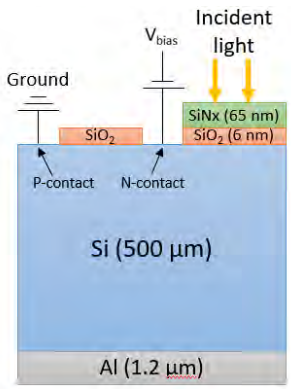

Fig. 1: Simplified schematic representation of the layer structure of the simulated photodetector.

The refractive indexes of different materials used in this model come from experimental values [4]. An "Interpolation Function" has been implemented for each material in the "Definitions" section of the component, which provides values of the real and imaginary refractive indexes that can be assigned to the corresponding material at the required wavelength.

The model employs a multiphysics approach by coupling the "Wave Optics" and the "Semiconductor" libraries. For the optical features of the model, the "Electromagnetic Waves, Frequency Domain" module has been chosen, in order to simulate the propagation and interaction of light within the device's multilayer structure. Frequency domain analysis allows steady-state simulations under monochromatic illumination, facilitating the coupling of optical processes with the semiconductor physics, although the use of other modules such as "Electromagnetic Waves, Beam Envelopes" may be considered given the thickness of the structure and its high wavelength-to-size ratio. To excite and to absorb the electromagnetic wave of the illumination, the Port boundary condition is applied in the model. One "Port" is defined on the top surface of the SiNx layer, with a varying input power distributed along the 250 µm surface, while Port 2 is applied at the underside of the Al layer with excitation turned off.

Meanwhile, the Semiconductor module captures the key recombination and generation processes that govern carrier dynamics in the photodiode. The semiconductor physics incorporates several critical phenomena, starting with the definition of analytic doping models which establish the doping profiles in the silicon bulk, with a background P-type doping of $2 \cdot 10^{12}$ cm^{-3}, N-type and P-type doping regions below the N-contact and P-contact respectively with a profile depth of 2 µm and peak doping concentrations of 10^{19} cm^{-3}, and a P-type doping layer right above the Al layer also with profile depth of 2 µm and concentration of 10^{19} cm^{-3} (these structures are not shown in Fig. 1). Metal contact boundaries

are assigned to the N-contact region and to the P-contact region. A reverse bias voltage is supplied between them. At the Si/SiO_2 interface, a surface charge density of $1.3 \cdot 10^{12}$ cm^{-2} is imposed with harmonic perturbation activated.

In addition, a "Trap-Assisted Recombination" feature is implemented using the Shockley-Read-Hall (SRH) formalism, with both electron and hole lifetimes set to 0.005 s and an energy offset of 0.25 V. Defect states within the bandgap capture carriers and facilitate recombination without the emission of light, and the trap occupancy is calculated based on the mid-gap energy level. This approach enables us to model the impact of bulk defects on carrier lifetimes, which is particularly important for understanding the dark current behavior.

Besides, a "Trap-Assisted Surface Recombination" feature is implemented using an explicit trap distribution with a trap occupancy formulation. At the surface, recombination can be significantly enhanced by interface defects, so in addition to radiative processes, the model also accounts for non-radiative recombination through trap-assisted mechanisms. This formulation captures the recombination dynamics at the Si/SiO_2 interface, where surface states can dominate the recombination process, and by incorporating both bulk and surface recombination processes, the model provides a comprehensive view of how defect states affect overall device performance.

Lastly, an "Optical Transitions" feature is also modeled using a matrix element approach corresponding to a spontaneous lifetime of 2.87 ns. This feature describes the radiative processes by which electrons recombine with holes via photon emission, ensuring that the radiative recombination methods are correctly represented. In combination with the "Wave Optics" module, these semiconductor physics elements yield a better insight into the interplay of optical and electronic phenomena, while considering the importance of defect states in the materials.

Two different studies are used in this simulation: the first one consists of a Frequency Stationary study, with a frequency corresponding to a wavelength of 550 nm, combined with a parametric sweep of either the N-contact reverse bias, from 0 V to 5 V, or the incident optical power, from 0 µW to 100 µW distributed along the active region. The wavelength of the incident light chosen for this study corresponds to the value where the physical samples have shown the lowest values of reflectance during measurement, so higher values of photogenerated current are expected due to better values of absorbance. The second study consists of a stationary study which only takes into account the "Semiconductor" module, with a parametric sweep of the reverse bias as the one previously mentioned; this study allows for calculation of the dark current of the photodiode, a parameter that will be used in the calculation of the IQD of the model.

3.- Results

This simulation provides the terminal current of the device and its responsivity for a range of values of the bias voltage, with a fixed incident power of 5 µW, represented in Fig. 2.

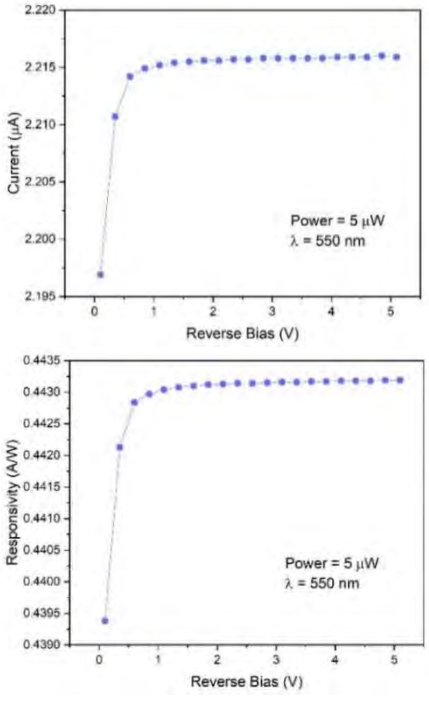

Fig. 2: Simulated terminal current (above) and responsivity (below) of the photodiode as a function of the reverse bias.

Terminal current as a function of the incident power, for a fixed bias voltage of 2 V, can also be simulated as shown in Fig. 3.

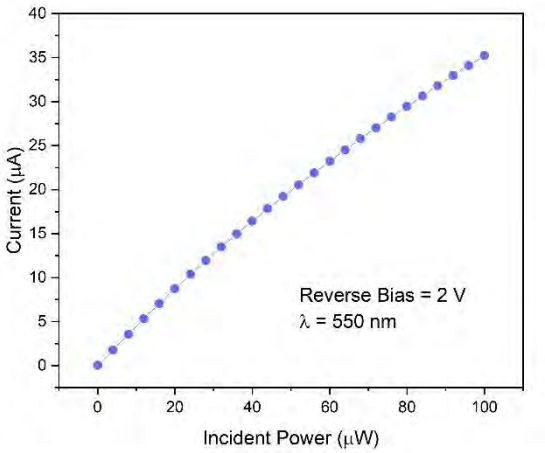

Fig. 3: Simulated terminal current of the photodiode as a function of the incident power.

Lastly, we represent in Fig. 4 the Internal Quantum Deficiency as a function of the bias voltage, whose value is given by the following equation:

$$IQD(V) = 1 - \frac{I(V) - I_{dark}}{\frac{e\lambda}{hc}\Phi\left(1 - \rho(\lambda)\right)}$$

Where $I(V)$ is the simulated terminal current, I_{dark} is the dark current of the photodiode, e is the charge of the electron, λ is the incident wavelength, h is the Planck constant, c is the speed of light, Φ is the incident radiant flux and $\rho(\lambda)$ is the reflectance of the photodiode at a given wavelength (in this case, 550 nm) [5].

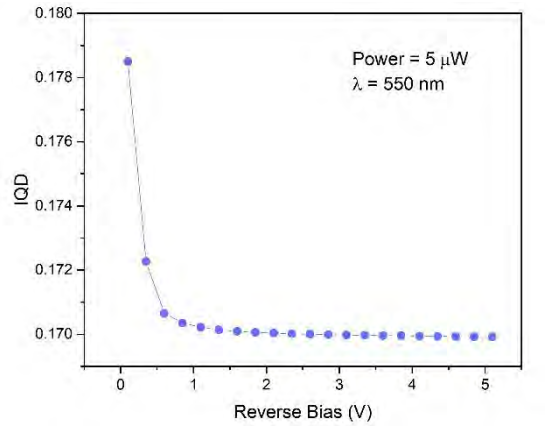

Fig. 4: Simulated Internal Quantum Deficiency of the photodiode as a function of the reverse bias.

4.- Conclusion

The results obtained by the simulation of the photodiode show that, for the simulated sample, the photogenerated current reaches an asymptotic value of approximately 2.216 μA at around 1 V of reverse bias, and this current doesn't significantly increase with bigger voltages. Something similar can be observed for the responsivity of the photodiode, which seems to cap for a value around 0.443 A/W. An asymptotic behavior can also be observed in the Internal Quantum Deficiency, capping at a value of 0.17, which makes sense since both the responsivity and the IQD are values derived from the photogenerated current. This value clearly differs from what we would expect, since the chipS-CALe photodiodes have an internal quantum efficiency close to the unity (and thus, the IQD is expected to be much closer to 0), this could be due to the model not having the full dimensions of the original chipS-CALe photodiode. Additionally, we observe on Fig. 3 that the photogenerated current doesn't seem to reach an asymptotic value (response saturation) at least in the range of incident power that has been evaluated. It could be interesting to simulate bigger values of the incident power, even one or two orders of magnitude higher, but the simulation has shown problems in the convergence with high values of incident power, so some modifications or a different approach to the model may be taken into account in order to reach a certain degree of consistency in the simulations.

The next steps that this work will take will be to simulate the complete structure of the photodiode, which has a full width of 11 mm, and to improve the model into a 3D version of it. As mentioned previously, the ultimate goal of this work is to develop a simulation system that can be used for future photodiodes, to be able to anticipate its responsivity and make adjustments to its structure prior to starting its process of fabrication.

Acknowledgements: This work has been carried within the project 22IEM06 S-CALe Up, funded by the program EPM, co-financed from the European Union's Research and Innovation Programme Horizon Europe and by the Participating States.

Bibliography

[1] Meelis SILDOJA et al., *"Predictable quantum efficient detector: I. Photodiodes and predicted responsivity"*, Metrologia, 50(4):385, 2013.

[2] Ingmar MÜLLER et al., *"Predictable quantum efficient detector: II. Characterization and confirmed responsivity"*, Metrologia, 50(4):395, 2013.

[3] Ozhan KOYBASI et al., *"High Performance Predictable Quantum Efficient Detector Based on Induced Junction Photodiodes Passivated with $SiO_2/SiNx$"*, Sensors, 21(23):7807, 2021.

[4] Ellipsometry measurements performed by Mauro RAJTERI from INRIM (Turin, Italy), unpublished.

[5] Trinh TRAN et al., *"Determination of the responsivity of a predictable quantum efficient detector over a wide spectral range based on a 3D model of charge carrier recombination losses"*, Metrologia, 59(4):045012, 2022.

Study of bandwidth and response saturation on PQED photodiode

Rubén GÓMEZ, Noelia CASTREJÓN, Juan GALINDO-SANTOS,
Joaquín CAMPOS, Pedro CORREDERA

Instituto de Óptica "Daza de Valdés", Consejo Superior de Investigaciones Científicas (CSIC), C. de Serrano 144, 28006 Madrid, Spain.

Contact: Rubén GÓMEZ (ruben.gomez@io.cfmac.csic.es).

ABSTRACT

Predictable Quantum Efficiency Detectors (PQEDs) are high-accuracy photodetectors that enable absolute optical power measurements. Their application to fiber optics could enhance measurement accuracy and traceability in optical communications, metrology, and quantum technologies. This work, part of the "S-CALe Up" project, evaluates a PQED composed of inversion layer silicon photodiodes under various operating conditions.

The measurements reveal a dependence of the PQED frequency response on wavelength, polarization, and bias voltage. Notably, we identify saturation effects related to absorption and reflectance properties of the photodetectors. We also demonstrate that applying a sufficiently high bias voltage mitigates saturation, achieving a flat frequency response for higher optical power values (up to 2 mW and up to 4 kHz). These findings provide valuable insights for the development of future PQEDs with improved performance in near-infrared range, paving the way for their integration into optical fiber-based measurement systems.

Key words: predictable quantum efficiency detector, optical fiber metrology.

1.- Introduction

Photodetectors are essential devices in optoelectronics, designed to convert incident light into an electrical signal. Their performance is typically characterized by parameters such as responsivity, noise, and quantum efficiency. Among them, the Predictable Quantum Efficiency Detector (PQED) stands out as a high-accuracy photodetector with a well-defined quantum efficiency, enabling absolute optical power measurements. PQEDs are based on silicon photodiodes operated in a predictable manner, ensuring near-unity internal quantum efficiency. These detectors are primarily used in fundamental radiometry, providing traceability for optical power measurements.

In the visible range of radiation, the applications of optical fibers in communications, sensors, integrated photonics, biomedical applications and quantum communications, where the precise detection of light is crucial, have opened up a new use for PQEDs as an easy-to-use, low-cost, high-precision absolute radiometer. The project "Self-calibrating photodiodes for UV and exploitation of induced junction technology" (EPM 22IEM06, "S-CALe Up"), in which this work is framed, attempts to extend the validity of previously produced absolute radiometers to the entire Si photodiode response range.

The aim of this work is to critically evaluate the applicability and integrability of PQEDs as an absolute standard radiometer in fiber optic applications. In order to develop procedures to study future PQEDs, we have performed measurements under different conditions of current readout circuits, repetition rates of chopped light, power levels and wavelengths, on a PQED composed of inversion layer Si photodiodes from a previous project (qu-Candela, Programme

iMERA-Plus, project number: T1.J2.3) whose response is well-known and stable. The same measurements can then be replicated on the improved S-CALe Up photodiodes once they have been produced to evaluate its performance.

2.- Basis and operation of PQED

Spectral responsivity of a silicon photodiode can be defined by the following function:

$$R(\lambda) = \frac{q\lambda}{hc} n(\lambda)[1 - \rho(\lambda)][1 - \delta(\lambda)]$$

Where $R(\lambda)$ is the spectral responsivity of the photodiode, q is the electron charge, λ is the wavelength of the optical signal, h is Planck constant, c is the speed of light, n is the refractive index of the medium, $\rho(\lambda)$ is the reflectance of the photodiode and $\delta(\lambda)$ is the carrier losses in the photodiode, with $1-\delta(\lambda)$ being the quantum efficiency of the photodiode at the working wavelength, which can be expressed as η. Responsivity $\frac{q\lambda}{hc} n(\lambda)$ corresponds to an ideal photodiode, where each incident photon produces an electron-hole pair that contributes to the measured current in the external electric circuit.

A PQED aims to reproduce this ideal behavior of the photodiode response by reducing the carrier losses to achieve unity internal quantum efficiency, this is attained by tailoring the doping in the structure of the photodiode material. Additionally, we try to keep the reflectance of the photodiode to a minimum, which is effectively achieved by placing several photodiodes in a geometrical light trap configuration. By replacing the values of the constants and expressing λ in micrometers, the responsivity of the PQED can be defined by the formula:

$$s(\lambda) = \eta \frac{q\lambda}{hc} \approx \eta \frac{\lambda}{1{,}24}$$

In order to achieve zero reflectance of the PQED, different light trap configurations have been described [1] [2] [3]. Fig. 1 shows the configuration selected in this project and the geometry and design of the PQED.

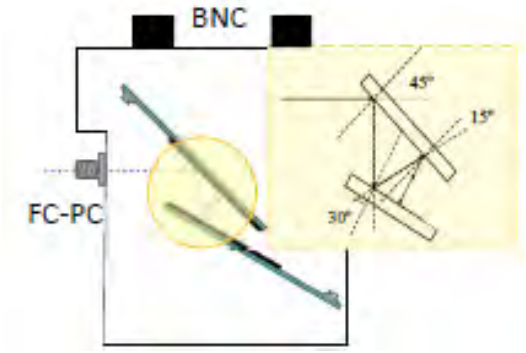

Fig. 1: Schematic representation of photodiode configuration in the PQED.

A maximum reflectance of 0.02 % is guaranteed for this configuration if Si photodiodes with a 30 % reflectance are used. The reflections inside the device occur at angles of 45º, 30º, 15º and 0º, all in the same plane; therefore, this device will manifest a dependence of its response on the polarization state of the incident light. For fiber optic applications this variation of response with polarization is a handicap (the polarization of the light cannot be controlled in the optical fiber), but within an uncertainty of 0.1 % a response can be considered good.

3.- Experimental setup

The PQED bandwidth study was performed by measuring the relative response of the PQED using diode lasers with fiber optic outputs of wavelengths 405 nm, 520 nm, 633 nm, 660 nm, 785 nm, 852 nm and 980 nm. To modulate the signal of these lasers, a chopper (Model SR540, Stanford Research Systems) has been used to vary the modulation frequency from 0 Hz to 4 kHz. During this work, the relative response of the detector has been measured for different chopper frequencies and different incident optical powers, for each of the lasers used.

Two experimental setups have been used depending on whether the optical radiation is impinging the PQED from a fiber or not, as shown in Fig. 2. In both setups the light from the single-mode fiber diode laser is collimated (either with a fiber collimator adapted to the

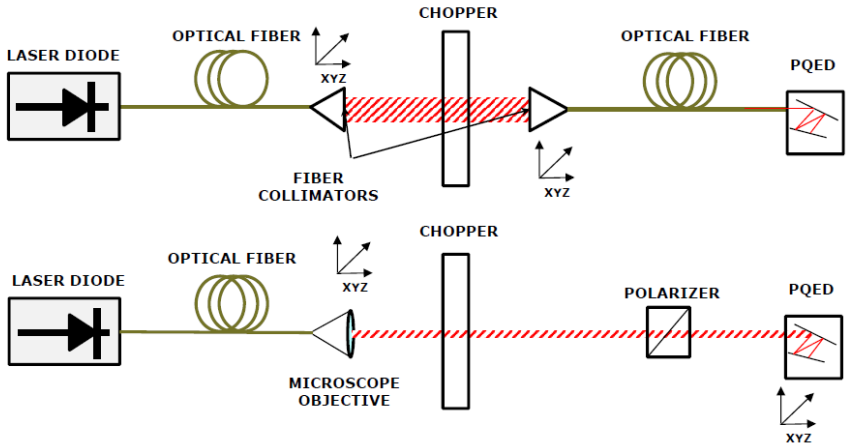

Fig. 2: Experimental setup used on fiber measurements (top) and air measurements (bottom).

working wavelength, or with a microscope objective) to modulate it in the chopper. In the first setup, the modulated radiation is collected with a fiber collimator and connected to the PQED input port by a fiber. In the second setup (designed to study the influence of light polarization) a polarizer is introduced into the optical path before reaching the PQED input port.

In order to achieve an adequate efficiency in the conversion of electron-hole pairs and to ensure electron collection, a bias voltage of 5 V is applied to both photodiodes of the PQED. The generated photocurrent is amplified with a low noise current preamplifier (Model SR570, Stanford Research Systems). This preamplifier is used in high bandwidth mode with amplification scales that guarantee bandwidths greater than 100 kHz. The amplified signal is displayed on a four-channel digital oscilloscope (Model DS6104, Rigol), which allows the measurement of all waveform parameters; specifically the peak-to-peak (P-P), the rms value and the ratio of negative cycle time to positive cycle time.

At low optical powers and low chopper frequencies, conditions under which we can be sure that the PQED is linear, the oscilloscope displays a symmetrical square wave analogous to the waveform produced by the chopper. As the optical power or modulation frequency increases, a deformation of the waveform appears, indicating a nonlinear behavior of the detector, or a drop in the detector bandwidth.

As usual for bandwidth measurements, P-P voltage variation and rms value of the signal were taken as figures of merit; however, in the case of this particular PQED, the values of P-P voltages and rms are not sensitive enough for the characterization of the dynamic behavior of the detector. Fig. 3 shows the PQED signal (total and of each individual photodiode) for 520 nm wavelength, 3.9 kHz modulation and 0.84 mA total current (equivalent to 2 mW). It can be seen that the signal is distorted maintaining the P-P ratio, but broadening of signal, so the ratio between the negative and positive cycle has been considered as the most appropriate parameter to characterize the dynamic behavior of the device.

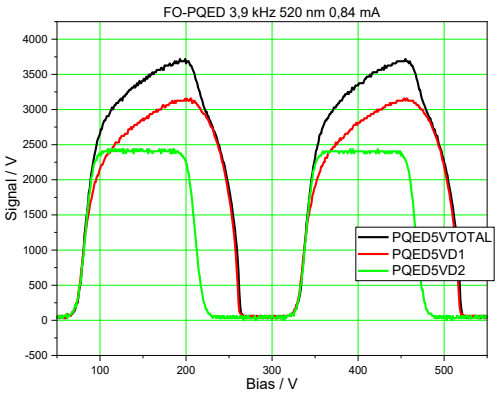

Fig. 3: Measured signal of the PQED (black), composed by the signal of the first detector (red) and the second detector (green).

4.- Measurements and discussion

Fig. 4 shows the relative response of the PQED with a bias of 5 V, for wavelengths of 520 nm and 852 nm using optical fiber (upper measurement setup from Fig. 2). The plots show the relative response at each wavelength for powers from 50 µW to 2 mW, varying the modulation frequency between 0 Hz and 4 kHz.

For incident powers below 500 µW, no significant drop in relative response can be observed at any modulation frequency, whereas above this power the relative response drops as the modulation frequency increases, being more pronounced for the 852 nm wavelength case. A similar behavior occurred at the other measured wavelengths, with more pronounced drops at longer wavelengths than at shorter ones.

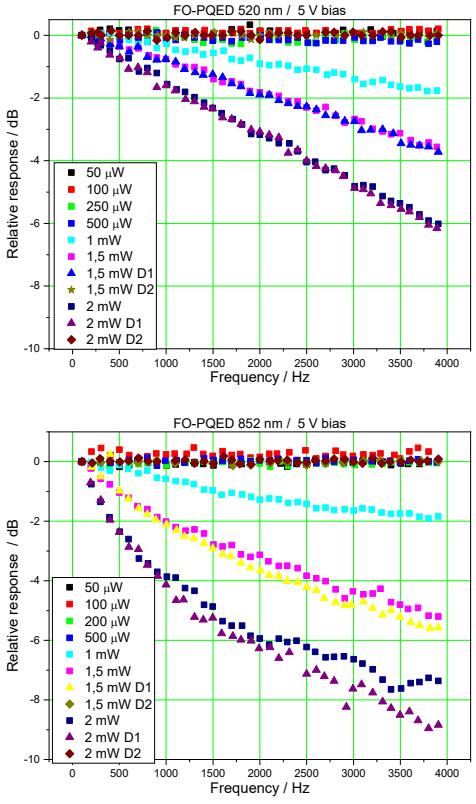

Fig. 4: Relative response of the PQED as a function of the chopper frequency for different values of incident power, for 520 nm (top) and 852 nm (bottom).

This behavior leads to think that the internal quantum efficiency of the PQED at long wavelengths may not be close to unity. Since long wavelengths are absorbed in the region farthest from the surface of the photodiode, an increase in the bias voltage leads to an enlargement in the depletion region of the photodiode, leading to a higher mobility of the generated carriers.

Under the same measurement conditions of the upper setup in Fig. 2, a study of the increase of the negative to positive width ratio with different bias voltages, for 1 kHz and 1.6 mW, at various wavelengths was performed. The result is shown in Fig 5, where we see that for this frequency and optical power, 5 V bias is not enough to achieve linear response and an adequate bandwidth in the PQED. Meanwhile, increasing the bias shows an improvement of the signal, achieving linear response at 12 V and covering the bandwidth of up to the measured frequencies. For 852 nm the bias voltage required for the linear behavior of the device is higher than for shorter wavelengths, which is congruent with the fact that photon absorption occurs in the area farthest from the photodiode surface. However, this behavior does not show for the 520 nm wavelength as it does for those of the 660 nm and 785 nm wavelengths, which need a lower bias voltage.

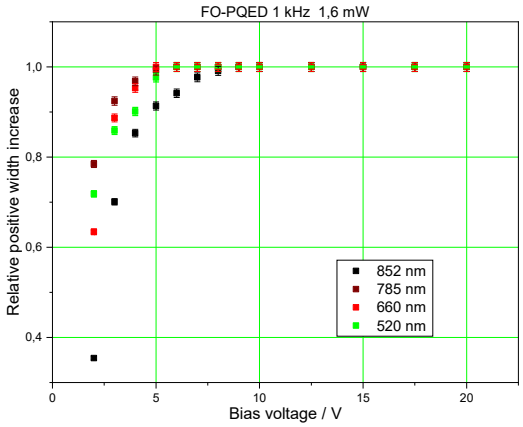

Fig. 5: Relative positive width increase of the bias voltage of the PQED as a function of the bias voltage for fiber optic signal.

To try to explain this anomalous behavior in the 520 nm wavelength, the experimental setup was modified to the one shown in the lower schematic of Fig. 2. In this setup, the optical fiber is eliminated and a linear polarizer of 10000:1 extinction ratio is included in the optical path, thus measuring the PQED response in the S- and P-polarization, with collimated beams of the same waist (2.5 mm), avoiding local saturation problems of the photodiodes.

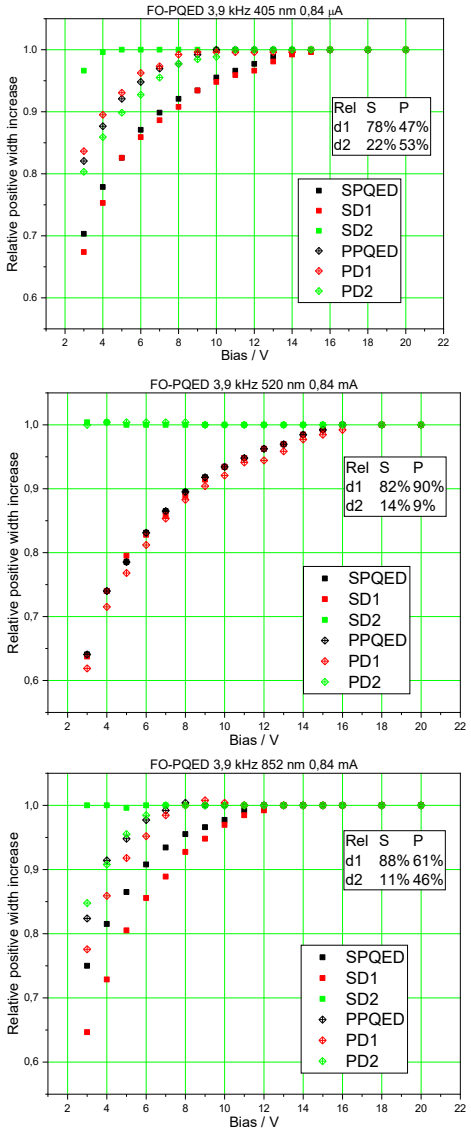

Fig. 6: Relative positive width increase as a function of the bias voltage of the PQED and each of its detectors for S-polarization and P-polarization, for 405 nm (top), 520 nm (middle) and 852 nm (bottom) of incident wavelength.

Fig. 6 shows the results for wavelengths of 405 nm, 520 nm and 852 nm, obtained at the highest frequency of light modulation in the chopper (3.9 kHz) and for a photogenerated current of 0.84 mA (equivalent to optical powers of 2.6 mW for 405 nm, 2.0 mW for 520 nm and 1.2 mW for 852 nm for the ideal PQED). A fixed output current has been decided to be used, because for an ideal PQED, each incident photon generates an electron-hole pair which is measured in the external circuit.

At the three wavelengths shown and for both polarizations, a bias voltage of 20 V guarantees a bandwidth of 3.9 kHz in the PQED. However, for 405 nm and 852 nm the bias voltages needed to achieve a flat frequency response are lower than those needed for 520 nm. Furthermore, for 520 nm, the first photodiode saturates regardless of the polarization of the light, while the second remains unsaturated for either polarization. This behavior leads to think of a certain connection with the reflectance of the photodiodes as a function of wavelength. Fig. 7 shows the reflectance measured in individual photodiodes of the same type as those composing our PQED, for P-polarized, S-polarized and unpolarized light, and for angles of incidence of 8°, 15°, 30° and 45° (corresponding to the angles of incidence shown in Fig. 1, with 8° being the minimum value that our spectrophotometer can measure and being considered equivalent to the value of 0°). These reflectance measurements show a minimum at wavelengths around 520 nm, which would cause the absorption of all radiation at those wavelengths in the first photodiode, and its saturation for certain power levels. It can be seen that, at wavelengths of 405 nm and 852 nm, the reflectances are higher and saturation of the first photodiode does not occur. The percentual contribution of electrical signal of each photodiode with respect to the signal produced by the PQED is shown in the boxes inserted in the graphs of Fig. 6.

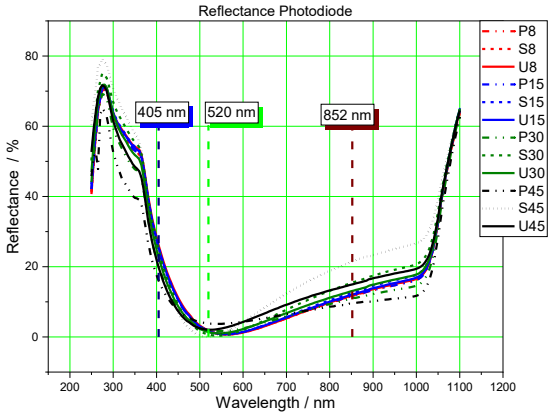

Fig. 7: Reflectance of the PQED detectors as a function of the wavelength, for different polarizations and angles of incidence.

5.- Conclusions

The bandwidth of a PQED has been measured for modulation frequencies between 0 Hz and 4 kHz. It has been found that, for bias voltage values recommended by the manufacturer (up to 5 V), the PQED presents a bandwidth of less than 2 kHz from powers of 1 mW.

It has been determined that an increase of bias voltage achieves an improvement of the device bandwidth, resulting in a value of 20 V ensuring a flat frequency response of the PQED for frequencies up to 4 kHz and powers of 2 mW.

Lastly, it has been verified that the bias voltage required to achieve flat response in PQED is very sensitive to wavelength, and it has been determined that it is related to the reflectance of the photodiode at different wavelengths; for wavelengths with a low reflectance, the first photodiode of the PQED absorbs most of the radiation and saturates at lower incident powers, requiring a higher bias voltage to achieve flat frequency response.

Acknowledgements: This work has been carried within the project 22IEM06 S-CALe Up, funded by the program EPM, co-financed by the European Union's Research and Innovation Programme Horizon Europe and by the Participating States. Giorgio Brida from INRIM is gratefully acknowledged for providing the studied PQED and for the fruitful discussions.

Bibliography

[1] Edward F. ZALEWSKI, C. Richard DUDA, *"Silicon photodiode device with 100% external quantum efficiency"*, Applied Optics, 22(18):2867, 1983.

[2] N.P. FOX, *"Trap detectors and their properties"*, Metrologia, 28(3):197, 1991.

[3] Meelis SILDOJA et al., *"Reflectance calculations for a predictable quantum efficient detector"*, Metrologia, 46(4):S151, 2009.

Detección de fugas en tuberías mediante redes de Bragg y algoritmos de Inteligencia Artificial

Javier MADRIGAL [(1)], Victor J. RUIZ [(1)], Beatriz DEFEZ [(2)], Jorge GOSÁLBEZ[(1)] y Salvador SALES[(1)]

1. Institute of Telecommunications and Multimedia Applications (iTEAM), Universitat Politècnica de València, Camino de Vera, s/n, 46022,Valencia, Spain
2. [b]Research Center in Graphical Technologies,Universitat Politècnica de València, Camino de Vera, s/n, 46022,Valencia, Spain.

Contact: Javier MADRIGAL (jamadmad@iteam.upv.es).

ABSTRACT:

This work presents an acoustic sensor based on fiber Bragg Gratings for pipeline leak detection. An artificial intelligence algorithm that utilizes autoencoders was implemented for real-time leak detection from the sensor's signals, regardless of the leak's acoustic frequency. Moreover, a mechanical amplification structure was designed and fabricated to enhance sensitivity leak detection, The sensors and the autoencoder-based detection approach were successfully tested on a real pipeline with a small leak. The amplified sensor achieved a 25 dB improvement in autoencoders-based detection performance.

Key words: Fiber Bragg Gratings, Optical Fibre Sensors, Leak detection, Mechanical Amplifiers, Artificial Intelligence, Autoencoders.

1.- Introducción

En las infraestructuras modernas, las tuberías son elementos esenciales que desempeñan un papel fundamental en el transporte de fluidos y gases en aplicaciones cotidianas e industriales. Sin embargo, las tuberías son elementos vulnerables a la aparición fugas producidas por varios factores, como la degradación del material o daños mecánicos entre otros. Estas fugas pueden ocasionar serios problemas de alto impacto ambiental y económico, como por ejemplo desperdicio de agua potable u otros fluidos. Además, pueden suponer graves riesgos para la seguridad y la salud como filtraciones, inundaciones, emisiones de sustancias tóxicas o incendios y explosiones en el caso de fluidos inflamables. Por lo tanto, un sistema de capaz de detectar y localizar fugas de manera rápida es crucial para garantizar la integridad operativa, optimizar la eficiencia, mantener la seguridad y prevenir eventos catastróficos. Existen distintas técnicas para la detección de fugas entre las que se incluyen, la monitorización de caudales, ondas de presión negativas, detección acústica y sensores ópticos distribuidos [1]. Los sensores basados en fibra óptica ofrecen múltiples ventajas sobre los sensores eléctricos derivadas de las propiedades intrínsecas de la fibra. Su ligereza y reducido tamaño permiten la integración de los sensores en tuberías sin afectar a su integridad estructural. Debido a su baja atenuación, permiten la monitorización a largas distancias. Su capacidad de multiplexación permite la medición en varios puntos utilizando una única fibra óptica, lo que reduce enormemente el cableado. Además, la fibra óptica, al ser un medio dieléctrico, es inmune a las interferencias electromagnéticas, es químicamente inerte, presenta bajo riesgo de ignición y no produce chispas, lo que la hace segura para para tuberías situadas en atmosferas explosivas (zonas ATEX) o que transportan líquidos o gases inflamables. En la bibliografía, se

pueden encontrar sensores de fibra óptica para la detección de fugas mediante los cambios de temperatura que se producen en los puntos de fuga [2]. Sin embargo, el tiempo de respuesta de estos sensores podría no ser lo suficientemente rápido como para detectar la fuga en tiempo real en determinadas circunstancias. Una alternativa es la detección por métodos acústicos, que se basan en el análisis del sonido producido por la fuga y permiten detectarla de una forma más rápida.

En este trabajo se propone la detección acústica de fugas mediante sensores en fibra óptica basados en redes de difracción de Bragg (FBGs por sus siglas en inglés) [3]. Una FBG puede detectar las deformaciones dinámicas inducidas por las vibraciones propias que provoca la fuga en una tubería. Sin embargo, la sensibilidad de la FBG está limitada por la rigidez de la fibra, lo que dificulta la detección de fugas muy pequeñas. Para mejorar la sensibilidad, se ha diseñado y fabricado un amplificador mecánico para la FBG basado en una estructura de masa en suspensión [4].

Las vibraciones de la fuga captadas por la FBG se analizan mediante técnicas de procesado de señal para determinar las frecuencias de oscilación. Estos datos se utilizan para obtener una firma acústica de la fuga que permitirá identificarla cuando se produzca. La frecuencia depende, entre otros parámetros de la geometría de la fuga y la tubería. De tal forma que, para detectar una fuga en un entorno real, deberíamos conocer de antemano todas la casuística de fugas y sus frecuencias, lo cual puede ser muy complicado. Para afrontar este problema proponemos el uso de algoritmos de inteligencia artificial basados en autocodificadores. Estos algoritmos se han entrenado con la firma acústica de la tubería en estado normal, sin fugas. Cuando se produce una fuga se altera la firma acústica de la tubería y algoritmo es capaz detectar la fuga independientemente de su frecuencia.

La evaluación de los autocodificadores junto con el sensor FBG amplificado mecánicamente para la detección de fugas se ha llevado a cabo en un entorno de laboratorio empleado un montaje de tubería real. El sensor FBG amplificado mecánicamente se ha comparado con un sensor FBG sin amplificar pegado directamente sobre la tubería con adhesivo epoxi. Ambas FBGs se han fabricado con características similares en fibra óptica monomodo. La fabricación se ha realizado utilizando el método de máscara de fase y un láser continuo de argón doblado frecuencia que emite una longitud de onda de 244 nm [3].

En las siguientes secciones se muestra el diseño del sensor amplificado mecánicamente. A continuación, se describe el montaje experimental de la tubería y el sistema de interrogación del sensor. Después, se describen procesado de señal junto con los autocodificadores empleados para la detección de fugas. Posteriormente se describen las pruebas de evaluación del sensor, se muestran los resultados y, por último, se indican las conclusiones.

2.- Diseño del amplificador mecánico para el sensor FBG

El amplificador mecánico diseñado para aumentar la sensibilidad a las vibraciones del sensor FBG se basa en un esquema de masa de plomo en suspensión (Figura 1).

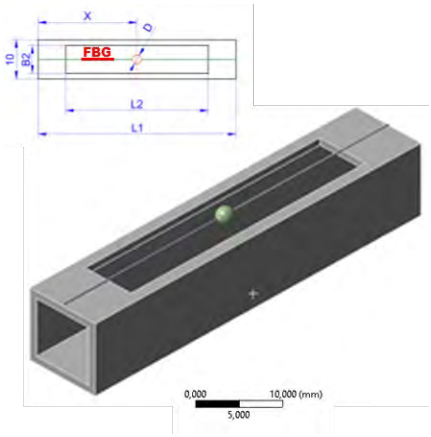

Figura 1: Esquema del amplificador mecánico en 2D y 3D.

El diseño conceptual se ha basado en el análisis de la literatura más relevante [4-9]. Se definió un modelo básico, y a continuación se realizó un estudio paramétrico y optimización mediante un software de elementos finitos

(Ansys® Academic Research Mechanical) para encontrar la mejor configuración geométrica en relación con la frecuencia de amplificación objetivo (7 kHz) y una ganancia significativa de sensibilidad. Los parámetros geométricos considerados se resumen en la Tabla 1.

Tabla 1 Parámetros del diseño del amplificador evaluados en las simulaciones.

Parámetro	***Descripción***	***Valor***
D	*Diámetro de la masa*	*2 mm*
X	*Posición de la masa*	*25 mm*
L1	*Longitud de la base*	*50 mm*
L2	*Longitud de la ventana*	*36 mm*
B2	*Anchura de la ventana*	*7mm*

Para obtener las frecuencias naturales del amplificador se han realizado simulaciones modales entre 0 y 25 kHz. Estos resultados se han utilizado como información de entrada para realizar las simulaciones armónicas y evaluar la respuesta del amplificador bajo una aceleración vertical 1 g entre 0 y 10 kHz. En la Figura 2 se muestra una representación de los modos más significativos.

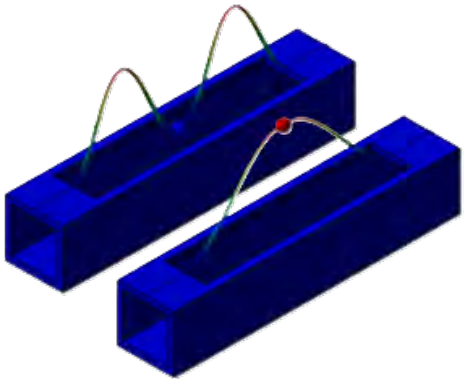

Figura 2: Representación de los modos de vibración más representativos en el rango de 1 a 10 kHz: altas frecuencias (izquierda) y bajas frecuencias (derecha).

En los resultados del análisis armónico se obtuvieron dos frecuencias naturales principales en el rango de la simulación (con variaciones en función del modelo paramétrico): una frecuencia baja, en torno a 0.4 kHz y una frecuencia media en torno a 5 kHz, relacionadas con el primer y tercer modo de vibración de la fibra óptica.

3.-Montaje experimental

Para la evaluación del sensor en el laboratorio, se ha utilizado una tubería conectada a la red de agua del edificio, la cual tiene una fuga (agujero 1mm de diámetro) que se puede cerrar manualmente con un tapón de plástico (Figura 3 y Figura 4).

Figura 3: Fotografía del sensor sobre la tubería con la fuga tapada.

Figura 4: Fotografía del sensor con la fuga activa.

La tubería dispone de una llave de paso de entrada para conectarla y desconectarla de la red de agua. Además, dispone de otra llave de paso en la salida que permite ajustar la presión del circuito. La presión se ha monitorizado mediante un manómetro analógico. En la Figura 5 se puede ver un esquema del montaje. Los dos sensores se han colocado sobre la parte superior de la tubería en la zona donde está el agujero Un sensor FBG se ha pegado en la tubería y al lado se ha colocado sensor FBG amplificado.

Para realizar una interrogación de los sensores FBG a alta velocidad se ha utilizado un

sistema de interrogación basado en amplitud (Figura 5). El sistema está formado por un láser sintonizable y un fotodetector balanceado (Thorlabs PD450) que permite amplificar la señal fotodetectada, y al mismo tiempo, reducir el ruido de intensidad. La salida del láser se divide en dos ramas mediante un acoplador 90:10. El 90% de la potencia se envía al puerto 1 de un circulador óptico, de esta manera podemos recibir la potencia reflejada por la FBG en el puerto 3. El 10% restante de la potencia del láser se envía al fotodetector. La potencia en cada rama se puede ajustar mediante sendos atenuadores ópticos variables. El balanceado de potencia en cada entrada del fotodetector se verifica mediante la medida del voltaje CC en sus salidas monitor.

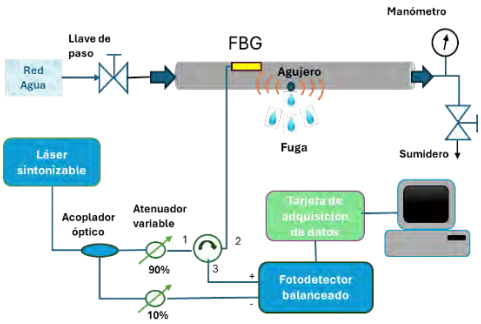

Figura 5. Esquema de la tubería y del sistema de interrogación de los sensores FBG.

Las vibraciones provocan el desplazamiento de la longitud de onda de la FBG, lo que modula la potencia óptica reflejada y, por lo tanto, la señal eléctrica fotodetectada (Figura 6). Para alcanzar la máxima sensibilidad, la longitud de onda del láser se ha sintonizado al punto donde la potencia reflejada de la FBG disminuye 3 dB con respecto a su máximo.

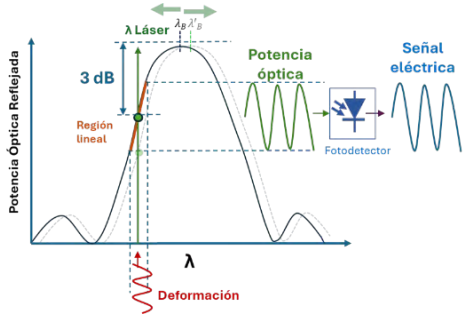

Figura 6: Detección de vibraciones por potencia reflejada en una FBG.

La señal eléctrica se adquiere en tiempo real mediante una tarjeta de adquisición de datos USB conectada a un ordenador.

4.- Procesado de las señales del sensor para la detección de fugas

Una vez adquiridas las señales del sensor FBG, la firma acústica de las vibraciones se ha obtenido mediante un análisis de tiempo-frecuencia (espectrograma) utilizando la transformada de Fourier de tiempo reducido (STFT por sus siglas en inglés). Después, se han procesado los espectrogramas mediante algoritmos de inteligencia artificial basado en autocodificadores [10,11] para detectar la presencia de la fuga. Los autocodificadores son un tipo de red neuronal artificial utilizada para el aprendizaje no supervisado. Su objetivo es aprender representaciones eficientes de los datos de entrada, lo que los hace útiles para la reducción de dimensionalidad o el aprendizaje de características (espacio latente). En esencia, un autocodificador intenta reconstruir una entrada con la mayor fidelidad posible a partir de una representación de menor dimensión.

Para la detección de fugas, previamente se entrena el autocodificador con los espectrogramas obtenidos en una situación sin fugas. Una vez entrenado el autocodificador, los espectrogramas de la señal del sensor se pasan como entrada al autocodificador $X(t_n, f)$, se comparan con los de salida $\hat{X}(t_n, f)$ y se obtiene el error. El error absoluto se calcula como $\varepsilon_{abs} = |X - \hat{X}|$ y el error relativo como:

$$\varepsilon_{rel}(t_n) = 10 \log_{10}\left(\frac{\varepsilon_{abs}(t_n)}{\bar{e}}\right) \qquad \bar{e} = \overline{\varepsilon_{abs}((1{:}t_{NTrain}))} \tag{1}$$

En una situación normal (sin fugas) los espectrogramas de salida serán similares a los de entrada y el error será bajo. Sin embargo, si se sale de la normalidad (se produce una fuga), el autocodificador no será capaz de reconstruir el espectrograma correctamente y el error será alto.

5.- Evaluación de los sensores FBG

La evaluación de los sensores FBG se ha llevado a cabo de forma independiente mediante la realización de fugas de baja intensidad. Primero para el sensor FBG directamente pegado a la tubería (sin amplificación mecánica) y después para el sensor amplificado mecánicamente. Las llaves de paso de la tubería se ajustaron para alcanzar una presión de 1 bar con la fuga tapada. Las señales de los sensores se adquirieron durante 120 s, de los cuales 50 s correspondieron a una situación sin fugas. Posteriormente, la fuga se abrió de forma manual durante 20 s, se cerró 20 s y se volvió a abrir 20 s. Los espectrogramas registrados con cada sensor se muestran en Figura 7 y Figura 8.

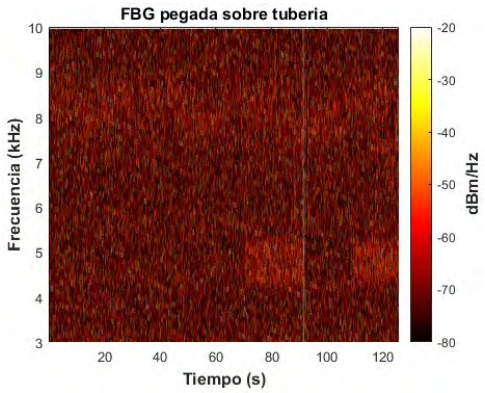

Figura 7: Espectrograma obtenido durante el ensayo de fuga con el sensor pegado directamente sobre la tubería.

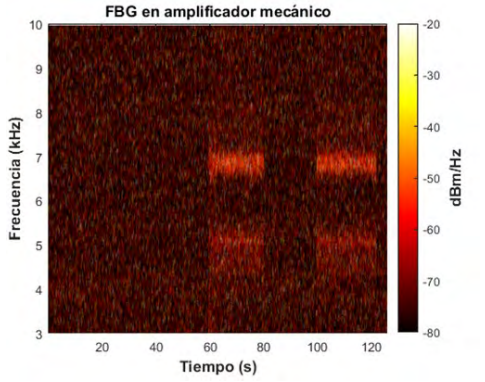

Figura 8: Espectrograma obtenido durante el ensayo de fuga con el sensor amplificado mecánicamente

En el espectrograma obtenido con el sensor pegado a la tubería sin amplificación mecánica se detectó la fuga en un rango de frecuencias entre 4 y 5 kHz. Sin embargo, con el sensor amplificado mecánicamente se detectó alrededor de 5 kHz con una densidad espectral de potencia ligeramente superior. Además, cabe destacar que, con el sensor amplificado, cerca de la frecuencia para la cual se ha diseñado el amplificador mecánico (7 kHz), la fuga se detectó con una densidad espectral de potencia aproximadamente 15 dB mayor que la detectada en 5 kHz con el sensor sin amplificar. Por otro lado, se puede observar que la fuga en cada caso se detecta a diferentes frecuencias. Esto se atribuye a que cada sensor detecta diferentes modos de vibración de la tubería.

En otros casos, si el agujero que causa la fuga tiene otra morfología, las frecuencias a las que se detecta también serán distintas. Esto dificultaría la detección de una fuga simplemente con el espectrograma, ya que en un escenario real, a priori, es difícil conocer el tipo de fuga que se va a producir. Sin embargo, este problema se puede solventar utilizando los autocodificadores propuestos.

Para el caso de los sensores evaluados, en las figuras Figura 9 y Figura 10 se muestra el error relativo de los autocodificadores (previamente entrenados para cada sensor en condiciones sin fugas). Se puede observar que, en ambos casos, la fuga se detecta como un aumento del error relativo del autocodificador. Cabe destacar que en el caso de la FBG amplificada, se alcanza una ganancia en la detección de 25 dB.

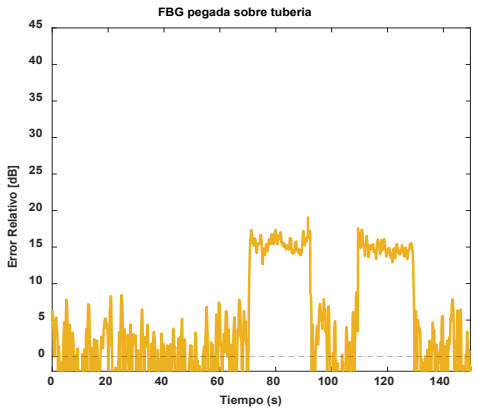

Figura 9: Error relativo a la salida del autocodificador durante el ensayo de fuga para el caso del sensor pegado directamente a la tubería.

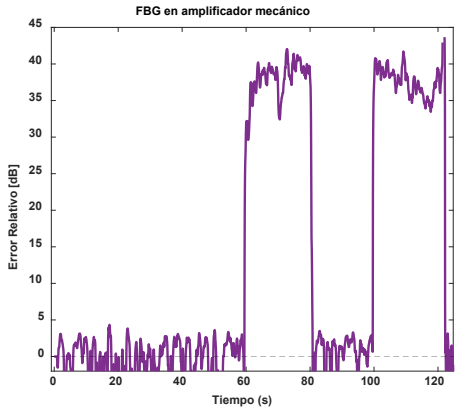

Figura 10: Error relativo a la salida del autocodificador para sensor amplificado mecánicamente.

6.- Conclusiones

En este trabajo se ha demostrado la detección acústica de fugas en tuberías utilizando sensores basados en FBGs y algoritmos de inteligencia artificial basados en autocodificadores. Además, se ha evaluado la posibilidad de aumentar la sensibilidad de detección a ciertas frecuencias mediante un amplificador mecánico. Los sensores, con y sin amplificación, se han evaluado en condiciones de fuga real. En la detección por espectrograma, el sensor amplificado ha mostrado una ganancia de unos 15 dB en la frecuencia de resonancia del amplificador mecánico. En la detección por autocodificadores, la fuga se ha detectado en ambos sensores mediante un aumento en el error relativo. En el caso del sensor amplificado se ha logrado una ganancia de 25 dB.

Agradecimientos: Ayudas a Primeros Proyectos de Investigación (PAID-06-23) y Ayudas (PAID-10-22) del Vicerrectorado de Investigación de la Universitat Politècnica de València, Programa para la Promoción de la investigación científica, el desarrollo tecnológico y la innovación en la Comunitat Valenciana, convocatoria 2023, anexo VII: Subvenciones para la realización de estancias de personal investigador doctor en empresas de la Comunitat Valenciana. Asimismo, por MCIN/AEI/10.13039/501100011033 y por la "Unión Europea", Grant number PID2020-120262GB-I00, INNOFIBER PID2023-152314OB-I00, SMARTMOORING Cetp-2022-00382 / PCI2023-145987-2, la Cátedra Chip Fotónico UPV TSI-069100-2023-0002), PROMETEO 2021/015 y Research Excellency Award financiado por la Generalitat Valenciana.

Referencias

[1] Naga Venkata KARLAPATI, Khan, Faisal KHAN,Quddus NOOR,irza, Saadat MIRZA, Sreeran Vassiraju, "Review and analysis of Pipeline Leak Detection Methods," J Pipeline Sci Eng. **2**(4), 100074 ,2022.

[2] Femi TANIMOLA, David Hill "Distributed fibre optic sensors for pipeline protection," Journal of Natural Gas Science and Engineering 1(4–5), 134–143,2009.

[3] Kenneth O. HILL, Gerald Meltz "Fiber Bragg Grating Technology Fundamentals and overview," JLT. 15(8), 1263–1276,1997.

[4] Tianliang LI, Yuegang TAN, Yi LIU, Yongzhi, QU, Mingyao Liu and Zude ZHOU "A fiber Bragg grating sensing based triaxial vibration sensor," Sensors 15(9), 24214–24229,2015.

[5] Ruiya LI, Yuegang TAN, Yiyang CHEN, Liu HONG, Zude ZHOU. "Investigation of sensitivity enhancing and temperature compensation for fiber Bragg grating (FBG)-based strain sensor." Opt. Fiber Technol., 48,2019.

[6] Luca SCHENATO, Qiangzhou RONG, Zhihua SHAO, Xueguang QUIAO, Alessandro PASUTO, Andrea GALTAROSSA "Highly Sensitive FBG Pressure Sensor Based on a 3D-Printed Transducer. J. Light. Technol, 37(18) ,2019.

[7] Shihao WEN, Qingsong XU, Bin ZI, "Design of a new piezoelectric energy harvester based on compound two-stage force amplification frame." IEEE Sensors Journal, 18(10) ,2018.

[8] Hao WU, Qijing LIN, Feng HAN, Libo ZHAO, Zhuangde JIANG "Design and analysis of high-frequency fiber Bragg grating vibration sensor." Meas. Sci. Technol. , 32(2), 2020.

[9] Zhengyi ZHANG,Chuntong LIU. "Design of vibration sensor based on fiber Bragg grating." Photonic Sensors, 7(4), 2017.

[10] Ian GOODFELLOW, Yoshua BENGIO, Aaron COURVILLE. (2016). Deep Learning. MIT Press.

[11] Geoffrey Hinton, Ruslan SALAKHUTDINOV. "Reducing the dimensionality of data with neural networks". Science, 313(5786), 504-507, 2006.

Dual-comb ranging using densified gain-switched optical frequency combs

Clara QUEVEDO-GALÁN, Antonio PÉREZ-SERRANO, José Manuel G. TIJERO, Ignacio ESQUIVIAS

CEMDATIC- E.T.S.I. Telecomunicación, Universidad Politécnica de Madrid, 28040 Madrid, Spain

Contact: Clara QUEVEDO-GALÁN (clara.quevedo.galan@upm.es).

ABSTRACT:

We present a dual-comb ranging system based on two mutually coherent densified gain-switched optical frequency combs. The system exploits the electrooptic densification technique to reduce the repetition rate of the gain-switched combs in a lossless approach. The low repetition rate characteristic of the generated combs allows to extend the non-ambiguity range of the system, enhancing its suitability for out-of-the-lab environments. We demonstrate the generation of dual optical frequency combs featuring a repetition rate of ~4 MHz enabling free-space interrogation of ranges up to 38 meters in a minimum measurement time of 25.4 ms. We conducted free-space differential ranging and successfully validated the system by measuring a distance of 2 mm with a precision of 46 µm.

Key words: optical frequency comb, dual comb interferometry, gain switching, electrooptic modulation, laser diodes.

1.- Introducción

Los sistemas LIDAR (*light detection and ranging*) permiten medir distancias con gran precisión utilizando fuentes láser, y se han consolidado como una tecnología esencial en diversas industrias como la automoción o la robótica. El avance continuo de estas industrias impulsa el desarrollo de nuevas técnicas LIDAR que puedan satisfacer las crecientes exigencias en términos de precisión, velocidad y coste. Entre estas técnicas, la medida de distancias mediante peines de frecuencia dual (*dual-comb ranging,* DCR*)* ha demostrado ser una solución prometedora que permite realizar medidas con gran precisión utilizando electrónica de bajo ancho de banda y coste reducido [1].

La técnica DCR se basa en el uso de dos peines de frecuencias ópticas (*optical frequency combs*, OFCs) con frecuencias de repetición ligeramente distintas, f_R y $f_R + \delta f_R$ (siendo $\delta f_R \ll f_R$). Uno de los peines interroga la distancia a determinar. El segundo peine, actúa como oscilador local (*local oscillator*, LO). La mezcla de ambos peines en un fotodetector genera un interferograma, cuya fase espectral contiene la información de la distancia interrogada. A través del análisis del interferograma en el dominio de la frecuencia es posible extraer la distancia con alta precisión, pues múltiples líneas espectrales del OFC interrogan de forma simultánea la distancia. La incertidumbre de la medida disminuye a medida que se incrementa el ancho de banda de los peines ópticos.

A pesar de sus ventajas, la técnica DCR presenta un compromiso entre el rango de no ambigüedad (*non-ambiguity range*, NAR) y el tiempo de medida. El NAR es inversamente proporcional a la frecuencia de repetición de

los peines, f_R. Por el contrario, f_R más altas permiten reducir el tiempo de medida, asociadas al aumento de δf_R. Como consecuencia de este compromiso, muchas de las demostraciones existentes se basan en el uso de OFCs con frecuencias de repetición altas (del orden de varios GHz) y priorizan velocidad de medida frente a NAR [2, 3]. Sin embargo, dichos sistemas están limitados a NARs de unos pocos milímetros, por lo que su uso práctico requiere de la implementación de técnicas para romper la ambigüedad.

Existen diferentes técnicas para romper la ambigüedad en sistemas DCR, siendo la más común la realización de una medida adicional intercambiando los roles del LO y el peine interrogador –basada en la explotación del efecto Vernier. No obstante, esta aproximación impide la realización de medidas dinámicas. En la búsqueda de métodos dinámicos para extender el NAR, en la literatura se han propuesto diferentes alternativas. Algunas de ellas están basadas en características específicas de los OFC, como la modulación de intensidad intrínseca [4] o la evolución no lineal de la polarización [5] en ciertos láseres de fibra de modo bloqueado. Sin embargo, dichos sistemas comprometen el enfoque de bajo coste de la técnica DCR ya que dependen de OFCs que requieren de complejos mecanismos de estabilización de la frecuencia de repetición.

En este trabajo, presentamos un sistema DCR basado en láseres de semiconductor que permite extender el NAR a través del uso de peines ópticos con baja frecuencia de repetición. En particular, el sistema se basa en dos OFCs mutuamente coherentes generados mediante la técnica de conmutación de ganancia (*gain-switching*). A través de la densificación de los dos peines ópticos utilizando modulación electroóptica de fase [6], demostramos la generación de dos OFCs con f_R ~4 MHz y δf_R ~40 Hz. Como resultado, el sistema propuesto permitiría interrogar un NAR en espacio libre de 38 metros en tiempos de medida tan rápidos como 25.4 ms. La validación del sistema se realiza a través de medidas de distancia diferenciales que permiten discriminar las posibles diferencias de longitudes ópticas existentes en el montaje experimental.

2.- Montaje experimental

El montaje experimental del sistema DCR propuesto se muestra en la Fig. 1. El extremo de generación de los dos OFCs (interrogador o *probe* y LO) comprende dos peines conmutados en ganancia densificados [7]. Las frecuencias de repetición del peine interrogador y del LO son $f_{R1} = f_R =$ 3.9369685 MHz y $f_{R2} = f_R + \delta f_R =$ 3.9370079 MHz, respectivamente. La coherencia mutua de los dos peines ópticos está proporcionada por un láser maestro operando en continua que inyecta los dos OFCs.

El sistema DCR sigue una configuración asimétrica, permitiendo la extracción de la información a partir del análisis de la fase del interferograma. Los interferogramas se detectan con fotodiodos balanceados (*balanced photodiodes* BPD); de esta forma, se recupera únicamente la componente de batido de la señal. Además, el montaje incluye dos fotodiodos: un fotodiodo que detecta la señal óptica que contiene la distancia interrogada (denominado Meas. BPD en la Fig. 1) y un fotodiodo de calibración (Cal. BPD). Este último permite compensar derivas en el sistema.

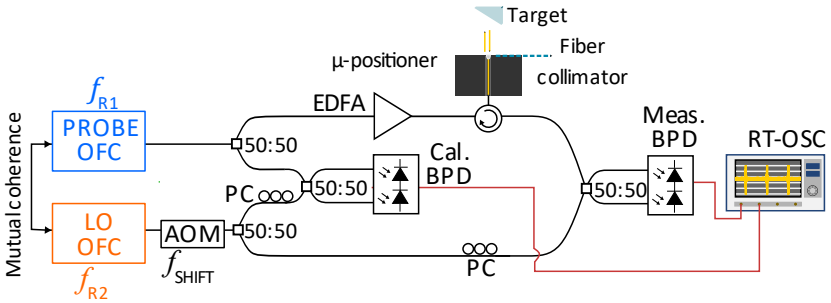

Fig. 1: Montaje experimental del sistema dual-comb ranging propuesto. AOM: acousto-optic modulator; EDFA: erbium-doped fiber amplifier, PC: polarization controller; Cal. BPD: calibration balanced photodiode; Meas. BPD: measurement balanced photodiode; RT-OSC: real-time oscilloscope.

La validación del sistema DCR se ha realizado mediante una medida en espacio libre. El peine de interrogación se dirige hacia el blanco (espejo) a través de un circulador óptico. En el puerto 2 del circulador la luz colimada se envía hacia el blanco. La fibra que lanza la señal al blanco está montada sobre un microposicionador que permite ajustar de forma manual la distancia recorrida por la luz hacia el blanco. Este microposicionador permite una variación máxima de 8 mm en pasos de 500 μm, con una resolución de 0.5 μm. La luz reflejada por el espejo es recogida por la misma fibra y redirigida al puerto 3 del circulador. La señal reflejada del peine de interrogación se combina con el LO y finalmente se detecta en el fotodetector de medida. En una adquisición consecutiva, se configura una nueva posición del microposicionador para realizar una medida diferencial de distancia. Como resultado, la distancia medida corresponde a la diferencia de distancias configuradas con el microposicionador. La limitación del recorrido del microposicionador impide la validación del NAR del sistema en espacio libre. Para evaluar la capacidad del sistema se han realizado medidas en fibra en las que se ha interrogado una fibra óptica de longitud conocida del orden del NAR, que no se incluyen en esta comunicación.

Adicionalmente, el peine LO se desplaza en frecuencia (f_{SHIFT} = 80 MHz) para asegurar un proceso de conversión del dominio óptico al dominio eléctrico sin ambigüedad. Además, el montaje incluye controladores de polarización para maximizar el acoplamiento entre el peine de interrogación y el LO. Las dos señales a la salida de los fotodetectores balanceados se digitalizan mediante un osciloscopio en tiempo real y se procesan *offline*.

3.- Resultados experimentales

3.1.- Espectro óptico del OFC

El peine interrogador, antes de ser lanzado al blanco, es amplificado con un amplificador de fibra dopada con Erbio (EDFA). La potencia óptica media tras la etapa de amplificación es de 1 mW. La Fig. 2 muestra el espectro óptico del OFC interrogador medido con un analizador de espectros ópticos de alta resolución (Aragon Photonics BOSA 400 C+L). La resolución del BOSA (10 MHz) no permite resolver las líneas espectrales del peine; no obstante, el OFC generado es un espectro coherente con líneas bien definidas, tal y como se demostrará a través del peine dual de radiofrecuencia (RF).

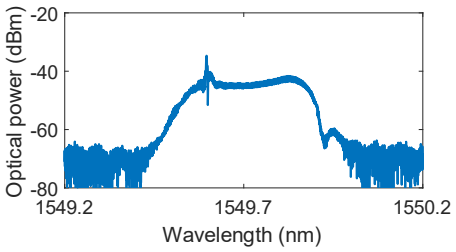

Fig. 2. OFC interrogador medido con un analizador de espectros ópticos (resolución 10 MHz).

Las condiciones de generación del OFC seleccionadas resultan en un espectro plano

cuyo ancho de banda a 10 dB ($\Delta\nu_{10dB}$) es de 48 GHz (12000 líneas espaciadas 4 MHz).

3.2.- Generación del peine dual de RF

Tras el batido de los dos OFCs en el fotodetector se obtiene el interferograma, que comprende ráfagas o secuencias de interferogramas cuyo periodo es $\delta f_R^{-1} = 25.4$ ms. Para la obtención de los resultados se han procesado trazas de duración 248 ms, que contienen 10 secuencias de interferogramas. Pese a que el tiempo mínimo de adquisición corresponde a la duración de una sola ráfaga, el procesado de una traza con varios interferogramas permite mejorar la relación señal a ruido (SNR) de la medida.

El módulo de la transformada de Fourier de la secuencia periódica de interferogramas revela el espectro del peine dual de RF mostrado en la Fig. 3 (a). Dicho espectro corresponde a la señal detectada con el fotodiodo de medida para una de las posiciones del microposicionador. Tal y como se puede observar en la Fig. 3 (b), el peine dual está formado por líneas bien definidas en frecuencia. El ancho de cada línea es mucho menor que $\delta f_R = 39.37$ Hz, lo que demuestra la coherencia mutua de los dos peines ópticos.

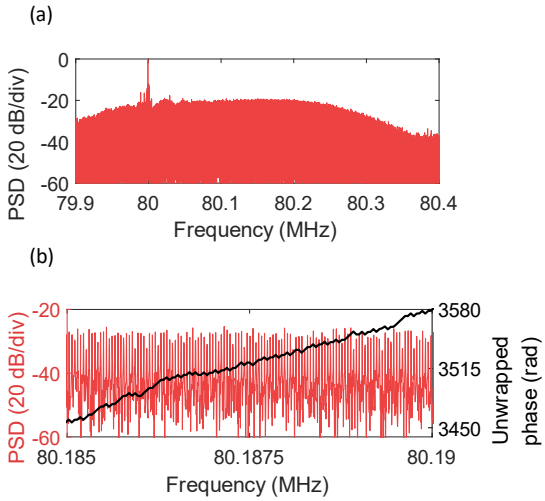

Fig. 3. (a) Espectro del peine dual de RF obtenido. (b) Vista ampliada del espectro de RF (rojo) y fase espectral desdoblada (negro).

La distancia interrogada se extrae del análisis de la fase espectral de 5080 líneas del peine dual de RF, comprendidas entre 80.05 MHz y 80.25 MHz. La región seleccionada para el análisis se caracteriza por una gran planitud espectral. Además, no incluye el tono correspondiente a la inyección óptica debido a inestabilidades observadas en esa región. La Fig. 3 (b) muestra también la evolución de la fase espectral para diferentes líneas del peine dual. Como se puede observar en la figura, la fase desdoblada sigue una evolución lineal con los tonos del peine, en concordancia con los resultados esperados.

3.3.- Extracción de la distancia diferencial

La validación del sistema se ha realizado a través de una medida de distancia diferencial en espacio libre de 2 mm. En una primera medida, se adquieren dos interferogramas (calibración y medida). A continuación, se varía de forma manual el camino recorrido por la señal hasta el blanco de forma que la distancia relativa entre las dos medidas sea de 2 mm, y se adquieren los dos interferogramas correspondientes. Para cada distancia, se sustrae del interferograma de medida la fase espectral del interferograma de calibración. Finalmente, la señal resultante de la diferencia de fases espectrales de las dos adquisiciones correspondientes a dos distancias d_1 y d_2 contiene la información de la distancia $d = d_2 - d_1 = 2$ mm.

La Fig. 4 muestra la fase espectral desdoblada $\Delta\Phi$ calculada como la diferencia de fases espectrales correspondientes a las distancias d_1 y d_2. Como se puede observar, en este caso también sigue una evolución lineal con los tonos del peine. La distancia se extrae de la pendiente de $\Delta\Phi$ como $d = b\frac{c}{4\pi n f_R}$, donde b es la pendiente en rad/Hz, y c/n es la velocidad de grupo.

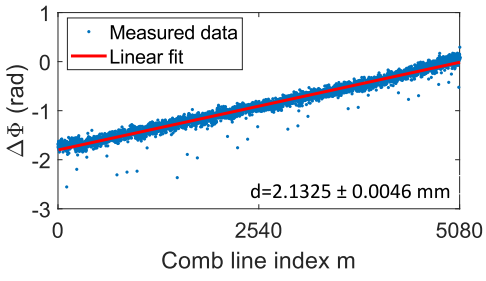

Fig. 4. Fase espectral desdoblada que contiene la información de la distancia interrogada (azul) y ajuste lineal (rojo).

Para obtener la distancia se ha realizado un ajuste lineal de los datos medidos, representado con una línea roja en la Fig. 4. La pendiente del ajuste lineal resulta en una distancia de 2.1325 mm. El error de la distancia, extraído a partir del error de la pendiente, es de 4.6 µm. Este error indica la precisión del sistema y, en sistemas donde la fuente predominante de ruido es ruido blanco, mejora con promediado espectral.

4.- Conclusiones

Se ha demostrado un sistema de medida de distancias basado en peines duales generados con láseres de semiconductor, capaz de incrementar el rango de no ambigüedad de los sistemas DCR existentes mediante el uso de OFCs con bajas tasas de repetición. A través de la densificación electroóptica de dos OFCs conmutados en ganancia, hemos generado dos peines ópticos con frecuencias de repetición de 4 MHz, permitiendo la medida dinámica de distancias en el rango de decenas de metros. El sistema se ha validado mediante una medida diferencial de distancias en espacio libre de 2 mm, obteniendo una precisión de 4.6 µm.

Además de las ventajas inherentes a la técnica dual-comb, el sistema propuesto se beneficia de las características de los láseres de semiconductor y podría integrarse monolíticamente en un chip fotónico. La capacidad de medir distancias de decenas de metros sin necesidad de emplear técnicas de desambiguación permite la operación en tiempo real del sistema (dentro de su tiempo mínimo de adquisición) y amplía su aplicación en entornos fuera del laboratorio.

Agradecimientos: Este trabajo es parte de los proyectos PID2021-1234590B-C21 *y* TED2021-131957B-100 financiados por MCIN/ AEI/10.13039/501100011033 y por la Unión Europea NextGenerationEU/PRTR y "FEDER Una manera de hacer Europa"

Referencias

[1] I. Coddington, W. C. Swann, L. Nenadovic, N. R. Newbury, *"Rapid and precise absolute distance measurements at long range",* Nat. Photonics 3, 351–356, 2009.

[2] M.-G. Suh, K. J. Vahala, *"Soliton microcomb range measurement"*, Science 359, 884–887, 2018.

[3] P. Trocha, M. Karpov, D. Ganin, M. H. P. Pfeiffer, A. Kordts, S. Wolf, J. Krockenberger, P. Marin-Palomo, C. Weimann, S. Randel, W. Freude, T. J. Kippenberg, C. Koos, "*Ultrafast optical ranging using microresonator soliton frequency combs"*, Science 359, 887–891, 2018.

[4] J. Fellinger, G. Winkler, P. E. C. Aldia, A. S. Mayer, V. Shumakova, L. W. Perner, V. F. Pecile, T. Martynkien, P. Mergo, G. Sobon, O. H. Heckl, "*Simple approach for extending the ambiguity-free range of dual-comb ranging"*, Opt. Lett. 46, 3677–368, 2021.

[5] X. Shao, H. Han, Y. Yan, J. Ma, C. Li, Z. Wei, *"Dual-comb interchanging absolute distance measurement with non-ambiguity range extension"*, Appl. Phys. Lett. 124, 171103, 2024.

[6] A. Rosado, M. R. Fernández-Ruiz, P. Corredera, J. M. G. Tijero, I. Esquivias, *"High-density and broadband optical frequency combs generated by pseudo-random phase modulation of optically injected gain-switched semiconductor lasers"*, Opt. Laser Technol. 163, 2023.

[7] C. Quevedo-Galán, A. Rosado, A. Pérez-Serrano, J. M. G. Tijero, I. Esquivias, *"Dual-comb spectroscopy with enhanced resolution by pseudo-random phase modulation of gain-switched optical pulses"*, J. Lightwave Technol. 42, 3954–3962, 2024.

Forward Stimulated Brillouin Scattering in Optical Fibers under Hydrogen Diffusion

Aleksander PATERNO [1,3], Carlos ALVAREZ-OCAMPO [1], Martina DELGADO-PINAR[1,2], Antonio DIEZ-CREMADES[1,2], José L. CRUZ[1,2], Miguel V. ANDRÉS[1,2]

1. Laboratory of Fiber Optics, ICMUV, Universitat de València, Dr Moliner 50, Burjassot, Spain
2. Departament de Física Aplicada y Electromagnetisme, Universitat de València, Dr Moliner 50, Burjassot, Spain
3. Department of Electrical Engineering, Center for Science and Technology (CCT), Santa Catarina State University, Rua Paulo Malshitzky, 200 – Zona Industrial Norte - 89.219-710 Joinville - Brazil

Contact: Aleksander PATERNO (aleksander.paterno@udesc.br).

ABSTRACT:

This study explores the use of the optomechanical interaction of forward-stimulated Brillouin scattering to investigate the effect on the elastic properties of optical fibers during hydrogen diffusion. The method employs a pump laser to excite acoustic modes and a probe laser to interrogate these modes. Torsional-radial acoustic modes are excited and detected in single-mode optical fibers. The experiment monitors resonance frequency shifts over time during hydrogen loading and outdiffusion phases. The results indicate distinct diffusion time constants for different torsional-radial mode families, suggesting multiple diffusion mechanisms. The analysis of resonance frequencies provides insight into hydrogen-induced mechanical changes in optical fibers.

Key words: Forward-stimulated Brillouin scattering, hydrogen diffusion, optical fiber sensors, optoacoustics, optomechanics.

1.- Introduction

Techniques based on forward-stimulated Brillouin scattering (FSBS) in optical fibers have been employed to sense several parameters by tracking the resonance frequencies of transverse acoustic resonant modes [1], as in monitoring the acoustic impedance of the surrounding medium of an optical fiber [2, 3], and to sense mechanical strain and temperature [4]. In previous studies, while operating as a backward Brillouin scattering-based sensor for strain and temperature, it was observed that the measured values were strongly affected by hydrogen diffusion [5], as the Brillouin gain was influenced by the presence of hydrogen. This effect has also been exploited to shape backward Brillouin gain profiles in fibers exposed to ultraviolet radiation, enabling customized profiles for optical communication applications [6].

Measuring hydrogen diffusion in optical fibers is relevant due to its impact on the refractive index, which affects applications in sensing and telecommunications [7, 8]. Some reported techniques to investigate hydrogen diffusion into optical fibers use long fibers and others use methods based on interferometry [7, 9, 10], to name a few. None of these techniques assess on the elastic or mechanical properties of the fiber, focusing mainly on the evaluation of refractive index changes [11].

Based on this, the study aims to provide a contribution on that issue through optomechanic techniques, utilizing the properties of FSBS-stimulated transverse

acoustic mode resonances of the optical fiber, which resonance frequency depends on the elastic properties of the fiber.

In single-mode optical fiber, two families of transverse acoustic mode resonances can be excited by FSBS, i. e., pure radial modes $R_{0,m}$ and torsional-radial (TR) acoustic modes of azimuthal order 2, $TR_{2,m}$ with *m* representing mode azimuthal order. Both modes provide a novel platform for studying optomechanical interactions and diffusion dynamics in SMFs. $TR_{2,m}$ modes can be categorized into $TR_{2,m}^{(1)}$ and $TR_{2,m}^{(2)}$, whose displacement field is predominantly azimuthal and radial, respectively. In this work, hydrogen diffusion processes are analized and their interaction with the fiber properties is based on the use of $TR_{2,m}$ modes.

Given this background, which highlights the potential of FSBS for measuring the mechanical characteristics of optical fibers, this study addresses the investigation of the elastic properties of optical fibers subjected to hydrogen diffusion.

2.- Methodology

The experiment was conducted using a setup designed to excite and detect optically torsional-radial ($TR_{2,m}$) acoustic modes in single-mode optical fibers (SMF). The experimental setup, illustrated in Fig. 1, includes a pulsed laser source (1064 nm, 750 ps, 19 kHz repetition rate, 140 mW average pump power) for TR mode excitation along an uncladded fiber section under test (FUT), a copropagating continuous-wave (CW) probe signal, and polarization control elements for optimal mode generation and detection. The pulsed laser induced acoustic oscillations via FSBS in the FUT. The oscillation of $TR_{2,m}$ acoustic modes modulates the birefringence of the FUT, resulting in the modulation of the CW probe signal polarization. The polarization modulation of the probe signal was converted into intensity modulation by a linear polarizer. Probe laser operated at 1550 nm with a power set at 5mW and linewidth of 10 kHz, having its state of polarization adjusted by a fiber polarizer, as shown in Fig. 1. The pump laser signal had an initial linear horizontal polarization, adjusted by waveplates to minimize radial mode contribution and ensure selective $TR_{2,m}$ mode detection. The radio-frequency (RF) spectrum of the probe signal contains a series of peaks, each peak is caused by the oscillation of a torsional radial mode. An example of RF spectrum recorded is shown in Fig. 2.

For each acoustic mode at each measurement, the resonance frequency was obtained using a Breit-Wigner-Fano function to fit the individual spectra recorded in the electronic spectrum analyzer (ESA). By this method, the uncertainty of the resonance frequency values was below 100 Hz,

The FUT was introduced into a sealed vessel in which a pressure of 50 bar H_2 was applied for loading. Outdiffusion measurements were performed at atmospheric pressure. The vessel was placed inside a temperature controlled chamber to keep the temperature constant (23 ºC) during the whole measurement.

The shift of the different peaks in the RF spectrum were measured during H_2 loading and outdiffusion processes to characterize hydrogen diffusion dynamics and determine time constants.

Measurements were conducted over 25 days, covering both the hydrogen loading phase and the fiber outgassing process. For each data point collected, the spectrum of 12 acoustic modes were recorded.

The hydrogen concentration dynamics inside the fiber can be described by the normalized concentration of hydrogen, $c(\rho,\tau)$, which is given by [7]:

$$c(\rho,\tau) = 1 - 2\sum_{s=1}^{\infty} exp(-\beta_s^2\tau)\left(\frac{J_0(\rho\beta_s)}{\beta_s J_1(\beta_s)}\right) \quad (1)$$

where $\rho = r/a$ is the normalized radius, r is the radial coordinate, a the fiber radius, $\tau = D \cdot t/a^2$ is the normalized time and D is the diffusivity constant, β_S are the roots of the first-order, zero-type Bessel function, $J_0(\beta_S) = 0$. For outgassing, the dynamics of the concentration reduction in the fiber has similar exponential dependencies [7] as seen in Eq. (2).

$$c(\rho,\tau)=\sum_{s=1}^{\infty}\exp\left(-\zeta_s^2\tau\right)\frac{2AJ_0(\rho\zeta_s)}{(\zeta_s^2+A^2)J_0(\zeta_s)} \quad (2)$$

Where ζ_s are the roots of the equation $AJ_0(\zeta_s)=\zeta_s J_1(\zeta_s)$, $A=ah/D$ and h is the gas-phase mass transfer coefficient.

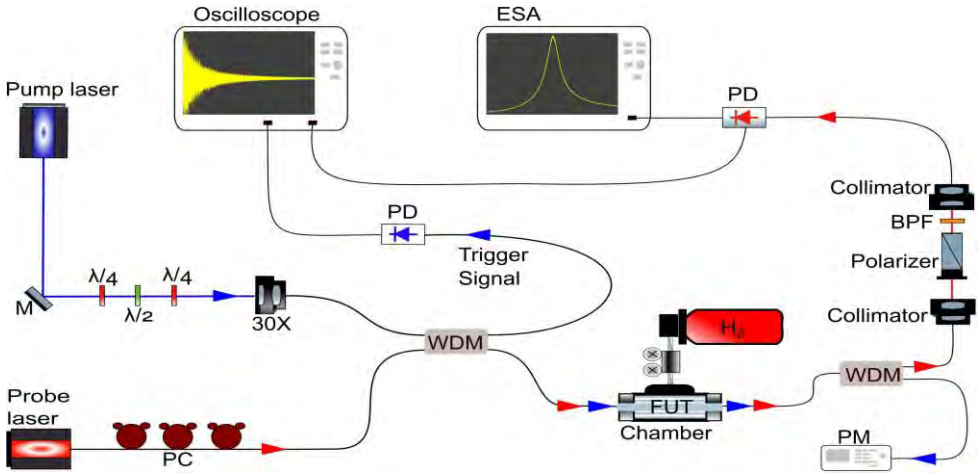

Fig. 1: Experimental setup illustrating pump and probe laser beams interacting in the hydrogen gas chamber (H_2) with the fiber under test (FUT). The setup includes an oscilloscope (OSC) and electrical spectrum analyzer (ESA) for signal detection, photodiodes (PD) also for triggering OSC, collimators for beam alignment, a bandpass filter (BPF) to remove the residual pump signal, fiber polarizers for polarization control, a 30X objective for coupling the pump signal to the fiber, a wavelength division multiplexer (WDM), a Glen Thompson polarizer, and a power meter (PM). Optical paths for pump (blue lines) and probe (red lines) lasers, mirrors (M), and waveplates (λ/4 and λ/2) are shown.

3.- RESULTS AND DISCUSSION

Figure 3 shows the resonance frequency of a dilatational-type and a shear-type $TR_{2,m}$ modes. The dilatational-type modes, $TR_{2,m}^{(1)}$, are associated mainly with radial displacements, leading to volumetric expansion and contraction of the fiber cross-section. In contrast, shear-type modes, $TR_{2,m}^{(2)}$, involve mainly azimuthal displacements, representing a torsional motion around the fiber axis. The results shown in Fig. 3 highlight the effect of hydrogen concentration on the fiber's elastic properties during diffusion process for two modes.

Distinct diffusion time constants for each mode family were found. For the H_2-loading process, the $TR_{(2,5)}^{(1)}$ mode showed time constants of t_1=0,40 ± 0,32 days and t_2=3,71±0,48 days, while the $TR_{(2,5)}^{(2)}$ mode showed t_1=3,42±0.22 days in this case a single exponential properly represented experimental data. For the outgassing, $TR_{(2,5)}^{(1)}$ mode had time constants of t_1= 1,89±0,19 days with a single exponential, and the $TR_{(2,5)}^{(2)}$ mode showed t_1=0,17±0,12 days and t_2=5,57±1,34 days with a double exponential.

These values indicate the presence of at least two diffusion mechanisms with different rates, and in the outgassing behavior with one fitting time constant.

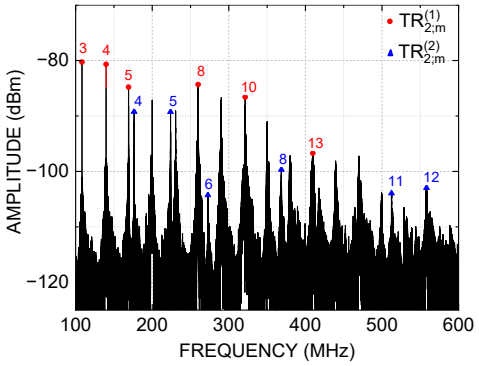

Fig. 2: FFT of photodetected signal. Resonance frequencies monitored during the experiment for $TR_{(2,m)}$ modes are shown: shear (red circles) and dilatational (blue triangles) with corresponding mode order m.

From the concentration model in Eq. (1), it would be expected the exponential behavior

during changes in resonance frequency for different modes. One must first observe that the experimental curves in Fig. 3 have some oscillation around the fitted curve.

This variation suggests non-uniformity in the diffusion process, with hydrogen potentially reacting with the silica network or encountering voids. Initially, resonance frequency shifts appear to correlate with normalized hydrogen concentration, exhibiting exponential behavior (mainly double exponential during diffusion). The initial values of resonance frequencies before hydrogen loading (169.096 MHz and 223.886 MHz) are not shown in the graphs. It is worth pointing out that they slightly differ from those measured after outgassing.

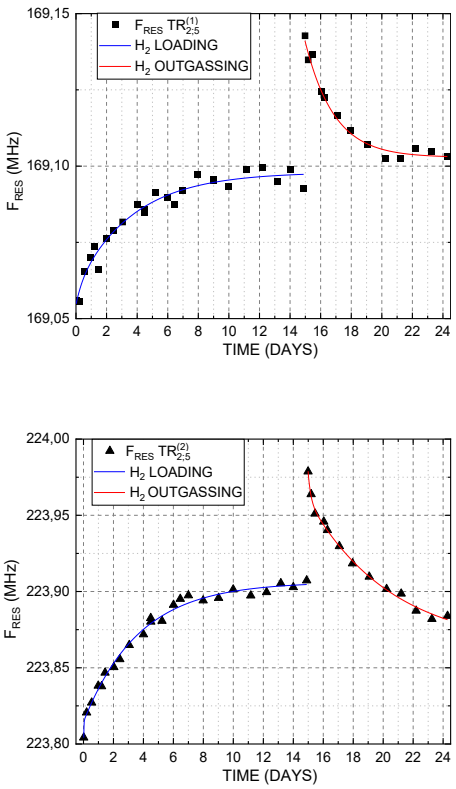

Fig. 3: Resonance frequency F_{RES} dynamics for two selected modes during hydrogen loading (14 days) F_{RES} $TR_{2,m}(t)$ *and outgassing (10 days)* F'_{RES} $TR_{2,m}(t)$ *at 50 bars and 23°C: (top) F_{RES} for shear mode $TR^{(1)}{}_{2,5}$, (bottom) for dilatational $TR^{(2)}{}_{2,5}$.*

This deviation may be due to residual hydrogen reacting within the silica network or structural modifications of the fiber glass after the pressurization. For the evaluation of individual modes, representation with double exponentials is associated with initial diffusion phases, where high concentration gradients drive rapid changes in material properties.

Conversely, whenever calculated, the slower time constants correspond to deeper diffusion into the fiber core and cladding, where equilibrium is reached over extended periods. The double-exponential behavior agrees with predictions of diffusion involving multiple spatial components of concentration, as shown in Eq. (1) and (2).

During the loading period, FUT is maintained at a pressure of 50bars. Ending the loading phase, the gas in the chamber is released and the initial effect is a positive shift in all resonance frequencies, as seen after 15 days in Fig. 3, related to the negative sensitivity of the mode resonant frequency with an increase in pressure, in other words, a reduction in fiber pressure would produce a positive shift in the mode resonance frequencies.

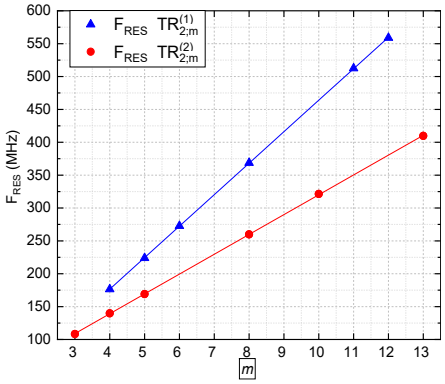

Fig. 4: Experimental resonance frequencies F_{RES} for torsional-radial modes $TR_{(2,m)}$, dilatational and shear types versus the azimuthal order m at 23 °C, and measured after the final loading period of 14 days and before outgassing, and the corresponding fits.

Analysis of the resonance frequencies of all modes together enables direct estimation of normalized dilatational or shear acoustic velocities as well as their evolution under hydrogen diffusion. For illustration purposes, the lines fitted from a set of 12 resonance

frequencies points, as selected in Fig. 2, as a function of mode order, after 14 days of hydrogen loading, are depicted in Fig. 4. In this case, the angular coefficient of the lines would allow the calculation of the shear and longitudinal speed, respectively from the shear and dilatational set of resonance frequencies.

Fitted lines are shown in Fig. 4. while each point was obtained from a set of resonances calculated from the acquired spectrum, as illustrated by the window centered at the peak points in the presented spectrum in Fig. 2. The angular coefficient for the shear sound velocity calculated for a set of 12 resonant frequencies after 14 days was $V_S/d=30.15528\pm0.10275\times10^6 s^{-1}$, with $d=125\mu m$ the diameter of the standard single mode fiber used. For the longitudinal velocity, one obtains $V_L/d = 47.90351\pm0.09346\times10^6 s^{-1}$, resulting, respectively in the velocities of V_S = 3769.41 ± 12.84 m/s and V_L= 5987.94 ± 11.68 m/s. This would indicate the procedures to evaluate the sound speed in the hydrogenated fiber based on the selected resonance frequencies from the acquired spectrum.

Table 1: Fitted models for resonant frequency shifts in silica SMF28 fiber under H_2 exposure (50 bar) during loading and outgassing at ambient pressure, both at 23°C

Mode	***Phase***	***Model***
$TR_{2,m}^{(1)}$	*Loading*	*Eq. (3)*
	Outgassing	*Eq. (4)*
$TR_{2,m}^{(2)}$	*Loading*	*Eq. (5)*
	Outgassing	*Eq. (6)*

The resonant frequency shifts in the SMF28 silica fiber under 50 bar H_2 pressure at 23°C for 14 days reveal distinct mechanical responses for shear and dilatational modes, and their models are organized as indicated in Table 1. A) For the shear mode during hydrogen loading, one must consider the pre-loading value (F_0=169.098 MHz), the frequency shift follows a double exponential function and Eq. (3) presents the model used to fit the resonant frequency of a shear mode behavior during the H_2 loading period:

$$F_{RES}\,TR_{2,m}^{(1)}(t)=F_0+A_1e^{(-t/t_1)}+A_2\,e^{(-t/t_2)} \qquad (3)$$

with t_1=0.41±0.32 days, t_2=3.71±0.48 days, having a two-stage diffusion mechanism: an initial rapid phase (surface adsorption) and a slower phase (diffusion deep into the network). The calculated negative amplitudes A_1=−0.003 MHz and A_2=−0.035 MHz align with the fiber's negative pressure sensitivity, where the applied 50-bar H_2 pressure induces compressive strain, shifting the frequency to lower values[4].

B) During shear mode outgassing, the process transitions to a single exponential decay, as in Eq.(4):

$$F'_{RES}\,TR_{2,m}^{(1)}(t)=F_0'+A_3\,e^{(-t/t_3)} \qquad (4)$$

with t_3=1.89±0.19 days, and the resonance frequency is related to a homogeneous release of hydrogen from the fiber matrix. The positive amplitude (A_3=0.040 MHz) signifies partial recovery of the original frequency, though the baseline (F_0'=169.103 MHz) remains slightly elevated compared to the pre-loading value, suggesting residual hydrogen retention.

C) For the dilatational mode during loading, the exponential growth model as in Eq. (5):

$$F_{RES}\,TR_{2,m}^{(2)}(t)=F_0''+A_4\,e^{(-t/t_4)} \qquad (5)$$

with t_4 = 3.43±0.23 days reveals a relatively more delayed saturation effect having F_0''= 223.905 ± 0.002 MHz.

D) During outgassing, the dilatational mode exhibits a double exponential, as in Eq. (6):

$$F'_{RES}\,TR_{2,m}^{(2)}(t)=F_0'''+A_1e^{(-t/t_5)}+A_2e^{(-t/t_6)} \qquad (6)$$

Time constants t_5=0.18±0.06 days and t_6=5.57±0.30 days, indicates two hydrogen populations: weakly bound H^+/H_2 with a fast release, t_5, and deeply trapped hydrogen (slow release, t_6). The positive amplitudes A_1=0.014 MHz and A_2=0.096 MHz suggest that hydrogen release partially restores the frequency, and full recovery is hindered by persistent network distortions, with F_0'''= 223.863 ± 0.001 MHz.

The quality of fits (R^2>0.95) and low residuals ($\chi_{red}^2 \approx 10^{-6}$) confirm the models' validity. The observed differences between shear and dilatational modes arise from their distinct strain dependencies: shear modes are governed by transverse stress, while dilatational modes respond to volumetric changes. These results underscore the anisotropic nature of hydrogen diffusion in silica fibers.

4.- Conclusion

This study emphasizes the value of acousto-optic techniques to investigate elastic properties of optical fibers. We have taken advantage of FSBS for monitoring the effects of hydrogen diffusion in the elastic properties of optical fibers. This method allowed the evaluation of the fiber's elastic parameters, such as longitudinal and shear sound velocities from resonance frequencies of acoustic modes, in the studied case and revealing some aspects of the behavior of hydrogen diffusion dynamics. The study provides insight into hydrogen-induced mechanical changes.

Acknowledgements:

This work has been partially funded by Horizon 2020 Framework Programme (H2020-MSCA-RISE-2019-872049); Generalitat Valenciana (CIPROM/2022/30); Ministerio de Ciencia, Innovación y Universidades (CNS2023-145717, PID2023-146725OB-I00).

References

[1] L. A. Sánchez, A. Díez, J. L. Cruz, and M. V. Andrés, "*Recent advances in forward Brillouin scattering: Sensor applications*," Sensors, vol. 23, no. 1, 2023.

[2] D. M. Chow and L. Thévenaz, "*Forward Brillouin scattering acoustic impedance sensor using thin polyimide-coated fiber*," Opt. Lett., vol. 43, no. 21, pp. 5467–5470, Nov 2018.

[3] H. H. Diamandi, Y. London, G. Bashan, and A. Zadok, "*Distributed opto-mechanical analysis of liquids outside standard fibers coated with polyimide*," APL Photonics, vol. 4, no. 1, p. 016105, 01 2019.

[4] M. Zhu, Y. Lu, Z. Zhang, P. Liu, and W. Zhang, "*High accuracy pressure and temperature simultaneous measurement based on forward Brillouin scattering in highly nonlinear fiber*," Opt. Fiber Technol., vol. 84, p. 103741, 2024.

[5] S. Delepine-Lesoille, J. Bertrand, L. Lablonde, and X. Pheron, "*Distributed hydrogen sensing with Brillouin scattering in optical fibers*," IEEE Photonics Technol. Lett., vol. 24, no. 17, pp. 1475–1477, 2012.

[6] F. Kong and L. Dong, "*Precise tailoring of acoustic velocity in optical fibers by hydrogenation and UV exposure*," Opt. Express, vol. 20, no. 25, pp. 27 810–27 819, Dec 2012.

[7] P. L. Swart, A. A. Chtcherbakov, W. L. Joubert, M.G. Shlyagin, "*Study of the pressure dependence of hydrogen diffusion in optical fiber by an interferometric technique*," Opt. Comm., vol. 217, no. 1–6, 2003, pp. 189–196.

[8] G. Meltz, W. W. Morey, and W. H. Glenn, "*Formation of Bragg gratings in optical fibers by a transverse holographic method,*" Opt. Lett., vol. 14, no. 15, pp. 823–825, 1989.

[9] K. Hayashi, A. Hongo, M. Nishimura, M. Ieda, and S. Tsujikawa, "*Measurement of the diffusion constant of hydrogen in silica optical fibers*," J. Appl. Phys., vol. 102, no. 7, p. 073108, 2007.

[10] G. Brochu, S. LaRochelle, and N. Ayotte, "*Dynamics of hydrogen diffusion as a key component of the photosensitivity response of hydrogen- loaded optical fibers*," J. Lightwave Technol., vol. 27, no. 15, pp. 3123–3134, 2009.

[11] L. B. Fu et al., "*Ultraviolet-initiated reactions of h with germanosilicate fibers*," Opt. Lett., vol. 25, no. 8, pp. 527–529, 2000.

[12] L. A. Sánchez, A. Díez, J. L. Cruz, and M. V. Andrés, "*Strain and temperature measurement discrimination with forward Brillouin scattering in optical fibers*," Opt. Express, vol. 30, no. 9, pp. 14384–14392, Apr 2022.

Microwave Frequency OTDR for High Strain-rate Sensing

Y. REN*(1), P. J. VIDAL-MORENO (1), M. R. FERNÁNDEZ-RUIZ (1), S. MARTIN-LOPEZ (1), L. COSTA (2), Z. ZHAN (2), M. GONZALEZ-HERRAEZ (1)

1. GRIFO - Sensors and Photonic Technologies, Universidad de Alcalá (UAH), Associate Unit to CSIC by Institute of Optics, 28805 Alcalá de Henares, Spain.
2. Seismological Laboratory, California Institute of Technology, 1200 E. California Boulevard, Pasadena, CA USA 91125-2100.

Contact: Yan REN (yan.ren@uah.es).

ABSTRACT:

Distributed acoustic sensing (DAS) systems have attracted significant attention from seismology. Unfortunately, conventional DAS systems are limited to measuring small strain rates, which limits their use to the measurement of relatively small events. This makes DAS systems appealing for scientific studies but not for early warning systems which are intended for alerting the population. In this paper, a novel DAS system based on microwave frequency OTDR with high saturation strain sensing ability is formulated and demonstrated. The system employs radiofrequency modulation on the probe pulse. A proof of principle experiment with an external perturbation of a few microstrain amplitude and 400 Hz frequency over a distance of 60 meter is well recovered over 4 km fiber. Hence, the new system is proved to broaden significantly the upper measurement limit of typical DAS, bringing a significant application prospect of extensive, real-time large strain sensing.

Key words: DAS, microwave frequency OTDR, strain sensing, seismicity detection

1.- INTRODUCCIÓN

En los últimos años, la detección acústica distribuida (DAS) ha despertado un interés creciente, especialmente en la comunidad sismológica [1-3]. Esta técnica permite medir el campo de ondas sísmicas a lo largo de decenas de kilómetros con una resolución espacial del orden de decenas de metros. Tal capacidad resulta particularmente atractiva para los sismólogos, dado que las longitudes de onda sísmicas suelen rondar el kilómetro. En consecuencia, un registro completo de DAS típicamente captura varios períodos de onda sísmica, con un muestreo de aproximadamente 10 a 100 puntos por período.

Aunque los sistemas DAS presentan sensibilidad direccional, el número extraordinariamente alto de sensores sísmicos sincronizados que incorporan permite capturar todas las características esenciales de una red sismológica, como la localización de la fuente y la estimación de la magnitud, entre otras [3]. Se ha demostrado que los sistemas DAS convencionales funcionan de manera efectiva para terremotos relativamente pequeños (aproximadamente entre magnitudes M1 y M4). No obstante, ante sismos de mayor magnitud, estos sistemas experimentan problemas de saturación [2-3]. En configuraciones típicas de DAS (resolución espacial de 10 metros y longitud de onda óptica de 1550 nm), la onda P de un sismo de magnitud 4 a una distancia de 10 km puede superar el rango de medición y provocar la saturación del dispositivo, lo que limita su utilidad para la alerta temprana de grandes terremotos (M > 6). Por ello, es fundamental incrementar significativamente

el rango de saturación en estos sistemas. El origen de esta limitación radica en el propio proceso de medición de los sistemas DAS. Estos dispositivos miden los cambios en la deformación de la fibra a partir de las variaciones de fase en el campo óptico retrodispersado por un pulso coherente incidente sobre la fibra. Los cambios de deformación en la fibra se manifiestan como variaciones de fase en la traza óptica retrodispersada. Sin embargo, los cambios de fase que superen los 2π entre ciclos consecutivos de interrogación no pueden medirse correctamente, lo cual restringe también el rango de deformación medible entre pulsos.

La interferometría de fibra óptica con frecuencia de microondas (MFFI) es una tecnología emergente que emplea señales de microondas estables propagadas a lo largo de un enlace de fibra óptica en una configuración de lazo cerrado para la detección de deformaciones [4]. En el campo de la monitorización sísmica, la MFFI se ha aplicado con éxito en transmisión para detectar la deformación global provocada por terremotos de magnitud media a alta a lo largo de tramos de fibra de varias decenas de kilómetros. Por ejemplo, en un experimento realizado en la región de Ática (Grecia), la MFFI capturó eficazmente las ondas sísmicas procedentes de un epicentro lejano, mostrando una elevada correlación con las señales registradas por acelerómetros nacionales y sistemas DAS comerciales [5]. Los sistemas MFFI ofrecen ventajas significativas en términos de coste, alcance máximo detectable y facilidad de implementación. No obstante, a diferencia del DAS, la MFFI no permite obtener mediciones espacialmente resueltas del campo de ondas sísmicas.

Inspirados por las ventajas de la MFFI, presentamos un sistema DAS novedoso basado en reflectometría óptica en el dominio del tiempo (OTDR), en el cual el pulso de sondeo incorpora una modulación de microondas impresa. La señal retrodispersada, que bate a la frecuencia de dicha modulación, se analiza para medir los cambios en el retardo de grupo de la microonda retrodispersada. Mediante métodos sencillos de demodulación de fase, es posible extraer con precisión la información de deformación a lo largo de la fibra, lo que permite una monitorización de alta resolución y un amplio rango dinámico para deformaciones de gran magnitud. Para sustentar y validar este enfoque, se presentan análisis teóricos junto con experimentos de prueba de concepto que demuestran su viabilidad.

2.- Fundamento teórico y principio de funcionamiento

2.1. Detección de deformaciones ópticas en sistemas DAS convencionales

En los sistemas DAS convencionales, se inyecta un pulso óptico coherente en la fibra y la detección de deformaciones dinámicas se basa en la medición de los cambios de fase en la señal retrodispersada por dispersión de Rayleigh [6]. Cuando la fibra está sujeta a perturbaciones externas, el camino óptico entre los centros de dispersión se modifica, lo que induce variaciones en la fase de la señal retrodispersada.

En condiciones estáticas, la diferencia de fase entre dos puntos de la fibra separados por la longitud de calibración Δz está relacionada con el índice de refracción de la fibra mediante:

$$\phi(z+\Delta z)-\phi(z)=2kn\Delta z \qquad (1)$$

donde k es el vector de onda, relacionado con la longitud de onda óptica λ mediante $k=2\pi/\lambda$, y n es el índice de refracción de la fibra. En caso de producirse un cambio de deformación $\Delta\varepsilon$, la diferencia de fase registrada entre estos dos puntos experimentará una variación $\Delta\phi$, que puede expresarse como:

$$\Delta\phi=2kn\left(\frac{1}{n}\frac{dn}{d\varepsilon}+1\right)\Delta z\Delta\varepsilon \qquad (2)$$

donde el término $dn/d\varepsilon$ depende de las propiedades elasto-ópticas de la fibra óptica utilizada. Para fibras ópticas estándar, estos coeficientes son bien conocidos, lo que permite expresar la deformación en función

del cambio de fase $\Delta\phi$ mediante relaciones explícitas.

El rango de deformación medible entre ciclos consecutivos de interrogación está limitado por el intervalo sin ambigüedad de 2π en la medición del cambio de fase. En fibras ópticas convencionales, con la resolución espacial típica de los sistemas DAS (~10 m), este límite se sitúa en unas pocas decenas de nanodeformaciones. Además, cuando se emplean longitudes de calibración mayores, la restricción se vuelve aún más severa, reduciéndose hasta unos pocos nanostrains para distancias de 100 m. Dado que los ciclos de interrogación típicos en fibras de decenas de kilómetros se encuentran en el orden de kHz, la tasa máxima de deformación medible por los sistemas DAS convencionales es del orden de 10^{-5} m/(m·s). Si bien este valor es suficiente para caracterizar sismos de magnitud 4, resulta insuficiente para terremotos de mayor magnitud, que generan deformaciones del terreno considerablemente más intensas.

2.2. OTDR de frecuencia de microondas

En el método propuesto en este trabajo, se introduce una modulación de radiofrecuencia (RF) en el pulso óptico de sondeo, lo que provoca que la señal retrodispersada también incorpore esta modulación. En lugar de medir los cambios en la fase óptica de la señal retrodispersada, nuestro sistema detecta las variaciones de fase en la modulación de RF impresa sobre dicha señal. Mediante un análisis teórico sencillo, se puede demostrar que la fase de la modulación de RF experimenta una variación entre dos posiciones de la fibra es:

$$\Delta\phi = 2k_{RF}n_g\left(\frac{1}{n_g}\frac{dn_g}{d\varepsilon}+1\right)\Delta z\Delta\varepsilon \quad (3)$$

donde el vector de onda $k_{RF} = 2\pi/\lambda_{RF}$ está relacionado con la longitud de onda de la modulación en frecuencia de radio (RF) dentro de la fibra, y el índice n_g corresponde al índice de grupo de la fibra a la longitud de onda del campo óptico. En general, los términos n_g y $dn_g/d\varepsilon$ tienen valores muy similares al índice de refracción ordinario de la fibra n en longitudes de onda ópticas. Como consecuencia, la sensibilidad de fase a la deformación de la señal retrodispersada en frecuencia de RF será, en esencia, una versión reducida de la sensibilidad de fase en el dominio óptico, reducida por un factor $k_{RF}/k = f_{RF}/f$, donde f_{RF} y f son, respectivamente, la frecuencia de la señal de radiofrecuencia y la frecuencia de la onda óptica.

Mientras que la longitud de onda de interrogación óptica en los sistemas DAS se encuentra generalmente fijada en torno a 1550 nm, la frecuencia de radiofrecuencia (RF) puede ajustarse de manera amplia, incluso utilizando la misma configuración óptica. Este ajuste permite controlar el grado de sensibilidad a la deformación en el sistema. Las frecuencias de RF más altas incrementan la sensibilidad a la deformación en comparación con frecuencias más bajas, y viceversa. Valores típicos de RF en el rango de los GHz conllevan una reducción en la sensibilidad de fase a la deformación de aproximadamente un factor de 10^5. Esto se traduce en un rango de tasa de deformación medible que es al menos 10^5 veces superior al de los sistemas DAS convencionales con la misma configuración óptica. Como resultado, este sistema permite utilizar pulsos significativamente más largos y mayores longitudes de calibración, sin alcanzar el umbral de saturación que limita a los sistemas DAS convencionales.

3.- Experimentos y resultados

3.1. Configuración experimental

La implementación experimental de la técnica OTDR con modulación de frecuencia de microondas se muestra en la Figura 1.

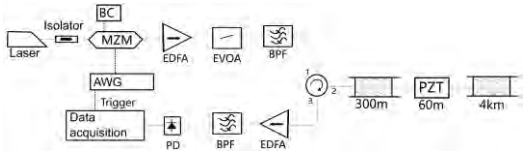

Figura 1. Sistema propuesto basado en OTDR de frecuencia de microondas. Las siglas se definen en el cuerpo del manuscrito.

Se emplea como fuente un láser de bajo ruido de fase, con un ancho de línea inferior a 100 Hz y operando a 1550.12 nm. Los pulsos de

interrogación se generan mediante un modulador electro-óptico (EOM), controlado por un generador de formas de onda arbitrarias (AWG), el cual produce pulsos super-Gaussianos de 1 μs de duración (equivalente a una resolución espacial nominal de 100 m) y una frecuencia de repetición de 10 kHz. Estos pulsos son modulados en doble banda lateral utilizando una señal de RF de 4.5 GHz. La señal óptica se amplifica mediante un amplificador dopado con erbio (EDFA) hasta alcanzar el nivel de potencia deseado, y un filtro de banda de 0.1 nm se utiliza para eliminar el ruido por emisión espontánea amplificada. Para ajustar la ventana temporal de los pulsos, se emplea un atenuador óptico variable electrónico (EVOA), asegurando una relación de extinción superior a 20 dB antes de inyectar la luz en la fibra bajo prueba (FUT) mediante un circulador óptico. La FUT consta de tres tramos: un primer tramo de fibra monomodo (SMF) de 300 metros; un segundo tramo con un transductor piezoeléctrico (PZT) de 60 metros, capaz de aplicar una deformación relativamente grande con una frecuencia de 400 Hz y una amplitud pico a pico de 1.8 με; y finalmente, un segmento de 4460 metros de SMF. Las señales retrodispersadas de la FUT se amplifican mediante un segundo EDFA y pasan por otro filtro de banda para eliminar el ruido. Posteriormente, estas señales ópticas se convierten en señales eléctricas mediante un fotodiodo con un ancho de banda de 10 GHz. Finalmente, las señales eléctricas se digitalizan con un osciloscopio que opera a 40 GSa/s.

Esta arquitectura permite un control preciso de toda la cadena de señal, logrando mediciones de alta resolución y bajos niveles de ruido.

3.2. Resultados

En la Figura 2, se muestra un conjunto de resultados obtenidos con el sistema experimental propuesto. Una vez digitalizada, la componente de 9 GHz se filtra y se desplaza a banda base. En la Figura 2(a) se presentan tres trazas consecutivas obtenidas tras desplazar la señal de RF a banda base.

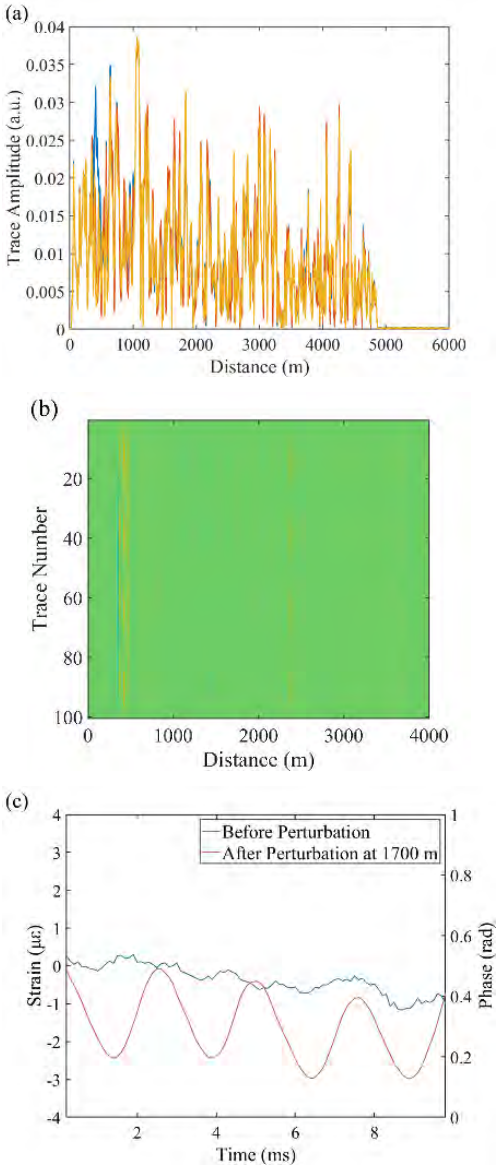

Figura 2. Resultados experimentales. (a) Trazas de señales a 9 GHz. (b) Mapa de fase tras la eliminación de saltos. (c) Señales de deformación recuperadas y fases correspondientes antes y después de la perturbación.

En principio, la fase demodulada debería proporcionar directamente la información sobre el cambio en la deformación. Sin embargo, al igual que en los sistemas DAS convencionales, este sistema también está limitado por la presencia de puntos de desvanecimiento (fading) [7]. En estas posiciones, la interferencia aleatoria de las señales retrodispersadas por Rayleigh dentro de una resolución espacial determinada

produce una amplitud muy baja, por debajo del umbral de detección. Para abordar este problema, se aplica un algoritmo de eliminación de fading durante el procesamiento de los datos. Adicionalmente, se observan saltos de fase de π a lo largo de la distancia, los cuales deben corregirse mediante un algoritmo diferencial basado en la transformada de Hilbert.Tras aplicar todas estas correcciones de fase, se obtiene la señal objetivo, aunque no todos los saltos de fase quedan perfectamente corregidos.

El resultado de la fase tras el procesamiento se presenta en la Figura 2(b), donde se observa su distribución en función del tiempo y la distancia El mapa de fase revela que la mayoría de los saltos fueron cancelados de manera eficaz, manteniéndose en buen estado el efecto de la perturbación, con una frecuencia correcta y una longitud aproximada de 100 m, debido a la resolución espacial del pulso de prueba. Además, las señales de deformación recuperadas se extraen del mapa de fase utilizando la ecuación de transformación fase-deformación, tal como se muestra en la Figura 2(c), con los valores de fase correspondientes. En esta figura se comparan visualmente diferentes casos antes y después de la perturbación, representados en curvas azul y roja. La curva azul muestra una fluctuación aleatoria de bajo nivel (ruido de fondo), mientras que la curva roja presenta una modulación de fase clara debida a la perturbación, que se mantiene estable a medida que aumenta la distancia. Aunque se observa una deriva lenta que eleva ligeramente la curva, la información de deformación se conserva de forma consistente, incluida la frecuencia de 400 Hz y el valor pico a pico de aproximadamente 2 με.

Los resultados experimentales demuestran que el nuevo método es viable y que la información sensorial obtenida es válida. El rendimiento del sistema se ajusta a las expectativas, especialmente en el contexto de aplicaciones para la detección de grandes deformaciones, como los sistemas de alerta temprana sísmica (EEW). Dadas las notables ventajas que ofrece el OTDR con modulación de frecuencia de microondas, la capacidad de medición y el potencial demostrados en este experimento podrían representar un avance significativo.

4.- Conclusión

Este trabajo presenta un diseño innovador de sistema DAS basado en OTDR con modulación de frecuencia de microondas. Su funcionamiento se basa en la inyección de un pulso de sondeo modulado en radiofrecuencia a través de la fibra, y la extracción de la información sensorial correspondiente mediante el análisis de la señal retrodispersada en esa frecuencia de microondas. Este sistema ofrece un rango de saturación en la medición de deformación que supera en varios órdenes de magnitud el de los sistemas DAS convencionales. Se han proporcionado pruebas tanto teóricas como experimentales que validan este nuevo esquema de interrogación. Consideramos que este sistema puede representar un avance significativo en la aplicación de las tecnologías DAS en los sistemas de alerta temprana sísmica (EEW).

Acknowledgements: P.J.V-M was supported by FPI-2021 Grant from the University of Alcalá Research Program. M.R.F-R. was supported by MCIN/AEI/10.13039/501100011033 and European Union «NextGenerationEU»/PRTR under grant RYC2021-032167-I. This work was supported in part by the Spanish MCIN/AEI/10.13039/501100011033 and the European Union NextGenerationEU/PRTR Program under Grant PSI ref. PLEC2021-007875 and REMO: ref. CPP2021-008869, in part by the Spanish MCIN/AEI/10.13039/501100011033 and FEDER, UE (grants, PID2021-128000OB-C21 and PID2022-140963OA-I00); in part by the European Innovation Council under Grant SAFE: ref. 101098992, and SUBMERSE: ref.101095055, and in part by the Grant SEASNAKE+, ref. PCI2023-145978-2 / MCIU/AEI/10.13039/501100011033/ European Union.

References

[1] E. Williams, M. Fernández-Ruiz, R. Magalhaes, et al., "Distributed sensing of microseisms and teleseisms with submarine dark fibers," Nat. Commun., vol. 10, no. 5778, pp. 1-9, December 2019.

[2] J. Yin, Z. Zhan and J Ajo-Franklin, "Sensing optical fibers for earthquake source characterization: A case study of the 2019 Ridgecrest sequence," J. Geophys. Res. Solid Earth, vol. 128, no. 5, pp. e2023JB027860, May 2023.

[3] J. Yin, Z. Zhan and J. Ajo-Franklin, "Earthquake magnitude with DAS: A transferable data-based scaling relation," Geophys. Res. Lett., vol. 50, no. 7, pp. e2023GL103045, April 2023.

[4] A. Bogris, T. Nikas, C. Simos, et al., "Sensitive seismic sensors based on microwave frequency fiber interferometry in commercially deployed cables," Sci. Rep., vol. 12, no. 14000, pp. 1-11, August 2022.

[5] E. Biondi, J. Li, J. Saunders, et al., "The frontiers of distributed acoustic sensing for seismological applications," presented at EGU24, no. EGU24-4186, Copernicus Meetings, March 2024.

[6] Z. He and Q. Liu, "Optical fiber distributed acoustic sensors: A review," J. Light. Technol., vol. 39, no. 12, pp. 3671-3686, June 2021.

[7] K. Shimizu and T. Horiguchi, "Characteristics and reduction of coherent fading noise in Rayleigh backscattering measurement for optical fibers and components," J. Light. Technol., vol. 10, pp. 982-987, July 1992.

Exploration of Optical Fiber Based Sensor Phenomena, Use Cases and Potential Calibration Method for Vibrations

Ángel REDONDO[(1)], José Antonio LÁZARO[(1)]

1. Department of Signal Theory and Communications, UPC - Universitat. Politècnica de Catalunya, Jordi Girona 31, 08034, Barcelona, Spain

Contact: angel.redondo@estudiantat.upc.edu, jose.antonio.lazaro@upc.edu.

ABSTRACT:

Optical fibers, beyond their role in data transmission, can also operate as distributed sensors capable of detecting strain, temperature, and vibration through light scattering phenomena. This paper provides an overview of the physical principles behind these capabilities and discusses real-world applications, such as seismic activity detection and infrastructure monitoring.

A calibration method for vibration sensing is proposed to ensure accurate correlation between optical responses and mechanical stimuli, which supports research and development. These capabilities enable early warning systems, increase infrastructure safety, and offer a scalable and cost-effective alternative to conventional sensor networks. The insights and methods presented in this paper reinforce the potential of distributed fiber-optic sensing for next-generation monitoring systems.

Key words: Optical Fibers, Sensors, Rayleigh Scattering, Temperature, Vibration.

1.- Introduction

The use of optical fiber for detecting irregularities in infrastructure is well-established. Nevertheless, it remains an effective tool for quality control and accident prevention, particularly by leveraging existing fiber optic deployment. This approach reduces installation costs while enabling continuous, real-time monitoring with minimal maintenance [1]. As a result, a wide range of sectors can benefit from early fault detection and data-driven decision-making.

2.- Optical Fibers as Physical Phenomena Sensors

A few physical phenomena can influence the structural properties of optical fibers. Although such effects may degrade transmission performance, they can be effectively repurposed for distributed sensing. The following subsections briefly describe these phenomena, and the methods used to quantify them.

2.1.- Strain

Strain in an optical fiber refers to the mechanical deformation experienced by the fiber when it is subjected to external forces. These forces may arise from natural events or inadequate infrastructure management, such as construction activities or improper installation and maintenance. A distributed Brillouin sensor assisted by counter-propagating Raman amplification [2] enables the measurement of both strain and temperature, as will be discussed in greater detail later. The sensing principle is based on the generation of a gain band at a frequency offset from the pump frequency, known as the Brillouin frequency shift. This shift, denoted as ν_B, can be detected using Brillouin scattering [3]:

$$\nu_B = \frac{2nV_a}{\lambda_0} \qquad (1)$$

where n is the refractive index of the fiber, V_a is the acoustic velocity in silica, which depends on both temperature and strain, and λ_0 is the pumping wavelength [2].

2.2.- Temperature

The temperature directly affects the properties of any material, including optical fiber. To mitigate environmental influences, fiber optic cables are typically enclosed within protective polyethylene tubes, which shield them from elevated temperatures and other factors. The thermal resistance of these enclosures can vary depending on the specific deployment context. For instance, in the ADIF railway network, the standard polyethylene tubes must withstand 110°C before losing their rigidity [4].

When the light propagates through optical fiber, a fraction of the photons undergoes inelastically scattering, known as Raman scattering. The photons in this context interact with the vibrational modes of the material, producing a shift in the wavelength and the energy. This scattering produces Stokes photons which lose energy and are shifted to lower frequencies (longer wavelengths) and Anti-Stokes photons which gain energy through thermal vibrations and are shifted to higher frequencies (shorter wavelengths). The intensity of Stokes scattering is constant when the temperature increases while the intensity of Anti-Stokes increases as the temperature rises, as shown in Fig. 1.

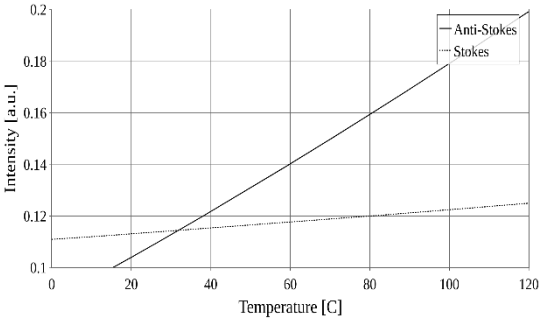

Fig. 1: Photon behavior as function of Temperature.

By analyzing the Anti-Stokes/Stokes ratio, it is possible to determine the local temperature along the fiber with high precision. This ratio follows an exponential dependence governed by the Boltzmann distribution, making it possible to calculate temperature variations with high spatial resolution [5], [6].

2.3.- Vibration

Vibrations are ubiquitous in most environments and can introduce mechanical stress into optical fibers. Although such vibrations are typically transient and, unless persistent and of high intensity, do not cause considerable damage to optical fibers. Specifically, vibrations may induce temporal bending or perturbations on the fiber, which in turn leads to localized variations in refractive index and scattering behavior, resulting in signal attenuation and spectral shifts [7].

In the context of optical communications, micro-bending is considered detrimental, as it can introduce losses in the range of 0.1 to 1 dB/km in standard single-mode fibers [8]. In contrast, these same mechanical effects are exploited in distributed sensing applications, where the fiber itself acts as a continuous sensor. One of the most widely used techniques in this domain is Distributed Acoustic Sensing (DAS) [1].

DAS technology relies on Rayleigh backscattering, a phenomenon in which incident light is scattered by intrinsic inhomogeneities within the fiber core. When the fiber undergoes a perturbation, such as a micro-bending event, the backscattered signal exhibits phase and intensity changes that correlate with the mechanical disturbance. By analyzing these variations, DAS systems can detect and localize vibration events with meter-scale spatial resolution and high temporal fidelity.

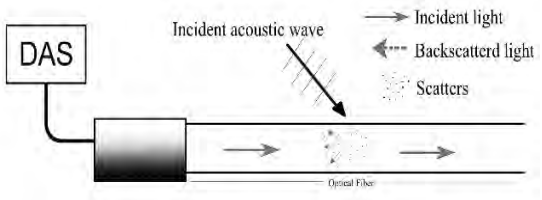

Fig. 2: Schematic representation of the DAS sensing principle.

3.- Use cases

In this section we explore some useful use cases of the distributed sensor as optical fiber.

3.1.- Railways/Roadway

Using a distributed fiber-optic sensor is a promising approach, given that fiber is already deployed throughout the Railways/Roadway infrastructure [9], [10]. This existing fiber can be leveraged to detect vibrations caused by events such as landslides, intrusions, or fractures on the traffic infrastructure, among other incidents. When combined with the strain detection capabilities of optical fiber, this solution would enhance system redundancy and security, particularly against unauthorized tampering with the infrastructure, thereby preventing both financial and time-related losses [11]. Additionally, using optical fiber as a temperature sensor could serve as a complementary mechanism to conventional fire detectors. However, relying on it as the primary fire detection system may result in delayed alarms due to the protective coating surrounding the fiber, so it should be used as an additional sensor to the system.

3.2.- Earthquake

Some earthquakes generate foreshocks that cannot be detected by humans [12]. However, there are methods capable of detecting these precursor shocks, providing a few seconds for society to prepare. Techniques such as DAS not only add redundancy to earthquake detection systems and offer valuable seconds of warning to the population but also allow us to capture seismic data for the study and analysis of such events [13].

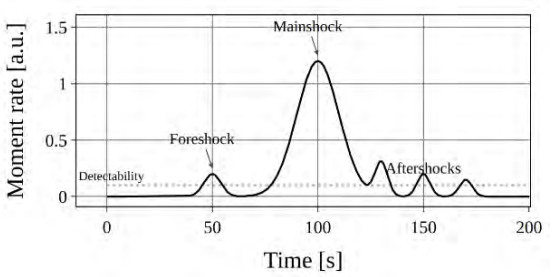

Fig. 3: Conceptual representation of seismic activity showing a detectable precursor earthquake preceding the main shock.

3.3.- Industries

Apart from the cases shown in [5], optical fiber could be deployed by intelligently wrapping it around large-diameter radio frequency (RF) cables typically found in broadcasting applications, to monitor the integrity of the current flow and mitigate RF signal attenuation. In factories where temperature monitoring is necessary, optical fiber wrapping could be applied to have an equivalent temperature sensor array.

4.- Calibration Method for Vibration

To accurately correlate the fiber's optical response with actual mechanical vibrations, a calibration procedure is performed in a controlled vibration environment. This setup involves a mechanical vibration system to induce known vibration patterns and the use of reference accelerometers to validate the excitation. These vibrations are produced by transductors that transform the signal into a mechanical/acoustic wave to observe the effects on the fiber. The input signal is controlled in terms of amplitude, frequency and pulse waveform for the different tests. The optical signal propagating through the fiber may be modulated with data or remain unmodulated. The specific fiber type is not critical for the calibration procedure. However, when studying the effect of vibrations on already deployed optical infrastructure, it is common to find standard single-mode fibers such as ITU-T G.652 and G.655 as shown in Fig. 4.

ITU-T Fiber type	Backbone / Core Transmission	Submarine / Undersea Systems	Point-to-Point / Digital Links	Access (FTTx) / PON Networks	Tight Bending Environments	Global Adoption
G.652	++	+	+	++	-	++
G.653	+	-	-	–	-	-
G.654	+	++	-	–	-	+
G.655	++	+	+	+	-	+
G.656	+	–	-	+	-	-
G.657	+	-	-	++	++	++

Fig. 4: Comparative assessment of the suitability of ITU-T standardized optical fiber types, based on their presence in the corresponding technical recommendations [14].

5.- Conclusion

Distributed sensors based on optical fibers are an efficient and versatile solution for real-time monitoring, transforming a passive transmission medium into a sensor array.

Calibration procedures for vibration-based sensing methods are essential not only for validating measurement accuracy but also for supporting research, development, and structural integrity prior to product launch. By enabling controlled experimentation and repeatable test conditions in an environment, calibration serves as the foundation for the design of future versions of distributed fiber-optic vibration sensing.

Acknowledgements: This article has been partially financed by Spanish MICIU founded, TRAINER-B (PID2020-118011GB-C22) and "Pla de Doctorats Industrials del Departament de Recerca i Universitats de la Generalitat de Catalunya" under Grant 2023-DI-0052.

References

[1] Wired España, (2024) https://es.wired.com/articulos/fibra-optica-de-internet-tambien-escucha-fallas-en-vias-ferreas

[2] Francisco RODRÍGUEZ-BARRIOS, et al., "*Sensor distribuido Brillouin de deformación y temperatura en fibra óptica asistido con Raman para aplicaciones de ingeniería civil*", in Proceedings of OPTOEL, 2009

[3] Govind P. AGRAWAL, "*Nonlinear Fiber Optics*" (Academic Press, 2007)

[4] Especificación técnica ET.03.366.751.0: Tubos de polietileno para tendido de cables de fibra óptica, https://www.adifaltavelocidad.es.

[5] Zakaria AMIRA, Mounir BOUYAHI, Tahar EZZEDINE, "*Measurement of temperature through Raman scattering*", Procedia Computer Science, 73, –, 350–357, 2015.

[6] Giovanni BOLOGNINI, Alex HARTOG, "*Raman-based fibre sensors: Trends and applications*", Optical Fiber Technology, 19, 6, 678–688, 2013.

[7] S. Steinblatt, *Optical waveguide mode coupling using mechanical wave interference*, European Patent EP0639781A1, Feb. 22, 1995.

[8] Zsolt VÁRALLYAY, et al., "*Microbending loss properties of different fiber designs*", in Proceedings of Optical Fiber Communication Conference, Th1A-49, 2021

[9] Adif Alta Velocidad, "*Telecomunicaciones*", https://www.adifaltavelocidad.es/telecomunicaciones

[10] Instalación de fibra óptica en la autovía A-7, https://avance.digital.gob.es/es-ES/Participacion/Paginas/Cerradas/fibra-optica-autoviaA7.aspx

[11] https://www.elmundo.es/espana/2022/08/08/62f09c53e4d4d83a528b4608.html

[12] Zhigang PENG, Xiaowei LEI, "*Physical mechanisms of earthquake nucleation and foreshocks: cascade triggering, aseismic slip, or fluid flows*?", Earthquake Research Advances, –, –, –, 2024.

[13] Itay LIOR, et al., "*Strain to ground motion conversion of DAS data for earthquake magnitude and stress drop determination*", Solid Earth Discussions, –, –, 1–30, 2021.

[14] ITU-T Recommendations Series G, https://www.itu.int/rec/T-REC-G/en

A Monte Carlo model of the propagation of polarized pulses in turbid media for modelling polarized lidar in fog

Maria BALLESTA-GARCIA [(1)], Aleix R. BOBI-OLMO [(1)], Santiago ROYO [(1,2)]

1. Centre de Desenvolupament de Sensors, Instrumentació i Sistemes, Universitat Politècnica de Catalunya (UPC-CD6), Rambla Sant Nebridi 10, E08222, Terrassa, Spain
2. Beamagine SL C/Bellesguard 16 E08755 Castellbisbal Spain

Contact: Maria BALLESTA-GARCIA (maria.ballesta.garcia@upc.edu).

ABSTRACT:

Fog is one of the main challenges for the use of lidar systems in autonomous vehicles. The interaction of light with droplets suspended in the air generates backscattering signals that add noise, reduce range and may blind the system. Polarization has proven useful in filtering out part of this undesired light.

We have developed a Monte-Carlo parallelized algorithm to model the propagation of polarized pulsed light through different turbid media, such as fog, to study such situations in a controlled way. Using this algorithm, backscattering signals are characterized, revealing their dependence on medium properties, as well as their connection to the polarimetric properties of the imaged targets. It also demonstrates the efficacy of circular polarization in mitigating scattering effects, highlighting the benefits of the polarization memory effect in these scenarios.

The algorithm can be used as a tool to predict different situations for designing polarimetric systems in complex outdoor environments..

Keywords: polarization, pulsed light, Monte Carlo, Lidar system, fog, scattering media, polarization memory effect.

1.- Introduction

In the last decade, lidar imaging systems have gained significant interest for their use in computer vision for outdoor applications where geometry is relevant. These applications span fields such as transportation, autonomous vehicles, and surveillance. Lidar systems provide precise, real-time imaging, capturing 3D information through active illumination and effectively measuring the environment in real-time [1].

However, there are still challenges that need to be addressed for their general adoption. In particular, adverse weather conditions present a significant problem for outdoor use. When the air is not clear and particles are suspended in it (for example, water droplets in fog), light interacts with these particles, generating undesired backscattering signals while limiting the range of the system.

There are three main issues associated with this phenomenon: 1) Scattering attenuates the light signal, reducing the system's range. 2) Backscattering interactions can generate false-positive detections, and deforming edges of objects, decreasing system reliability. 3) In active systems like lidar, strong backscattering signals can return to the system, risking saturation of the detector and hampering its sensitivity for some time.

Several strategies have been proposed to address these challenges. Among them, polarization has been shown to mitigate the effects of backscattering [2,3]. Experimental tests using a polarimetric lidar have demonstrated that polarization can reduce the

scattering effects of fog [4]. These studies also highlight the ability of circularly polarized light to effectively minimize the impact of backscattered light.

However, creating controlled experimental conditions for each of the variables that can influence system performance is extremely difficult, if not unfeasible. Several factors that are difficult to control can affect the medium, such as particle density, distribution, geometry, and composition. The temporal stability of fog is also a major issue. As a result, the variety of potential scenarios and use cases is vast, and real-world adverse weather conditions are dynamic, making precise parameterization a challenging task. Moreover, setting up these experiments is time-consuming and complex, as is preparing the system for each possible configuration. In this context, the use of models to predict expected trends, test various experimental configurations, and determine the optimal setup in a broader range of controlled situations becomes necessary.

Monte Carlo (MC) algorithms for polarized light transport are widely recognized as a powerful tool for addressing complex light propagation scenarios [5,6]. Following this approach, we have developed and validated an MC algorithm designed to model polarimetric optical systems in turbid environments, in particular a time-of-flight lidar operating in fog. This algorithm accounts for key factors such as time dynamics, polarization effects, various geometries, optical obstacles, target interactions, and the presence of both regular and irregular particles in the medium.

In this contribution, we present the MC algorithm developed for time-resolved polarized light propagation in turbid media, incorporating realistic media characterization and features of existing pulsed lidar prototypes. We also show and discuss some interesting results obtained using it.

2.- Methods and Materials

2.1.- Algorithm description and implementation

The algorithm uses the Mueller-Stokes formalism, in which polarization is defined by a Stokes vector ($\vec{S}$):

$$\vec{S} = [I\ Q\ U\ V] \quad (1)$$

A turbid medium is defined by the presence of localized non-uniformities (particles) that are randomly distributed throughout it. In non-absorbing media, these particles are responsible for the scattering and the absorption of light. Consequently, the optical properties that characterize the media are closely linked to the characteristics of the particles it contains.

Propagation through turbid media composed of regular or irregular particles is similar, with differences arising only during the modeling of scattering events, where light interacts with these particles. When using the Mueller-Stokes formalism, this interaction is always described by a Mueller matrix (M) and the scattering angles (θ, ϕ):

$$\vec{S}_{out} = M(\theta, \phi) \cdot \vec{S}_{in} \quad (2)$$

However, the characteristics of M and the method for sampling the scattering angles differ between regular and irregular particles. Additionally, irregularity introduces another variable into the system: the orientation of the particle, which must also be considered.

To compute M in a medium with regular particles, we use Mie theory. For our calculations, we rely on gmie_cpp —a general-purpose Mie scattering code written in C++ by Moteki [7], which has been modified to suit our specific needs. However, for irregular particles, we adopt a different approach: the T-matrix method. To implement this, we utilize the open-source Python library pytmatrix (version 0.3.2), developed by Leinonen [8]. This library, built upon a Fortran code created by Mishchenko and Travis, enables us to compute media parameters that account for polarization effects while considering the irregularity of the particles [9].

We also introduce a method for calculating the particle density required to characterize the medium using the concept of visibility [10].

A key strength of this algorithm is its ability to simulate the interaction of pulsed, polarized light with objects in the scene. These objects are defined by their unique M, which describes how they interact with polarized light. In this contribution, we use a mirror [11], a metallic plate as a reflective target, and sand as a diffusive target [12]. This capability makes our model a versatile tool for a wide range of simulation scenarios, from fog to underwater turbulence.

For more detailed information on the characteristics and implementation of this algorithm, refer to [13].

The algorithm was developed in C++ and optimized with NVIDIA® CUDA® for parallel computation. Simulations were performed on a high-performance server with two NVIDIA A40 GPUs, each equipped with 46GB of dedicated memory.

2.2.- Simulated scenarios

The scene is modeled in air, having a refractive index $n = 1.0$, and water particles suspended in it to simulate fog. These particles have a diameter of 2 µm, with $n = 1.33 + i2.4 \times 10^{-9}$. The concentration of droplets varies depending on the selected visibility. There are two types of particles: regular particles (spheres) and irregular particles (spheroids). For the irregular particles, the degree of irregularity is defined by the aspect ratio (AR), which is the ratio of the equatorial radius of the spheroid to the distance from the center to the pole along the symmetry axis.

In all cases, a Gaussian pulse of 1064 nm with a Full Width at Half Maximum pulse of 1 ns, centered at 0 ns, is emitted from a point source. This pulse is directed toward a target that occupies the entire plane, located 10 meters away. The target is characterized by its specific Mueller matrix (M).

Two polarization cases are simulated: one with the initial pulse exhibiting horizontal (H) linear polarization (LP): $\vec{S} = (1,1,0,0)$, and another with right-handed (R) circular polarization (CP) $\vec{S} = (1,0,0,1)$. For each case, the resulting signal is analyzed using a polarizer with identical polarimetric characteristics to the initial light (CO), as well as another polarizer with orthogonal polarimetric characteristics to the initial light (CROSS). For CO detection, an H polarizer is used for the LP case, and an R polarizer is used for the CP case. For CROSS detection, a vertical (V) polarizer is used for LP, and a left (L) polarizer is used for CP. Additionally, the total irradiance (I) is recorded without any polarizers in front of the sensor.

From the collected data, we can compute the Degree of Polarization (DOP), the Degree of Linear Polarization (DOLP), and the Degree of Circular Polarization (DOCP), directly derived from the resulting Stokes vector $\vec{S}$:

$$\mathrm{DOP} = \frac{\sqrt{Q^2+U^2+V^2}}{I}; \mathrm{DOLP} = \frac{\sqrt{U^2+Q^2}}{I}; \mathrm{DOCP} = \frac{V}{I} \quad (3)$$

We recorded all the reflected light returning to the illumination plane, which also serves as the detection plane, as a function of time. We consider t = 0 ns as the center of the Gaussian pulse. The data is presented as optical power (OP) normalized to the peak power of the initial pulse.

3.- Results

Fig. 1 shows the detected light response when a pulse is directed towards a mirror placed 10 m away, in a fog medium composed of regular particles with a visibility of 25 m.

In Fig. 1(a), the temporal profiles of the OP, normalized to the peak power of the initial pulse, are shown for each polarization case: CO_L and $CROSS_L$ for LP, and CO_C and $CROSS_C$ for CP, along with the total OP without polarizers (I).

Two different peaks can be observed. The first one, occurring from 0 to around 40 ns, results from the initial direct backscattering with the medium. The second peak, centered around 67 ns, corresponds to the reflection of the pulse due to the interaction with the target.

The LP signals from both channels (CO and CROSS) are superimposed throughout the entire time span, indicating a loss of the initial plane of polarization. In contrast, for CP, the first peak shows more signal in the CO channel, indicating that the polarization is

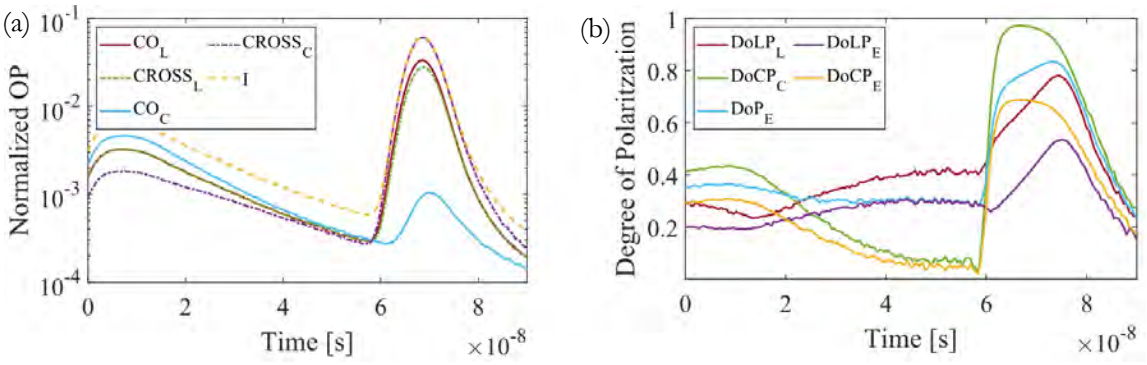

Fig. 1: In a turbid medium characterized by regular particles with a visibility of 25 m, for a Gaussian pulse encountering a mirror at 10 m: (a) Detected backscattering for different polarimetric configurations in the form of optical power and (b) different degrees of polarization.

maintained during the first backscattering. For the second peak, the CROSS channel has a higher signal, showing that polarization is also maintained but has been inverted due to the reflection at the target.

Fig. 1(b) shows the DOP, DOLP and DOCP, as defined by Eq. 3, for the described scenario. DOLP is presented for the LP case, while DOCP is shown for the CP case. Additionally, an initial pulse characterized by an elliptically polarized state, $\vec{S} = (1,0.5,0.5,\sqrt{0.5})$, is also analyzed. In this latter case, DOP, DOLP and DOCP are shown (identified with a small "E"). In all cases, the DOP of photons returning from interactions with the medium (first peak) is consistently smaller compared to those returning from the mirror (second peak). Additionally, the DOCP exceeds the DOLP whenever a notable number of photons are recorded.

Fig. 2 shows the detected light response when a pulse is directed towards a mirror placed 10 m away, composed of irregular particles, with a visibility of 15 m. These particles are characterized by M computed using the T-matrix method, based on their defined AR: 0.5, 1 (regular particles), and 1.5. Their orientations are randomized in each interaction. Additionally, a fourth case was considered: a medium where all three types of particles were combined (RND), with an equal probability of encountering each particle type.

Fig. 2(a) shows the temporal OP profiles of the reflected light for the four distinct types of media, normalized to the peak power of the initial pulse. In this case, no polarizers are used for detection. The recorded OP varies depending on the AR of the particles.

In Fig. 2(b), similar results to those in Fig. 2(a) are presented. However, in this case, only CP is considered. The exploration of LP is omitted, as previous findings indicate the

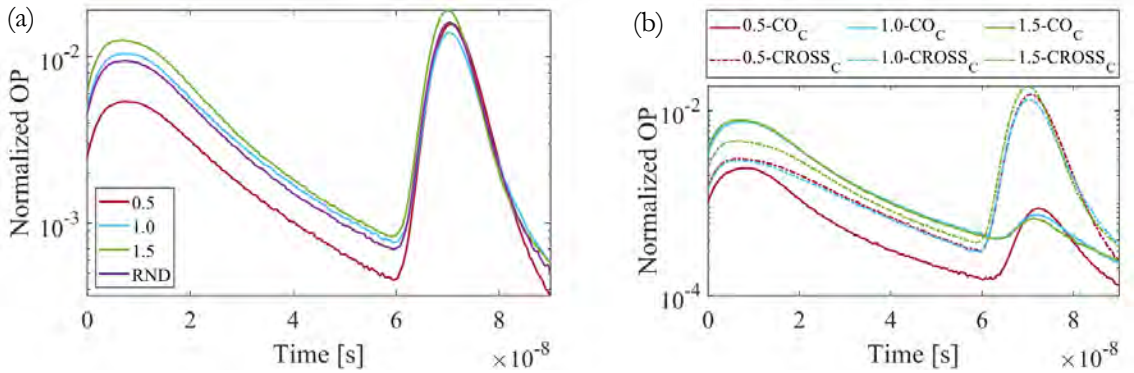

Fig. 2: In a turbid medium characterized by irregular particles with a visibility of 15 m, for a Gaussian pulse encountering a mirror at 10 m: (a) Detected backscattering in the form of total optical power for different AR and (b) different polarimetric configurations of polarization.

rapid loss of this polarization. For this case, when AR < 1, the behavior of the polarization in the first backscattered light is the opposite of that observed for AR = 1 and AR > 1.

Finally, in Fig. 3, the results show simulations conducted in fog with regular particles at three distinct visibilities: 15 m, 25 m, and 35 m. Once again, four cases are considered for study: LP with CO and CROSS detection, and CP with CO and CROSS detection. Now, the target placed at 10 m is not a mirror. Two different scenarios are explored: one with a highly reflective target (polished steel) and another with a diffusive target (sand).

Fig. 3(a) shows the energy corresponding to the integration of areas beneath the backscattering response from the fog (the first peak in Figs. 1 and 2, from 0 to 40 ns), normalized to the energy of the initial pulse. The energy decreases as visibility increases. All polarization cases can be accurately fitted by a negative power law. LP signals are superimposed, while $CROSS_C$ channel always presents greater energy than CO_C channel.

In Fig. 3(b), the depicted data shows the amount of energy associated with the reflected light (the second peak in Figs. 1 and 2, starting at 40 ns) returning from both diffusive (d) and reflective (r) objects. Once again, the reflected light as a function of visibility can be fitted using a power law. For the diffusive targets, all polarization cases show similar values, indicating the loss of the initial polarization plane. For the reflective target, LP also exhibits depolarization, while for CP, the CO_C channel presents greater energy than the $CROSS_C$ channel. This behavior is inverted compared to the first peak of backscattering.

4.- Discussion and Conclusions

In this contribution, we have studied the polarization properties of a pulsed light propagating through a turbid media, in particular fog. Two polarization states, linear and circular, were examined in relation to different targets and media.

For a mirror in a media composed of regular particles, LP exhibited a complete loss of its initial polarization state, emphasizing the challenges of maintaining the polarization plane under such conditions. In contrast, CP demonstrated a more favorable response, allowing the effective filtering of backscattered light from the fog while enabling clear detection of the target using CROSS detection. The DOCP consistently exceeded the DOLP, reinforcing CP as a more effective tool for mitigating scattering effects within the medium.

Then, irregular particles were introduced into the medium to assess their impact on the previously observed results. Differences in the backscattered signal were observed depending on the AR of the particles. In particular, particles with AR < 1 showed different behavior compared to the other cases. This finding underscores the complexity of real-world scattering environments, emphasizing the relevance of

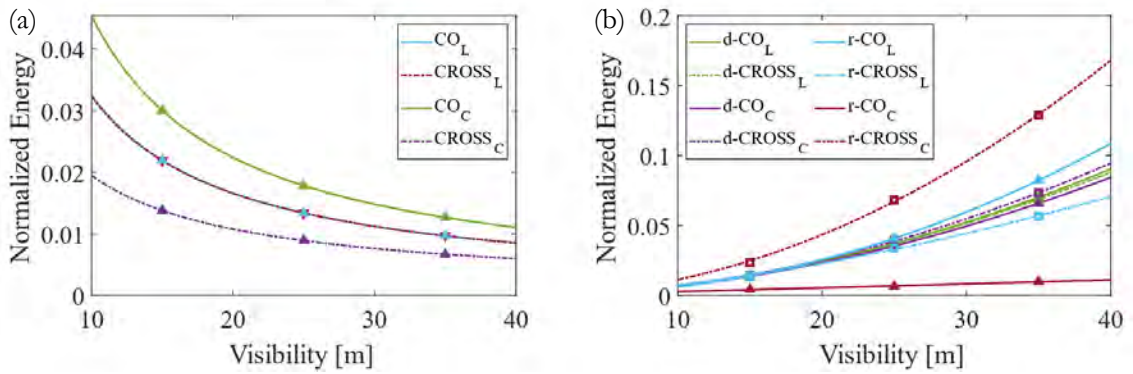

Fig. 3: (a) Relation of the energy associated with the backscattering signal as a function of visibility for different polarimetric configurations. Fitted with a power law. (b) Relation of the energy associated with the reflected signal of diffusive (d) and reflective (r) objects as a function of visibility for different polarimetric configurations. Fitted with a power law.

particle shape and the need for further studies to optimize detection strategies based on the specific characteristics of the medium.

Our simulations also showed that as visibility decreases, both the optical power and the energy of the backscattered signal from fog exhibited a noticeable decline, following a negative power-law trend. Additionally, by introducing different types of targets at varying visibilities, we observed that the same power-law model could be applied to the reflected pulse returning from targets. Positive exponent values in the power-law relationship indicated an increase in energy arrival with visibility, depending on the visibility. Furthermore, we demonstrated that the polarimetric properties of the material could influence the optimal system configuration, as diffusive targets significantly contributed to depolarization.

The insights derived from this study have substantial implications for the design and optimization of pulsed lidar systems, in particular at a wavelength of 1064 nm. The adoption of circular polarization stands out as a promising strategy for enhancing contrast and improving performance in foggy conditions, particularly in the detection of objects with reflective properties. The study contributes valuable knowledge for engineers and researchers engaged in the development of these types of systems, providing an understanding of the intricate interplay between various parameters.

Acknowledgments: This work has been sponsored by the Spanish Ministry of Science through projects TED2021-132338B-I00 and PID2023-152427OB-I00 and by the European Commission through project GA-101139941

References

[1] S. ROYO, M. BALLESTA-GARCIA, "*An overview of lidar imaging systems for autonomous vehicles*," Appl. Sci. 9, 19, 4093, 2019.

[2] F. SNIK, et al., "*An overview of polarimetric sensing techniques and technology with applications to different research fields*," in Proc. SPIE Polarization: Measurement, Analysis, and Remote Sensing XI, Vol. 9099, p. 90990B, 2014.

[3] J. G. WALKER, et al. "*Visibility depth improvement in active polarization imaging in scattering media*," Appl. Opt. 39, 27, 4933-4941, 2000.

[4] M. BALLESTA-GARCIA, et al., "*Analysis of the performance of a polarized LiDAR imager in fog*," Opt. Express 30, 23, 41524-41540, 2022.

[5] J. D. VAN DER LAAN, et al., *"Range and contrast imaging improvements using circularly polarized light in scattering environments*," in Proc. SPIE Infrared Imaging Systems: Design, Analysis, Modeling, and Testing XXIV, Vol. 8706, p. 87060R, 2013.

[6] J. RAMELLA-ROMAN, et al., "*Three Monte Carlo programs of polarized light transport into scattering media: part I*," Opt. Express 13, 12, 4420–4438, 2005.

[7] N. Moteki, ""gmie_cpp" -- A general purpose Mie scattering code in C++," https://github.com/nmoteki/gmie_cpp

[8] J. Leinonen, "pytmatrix · PyPI," https://pypi.org/project/pytmatrix/#description.

[9] M. I. Mishchenko, L. D. Travis, and D. W. Mackowski, "NASA GISS: Scattering — T-Matrix Codes," https://www.giss.nasa.gov/staff/mmishchenko/tmatrix/.

[10] M. NEGRU and S. NEDEVSCHI, "*Assisting navigation in homogenous fog,*" in Proc. IEEE International Conference on Computer Vision Theory and Applications (VISAPP), p. 619–626, 2014.

[11] G. VAN HARTEN, et al., "*Polarization Properties of Real Aluminum Mirrors, I. Influence of the Aluminum Oxide Layer*," Publ. Astron. Soc. Pacific 121, 878, 377–383, 2009.

[12] F. LE ROY-BREHONNET and B. LE JEUNE, "*Utilization of Mueller matrix formalism to obtain optical targets depolarization and polarization properties*," Prog. Quantum Electron. 21, 2, 109–151, 1997.

[13] M. BALLESTA-GARCIA, S. ROYO, "*Modelling polarized pulsed LiDAR signals in scattering media: an approach for optimizing systems in real-world scenarios*." Opt. Express, 32, 13, 22837-22857, 2024.

Development of a LiDAR-integrated multimodal system for underwater sensing

Aleix.R BOBI-OLMO [(1)], Eduardo BERNAL [(1)], Pablo GARCÍA-GOMEZ [(2)], Maria BALLESTA-GARCIA [(1)], Santiago ROYO [(1-2)]

1. Center for Sensors, Instruments and Systems Development (UPC-CD6), Universitat Politècnica de Catalunya, Rambla de Sant Nebridi 10, 08222, Terrassa, Spain
2. Beamagine S.L., Carrer de Bellesguard 16, 08755, Castellbisbal, Spain

Contact: Aleix.R BOBI-OLMO (aleix.ramon.bobi@upc.edu).

ABSTRACT:

Exploring oceans and seas, as well as the elements within them, including both manufactured and natural elements, is critical for many disciplines. Traditional optical imaging and sonar have advantages and disadvantages, but underwater LiDAR devices can complement them in terms of range and resolution. This article describes the design and construction of an innovative novel LiDAR integrated multimodal system for underwater sensing. The device can retrieve 3D information on the geometry of its surroundings thanks to the LiDAR, as well as RGB images with both wide and narrow FOV, and polarimetric images. Designed for modularity and ease of improvement, it improves range compared to a first proof of concept that was carried out last year. As future work, different lines of research will take place taking advantage of the multiple data that can be retrieved from the system in different environments, as well as the ability to retrieve new data.

Key words: LiDAR, underwater, multimodal, polarimetric, RGB imaging, marine research, 3D point cloud

1.- Introduction

The oceans have been integral to human civilization since its earliest days, providing both sources of sustenance and trade routes. This historical importance makes oceanic research compelling for various reasons, with formal scientific studies dating back to the early 1700s [1].

Contemporary marine research covers a wide range of fields, including environmental and energy studies, biodiversity research, and, as indicated by recent publications, national security applications. Accurate seafloor mapping is a critical need across these domains.

Despite sustained interest in the field, technical challenges in deploying mapping technologies in marine environments, especially beneath the surface, have resulted in large portions of the underwater landscape remaining inadequately documented and unmapped [2].

Traditionally, underwater imaging and mapping have relied on two main technologies: optical imaging and sonar.

Optical stereo imaging provides high-quality results at a low cost but is limited by range, computational demands, and difficulties with texture-less surfaces [3].

Sonar, on the other hand, is effective over long distances and in turbid waters but has a limited resolution due to its wavelength [4], requires large equipment, and can suffer from signal distortions on metallic structures.

More recently, underwater LiDAR has emerged as a complementary technology, bridging the gap between these methods, as

shown in figure 1, by offering detailed 3D data and improved environmental analysis for close- to mid-range underwater applications.

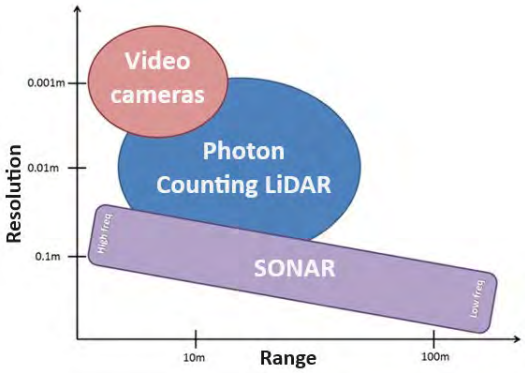

Fig. 1: Comparison of resolution versus range for underwater LiDAR, traditional optical imaging techniques and sonar based methods.

In this work, we present the design and development of a novel multimodal LiDAR system for underwater applications.

Unlike existing solutions, which are often highly specialized, expensive, and limited in availability, our system integrates multiple sensing modalities: traditional LiDAR point cloud acquisition, polarimetric imaging, and RGB imaging with both wide and narrow fields of view.

This unique combination enhances data collection capabilities, providing richer environmental information and improving object detection and classification in underwater scenarios. The proposed system represents the first implementation of such a comprehensive multimodal approach.

The following sections begin with a review of the state of the art in underwater LiDAR technology, providing context for our system's development. We then present the design and implementation of our multimodal sensing system, detailing the integration of different sensors and their functionalities. To validate our approach, we include preliminary results obtained last year with an earlier, more compact prototype that featured only two sensors. Finally, we present the results from the current system, highlighting its performance and potential applications in underwater exploration and mapping.

2.- State of the Art

2.1.- Light detection and ranging

LiDAR (Light Detection and Ranging) systems are remote sensing technologies that have existed since the 1960s, using light to measure distances by analyzing the backscattered signal. These systems operate using different principles, such as Time-of-Flight (ToF), Amplitude Modulated Continuous Wave (AMCW), Frequency Modulated Continuous Wave (FMCW), and triangulation. Each principle has its advantages depending on the specific requirements needed.

2.2.- Underwater LiDAR

Underwater LiDAR (UW-LiDAR) is still a relatively unexplored area, with limited commercially available systems, often accompanied by high operational costs.

The underwater absorption spectrum, as shown in figure 2 , makes it impossible to employ infrared lasers, which are commonly used in classic LiDAR systems.

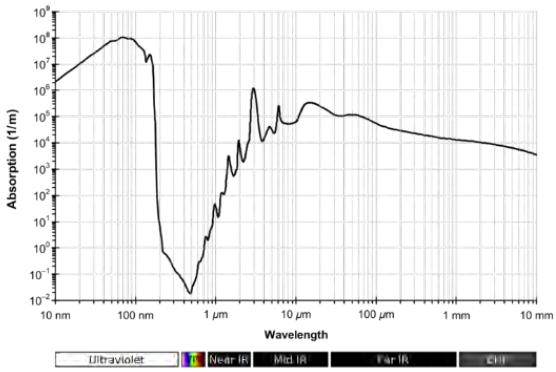

Fig. 2: Absorption spectrum for pure water.

The key challenge in underwater LiDAR is selecting the appropriate wavelength to maximize penetration and minimize attenuation. For oceanic waters, wavelengths between 420–520 nm are optimal, while for coastal waters, wavelengths between 520–580 nm are more effective due to increased turbidity [5]. The 532 nm wavelength (green light) is commonly used due to its relatively high transmission in water, even though it is not ideal for all conditions.

Additionally, technologies that are often taken for granted in conventional systems outside of water, such as GPS (Global Positioning System) that works with radio waves, are quickly absorbed in water within just a few meters, making underwater navigation even more challenging. This limitation requires generally alternative positioning methods, such as acoustic-based navigation or inertial measurement units (IMUs), adding complexity to underwater exploration and mapping.

Depending on the vehicle on which the system is mounted on, we can talk of airborne oceanic LiDAR or purely UW-LIDAR.

Airborne oceanic LiDAR is a system installed in aerial vehicles like planes, helicopters, and drones, used to scan the ocean's surface, water column, and potentially the upper ocean floor. It typically uses infrared light to detect the ocean surface and visible light (green or blue) to reach the bottom. One of its advantages is the ability to cover large areas quickly, something underwater systems can't do due to water resistance. However, its limitations include depth constraints due to water absorption, reduced reflection from the surface, and the inability to scan from other directions that are not downwards.

Subsea LiDAR, or purely underwater LiDAR, is mounted on a vehicle or pod that is fully submerged. It mainly uses visible light, typically green or blue. It can achieve greater depths and offers higher resolution, better accuracy, and the ability to scan closed spaces like underwater caves in real time, without further processing. However, it covers a smaller area compared to airborne systems, lacks GPS/GNSS data, and requires robust waterproof casing for protection.

2.3.- UW-LiDAR variations and applications

UW-LiDAR in its various forms has been used for a wide range of applications. In its conventional version it has been utilized for numerous applications, such as to discover new underwater archaeological sites as well as to study known ones [6]. It has also been used for scanning various marine structures such as offshore platforms, underwater locks, submarine connectors, pipelines [7], and anchor marks on the seabed among others. It has been used too, to study fish and fish schools [8], both with red and green light. Additionally, it has also been used to locate mines [9] and other objects with projects such as ALMDS (Airborne Laser Mine Detection System) which is mounted on a helicopter and scans the coastline.

In some of its variants UW-LiDAR has been employed for identifying material types based on the DOP (Degree of Polarization) response obtained [10], identifying species of macroalgae and coral based on their spectral response with a multispectral UW-LiDAR [11], and determining the attenuation coefficient as well as the beam profile and types of algae present in the water using a Scheimpflug UW-LiDAR [12].

3.- System design and implementation

To begin with, the system design has been developed to withstand pressures of up to two atmospheres. The main housing includes various electronic components and sensors, including a LiDAR scanner, a reception camera, RGB and polarimetric cameras, and a camera with a wide field of view. The system was also designed with a modular architecture to facilitate modifications and upgrades without requiring a complete redesign. This approach ensures that any changes (e.g. in imaging modes) can be implemented efficiently and cost-effectively, making the system adaptable to future improvements.

One of the key design elements is the front glass windows, which allow light and the scanning beams to pass through without compromising the system's waterproofing. To ensure structural integrity, a strength calculation was performed to confirm that the selected glass can withstand depths greater than initially required, even though these windows are the most critical components of the system.

The system's waterproofing relies on a set of mechanisms that protect internal components from water intrusion. Nitrile O-Rings with appropriate hardness have been used to ensure proper compression and sealing at the joints. These O-Rings have been strategically placed at critical points, such as the front cover, optical windows, and the connection between the main housing and the covers. Additionally, mounting rings have been designed to enhance sealing and provide a secure attachment.

The housing structure is made of high-strength aluminum and treated to withstand marine corrosion. To enhance durability, an anodized coating has been applied to protect the surface from oxidation. Simulation studies have shown that the housing can withstand pressures far exceeding the requirements for its current application, providing an additional safety margin.

Power supply and data transmission have been addressed with the selection of high-resistance submersible cables. The power cable is designed to withstand high current intensities, while data transmission is carried out via a Category 7 Ethernet cable. Both cables are protected by a water-resistant sheath and enter the housing through sealed cable glands, preventing leaks and ensuring stable operation.

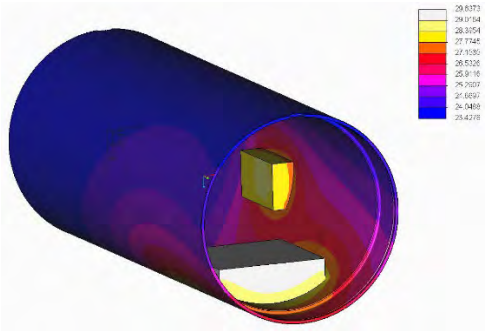

Fig. 3: Thermal simulations for the system supposing a 23°C water temperature. Maximum temperature for the surface in contact with the dissipators reaches 30°C.

Another important aspect of the design is heat dissipation, as several electronic components generate heat during operation. To prevent excessive temperature increases, heat sinks have been integrated in direct contact with the aluminum housing, taking advantage of the material's thermal conductivity and the natural cooling provided by the surrounding water. Thermal studies have confirmed that, under normal operating conditions, the internal temperature remains within safe limits. Long-duration tests with the system running at full power have also validated these findings.

Regarding possible system improvements, several options could be considered to enhance its durability and versatility. One proposal would be the incorporation of tempered glass windows, which would improve impact resistance and reduce the risk of fractures. Additionally, the cable glands could be reinforced to ensure an even more effective seal under extreme conditions.

Finally, in terms of safety, potential failure scenarios have been considered. Severe damage to the cables could disrupt power supply or data transmission, so additional protective measures are always taken during transport and deployment. Nevertheless, the presence of an internal pair of cable glands, the double shielding of the Ethernet cable with different diameters, and the use of a submarine power cable with no gaps for water ingress ensure that such hypothetical situations would not lead to system failure in most cases. Similarly, while the likelihood of window breakage is low, an additional protective system may be considered to minimize any risk in demanding work environments.

This design has been developed through a combination of structural analyses, material studies, and simulations to ensure its proper functioning in underwater applications, maintaining a balance between safety, efficiency, and future expansion possibilities.

4.- Results

A first proof of concept was carried out to confirm main hypotheses. This design was quite different from the one being presented in this work. It only contained a LiDAR within the POD, as well as a GoPro camera at the outside, which wasn't screwed but attached by a Velcro. The laser used by this previous system had a peak power of 33W, compared to the 2000W of the new laser, resulting in a very moderate range. With a color checker a range of 4 meters was obtained. The tests were carried out at LIM (Laboratory of Mechanical Engineering) at Campus Nord-UPC.

Fig. 4: Photography of the LIM test site with the system.

Fig. 5: Photo of the scene, with the proof of concept system at the right, and at the left a platform with 4 ropes and a cylindrical and brick like objects.

Fig. 6: Visualization of a point cloud retrieved from the scene we can see in figure 5.

The current system has already been assembled, and tested underwater for a depth of 50 centimeters. Further deeper submersion tests are planned to be carried out soon to test the sealing of the system. The calibration of the system in air has been carried out using a chessboard-style pattern, and the perfected underwater calibration method is still under evaluation, but initial approach considers Snell's law and scanner's normal angle. As mentioned before, long duration test have been caried out in order to check that internal temperature don't reaches a critical point. Potential high pressure hose test could also be done to check the waterproofness of the system.

Fig. 7: Photography of the current system.

5.- Conclusion

In this work, we have presented the development of an innovative multimodal LiDAR system for underwater applications, integrating different sensing modalities: traditional LiDAR point cloud acquisition, polarimetric imaging, and RGB imaging with both wide and narrow fields of view. This multimodal approach is pioneering, as no similar implementations exist today.

The modular and robust design of the system, capable of withstanding pressures up to two atmospheres, has demonstrated optimal performance in initial submersion tests. Thermal management and waterproofing have been validated through simulations and extended operation testing.

Preliminary results confirm the system's viability, representing a significant advancement over the previous lower-power prototype.

This new device offers considerable potential for improving the study of various underwater environments, constituting a valuable tool for oceanic research.

As future work, different lines of research will take place taking advantage of the multiple data that can be retrieved from the system in different environments.

Acknowledgements: This work is part of a Ph.D. Thesis with grant number 2024 FI-1 00222 given by the Joan Oró from the Secretaria d'Universitats i Recerca from the department of Recerca i Universtitats of Generalitat de Catalunya. This work has been sponsored by the Spanish Ministry of Science through projects TED2021-132338B-I00 and PID2023-152427OB-I00 and by the European commission through project GA-101139941.

References

[1] Nadia PINARDI, Emin ÖZSOY, Mohamed A. LATIF, Fabio MORONI, Alessandro GRANDI, Giovanni MANZELLA, Federica DE STROBEL, Vladimir LYUBARTSEV, "Measuring the Sea: Marsili's Oceanographic Cruise (1679–80) and the Roots of Oceanography", Journal of Physical Oceanography, 48, 4, 845–860, 2018.

[2] NOAA Office of Ocean Exploration and Research, https://oceanexplorer.Noaa.gov/facts/explored.html

[3] A. FILISETTI, A. MAROUCHOS, A. MARTINI, T. MARTIN, S. COLLINGS, "Developments and applications of underwater LiDAR systems in support of marine science", in Proceedings of OCEANS Conference, 1-10, 2018.

[4] J. DILLON, R. CHARRON, "Resolution Measurement for Synthetic Aperture Sonar", in Proceedings of OCEANS 2019 MTS/IEEE SEATTLE, 1-6, 2019.

[5] S. CHEN, C. XUE, T. ZHANG, L. HU, G. CHEN, J. TANG, "Analysis of the Optimal Wavelength for Oceanographic Lidar at the Global Scale Based on the Inherent Optical Properties of Water", Remote Sensing, 11, 22, 2705, 2019.

[6] Jessica W. COOK HALE, Dylan S. DAVIS, Matthew C. SANGER, "Evaluating the Archaeological Efficacy of Bathymetric LiDAR across Oceanographic Contexts: A Case Study from Apalachee Bay, Florida", Heritage, 6, 2, 928-945, 2023.

[7] Albert PALOMER, Pere RIDAO, David RIBAS, *"Inspection of an underwater structure using point-cloud SLAM with an AUV and a laser scanner"*, Journal of Field Robotics, 36, 8, 1333-1344, 2019.

[8] Elizaveta DUBROVINSKAYA et al., "Underwater LiDAR Signal Processing for Enhanced Detection and Localization of Marine Life", in Proceedings of (2018 OCEANS - MTS/IEEE Kobe Techno-Oceans), 1-8, 2018.

[9] IDST – International Defence Security & Technology,https://idstch.com/military/navy/lidar/

[10] Yong ZHU, Qingyi HE, Qiang FU, Chao DONG, Jianhua LIU, Jin DUAN, *"Detection of Underwater Targets Using Polarization Laser Assisted Echo Detection Technique"*, Applied Sciences, 13, 5, 3222, 2023.

[11] M. HUOT, F. DALGLEISH, D. BEAUCHESNE, M. PICHÉ, P. ARCHAMBAULT, "Machine learning for underwater laser detection and differentiation of macroalgae and coral", Front. Remote Sens., 4, 1135501, 2023.

[12] H. ZHANG, Y. ZHANG, Z. LI, B. LIU, B. YIN, S. WU, "Small Angle Scattering Intensity Measurement by an Improved Ocean Scheimpflug Lidar System", Remote Sensing, 13, 12, 2390, 2021.

Optical Characterization of a Novel Concept of Deformable Primary Mirror for CubeSat Telescopes

Sara GIMÉNEZ-ARAGÓN [1], Toni RUIZ-VALVERDE [1], Alejandro SANTILLÁN [2], Armengol TORRES [2], Eduardo FERRER [2], Santiago ROYO [1]

1. Centre for Sensors, Instruments and Systems Development, Universitat Politècnica de Catalunya (CD6-UPC), Rambla de Sant Nebridi 10, E08222, Terrassa, Spain
2. SLIMOp Space S.L., C/Sancho de Ávila 119, E08018, Barcelona, Spain

Contact: Sara GIMÉNEZ-ARAGÓN (sara.gimenez@upc.edu).

ABSTRACT:

The increasing demand for compact and affordable satellite technologies has driven the adoption of CubeSats for Earth observation and space research. This study examines the optical characterization of a novel concept of deformable primary mirror developed for CubeSat missions, conceived by SLIMOp Space. The Shack-Hartmann wavefront sensor (SHWFS) and Bath interferometer techniques were successfully implemented and validated against a reference mirror, offering complementary insights into the mirror's optical quality and surface performance. Finite element analysis using SolidWorks and MATLAB identified wafer warp as the primary cause of surface defects due to undesired surface deformations. These findings aid in refining the mirror's design to meet the stringent optical requirements of CubeSat missions. With its lightweight and scalable design, the mirror shows great potential not only for Earth observation but also for free-space optical communications. Future work will focus on exploring alternative wafer materials to further optimize the mirror's surface shape.

Key words: CubeSat, deformable mirror, Shack-Hartmann wavefront sensor, Bath Interferometer, finite element analysis, wafer warp

1.- Introduction

Earth observation through satellites plays a crucial role in fields such as environmental monitoring, agriculture, disaster management, and urban planning. The growing demand for high-resolution space-based imaging must be balanced with compact, lightweight, cost-effective, and scalable satellite technologies.

This challenge has driven the development of smaller, more accessible satellite platforms, contrasting with large-scale observatories like the James Webb and Hubble Space telescopes. Among the most promising solutions are nanosatellites, a category that includes CubeSats, custom nanosatellites, PocketQubes, and picosatellites. These platforms offer an affordable and flexible approach to space-based imaging, with CubeSats, in particular, emerging as key players, due to their standardized designs, as an expanding ecosystem supporting technology development [1].

A CubeSat's basic unit (1U) measures 10 cm per side and weighs 1.33 kg. Larger configurations, referred to as 'XU' CubeSats, are created by coupling multiple units, ranging from 0.25U to 27U. This modular design has revolutionized CubeSat-based astronomical telescopes, with missions like ASTERIA, SPARCS, and CUTE demonstrating their capability for high-precision photometry and spectroscopy. Originally intended for educational purposes, CubeSats have evolved into powerful tools for

scientific research, with applications in astrophysics, atmospheric studies, and Earth observation [2].

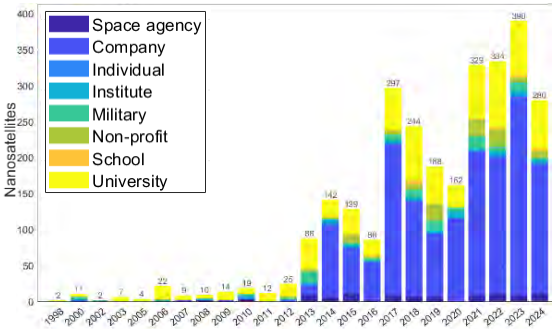

Fig. 1: Yearly nanosatellite launches by organization type (reproduced from [2]).

Fig. 1 illustrates the annual nanosatellite launches by organization type, highlighting the growing adoption of CubeSats across academia, government, and especially the commercial sector, driven by large-scale constellation deployments.

A critical factor in improving CubeSat telescope performance is addressing optical distortions arising from misalignment, component imperfections, and environmental disturbances such as temperature fluctuations. Adaptive optics, particularly deformable mirrors, offer a solution by dynamically correcting wavefront errors to enhance image quality. Deformable mirrors are widely used in astronomy, microscopy, and laser systems to achieve real-time correction of optical aberrations [3]. While conventional deformable mirrors use actuators to reshape their surface and compensate for optical aberrations, this work investigates an alternative approach within adaptive optics: a pressure-controlled flexible membrane mirror capable of modulating its global curvature. Instead of correcting fine wavefront distortions, this system enables dynamic tuning of the focal length. The result is a lightweight, cost-effective, and scalable solution well-suited for CubeSat telescopes.

This research is part of a collaboration between the Centre of Sensors, Instruments and Systems Development (CD6) and the New Space startup SLIMOp Space. SLIMOp specializes in the development of CubeSat telescopes, focusing on affordability, scalability, and high-resolution imaging for space applications. CD6 contributes by designing an innovative deformable primary mirror, forming the core of a compact Optical Tube Assembly (OTA) tailored for CubeSat missions. By integrating this novel optical system, the project aims to enhance Earth observation capabilities, offering a practical and efficient solution for high-resolution imaging in small satellite platforms.

2.- Methodology

The deformable primary mirror developed for this study consists of a vacuum chamber housing a glass mirror wafer that flexes under pressure. To evaluate its optical quality, two experimental characterization techniques were employed: the Shack-Hartmann Wavefront Sensor (SHWFS) and the Bath Interferometer. Additionally, numerical simulations were conducted to validate the experimental results and assess their consistency.

2.1.- Experimental Characterization

2.1.1.- Shack-Hartman Wavefront Sensor (SHWFS)

The Shack-Hartmann Wavefront Sensor (SHWFS) is a non-interferometric device based on deflectometry, designed to evaluate the wavefront emerging from an optical surface by comparing it to an ideal reference wavefront. It consists of an array of lenslets, each producing a light spot on a detector (see Fig. 2). The position of each spot corresponds to the local slope of the wavefront, enabling the reconstruction of the aberrated wavefront using the Zernike modal basis [4].

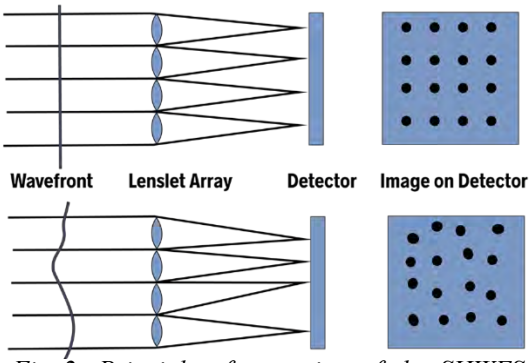

Fig. 2: Principle of operation of the SHWFS (adapted from [5]).

In addition to characterizing the aberrations present on the primary mirror's surface, the SHWFS can determine the radius of curvature (RoC) of the mirror using the expression:

$$RoC\ [mm] = \frac{2000}{P} + d \qquad (1)$$

where P is the optical power (in diopters) and d is the distance from the mirror to the SHWFS (in mm). The relationship between optical power P and focal length f is $f = 1/P$, and since $RoC = 2f$, it can be used to compute the radius of curvature.

The experimental setup (see Fig. 3) used for this measurement consists of a diode laser emitting at 635 nm, coupled to a 2-inch aperture collimator, followed by a 50:50 non-polarizing Beam Splitter (BS) cube (400-700 nm). The mirror under study is placed in one of the directions where the BS redirects the beam. Upon reflection from the mirror, the beam returns to the BS, which then redirects it toward the Shack-Hartmann sensor.

Before taking measurements, the precision and accuracy of the system were evaluated using a known non-aberrated plane mirror as a reference. The results showed a relative error of 0.1% in focal length determination, while the Zernike coefficients for aberrations were on the order of 10^{-2}, indicating negligible aberrations. These findings confirm the high precision and accuracy of the SHWFS system.

However, the maximum measurable diameter in the SHWFS setup is limited to a central Ø50 mm pupil due to the sizes of the collimator and beam splitter, while the primary mirror's working diameter extends up to 200 mm. As a result, a complementary characterization technique, such as the Bath interferometer, is required to fully assess the mirror's surface.

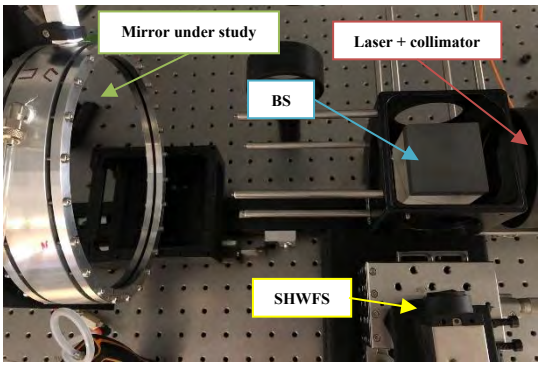

Fig. 3: Shack-Hartmann setup: deformable primary mirror as the mirror under study.

2.1.2.- Bath Interferometer

The Bath Interferometer is an interferometric technique used to compare the light reflected by the mirror under study (test beam) with a known reference beam. When the two beams interfere, the resulting fringe pattern reveals the shape of the mirror's surface. Deviations from the ideal spherical wavefront distort the fringe pattern, enabling the analysis of imperfections and aberrations. This technique is commonly employed for the characterization of telescope mirrors [6].

The interferometer setup (see Fig. 4) consists of a laser source emitting at 657 nm, a 15 mm 50:50 non-polarizing BS cube, a 20 mm divergent lens for the test beam, and a flat mirror for the reference beam, all mounted on an XYZ stage. A polarizer is placed after the BS to suppress residual scattering and enhance interference fringe contrast. The interferogram is captured at the polarizer's output using a CANON EOS 1100D camera.

As a preliminary step before characterizing the deformable primary mirror, a reference object is measured to evaluate and calibrate the system, ensuring the accuracy of subsequent measurements. A parabolic f/5 mirror with a focal length of 1000 mm and a diameter of Ø200 mm has been used as the aspheric reference. This mirror shares the same dimensions as the one used in the deformable primary mirror.

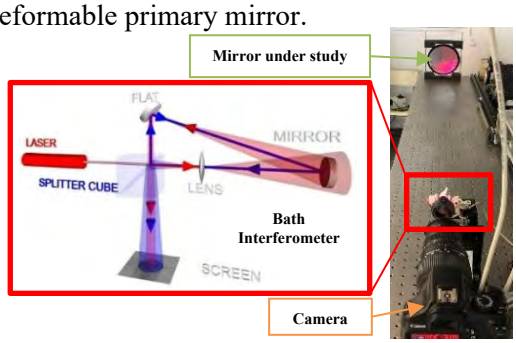

*Fig. 4: **Left:** Principle of operation of the Bath Interferometer (reproduced from [7]). **Right:** Bath Interferometer setup: parabolic f/5 reference mirror as the mirror under study.*

To further validate the measurements obtained from both the reference mirror and the mirror under study, an interferogram simulator open-source [8] has been employed.

2.2.- Numerical Simulation of Deformable Mirror Behaviour

In practice, the obtained interferogram deviated significantly from those of the aspheric reference, exhibiting uncontrolled astigmatism of several wavelengths. To better understand the surface deformations of the mirror wafer under vacuum conditions, numerical simulations were performed using SolidWorks and MATLAB. This study aimed to identify the sources of deformation, optimize mirror performance, validate experimental results, and assess their consistency with theoretical predictions.

The vacuum chamber and mirror assembly were modeled in SolidWorks, replicating the experimental conditions by defining key parameters such as material properties, temperature, pressure levels, and screw torque. The simulations explored various deformation scenarios by adjusting defect distributions and mounting configurations, refining the design, and providing deeper insight into the mirror's mechanical response.

3.- Results

3.1.- Shack-Hartmann Wavefront Sensor (SHWFS)

To evaluate the optical quality of the deformable primary mirror, wavefront measurements were performed using the SHWFS. This technique allows for the characterization of the mirror's surface by analyzing the local wavefront slopes and reconstructing the phase profile.

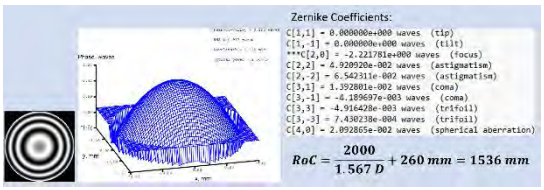

Fig. 5: SHWFS measurement of the central Ø50 mm pupil of the Ø200 mm deformable primary mirror at RoC = 1536 mm. The results include the interference ring pattern, 3D representation of the measured phase surface, calculated RoC, and Zernike coefficients, all indicating the absence of aberrations in the measured pupil.

The results indicate that within the central Ø50 mm pupil—the maximum measurable diameter in our setup—the mirror is free of aberrations across the RoC range of 3200–1200 mm (Fig. 5 presents the specific case of RoC = 1536 mm). This confirms the stability and optical performance of the mirror within this region, validating its suitability for precision applications.

3.2.- Bath Interferometer

To evaluate the entire surface of the deformable primary mirror, measurements were conducted using the Bath interferometer. As a preliminary step, an interferogram simulation [8] was performed, replicating the parameters of our experimental setup: an f/5 system, a 200 mm mirror diameter, a conic constant $K = -1$ (parabolic), a wavelength of 657 nm, and a defocus of 3.34 waves. The resulting simulated interferogram is shown in Fig. 6 (left).

Next, an experimental interferogram was captured from the parabolic reference mirror (Fig. 6, center). The strong agreement between the simulated and experimental results confirms the accuracy of the interferometer as a measurement tool and validates the expected fringe pattern of an aberration-free parabolic mirror.

Finally, the deformable primary mirror was measured. The resulting interferogram (Fig. 6, right) exhibits significant deviations from both the simulated and reference mirror interferograms, indicating unexpected surface

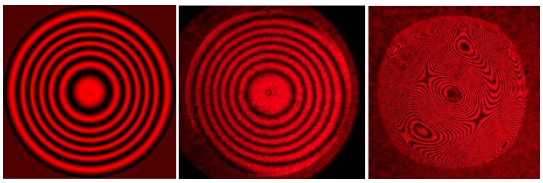

Fig. 6: Interferograms for a parabolic mirror (f/5, Ø200 mm, K=-1, λ = 657 nm). Left: Simulated interferogram [8]. Center: Experimental interferogram of the reference mirror. Right: Experimental interferogram of the deformable primary mirror. Both captured images were taken with a camera (f = 300 mm, f/5.6, exposure = 1/4000, ISO = 100) using a polarizing lens.

deformations. These observations prompt a critical question: what is the origin of these deformations?

3.3.- Numerical Simulations

Numerical simulations of mirror wafer bending were conducted using SolidWorks and MATLAB to identify the source of surface deformations.

3.3.1.- Simulation 1: mirror wafer bending under pressure

The simulation of the deformable mirror bending in the vacuum chamber showed no significant surface deformations. The contour plot exhibited a nearly symmetrical distribution, matching the simulated interferogram (Fig. 6, left), indicating that neither the screws nor the applied pressure caused the observed deformations.

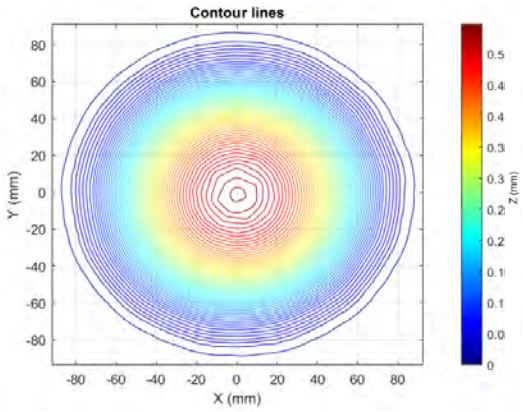

Fig. 7: Simulation of mirror wafer surface deformation at 51.3 mbar, with contour lines at 10 µm intervals, when resting on the vacuum chamber.

3.3.2.- Simulation 2: Thermal Analysis

A thermal analysis was performed to assess the effect of temperature on the mirror surface. The results showed that as temperature increases, the radius of curvature decreases (i.e., the mirror becomes less flat), following a linear trend. This behavior is due to thermal expansion, which alters the material properties. However, all contour plots exhibited symmetrical bending similar to Fig. 7, confirming that temperature is not the source of the observed defects.

3.3.3.- Simulation 3: Mechanical Tolerances of the Vacuum Chamber

Profilometry studies identified three deformation points on the vacuum chamber's support ring where the mirror wafer rests. To investigate their impact, a simulation was performed by introducing three semi-cylindrical defects (0.25 mm radius), evenly spaced at 120° intervals.

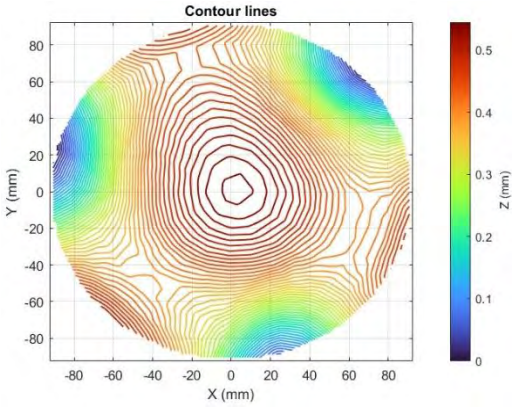

Fig. 8: Simulation of mirror wafer surface deformation at 32 mbar due to three deformation points on the vacuum chamber (cylindrical defects of 0.25 mm spaced 120° apart), with contour lines at 10 µm intervals.

Fig. 8 reveals significant irregularities at the wafer's outer region. While some manufacturing defects in the vacuum chamber may contribute to peripheral distortions, they do not match the deformations observed in the experimental interferograms, ruling out mechanical tolerances as the primary cause.

3.3.4.- Simulation 4: Wafer Warp

Warp refers to the maximum deviation of the wafer surface from an ideal flat surface. Since wafer warp is inherently random, according to the manufacturer, and varies from one wafer to another, multiple simulations were conducted to analyze different possible scenarios.

Simulations were conducted with both negative and positive cylindrical warps applied to the mirror wafer at 50 mbar. As shown in Fig. 9, the simulated warps closely correspond to the experimental results, replicating the key deformation features observed in the interferograms. Although each wafer has an inherent, unpredictable warp that cannot be precisely modeled in SolidWorks, the results confirm that wafer warp is the dominant factor causing the observed surface deformations.

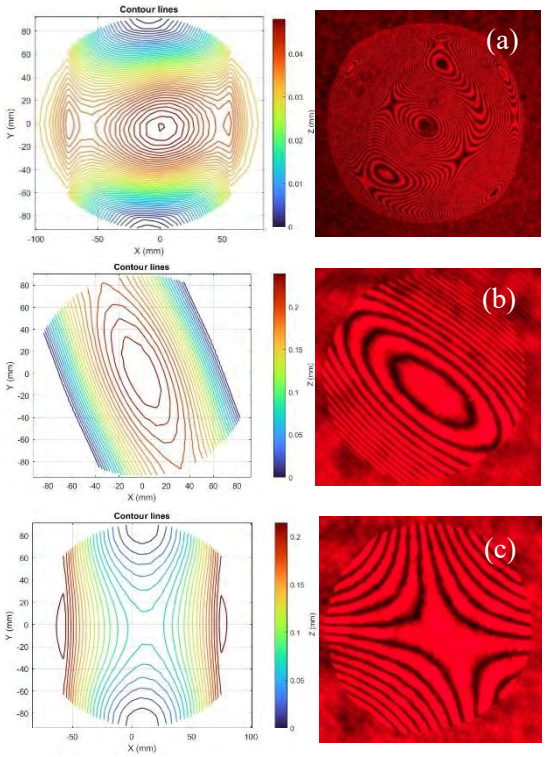

Fig. 9: Simulations of mirror wafer surface deformation due to cylindrical warp at 50 mbar, compared with experimental interferograms captured using the Bath Interferometer. (a) Negative cylindrical warp of 30 µm, matching the captured interferogram. Contour lines are spaced at 1 µm intervals. (b) and (c) show negative and positive cylindrical warps of 200 µm, respectively, corresponding to interferograms from a different wafer. Contour lines are spaced at 10 µm intervals.

4.- Conclusion

This study presents the optical characterization of a novel deformable primary mirror designed for CubeSat missions, aiming to enable ultra-lightweight, low-cost, and high-resolution imagers with rapid deployment, scalable for Earth observation satellite constellations.

The Shack-Hartmann and Bath interferometer techniques have been successfully validated, providing a robust and reliable reference for assessing the mirror's optical quality. These methods offered complementary insights into the mirror surface and its optical performance, ensuring a thorough characterization.

To strengthen the theoretical foundation, a finite element analysis of wafer deformation under static pressure was conducted using SolidWorks and MATLAB. This analysis provided valuable insights into surface deformation, thermal effects, and surface warping, deepening the understanding of the mirror's mechanical response. The results confirm that wafer warp is the primary cause of the observed surface defects.

Future work could explore different wafer types and materials to optimize performance further. Given its lightweight, cost-effective, and scalable design, this system holds significant potential for CubeSats, not only for Earth observation imaging but also for free-space optical communications.

Acknowledgements: This work has been sponsored by the Spanish Ministry of Science through projects TED2021-132338B-I00 and PID2023-152427OB-I00 and by the European commission through project GA-101139941.

References

[1] Daniel SELVA and David KREJCI, "*A survey and assessment of the capabilities of Cubesats for Earth observation*", Acta Astronautica, vol. 74. Elsevier BV, pp. 50–68, 2012.

[2] Nanosats database. https://www.nanosats.eu/

[3] Pierre-Yves MADEC, "*Overview of deformable mirror technologies for adaptive optics and astronomy*", Proceedings of SPIE, 2012.

[4] Ethan CHU et al., "*Improved wavefront reconstruction for Shack–Hartmann wavefront sensor in the presence of shock-related distortions*", Optics & Laser Technology, 187, 2025.

[5] Bettina MIKULEC et al., "*A novel high resolution, high frame rate detector based on a microchannel plate read out with the Medipix2 counting CMOS pixel chip*", IEEE Symposium Conference Record Nuclear Science, 2004.

[6] The Bath Interferometer. George Roberts Website. https://gr5.org/bath/

[7] Bath interferometer light paths. Vladimir Galogaza Website. https://vladimirgalogaza.wordpress.com/2009/06/29/bath-interferometer-light-paths/

[8] Interferogram Simulator. George Roberts Website. https://gr5.org/bath/fringes.html

Phi-OTDR de pulso chirpeado largo para medidas en fibra de nanodeformaciónes de kHz a 24h con alto rango dinámico

Hugo F. MARTINS [1]

1. Instituto de Óptica "Daza de Valdés" IO-CSIC, C/Serrano 121, 28006 Madrid, España

Contact: Hugo F. MARTINS (hugo.martins@csic.es).

Resumen:

Los OTDR sensibles a fase (φOTDR) con pulsos chirpeados (CP-ΦOTDR) ofrecen una alternativa de detección directa sencilla pero eficiente a los sistemas DAS (sensado acústico distribuido) tradicionales de medición de fase. CP-ΦOTDR se han utilizado académica/comercialmente hasta ≈1GHz, pero el uso de grandes chirps se ha evitado en gran medida debido al aumento de coste/complejidad. En este trabajo, se investigan los límites de rendimiento de CP-ΦOTDR con grandes chirps ópticos (8 GHz). Resultados preliminares muestran un aumento supralineal del rango de deformación dinámica con el contenido de chirp óptico y una mejora disruptiva de medidas a largo plazo. El ruido instrumental 1/f se elimina prácticamente hasta mHz, mientras se miden perturbaciones equivalentes a cientos de MHz. Se obtuvieron fácilmente variaciones de deformación traza-a-traza (kHz) de ±3με, un nivel de ruido ASD de <100 pε/√Hz y una incertidumbre instrumental de ≈nε estimada durante mediciones de una hora de duración.

Palabras clave: Sensado distribuido, OTDR sensible a fase, sismología, fibra óptica, scattering Rayleigh, pulsos con chirp, sensado acústico distribuido

1.- Introduction

La reflectometría de dominio óptico sensible a la fase con pulsos chirpeados (CP-ΦOTDR) se ha utilizado ampliamente tanto académica como comercialmente en el rango de ≈1 GHz. Sin embargo, hasta la fecha, el uso de grandes chirps se ha evitado en gran medida debido al aumento de costo y complejidad [1]. Se han presentado estudios prometedores que amplían considerablemente el rango de deformación dinámica [2] y la estabilidad a largo plazo [3] del CP-ΦOTDR, pero estos se realizaron a expensas de un empeoramiento drástico de la sensibilidad del sensor (aumentada a cientos de ne/√Hz), en comparación con los cientos de pe/√Hz alcanzables con el CP-ΦOTDR tradicional. En este trabajo, investigamos los límites de rendimiento al operar con CP-ΦOTDR de gran chirp (LCP-ΦOTDR) - 8 GHz, demostrando en una única configuración un aumento significativo tanto en el rango de deformación dinámica de traza-a-traza alcanzable como en la estabilidad de referencia de la fibra a largo plazo, manteniendo el bajo nivel de ruido de ASD asociado a la técnica.

2.- Metodología

Este trabajo ha utilizado una configuración experimental basada en la operación típica de CP-φOTDR [1] con modulación externa, modificada para mejorar el rendimiento con un mayor contenido de chirp, como se muestra en la Figura 1a. La rama superior del diagrama está dedicada a la generación de pulsos, utilizando un láser de bajo ruido de fase (ancho de línea ≤100 Hz, 1550,12 nm) como fuente de luz. Su salida fue modulada por un modulador IQ-MZM controlado por un Generador de Forma de Onda Arbitraria (AWG) para producir un tren de pulsos chirpeados (chirp lineal de 8 GHz, sobre 80 ns y tasa de repetición de 1 kHz). Estos pulsos son amplificados por un amplificador de fibra dopada con erbio (EDFA) y pasan a través de un multiplexor por división de longitud de

onda densa (DWDM) comercial de 100 GHz, utilizado como un paso de banda óptico para filtrar el ruido ASE del EDFA. Se utilizan atenuadores ópticos variables (VOA) para regular y optimizar los niveles de potencia en ambas ramas. La potencia pico de los pulsos se fijó en 200 mW (el límite antes de la aparición de no linealidades en fibras largas), antes de inyectarse en la fibra bajo prueba (FUT) a través de un circulador óptico. La FUT estaba compuesta por 4 km de fibra SMF seguida de un PZT comercial (alimentado por un generador de señales de voltaje), lo que permitió aplicar perturbaciones de deformación calibradas a lo largo de 60 metros de fibra (enrollada alrededor del PZT, en 3 capas de 20 m, fig. 1b).

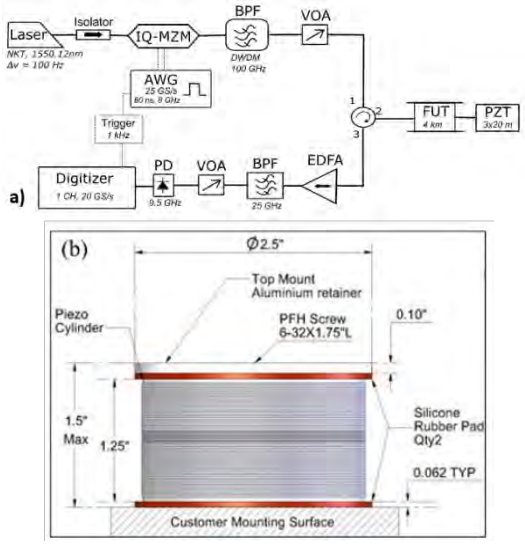

Fig. 1: (a) Configuración experimental del ΦOTDR de pulsos chirpeados grandes y (b) el PZT utilizado para introducir perturbaciones de deformación calibradas. Véase el texto para más detalles sobre cada componente.

La rama inferior del diagrama muestra los elementos que intervienen en la detección de señales. La señal retrodispersada de Rayleigh es amplificada por un EDFA, pasa por un filtro paso banda óptico sintonizable de 25 GHz para reducir el ruido ASE del EDFA, antes de ser detectada por un fotodetector (PD) de alta velocidad (detección directa, 9,5 GHz) y registrada por un digitalizador (1 canal, 20 GS/s). La generación y adquisición de señales se sincronizan mediante un disparador común. El sistema completo es capaz de generar y analizar grandes pulsos chirpeados para la operación del CP-φOTDR con alta calidad y una resolución espacial de 8 m, manteniendo una buena relación señal-ruido (SNR) a lo largo de todo el FUT durante largos periodos de tiempo.

Cabe mencionar que, si bien la respuesta dinámica del LCP-ΦOTDR pudo caracterizarse con una medida de calibrada (las perturbaciones de nanodeformación calibradas con el PZT fueron factibles), esto no fue posible para las mediciones lentas, que se vieron limitadas fundamentalmente por el ruido ambiental. Dado que no era experimentalmente factible aplicar o medir variaciones de temperatura de la fibra del orden de 1 mK en nuestro laboratorio durante largos periodos para una caracterización directa del ruido ambiental, no era estrictamente posible una medición verdaderamente directa del ruido de fondo instrumental para mediciones lentas. Por lo tanto, para proporcionar límite superior al error de medición, se utilizó una medición diferencial entre las tres capas de PZT. Debido a su configuración geométrica, se espera (según el fabricante) que el coeficiente de conversión de deformación-voltage sea ligeramente diferente para cada una de las capas de 20 m. Las capas externas presentan menos desplazamientos (0-20 m). También se espera que la temperatura a lo largo de las tres capas presente un gradiente de temperatura, con las capas externas (0-20 m) en "contacto" con el aire, presentando una variación mayor que las capas internas (en contacto con el piezocilindro y mecánicamente en contacto con una mesa óptica, que actuó como un disipador de calor). Más importante aún, se observó que estos gradientes variaban linealmente a lo largo de grandes variaciones, lo que permitió evaluar el ruido instrumental mediante la medición diferencial: (capa 1 [0-20 m] + capa 3 [40-60 m])/2- (capa 2 [20-40 m]). Cabe destacar que la resolución espacial de la medición (80 ns) y el tamaño de la ventana temporal para el cálculo del retardo temporal mediante correlación cruzada (también 80 ns) se eligieron para garantizar que las mediciones en las 3 capas (cada una de 20 metros) presentaran 3 mediciones no

correlacionadas y, por lo tanto, que la medición diferencial proporcionara una estimación real del ruido de fondo instrumental, en lugar de una reducción virtual del ruido debido al uso de la medición diferencial de puntos que no proporcionaron ruidos verdaderamente no correlacionados.

3.- Resultados

Mediciones de deformación dinámica: En primer lugar, se caracterizaron las mediciones dinámicas aplicando una señal sinusoidal de 10 Hz pico a pico de 2,5 με (fig. 2 a-c) y 10 nε (fig. 2 d-f) al PZT. Se registraron 1000 trazas adquiridas a 1 kHz (1 s). Gracias al uso de un chirp óptico grande, fue posible cubrir todo el rango de medición utilizando solo una traza óptica (la primera) como referencia de fibra, y sin actualizaciones de referencia adicionales, como suele ser el caso para grandes perturbaciones [2]. En este caso, se observó la eliminación del ruido DAS 1/f tradicional (fig. 2 a, b, d, e). Se presenta una medición de control, donde la referencia de fibra se actualizó en todo momento para su comparación (fig. 2 c, f), que representa un ruido 1/f que impidió mediciones de alta sensibilidad a bajas frecuencias. El ruido de fondo ASD (<100 pε/√Hz) es comparable al CP-ΦOTDR del estado-del-arte [1].

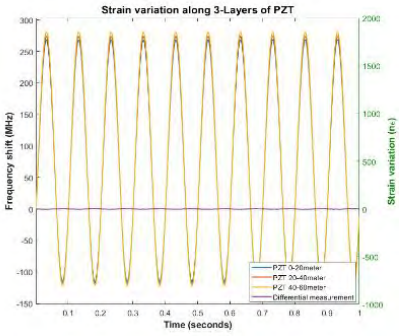

a)

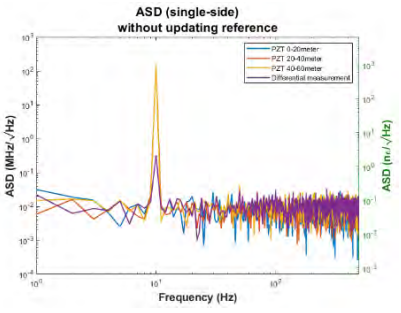

b)

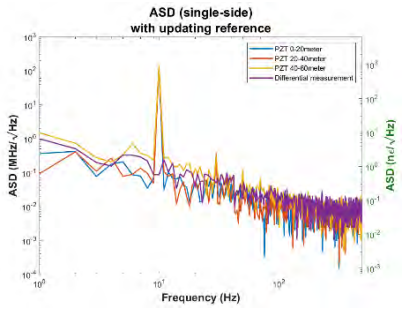

c)

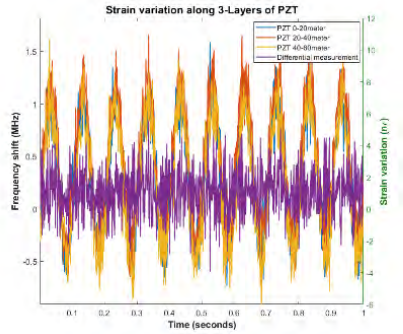

d)

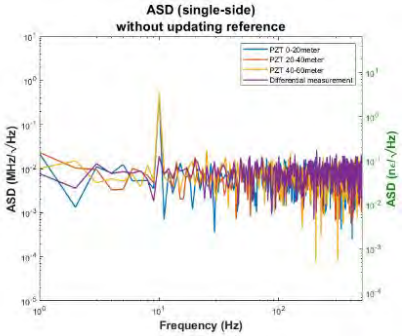

e)

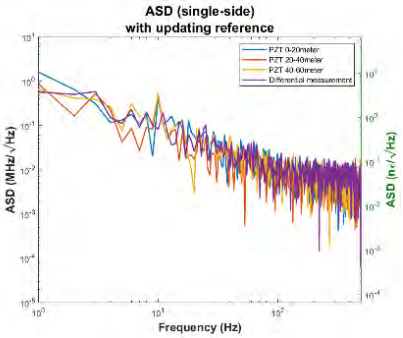

f)

Fig. 2: Mediciones de deformación dinámica para una señal sinusoidal de 10 Hz pico a pico de 2,5 με (fig. a-c) y 10 nε (fig. d-f) hacia el PZT. Estas mediciones se realizaron utilizando una única referencia de fibra (la primera traza óptica) sin actualizaciones de referencia (a, b, d, e) y se compararon con el caso en

el que la referencia de fibra se actualiza en todos los instantes (c, f).

Rango de deformación dinámica traza-a-traza: Luego, para caracterizar el límite del sistema en términos de rango de deformación dinámica traza-a-traza, se aplicó una onda cuadrada de 2,5 $\mu\varepsilon_{pp}$ a 100 Hz (fig. 3). Se registraron 1000 trazas adquiridas a 1 kHz (1 s). La variación de deformación traza-a-traza de la medición se presenta en la fig. 3b, pudiendo medir ±3 με (señal aplicada + sobreimpulso). La medición se realizó de nuevo tomando una única traza óptica (la primera) como referencia, sin que se requirieran actualizaciones de referencia adicionales. A pesar de la deformación aplicada grande y rápida, el uso de una única traza de referencia conduce de nuevo a un espectro ASD plano sin ruido 1/f (los armónicos son totalmente esperados considerando la onda cuadrada aplicada). Considerando la naturaleza repetitiva de la señal, se estima que los sobreimpulsos de deformación se deben a las señales aplicadas por el PZT y no al ruido instrumental.

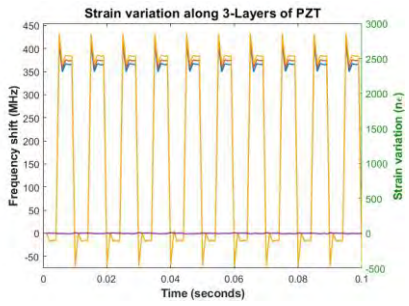

a)

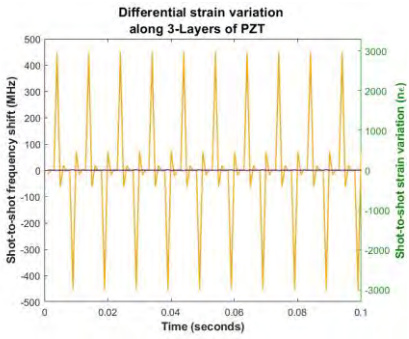

b)

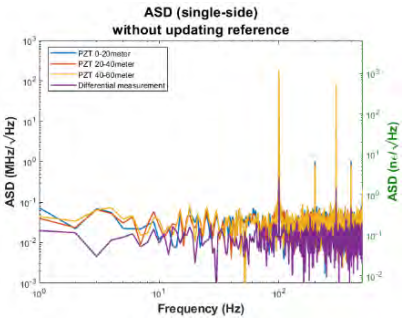

c)

Fig. 3: Rango dinámico traza-a-traza para una onda cuadrada de 2,5 $\mu\varepsilon_{pp}$ de 100 Hz (a) Zoom de la medición de la señal temporal (0,1 s de 1 s) (b) diferenciación de (a), que representa la variación de la deformación traza-a-traza (c) ASD para la medición presentada en (a).

Medición de deformación lenta: Para caracterizar la respuesta del sistema a frecuencias lentas, se aplicó una onda sinusoidal de 2,5 $\mu\varepsilon_{pp}$ de 0,01 Hz (fig. 4). Debido a las limitaciones de la memoria del digitalizador, se registró 1 de cada 500 trazas del disparo original de 1 kHz (sin promediar, para no cambiar las estadísticas de la señal), durante 500 s (1000 trazas). La medición se vio afectada por el ruido ambiental (deriva de temperatura, fig. 4a), que introdujo un ruido 1/f en el dominio espectral (fig. 4 b, c). Sin embargo, utilizando una medición diferenciada entre las 3 capas PZT (discutidas previamente), se recupera una vez más una respuesta instrumental libre de ruido 1/f para el caso en que se utiliza la primera traza como referencia y no se utilizan actualizaciones de referencia (fig. 4b) VS un ruido 1/f persistente para el caso en que la referencia de fibra se actualiza en todos los instantes (fig. 4c). Obsérvese que el ruido de fondo del ASD se incrementa virtualmente en unos 13,5 dB [= 10*log10(√500)] simplemente debido a una disminución de la velocidad de adquisición de la traza óptica (1 kHz => 2 Hz, debido a limitaciones de la memoria del digitalizador), lo que altera la resolución espectral del ASD. Sin embargo, un muestreo similar de 1 kHz durante 500 s debería revelar un ruido de fondo del ASD similar al presentado en la figura 2-3.

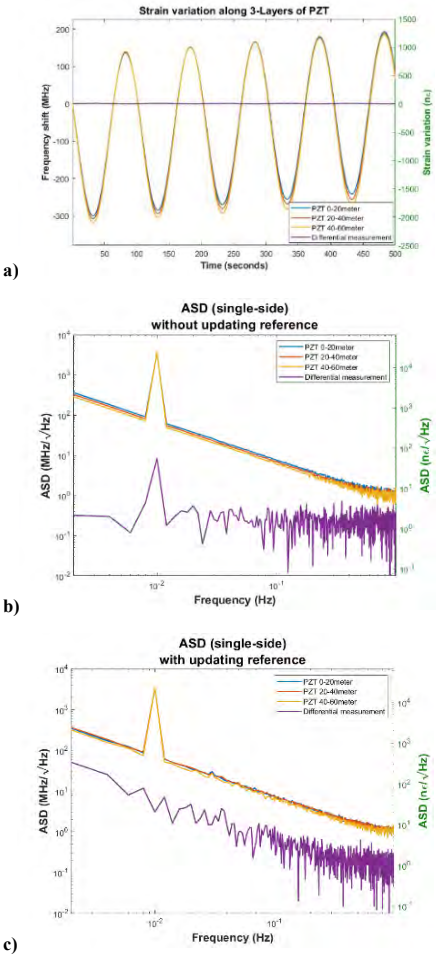

Fig. 4: Mediciones de deformación lenta para una onda sinusoidal de 0,01 Hz y 2,5 $\mu\varepsilon_{pp}$. Debido a las limitaciones de la memoria del digitalizador, se registró 1 de cada 500 trazas de la señal original de 1 kHz (sin promediar, para no alterar las estadísticas de la señal) durante 500 s (1000 trazas). Estas mediciones se realizaron utilizando una única traza de referencia (la primera traza óptica) sin actualizaciones de referencia (a, b) y se compararon con el caso en el que la fibra se actualiza en todos los instantes (c).

Mediciones a largo plazo: Finalmente, se caracteriza el rendimiento del LCP-ΦOTDR para mediciones a largo plazo (durante más de un día) (fig. 5). En este caso, se registraron las variaciones de la fibra en las 3 capas de PZT durante 36 h, aplicando permanentemente una onda sinusoidal de 0,01 Hz y 100 $n\varepsilon_{pp}$, con el objetivo de simular el ruido ambiental de deformación, en lugar de medir una fibra de laboratorio sin perturbaciones. Se comparó con el seguimiento de temperatura de un termómetro tradicional (en verde), que presentó una respuesta proporcional, como se esperaba (fig. 5a). Se rastrearon grandes perturbaciones de la fibra (equivalentes a > 4 GHz, es decir, que superan el 50 % del contenido de frecuencia de pulso), requiriendo solo actualizaciones de referencia cada pocas horas (con 15 actualizaciones de referencia a lo largo de las 36 h). Considerando el disparo de 1 kHz, esto significa una actualización promedio de la traza de referencia de 1 en $\approx 10^7$ trazas adquiridas, lo que, como se esperaba, reduce considerablemente el ruido 1/f registrado y mejora la estabilidad/sensibilidad a largo plazo. Como se mencionó previamente, una evaluación precisa del verdadero ruido de fondo instrumental es fundamentalmente imposible, considerando que el ruido ambiental (causado principalmente por variaciones de temperatura) es órdenes de magnitud mayor que dicho ruido. Sin embargo, una medición diferencial de las tres capas PZT (fig. 5b) permite estimar un límite superior del error, que se observa en <1% de la perturbación (error máximo de ±20 MHz para perturbaciones que superan el 50% del contenido chirp del pulso - 4 GHz). Este error, considerando el mayor valor cuando se produjeron variaciones de temperatura más rápidas y una serie de cruces por cero cuando la temperatura se estabilizó, aún parecía estar limitado en gran medida por la estabilización térmica de las capas PZT, es decir, por el ruido ambiental, en lugar de una verdadera limitación del ruido instrumental. Luego, el error instrumental estimado para mediciones de una hora de duración (calculado a través de la STD de la medición diferencial de 36 h después de un filtro de paso alto de 1 h, (fig. 5c) fue del orden de 0,1 MHz, equivalente a ≈1 ne/0,1 mK en fibras SMF tradicionales [1].

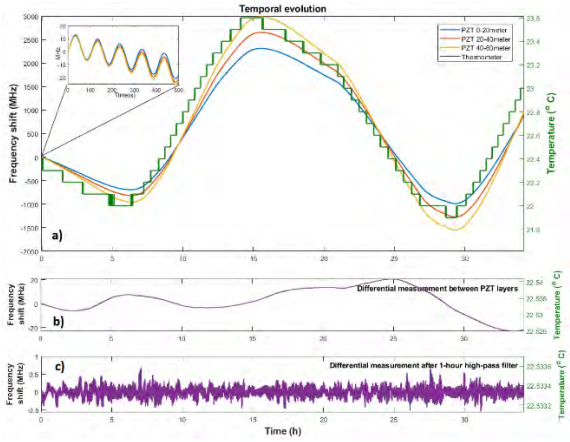

Fig. 5: Mediciones a largo plazo, registradas durante 36 h y aplicando una onda sinusoidal de 0,01 Hz y 100 $n\varepsilon_{pp}$, con el fin de simular el ruido ambiental (en lugar de medir una fibra sin perturbaciones). Debido a limitaciones de memoria, las trazas se adquirieron a 1 Hz, sub-muestreadas a partir del disparo original de 1 kHz. (a) Evolución temporal del desplazamiento de frecuencia a lo largo de las tres capas de PZT de 20 m (azul, naranja, amarillo) y temperatura ambiente, registrada con un termómetro convencional (verde). (b) Medición diferencial entre las capas de PZT. (c) Medición diferencial presentada en b, tras aplicar un filtro paso alto de 1 hora.

4.- Conclusiones

Se investigan los límites de rendimiento del CP-ΦOTDR al operar con altos chirps ópticos (8 GHz). Los resultados preliminares muestran un aumento supralineal del rango de deformación dinámica con el contenido de chirp óptico, así como un aumento disruptivo del rendimiento a largo plazo, con una drástica disminución del ruido instrumental 1/f, que prácticamente se elimina hasta mHz, al medir perturbaciones equivalentes a cientos de MHz de desplazamiento de frecuencia. Si bien trabajos previos se centraron en la optimización de una única métrica, los resultados aquí presentados permitieron obtener fácilmente variaciones de deformación traza-a-traza de ±3 με con un disparo de 1 kHz, un nivel de ruido de fondo ASD <100 pε/√Hz y una incertidumbre instrumental estimada de nε en mediciones de una hora, para una única configuración experimental.

Agradecimientos:

Este trabajo ha sido financiado por MCIN/AEI/10.13039/501100011033 e European Union «NextGenerationEU»/PRTR con los proyectos RYC2021-035009-I, CNS2022-135925, CPP2022-009772.

Referencias

[1] Fernández Ruiz, M. R., Costa, L. and Martins, H. F., "Distributed Acoustic Sensing Using Chirped-Pulse Phase-Sensitive OTDR Technology", Sensors 19(20), 4368(2019). https://doi.org/10.3390/s19204368

[2] H. D. Bhatta et al., "Dynamic Measurements of 1000 Microstrains Using Chirped-Pulse Phase-Sensitive Optical Time-Domain Reflectometry," in Journal of Lightwave Technology, 37(18), (2019) 10.1109/JLT.2019.2928621

[3] Pedro J. Vidal-Moreno et al., "Cancellation of reference update-induced 1/f noise in a chirped-pulse DAS," Opt. Lett. 47, 3588-3591 (2022) https://doi.org/10.1364/OL.465367

Autocorrección de referencias en MFDD-DAS: Hacia medidas absolutas en condiciones reales

Pedro J. Vidal-Moreno[1], Marcos G. Barriopedro[2], Alejandro Rosado[2], Laura Hernández-Martín[3], Sonia Martin-Lopez[1], Hugo F. Martins*[3]

1. Universidad de Alcalá, Departamento de Electrónica, 28805 Alcalá de Henares, Spain
2. Universidad Politécnica de Madrid, 28040 Madrid, Spain.
3. Instituto de Óptica "Daza de Valdés" IO-CSIC, C/Serrano 121, 28006 Madrid, Spain

Contact: Hugo F. Martins (hugo.martins@.csic.es).

ABSTRACT:

Chirped-pulse phase-sensitive OTDR (CP-φ-OTDR) enhanced with Multi-Frequency Database Demodulation (MFDD) offers improved long-term stability and 1/f noise reduction in distributed acoustic sensing (DAS). However, its applicability has been limited by the need for an undisturbed fiber during the calibration stage, as any perturbation during reference matrix acquisition compromises later measurements. This work proposes a self-correction method that treats the reference matrix itself as a CP-φ-OTDR trace, allowing post-processing compensation of disturbances during calibration. We validate this approach experimentally by comparing two measurements: one with strong perturbations during calibration (later corrected) and another performed without disturbances, serving as a baseline. Both cases show similar performance under dynamic (100 Hz) and static conditions. The results demonstrate that accurate reference matrices can be retrieved even in noisy environments, improving the practicality of MFDD-CP-φ-OTDR systems for field deployment.

Key words: Distributed Acoustic Sensing, φOTDR, Chirped Pulses, Long-term Stability, Low Frequency Sensitivity, Signal Processing, Geophysics

1.- Introducción

La detección acústica distribuida (*Distributed Acoustic Sensing*, DAS), basada principalmente en la reflectometría optica en el dominio del tiempo sensible a la fase (φ-OTDR), es una técnica ampliamente utilizada para detectar perturbaciones de frecuencia acústica con alta sensibilidad y resolución espacial [1]. Sin embargo, el monitoreo continuo de cambios de baja frecuencia en temperatura o deformación es fundamental para comprender y predecir fenómenos a gran escala, ya que estos cambios suelen indicar procesos graduales que pueden afectar significativamente la integridad estructural o las condiciones ambientales durante periodos de días, meses o incluso años.

Un avance reciente en el campo de DAS, el sistema MFDD-CP-φ-OTDR (*Multi-Frequency Database Demodulation* CP-φ-OTDR), permite realizar medidas cuasi-absolutas de alta sensibilidad durante largos periodos, utilizando una fibra previamente calibrada (matriz de trazas de referencia adquiridas mediante un barrido en frecuencia). Este enfoque elimina la necesidad de actualizaciones frecuentes de la medida de

referencia, lo que elimina el ruido 1/f proveniente de dichas actualizaciones de referencia y permite mediciones precisas en un amplio rango de frecuencias, desde perturbaciones de baja frecuencia, hasta señales en banda acústica [2]. Esta doble capacidad amplía la utilidad de los sistemas DAS en aplicaciones como la geofísica, el monitoreo ambiental o la seguridad de infraestructuras, donde tanto el monitoreo dinámico como el de largo plazo son esenciales.

No obstante, la precisión del método MFDD depende de la estabilidad durante el proceso de calibración de la fibra, el cual asume perturbaciones mínimas en la fibra y una alta estabilidad en frecuencia del láser durante la adquisición de la matriz de referencia. En escenarios reales, alcanzar estas condiciones ideales puede resultar difícil. Perturbaciones externas como vibraciones o fluctuaciones térmicas, así como el ruido de fase del láser, pueden introducir errores en la matriz de calibración que se traducen en distorsiones en las mediciones posteriores, afectando finalmente la fiabilidad de la técnica MFDD.

Para mitigar este problema, en [3] se propuso un método de postprocesado 2D para mejorar la relación señal-ruido (SNR) de la matriz de referencia sin necesidad de promediar temporalmente las trazas. Esto incrementa la estabilidad de la técnica, ya que reduce el tiempo de calibración (y, por tanto, el impacto del ruido ambiental lento). Sin embargo, las perturbaciones que ocurren durante la etapa de calibración (aunque esta sea más rápida) siguen afectando a la medición final, ya que no son corregidas de forma fundamental.

Este trabajo presenta un método novedoso para abordar estos desafíos mediante la incorporación de una autocorrección durante la etapa de calibración de la fibra. Dado que la matriz MFDD puede tratarse como una medida CP-φ-OTDR tradicional, es posible medir y compensar en Postprocesado las perturbaciones ocurridas durante la calibración. El método explota la naturaleza secuencial de la adquisición de la matriz de referencia, tratando cada traza como una medición y estimando/compensando el ruido de fase y las perturbaciones en la fibra mediante la comparación de trazas consecutivas usando estimación de retardo temporal (TDE) por correlación cruzada.

Este enfoque mejora la fiabilidad de la matriz de referencia al compensar activamente el ruido ambiental e instrumental, asegurando mediciones precisas incluso en condiciones no ideales. Para validar experimentalmente este concepto, se realizan mediciones MFDD-CP-φ-OTDR en una posición de fibra donde se aplican perturbaciones intensas durante la etapa de calibración. El rendimiento tras la autocorrección y el postprocesado para eliminar dichas perturbaciones se cuantifica y compara con una medición de referencia MFDD-CP-φ-OTDR realizada en una posición de fibra sin perturbaciones durante la calibración (utilizada como control para establecer la línea base de rendimiento de la técnica). Ambas mediciones mostraron un rendimiento similar, lo que valida el método propuesto, capaz de compensar con precisión las perturbaciones ambientales y/o el ruido instrumental y garantizar una matriz de referencia fiable, incluso en condiciones no ideales.

Este avance mejora la robustez de los sistemas MFDD-CP-φ-OTDR, abriendo la puerta a una adopción más amplia en aplicaciones reales exigentes.

2.- Métodos y montaje experimental

La configuración experimental utilizada en este trabajo se basa en la descrita en [2], con modificaciones destinadas a mejorar el rendimiento y la calidad de la señal. El sistema consta de dos ramas principales: la rama superior dedicada a la generación de pulsos y la rama inferior encargada de la recepción y procesamiento de la señal.

En la rama superior, se emplea como fuente de luz un láser de bajo ruido de fase (ancho de línea <100 Hz) con una estabilidad espectral a largo plazo de 0.1 pm (12.5 MHz). Este láser opera a una longitud de onda central de 1550.12 nm y permite ajustes en pasos de 0.1 pm (12.5 MHz). La salida del láser se modula mediante un modulador IQ controlado por un generador de formas de onda arbitrarias

(AWG) de 25 GS/s, produciendo pulsos chirpados de 100 ns de duración y 10 GHz de contenido espectral, con una tasa de repetición de 1 kHz.

Los pulsos generados se amplifican mediante un amplificador de fibra dopada con erbio (EDFA) y se filtran a través de un filtro de banda pasante de 100 GHz (BPF) basado en multiplexación por división en longitud de onda densa (DWDM), con el fin de reducir el ruido por emisión espontánea amplificada antes de ser inyectados en la fibra bajo prueba (FUT) a través de un circulador óptico.

La FUT consiste en 4000 m de fibra, al final de los cuales se encuentran 60 m enrollados sobre un actuador piezoeléctrico (PZT), distribuidos en tres capas de 20 m, que permiten aplicar deformaciones calibradas sobre la fibra.

La rama inferior se encarga del procesamiento de la señal retrodispersada desde la FUT. La señal de retorno se amplifica inicialmente con un EDFA y se filtra de nuevo mediante un filtro óptico DWDM de 100 GHz para reducir el ruido. A continuación, un fotodetector de detección directa de alta velocidad con un ancho de banda de 9.5 GHz convierte la señal óptica en una señal eléctrica, que se digitaliza mediante un digitalizador de un canal con 20 GSa/s.

En ambas ramas se utilizan atenuadores ópticos variables para optimizar los niveles de potencia tanto del pulso incidente como de la traza retrodispersada. Esta configuración permite generar pulsos chirpados de alta calidad, alcanzando una resolución espacial de 10 metros y una relación señal-ruido (SNR) mejorada para mediciones de alta sensibilidad y larga duración [2,4].

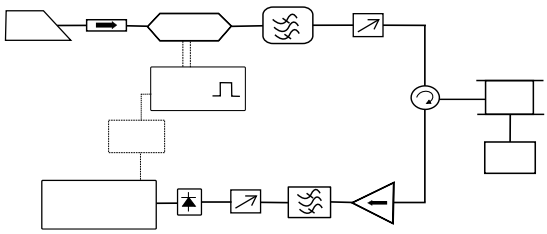

Fig. 1: Esquema experimental de un Sistema DAS basado en φ-OTDR. La descripción detallada se encuentra en el texto.

3.- Resultados

Utilizando la configuración experimental descrita en la Fig. 1, se adquirió una matriz de referencia inicial. Se lanzaron pulsos ópticos (modulados con un chirp de 100 ns y 10 GHz de contenido espectral, disparados a 1 kHz) de forma continua mientras se realizaba un barrido óptico de la frecuencia central del láser a una velocidad de 60 MHz/s sobre un rango de 30 GHz. La matriz de referencia se obtuvo registrando una traza cada 1000 disparos (es decir, una cada segundo, debido a las limitaciones de memoria digital), sin promediado, resultando en 500 trazas adquiridas con pasos de frecuencia de 60 MHz a lo largo de 30 GHz, durante 500 s. Durante este tiempo, los 4 km de fibra se mantuvieron sin perturbaciones, salvo la sección del PZT, que fue sometida a una perturbación calibrada de 2.5 με pico a pico (equivalente a ≈380 MHz pico a pico) mediante una señal sinusoidal de periodo 20 s. Los resultados se presentan en la Fig. 2a.

En este caso, el desplazamiento de frecuencia de la traza N-ésima de referencia, $\Delta\upsilon_N$ (N=1 a 500), respecto a la primera traza (N=1), fue $\Delta\upsilon_N = 60\cdot(N-1)$ MHz en la fibra sin perturbar, pero $\Delta\upsilon_N = 60\cdot(N-1)$ MHz + perturbación del PZT en la sección perturbada. Esto se midió con precisión integrando el desplazamiento de frecuencia calculado entre trazas consecutivas en cada posición: $\Delta\upsilon_N = \sum_{i=2}^{N} \Delta\upsilon_i - \Delta\upsilon_{i-1}$

Cabe destacar que, en este caso, la perturbación aplicada por el PZT (representada en amarillo) puede medirse con precisión al calcular la diferencia entre $\Delta\upsilon_N$ en la zona del PZT (azul) y $\Delta\upsilon_N$ en la fibra sin perturbar (rojo).

Una vez adquirida la matriz de referencia, se probó el funcionamiento del sistema MFDD-CP-φ-OTDR en todo el rango de frecuencias de dicha matriz. Dado que no era experimentalmente factible aplicar perturbaciones equivalentes a 30 GHz (≈200 με o ≈22 ºK, no aplicables de forma calibrada en nuestro laboratorio), esta verificación se realizó adquiriendo un segundo conjunto de 500 trazas mientras se barría la frecuencia óptica central del láser con pasos de 60 MHz

a lo largo de 30 GHz (un desplazamiento de la frecuencia del láser es equivalente a una perturbación en un sistema CP-φ-OTDR), manteniendo la fibra y el PZT sin perturbar. Este desplazamiento también se midió con precisión mediante integración entre trazas consecutivas (como antes), y los resultados se muestran en la Fig. 2b, tomados como referencia ("ground truth") para esta serie de mediciones. El error máximo de esta referencia, debido al método CP-φ-OTDR tradicional, se estimó en <1 MHz [4].

Utilizando la matriz de referencia (Fig. 2a) y el conjunto de mediciones (Fig. 2b), se ejecutó la operación MFDD-CP-φ-OTDR siguiendo el procedimiento detallado en [2]: cada traza del conjunto de medición se comparó con toda la matriz de referencia para seleccionar la traza con mayor correlación, y posteriormente se estimó el desplazamiento fino de frecuencia entre ambas mediante estimación de retardo temporal tradicional CP-φ-OTDR.

Usando la operación tradicional MFDD-CP-φ-OTDR, sin autocorrección de la matriz (es decir, asumiendo simplemente que la frecuencia de cada traza de referencia era $\Delta\upsilon_N = 60\cdot(N-1)$ MHz, sin perturbaciones), se obtuvieron los resultados de la Fig. 2c. El error de esta medición (Fig. 2e) se estimó como la diferencia entre la referencia (Fig. 2b) y la medición sin corrección (Fig. 2c). Cuando la fibra no fue perturbada durante la adquisición de la matriz, el error fue bajo (Fig. 2e, naranja, error estimado de ≈MHz en todo el conjunto). No obstante, cuando hubo perturbaciones durante la calibración, estas se transfirieron de forma no lineal a la medición final, generando errores del orden de la propia perturbación, pero no compensables (Fig. 2e, azul, error estimado de ≈380 MHz).

Por otro lado, al aplicar la operación MFDD-CP-φ-OTDR con la autocorrección y postprocesado propuestos (es decir, usando los desplazamientos de frecuencia realmente medidos en la matriz de referencia: $\Delta\upsilon_N = 60$ (N-1) MHz + perturbación del PZT), los resultados obtenidos se muestran en la Fig. 2d. El error correspondiente (Fig. 2f), calculado como la diferencia entre la referencia (Fig. 2b) y la medición corregida (Fig. 2d), fue bajo y del mismo orden tanto en los casos con matriz de referencia perturbada como sin perturbar, lo que demuestra la validez del método propuesto.

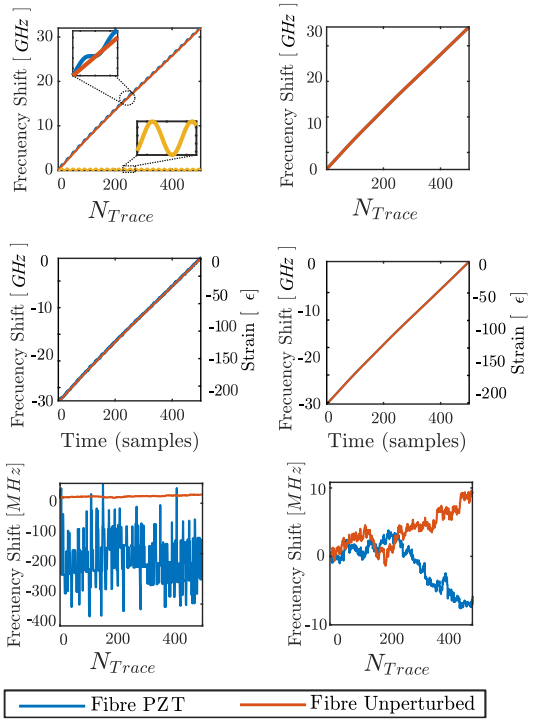

Fig. 2: Mediciones estáticas, para la sección perturbada con el PZT (azul) y la sección de fibra sin perturbaciones (naranja). (a) Desplazamientos de frecuencia de la matriz de referencia medidos, adquiridos con una perturbación PZT de 2.5 με pico a pico durante 100 s. (b) Valor de referencia (ground truth) de los desplazamientos de frecuencia del conjunto de medición, adquiridos sin perturbación del PZT, calculados mediante CP-φ-OTDR tradicional. (c) Desplazamientos de frecuencia del conjunto de medición medidos mediante MFDD-CP-φ-OTDR sin autocorrección de la matriz de referencia. (e) Error estimado de la medición correspondiente (calculado como la diferencia entre (b) y (c), es decir, medición sin corrección frente a su valor de referencia). (d) Desplazamientos de frecuencia del conjunto de medición medidos mediante MFDD-CP-φ-OTDR con autocorrección de la matriz de referencia. (f) Error estimado de la medición correspondiente (calculado como la diferencia entre (b) y (d), es decir, medición corregida frente a su valor de referencia).

Para demostrar la capacidad del método en la medición de perturbaciones dinámicas, se repitió el procedimiento descrito en la Fig. 2 para una medición dinámica. En este caso, se

reutilizó la misma matriz de referencia (Fig. 3a = Fig. 2a), y se adquirió un nuevo conjunto de mediciones (0.5 s a 1 kHz, con frecuencia óptica fija del láser), mientras se aplicaba una perturbación sinusoidal de 2.5 με pico a pico (≈380 MHz) al PZT, con una frecuencia de 100 Hz.

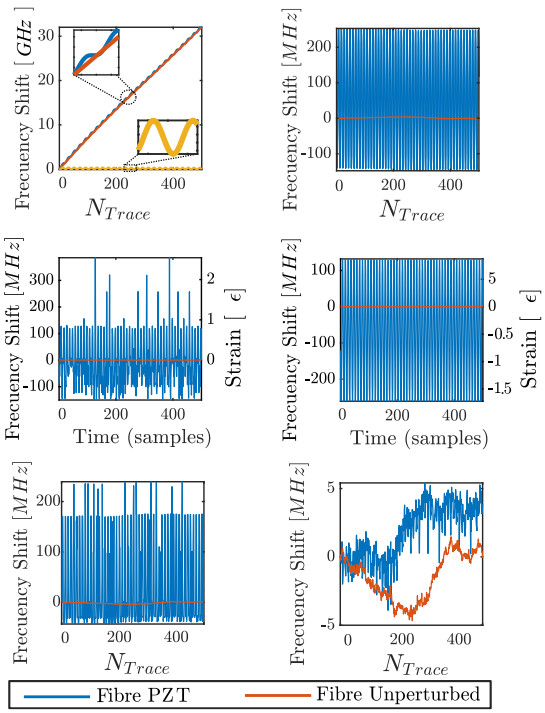

Fig. 2: Mediciones dinámicas, para la sección perturbada con el PZT (azul) y la sección de fibra sin perturbaciones (naranja). (a) Desplazamientos de frecuencia de la matriz de referencia medidos adquiridos con una perturbación del PZT de 2.5 με pico a pico durante 100 s. (b) Valor de referencia (ground truth) de los desplazamientos de frecuencia del conjunto de medición, adquiridos con perturbación del PZT de 2.5 με pico a pico a 100 Hz, calculado mediante CP-φ-OTDR tradicional. (c) Desplazamientos de frecuencia del conjunto de medición obtenidos mediante MFDD-CP-φ-OTDR sin autocorrección de la matriz de referencia. (e) Error estimado correspondiente (calculado como la diferencia entre (b) y (c), es decir, medición sin corrección frente a su valor de referencia). (d) Desplazamientos de frecuencia del conjunto de medición obtenidos mediante MFDD-CP-φ-OTDR con autocorrección de la matriz de referencia. (f) Error estimado correspondiente (calculado como la diferencia entre (b) y (d), es decir, medición corregida frente a su valor de referencia).

Los resultados son conceptualmente similares a los de la Fig. 2, pero con una perturbación real de deformación (en lugar de un desplazamiento equivalente de frecuencia del láser) y a una velocidad mucho mayor (estática, 500 s → dinámica, 100 Hz). La operación sin corrección (Fig. 3c, 3e) provocó errores de medición no compensables, equivalentes a la perturbación en la adquisición de la matriz. Sin embargo, al aplicar el método de autocorrección con postprocesado (Fig. 3d, 3f), el error fue bajo y del mismo orden en ambos casos, validando nuevamente la eficacia del enfoque propuesto.

4.- Conclusiones

Se ha propuesto un método de autocorrección de la matriz de referencia que permite compensar las perturbaciones ocurridas durante la etapa de adquisición de dicha matriz (calibración de la fibra) en sistemas MFDD-CP-φ-OTDR. Dado que la matriz de referencia MFDD puede tratarse como una medición CP-φ-OTDR tradicional, las perturbaciones durante esta fase pueden medirse y corregirse mediante postprocesado.

Este concepto se ha demostrado experimentalmente tanto para mediciones rápidas (100 Hz) como para mediciones lentas o estáticas, mostrando un rendimiento similar entre una calibración sin perturbaciones y otra con fuertes perturbaciones seguida de autocorrección y compensación en postprocesado. Esto valida plenamente la eficacia del método propuesto.

Al compensar las perturbaciones dinámicas durante la calibración, este enfoque garantiza la fiabilidad de la matriz de referencia y mantiene la precisión de las mediciones en condiciones no ideales, ampliando así la aplicabilidad del enfoque MFDD-CP-φ-OTDR en entornos reales.

Acknowledgements: *P.J.V-M was supported by FPI-2021 Grant from the University of Alcalá Research Program. We acknowledge financial support from the Spanish Ministry of Science and Innovation under grants PID2021-128000OB-C21 and PRE2022-104176. From the MCIN/AEI/10.13039/501100011033 and European Union «NextGenerationEU»/PRTR Program under grants RYC2021-035009-I, CNS2022-135925, CPP2022-009772, Grant PSI ref. PLEC2021-007875 and REMO: ref.*

CPP2021-008869. From the Spanish MCIN/AEI/10.13039/501100011033, and FEDER (grants, PID2021-128000OBC21 and PID2021-128000OB-C22). And from the European Innovation Council under Grant SAFE: ref. 101098992, and SUBMERSE: ref.101095055.

References

[1] J. Pastor-Graells, et al. “Single-shot distributed temperature and strain tracking using direct detection phase-sensitive OTDR with chirped pulses,” Opt. Express, 24, 12, 13121–13133, (2016).

[2] P. J. Vidal-Moreno, et al, "Cancellation of reference update-induced 1/f noise in a chirped-pulse DAS," Opt. Lett. 47, 3588-3591 (2022)

[3] P. J. Vidal-Moreno, et al., "Frequency-Time 2D Correlation for SNR Improvement in Multifrequency Database Demodulation CP-ΦOTDR," in 28th International Conference on Optical Fiber Sensors, (2023), paper Tu2.5.

[4] Luís Costa, et al. "Fully Distributed Optical Fiber Strain Sensor With 10−12 ε/√Hz Sensitivity," J. Lightwave Technol. 37, 4487-4495 (2019)

Phi-OTDR con pulsos chirpados de gran tamaño asistido por Raman para termometría de fibra distribuida en milikelvin de largo alcance

Laura HERNÁNDEZ-MARTÍN [(1)], Javier PRECIADO-GARBAYO [(2)], Jorge CANUDO[(2)], Juan D. ANIA-CASTAÑÓN [(1)], Hugo F. MARTINS [(1)]

1. Instituto de Óptica "Daza de Valdés" IO-CSIC, C/Serrano 121, Madrid 28006, Spain
2. Aragon Photonics Labs, S.L., 5 Prado, Zaragoza 50009, Spain

Contact: Laura HERNÁNDEZ-MARTÍN (laura.hernandez@io.cfmac.csic.es).

ABSTRACT:

Chirped-pulse phase-sensitive optical time domain reflectometry (CP-φOTDR) has become of standard use in a number of distributed fiber sensing applications, with particularly promising results in long-term highly sensitive measurements. However, so far, the use of large chirps has been largely avoided due to the cost/complexity increase, with the majority of academically and commercially studies operating in the ≈1GHz regime. In this paper Large Chirped-Pulse φOTDR (LCP φOTDR) employing large chirps (8GHz) and assisted by optimized distributed Raman amplification was used to extend traditional DAS bandwidth to day long high-sensitivity temperature measurements in the order of mK over 50 km of fiber.

Key words: distributed optical fiber sensing, Rayleigh scattering, chirped-pulse φOTDR, distributed acoustic sensing, distributed Raman amplification, fiber thermometry

1.- Introducción

La reflectometría óptica en el dominio del tiempo sensible a la fase de pulso chirpado (CP-ΦOTDR) es una herramienta estándar para un gran número de aplicaciones del sensado distribuido de fibra [1], con resultados particularmente prometedores para medidas de gran sensibilidad durante largos períodos de tiempo [2]. El rango espacial de la técnica puede extenderse mediante el empleo de amplificación Raman [3], aunque hasta la fecha su uso ha estado limitado a chirps en el régimen de 1 GHz. En este artículo se exploran los límites de CP-ΦOTDR al operar con pulsos altamente chirpados (8 GHz) y amplificación Raman, presentando un análisis detallado de los efectos no lineales del sistema, además de la mejora en medición a largo plazo y grandes distancias, debido a la estabilidad de la referencia de la fibra, llegando a medir con gran sensibilidad durante 72 h a lo largo de 50 km.

2.- Metodología

El montaje experimental en este trabajo, mostrado en la Figura 1ª, está basado en una configuración típica de CP-OTDR [1,2], utilizando modulación externa para operar con el chirp incrementado y asistido por amplificación Raman distribuida. La rama superior del diagrama corresponde a la generación del pulso, empleando como fuente de luz un láser con bajo ruido de fase centrado en 1550.12 nm y con una anchura espectral menor a 100 Hz. La luz emitida pasa por un modulador IQ-MZM controlado por un generador de funciones arbitrarias (AWG) y forma un tren de pulsos chirpados con duración de 80 ns, chirp lineal de 8 GHz y frecuencia de repetición de 1 kHz. Los pulsos

son amplificados por un amplificador de fibra dopada con erbio (EDFA) y pasan por un multiplexador denso por división en longitudes de onda (DWDM), que actúa como un filtro paso banda para filtrar el ruido ASE del EDFA antes de la señal sea inyectada en la fibra a monitorizar (FUT) mediante un circulador óptico. En este punto es cuando se introduce también un bombeo Raman de 400mW en onda continua, centrado en 1455 nm, que se propagará en la misma dirección que el tren de pulsos y le proporcionará una amplificación distribuida para compensar las pérdidas a lo largo de la FUT. Esta FUT comprende 50 km de fibra monomodo estándar (SMF) y es seguida de un dispositivo comercial de 60 m de fibra enrollados en 3 capas de 20 m alrededor de un piezoeléctrico (PZT) que, controlado por un generador de señales de voltaje, permite introducir deformaciones controladas. Después de este último elemento se empleó un analizador de espectro óptico (OSA) con resolución de 10 pm para registrar el espectro óptico de los pulsos tras su propagación y estudiar las no-linealidades acumuladas.

La rama inferior del esquema muestra los elementos involucrados en la detección de la señal que llega reflejada debido a la dispersión Rayleigh. La señal dispersada es amplificada por un EDFA y pasa por un filtro óptico de 25 GHz para reducir el ruido ASE del EDFA antes de llegar a un fotodiodo de alta velocidad (detección directa, 9.5 GHz) y ser registrada por una digitalizadora (1 canal, 20 Gs/s). La potencia en ambas ramas es regulada mediante atenuadores ópticos variables (VOA), y la generación y detección de la señal están sincronizadas. El sistema completo es capaz de generar y analizar pulsos altamente chirpados de gran calidad, con una resolución espacial de 8 m y manteniendo una buena relación señal-ruido (SNR) a lo largo de toda la FUT durante largos períodos.

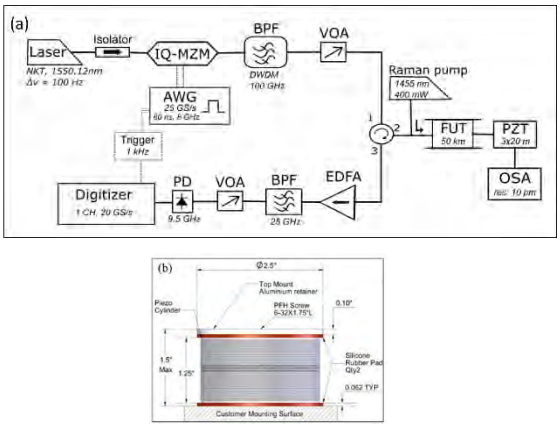

Fig. 1: (a) Montaje experimental del LCP-φOTDR asistido por Raman y (b) el PZT utilizado para introducir perturbaciones de deformación calibradas.

3. - Resultados

El impacto de efectos no lineales en LCP-φOTDR asistido con amplificación Raman fue detalladamente estudiado antes de pasar a medidas largas, caracterizando el espectro óptico, las trazas adquiridas mediante la digitalizadora y la respuesta medida ante deformaciones.

3.1.- Espectro óptico

En primer lugar, se midió la densidad de potencia espectral de los pulsos tras su propagación a lo largo de los 50 km de FUT mediante un OSA. A medida que la potencia de pico inicial de los pulsos aumenta, los fenómenos no lineales que ocurren a lo largo de su propagación ganan importancia y llevan a la generación de dos bandas laterales, una a cada lado de la frecuencia portadora, que pueden ser atribuidas a la inestabilidad de modulación [1]. La potencia de señal y bandas laterales ha sido computada en base a las regiones espectrales mostradas en la Figura 2b, observándose en la Figura 2c cómo un aumento de la potencia inicial puede ser activamente contraproducente a partir de cierto umbral, ya que no solamente aumenta la potencia de las bandas laterales, sino que además la potencia final del pulso se estanca o incluso disminuye.

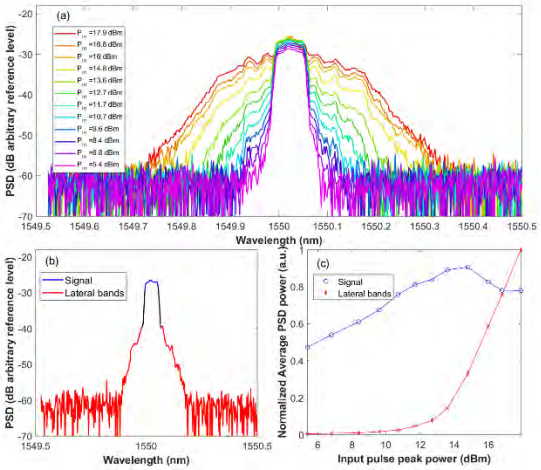

Fig. 2: (a) Densidad espectral de potencia (PSD) medida después de la propagación a lo largo de FUT para distintas potencias pico del pulso de entrada. (b) Regiones espectrales consideradas para calcular la PSD de la señal (azul) y la PSD de las bandas laterales (roja), mostradas en (c).

3.2.- Traza óptica

El análisis de las trazas ópticas registradas por la digitalizadora muestra resultados esperables de la amplificación Raman, con una amplitud máxima alrededor de los 20 km (Figura 3a). La desviación estándar (STD) de la traza sobre ventanas del tamaño del pulso óptico se muestra en la Figura 3b para diferentes potencias de pico iniciales, normalizada por la STD del ruido registrado tras el final de la fibra, tradicionalmente asociado a la SNR de la traza óptica. La dependencia con la potencia de pico inicial observada en la Figura 3c corrobora los resultados de la Figura 2, ya que después de cierto punto óptimo, un mayor aumento de la potencia óptica de entrada puede provocar una disminución de la amplitud de la traza hacia el extremo de la fibra debido a la aparición de no linealidades.

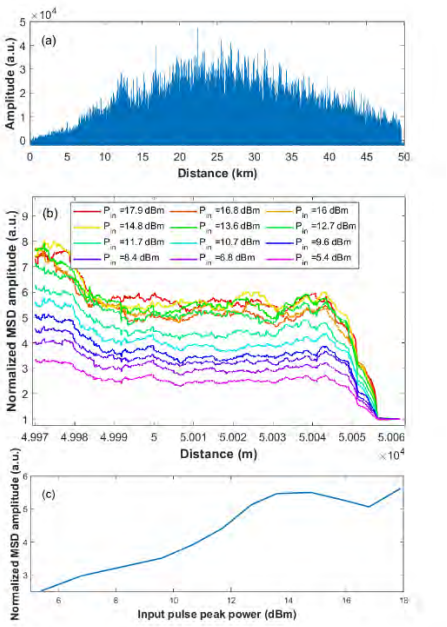

Fig. 3: (a) Traza óptica a lo largo de 50 km (b) Desviación estándar móvil (MSD) de trazas ópticas (correlacionados con la SNR óptica) a lo largo de los últimos 80 m de FUT para distintas potencias pico del pulso de entrada. (c) Mediana de las curvas MSD presentadas en (b).

3.3.- Respuesta dinámica del mensurando

La respuesta del sistema a la deformación dinámica fue probada aplicando una perturbación sinusoidal de 0,5 Hz al PZT situado al final de la FUT, el punto de menor SNR de la traza óptica. Se observa cómo, mientras que el régimen lineal de LCP-φOTDR presenta una respuesta de deformación lineal como cabría esperar, el sistema exhibe una respuesta no lineal en la medición de deformación al entrar en regímenes fuertemente no lineales (Figura 4a). Esto se cuantificó mediante la medición del tono de 0,5 Hz y su armónico (1 Hz) en la transformada rápida de Fourier (FFT), mostrada en la Figura 4b, con la variación en función de la potencia de pico del pulso inicial representada en la Figura 4c. Cabe destacar que las potencias de entrada para los regímenes lineal/no lineal coinciden nuevamente con los resultados de las Figuras 2 y 3.

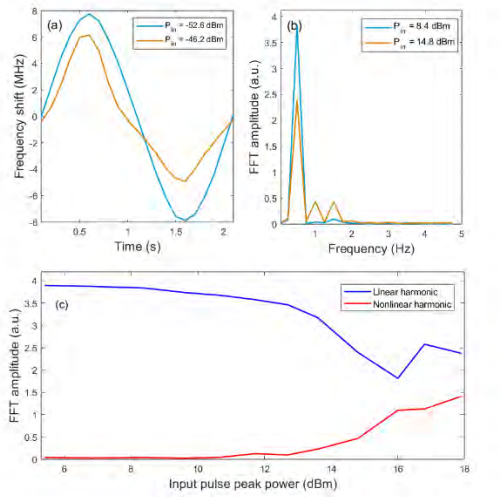

Fig. 4: (a) Desplazamiento de frecuencia medido al aplicar una vibración sinusoidal en el PZT y (b) su FFT) para potencias pico de entrada -8,4 dBm (azul claro) y 14,8 dBm (naranja). (c) Respuesta armónica lineal (0,5 Hz, azul) y primera no lineal (1 Hz, rojo) en función de las potencias pico del pulso de entrada.

3.4.- LCP-φOTDR asistido por Raman para termometría de fibra distribuida en milikelvin de largo alcance

Tras caracterizar y optimizar el funcionamiento del LCP-φOTDR, nos propusimos explorar el potencial de mediciones de alta sensibilidad, superando las 24 h de medida.

En este punto, cabe mencionar que no se disponía experimentalmente de una medición de temperatura de referencia que coincidiera con la sensibilidad (mK) del LCP-φOTDR. El error de medición se limitó registrando la temperatura del aire con un termómetro con una precisión de 0,1 K, pero la medición de variaciones de temperatura de la fibra del orden de mK, que proporcionaría una medición directa del ruido de fondo instrumental, resultó estar fuera del alcance de nuestras condiciones experimentales. Este problema se mitigó calculando una medición diferencial entre las tres capas de fibra alrededor del PZT, lo que proporcionó una estimación del límite superior del error de medición y, por lo tanto, permitió la caracterización del ruido de fondo instrumental.

Según el fabricante, se espera (y se ha medido) que la configuración geométrica del dispositivo provoque una conversión voltaje-deformación ligeramente diferente para cada capa de 20 m, siendo la capa exterior (0-20 m) la que presenta el menor desplazamiento. Se espera que esta capa, en contacto con el aire, experimente una mayor variación de temperatura que las capas internas, en contacto con el piezocilindro (que a su vez está en contacto con una mesa óptica que actúa como un gran disipador de calor), generando un gradiente de temperatura. Se observó que ambos gradientes varían linealmente ante grandes variaciones, lo que permite estimar el ruido instrumental mediante la medición diferencial: (capa 1 [0-20 m] + capa 3 [40-60 m])/2- (capa 2 [20-40 m]). Cabe destacar que la resolución espacial de la medición (80 ns, equivalente a 8 m) y el tamaño de la ventana temporal para el cálculo del retardo temporal mediante correlación cruzada (también 80 ns) se eligieron para garantizar que las mediciones en las tres capas, cada una de 20 metros, presentaran tres mediciones no correlacionadas y, por tanto, que la medida diferencial entre ellas proporcionara una estimación real del ruido de fondo instrumental, en lugar de una reducción virtual del ruido debido al uso de puntos que no presentaban ruidos no correlacionados.

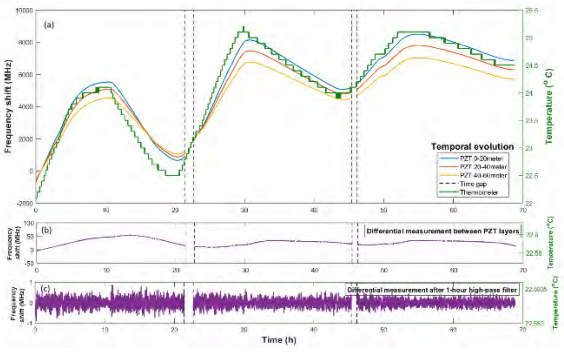

Fig. 5: (a) Evolución temporal del desplazamiento de frecuencia a lo largo de las tres capas de PZT de 20 m (azul, naranja, amarillo) y temperatura ambiente (verde) durante un período de 3 días. (b) Medición diferencial entre las capas de PZT. (c) Medición diferencial en (b) tras aplicar un filtro paso alto de 1 hora. Las líneas discontinuas indican dos pausas de aproximadamente 1 hora en la medición del LCP-φOTDR.

4.- Conclusiones

En este trabajo, se ha estudiado el comportamiento de CP-φOTDR utilizando chirps grandes (8 GHz) y asistido por amplificación Raman de copropagación junto con su aplicación para la termometría de fibra distribuida en milikelvin de largo alcance (50 km). Se presenta un estudio exhaustivo sobre el impacto de las no linealidades en diversos dominios (espectro óptico, trazas ópticas adquiridas y respuesta a la medición de deformación). Posteriormente, se caracterizó el rendimiento del sistema durante una medición de 72 h, demostrando un aumento considerable de la estabilidad de la referencia de fibra gracias al uso de un chirp óptico, ya que las referencias de fibra solo se actualizaron cada 2 h aproximadamente. Si bien no fue posible realizar una medición experimental directa del ruido de fondo instrumental debido a la falta de una referencia de mK, se estimó un límite superior del error inferior al 1 % de la perturbación (error de ±30 MHz para perturbaciones que superan el contenido del chirp de 8 GHz). Sin embargo, esto parece estar limitados en gran medida por la estabilización térmica (es decir, el ruido ambiental) de los puntos de medición, más que por un verdadero ruido instrumental. El error instrumental estimado para mediciones de una hora fue del orden de 0,1 MHz, equivalente a $1n\epsilon$ o 0,1 mK en fibras SMF tradicionales. El sistema propuesto amplía los límites conocidos del φ-OTDR de pulsos chirpados, permitiendo medir magnitudes físicas como la deformación y la temperatura con gran sensibilidad y mayor estabilidad. También destaca la importancia de optimizar los esquemas de amplificación Raman y se demuestra su efecto en sistemas de detección distribuida. En general, el LCP-φOTDR muestra un potencial prometedor para aplicaciones que requieren medición constante a largas distancias y durante largos períodos de tiempo, como el monitoreo del estado de infraestructuras o la detección de ondas sísmicas. Futuros trabajos pretenden explorar la ampliación del rango de distancia operativa y una caracterización más precisa de los errores de esta técnica con la ayuda de un mejor aislamiento y control de la fibra monitorizada.

Agradecimientos: este trabajo ha sido posible gracias al del Ministerio de Ciencia e Innovación de España mediante las subvenciones PID2021-128000OB, PRE2022-104176 y MCIN/AEI/10.13039/501100011033, así como del programa europeo «NextGenerationEU»/PRTR mediante las RYC2021-035009-I, CNS2022-135925 y CPP2022-009772.

References

[1] Maria R. FERNÁNDEZ-RUIZ, Luis COSTA, Hugo F. MARTINS, *"Distributed Acoustic Sensing Using Chirped-Pulse Phase Sensitive OTDR Technology"*, Sensors 19(20), 4368(2019).

[2] Juan PASTOR-GRAELLS, Javier NUÑO, María R. FERNÁNDEZ-RUIZ, Andres GARCIA-RUIZ, Hugo F. MARTINS, Sonia MARTIN-LOPEZ, Miguel GONZALEZ-HERRAEZ., "*Chirped-Pulse Phase-Sensitive Reflectometer Assisted by First-Order Raman Amplification*", Journal of Lightwave Technology, 35(21), (2017).

[3] Regina MAGALHÃES, Tiago NEVES, Lorenzo SCHERINO, Sonia MARTIN-LOPEZ y Hugo. F. MARTINS, "*Reaching Long-Term Stability in CP-ϕOTDR*", Journal of Lightwave Technology, 40(12), (2022).

High-Finesse Fiber-Optic Fabry-Perot Interferometer for Gas Pressure Sensing with Minimal Temperature Influence

Elena LORENTE [(1)], Luis A. SÁNCHEZ [(2)], Bryan SANIPATIN [(1)], Daniel MALDONADO-HURTADO [(1)], Salvador SALES [(1)]

1. Photonics Research Labs, ITEAM, Universitat Politècnica de València, Camino de Vera, s/n, 46022, Valencia, Spain.
2. CalSens S.L., 8F Building Office, Universitat Politècnica de València, Camino de Vera s/n 46022, Valencia, Spain.Department, Center, University, Address.

Contact: Elena LORENTE (elorcan@etsii.upv.es).

ABSTRACT:

An optical fiber gas pressure sensor based on a Fabry-Perot interferometer has been developed by inserting two single-mode fibers at opposite ends of a silica capillary, leaving an internal open cavity between the two fibers. The interrogation fiber has been fused at the end to create a ball-lense and the reflective fiber has been sputtered with gold, thus minimizing the divergence of the emitted beam and improving the reflectivity, respectively. A microhole was drilled on the capillary by a femtosecond laser that allows the flow of air and, therefore, the measurement of pressure changes from the variation of the refractive index inside the cavity. The optical path length of the cavity showed a linear response with pressure in the range from 0 to 1 MPa. Additionally, the influence of temperature was evaluated in the range of -10 ° C and 70 °C, with negligible impact. These results demonstrate that the proposed sensor combines high sensitivity and thermal stability, making it ideal for demanding environments.

Key words: Fiber optic sensors, Fabry-Perot interferometers, pressure sensor, silica capillary, femtosecond laser.

1.- Introduction

Static and dynamic pressure monitoring is essential in processes ranging from industrial to biochemical applications [1, 2]. However, most of these processes are exposed to extreme temperature conditions and electromagnetic interference (EMI), making it difficult to implement conventional pressure sensors that have many limitations [3]. Optical fiber sensors (OFS) present several advantages that make them an attractive alternative to conventional sensors. Their immunity to electromagnetic interference, high temperature resistance, electrical isolation, resistance to aggressive environments, small size, light weight, and the possibility of multiplexing several sensors on the same optical fiber are some of the features that make OFS an effective solution for pressure measurement [1, 4, 5]. Some examples of applications of this type of sensors include the measurement of pressure in the underground oil reservoir and in vivo medical applications [6, 7].

In recent years, extrinsic Fabry-Perot interferometers (EFPI) applied to pressure sensors [8] have gained relevance due to their advantages, such as their high sensitivity. Depending on the construction of the sensor, two types of EFPI sensors can be distinguished: those that depend on the variation of the physical length of the cavity, and those that depend on the variation of the refractive index inside the cavity [9]. In this paper, we develop an optical fiber gas pressure sensor based on the second type of

EFPI by inserting a single-mode fiber at one end of a silica capillary tube and a gold-sputtered fiber at the other end, leaving an internal air cavity between the two fibers. In the center of this air cavity, a micro-hole is drilled by a femtosecond laser, allowing air flow and thus measurement of pressure changes. First, we describe the fabrication and design of the device. Next, the physical principles on which the device is based are presented. Finally, the sensor characterization at different pressures and temperatures is shown, in order to demonstrate the efficiency and reliability of the pressure sensor.

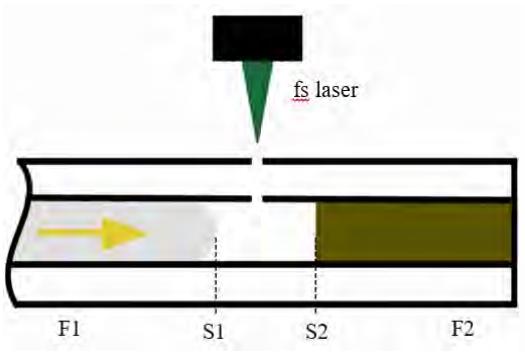

Fig. 1: Representative image of the silica capillary tube and the inserted fibers.

2.- Device Fabrication and Operating Principles.

The developed pressure sensor is based on an optical fiber Fabry-Perot interferometer implemented in a silica capillary tube, whose inner diameter was 150 µm and outer diameter was 363 µm. In the center of the capillary a microhole with dimensions 40x60 µm was drilled by using a femtosecond laser, specifically a frequency-doubled Yb laser emitting pulses at 515 nm with a repetition rate of 1 kHz.

To improve optical coupling efficiency, the end of the fiber (F1, Fig. 1) was fused using a CO_2 laser (Fujikura LZM-10), forming a ball-lense with a diameter of 140 µm. This curvature allows the output beam to reduce its divergence, enhancing transmission to the mirror fiber (F2). Furthermore, the straight cut of the mirror fiber was coated with a 150 nm gold layer through a sputtering process to increase its reflectivity.

Both fibers were inserted into the capillary from opposite ends using a conventional fiber fusion machine (FITEL s178) in manual mode. To complete the alignment, the spectrum was monitored in real time, looking for the maximum contrast of the resonances, and a camera with an x10 objective was used to position the microhole between the two reflective surfaces (S1 and S2). Once the maximum spectral contrast position was reached, the fibers were fixed to the capillary with UV glue. The final result of the sensor is shown in Figure 2.

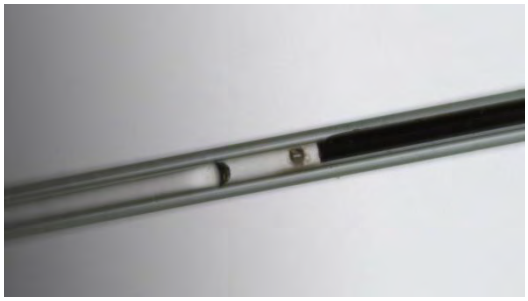

Fig. 2: Image taken with a x10 objective camera of the finished pressure sensor.

This configuration forms a Fabry-Perot cavity bounded by the two reflecting surfaces separated at a fixed distance L. The reflection spectrum of the Fabry-Perot cavity is characterized by periodic minima corresponding to the resonant wavelengths satisfying the constructive condition:

$$2n_{air}L = m\lambda \qquad (1)$$

where m is the order of interference (integer), n_{air} is the refractive index of the internal medium, L is the length of the cavity and λ is the resonant wavelength.

The spectral position of the peaks or valleys can be affected by changes in the refractive index (RI) and the length of the cavity caused by variations in temperature and pressure [10].

$$n_{air} = 1 + \frac{a\,P}{1 + b\,T} \qquad (2)$$

where a and b are coefficients affected by gas composition and P, T and n_{air} are the pressure, temperature and refractive index of the cavity respectively. For a change in pressure, since there is no variation in the

cavity length, the spectral shift of the resonant lengths is due only to the variation of the refractive index. If we assume that temperature remains constant, we can estimate that the pressure sensitivity of the Fabry-Perot air cavity is:

$$\frac{d\lambda_m}{dP} = \frac{d\lambda_m}{dn_{air}} \frac{dn_{air}}{dP} \quad (3)$$

To analyze this behavior of the sensor, we observe the evolution of the optical path length (OPL) as a function of time; this magnitude represents the product between the refractive index of the medium and the physical length of the cavity.

$$OPL = nL \quad (4)$$

Specifically in the developed sensor, the OPL variation reflects only the air refractive index variation induced by pressure and temperature changes. Combining the definition of the OPL with the wavelength resonant condition of order m (1), and considering two nonadjacent minima for a more accurate calculation of the free spectral range (FSR), we obtain:

$$OPL = \frac{\lambda_1 \lambda_2}{2\, FSR\, (m_1 - m_2)} \quad (5)$$

where λ_1 and λ_2 are the wavelengths corresponding to the interference orders m_1 and m_2, respectively.

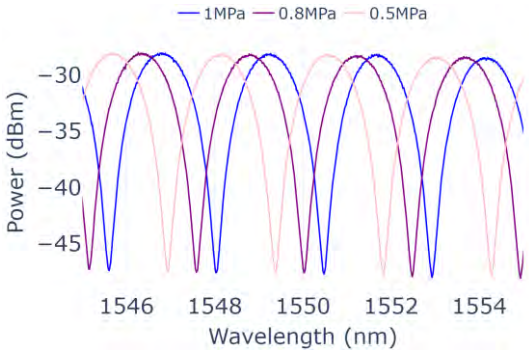

Fig. 3: Comparison of Fabry-Perot Spectra at Different Pressures

3.- Experimental results

3.1.- Pressure characterization

The pressure's sensor response was characterized by using a pressure chamber and a compressor. The reflection spectra of the sensor was obtained by using an optical interrogator (Micron Optics, SM125). Figure 3 shows the reflection spectra at different pressure values, within the wavelength range of 1545 to 1555 nm. The resonances exhibited high contrast (> 15 dB) due to the sensor's structure containing a ball lense and a metallic mirror. A shift of the resonance minima to lower wavelengths is clearly observed as the pressure decreases. This agrees with the theory that, as the pressure decreases, the refractive index of the air inside the cavity decreases (4), leading to smaller resonant wavelengths to fulfill the interference equation (1).

To verify this effect, the sensor was characterized in the pressurized chamber at room temperature. The minimum measurable value of the barometer used to monitor pressure was 0.3 MPa, so the pressure was initially reduced from 1 MPa to 0.3 MPa with a step of 0.1 MPa, and then the pressure was released directly to 0 MPa. The pressure level was maintained for approximately 40 seconds to ensure spectral stability.

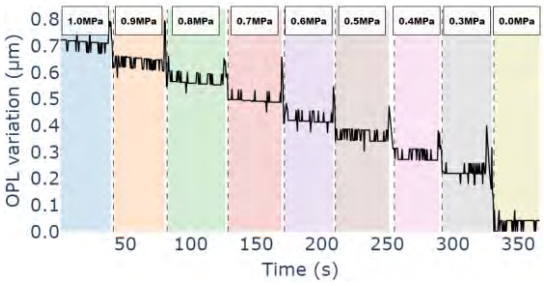

Fig. 4: OPL response of the cavity with pressure variation.

The steps defined in Figure 4, which represent the OPL of the cavity as a function of time, verify the stability at each pressure level. It should be noted that the zero value (0.0 µm) on the vertical axis corresponds to the minimum OPL measured during the experiment (490.98 µm), while all other values represent the positive difference with respect to this baseline value. In addition, a fast response time of the sensor to pressure changes is observed, as evidenced by the abrupt transition of the OPL between the different levels. Some noise can be observed, possibly caused by limitations in the resolution of the optical interrogator.

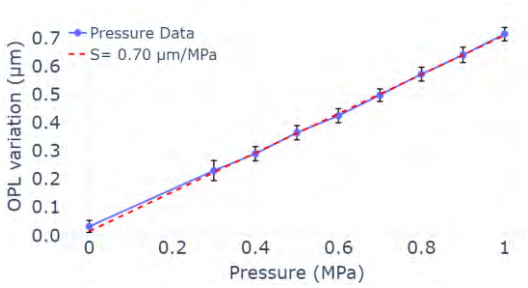

Fig. 5: Sensor linearity checks with pressure changes

As expected, a practically linear trajectory is observed in Figure 5 with $R^2 = 0.9993$, which confirms that the sensor responds proportionally to the pressure in the applied range. The sensor yielded a sensitivity of 0.7 µm/MPa, which demonstrates the potential of the sensor as a pressure gauge.

3.2.- Influence of temperature

The influence of temperature on the device was tested by placing it in a climatic chamber. The temperature within the chamber was varied from -10 °C to 70 °C with a 10 °C step, and was maintained at each level for 20 min to ensure thermal stabilization. Throughout the process, the reflection spectrum was monitored by using the same optical interrogator as before.

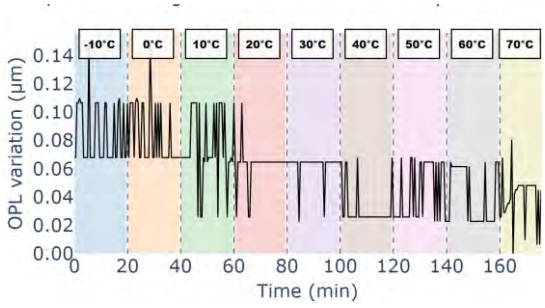

Fig. 6: OPL response of the cavity with temperature variation.

As shown in Figure 6, the sensor does not show a strong time-dependence in the OPL as in Fig. 4, which means that the OPL remains practically constant in the temperature range. In this representation, the zero value (0.0 µm) on the vertical axis corresponds to the minimum OPL measured during the temperature experiment (490.99 µm), with all other values indicating the positive difference with respect to this baseline. Figure 7 shows the averaged variation of OPL for each temperature step, maintaining the same reference where 0.0 µm represents the minimum measured value.The small dependence observed between these magnitudes indicates that temperature changes have little influence on the refractive index variation, as well as in the physical length of the cavity due to thermal expansion, which demonstrates that cross sensitivity between pressure and temperature is negligible, therefore there is no need for thermal compensation.

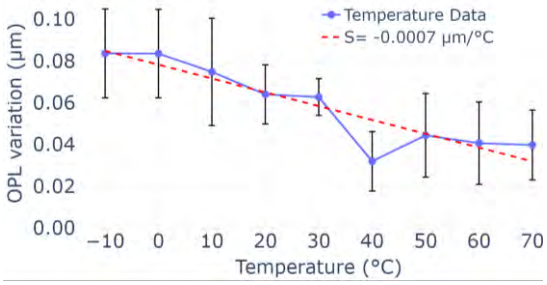

Fig. 7: Sensor linearity checks with temperature changes.

4.- Conclusion

A fiber optic pressure sensor based on an extrinsic Fabry-Perot interferometer, whose sensitivity is derived solely from changes in the refractive index of air in the cavity, has been successfully developed and characterized. The results obtained show a linear behavior between the optical path length of the cavity and the applied pressure, with a sensitivity of 0.7 µm/MPa, which confirms the accuracy and stability of the sensor to detect changes in pressure. Furthermore, it has been shown that the effect of temperature on the spectral response is negligible in the range of -10°C to 70°C, eliminating the need for thermal compensation. We conclude that the gas pressure can be monitored in real time by measuring the OPL through the shift of resonance lengths caused by the change of refractive index. This positions the developed pressure sensor as an effective and reliable option for pressure monitoring in environments with varying thermal conditions.

Acknowledgements: This work is partially supported by the I+D+I projects INNOFIBER PID2023-152314OB-I00 funded by the MICIU/AEI/501100011033/ and by the "European Union NextGenerationEU/PRTR/. Luis A. Sánchez acknowledges financial support from the "Ministerio de Ciencia, Innovación y Universidades/Agencia Estatal de Investigación" through the Torres-Quevedo research grant PTQ2023-013004.

References

[1] Marcelo F. DOMINGUES, Carlos TAVARES, Nélia ALBERTO, Paulo ANTUNES, Rui NOGUEIRA, "Cost-effective optical fiber pressure sensor based on intrinsic Fabry-Perot interferometric micro-cavities," Optical Fiber Technology, Volume 42, pp. 56–62, 2018.

[2] edro RORIZ, Orlando FRAZÃO, Ana B. LOBO-RIBEIRO, José L. SANTOS, Joaquim A. SIMÕES, "Review of fiber-optic pressure sensors for biomedical and biomechanical applications," Journal of Biomedical, Volume 18, Number 5, p. 050903, 2013.

[3] Guangyi HONG, Tingting LIU, Bowen YU, Yifei WANG, Yundong ZHANG, Zhaofang LI, Yiping WANG, "Optical fiber acoustic sensor with gold diaphragm based Fabry-Perot interferometer," Sensors and Actuators A: Physical, Volume 366, p. 114930, 2024.

[4] engyu CHEN, Yitang DAI, Dachuan ZHANG, Xiaohui WEN, Minghong YANG, "Cascaded-cavity fabry-perot interferometric gas pressure sensor based on vernier effect," Sensors, Volume 18, Number 11, p. 3677, 2018.

[5] Nélia ALBERTO, Carlos TAVARES, Marcelo F. DOMINGUES, Paulo ANTUNES, Humberto VARUM, Rui NOGUEIRA, "Relative humidity sensing using micro-cavities produced by the catastrophic fuse effect," Optical and Quantum Electronics, Volume 48, Number 12, p. 216, 2016.

[6] Steffen POEGGEL, Tino T. NAHRSTEDT, Stephanus P. PRAHER, Christian S. TAUSCHER, Hubert K. H. PUOLANNE, Dirk PLETTEMEIER, "Fiber-optic EFPI pressure sensors for In Vivo urodynamic analysis," IEEE Sensors Journal, Volume 14, Number 7, pp. 2335–2340, 2014.

[7] Qingming YU, Xiaodong ZHOU, "Pressure sensor based on the fiber-optic extrinsic fabry-perot interferometer," Photonic Sensors, Volume 1, Number 1, pp. 72–77, 2011

[8] Kent A. MURPHY, Michael F. GUNTHER, Ashish M. VENGSARKAR, Richard O. CLAUS, "Quadrature phase-shifted extrinsic Fabry-Perot optical fiber sensors," Optics Letters, Volume 16, Number 4, pp. 273-275, 1991.

[9] Bo XU, Yan LIU, Dongdong WANG, Dagong JIA, Chunshui JIANG, "Optical fiber Fabry–Pérot interferometer based on an air cavity for gas pressure sensing," IEEE Photonics Journal, Volume 9, Number 2, Art. no. 7102309, 2017.

[10] Lin ZHANG, Zongda ZHU, Chenjie LUAN, Yidan WANG, Libo YUAN, "Simultaneous measurements of temperature and pressure with a dual-cavity fabry-perot sensor," IEEE Photonics Technology Letters, Volume 31, Number 1, pp. 106–109, 2019.

Development and Experimental Validation of a Fiber Bragg Grating-Based Hydrogen Sensor Using Pt-Doped WO_3

Pablo SANCHO-VILLACH [(1)], Bryan SANIPATIN [(1)], Rubén MARTÍN-CABEZUELO [(1)], Laurent SAUVANAUD [(X)], Luis A. SÁNCHEZ [(2)], Salvador SALES [(1)]

1. Photonics Research Labs, ITEAM, Universitat Politècnica de València, Camino de Vera, s/n, 46022, Valencia, Spain.
2. CalSens S.L., 8F Building Office, Universitat Politècnica de València, Camino de Vera s/n 46022, Valencia, Spain.

Contact: Pablo SANCHO-VILLACH (psanvil1@upv.edu.es).

ABSTRACT:

We present the experimental development and validation of a fiber Bragg grating (FBG)-based hydrogen sensor using a Pt-doped WO_3 transducer in disk form. The sensor operates via an exothermic reaction between H_2 and the catalytic material, resulting in a localized temperature increase that causes a measurable shift in the Bragg wavelength. The pill, with an innovative encapsulation using a 3D-printed structure, shows excellent stability features and avoids condensation-related phenomena which compromised previous models studied. The results of a total wavelength shift of 540 pm under a 4% H_2 concentration demonstrated a smooth, and consistent spectral response following. Moreover, the system shows a response time to reach stability for a 1% change of approximately 10 minutes. This compact and cost-effective sensor configuration demonstrates a reliable, robust, remote and multi-point sensing alternative to traditional detection methods suitable for industrial safety monitoring and leak detection safety.

Key words: Hydrogen sensing, Fiber Bragg Grating (FBG), Pt-doped WO_3, Optical fiber sensor, Exothermic reaction, Gas sensor encapsulation, Molar ratio tuning, Remote sensing.

1.- Introduction

Hydrogen is progressively standing out as one of the most hopeful alternative energy sources to overcome serious environmental issues such as ozone layer depletion, acid rain and the greenhouse effect associated with traditional fossil fuels.

Hydrogen is established as a clean energy carrier [1], as not only its only byproduct during its combustion reaction is water vapor but also it is not based on carbon-base sources.

These properties mentioned above grant an outstanding potential for hydrogen-based energy systems, calling attention across several industries which already have used them in aerospace, petrochemicals, metallurgy and more emerging technologies.

However, its widespread adoption becoming stable in our market is still yet to be unresolved due to technical challenges present in transportation, storage, and production methods. But the critical issue is its tendency for leakage, along with the fact that concentrations above 4% in air represent a significant explosion hazard according to multiple studies [2].

Consequently, robust, safe and reliable systems are required in order to detect its presence and measure its concentration in the

environment and avoid such problems and risks.

The initial detection schemes were based on electrochemical sensors [3] that are still widely used in a variety of industrial processes. However, one major drawback with them is the exposure to hydrogen directly; this can lead to the generation of sparks and, by extension, explosion risks.

Since it is so much safer and more versatile compared to conventional solutions, fiber optic hydrogen sensors have grown more and more prominent in recent years [4]. They offer numerous advantages over traditional solutions like immunity against electromagnetic interference, high resistance to corrosion and harsh environments, high chemical selectivity, and remote monitoring and distributed sensing on an extensive scale.

Among the several fiber optic configurations available, fiber Bragg gratings (FBGs) are notable for their accuracy, miniaturization, and scalability. Besides uniform FBGs, more sophisticated configurations like long-period gratings (LPGs)[5], tilted FBGs (TFBGs) [6], or even composite gratings are considered in hydrogen sensing and provide transduction mechanisms, and an improved sensitivity based on the particular application.

Here, uniform FBGs are used in a hydrogen sensor with the sensing element being a Pt-doped tungsten trioxide (Pt-WO_3). The reactive material experiences an exothermic reaction on detection of hydrogen and generates localized heat that is responsible for creating a discernable wavelength shift in the FBG spectrum.

2.- Implementation and theoretical foundations

This section presents the experimental setup developed for the implementation of the sensor, along with the theoretical background that supports its operation.

The aim is to provide an overview of the design, fabrication, and working principles of the sensor, which is based on a fiber Bragg grating (FBG) coated with a catalytic active material. The components of the sensing capsule and the measurement system are described first, followed by a discussion of the physical and chemical mechanisms involved in hydrogen detection, with a particular focus on the role of platinum-doped tungsten trioxide and its interaction with the optical fiber.

2.1.- Chemical background

Tungsten trioxide (WO_3) is a traditional wide-bandgap metal oxide semiconductor with extensive application in hydrogen sensors owing to its exothermic reaction with hydrogen and its discoloration effect by hydrogen [7][8]. The compounds are very well researched with considerable work being conducted on them in several forms, including thin films [9] and powders [10].

In our application, hydrogen detection is performed by using a platinum-doped tungsten trioxide (Pt-WO_3) disk with high molar concentration of the active compound, it was elected due to its balance between fast stabilization time and reliable spectral response. When this capsule is exposed to hydrogen, it experiences an exothermic reaction that makes its detection possible and which is reversible.

$$WO_3+H_2 \leftrightarrow WO_2+H_2O$$

$$WO_2+\frac{1}{2}O_2 \leftrightarrow WO_3$$

The reaction between WO_3 and H_2 is inherently slow and requires a noble metal such as platinum to act as a catalyst, enabling the dissociation of the hydrogen molecule [11]. The presence of platinum significantly accelerates the reaction, thereby reducing the device's response time. The resulting temperature increase from the reaction radiates to the surrounding environment, altering the optical properties of the fiber.

2.2.- Principles of fiber Bragg gratings

Fiber Bragg gratings (FBGs) are passive optical devices consisting of a periodic modulation of the refractive index inscribed in the core of an optical fiber. This structure acts as a wavelength-selective mirror, reflecting only those wavelengths that satisfy the Bragg condition, given by the following equation:

$$\lambda_{Bragg} = 2n_{eff}\Lambda$$

Where λ_{Bragg} is the Bragg wavelength, n_{eff} is the effective refractive index of the guided mode, and Λ is the grating period.

This condition can be affected by external perturbations such as temperature (which can be compensated) or axial mechanical strain. These effects result in a wavelength shift in the reflected spectrum, without altering its shape. This shift can be accurately measured using a laboratory-grade optical interrogator.

A sensitive material layer is deposited on the fiber in the region of the FBG, which triggers a controlled exothermic reaction in the presence of hydrogen. This reaction primarily affects the thermal expansion of the FBG, leading to a modulation of the effective refractive index and resulting in a shift of the Bragg wavelength. Therefore, there is a direct relationship between hydrogen concentration and the Bragg peak variation.

2.3.- Sensor assembly and experimental setup

A custom gas mixing setup was implemented for the characterization, using two mass flow controllers to regulate the flow of air and hydrogen in order to achieve the desired gas concentrations (Fig. 1).

The constant flow rate of 300 ml/min was maintained during the process. The gases were blended under room temperature prior to being introduced into the chamber of the sensor, which had an enclosed feedthrough to the optical fiber and individual inlet and outlet ports for the gas flow.

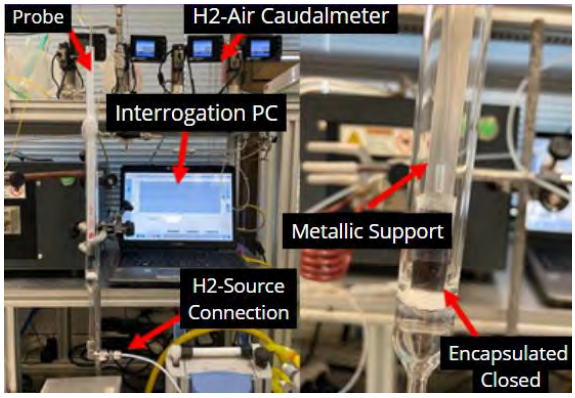

Fig. 1: Experimental set-up with laboratory container for the gas flow.

After passing through the chamber, the mixtures could be recovered if further analysis is required. All sensor setups were tested under hydrogen concentrations with ranges from 0 to 4% vol to ensure secure operation under levels below the flammability level.

The sensor that is suggested uses an active material pellet as the reactive element and an FBG to sense the temperature changes induced by the presence of hydrogen. Both are supported and anchored in place using a 3D-printed structure designed specifically to shield them and provide adequate exposure to the reactive from external gases (Fig. 2).

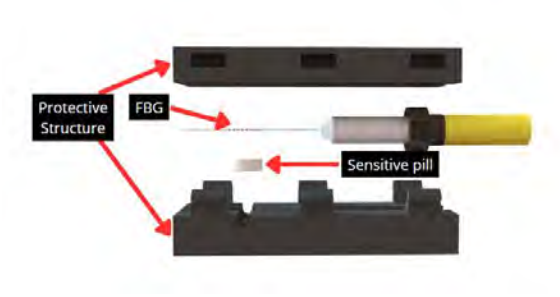

Fig. 2: 3D model of the hydrogen sensor structure.

To provide increased longevity in the event of being deployed in the field, the optical fiber outside the sensing area is covered in a 3.5 mm protective covering. It makes handling better and allows the sensor to work under harsh environments without damaging the very sensitive fiber located within the sensing area.

3.- Results

The operation of the H_2 sensor prototype was experimentally tested under several controlled conditions. The work highlights the spectral behavior of FBG when H_2 with varying concentrations is introduced in the presence of the active disk made of Pt-WO_3 with a molar ratio of W/Pt=13 [12]. The wavelength-shifted reflectance is traced with elapsed time to certify that the sensor is able to identify hydrogen through repeatable and measurable Bragg peak shifts.

The tests were performed with increasing hydrogen concentrations (0.2–4%) and the real-time Bragg wavelength displacement monitored (Fig. 3). Data revealed well-

defined spectral shifts with exposure to the gas and consistent behavior and patterns with repeated trials. These findings confirm the efficacy and resilience of the suggested structure and its suitability to be applied in practice.

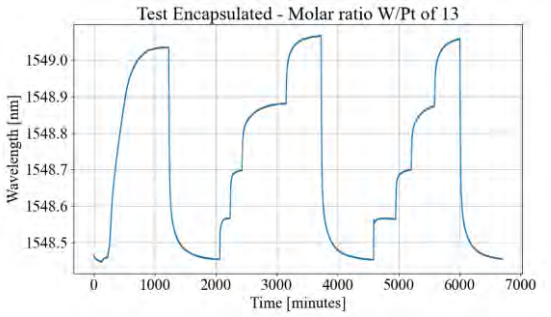

Fig. 3: Response of high molar concentration pill sensor with 1% H2 concentration increases.

The system is stabilized by the behavior of the disk under the encapsulation against fluctuations induced by condensation and thus achieves a smooth and uniform wavelength change in accordance with H_2 level changes. In the disk of the study, it takes the system approximately 10 minutes to stabilize following 1% H_2 level change. A 4% level rise in H_2 level presents a net wavelength change of 540 pm.

Further to this, an examination has been made on the reflectance spectra acquired by the Hyperion si255 sensor working in 1500 nm to 1600 nm and measuring one thousand points within this window. The results are shown on Fig. 4.

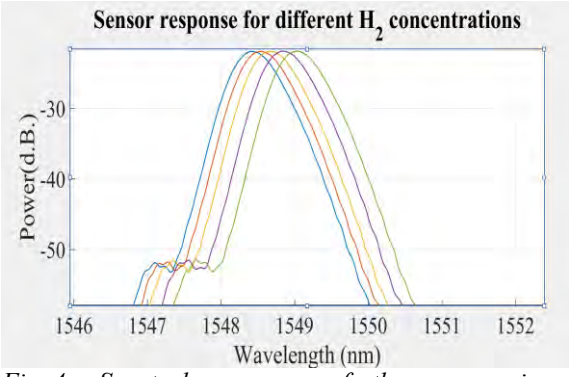

Fig. 4: Spectral response of the sensor in reflection with increasing hydrogen concentration levels.

The spectral profile in intensity (dB) does not vary and shifts to the right when the hydrogen level in the environment is increased from 0% to 4% with 1% intervals. The quantitative shift attests to the sensor's correct operation and its sensitivity to different hydrogen concentrations.

4.- Conclusion

In this work, a H2 sensor prototype was built, tested and validated in lab. It is a compact, reproducible and strong module that is ideal to deploy in any real-world scenario. The suggested setup takes into account past problems with wavelength shifts through condensation by using the disk form of the active material that has been found to be more stable, easy to incorporate into the system, and offers a uniform and stable response compared to powders or pellets.

The experimental results confirm the feasibility and performance of the sensor. The integration of the FBG with Pt-doped WO_3 reactive material presents an obvious and measurable sensitivity to the hydrogen percentage and therefore confirms the approach both in sensitivity and robustness aspects. Furthermore, the mechanical setup based on 3D printing of a customized holder and protective sleeve ensures protection to the optical fiber and functional exposure to the environment to which it should react.

This design not just provides simplicity and robustness but is itself an excellent foundation for future realizations with remote sensing and multipoint detection capabilities with further prospects in huge or hard-to-reach environments.

Acknowledgements: This work is partially supported by the I+D+I projects INNOFIBER PID2023-152314OB-I00 funded by the MICIU/AEI/501100011033/ and by the "European Union NextGenerationEU/PRTR/. Luis A. Sánchez acknowledges financial support from the "Ministerio de Ciencia, Innovación y Universidades/Agencia Estatal de Investigación" through the Torres-Quevedo research grant PTQ2023-013004.

References

[1] Yang, S., Wang, Z., Hu, Y., Luo, X., Lei, J., Zhou, D., ... & Gu, H. (2015). Highly responsive room-temperature hydrogen sensing of α-MoO3 nanoribbon membranes. *ACS applied materials & interfaces*, *7*(17), 9247-9253.

[2] Crowl, D. A., & Jo, Y. D. (2007). The hazards and risks of hydrogen. *Journal of Loss Prevention in the Process Industries*, *20*(2), 158-164.

[3] Hunter, G. W. (1992). *A survey and analysis of commercially available hydrogen sensors* (Vol. 105878). Lewis Research Center.

[4] Shen, C., Xie, Z., Huang, Z., Yan, S., Sui, W., Zhou, J., ... & Zeng, X. (2023). Review of the status and prospects of fiber optic hydrogen sensing technology. *Chemosensors*, *11*(9), 473.

[5] Kim,Y.H.; Kim, M.J.; Park, M.S.; Jang, J.H.; Lee, B.H.; Kim, K.T. Hydrogen Sensor used on A Palladium-Coated Long-Period Fiber Grating Pair. J. Opt. Soc. Korea 2008, 12, 221–225.

[6] Zhang, C., Shen, C., Liu, X., Liu, S., Chen, H., Huang, Z., ... & Zhang, Y. (2022). Pd/Au nanofilms based tilted fiber Bragg grating hydrogen sensor. *Optics Communications*, *502*, 127424.

[7] Yang, M., Wang, G., Dai, J., Yang, Z., Li, Z., Wang, Y., ... & Zhuang, Z. (2014). Fiber Bragg grating sensors with Pt-loaded WO3 coatings for hydrogen concentration detection down to 200 ppm. Measurement Science and Technology, 25(11), 114004.

[8] C.-C. Chan, W.-C. Hsu, C.-C. Chang, and C.-S. Hsu, “Hydrogen incorporation in gasochromic coloration of sol–gel WO3 thin films,” Sens. Actuators B, Chem., vol. 157, no. 2, pp. 504–509, Oct. 2011.

[9] P. Ngene, R. J. Westerwaal, S. Sachdeva, W. Haije, L. C. de Smet, and B. Dam, “Polymer-induced surface modifications of Pd-based thin films leading to improved kinetics in hydrogen sensing and energy storage applications,” Angew. Chem. (Int. ed. English), vol. 53, no. 45, pp. 12081–12085, Nov. 2014

[10] Y. Li, W. Shen, C. Zhao, B. Xu, D. Wang, and M. Yang, “Optical hydrogen sensor based on PDMS-formed double-C type cavities with embedded pt-loaded WO3/SiO2,” Sens. Actuators B, Chem., vol. 276, pp. 23–30, Dec. 2018.

[11] C. Caucheteur, M. Debliquy, D. Lahem and P. Megret, "Catalytic Fiber Bragg Grating Sensor for Hydrogen Leak Detection in Air," in IEEE Photonics Technology Letters, vol. 20, no. 2, pp. 96-98, Jan.15, 2008, doi: 10.1109/LPT.2007.912557.

[12] J. A. Villatoro et al., “Sensor de hidrógeno basado en fibra óptica con capa sensible de óxidos metálicos”, ES2856167B2, Spain, 15 Dec. 2021.

Análisis exhaustivo y modelo simplificado de un sensor de fibra óptica para desplazamiento angular

Gorka ZUBIA[(1)], Joseba ZUBIA[(2,3)], Josu AMOREBIETA[(4)], Gotzon ALDABALDETREKU[(2)], Gaizka DURANA[(2)]

1. Dpto. Exp. Gráfica y Proyectos de Ingeniería, Universidad del País Vasco EHU, Bilbao, 48013
2. Dpto. Ingeniería de Comunicaciones, Universidad del País Vasco EHU, Bilbao, 48013, España
3. EHU Quantum Center, Universidad del País Vasco EHU, Bilbao, 48013, España
4. Dpto. Matemática Aplicada, Universidad del País Vasco EHU, Bilbao, 48013, España

Contact: Gorka ZUBIA (gorka.zubia@ehu.eus).

ABSTRACT: (format: 12pt, bold, border at 12pt from text...)

Accurate tilt-angle measurement is vital in applications ranging from aerospace to civil infra structure monitoring, especially under harsh conditions where conventional inclinometers may fail. In this work, we present a comprehensive analytical model for intensity-based optical fiber displacement sensors (OFDS) capable of measuring multi-axis tilt. We model how a beam reflected from an inclined surface couples into arrays of receiving fibers (RF). It relates geometric fiber parameters, numerical aperture (NA), and target distance to predict measured optical power across different tilt angles and directions. It experimentally validated using various fiber bundle configurations: bifurcated, trifurcated, differential, symmetric, and quasi-random 19-fiber collections, demonstrating accurate operation up to ±20◦ tilt over distances up to 15 mm. Theoretical predictions match well with measurements, revealing that differential fiber configurations suppress noise and eliminate directional ambiguity. Moreover, we demonstrate how multi-fiber geometries discriminate tilt axes and enhance sensitivity through differential measurements. These findings highlight the potential for cost-effective, real-time, multi-axis tilt sensors that can address Industry 5.0 and advanced physics lab instrumentation needs.

Key words: instrumentation, optical fiber sensors, optical fiber displacement sensor, pho- tonic sensor, structural health monitoring, optical fiber devices.

1.- Introduction

La Industria 5.0 plantea una fabricación más humana, sostenible y resiliente, donde la monitorización avanzada es clave para integrar máquinas y personas [1]. En este contexto, medir ángulos de inclinación con precisión es esencial para la seguridad y rendimiento estructural e industrial, por ejemplo, en álabes de turbinas aeroespaciales o detección temprana en puentes y presas. Los sensores de fibra óptica, inmunes a EMI/EMC, compactos y capaces de sensado remoto, son ideales para estos entornos [2, 3]. Aunque los FBG y Fabry–Pérot ofrecen alta precisión, requieren sistemas complejos. Los sensores ópticos basados en intensidad (OFDS) son más económicos y simples, midiendo potencia óptica reflejada en superficies inclinadas [4, 5, 6], pero necesitan calibración y es difícil distinguir ejes. Aunque estas limitaciones mejoran mediante configuraciones diferenciales avanzadas [7], aún no existe un modelo analítico unificado para sensores multieje basados en intensidad [8]. Presentamos un modelo matemático que relaciona la inclinación y la potencia medida en configuraciones multifibra, analizando cómo parámetros geométricos, NA y distribución espacial afectan la sensibilidad,

linealidad y rango. Validamos experimentalmente el modelo con haces bifurcados, trifurcados, diferenciales, simétricos y cuasi-aleatorios, con precisión hasta $\pm 15°$ y distancias hasta 15 mm. Nuestro diseño trifurcado mide simultáneamente distancia y ángulo.

2.- Modelo matemático

El principio de operación de un sensor angular de fibra óptica (OFDS) se ilustra en la Fig. 1, donde se presenta el problema general de medición abordado en este trabajo: un haz de fibras ópticas emite luz hacia un objetivo que puede desplazarse en la dirección z e inclinarse en los ángulos $\{\alpha_x, \alpha_y\}$. El sensor captura las reflexiones a distintas distancias y orientaciones sin necesidad de óptica externa. La luz que emerge de la fibra transmisora (TF) puede describirse con un perfil gaussiano. En [9] se presentó el perfil del haz gaussiano en coordenadas polares, ahora lo reescribimos en cartesianas. La potencia óptica total incidente es P_0 y el radio de la cintura del haz [10],

$$\omega(z) \approx z^2 \tan^2\theta_0 \quad \text{con NA} = \sin\theta_0, \qquad (1)$$

la irradiancia $I(x, y, z)$ a distancia z [11,12]:

$$I(z) = \frac{2P_0}{\pi\,\omega^2(z)} \exp\left(-\frac{2(x^2+y^2)}{\omega^2(z)}\right). \qquad (2)$$

2.1.- Efecto de la inclinación del espejo

Al inclinar el espejo un ángulo α alrededor del eje X, se generan desplazamientos tanto angulares como lineales en el punto de incidencia del haz en la fibra receptora (RF). Para describir este desplazamiento, resulta conveniente definir un nuevo sistema de coordenadas $\{x_R, y_R, z_R\}$ rotado un ángulo 2α con respecto al sistema original $\{x, y, z\}$. Este giro de 2α se debe a que, en una reflexión especular, el ángulo reflejado se duplica respecto al ángulo incidente, Fig. 2. Sea d la posición del centro del espejo inclinado sobre el eje Y en el sistema original. La transformación al sistema rotado (en torno al eje X) queda definida por las coordenadas,

$$x_R = x, \qquad (3)$$

$$y_R = y\cos 2\alpha - d\sin 2\alpha, \qquad (4)$$

$$z_R \approx d\left(1 + \frac{1}{\cos 2\alpha}\right). \qquad (5)$$

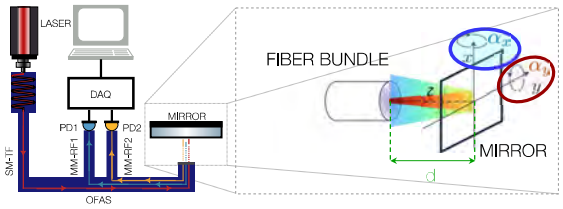

Fig. 1: Montaje experimental típico de un OFDS.

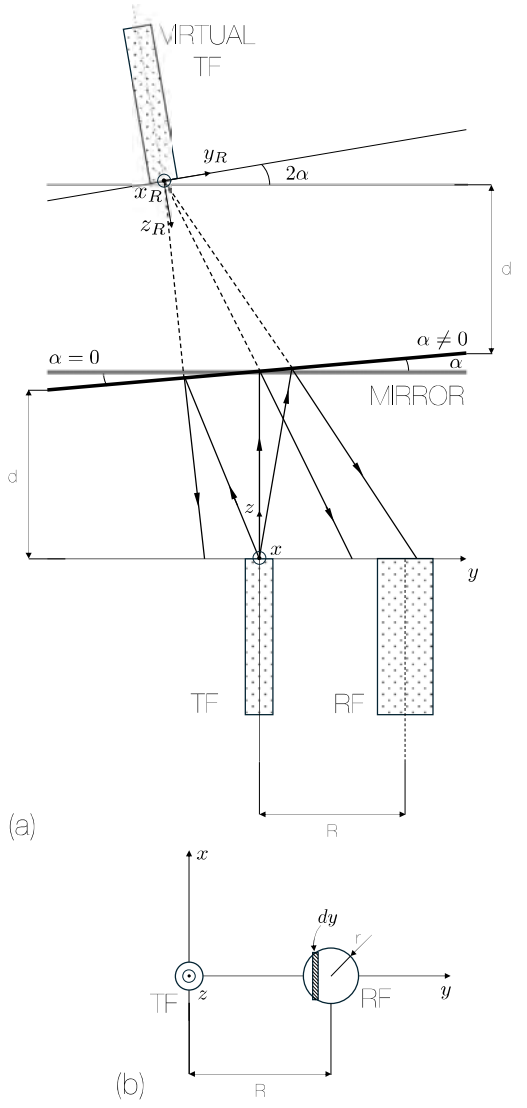

Fig. 2: Definición de los parámetros geométricos del problema. (b) Integración en la RF.

En el sistema rotado, el haz reflejado llega a la RF con un factor adicional $\cos 2\alpha$:

$$I(z) = \frac{2\Gamma P_0 \cos 2\alpha}{\pi\,\omega^2(z_R)} \exp\left(-\frac{2(x^2+y_R^2)}{\omega^2(z_R)}\right), \qquad (6)$$

donde,

$$\omega^2(z_R) \approx d^2(1+\cos 2\alpha)^2 \frac{\tan^2\theta_0}{\cos^2(2\alpha)}. \qquad (7)$$

2.2.- Potencia total recolectada

Para determinar la potencia total recolectada por la RF, se integra $I(z)$ sobre la superficie de la RF. Sea r el radio de la RF, que está ubicada a una distancia R del eje de rotación del espejo, Fig. 2. Entonces,

$$P_R(R,\alpha,d) = \Gamma \frac{2P_o \cos^3 2\alpha}{\pi\, d^2\,(1+\cos 2\alpha)^2 \tan^2\theta_0} \times$$

$$\iint_{R_x} \exp\left(-\frac{2\,(x^2+y_R^2)\cos^2 2\alpha}{d^2(1+\cos 2\alpha)^2\tan^2\theta_0}\right) dx \qquad (8)$$

donde R_x indica la región de integración del área de la RF y Γ la reflectividad del espejo. Integrando respecto a x,

$$\int_{-\sqrt{r^2-(y-R)^2}}^{\sqrt{r^2-(y-R)^2}} exp\left(-\frac{2\,x^2\cos^2 2\alpha}{d^2(1+\cos 2\alpha)^2\tan^2\theta_0}\right) dx \qquad (9)$$

donde erf(·) es la función error y

$$a = \frac{2\cos^2(2\alpha)}{d^2,(1+\cos 2\alpha)^2,\tan^2\theta_0}.$$

La integral restante queda:

$$\sqrt{\frac{\pi}{a}} \int_{R-r}^{R+r} \mathrm{erf}\left(\sqrt{a}\sqrt{r^2-(y-R)^2}\right) \times$$

$$\exp(-a(y\cos 2\alpha - d\sin 2\alpha)^2)dy. \qquad (10)$$

2.3.- Solución aproximada

La integral derivada en Eqs. (9) y (10) puede evaluarse numéricamente. Sin embargo, es más conveniente aproximarla para observar explícitamente cómo la potencia detectada depende de distintos parámetros. Aplicando el teorema del valor medio, aproximamos evaluando la irradiancia en el centro de la RF, $y = R$. Por lo tanto,

$$P_{R_i} = \frac{2\sqrt{2}\, r\, \Gamma\, P_0 \cos^2(2\alpha)}{\sqrt{\pi}\, d\,(1+\cos 2\alpha)\tan\theta_0}$$

$$\times \mathrm{erf}\left(\frac{\sqrt{2}\, r\cos 2\alpha}{d\,(1+\cos 2\alpha)\tan\theta_0}\right)$$

$$\times \exp\left(-\frac{2\,(R\cos 2\alpha - d\sin 2\alpha)^2\cos^2(2\alpha)}{d^2\,(1+\cos 2\alpha)^2\tan^2\theta_0}\right). \qquad (11)$$

3.- Resultados

3.1.- Haz bifurcado

La Fig. 3 muestra la respuesta representativa de un haz con una TF y una RF, de acuerdo con la de la Fig. 2b. Los parámetros son NA = 0.09, $r = 50\,\mu$m, $R = 600\,\mu$m, y ángulos de inclinación $\alpha_x \in \{0{,}20\}^\circ$ en incrementos de 2° (Fig. 3a). En la Fig. 3b se detalla la respuesta para ángulos de 0° a 2°, cada 0.2°. La potencia detectada aumenta al inclinar la superficie reflectante; a 20° se recibe aproximadamente 60 veces más potencia que a 0°. La respuesta del haz bifurcado es *bivaluada*; una misma potencia detectada corresponde a dos distancias diferentes, com-plicando así su uso en diseños de sensores, salvo que se restrinja el rango operativo a una sola región.

3.2-Haz bifurcado simétrico

Una forma de obtener una respuesta equilibrada frente a ángulos positivos y negativos es utilizar dos RFs idénticas dispuestas simétricamente respecto a la TF, a $+R$ y $-R$. Definimos la responsividad $\eta(\alpha_x, d)$ como,

$$\eta(\alpha_x, d) = \frac{P_{R_2}(-R)}{P_{R_1}(R)}$$

$$= \exp\left(-\frac{8\,R\sin 2\alpha_x \cos^3 2\alpha_x}{d\,(1+\cos 2\alpha_x)^2\tan^2\theta_0}\right). \qquad (12)$$

Una ventaja de esta configuración es la cancelación del ruido común mediante la relación de potencias, una respuesta simétrica para rotaciones positivas y negativas.

4.- Validación del modelo

Para validar el modelo teórico de la Sec. 2, diseñamos el montaje experimental de la Fig. 4. Este consta de siete elementos: una fuente láser Fabry-Perot de sobremesa de 660 nm (Thorlabs), el haz de fibras, un espejo que actúa como superficie reflectante, unas etapas de desplazamiento lineal y angular (Zaber), vario fotodetectores (Thorlabs) y una tarjeta de adquisición (Keithley). Para la validación se utilizaron cuatro haces bifurcados con diferentes diámetros de núcleo y número de fibras, además de un haz trifurcado. Tres de estos haces están construidos a partir de dos fibras con diámetros de núcleo de $\{50, 200, 600\}\,\mu$m. Además, incluimos un haz comercial distribuido aleatoriamente (Thorlabs), con 19

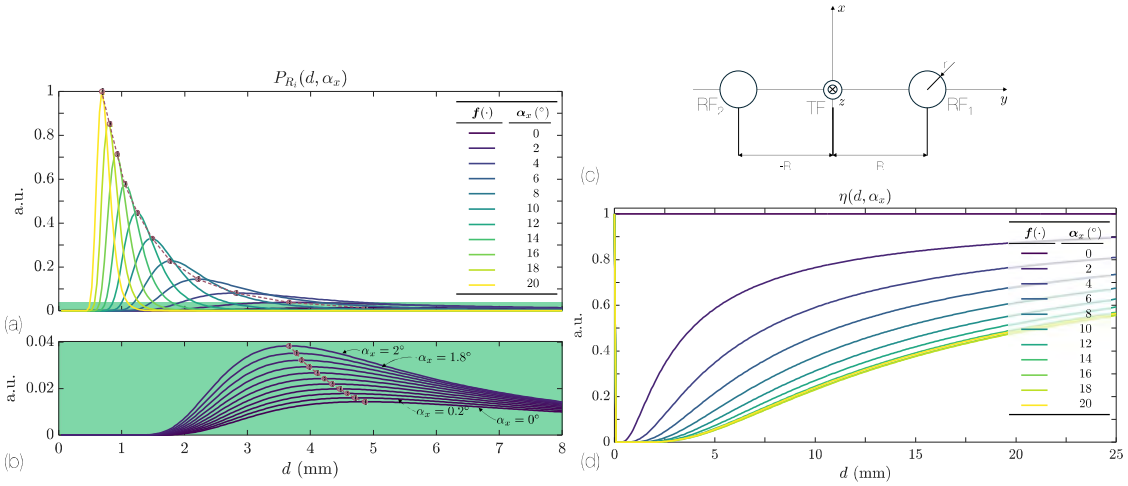

Fig. 3: Izquierda: potencia recibida por la RF de un haz bifurcado según Ec. (11) *para* α_x. *Los puntos rojos indican la posición del máximo* d_{max}. *(a) Respuesta para NA* $= 0.09$, $r = 50\,\mu m$, $R = 600\,\mu m$ *y* $\alpha_x \in \{0{,}20\}°$. *(b) Detalle entre* $\alpha_x = 0°$ *y* $2°$ *cada* $0.2°$. *Derecha: (c) Geometría del haz bifurcado simétrico. (d) Relación de potencia detectada* $\eta(\alpha_x, d)$ *según la Ec.* (12) *para* $\alpha_x \in \{0{,}20\}°$, *con pasos de* $2°$ *y* $\theta_0 = 12.71°$, $r = 50\,\mu m$ *y* $R = 600\,\mu m$.

fibras (9-TF y 10-RF), todas con núcleos de 200 µm y NA = 0.22. En comparación, este proporciona una iluminación más uniforme y más potencia.

4.1.- Haces bifurcados

La Fig. 5a muestra las medidas de desplazamiento lineal, y la Fig. 5b, el desplazamiento angular. Observamos una muy buena concordancia entre los resultados experimentales y el modelo teórico desarrollado. En el desplazamiento lineal, apreciamos que la posición del máximo de potencia se desplaza hacia mayores distancias a medida que aumenta la separación TF-RF. El modelo predice una disminución abrupta después del máximo, aunque a grandes distancias la potencia experimental y la teórica convergen asintoticamente. Las diferencias observadas a grandes distancias se deben a dos razones: el haz reflejado se expande más allá del núcleo de la fibra, siendo parcialmente recortado por el revestimiento, lo que disminuye la potencia detectada. También, la excitación de modos superiores en la fibra TF distorsiona el perfil gaussiano ideal del haz, aumentando su divergencia y reduciendo la eficiencia del acoplamiento en la RF. La Fig. 5b muestra las medidas angulares para diferentes distancias. Se observa una respuesta asimétrica (Sec. 3.1), con un máximo desplazado hacia ángulos positivos. La potencia detectada disminuye con la distancia y la respuesta se vuelve más simétrica, acercándose el máximo a $\alpha_x = 0°$. Esto ocurre con más rapidez cuanto menor es el tamaño del haz bifurcado. Por ejemplo, para el haz de 50 µm la respuesta se vuelve simétrica a solo 2 mm, mientras que para el de 600 µm se requiere una distancia de 8 mm.

4.2.- Haz bifurcado de 19 fibras

La Fig. 6c muestra los resultados del haz de 19 fibras. En este caso, la coincidencia con el

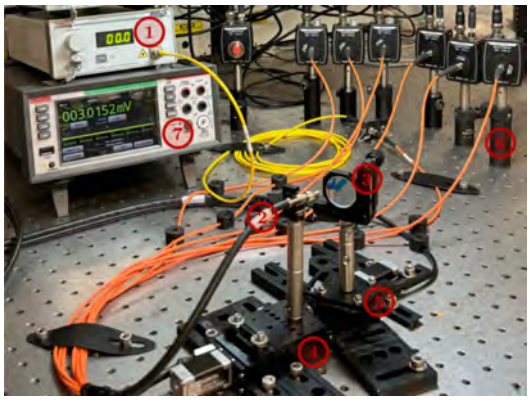

Fig. 4: Sensor angular típico de fibra óptica (1) fuente láser de 660 nm, (2) haz de fibras ópticas, (3) un espejo, (4) una etapa lineal y otra (5) angular, (6) fotodetectores cuadráticos PD_i *y (7) una tarjeta DAQ.*

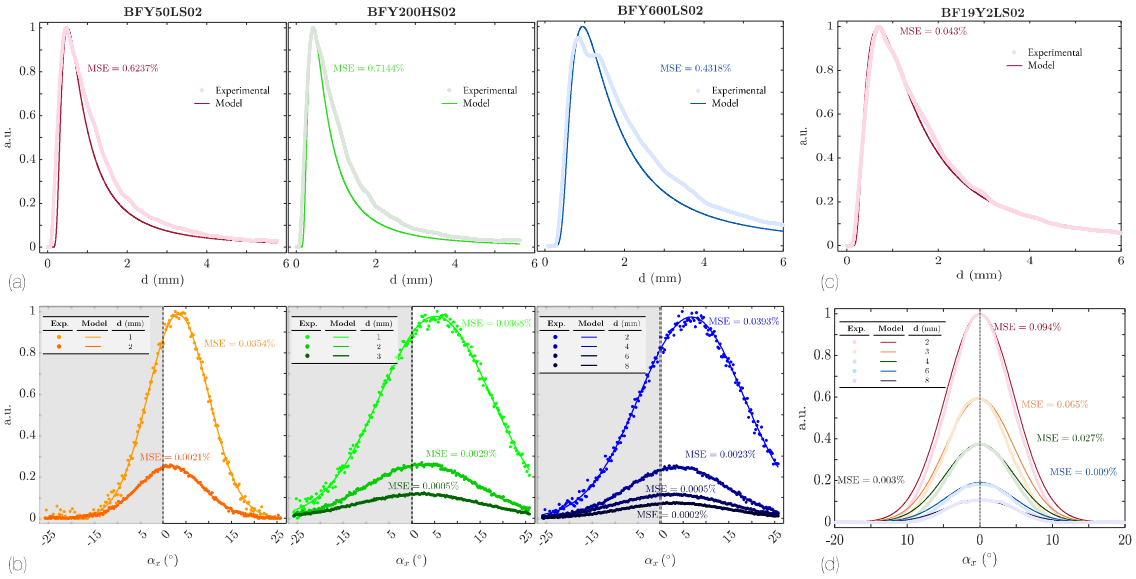

Fig. 5: Respuestas experimentales y teóricas de los tres haces bifurcados con diámetros {50,200,600} *μm. (a) Distancia para* $\alpha_x = 0°$. *(b) Ángulo para distancias fijas, con* $\alpha_x \in [-25,25]°$. *Derecha: lo mismo pero para el BF19Y2LS02. (c) Respuesta frente a la distancia para* $\alpha_x = 0°$. *(d) Respuesta frente al ángulo para distancias fijas y* $\alpha_x \in [-25,25]°$.

modelo teórico es aún mejor, atribuible al efecto promediado del conjunto de fibras, que minimiza desalineamientos individuales. Gracias a la casi aleatoriedad, la respuesta angular es simétrica, con un máximo centrado en $\alpha_x = 0°$. Este haz presenta una sensibilidad inversamente proporcional a la distancia, aunque pierde sensibilidad rápidamente fuera del rango $\alpha_x \in [-10,10]°$. La respuesta sigue siendo bivaluada, lo que impide distinguir el sentido de rotación.

4.3.- Haz trifurcado

Las medidas experimentales y el modelo se muestran en la Fig. 7.

Este consta de dos colecciones de RF en $\{R_1 \approx 200, R_2 \approx 400\}$ μm. La coincidencia es buena pero inferior respecto a los anteriores, dado que el modelo considera una configuración lineal mientras que la experimental es azimutal. La discrepancia aparece en la zona muerta de la segunda colección RF, que es mayor en el modelo teórico debido a proyecciones más cortas en la estructura experimental.

5.- Conclusiones

En este trabajo desarrollamos y validamos experimentalmente un modelo analítico unificado para sensores angulares de fibra óptica basados en intensidad, capaces de medir inclinaciones respecto a uno o más ejes ortogonales. El modelo integra propagación gaussiana, geometría y reflexión, vinculando analíticamente la potencia detectada con los ángulos de inclinación sin recurrir a calibraciones puramente empíricas. Analizamos diversas configuraciones: haces

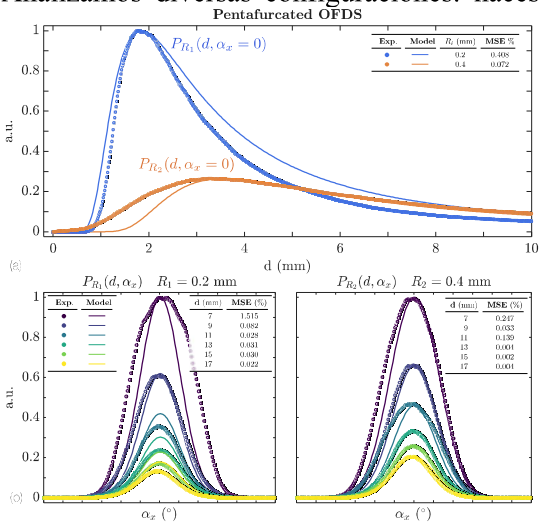

Fig. 6. Respuestas experimentales y teóricas de las dos colecciones RF del haz trifurcado. (a) Respuestas en distancia para $a_x = 0°$. *(b) Respuestas angular para* $a_x \in [-15, 15]°$.

bifurcados simples, simétricos, diferenciales, trifurcados y distribuidos aleatoriamente con 19 fibras. La simetría geométrica y la detección diferencial reducen considerablemente el ruido y la ambigüedad en las medidas. La validación experimental para distancias de hasta 15 mm y ángulos hasta $\pm 20°$ confirma que el modelo describe con precisión el comportamiento tanto angular como dependiente de la distancia. Haces con mayor número de fibras muestran respuestas más estables y menos ambiguas, ideales para la detección multiaxial fiable. En comparación con otros sensores angulares de fibra óptica reportados, nuestro modelo ofrece tres ventajas. Una expresión analítica cerrada para inferir directamente la inclinación; adaptabilidad flexible a diversas configuraciones de fibras y mayor rechazo al ruido mediante detección diferencial. Estas permiten mediciones angulares multieje compactas y fiables, adecuadas para entornos hostiles o con limitaciones de espacio, desde inclinómetros industriales hasta componentes aeroespaciales. Como trabajo futuro ampliaremos el modelo a rangos angulares mayores y blancos no especulares.

Acknowledgements: This research was supported by the grants I+D+i/PID2021-122505OBC31, TED2021-129959B-C21 and PID2024-155582OB-C31, funded by MCIN/AEI/10.13039/501100011033, by "ERDF A way of making Europe", by the "European Union Next Generation EU/PRTR". The research work is also supported by the Grant No. IT11452-22 and funded by the Basque Government, by ELKARTEK 2023 (µ4Smart-KK-2023/00016 and Ekohegaz II-KK-2023/00051), by ELKARTEK 2025 (Smart-SmartµS and Newhegaz) and by the University of the Basque Country (UPV/EHU) Translight.

References

[1] European Commission, ''Industry 5.0,'' *Tech. Rep.*, 2021.

[2] A. Sharbirin et al., ''High-performance and 3d-printed two-mode fiber optic tilt sensor,'' *Journal of Lightwave Technology,* vol. 37, no. 4, pp. 1140–1146, 2019.

[3] J. Wang, *et al.*, ''A bio-inspired fiber-optic attitude sensor for multi-axis tilt measurement,'' *Journal of Lightwave Technology*, vol. 41, no. 21, pp. 6844–6851, 2023.

[4] G. Zubia *et al.*, ''High-perfomance optical fiber displacement sensor with extended linear range and sensitivity,'' *Sensors*, vol. 13, no. 6, pp. 7385–7398, Jan. 2025.

[5] G. Zubia *et al.*, ''Design and performance analysis of tetrafurcated optical fiber displacement sensors for enhanced range and linearity,'' in *SPIE*, vol. 12893. 2024, pp. 199–206.

[6] G. Zubia *et al.*, ''An algorithm to optimize the optical sensor design for tip clearance and tip timing measurements,'' in *SPIE*, vol. 12139., May 2022, pp. 194–200.

[7] Vadapalli, K *et al.*, ''Optical fiber-based intensity-modulated cost-effective small lean angle measurement sensor,'' *MAPAN* -, vol. 36, no. 4, pp. 925–930, 2021.

[8] Y. Shimizu *et al.*, ''Optical Sensors for Multi-Axis Angle and Displacement Measurement Using Grating Reflectors,'' *Sensors*, vol. 19, no. 23, p. 5289, Jan. 2019.

[9] G. Zubia *et al.*, ''In-depth analysis of optical fiber displacement sensor design process,'' *Journal of Optics*, Aug. 2024.

[10] G. Zubia *et al.*, ''Mathematical modeling and experimental validation of optical fiber sensors for simultaneous measurement of angular and linear displacements,'' in *SPIE*, vol. 12999. *SPIE*, 2024, pp. 40–47.

[11] G. Zubia *et al.* ''A new method to design trifurcated optical fiber displacement sensors,'' *IEEE Sensors Journal*, vol. 24, no. 2, pp. 1532–1545, Jan. 2024.

[12] G. Zubia *et al.*, ''Theoretical method for the design of bifurcated fiber optic displacement sensors,'' in *OPTOEL* 2023, 2024

Dispositivos fotónicos

Improving the Efficiency of Blazed gratings in Vertical Aligned LCoS device

Guillem NAJAR [1,2], Fco. J. MARTÍNEZ-GUARDIOLA [1,2], Andrés MÁRQUEZ [1,2], Jorge FRANCÉS [1,2], Sergi GALLEGO [1,2], Inmaculada PASCUAL[1,3], Augusto BELÉNDEZ [1,2]

1. Department of Physics, System Engineering and Signal Theory, University of Alicante, Crta. San Vicent del Raspeig s/n.
2. University Institute of Physics Applied to Sciences and Technologies, University of Alicante, Crta. San Vicent del Raspeig s/n.
3. Department of Optics, Pharmacology and Anatomy, University of Alicante, Crta. San Vicent del Raspeig s/n.

Contact: Francisco J. MARTINEZ-GUARDIOLA (fj.martinez@ua.es).

ABSTRACT:

The use of Liquid Crystal on Silicon devices (LCoS) has extended to a multitude of optical applications. We are working with an LCoS that works as a pure phase spatial light modulator (SLM) and it has a wide range of wavelengths.

The pixelation of these devices implies that some degradation effects, such as the fringing field or crosstalk, can affect the efficiency of our programmed diffraction optical elements. In our case we want to test if we can improve the efficiency of a blazed grating when we use the device in visible range. We have been working with a Vertical Aligned (VA) device that works on a wide range of wavelengths from 450 to 1600nm, we will see how efficiency can be improved by using different configurations that the manufacturer offers.

Key words: VA-LCoS, Blazed Gratings, Diffractive Optical Element, SLMs, Fringing Field, Crosstalk

1.- Introduction

The LCoS (Liquid Crystal on Silicon) devices have been used in almost all fields of optics because of their versatility and ease of use. In our case we use a VA-LCoS (Vertical Alligned Liquid Crystal on Silicon) device designed to be used in the wavelength range that goes from infrared to visible (1600 to 450nm).

The device operation implies the application of a certain voltage in each pixel that makes the liquid crystal molecules to be reoriented in the direction of the electrical field [1]. The difference in the optical path due to the birefringence of the material implies the introduction of a retardance. The device works as a tunable waveplate.

For the implementation of a Diffractive Optical Element (DOEs) we usually need a 360º phase-shift, that is the reason why the manufacturer allows us to configure the display with different parameters depending on the incident wavelength. The pixelation implies that the efficiency is reduced from an ideal blazed grating [2].

We will see how, despite the limited configuration capabilities that we have available, we can improve the efficiency of a well-known multilevel DOE such as a blazed grating.

2.- Experiment and results

For the experiment we will use a VA-LCoS manufactured by Santec, the model SLM-200 with a WUXGA (1920x1200) pixel

resolution, with a 10-bit addressing scheme (1024 gray levels). The model that we use has an antireflection coating with a wavelength range from 450nm to 1600nm (SLM-200-01-0001-21). In previous works we have done calibration experiments to test the behavior for different configurations, and we saw that the phase response is linear for all configurations [3].

The manufacturer, by using its software, allows us to select the retardance range and the wavelength that we need for the DOEs that we want to implement. Internally the device will change the range of the voltage that is applied for the different 1024 gray levels and its look up table (LUT) to avoid non linearities on the response due to the liquid crystal behavior. In this sense, the maximum range of applied voltage will be used for the larger wavelengths (infrared) and the range of voltage has to be reduced to obtain a 360º phase retardance in the visible range [4].

We want to test if the configurations designed by the manufacturer are the best option to implement a blazed grating with different period.

In the first place we want to measure the diffraction efficiency for the full range of voltage; to do so, we measure the first 4 orders for a 20 pixel per period blazed grating.

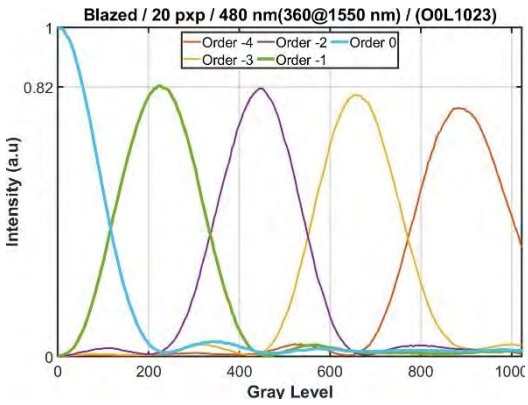

Fig. 1: Diffraction efficiency for the 4 orders as a function of the gray level of the last step of the grating, when using a configuration for 1550nm and 480nm in the incident beam. 20pix/per

We produce a blazed grating of 20pix/per where the first pixel has a gray level equal to 0 and the last pixel is increasing its value until its maximum value (1023 gray level). The intermediate values are calculated following a linear progression.

In Fig.1, we can see the normalized intensity measurements of the first 4 orders of a blazed grating with a 20 pixel per period. In this case, the configuration for the VA-LCoS is the one that allows a 360º phase-shift for the 1550nm wavelength, but we are using a blue laser (480nm). That means that we are using the full range of the voltage applied and see that for that wavelength (480nm) we have more than 360º of phase-shifting. We can observe that the phase-shift introduced in the incident beam is more than 1440º (4x360º) [3]. If we focus our attention on the first order, we see that the maximum efficiency for this order is 82%.

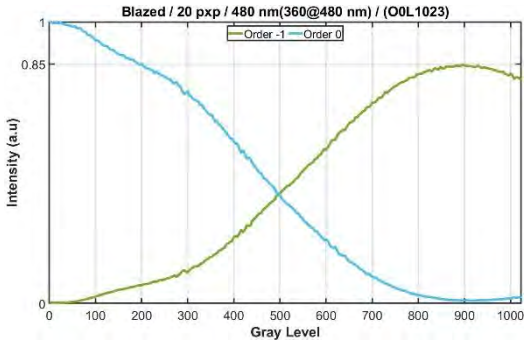

Fig. 2: Diffraction efficiency for the 1 order as a function of the gray level of the last step of the grating when using a configuration for 480nm as the incident beam.20pix/per.

In Fig.2 we obtain the results for the same experiment but in this case, we use the configuration designed by the manufacturer for the used wavelength (480nm). We see how in this case the maximum introduced retardance is a bit more than 360º and the maximum efficiency is 85%, slightly better than the one obtained with the configuration for 1550nm.

At this point, we want to check if we can improve the efficiency of our grating using different range of voltage. The manufacturer does not allow us to directly change this range as other manufacturers [5]. As we present in Fig.1 we have enough range for the phase-

shifting, so we do not need the 1023 available gray levels, we can just use about 300 levels for the 360º phase-shift needed. And we can select these 300 levels in the range from 0 to 1023. So, in this case the experiment is the same as before, but the first pixel of the blazed grating will not have the 0 value, we will start from a greater value (we have selected 700).

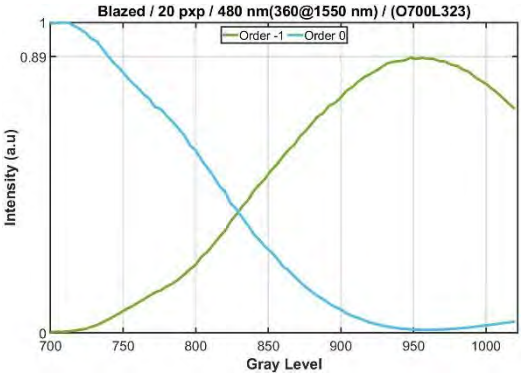

Fig. 3: Diffraction efficiency for the 1 order as a function of the gray level of the last step when using a configuration for 1550nm and 480nm in the incident beam. 20pix/per

In Fig. 3 we see the results for the case of a blazed grating of 20pix/per and the configuration for 1550nm and the same incident beam of 480nm, but this time we insert an offset in the blazed. We use a blazed grating that starts from gray level 700 instead of 0, and we increase the last step until its maximum gray level (1023). We can observe that the efficiency of the first order is slightly better (89%) than the one obtained with the configuration specifically designed to 480nm (85%) reflected in Fig 2.

We have seen how efficiency has slightly increased, just but applying an offset to the blazed grating. Now, we want to check how this can be affected when we select other period for the grating. So, we repeat the measurements for a blazed grating with 4 pix/per.

In Fig. 4 we have diffraction efficiency, for the first 2 orders, in this case we show less orders because the CCD camera used to make measurements cannot capture all the orders, because in this case the orders are more spatially separated. With this experimental configuration we obtain an efficiency of 44% for the first order.

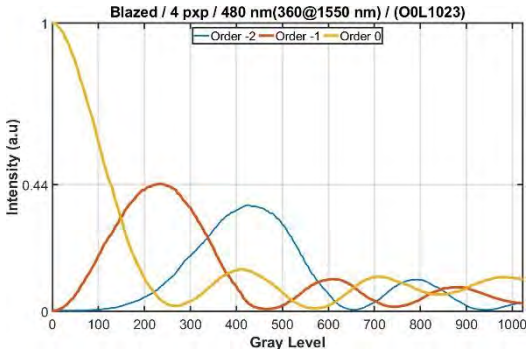

Fig. 4: Diffraction efficiency for the first 2 orders as a function of the gray level of the last step of the grating, when using a configuration for 1550nm and 480nm in the incident beam. 4pix/per

As in the previous configuration, we are interested in the efficiency obtained with the manufacturer configuration for the 480nm. In Fig.5 we have the results for this case, and we clearly observed that efficiency has increased, and now we obtain 52% for the first order.

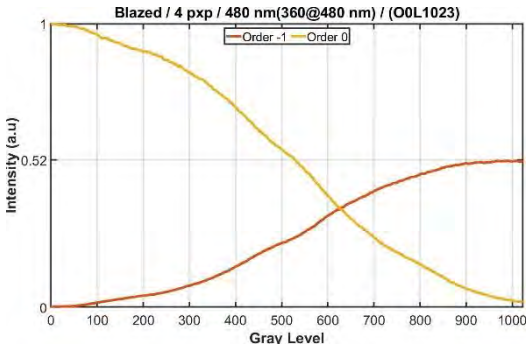

Fig. 5: Diffraction efficiency for the first order as a function of the gray level of the last step of the grating, when using a configuration for 480nm and 480nm in the incident beam. 4pix/per

Finally, we want to check if by using the same method than before, that means, to make the blazed grating with an offset the efficiency improves. We select the same values as before. Gray level 700 will be our value for the first step, and we will increase the last step until its maximum value.

In Fig.5 we see that the efficiency of the grating has increased to a 58%, just by adding an offset to all the blazed grating.

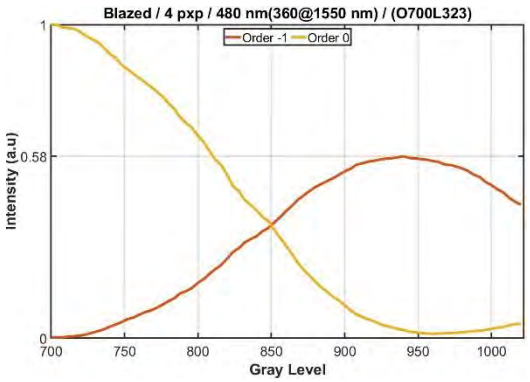

Fig. 5: Diffraction efficiency for the first order as a function of the gray level of the last step of the grating, when using a configuration for 1550nm and 480nm in the incident beam. 4pix/per

3.- Conclusion

In this work we have seen how despite the limitations to configure the device, since we cannot access the LUT of the voltages, we can make some changes to the configuration. By selecting the configuration for a lower wavelength, we can slightly improve the efficiency of blazed gratings, just by designing these gratings in other voltage ranges (in our case this is translated to a gray level offset.) We even achieved better efficiency than when the configuration for the specific wavelength is used.

Acknowledgements This work was supported by the Ministerio de Ciencia, Innovación y Universidades/AEI (Spain), cofunded by ERDF/EU (PID2021-123124OB-I00, PID2023-148881OB-I00).

References

[1] Grigory LAZAREV, Po-Ju CHEN, Johannes STRAUSS, Nicolas FONTAINE, Andrew FORBES, *"Beyond the display: phase-only liquid crystal on Silicon devices and their applications in photonics [Invited]"*, Opt. Express 27, 16206 (2019).

[2] Andrés MÁRQUEZ, Francisco J. MARTÍNEZ-GUARDIOLA, Jorge FRANCÉS, Cristian NEIPP, Manuel G. RAMÍREZ, Eva M. CALZADO, Marta MORALES-VIDAL, Sergi GALLEGO, Augusto BELÉNDEZ, and Inmaculada PASCUAL, *"Analytical modeling of blazed gratings on two dimensional pixelated liquid crystal on silicon devices"*, Optical Engineering 59, 041208 (2020).

[3] Guillem NÁJAR, Francisco J. MARTÍNEZ-GUARDIOLA, Adriana R. SÁNCHEZ-MONTES, Andrés P. BERNABEU, Eva M. CALZADO, Daniel PUERTO, Andrés MÁRQUEZ *"Higher orders enhancement in gratings produced by a vertically aligned LCoS"*, in Proceedings of SPIE Vol. 13015, 130150Z, 2024.

[4] Z. ZHANG, Z. YOU, D. CHU "*Fundamentals of phase-only liquid crystal on silicon (LCOS) devices*". Light Sci.Amp. Appl. 3, e213, 2014.

[5] Francisco J. MARTÍNEZ, Andrés MÁRQUEZ, Sergi GALLEGO, Manuel ORTUÑO, Jorge FRANCÉS, Augusto BELÉNDEZ, Inmaculada PASCUAL "*Electrical dependencias of optical modulation capabilities in digitally addressed parallel aligned liquid crystal on silicon devices*". Optical Engineering 53(6), 067104, 2014.

Fabrication and characterization of photoaligned MR-based liquid crystal cells

Adrián Moya [(1*)], Eva M. Calzado [(1,2)], Emilio J. Mena[(1,2)], Guillem Najar[(1,2)], Andrés Márquez[(1,2)] Augusto Beléndez[(1,2)] and Inmaculada Pascual[(1,3)]

1. I.U. Física Apl. A las Ciencias y las Tecnologías, Univ. Alicante, P.O.Box 99, E-03080, Alicante, Spain
2. Dept. de Física, Ing. De Sistemas y T. Señal, Univ. Alicante, P.O.Box 99, E-03080, Alicante, Spain
3. Dept. de Óptica, Farmacología y Anatomía, Univ. Alicante, P.O.Box 99, E-03080, Alicante, Spain

*Contact: Adrián Moya (adrian.moya@ua.es).

ABSTRACT:

In this work, liquid crystal cells with photoaligned substrates were fabricated and characterized using the commercial azo dye Methyl Red (MR) in combination with the commercial liquid crystal mixture E7. The main objective was to develop a device operating as a Liquid Crystal Variable Retarder (LCVR) and to investigate the influence of key parameters on its performance, including thickness, temperature and degree of polarization (DOP). These studies constitute a fundamental step towards our future research.

Key words: Liquid Crystal, Photoalignment, Methyl Red, LC Variable Retarder, Temperature, Thickness, Polarization

1.- Introduction

The study, design, and fabrication of optical elements based on photoaligned liquid crystals (LCs) is an area of considerable interest, given the flexibility these materials provide for diverse technological applications [1-3]. The thin alignment coatings that define the LC orientation are essential, as they directly influence both the optical performance of the device and the alignment control within the cell [4, 5]. By adjusting the orientation of the LC molecules, it is possible to manipulate the effective refractive index, a process that depends directly on the properties and configuration of the alignment layers. Moreover, liquid crystal devices can respond to applied electric fields, enabling the creation of adaptive and reconfigurable optical systems. Importantly, photoalignment techniques make it possible to generate spatial variations in the optical axis across the LC layer, a critical feature for the development of geometric-phase elements.

2.- Experimental Section

2.1.- Sample Preparation

The first step in the fabrication of the liquid crystal devices studied was the treatment of surfaces. In our case, ITO substrates were cleaned with acetone and an ultrasonic bath for 15 minutes was applied. After that, the substrates were dried in the oven for 20 minutes at about 120 ºC, and finally UV/03 treatment for 15 minutes was used.

Then, the cleaned ITO substrates were assembled using UV curing optical adhesives and silica spacers of three different sizes (5.5 µm, 10 µm and 25.6 µm) for controlling the thickness of the cell. Next, a mixture consisting of 99% LC E7 and 1% MR was introduced inside the cell by capillary action.

For this, it is important that the LC is in the isotropic phase, at 65 ºC approximately. Finally, the cell was sealed with the adhesive.

2.2.- Experimental Set-Up

Figure 1 shows the setup for measuring the cell thickness, which simply consists of passing a beam from a supercontinuum laser with the maximum spectral bandwidth ($\Delta\lambda$ = 500 nm) through the cell and collecting it with an optical fiber, which takes the light to the spectrophotometer, where the transmission spectrum can be analyzed.

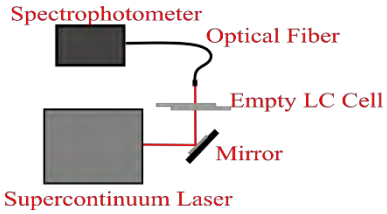

Fig. 1: Set-up used to measure the thickness of the empty cell.

The set-up used to perform the photoalignment is shown in Figure 2. First, the beam was expanded with a spatial filter, pass it through a linear polarizer and finally a spot of 1 cm diameter in the cell was illuminated with 532 nm linearly polarized light along the vertical of the laboratory.

As it can be seen, a heating plate is used to achieve the isotropic phase of the LC. It is necessary to be careful with the temperature because it is an important parameter as it will be discussed further in the results section. Another important parameter for the manufacturing of the devices are the power density and the exposure time, that also will be discussed in detail in the next section.

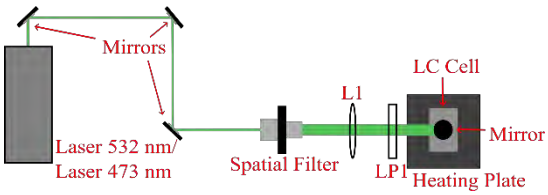

Fig. 2: Set-up used to perform the photoalignment in MR-based cells.

Finally, the set-up used to characterize the quality of the devices manufactured is shown in Figure 3. The devices were illuminated with linearly polarized light at 45º and a polarimeter was used to measure the azimuth and the degree of polarization (DOP) of the output beam.

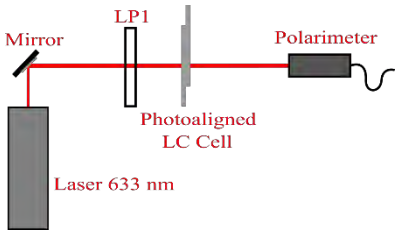

Fig. 3: Set-up used to characterize the devices fabricated.

3.- Results

3.1.- Thickness Measurements

First, despite knowing the size of the spacers and therefore the thickness of the cell using the set-up described in Figure 1, it is important to check exactly how thick they are, as this directly affects the retardance introduced by the liquid crystal device.

When the empty liquid crystal cell is illuminated with coherent light, multiple reflections/transmissions occur at the air-glass interfaces within the cell. In addition, the beam, when enters parallel to the cell, all reflections and transmissions are parallel, allowing a superposition of several beam interferences to happen, i.e. showing the well-known spectral ondulations given by Fabry-Pérot effects. By measuring the transmitted light using the set-up shown in Figure 1, transmission spectra were obtained (Figure 4), where the distance between "peaks" provides us information regarding the thickness of the cell.

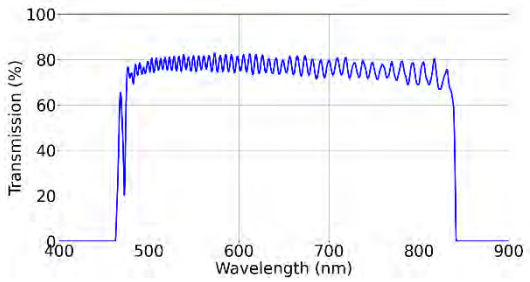

Fig. 4: Transmission spectrum of an empty cell of 25.5 μm thickness.

With Eq. (1) it is possible to calculate approximately the thickness of the cell where

d is the thickness, λ_1 and λ_2 are the wavelengths of two peaks and N is the number of peaks between both λ's.

$$d = \frac{\lambda_1 \lambda_2 N}{2(\lambda_2 - \lambda_1)} \qquad (1)$$

In Table 1, we can see that the thicknesses of the manufactured devices are pretty similar to the theoretical ones

Table 1: Experimental thickness by the spectrophotometer which is the average value of 4 measures of the cell for each spacer.

Theoretical Thickness (µm)	***Experimental Thickness (µm)***
5.5	*7.2*
10.0	*10.7*
25.6	*26.2*

3.2.- Temperature Measurements

As it has been explained in Section 2.2, it is necessary to heat the cell to the isotropic state of the liquid crystal, in this way, the E7 behaves as a liquid and loses its birefringence, which makes it possible to photoalign this kind of devices.

However, there is a temperature above which the liquid crystal oxidizes, turning yellowish in color and greatly reducing the clearing point. In an inert atmosphere, this oxidation temperature is around 160 ºC, but in the presence of oxygen, the material begins to oxidize very slowly from 60 ºC. In addition, it also depends on the incident light and the surface of the substrate. This makes it difficult to estimate when the material oxidizes and is therefore no longer usable. The higher the temperature, the faster the oxidation process.

Therefore, it is of great importance to have a good control of the sample temperature. On the one hand, the heating plate heats the sample to 65 ºC, but light is also incident, which is responsible for photoalignment. If a very high-power density is used, what happens is that the sample is also heated, which means that it is at a higher temperature than the expected 65 degrees.

Using an infrared thermometer, it is possible to measure the temperature of the sample at the same time as it is photoaligned.

Figure 5 shows the kind of temperatures that the LC can achieve under high energy beams. So, it is important to find an equilibrium between high density power and temperature of the photoaligned area.

Fig. 5: Temperature of the photoaligned area with a power density around 1 W/cm^2.

3.3.- Characterization of Devices

To evaluate the device quality, the degree of polarization (DOP) and azimuth were analyzed using the set-up described in Figure 3. The DOP quantifies the degree of polarized light, while the azimuth defines the orientation angle of the polarization state.

The azo dye molecules align perpendicularly to the polarization direction of the incident beam. Thus, if linearly polarized light is incident along the vertical axis during photoalignment, the molecules should align along the horizontal. Assuming proper photoalignment and liquid crystal director alignment, an incident beam polarized at 45° should produce a response characteristic of an LCVR. This would allow voltage application to modulate the device's retardance, generating various output polarization states, including linear, elliptical, and circular. In our case, the 633 nm input beam is 100% linearly

polarized with a 45° azimuth. Ideally, the output should exhibit different polarization states while maintaining the same DOP and azimuth.

As mentioned at the beginning, devices with three types of thicknesses have been fabricated and characterized: 5.5 µm, 10.0 µm and 25.6 µm. It is interesting to be able to operate several thicknesses, because the range of the retardance that the device can apply to the light depends on the thickness.

In Figures 6, 7 and 8 and Tables 2, 3 and 4, the results obtained by the characterization are shown.

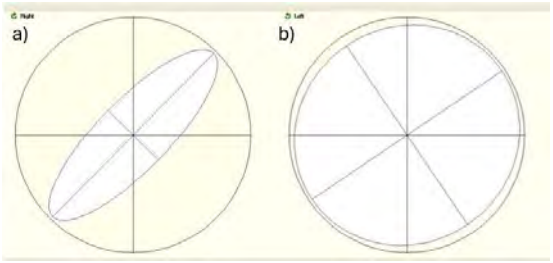

Fig. 6: Polarization states of E7 cell with MR photoaligned layer with a thickness of 5.5 µm for a) 0 V and b) 5.0 V.

Table 2: Characterized parameters of 5.5 µm MR cell.

Voltage (V)	***DOP (%)***	***Azimuth (º)***
0	*98.0*	*45.5*
5.0	*98.9*	*34.1*

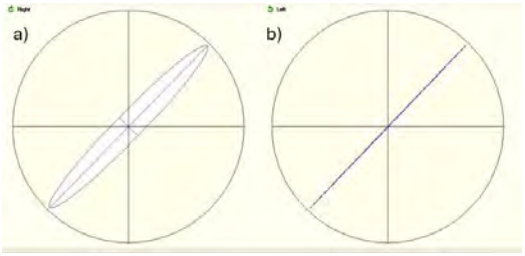

Fig. 7: Polarization states of E7 cell with MR photoaligned layer with a thickness of 10.0 µm for a) 0 V and b) 1.5 V.

Table 3: Characterized parameters of 10.0 µm MR cell.

Voltage (V)	***DOP (%)***	***Azimuth (º)***
0	*99.6*	*45.6*
1.5	*96.9*	*46.1*

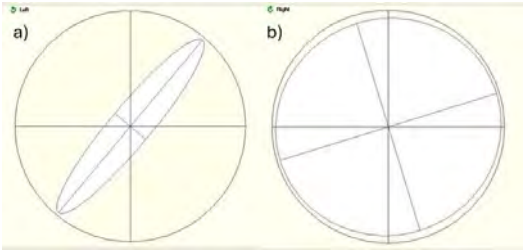

Fig. 8: Polarization states of E7 cell with MR photoaligned layer with a thickness of 25.6 µm for a) 0 V and b) 7.0 V.

Table 4: Characterized parameters of 25.6 µm MR cell.

Voltage (V)	***DOP (%)***	***Azimuth (º)***
0	*56.2*	*50.0*
7.0	*87.8*	*17.1*

Tables 2, 3 and 4 show that the devices of thickness 5.5 and 10.0 µm behave really well, with nearly 100 % DOPs and azimuths around 45º. In addition, good defined linear, circular and elliptical states were obtained. However, with 25.6 µm, the DOP is low, specially with low voltages, and the azimuth behavior is more irregular.

Finally, the photoalignment is a process that depends on many external parameters like the humidity, the illumination and the temperature, and other internal ones like the power density and time. This makes the photoalignment process very complicated to optimize.

Two of the main parameters that most affect photoalignment and are easier to control are the power density and the exposure time of the sample to light. In Table 5, it can be seen the parameters for the best devices (one for each

thickness) we have managed to create until now. It is important to notice that these values are not unique, and the same result can be obtained combining these two parameters.

Table 5: Power density and time required for an effective photoalignment.

Thickness (µm)	***Power Density (mW/cm²)***	***Time (minutes)***
5.5	*137*	*180*
10.0	*101*	*90*
25.6	*63*	*165*

4.- Conclusion

The methodology for the fabrication and characterization of LCVRs devices based on the photoalignment technique has been shown. In general, satisfactory results have been obtained both in cell thickness and in DOP and azimuth, especially for small cell thicknesses.

Acknowledgements: *This work was supported by the Ministerio de Ciencia, Innovación y Universidades/AEI (Spain), cofunded by ERDF/EU (PID2021-123124OB-I00, PID2023-148881OB-I00).*

References

[1] Xiaochuan Xi, Cenqui Yan, Larry Zhongxin Shen, Yinghan Wang and Pei Cheng, "Liquid crystal photoalignment technique: Basics, developments and flexible/stretchable devices applications", Materials Today Electronics, 6, 100069, 2023.

[2] Oleg Yaroshchuk and Yuriy Reznikov, "Photoalignment of liquid crystals: basics and current trends", Journal of Materials Chemistry 22, 286-300, 2012.

[3] Vladimir Chigrinov, Hoi Sing Kwok, Hirokazu Takada and Haruyoshi Takatsu, "Photo-aligning by azo-dyes: Physics and applications", Liquid Crystals Today 14, 1-15, 2005.

[4] Chia-Yi Huang, Yi-Ru Lin, Kuang-Yao Lo and Chia-Rong Lee, "Dynamics of photoalignment in azo-dye-doped liquid crystals", Applied Physics Letters, 93, 181114, 2008.

[5] Cheg-Kai Liu, Shao-Hao Liao, Chi-Tang Huang and Ko-Ting Cheng, "Fabrication of azimuthally/radially symmetric liquid crystal plates using- two-step photoalignments", Optics Express 31, 21962 (2023).

Effects of addition of terminal emitter on device performance in hyperfluorescent OLEDs

Thomas SAYNER(1), Arvydas Ruseckas(1), Ifor D. W. Samuel(1)

1. Organic Semiconductor Centre, SUPA, School of Physics and Astronomy, University of St. Andrews, St. Andrews, Fife KY16 9SS, U.K.

Contact: Thomas SAYNER (ts234@st-andrews.ac.uk).

ABSTRACT:

Hyperfluorescent OLEDs have gained a lot of attention in the past few years as a potential pathway to efficient OLEDs with narrow pure emission.[1–5] However, the efficiency roll-off of devices at higher luminance remains a persistent problem and the connections between photophysical characteristics and device performance are not fully understood.[6,7] In order to better understand these OLEDs we have investigated the photophysical and device characteristics of the hyperfluorescent blend 1%TBRb:15%4CzIPN:mCP.

Key words: Hyperfluorescence, OLEDs, photophysics, efficiency roll-off, time resolved photoluminescence.

1.- Introduction

OLEDs are now a leading display technology, due to their use in high contrast, thin and flexible displays made from cheap, non-toxic materials.[8,9] These devices operate by injecting charges into an emission layer where they combine to form excitons that then radiatively decay. Due to the spin statistics of the injected charges however, only 25% of excitons (singlets) are able to radiatively decay in conventional fluorescent emitters. This significantly limits the maximum possible efficiency to 25%, and the remaining long lived “triplet” excitons reduce the efficiency even further via annihilation interactions. The development of phosphorescent emitters overcame this issue by utilizing strong spin orbit coupling to harvest triplets and these are now widely used in modern display technology for red and green pixels.[10,11] Unfortunately, these emitters rely on the use of heavy metals in order to achieve the strong spin-orbit coupling, and the success of the red and green OLEDs could not be replicated in the blue due to the higher exciton energies greatly affecting the material stability.[3] Blue industry OLEDs therefore still use the inefficient but stable fluorescent emitters so significant attention has been focused on finding alternative methods of triplet harvesting. One such method, known as thermally assisted delayed fluorescence (FRET) can utilize the non-radiative triplet population via reverse intersystem crossing (RISC).[12,13] This leads to the characteristic feature of TADF materials which is that they have two distinct emission lifetimes. A shorter (prompt) lifetime from the initial singlet population and a longer (delayed) lifetime from the singlets produced by the RISC process. Unfortunately, TADF emitters often exhibit broad emission and suffer from reduced external quantum efficiency (EQE) at higher driving currents. This phenomenon, which also affects phosphorescent OLEDs, is known as efficiency roll-off.[14–18] It is often attributed to annihilation interactions from the higher density of singlets, triplets and polarons present within the device at the higher driving currents. Thus, long-lived triplet states need to be harvested efficiently in order to minimize annihilation

interactions. A further development upon the TADF mechanism is hyperfluorescence. In hyperfluorescent (HF) OLEDs, an emitter with an optimal spectrum but poor ability to utilize its triplets can be paired with a TADF material that is optimized for triplet harvesting.[1,4,5,19] These are respectively referred to as the terminal emitter and sensitizer. In this work we compare how the photophysics and device performance of a TADF device using the material 4CzIPN changes when the fluorescent terminal emitter TBRb is added.

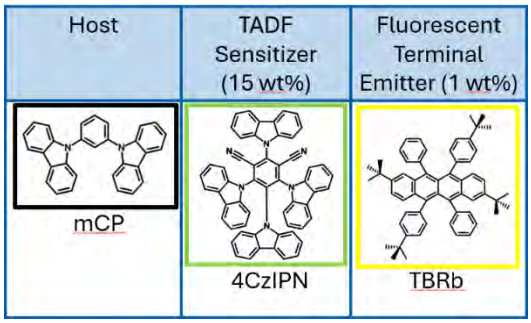

Fig. 1: Materials studied. Host mCP, TADF emitter/sensitizer 4CzIPN, fluorescent terminal emitter TBRb.

2.- Results and discussion

The materials used in this study (Fig.1) are host 1,3-Bis(N-carbazolyl)benzene (**mCP**), TADF emitter/sensitizer 1,2,3,5-tetrakis(carbazol-9-yl)-4,6-dicyanobenzene, 2,4,5,6-tetrakis(9H-carbazol-9-yl) isophthalonitrile (**4CzIPN**), and fluorescent terminal emitter 2,8-Di-*tert*-butyl-5,11-bis(4-*tert*-butylphenyl)-6,12-diphenyltetracene (**TBRb**). Thin films and devices of 15%4CzIPN:mCP and 1%TBRb:15%4CzIPN:mCP were thermally evaporated in a vacuum chamber. These will respectively be referred to as **TADF** and **HF-TBRb.** A fluorescent thin film of 1%TBRb:mCP (**F-TBRb**) was also fabricated. 50 nm thick films were deposited on fused silica substrates, and devices were made with the structure ITO/HATCN (5 nm)/TAPC (40 nm)/mCP (10 nm)/active layer (20 nm)/TmPyPB (50 nm)/LiF/Al (50nm).

2.1.- Devices

Device characterization (Table. 1 Fig.2) shows that maximum EQE drops significantly upon the addition of TBRb from 25.5% in the TADF OLED to 14.8% in the HF-TBRb.

Table 1: Table of PLQY for TADF, hyperfluorescent (HF-TBRb), and fluorescent (F-TBRb) films. Max EQE and J_{90} (efficiency roll-off) for the TADF and hyperfluorescent devices.

Film	PLQY (%)	Max EQE (%)	J_{90} (mA/cm^2)
TADF	60	25.5	2.0
HF-TBRb	59	14.8	1.44
F-TBRb	57	-	-

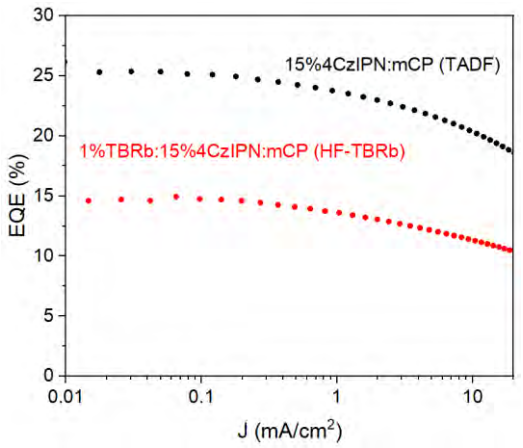

Fig. 2: External quantum efficiency vs driving current J of TADF and HF-TBRb OLEDs.

This is still better performance than a fluorescent TBRb OLED which typically have EQE <5%, but it is clear that there has been significant max EQE loss.[1] Also observed is that the reduction in EQE at higher current density (efficiency roll-off) is largely unchanged. The roll-off is characterized by the current density at which the EQE drops to 90% of its maximum (J_{90}).[20] The two devices have similar J_{90} values of 2 mAcm^{-2} and 1.44 mAcm^{-2} for the TADF and HF-TBRb devices respectively. This suggests that the ability of the 4CzIPN to manage the triplet population at higher driving currents is largely unaffected by the addition of TBRb, and that whatever loss

mechanisms have been introduced are not dependent on the driving current.

2.2.- Photophysics

Photophysical measurements on films with the same composition as the emission layers of the devices were performed to investigate potential causes of this loss. Steady state Photoluminescence (PL) and Electroluminescence (EL) (Fig.3a,b) show that most of the emission comes from the TBRb, with a small contribution from the 4CzIPN. This evidences that there is not complete sensitization of the TBRb and inefficient Förster Resonance Energy Transfer (FRET).

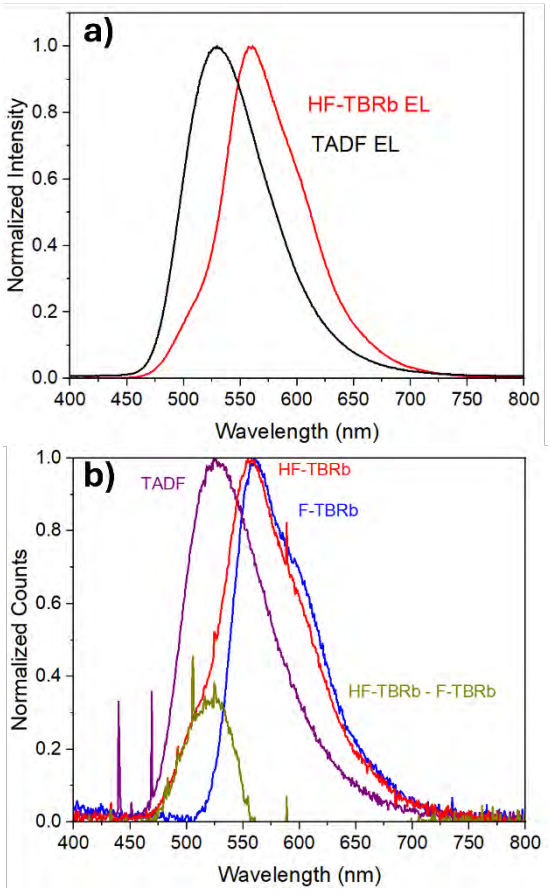

Fig. 3: Steady state device electroluminescence (a) and film photoluminescence (b).

The photoluminescence quantum yield PLQY is similar across the F-TBRb, TADF and HF-TBRb films at 58%±1%, which obscures how PLQY is affected by the addition of the terminal emitter. However, it is clear that the PLQY values do not correlate with the EQE drop from 26% to 15%. It has previously been suggested that the EQE drop is due to CT state formation between TBRb and the host, leading to singlet to triplet conversion on the TBRb molecules.[18] We would expect this to cause a corresponding drop in the PLQY and the lack of such a drop suggests that other factors are the cause of EQE loss.

Time correlated single photon counting (TCSPC) measurements were also performed on the films in order to gain insight into how the PL decay changes with the addition of the TBRb (Fig.4a,b). On the short prompt lifetime of the decay, the 4CzIPN emission (measured at 520 nm) is faster after the addition of the TBRb. This faster emission is due to the FRET from the 4CzIPN to the TBRb as excitons that do not emit very quickly will transfer instead.

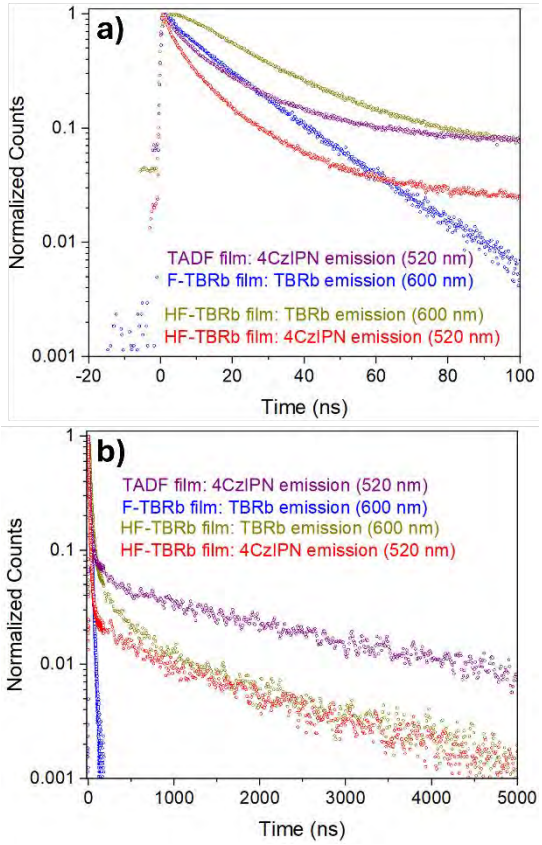

Fig. 4: Prompt (a) and delayed (b) PL decays of the F-TBRb, TADF, and HF-TBRb films, with 4CzIPN emission detected at 520 nm, and TBRb emission at 600 nm.

This is confirmed by a rise component at the start of the TBRb decay (measured at 600 nm). Furthermore, the overall TBRb lifetime increased from approximately 19 ns to 25 ns due to the delay from the FRET. Meanwhile in the delayed regime, the 4CzIPN decay is again quenched and has a lower amplitude. The lower amplitude is likely due to the FRET outcompeting intersystem crossing (ISC) so there is a smaller contribution to the emission from the ISC RISC cycle. The delayed emission of the TBRb closely follows the 4CzIPN because TBRb has no delayed emission of its own, so this decay is entirely controlled by the delayed processes on the 4CzIPN. Despite these insights, the connections between the photophysics and device performance remain unclear. Photophysics results suggest that the hyperfluorescence device should be just as efficient as the TADF. It is possible that Dexter energy transfer (DET) plays a role in transferring triplets from the 4CzIPN to the TBRb in devices, however the rates of this process cannot be accessed optically in photoluminescence measurements of films.[6]

4.- Conclusion

The links between the difference in device performance of hyperfluorescent OLEDs and their photophysical characteristics is unclear. PLQY and photoluminescence decays suggest that both the hyperfluorescent and TADF devices studied in this work should have similar performance and do not explain the large EQE drop. Therefore, the reasons for the differing performance may not be in the emission mechanism, but in charge related processes such as charge trapping on the TBRb. Further research would be to attempt to model the hyperfluorescence PL decay in order to better understand how the photophysical processes interact, and also to investigate how charges interact in hyperfluorescent OLEDs vs TADF OLEDs.

Acknowledgements: The authors are grateful to the Engineering and Physical Sciences Research Council of the UK for financial support through grants ER/R035164/1 and EP/W524505/1.

References

[1] Nakanotani, H., Higuchi, T., Furukawa, T., Masui, K., Morimoto, K., Numata, M., *et al.* High-efficiency organic light-emitting diodes with fluorescent emitters. *Nat. Commun.* **5**, 4016 (2014).

[2] Chan, C.-Y., Tanaka, M., Lee, Y.-T., Wong, Y.-W., Nakanotani, H., Hatakeyama, T., *et al.* Stable pure-blue hyperfluorescence organic light-emitting diodes with high-efficiency and narrow emission. *Nat. Photonics* **15**, 203–207 (2021).

[3] Monkman, A. Why Do We Still Need a Stable Long Lifetime Deep Blue OLED Emitter? *ACS Appl. Mater. Interfaces* **14**, 20463–20467 (2022).

[4] Baldo, M. A., Thompson, M. E. & Forrest, S. R. High-efficiency fluorescent organic light-emitting devices using a phosphorescent sensitizer. *Nature* **403**, 750–753 (2000).

[5] Samuel, I. D. W. & Beeby, A. Sidestepping the selection rules. *Nature* **403**, 710–711 (2000).

[6] Haase, N., Danos, A., Pflumm, C., Stachelek, P., Brütting, W. & Monkman, A. P. Are the rates of dexter transfer in TADF hyperfluorescence systems optically accessible? *Mater. Horiz.* **8**, 1805–1815 (2021).

[7] Cho, E., Hong, M., Yang, Y. S., Cho, Y. J., Coropceanu, V. & Brédas, J.-L. Energy transfer processes in hyperfluorescent organic light-emitting diodes. *J. Mater. Chem. C* **10**, 4629–4636 (2022).

[8] Hong, G., Gan, X., Leonhardt, C., Zhang, Z., Seibert, J., Busch, J. M., *et al.* A Brief History of OLEDs—Emitter Development and Industry Milestones. *Adv. Mater.* **33**, 2005630 (2021).

[9] Tsuboi, T. 1 - Brief history of OLEDs and TADF materials for OLEDs. in *Thermally Activated Delayed Fluorescence Organic Light-Emitting Diodes (TADF-OLEDs)* (ed. Duan, L.) 1–69 (Woodhead Publishing, 2022). doi:10.1016/B978-0-12-819810-0.00002-8.

[10] Baldo, M. A., O'Brien, D. F., You, Y., Shoustikov, A., Sibley, S., Thompson, M. E., *et al.* Highly efficient phosphorescent emission from organic electroluminescent devices. *Nature* **395**, 151–154 (1998).

[11] Baldo, M. A., Lamansky, S., Burrows, P. E., Thompson, M. E. & Forrest, S. R. Very high-efficiency green organic light-emitting devices based on electrophosphorescence. *Appl. Phys. Lett.* **75**, 4–6 (1999).

[12] Endo, A., Sato, K., Yoshimura, K., Kai, T., Kawada, A., Miyazaki, H., *et al.* Efficient up-conversion of triplet excitons into a singlet state and its application for organic light emitting diodes. *Appl. Phys. Lett.* **98**, 083302 (2011).

[13] Goushi, K. & Adachi, C. Efficient organic light-emitting diodes through up-conversion from triplet to singlet excited states of exciplexes. *Appl. Phys. Lett.* **101**, 023306 (2012).

[14] Ligthart, A., de Vries, X., Zhang, L., Pols, M. C. W. M., Bobbert, P. A., van Eersel, H., *et al.* Effect of Triplet Confinement on Triplet–Triplet Annihilation in Organic Phosphorescent Host–Guest Systems. *Adv. Funct. Mater.* **28**, 1804618 (2018).

[15] Coehoorn, R., van Eersel, H., Bobbert, P. & Janssen, R. Kinetic Monte Carlo Study of the Sensitivity of OLED Efficiency and Lifetime to Materials Parameters. *Adv. Funct. Mater.* **25**, 2024–2037 (2015).

[16] Masui, K., Nakanotani, H. & Adachi, C. Analysis of exciton annihilation in high-efficiency sky-blue organic light-emitting diodes with thermally activated delayed fluorescence. *Org. Electron.* **14**, 2721–2726 (2013).

[17] Hasan, M., Saggar, S., Shukla, A., Bencheikh, F., Sobus, J., McGregor, S. K. M., *et al.* Probing polaron-induced exciton quenching in TADF based organic light-emitting diodes. *Nat. Commun.* **13**, 254 (2022).

[18] Gottardi, S., Barbry, M., Coehoorn, R. & van Eersel, H. Efficiency loss processes in hyperfluorescent OLEDs: A kinetic Monte Carlo study. *Appl. Phys. Lett.* **114**, 073301 (2019).

[19] Stavrou, K., Franca, L. G., Danos, A. & Monkman, A. P. Key requirements for ultraefficient sensitization in hyperfluorescence organic light-emitting diodes. *Nat. Photonics* (2024) doi:10.1038/s41566-024-01395-1.

[20] Diesing, S., Zhang, L., Zysman-Colman, E. & Samuel, I. D. W. A figure of merit for efficiency roll-off in TADF-based organic LEDs. *Nature* **627**, 747–753 (2024).

Optical generation, measurement and tuning of optomechanical spheroidal resonances in a silica microsphere

Juan JULIAN-BARRIEL[(1)], Martina DELGADO-PINAR[(1,2)], Antonio DÍEZ[(1,2)], Miguel V. ANDRÉS[(1,2)]

1. Laboratory of Fiber Optics, ICMUV, Universitat de València, Dr. Moliner 50, 46100, Burjassot, Spain.
2. Departamento de Física Aplicada y Electromagnetismo, Universitat de València, Dr. Moliner 50, 46100, Burjassot, Spain.

Contact: Juan JULIAN-BARRIEL (juan.julian@uv.es)

ABSTRACT:

In this work we present an experimental characterization of the spheroidal acoustic mode resonances of a silica microsphere, and its frequency tuning. Excitation, detection and tuning of the acoustic resonances are carried out optically, using pump and probe signals. The experimental results show the excitations and detection of up to 34 harmonics of the spheroidal modes in the range of 11 MHZ to 500 MHz. These results are compared with a theoretical model that includes the interaction of the acoustic fields with the pump and probe optical fields. Finally, a technique for fine tuning the frequency of the acoustic modes by optical means is demonstrated. For the R_{12} acoustic mode whose resonance frequency and linewidth are 248,98 ± 0,02 MHz and 32 ± 5 kHZ, respectively, a tuning range of up to 4.84 MHz is demonstrated.

Key words: Optomechanics, optical fibers, microresonators, microsphere, WGM, acoustics, FSBS.

1.- Introduction

Dielectric microspheres, along with other resonators as microbubbles, microtoroids or microcylinders, are known to be high-quality optical resonators. In them, it is possible to excite optical azimuthal resonances, also known as whispering-gallery mode (WGM) resonances, usually employing an auxiliary tapered fiber. These microresonators also support a huge variety of mechanical modes, some of them consist in surface oscillations (as wineglass acoustic modes), others in a resonance of the whole structure (transversal acoustic modes in optical fibers, for instance).

The interaction between optical and mechanical resonances in the listed resonators is of high interest in the field of optomechanics. It is employed in different applications as phonon lasers [1] or sensing [2], beyond its interest in fundamental applied physics.

In this work, we excited and measured the spheroidal acoustic modes of a silica microsphere. Both excitation and detection of these modes is carried out by exploiting different optomechanical effects. The modes are excited by Forward Stimulated Brillouin Scattering (FSBS) [3], thanks to the electrostriction produced by an intense optical pulse, from now, the pump laser. On the other hand, the detection is made measuring the intensity fluctuations of a probe laser tuned to the edge of one WGM of the microsphere after the pass-through of the pulse.

Finally, we have also investigated the possibility of tuning the resonance spectrum

of the microsphere through temperature by optical means. For this purpose, we have used an Er/Yb doped fiber, highly absorbing at 980 nm, and a continuous laser at that wavelength. The absorption of the optical radiation is a way to control the temperature rise of the sphere [4], and thus tune the spectrum of acoustic modes.

2.- Theory

In this section we explain the fundamentals behind the experiments performed in this work. We will describe what are the spheroidal resonances, how is possible to optically excite them and how to measure them with WGM.

2.1.- Spheroidal acoustic modes

An elastic sphere can support many families of acoustic modes. Most of them are a combination of radial and torsional movements, but there is a family of modes that only have oscillation in the radial direction. These are the called spheroidal modes, and they consist of a radial oscillation of the whole volume of the sphere [5]. The displacement field of spheroidal modes contains only the radial component that depends only on the radial coordinate. For example, the fundamental mode (R_1) of this family is a dilation and contraction movement of the whole sphere, like a heart-beat. In the R_2 mode the movement splits in two spherical shells: the inner shell expands while the outer shell contracts and vice versa. In this case, between shells there is a node with null motion. The generalization of the movement for higher harmonics is straightforward. This is represented in Fig. 1.

In order to find the acoustic fields and resonant frequencies of these modes one must solve the acoustic wave equation in a sphere:

$$\rho\{V_L^2\nabla\cdot(\nabla\cdot\mathbf{U}) - V_S^2\nabla\times(\nabla\times\mathbf{U}) - \frac{\partial^2\mathbf{U}}{\partial t^2}\} = 0 \qquad (1)$$

where $\mathbf{U}$ is the acoustic field and V_L, V_S the acoustic longitudinal and shear velocity of silica. Considering harmonic fields with frequency Ω and applying the corresponding boundary conditions, the solution for each mode of order n is found. The displacement acoustic field in spherical coordinates for the spheroidal modes is:

$$\mathbf{U_n}(r,t) = B_n\cdot\nabla j_0(k_n r)e^{i\Omega_n t} \qquad (2)$$

where r is the radial coordinate, B_n is the mode amplitude, j_0 is the spherical zero-th order Bessel function of first kind, and Ω_n and $k_n = \Omega_n/V_L$ are, respectively, the resonance frequency and wavevector of the n-th order acoustic mode. The characteristic equation fulfilled by spheroidal acoustic modes, from which the values of k_n are found, is given by [5]:

$$\tan(k\cdot a) = \frac{k\cdot a}{1-\frac{(k\cdot a)^2}{4\cdot\alpha^2}} \qquad (3)$$

where a is the sphere radius and $\alpha = V_S/V_L$.

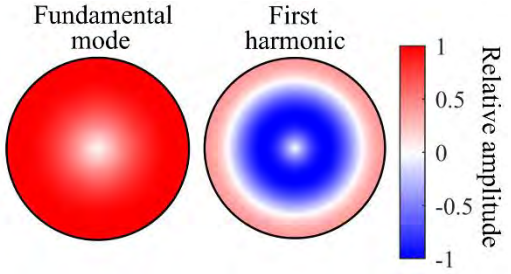

Fig. 1: Transversal profile of the radial acoustic field of the fundamental and first harmonic of the spheroidal modes.

2.2.- Optical excitation of acoustic modes

In our experiment the acoustic resonances are stimulated by the electrostrictive force, $\mathbf{F}_{es}$ (per volume unit), produced by a pump laser. As our pump laser emits optical pulses, we must consider its spectral components. Therefore, we will calculate the spectral electrostrictive force $\tilde{\mathbf{F}}_{es}(\Omega)$. Normalizing the acoustic fields, and adding the electrostrictive force and a damping term in Eq. (1), is possible to find the amplitude B_n and spectral amplitude $\tilde{B}_n(\Omega)$ of each mode [3]:

$$\tilde{B}_n(\Omega) = \frac{\int_{\mathbb{R}^3}\mathbf{u}_n^*(r)\cdot\tilde{\mathbf{F}}_{es}(\Omega_n)dV}{\rho(-\Omega^2+i\Omega\Gamma_n+\Omega_n^2)} \qquad (4)$$

where $\mathbf{u}_n(r)$ is the normalized acoustic field.

2.3.- Optical detection by means of WGMs

Spheroidal modes were probed by an optical WGM propagating along the equator of the microsphere, which was excited by evanescent coupling using a thin tapered fiber. As in other geometries, spherical WGMs are divided in two families according to the polarization of fields. Control of the light beam polarization allows the excitation of TE_r modes, whose electric field is transverse to the radial direction, and TM_r modes, in which case it is the magnetic field that is transverse.

There are two mechanisms by which acoustic modes can affect the WGM: photoelasticity and the geometric perturbation of the sphere radius. Photoelasticity is the perturbation produced in the dielectric tensor by the strain ($\bar{S}$) generated by the acoustic field. The change in the relative dielectric tensor ($\Delta\bar{\varepsilon}$) is:

$$\Delta\varepsilon_{ij} = -{n_0}^4 \sum_{k,l} p_{ijkl} S_{kl} \qquad (5)$$

being p_{ijkl} the photoelastic coefficients and n_0 the refractive index. The effect of the acoustic modes on WGMs is quantified by the shift they produce in their resonant wavelength caused by the change in the refractive index. This can be calculated, for each acoustic mode, using [6]:

$$\frac{\Delta\lambda_{PH,n}}{\lambda_0} \approx \frac{\varepsilon_0 \int_V \mathbf{E}^* \cdot \Delta\bar{\varepsilon}_n \cdot \mathbf{E}\, dV}{\int_V (\varepsilon_0 \varepsilon \mathbf{E}^* \cdot \mathbf{E} + \mu_0 \mathbf{H}^* \cdot \mathbf{H}) dV} \qquad (6)$$

where **E** and **H** are the electric and magnetic field of the WGM. The geometric contribution relates to the change in the fiber radius caused by the acoustic oscillation. To a first order approximation, the relative WGM wavelength shift is given by the relative radius change, which can be related with the acoustic displacement,

$$\frac{\Delta\lambda_{GE,n}}{\lambda_0} = \frac{\Delta a}{a} = \frac{U_{r,n}(a,t)}{a} \qquad (7)$$

being $U_{r,n}$ the radial component of the acoustic field of the mode.

Finally, is possible to estimate the relative wavelength shift of the WGM wavelength if (6) and (7) are calculated using the normalized acoustic field $\mathbf{u}_n(r)$:

$$\frac{\Delta\tilde{\lambda}(\Omega)_n}{\lambda_0} = \tilde{B}_n(\Omega)\left[\frac{\Delta\lambda_{PH,n}}{\lambda_0} + \frac{\Delta\lambda_{GE,n}}{\lambda_0}\right] \qquad (8)$$

With this expression, it is possible to simulate the spectral response of the probe laser and its temporal dependance by addition of each mode contribution and performing a Fourier transform. An example of this is shown in Fig. 2.

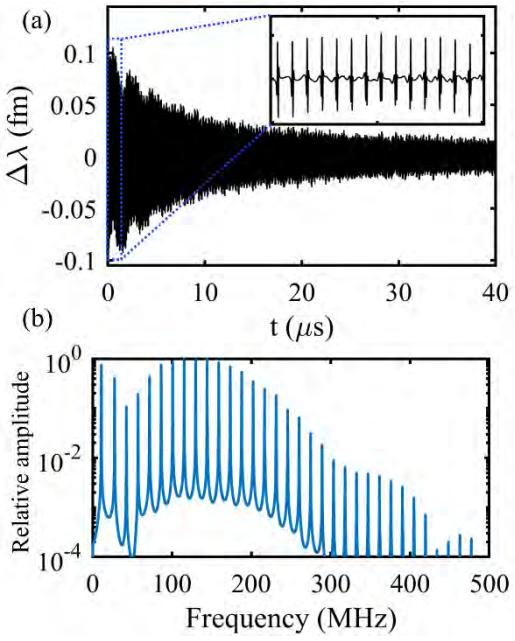

Fig. 2: (a) Simulation of the WGM resonant wavelength perturbation after a pump pulse with an inset of the first μs of the trace. (b) Theoretical amplitude spectrum of the spheroidal modes, normalized to the maximum value. Simulation parameters: $a = 205{,}8$ μm, $\lambda_{WGM} = 1549{,}49$ nm, *WGM azimuthal order:* 1140, *WGM radial order:* 3, $P_{peak} = 6$ kW.

3.- Experiment

3.1.- Experimental setup

The experimental setup is shown in Fig. 3. Our probe laser is a NKT Koheras tunable laser at 1550 nm with 100 Hz linewidth. This signal is launched into a fiber polarization controller to select the WGM family. In order to couple the probe beam into the microsphere we employ a 3 μm waist tapered fiber fabricated at our facilities. The transmitted signal of the WGM is sent into a 90/10 fiber coupler. The 10% signal is employed to monitor the WGM spectrum and to tune the probe laser to its edge. The 90% arm is

delivered to a 1 GHz photodetector connected to a 1 GHz oscilloscope, where the intensity fluctuations of the probe are measured.

The pump signal for exciting the mechanical modes is a diode pulsed laser emitting at 1064 nm (DC power of 100 mW, 20 kHz repetition rate and 700 ps timewidth). The pulses are sent to a 99/1 fiber coupler, being the 1% signal employed as a trigger to the oscilloscope and the 99% left to excite the mechanical modes.

In the tuning experiment, a second pump laser is employed to change the temperature of the resonator. This laser is a continuous wave laser at 980 nm with a maximum output power of 400 mW. Both pump signals are delivered to the sphere by a 1064/980 WDM.

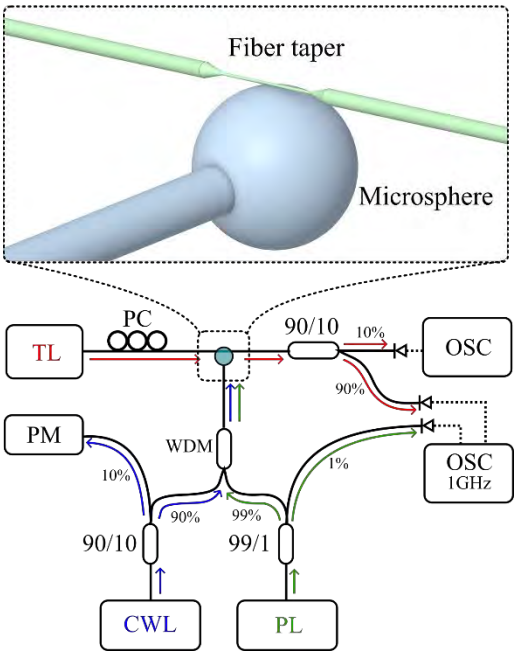

Fig. 3: Experimental setup. TL: tunable laser, PL: pulsed laser, CWL: continuous laser, PM: power-meter, OSC: oscilloscope, PC: polarization controller, WDM: wavelength division multiplexer.

3.2.- Characterization of spheroidal resonances in silica microspheres

In the first experiment, the spheroidal modes of a silica microsphere were excited and characterized. The sphere was fabricated at the tip of a SMF-28 fiber by surface tension, using the electrical arc of a commercial fiber splicer. Using the setup shown in Fig. 3 the transmittance of the system was recorded. Knowing the linewidth and visibility of the WGM ($\Delta\lambda_{3dB} = 0{,}89$ fm, $V = 0{,}85$) is possible to calculate the experimental resonant wavelength perturbation. Figure 4(a) shows the temporal trace obtained with a microsphere of $207{,}6 \pm 0{,}9$ µm radius. By performing the FFT, the experimental spectrum is calculated (Fig. 4(b)).

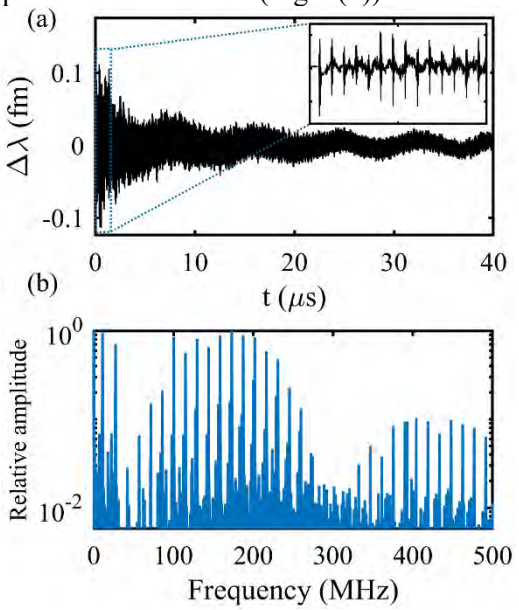

Fig.4: (a) Experimental resonant wavelength perturbation with an inset of the first micro-second of the trace. (b) Experimental frequency spectrum of spheroidal modes. Normalized to the maximum value.

The experimental spectrum shows a series of peaks, each one centered at a frequency that corresponds to resonant frequency of a spheroidal mode. Comparing Fig. 2 and Fig. 4 we find that the simulation and experimental results show a good agreement. Despite that, some differences are observed, especially in the spectrum. These differences may be due to several factors. On the one hand, the radial order of the WGM used in the experiment is unknown, which affects the shape of the spectrum. On the other hand, the theory does not take into account the effect of the fiber supporting the microsphere, which can affect the linewidth and amplitude of the resonances, and also can allow the excitation of resonant acoustic modes of another family, in addition to the spheroidal modes.

The experimental resonant frequencies are fitted to Eq. (3) leaving the sphere radius as a free parameter. The fitted radius is $205{,}8 \pm 0{,}4\ \mu m$, which has a good agreement with the direct measurement.

3.3.-Frequency tuning of resonances

In this second experiment the previous microsphere is replaced by a microsphere fabricated using the DF 1500 Er/Yb doped optical fiber. The increase in temperature [4] of the fiber under 980 nm pump absorption is exploited to heat the microsphere, and as a mechanism for optically tuning the acoustic mode resonances.

Fig. 5 shows the obtained results with a microsphere of $174{,}8 \pm 0{,}5$ µm radius. The peak corresponds to the 12th acoustic mode resonance.

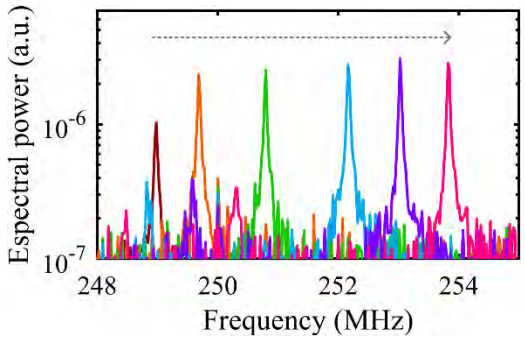

Fig. 5: Frequency spectrum of the 12th spheroidal mode for different pump values.

The relative frequency shift of all resonances is the same. In Fig. 6, the mean relative shift of all resonances as the pump increases is represented. Some saturation of the pumping effects can be observed, since the absorption is caused by the dopant ions [4]. The maximum relative shift is 1,93% which corresponds to a velocity change of 115 m/s and a temperature change of 191 ºC.

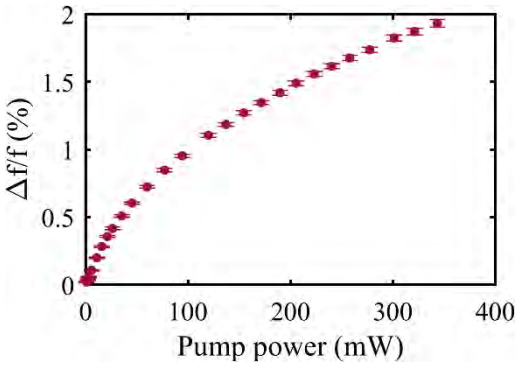

Fig. 6: Mean relative shift of the spheroidal modes as the 980 nm pump increases.

4.- Conclusions

In this work we present a comprehensive study of the spheroidal mechanical modes of a silica microsphere using a pump and probe scheme. We measured the radiofrequency spectrum of the generated spheroidal modes, finding up to 34 harmonics, with good signal to noise ratio.

In parallel, we developed a theoretical model to explain the experimental results, which takes in to account the interaction between acoustic and optical waves, both in the excitation and detection processes. Experiment and theory showed a good agreement.

In addition, we investigated a method for tuning the acoustic frequency spectrum, rising the sphere temperature with a second pump laser. We found that is possible to tune the frequency of modes several MHz, which could be useful for future optomechanical applications.

Acknowledgements: Authors thank to the funding agencies of the following grants: PID2023-146725OB-I00, CNS2023-145717, co-funded by AEI of Spain and EU by means of Fondo Europeo de Desarrollo Regional (FEDER) and "NextGenerationEU"/PRTR", CIPROM/2022/30 and CIACIF/2022/345 funded by the Generalitat Valenciana (Spain); and H2020-MSCA-RISE-2019-872049, funded by the European Union's Horizon 2020 research and innovation programme under the Marie Skłodowska-Curie grant agreement No 872049.

References

[1] Ivan S. GRUDININ, Hansuek LEE, Oskar PAINTER, Kerry J. VAHALA, *"Phonon Laser Action in a Tunable Two-Level System"* Physical Review Letters, 104, 083901, 2010.

[2] Luis A. SÁNCHEZ, Antonio DÍEZ, José L. CRUZ, Miguel V. ANDRÉS, *"Strain and temperature measurement discrimination with forward Brillouin scattering in optical fibers"*, Optics Express, 30, 9, 14384 – 14392, 2022.

[3] Avi ZADOK, Hilel H. DIAMANDI, Yosef LONDON, Gil BASHAN, *"Forward Brillouin Scattering in Standard Optical Fibers"* (Springer, 2022).

[4] Emmanuel RIVERA-PÉREZ, Irma L. VILLEGAS, Antonio DÍEZ, Miguel V. ANDRÉS, José L. CRUZ, Amparo RODRÍGUEZ-COBOS, *"Measurement of Pump-induces temperature Increase in Doped Fibers using Whispering-Gallery Modes"*, IEEE Photonics Technology Letters, 25, 24, 2498-2500, 2013.

[5] B. Alexander AULD, *"Acoustic waves and fields in solids"* (Krieger Publishing Company, 1990).

[6] David M. POZAR, *"Microwave Engineering, 4th Edition"* (Wiley, 2012).

Performance of gravity-compensated focus-tunable lens

Fátima CUÉLLAR, Elisabet PÉREZ-CABRÉ, Laura CLAVÉ, María Sagrario MILLÁN

Optics & Optometry Department, Applied Optics and Image Processing Group (GOAPI), Universitat Politècnica de Catalunya − BarcelonaTech (UPC), Violinista Vellsolà 37, 08222 Terrassa (Barcelona).

Contact: Elisabet PÉREZ-CABRÉ (elisabet.perez@upc.edu).

ABSTRACT:

An electrically controlled focus-tunable lens (FTL) allows for precise, continuous, and dynamic power adjustment over a range of diopters. While the FTLs are often positioned horizontally with a vertically aligned optical axis, certain applications require alternative orientations, which can introduce coma aberration due to gravitational effects on the optical fluid and elastic membrane of the device. This study examines the optical performance of a newly designed gravity-compensated FTL (Optotune EL-16-40-GTC-VIS-5D) by evaluating its addressed optical power and measured wavefront error, in both horizontal and vertical lens orientation. The results were compared to two standard, non-compensated models from the same manufacturer. All tested FTLs exhibited excellent optical power performance regardless of orientation, while the gravity-compensated model effectively corrected vertical coma when positioned upright.

Key words: Focus-tunable lens, wavefront analysis, aberrations, active optics, optoelectronic devices.

1.- Introduction

Electrically focus-tunable lenses (FTL) are becoming common components in optical setups, eliminating moving parts and reducing size, weight, response time and power consumption. Comprehensive reviews describe the working principles, advantages and limitations of various tunable lens technologies [1-3]. Among tunable lens technologies, electromagnetic-driven liquid lenses stand out due to their relatively larger apertures [3]. These lenses enclose an optical fluid within a sealed container with an elastic membrane. An electromagnetic actuator applies pressure to the container, altering the curvature of the lens. Optical power is controlled by adjusting the current through the actuator's coil.

Optotune Switzerland AG is a prominent industry supplier of this lens technology [4-5]. Since the initial model, Optotune has commercialized various lens versions, with manual or electronic controls, larger apertures and extended focal ranges. Beyond lens technology, experimental characterization and calibration are essential prerequisites enabling the use of a given component to its maximal capacity. In many applications, the FTL is oriented horizontally, with the optical axis vertical. However, certain applications may require alternative orientations. Thus, vertical coma aberration can arise when the lens is positioned upright (i.e., with the optical axis horizontal) due to the gravitational force effects on the optical fluid. Although the lenses might still offer sufficient optical quality for imaging, the issue of induced coma, already highlighted by various authors [6-11], can have a negative impact on the wavefront control, which can be critical for adaptive optics systems. For applications where vertical placement is essential, a novel gravity-compensated version of the Optotune tunable lens was launched on the market in 2024. The EL-16-40-GTC-VIS-5D model

was designed to mitigate coma in vertical orientation while retaining the specifications of standard models [12].

This study analyses the performance of the gravity-compensated FTL compared to two uncompensated models. Wavefront characterization across their addressable power range, as well as a comparison of optical performance and induced coma aberration, are evaluated in both horizontal and vertical orientations.

2.- Material and method

2.1.- FTLs specifications

Three Optotune FTL models were evaluated: two standard models, EL-16-40-TC-VIS-5D (TC) and EL-16-40-TC-VIS-5D-E (TC-E) and a gravity-compensated model, EL-16-40-GTC-VIS-5D (GTC). All three offer a 5D focus tunable range (-2.0 to +3.0D).

The TC and GTC models were controlled via an ICC-4C external controller, while the TC-E model featured embedded electronics in the lens mount, enabling direct USB connection to a computer. The GTC model incorporates an integrated mechanism intended to counteract gravitational effects when the lens is positioned vertically.

Two different commercial formats of the evaluated FTLs are displayed in Fig. 1.

Each lens has a 16 mm clear aperture and an integrated temperature sensor to regulate optical power deviations due to electronic heating [8, 13-14]. Manufacturer specifications indicate a ~5 ms response time with high repeatability (±0.02 D), a refractive index of n_D=1.30 and an Abbe number of ν=100 [12].

Table 1 summarizes the nominal RMS wavefront error at 0D optical power, measured at 80% of the aperture for λ=532 nm [12].

Additionally, the manufacturer provides a numerical evaluation of coma aberration when comparing the uncompensated TC to the gravity-compensated GTC in upright position. At 525 nm, the RMS error for the TC due to gravity-induced coma is ~0.5λ, whereas in the GTC model, it is significantly reduced to <0.05λ [12].

Fig. 1: Two commercial formats for the FTLs used in the experiments.

Table 1: Nominal RMS error for the three FTLs in horizontal and vertical orientation.

Model	*Horizontal*	*Vertical*
TC	*<0.25λ*	*<0.50λ*
TC-E	*<0.25λ*	*<0.50λ*
GTC	*<0.25λ*	*<0.26λ*

2.2.- Optical setup and measurements

Figure 2 illustrates the optical setup used in the experiments. A 530nm LED serves as the light source, with a microscope objective (MO) focusing the light onto a pinhole (P). A 100 mm focal length collimating lens (L_C) provides on-axis plane wave illumination onto the FTL aperture. The optical arrangement facilitates sequential evaluation of the lens in two orientations: vertical (black path between Lc and L_1 in Fig.2), where gravity affects the lens geometry, and horizontal (alternative green path between Lc and L_1 in Fig. 2), where gravity's effect is minimized. When the FTL is vertical, the optical axis of the whole setup remains horizontal. An iris diaphragm (ID), next to the FTL controls the aperture. A 4f-relay system (L_1 and L_2, with focal lengths $f_1 = 160$ mm and $f_2 = 100$ mm) projects the FTL pupil and adjust the beam diameter to match the area of the Hartman-Shack (HS) wavefront sensor. A double upright periscope (λ/10 flat mirrors M_1 to M_4 in the alternative green path of Fig. 2) redirects light for FTL horizontal testing. In both configurations, the

FTL is located at the same distance from the HS sensor, which in turn is conjugated with the lens plane.

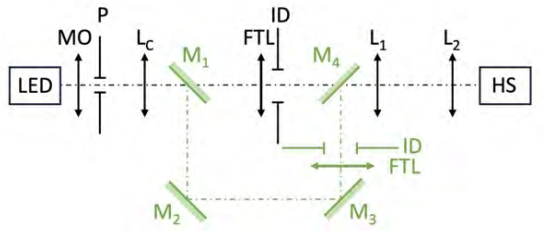

Fig. 2: Experimental optical setup.

The evaluated FTL region was a central area of about 6 mm diameter in all cases. It has to be noted that, in general, all the high-order aberrations found in this central region would rapidly increase if the analysed diameter of the lens was larger.

Before introducing an FTL into the setup, the incident wavefront on the HS sensor was recorded to serve as a reference. Any subsequent variation in the wavefront was then attributed to the effect of the lens.

Different Zernike coefficients were recorded for each lens using the HS sensor, followed by analysis and comparison. The Zernike coefficient for defocus c_2^0 specifically correlates with the optical power introduced by the FTL, which in turn, should align with the addressed value. In addition to defocus, high-order aberrations (HOAs) include third-order coma (c_3^{-1}, c_3^1). Ideally, only defocus should be present; any additional aberrations would indicate undesirable distortions.

3.- FTLs performance

The following subsections present the measured Zernike coefficients as a function of the optical power addressed to each FTL with 6 mm pupil. The obtained results for the FTLs are graphically depicted to facilitate the analysis. Vertical and horizontal FTL performances are compared and the main differences highlighted.

3.1.- Defocus and optical power

The defocus Zernike coefficient (c_2^0), is, in a first approximation, directly related to the wavefront curvature, *S*, as defined by [15]

$$S = -\frac{4\sqrt{3}c_2^0}{R^2}, \qquad (1)$$

where *R* is the pupil radius. The optical power of the tunable lens is then calculated by considering the magnification $m = -f_2/f_1$ of the 4f-relay system [16]

$$P = -S \cdot m^2. \qquad (2)$$

Figure 3 shows the measured optical power of the three 6mm-pupil FTLs versus the addressed value when it runs from -2.0 to +3.0 D in 0.2 D increments.

In all cases, the measured optical power, computed using Eqs. (1) and (2), closely matches the expected values. The TC, TC-E, and GTC lens behaviours show no significant differences between the horizontal and vertical orientations. Thus, these results illustrate the satisfactory optical power tuning performance of all the three lens models in both orientations: horizontal (the recommended orientation for the uncompensated standard TC and TC-E models) and vertical (where the gravity-compensated GTC model might be expected to perform better).

3.2.- Primary coma

Figures 4 and 5 display the measured Zernike coefficient c_3^1 and c_3^{-1} corresponding to the induced horizontal and vertical coma, respectively, for a 6 mm pupil size.

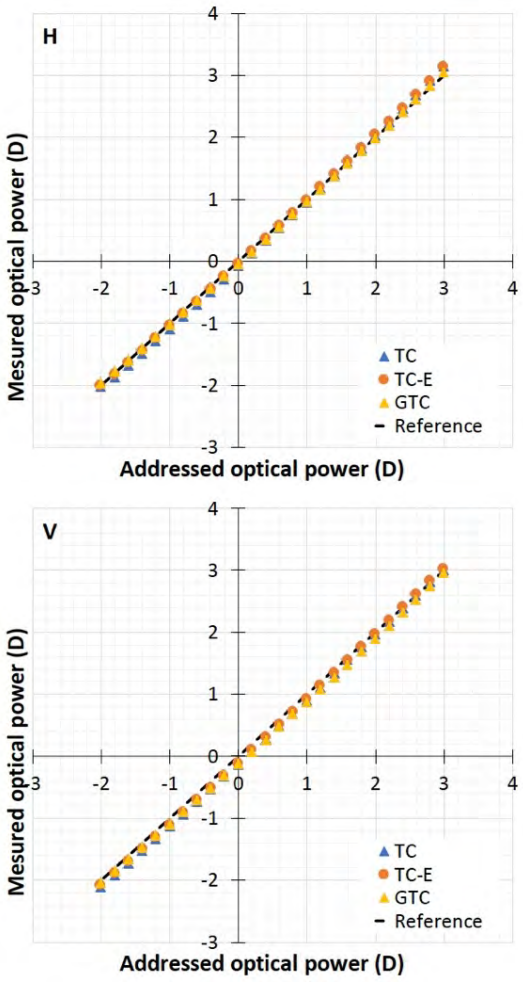

Fig. 3: Measured optical power (D), calculated from the defocus c_2^0, versus the addressed power (D) for FTLs in horizontal (H) and vertical (V) orientations. Reference indicates ideal performance.

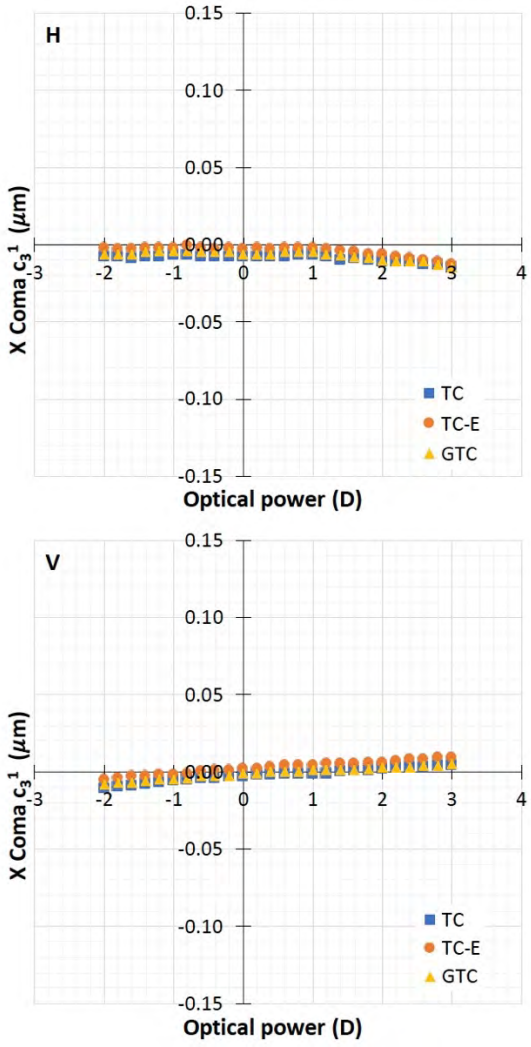

Fig. 4: Zernike coefficient c_3^1 (horizontal coma), versus the addressed power (D) for FTLs in horizontal (H) and vertical (V) orientations.

Figure 4 demonstrates that all three FTLs exhibit a reduced c_3^1 coma coefficient across the entire addressable range of optical power, regardless their horizontal or vertical position. The maximum c_3^1 coma error observed in this experiment (about -0.02 microns) occurred for all three lenses positioned horizontally, at addressed power values approaching the upper limit of +3.0 D.

In contrast, the FTL's behaviour changes with orientation when c_3^{-1} coma is considered (Figure 5).

When the lenses are positioned horizontally, c_3^{-1} values remain low and comparable in magnitude to c_3^1 values. However, when the lenses are oriented vertically, the two standard models (TC and TC-E) exhibit certain amount of induced c_3^{-1} coma, as highlighted by the manufacturer warnings. This induced c_3^{-1} coma, however, keeps below 0.04 microns quite uniformly within the power range. In the gravity-compensated GTC model, this c_3^{-1} coma is substantially reduced -almost entirely suppressed- resulting in a magnitude comparable to that of c_3^1 coma.

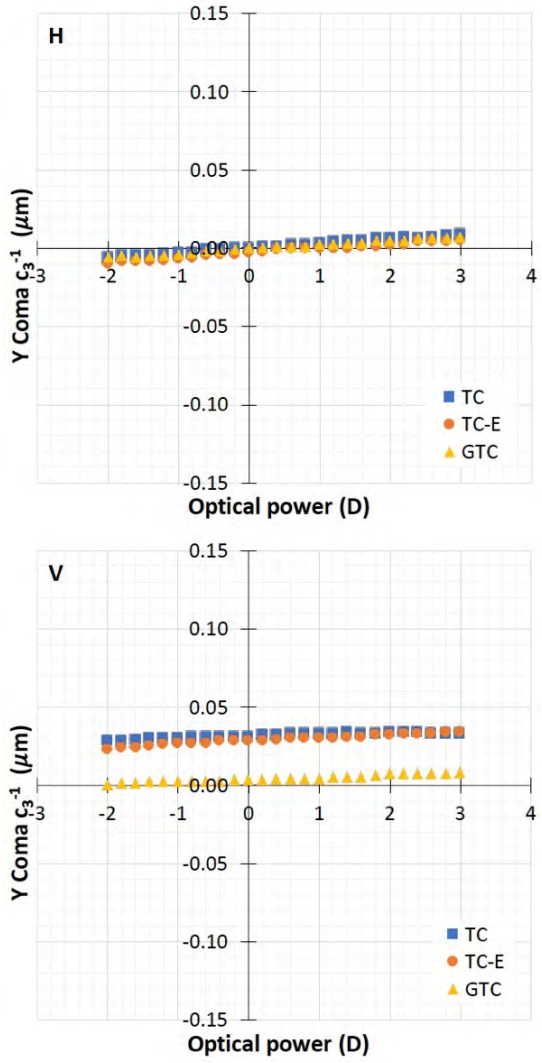

Fig. 5: Zernike coefficient c_3^{-1} (vertical coma), versus the addressed power (D) for FTLs in horizontal (H) and vertical (V) orientations.

Table 2 contains the RMS error due to coma, computed from the Zernike coefficients as $\left([(c_3^{-1})^2 + (c_3^1)^2]^{1/2}\right)$, for the three FTLs in horizontal and vertical positions. These numerical results (mean values ± standard deviations across the power range) confirm that the GTC lens effectively corrects the vertical coma caused by gravity when the lens is upright. The residual coma is of the same order of magnitude as that observed when tunable lenses are placed in a horizontal position.

Table 2: RMS error (in μm) due to coma for the FTLs in horizontal (H) and vertical (V) positions (6 mm pupil).

	TC	***TC-E***	***GTC***
H	*0.010 ± 0.003*	*0.007 ± 0.003*	*0.008 ± 0.003*
V	*0.032 ± 0.001*	*0.024 ± 0.003*	*0.006 ± 0.002*

4.- Conclusions

This work presents a comparative analysis of a recently developed gravity-compensated focus tunable lens (GTC) against two standard counterparts (TC and TC-E) from the same manufacturer, sharing identical material and optical specifications (clear aperture, addressable power range, response time, integrated temperature sensor).

Our results indicate that all three lens models performed exceptionally well within their intended optical power range, regardless of whether they were oriented horizontally or vertically.

Regarding coma aberration, this study shows that horizontal coma (c_3^1) remained negligible for all three lenses in both orientations. It also demonstrates a substantial reduction in vertical coma (c_3^{-1}) for the gravity-compensated GTC lens when positioned upright (0.006 μm RMS) compared to the uncompensated TC (0.032 μm RMS) and TC-E (0.024 μm RMS) lenses. These findings confirm that the GTC model effectively minimizes the vertical coma observed in the standard models when used upright, as intended.

The impact of induced aberrations depends on the intended application. In scenarios requiring strict aberration control, the aberrations introduced by FTLs can be significant, potentially masking the effects of other optical elements. In such cases, when the FTL must be positioned vertically, the gravity-compensated model effectively mitigates the vertical coma caused by the gravitational force.

Acknowledgements: This work has been sponsored by the Agencia Estatal de Investigación (PID2020-114582RB-I00/AEI/ 10.13039/501100011033).

References

[1] Mishra, K., van den Ende, D., & Mugele, F., "*Recent developments in optofluidic lens technology,*" Micromachines, 7 (6), 102 (2016).

[2] Chen, L., et al., *"Electrically Tunable Lenses: A Review,"* Frontiers in Robotics and AI, 8, 678046 (2021).

[3] Liu, C., et al., *"Tunable Liquid Lenses: Emerging Technologies and Future Perspectives,"* Laser and Phot. Reviews, 17 (11), 2300274 (2023).

[4] Blum, M., et al., *"Optotune focus tunable lenses and laser speckle reduction based on electroactive polymers,"* MOEMS and Miniaturized Systems XI, 8252, 825207 (2012).

[5] Casutt, S., et al., *"Fast and precise continuous focusing with focus tunable lenses,"* Optical Components and Materials XI, 8982, 89820Y (2014).

[6] Suchkov, N., Fernández, E. J., & Artal, P., *"Wide-range adaptive optics visual simulator with a tunable lens,"* JOSA A, 36 (5), 722 (2019).

[7] Dorronsoro, C., et al., *"Tunable lenses: dynamic characterization and fine-tuned control for high-speed applications,"* Opt. Express, 27 (3), 2085 (2019).

[8] Torres-Sepúlveda, et al., *"Hysteresis characterization of an electrically focus-tunable lens,"* Opt. Eng., 59 (4), 044103 (2020).

[9] Yan, Y., et al., *"Optical performance evaluation and chromatic aberration correction of a focus tunable lens used for 3D microscopy,"* Biomed. Opt. Express, 10 (12), 6029 (2019).

[10] Gowda, H. G. B., et al., *"Reliability of tunable lenses: feedback sensors and the influence of temperature, orientation, and vibrations,"* Appl. Opt., 62 (12), 3072 (2023).

[11] Salvador-Roger, R., Esteve-Taboada, J. J., & Micó, V., *"Optical characterization of a manual tunable lens for eye-care applications,"* Appl. Opt., 63 (34), 8732 (2024).

[12] Optotune. (2024). *Datasheet: Electrically tunable lens EL-16-40 (5D version)*. www.optotune.com

[13] Marrakchi, Y., et al., *"Experimental characterization, modelling and compensation of temperature effects in optotunable lenses,"* Sci. Rep., 13 (1), 1575 (2023).

[14] Oliva-García, R., et al., *"Real-Time Wavefront Sensing at High Resolution with an Electrically Tunable Lens,"* Sensors, 23 (15), 6651 (2023).

[15] Dai, G.M. *Wavefront Optics for Vision Correction*, (SPIE Press, USA, 2008).

[16] Arines, J., *"What should be done to the measured Zernike coefficients when conjugating the pupil and wavefront sensor planes with a 4f system: discussion,"* JOSA A, 38 (3), 437 (2021).

Desarrollo de películas delgadas de AlN amorfo sobre ITO-vidrio e ITO-PET a baja temperatura mediante rf-sputtering

Miriam CADENAS [(1)], Michael SUN [(1)], Susana FERNÁNDEZ [(2)], Sirona VALDUEZA-FELIP [(1)], Fernando B. NARANJO[(1)]

1. Grupo de Ingeniería Fotónica, Universidad de Alcalá, 28871, Alcalá de Henares, España. Unidad Asociada Instituto de Óptica-CSIC, Tecnologías Fotónicas y de Sensores.
2. Departamento de Energía, CIEMAT, Av. Complutense 40, 28040 Madrid, Spain.

Persona de contacto: Miriam CADENAS (miriam.cadenas@uah.es)

ABSTRACT:

In this work, the deposition and characterization of AlN thin films by reactive sputtering at low temperature (room temperature and 100ºC) on ITO-glass and ITO-PET substrates are presented. The structural, optical, and electrical properties of the samples were analysed as a function of the sputtering power and the deposition temperature. The results show the formation of homogeneous and compact layers with a bandgap around 5.82 eV, depending on the deposition conditions. These findings confirm the potential of amorphous AlN for applications in flexible optoelectronic devices.

Key words: AlN thin films, reactive sputtering, flexible electronics, optoelectronic devices.

1.- Introducción

El nitruro de aluminio (AlN) es un material de amplio interés en la industria de la optoelectrónica y la electrónica de alta potencia debido a su gran estabilidad térmica, alta conductividad térmica y excelente aislamiento eléctrico. Su ancha banda prohibida (~6.2 eV en su fase cristalina) lo convierte además en un material atractivo para aplicaciones en ventanas ópticas en el ultravioleta profundo, sensores y transistores de alta frecuencia [1,2].

La deposición de películas delgadas de AlN a temperatura elevada es un proceso bien establecido, pero su implementación en sustratos flexibles con óxidos conductores, como el ITO-vidrio o ITO-PET plantea desafíos debido a la degradación térmica de estos materiales. Por ello, es crucial desarrollar métodos de depósito a baja temperatura que mantengan las propiedades ópticas y eléctricas del AlN sin comprometer la integridad del sustrato [3-5].

En este trabajo, se estudia la deposición de AlN amorfo mediante pulverización catódica (*sputtering*) reactivo y su caracterización estructural, óptica y eléctrica. En concreto, se analiza la influencia de la potencia de radiofrecuencia (rf) aplicada al blanco de Al (P_{Al}) y la temperatura de crecimiento sobre la calidad de las películas obtenidas, con el objetivo de evaluar su viabilidad para aplicaciones en dispositivos electrónicos flexibles y optoelectrónicos avanzados [6].

2.- Metodología

En este estudio, las películas de AlN se depositaron utilizando la técnica de *sputtering* de radiofrecuencia en atmósfera reactiva. Durante el proceso, se mantuvo una presión constante de 0,47 Pa y una P_{Al} que se fijó en cada muestra de la serie entre 100 W y 175 W, con intervalos de 25 W. Estas condiciones de depósito se fijaron teniendo en cuenta la experiencia previa del grupo de investigación en el crecimiento de nitruros a alta temperatura

[7,8]. En cuanto a los sustratos utilizados fueron: ITO depositado sobre vidrio e ITO depositado sobre PET, ambos comerciales. Todas las muestras se realizaron simultáneamente sobre zafiro como sustrato cristalino de referencia. Las capas se depositaron tanto a 100ºC como a temperatura ambiente.

Una vez depositadas, las películas fueron caracterizadas mediante diferentes técnicas, con el fin de poder evaluar sus propiedades estructurales, ópticas y eléctricas. La cristalinidad de las muestras se analizó mediante difracción de rayos X (XRD), una técnica que permite estudiar la calidad cristalina de las capas. Por otro lado, la espectroscopia de energía dispersiva (EDX) se empleó para confirmar la presencia de los elementos aluminio (Al) y nitrógeno (N) en las películas, lo cual es fundamental para verificar la composición de las muestras.

Además, se realizaron análisis de la morfología y la estructura en sección transversal mediante microscopía electrónica de barrido (SEM), lo que permitió observar la topografía y las características microestructurales de las películas. Para medir la rugosidad superficial, se utilizó microscopía de fuerza atómica (AFM), una técnica que proporciona información detallada sobre las irregularidades en la superficie de las películas, siendo esto de gran importancia para evaluar la calidad de las mismas en términos de uniformidad y posibles defectos.

También se realizaron medidas de transmisión óptica para determinar el ancho de banda prohibido de las películas, lo que proporciona datos importantes sobre las propiedades ópticas de las muestras. Finalmente, se evaluó la resistividad de las películas mediante medidas eléctricas utilizando el método de línea de transmisión (TLM, por sus siglas en inglés), lo que es fundamental para estimar su potencial en diversas aplicaciones tecnológicas, obteniendo información sobre la conductividad eléctrica de las películas de AlN depositadas. Para estas medidas se emplearon contactos de Al de 100 nm de espesor sin aleado posterior.

3.- Resultados y Discusión

3.1. Caracterización estructural

Los análisis de XRD revelaron la ausencia de picos característicos de AlN cristalino (esperable en torno a 2θ~36º para los planos (0002)) en muestras sobre ITO, tal y como se observa en la **figura 1**, lo que podría indicar la formación de una fase amorfa. Las mediciones de EDX que se realizaron sobre el sustrato de ITO-vidrio con P_{Al} = 175 W, depositada a 100ºC, confirmaron la presencia de Al y N, lo que corrobora la deposición de AlN al menos sobre esta muestra, pudiendo estar presentes de esta manera en los tres substratos

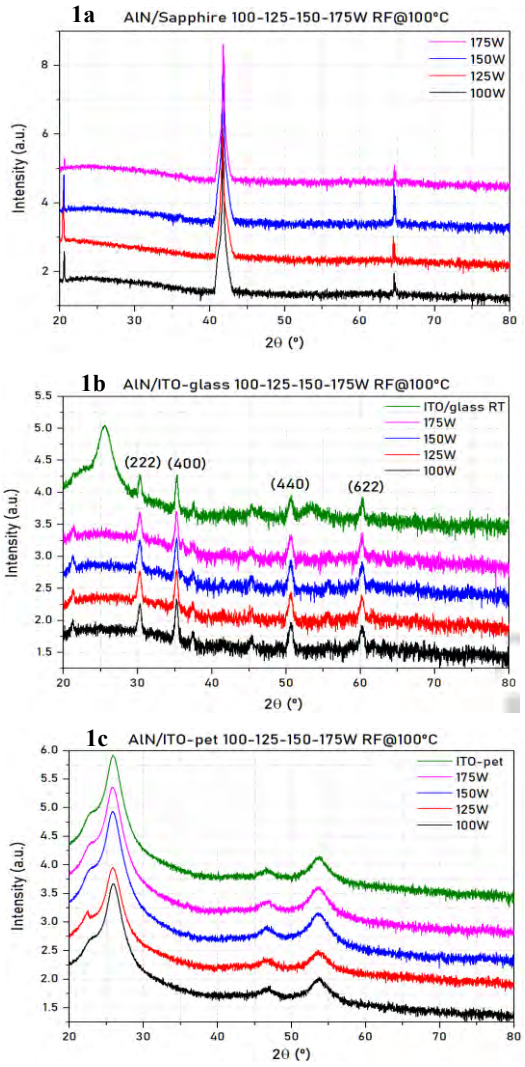

***Figura 1**. Mediciones de difracción de rayos X de las muestras AlN/Zafiro (1a), AlN/ITO-vidrio (1b) y AlN/ITO-PET (1c) con diferentes P_{Al}, depositadas a 100ºC.*

La **figura 2** muestra una medida característica de las oscilaciones detectadas en la intensidad (cuentas) de los rayos X reflejados en la medida de XRR. En concreto, se representa la medida de la capa de AlN depositada sobre zafiro, a RT y con P_{Al}=175 W, lo que permite la estimación del espesor de la capa. Estas oscilaciones no están presentes en las capas crecidas sobre ITO-vidrio ni ITO-PET, lo que podría estar relacionado con una intercara AlN/ITO menos abrupta. La gráfica insertada muestra el ajuste realizado para la obtención del espesor. La **tabla 1** resume los valores del espesor de las capas de AlN/Zafiro depositadas a diferentes temperaturas en función de la potencia de aluminio.

El espesor de las capas se estimó mediante reflectividad de rayos X (XRR) en muestras depositadas sobre zafiro, obteniéndose valores en el rango de 50 a 150 nm, correspondiendo a una tasa de crecimiento proporcional a P_{Al}, desde 25 nm/h hasta 65 nm/h para 100 W y 175 W, respectivamente.

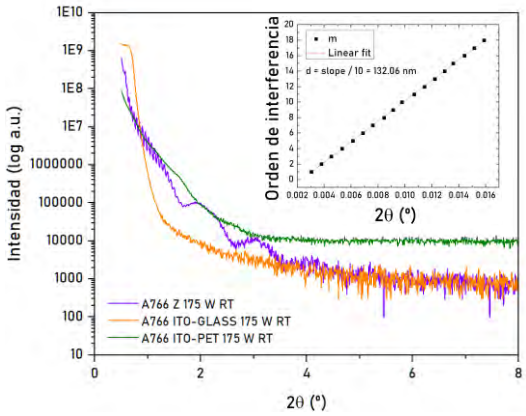

Figura 2. *Curvas de XRR medidas en las muestras AlN/Zafiro, AlN/ITO-vidrio y AlN/ITO-PET a una potencia de 175 W y a temperatura ambiente.*

Tabla 1. *Resumen de los valores del espesor (obtenido mediante mediciones de reflectividad de rayos X) de las capas de AlN/Zafiro bajo estudio, depositadas tanto a 100ºC como a temperatura ambiente, en función de P_{Al}.*

	Espesor XRR (nm)	
P_{Al} (W)	***AlN/Zafiro 100ºC***	***AlN/Zafiro RT***
100	*51.3*	*51.9*
125	*74.7*	*72.9*
150	*97.9*	*105.5*
175	*127.9*	*132.1*

3.2. Caracterización morfológica

La imagen de SEM de la **figura 3** muestra películas compactas y homogéneas en la muestra AlN/ITO-vidrio a 175 W y 100ºC. Lo anterior confirma que las capas son compactas, siendo el espesor el esperado, según lo obtenido a partir de la técnica de XRR en la muestra depositada sobre zafiro. Además, las mediciones de espectroscopía de rayos X por dispersión de energía muestran la presencia de Al y N en las capas, lo que indica que las películas están formadas principalmente por AlN amorfo.

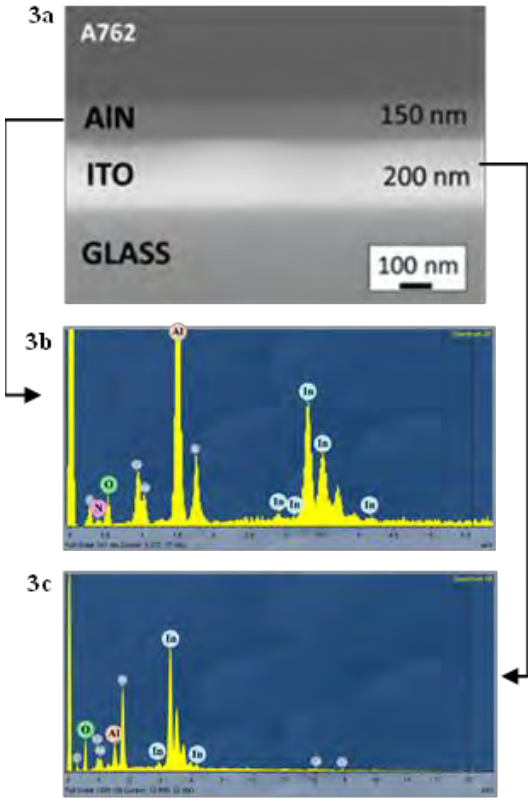

***Figura 3**. Imagen SEM de la capa de AlN sobre el sustrato de ITO-vidrio con P_{Al} = 175 W, depositada a 100ºC (3a). Mediciones EDX en la capa de AlN y en la capa de ITO de la misma muestra (3b y 3c, respectivamente).*

Por otro lado, los estudios mediante AFM mostraron que la rugosidad RMS en AlN/Zafiro fue inferior a 1 nm, mientras que para las muestras depositadas sobre ITO-vidrio e ITO-PET este valor está en el rango de 4-5 nm y 1.5-3 nm, respectivamente. La **figura 4** muestra una imagen representativa de las muestras AlN/ITO-vidrio, AlN/ITO-PET y AlN/Zafiro, crecidas a una potencia de 100 W y a 100 ºC, en un área de 2×2 μm^2, aunque el valor del RMS se obtuvo haciendo una media de las medidas de rugosidad obtenidas en áreas de 5×5, 2×2 y 1×1 μm^2.

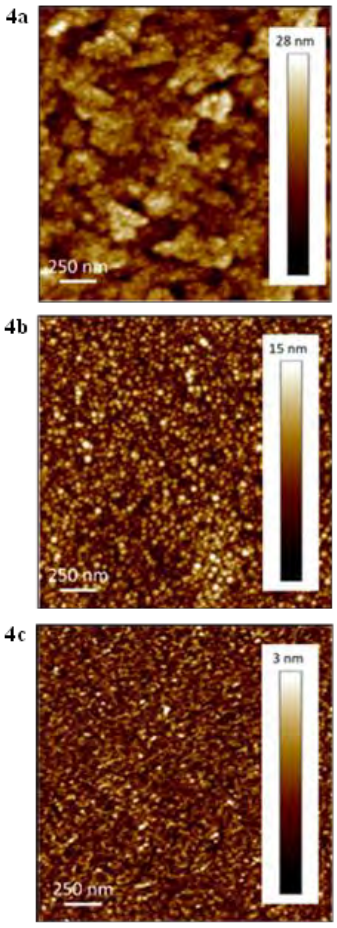

***Figura 4.** Imágenes AFM de las muestras AlN/ITO-vidrio (4a), AlN/ITO-PET (4b) y AlN/Zafiro (4c), crecidas a una potencia de 100 W y a 100 ºC.*

3.3. Caracterización óptica

El ancho de banda prohibida de las películas de AlN se estimó con mediciones de transmisión óptica en muestras depositadas sobre zafiro, con el fin de evitar el efecto de absorción por la capa de ITO, con ancho de banda de alrededor de 3.4 eV, por debajo del valor teórico del AlN (6.2 eV). Para las capas depositadas a temperatura ambiente, el ancho de banda estimado fue aproximadamente de 5.7 eV. Como se resume en la **tabla 2**, en el caso de las películas depositadas a 100 °C, el ancho de banda aumentó con P_{Al}, desde 5.47 eV hasta 5.82 eV (100 W y 175 W, respectivamente). Todos estos valores están por debajo del valor teórico del AlN cristalino. Esto puede estar relacionado con la presencia de defectos y estados

electrónicos dentro de la banda prohibida en la estructura desordenada de la forma amorfa, lo que conduce a una reducción del borde de absorción de la banda prohibida [1].

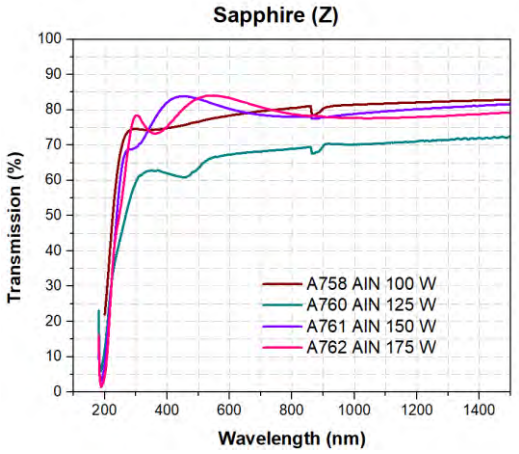

Figura 5. *Espectros de transmisión de las muestras AlN/Zafiro depositadas a 100 ºC con diferentes valores de P_{Al}.*

Tabla 2. *Resumen del ancho de banda óptico (estimado a partir de mediciones de transmisión) de las capas de AlN/Zafiro bajo estudio, depositadas tanto a 100 ºC como a temperatura ambiente, en función de P_{Al}.*

	E_g (eV)	
P_{Al} (W)	AlN/Zafiro 100ºC	AlN/Zafiro RT
100	5.5	5.8
125	5.8	5.8
150	5.8	5.6
175	5.8	5.9

3.4. Caracterización eléctrica

Las medidas de resistividad realizadas con el método de línea de transmisión indicaron altas resistividades en las muestras sobre zafiro, siendo menores para las muestras depositadas sobre ITO-PET e ITO-vidrio, en especial, para las muestras depositadas a RT, sugiriendo un comportamiento aislante. Sin embargo, en algunos casos se detectó conducción paralela a través del sustrato de ITO, en especial las de ITO-PET, debido a la existencia de grietas en el sustrato.

4.- Conclusión

En este estudio se ha demostrado la viabilidad del depósito de películas delgadas de AlN amorfo sobre sustratos de ITO a baja temperatura mediante *sputtering* reactivo. Las películas obtenidas presentan una morfología compacta, una energía de banda prohibida alrededor de 5.82 eV, y una alta resistividad.

Estos resultados indican que el AlN amorfo depositado sobre ITO-vidrio e ITO-PET puede ser una alternativa viable para aplicaciones en electrónica flexible y dispositivos optoelectrónicos.

Agradecimientos: Este trabajo ha sido financiado por los proyectos RELY (PDC2023-145888-I00) project (MICIU/ AEI/ 10.13039/ 501100011033 Next Generation EU/ PRTR) y el proyecto PTUAH24/016, financiado por la Universidad de Alcalá.

Referencias

[1] Fabio Felipe CHALÉ LARA, "*Propiedades estructurales y ópticas del nitruro de aluminio*", PhD Thesis, CICESE, **2011**.

[2] AIP Advances. "*Low temperature aluminum nitride thin films for sensory applications*." *AIP Advances*, **2016**.

[3] Ke ZHU and Kaiwei YANG, "*Low-temperature deposition of AlN films for flexible electronics*", Applied Physics *A*, vol. 128, no. 1038, **2022.**

[4] Christopher PEREZ, et al., "*High Thermal Conductivity of Submicrometer Aluminum Nitride Thin Films Grown by Low-Temperature Sputtering*," Nano Letters, **2023**.

[5] Jihong KIM, "*Low-Temperature Epitaxial Growth of AlN Thin Films on a Mo Electrode/Sapphire Substrate Using Reactive Sputtering*," *Coatings*, vol. 11, no. 4, pp. 443-450, **2021**.

[6] Martin Fischeneder, et al., "*Enhanced process stability for the low temperature sputter deposition of AlN thin films*," Microelectronic Engineering, **2018**.

[7] Sirona VALDUEZA-FELIP, "*Influence of the AlN interlayer thickness on the photovoltaic properties of in-rich AlInN on Si heterojunctions deposited by RF sputtering*", AIP Advances, vol. 8, p. 115315, **2018**.

[8] Laura MONTEAGUDO-LERMA, "*Two-step method for the deposition of AlN by radio frequency sputtering*", Thin Solid Films, vol. 545, pp. 149-153, **2013**.

Orbital Angular Momentum Multiplexing employing Liquid Crystal Reconfigurable Devices

Javier Pereiro-García, Byron Ganazhapa, José Jaraba, Pablo de la Rosa, Xabier Quintana, Morten A. Geday

CEMDATIC, ETSI Telecomunicación, Universidad Politécnica de Madrid, Av. Complutense 30, 28040 Madrid, Spain

Contact: Javier Pereiro García (javier.pereiro.garcia@upm.es).

ABSTRACT:

Orbital Angular Momentum (OAM) multiplexing is a promising technique to increase transmission capacity over Free Space Optical (FSO) communication systems. The implementation of this modulation technique is limited due to the technological difficulty of generating vortex beams, light beams carrying a helical wavefront, in a reconfigurable way. This work presents the development of liquid crystal (LC) spiral phase plates (SPP) that can generate up to 48 different vortex beams without moving parts. These devices have been characterized, and integrated in an optical setup to preliminary study their employment in an OAM multiplexing system. Employing this setup, the potential to generate and recover a specific vortex beam carrier has been proved.

Key words: Orbital Angular Momentum, Liquid Crystals, Adaptive Optics, Spiral Phase Plate, Multiplexing.

1.- Introduction

In recent years, the increasing demand for data transmission has driven the development of new technologies to expand communication capacity. In this context, optical communications have played a key role in the widespread deployment of fiber-optic networks. More recently, free-space optical (FSO) communications have gained significant relevance, particularly due to the growing need for high-speed data transmission between satellites. The deployment of satellite constellations has increased substantially, fueled by both private initiatives, such as Starlink, and public projects, like the upcoming European IRIS² satellite network. These strategically valuable infrastructures require advanced multiplexing and modulation technologies to enhance data transmission capacity while ensuring secure communication.

One promising technology that has attracted considerable interest in recent years is orbital angular momentum (OAM) multiplexing of light [1]. This technique introduces a new degree of freedom in data transmission and is compatible with widely used multiplexing schemes such as wavelength-division and frequency-division multiplexing [2]. OAM multiplexing relies on vortex beams, light beams characterized by an azimuthal phase variation, resulting in a helical wavefront. The key parameter of these vortices is their topological charge (l), defined by the number of helices in the wavefront [3]. These beams are also characterized by having a phase singularity leading to an intensity destructive interference around the optical axis.

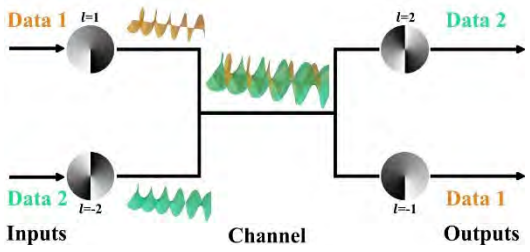

Fig. 1: Orbital Angular Momentum (OAM) multiplexing sketch depicting how data multiplexed over the same transmission channel can be demultiplexed by using a device with an opposite topological charge (l).

The core principle of this multiplexing technique is the orthogonality between optical vortices with different topological charges. Additionally, an optical vortex encoded with a specific topological charge can only be accurately demultiplexed by a device with the opposite topological charge, enabling secure and selective channel separation. Theoretically, an infinite number of topological charges exist, making it possible to multiplex a vast number of channels, thereby drastically increasing data transmission capacity.

Despite its potential, current technologies for generating optical vortices are not yet fully mature. The most widely used devices today are Q-plates [4], typically made from polymerizable liquid crystals. However, these components are not reconfigurable and are limited to a small set of discrete topological charges. To overcome this limitation, various research groups have explored the use of spatial light modulators (SLMs) [5]. These devices offer high versatility and tunability of topological charge. However, as general-purpose components, their high cost and bulkiness present challenges for real-world implementation beyond laboratory environments.

A promising solution to this challenge lies in the development of reconfigurable spiral phase plates (SPPs) [6], [7]. These specialized devices generate optical vortices by inducing an azimuthal phase delay in the incident light. By offering a compact and efficient means of controlling topological charge, SPPs hold significant potential for advancing OAM-based optical communication systems.

In this work we present a preliminary implementation of liquid crystal SPPs in an orbital angular momentum multiplexing system achieving both the generation of vortex beams with a certain topological charge and their recovery.

2.- Materials and Methods

2.1.- Liquid Crystal Cell Manufacturing

The liquid crystal (LC) spiral phase plate (SPP) consists of two indium tin oxide (ITO)-coated glass substrates arranged in a sandwich-like configuration. One substrate serves as the ground backplane, while the other is pixelated using direct laser writing (DLW).

The pixelated layer comprises 48 independently addressable pie-slice-shaped electrodes within a 2.54 cm active area. These electrodes, separated by laser-ablated ITO, enable the generation of 24 positive or 24 negative topological charges (l). The electrode design allows efficient routing to the periphery, where connections to a custom electronic driver are established using a flexible connector and anisotropic conductive adhesive (Hitachi).

The uniform alignment of the liquid crystal (LC) is achieved using polyimide PIA-2304 (Chisso Lixon, Japan). Both ITO-coated surfaces are spin-coated with a polyimide solution (30s @ 2500 rpm) and polymerized at 180°C for 45 minutes. The alignment direction is then defined by rubbing the polymerized polyimide with a velvet cloth. The LC cell maintains a uniform 7.2 µm thickness using cylindrical silica spacers and is filled with a high-birefringence nematic liquid crystal, MDA-98-1602 (Merck GmbH), before being sealed with an epoxy adhesive (Araldite).

2.2.- Calibration and Driving

Each pixel of the developed device will induce a phase delay depending on the applied RMS voltage signal. To calibrate the LC SPP, the device is placed between crossed polarizers at +/-45 degrees respect to rubbing direction. The relation between the phase delay (δ) and duty cycle (dc) has been empirically fitted with a pseudo-exponential function given by:

$$\delta = A \cdot e^{-B \cdot dc} + C$$

where A, B, C are fitting parameters as previously described [6], [8].

The driving signals are produced employing a custom electronic driver able to generate the 48 independent 12-bit pulse width modulation (PWM) outputs. These signals modulate 1kHz square wave, precisely adjusting the RMS voltage applied to each pixel, thereby determining the phase delay and controlling the spiral phase plate topological charge.

3.- Results

Three different spiral phase plates composed of 48 different pixels were manufactured and calibrated. After that, the intensity generated patterns for different topological charges (l) were measured. The recorded measurements are in agreement with carried out simulations based on scalar diffraction theory.

An optical setup was assembled to test the potential use of the developed LC SPPs for OAM multiplexing systems.

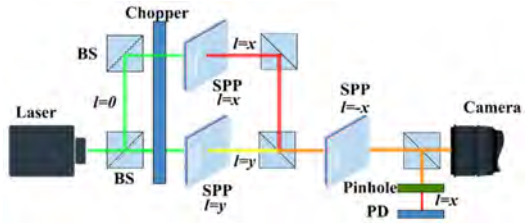

Fig. 2: Employed OAM multiplexing setup diagram.

A He-Ne laser (λ=543.5 nm) is employed as light source. The laser beam is divided in two branches employing beam splitters. The use of this beam splitters configuration means that each path will have a different intensity loss, however this will not affect our ability to discriminate between channels as we will separate them according to the frequency of the intensity modulation as explained below. Furthermore, each path will go through a polarizer (aligned with the LC cell rubbing direction) and a LC SPP. The two paths are recombined later (or multiplexed) for impinging together over a third LC SPP. Finally, the outcome of the system is measured both with a photodiode and a camera.

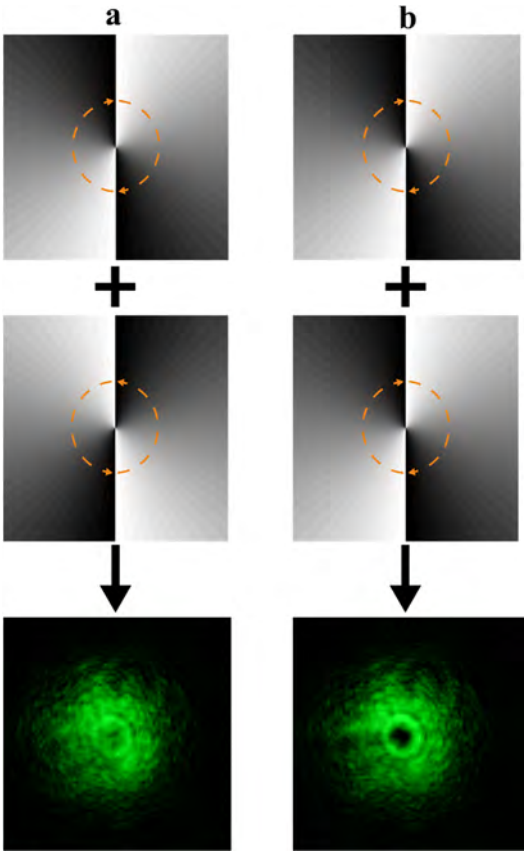

Fig. 3: Vortex beam intensity recovery. (a) Two SPPs with opposite topological charge will recover the intensity around the optical axis. (b) Two SPPs with the same topological charge will present the intensity singularity around the center of the beam as they are not compensating each other.

Additionally, a mechanical chopper has been added to perform intensity modulation of each light path with different frequencies, so they could be discriminated in the photodiode. The mechanical chopper has two different slit spacings, light path will pass through one of them, thus corresponding to an intensity

modulation with a different frequency. This type of modulation has been chosen to validate the concept of OAM multiplexing with the equipment available in our laboratory, however theoretically this type of multiplexing is compatible with more advanced phase modulation techniques (i.e. Quadrature Amplitude Modulation (QAM)).

Employing this setup, it was tested that a vortex beam could be generated in each path. Moreover, the received intensity around the optical axis could be recovered by the third SPP, only if it was configured with the opposite topological charge of the transmitted beam. Otherwise, if their topological charge does not compensate each other, the intensity destructive interference will still be present.

4.- Conclusion

This work presents the employment of purpose build liquid crystal spiral phase plates in an orbital angular multiplexing setup. Employing these devices vortex beams were generated and recovered by electronically configuring them with opposite topological charge.

The preliminary results showcase the potential of these devices as OAM multiplexers/demultiplexers. Further research must be carried out to test the performance of the developed system with multiple transmitted channels.

Acknowledgements: The authors are grateful to the ETSIT-UPM for funding the project “OrbItal aNgular momenTum mUltiplexing lIquid crysTal reconfIgurable deVicEs” (INTUITIVE), that has been funded by the “Primeros Proyectos” call within the research support funding framework of ETSIT-UPM.

References

[1] L. Zhu, M. Deng, B. Lu, X. Guo, and A. Wang, *"Turbulence-resistant high-capacity free-space optical communications using OAM mode group multiplexing"*, Optics Express, vol. 31, no. 9, pp. 14454–14463, 2023.

[2] Lei Gong, Qian Zhao, Hao Zhang, Xin-Yao Hu, Kun Huang, Jia-Miao Yang, Yin-Mei Li, *"Optical orbital-angular-momentum-multiplexed data transmission under high scattering"*, Light: Science & Applications, vol. 8, no. 1, Art. no. 1, 2019.

[3] Yijie Shen, Xuejiao Wang, Zhenwei Xie, Changjun Min, Xing Fu, Qiang Liu, Mali Gong, Xiaocong Yuan, *"Optical vortices 30 years on: OAM manipulation from topological charge to multiple singularities"*, Light: Science & Applications, vol. 8, no. 1, Art. no. 1, 2019.

[4] A. Rubano, F. Cardano, B. Piccirillo, and L. Marrucci, *"Q-plate technology: a progress review"*, Journal of the Optical Society of America B, vol. 36, no. 5, pp. D70–D87, 2019.

[5] Yongxiong Ren, Long Li, Zhe Wang, Seyedeh Mahsa Kamali, Ehsan Arbabi, Amir Arbabi, Zhe Zhao, Guodong Xie, Yinwen Cao, Nisar Ahmed, Yan Yan, Cong Liu, Asher J. Willner, Solyman Ashrafi, Moshe Tur, Andrei Faraon, Alan E. Willner, *"Orbital Angular Momentum-based Space Division Multiplexing for High-capacity Underwater Optical Communications"*, Scientific Reports, vol. 6, no. 1, p. 33306, 2016.

[6] M. Caño-García, X. Quintana, J. M. Otón, and M. A. Geday, *"Dynamic multilevel spiral phase plate generator"*, Scientific Reports, vol. 8, no. 1, Art. no. 1, 2018.

[7] T. Jankowski, N. Bennis, P. Morawiak, D.C. Zografopoulos, A. Pakuła, M. Filipiak, M. Słowikowski, J.M. López-Higuera, J.F. Algorri, *"Optical vortices by an adaptive spiral phase plate"*, Optics & Laser Technology, vol. 176, p. 111029, 2024.

[8] J. Pereiro-García, M. García-De-Blas, P. D. L. Rosa, M. A. Geday, X. Quintana, and M. Caño-García, *"Reconfigurable perfect vortex beam generator based on a liquid crystal spiral phase plate"*, Optics Express, vol. 31, no. 23, pp. 37653–37662, 2023.

Low cost optical device to measure blood plasma coagulation

Gemma García Mandayo [1,2], Lucía Ruiz Fernández de Bobadilla [1,2], María Guijo[2], Oihane Beldarrain[1,2], Aitor Larrañaga-Jaio[1,2], Javier Gallego [4], Patricia Blanco[3], Carles Pizarro[3], Santiago M. Olaizola[1,2]

1. CEIT-Basque Research and Technology Alliance (BRTA), Manuel Lardizábal 15, 20018 Donostia / San Sebastián, Spain.
2. Universidad de Navarra, Tecnun, Manuel Lardizábal 13, 20018 Donostia / San Sebastián, Spain.
3. SnellOptics, Sant Quirze 91 5º2, 08221 Terrassa, Barcelona, Spain SnellOptics, Sant Quirze 91 5º2, 08221 Terrassa, Barcelona, Spain
4. RAL Tecnica para el laboratorio SA, Avda.Madere de Deu de Montserrat, 51, St Joan Despi, 08970, Barcelona, Spain

Contact: Gemma García Mandayo ggmandayo@ceit.es.

ABSTRACT

This work presents some key aspects of the development of a device to measure the coagulation velocity of blood plasma, which is a marker for several relevant diseases. We present the validation of the sensing principle and an optimized design of a sensing device, based on simulation and experimental evidence. Regarding manufacturing, the fabrication process of an injection mould for a Fresnel lens integrated in the device has been developed and the main features of the mold characterized. Finally, an auxiliary method to position the plasma clot in the device is proposed and a preliminary test to validate it have been carried out.

Key words: coagulation, femtosecond laser, Fresnel lens, optical device

1.- Introduction

Some relevant diseases such as several inflammatory processes and neoplasia have been linked to an increase in the coagulation time of blood and blood plasma [1, 2]. This means that those diseases can be early detected by measuring the coagulation speed of a plasma sample. For this reason, this research work proposes the measurement of the plasma coagulation using a low-cost optical device. The final objective of the proposed device is to serve as an early detection tool for medical doctors to have markers of certain diseases at a primary stage.

The Point-of-Care (POC) devices allow to make fast coagulation analysis in environments where results need to be fast to manage hemorrhage or detect coagulopathies. Several devices that include optical principles are already available in the market, such as the Coag-Sense PT/INR, which relies on a mechanical part that combined with the use of IR light [3], or the microINR, using a disposable microchip with to microcapilary channels combined with an artificial vision system [4]. Other devices take advantage of other measuring principles, such as the ClotChip, which is a new development that uses impedance spectroscopy applying an electric field to the sample and then correlating the impedance measurement with coagulation parameters [5].

2.- Measurement principle validation and first prototype

2.1.- Measuring principle

The device is based on the idea that the coagulated plasma changes its refractive index with respect to non-coagulated plasma.

Hence, by detecting this change, coagulation velocity can be measured. We intend to take advantage of this idea by putting the plasma sample in a transparent cuvette and using a light beam, which is diffracted through the bottom of the cuvette, as Fig.1 depicts. The device will be designed so the proportion of diffracted and refracted light can be linked to a certain change in the refractive index, and thus to the coagulation process.

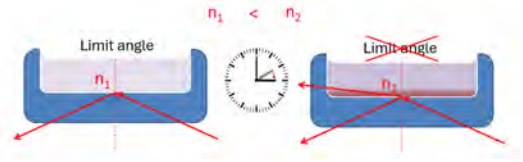

Fig. 1: Scheme of the concept to measure the coagulation through the refractive index change

2.2.- Validation setup and simulations

A preliminary setup was designed to validate the measurement principle. It mainly consisted of a cuvette with a transparent bottom (PMMA), a laser pointer as a light source and an observation area (a piece of paper). After adjusting the initial conditions of the sample so the light was fully reflected, the validation was made under the hypothesis that when the diffraction index of the sample increased, a proportion of the light would be refracted.

Experiments were carried out with salty water in different concentrations, because the refractive index of this dissolution, according to bibliography, is similar to the refractive index of blood plasma.

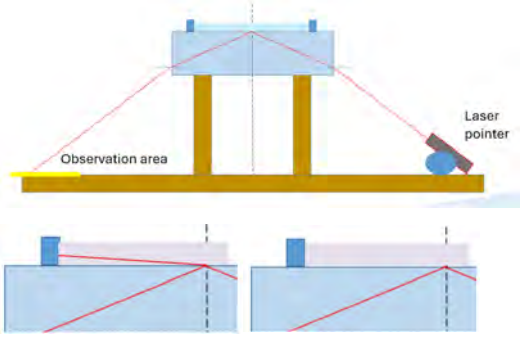

Fig. 2: Scheme of the setup (top). Scheme of how lighg is partially or fully reflected for different refractive indexes (center). Photograph of setup (bottom).

This experiment allowed to observe the phenomenon of having all the light reflected (Fig.2-centre-right) or only partially reflected (Fig.2-centre-left).

Some simulations were also carried out in order to find the optimum thickness of the plasma sample on the bottom of the cuvette. The thickness was adjusted so the maximum amount of light reached the detector receiving the reflected light. The simulations showed that the sample thickness should be over 4 mm.

Once the optimum sample thickness was established, the amount of light reaching the detector was also simulated, and a relationship between the energy arriving at the detector (E in arbitrary units) and the variation of the refractive index (n) in Fig.5. For these simulations, an incident light with a wavelength of λ=632.8 nm was used. The material of the cuvette was PMMA, whose refractive index is n=1.4887. Salty water was used in concentrations ranging from 0% (n=1.32921) to 4% (n=1.36844).

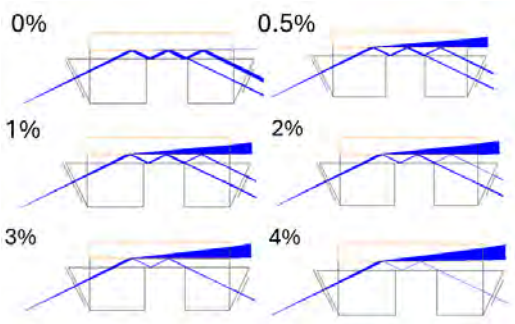

Fig. 3: Simulation of light reaching the detector (right side of the cuvette) for different salt concentrations (different refractive indexes)

2.3.- First prototype validation

With these results a prototype was built to be validated with salty water, using the same light source and salty water concentrations as in the simulations.

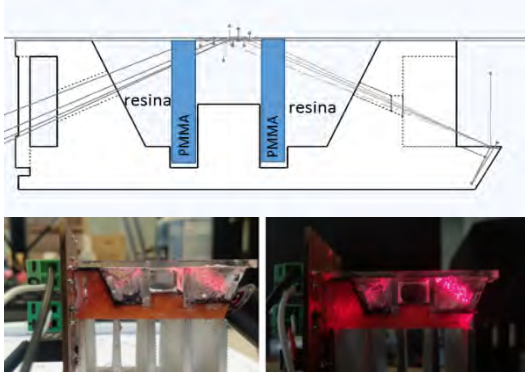

Fig. 4: Scheme and photographs of the prototype

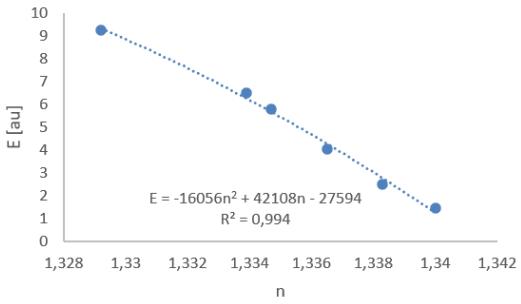

Fig. 5: Correlation between the energy reaching the detector (a.u.) and the refractive index of the samples in the cuvette

As a result, a minimum refraction angle of 63.2° and a maximum of 66.8° were measured, as can be seen in Fig.6.

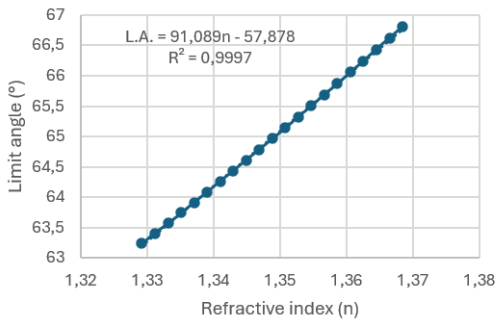

Fig. 6: Linear relationship between the angle and the refractive index

The resin used for the fabrication presented bubbles that led to a bad diffusion of the light, and for this reason the prototype was re-designed.

3.- Optimized prototype

Based on the results obtained, the next step taken was to fabricate a cuvette fully based on PMMA with polished optical finish. By doing this, the refractive index changes happening between the PMMA parts and the resin and the bubbles were completely avoided.

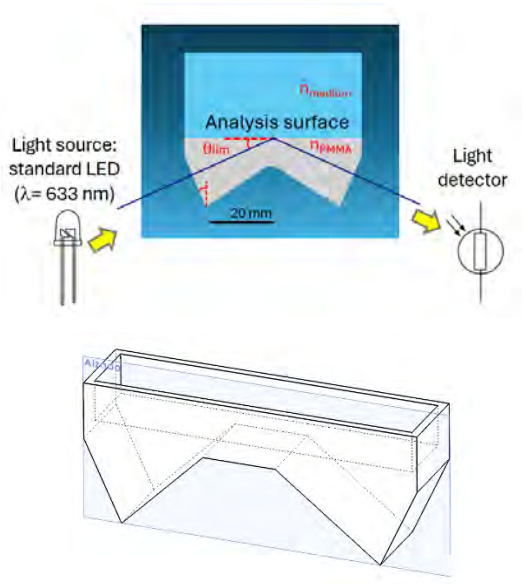

Fig. 7: Scheme of the cuvette with the position of the light source and detector (top). 3-dimensional image of the PMMA cuvette (bottom).

For collimating the incident light, we considered including a custom Fresnel lens on the cuvette surface on the side where light impinges.

Table 1: Fresnel lens dimensions

Parameter	***Value***
Diameter	*11 mm*
Grooves	*2.2 mm*
Inactive facet angle	*0.505°*
Curvature radius	*9.383 mm*
Maximum depth of the grooves	*0.67 mm*

3.2- Fresnel lens optimization and fabrication

In the framework of this work, injection moulding is the chosen fabrication process for the cuvette, so the device can be mass-produced in the future. The surface finishing required for a Fresnel lens, requires a very fine-tuning of the surface roughness, which must be smaller than 60 nm. Femtosecond lasers are becoming a versatile tool to mechanize injection mould surfaces with complex geometries while achieving low-roughness [6]. Over the first design some problems had to be solved in order to adapt the design into an optimized laser process:

(a) The slope of the lens walls needs to be adjusted so it has a minimum value for the demoulding process, and the angle is easy to achieve with the laser process.
(b) The amount of material to be eliminated by laser should be minimized for an optimum performance.
(c) The roundness of the peaks and valleys of the lens facets need to have a minimum value.

With all these constraints in mind, a final lens design was achieved, increasing the number of rings, and thus decreasing the thickness of the lens and also the amount of material to remove.

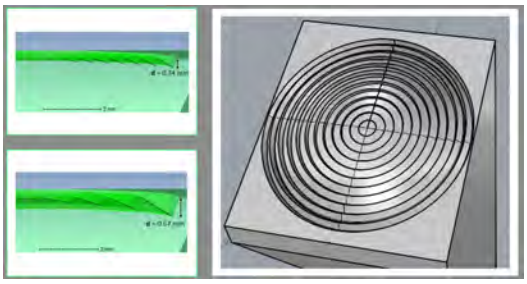

Fig. 8: Detail of the re-dimensioning of the number of rings and depth of the lens

As this lens will be fabricated by injection moulding, in the first place we manufactured some mould prototypes to study the influence of the mould surface finishing and coatings (such as silicon dioxide or titanium dioxide) in the injection and demoulding process. The final aim is to enhance the mould duration while easing the demoulding process [7].

The fabrication was carried out in AISI 304 stainless steel samples of 30 mm x 30 mm x 2 mm using a laser source Amplitude Satsuma HP, with a central wavelength of 1030 nm, maximum power of 10W, maximum pulse energy of 20µJ @ 500kHz and pulse widths between 350fs-10 ps. We carried out an optimization of the laser parameters to decrease roughness and eliminate directional texturing, while keeping a reasonable processing time. This was achieved by an experimental matrix of parameters playing with the (1) distance between processing planes, (2) velocity of the process, (3) angle of the processing direction between planes and (4) power of the laser source.

The topography of the mould was performed with the Sensofar S-Neox optical profilometer. The main conclusions obtained from the analysis are that (a) the designed topography is precisely reproduced by the laser engraving and (b) the surface roughness achieved is Sa=130 nm.

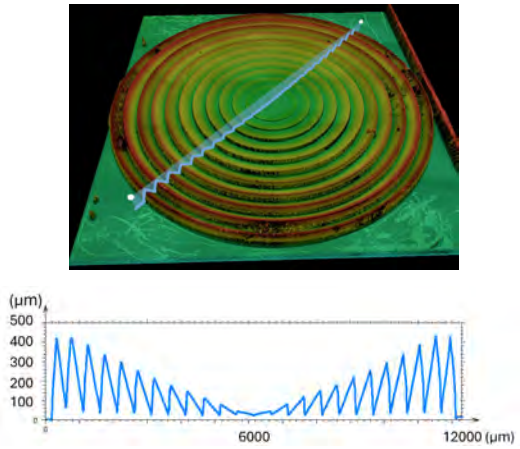

Fig. 9: 3D image of the mold surface and lateral profile across the diameter of the processed area

4.- Control of the position of the coagulated sample

From the results obtained, it becomes clear that it is important to have the plasma clot close to the bottom of the cuvette for an effective measurement of the refractive index. In the bibliography, there are several methods to position the fibers inside a plasma or blood clot: centrifugation, magnetic forces or electrical forces [8].

To evaluate the feasibility of using an electric field to place the clot in the best position on the cuvette for the refractive index measurement, we made some experiments to analyze the influence of applying a voltage to the clot.

To that end, we manufactured some platinum electrodes on alumina by sputtering and passivated them with silicon nitride obtained by Plasma Enhanced CVD (Chemical Vapour Deposition).

We used three different plasma coagulation tests, based on different principles: prothrombin (PT), Activated Partial Thromboplastin Time (APTT) and fibrinogen. In order to evaluate the coagulation times, we used commercially available normal and abnormal plasma (N and P respectively).

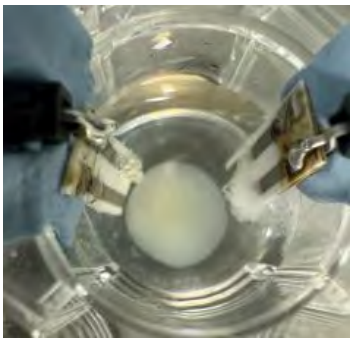

Fig. 10: Top view of a well in a well-plate with the two electrodes at both sides of a clot

Following this procedure, we applied increasing voltage values to analyze the behaviour of the clots formed with N and P plasma and the three different coagulation tests. As an example, we show in Fig.11 the average values of the curves obtained with the PT coagulation test for N and P plasmas. The difference in the behaviour of plasmas can be clearly seen. Similar trends are observed for all the coagulation tests, and also a difference between the two curves. In all cases, there is a point in the curve where the trend changes from increasing to decreasing current. This happens when the clot gets close to the anode side of the electrodes.

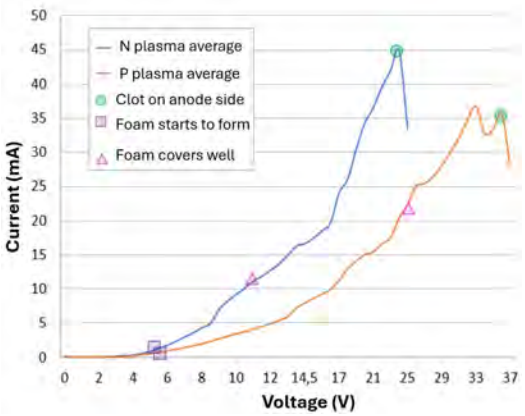

Fig. 11: Current vs voltage curves when applying increasing voltage values within the sides of a well with a formed clot, with the PT coagulation test

4.- Conclusion

In this work a principle to measure plasma coagulation through the measurement of a refractive index change has been validated. Based on it, a prototype to measure the blood plasma coagulation has been designed and some aspects of its performance have been simulated and characterized with the prototype. Finally, an additional method to position the plasma clot, that could be integrated into the device has been proposed and preliminary tests have been performed to validate its feasibility.

Acknowledgements: This work has been carried out within the BIOFOT project (CPP2021-009001), funded by the call Retos Colaboración 2021 of the "Ministerio de Economía y Competitividad" in Spain.

References

[1] Grzegorz Wilhelm, Paulina Mertowska, Sebastian Mertowski, Anna Przysucha, Jerzy Struzyna, Ewelina Grywalska, Kamil Torres, *"The Crossroads of the Coagulation System and the Immune System: Interactions and Connections"*, International Journal of Molecular Sciences, Vol. 24, 12563, 2023.

[2] Maria Grazia Lazzaroni, Silvia Piantoni, Stefania Masneri, Emirena Garrafa, Giuliana Martini, Angela Tincani, Laura Andreoli, Franco Franceschini, "*Coagulation dysfunction in COVID-19: The interplay between inflammation, viral infection and the*

coagulation system", Blood Reviews, Vol. 46, 100745, 2021.

[3] V. C.-L. L. F. Harris and A. J. Killard, "Coagulation monitoring devices: Past, present, and future at the point of care" TrAC Trends in Analytical Chemistry, vol. 50, 85, 2013.

[4] iLine Microsystems, microINR: The Next Generation Point-Of-Care and Self Testing System for OAT Monitoring. Donostia-San Sebastián, Spain: iLine Microsystems, 2014.

[5] "Technology - clotchip," Clotchip, May 16 2024. [Online]. Available: https://www.clotchip.com/technology/

[6] F. Bouchard, W. Wang, M. Soldera, A. F. Lasagni, *"Influence of Structure Size and Geometry on Wetting Behavior of PMMA Surfaces Imprinted with Laser-Textured Stamps"*, JLMN-Journal of Laser Micro/Nanoengineering Vol. 17, No. 2, 2022.

[7] G. Lucchetta, D. Masato, M. Sorgato, L. Crema, E. Savio, *"Effects of different mould coatings on polymer filling flow in thin-wall injection moulding",* CIRP Annals - Manufacturing Technology 65, 537–540, 2016.

[8] E. Hardy, Y. Sakurai, N. Sanjaya, A. Wolberg, *"Effect of Locally Applied Electricity On Clot Formation and Hemostasis",* Blood, 120(21), 2220, 2012

Caracterización robusta de retardadores mediante el uso de un interferómetro de doble rendija de Young

Robust characterization of waveplates by using a double slit Young interferometer

Inés M. DÍAZ-GARCÍA [(1)], Jesus DEL HOYO [(1)], Armando GONZÁLEZ-GARCÍA [(1)], Joaquín ANDRES-PORRAS [(1)], Angela SORIA-GARCIA [(1)], Isabel GONZÁLEZ-MARTÍNEZ [(1)], Karen P. SOTO-GONZÁLEZ [(1)], Javier ALDA [(2)], Luis Miguel SANCHEZ-BREA [(1)]

1. Universidad Complutense de Madrid, Facultad de Ciencias Físicas, Departamento de Óptica, Plaza de Ciencias 1, 28040, Madrid.
2. Universidad Complutense de Madrid, Facultad de Óptica y Optometría, Departamento de Óptica, Arcos de Jalón 118, 28037, Madrid.

Persona de contacto: Jesús DEL HOYO (*jhoyo@ucm.es*).

RESUMEN:

Se propone un nuevo método robusto para la caracterización experimental de elementos retardadores (retardancia y acimut) mediante un dispositivo que utiliza elementos polarizadores no ideales y sin necesidad de emplear otros retardadores previamente calibrados. El método consiste en la medida del desplazamiento de las franjas de interferencia producidas por un sistema de doble rendija, donde se añade un polarizador lineal en cada una de las rendijas, orientados ortogonalmente entre sí. Los resultados experimentales demuestran las capacidades del método, y los valores de retardancia y acimut obtenidos son coincidentes con el modelo teórico desarrollado y las especificaciones comerciales de los elementos medidos.

Palabras clave: Retardador, Eje Rápido, Retardancia, Interferencia, Doble Rendija de Young, Polarización.

ABSTRACT:

A novel robust method is proposed for the experimental characterization of retarder elements (retardance and azimuth) using a device that employs non-ideal polarizing elements, without the need for pre-calibrated retarders. The method consists of measuring the shift of interference fringes produced by a double-slit system, where two linear polarizers are placed at each slit, oriented orthogonally to each other. The experimental results demonstrate the capabilities of the method and provide reliable values of retardance and azimuth that are consistent with the developed theoretical model and the commercial specification of the elements under test.

Key words: Retarder, Fast axis, Retardance, Interference, Young Double Slit Interferometer, Polarization.

1.- Introducción

La polarización de la luz es una característica intrínseca de la radiación luminosa debido al carácter transversal de las ondas electromagnéticas [1]. El conocimiento del estado de polarización de un haz de luz informa de una serie de propiedades ligadas a la interacción de la radiación con los medios por los que se propaga e interacciona. Para la adecuada medida y control del estado de polarización se utilizan elementos que pueden calificarse, de manera simplificada, en dos grandes grupos: polarizadores y retardadores. Los polarizadores, o diatenuadores, seleccionan un estado de polarización convirtiéndose en proyectores o generadores de ese estado. Además, permiten variar la intensidad de la luz que les atraviesa. Los retardadores añaden un desfase, la retardancia, entre sus componentes propias. Existen muchos tipos de retardadores en función del material utilizado y de la geometría del mismo. Estos elementos, junto con los polarizadores, se utilizan en multitud de aplicaciones y sistemas ópticos que van desde la microscopía hasta los láseres [2].

Así pues, todo retardador tiene dos autoestados, que corresponden a los estados de polarización de la luz que no varían al atravesar el retardador. Uno de los autoestados, el autoestado rápido, se propaga más rápidamente que el otro, el autoestado lento. La diferencia de fase inducida entre estos dos autoestados es la retardancia. En la mayoría de las ocasiones, estos autoestados son estados linealmente polarizados y aparecen dos orientaciones, o ejes, de luz linealmente polarizada que, al atravesar el retardador, conservan su mismo estado de polarización. A estos ejes se les conoce como ejes rápido y lento, ya que están asociados a la velocidad de propagación de las componentes del vector de campo eléctrico asociado a cada una de las direcciones. Además, estos estados son ortogonales entre sí en la mayoría de casos, por lo que normalmente solo se trabaja con el autoestado rápido. A la orientación del eje rápido se le conoce como acimut.

Para conocer la retardancia y el acimut existen diversos métodos que utilizan moduladores ópticos o sistemas interferométricos que típicamente requieren dos longitudes de onda para su funcionamiento [3-7]. Algunos otros métodos emplean elementos retardadores de los cuales ya se conoce su retardancia y acimut, pero suelen requerir elementos de posicionamiento muy preciso y necesitan retardadores y polarizadores de muy alta calidad.

En esta contribución presentamos un método interferométrico para la caracterización de retardadores [8-10]. Este método se basa en el análisis del desplazamiento producido en un interferograma creado mediante una doble rendija de Young. La ventaja de esta propuesta es su robustez frente a tolerancias experimentales, a la vez que permiten el empleo de elementos polarizadores no ideales. Por otro lado, esta contribución puede considerarse como una evolución de la presentada previamente en la que se utilizaba un interferómetro de Michelson [8]. A pesar de que el esquema interferencial ha sido probado positivamente, su realización práctica ha puesto de manifiesto ciertos problemas del montaje, básicamente ligados a la necesidad de controlar de forma muy precisa la diferencia de caminos ópticos que se producen entre los brazos del interferómetro, especialmente cuando se utilizan fuentes de luz espectralmente no estables. Estos problemas experimentales han permitido evaluar otras opciones interferenciales que usan interferómetros por división del frente de onda, tales como el biprisma de Fresnel y la doble rendija de Young [10].

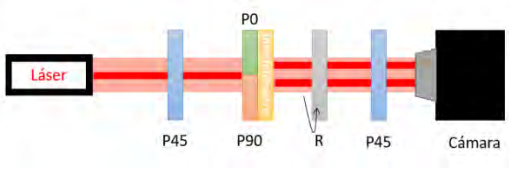

Fig. 1: Esquema experimental basado en un interferómetro de doble rendija. El haz láser es polarización linealmente y orientado a 45º mediante un polarizador, P45. La doble rendija (interferómetro) tiene cada una de las rendijas individuales asociadas a dos polarizadores lineales con orientaciones a 0º y 90º (elementos P0 y P90). El elemento que se desea caracterizar, R, se coloca tras la doble rendija sobre un soporte rotatorio. Antes de llegar a la cámara, se sitúa otro polarizador lineal, P45. La fuente de luz es un láser de diodo emitiendo a 635 nm.

2.- Método experimental

El sistema utilizado en esta contribución puede verse en la Fig. 1, donde se indica la disposición de los elementos polarizadores. El retardador que se desea caracterizar, R, se coloca detrás de la doble rendija, de manera que está iluminado por el campo interferencial producido [10].

El elemento esencial de este montaje es la doble rendija, donde cada una de ellas está asociada a un polarizador lineal. El montaje de estos polarizadores se puede observar en la fotografía de nuestro sistema (Fig. 2).

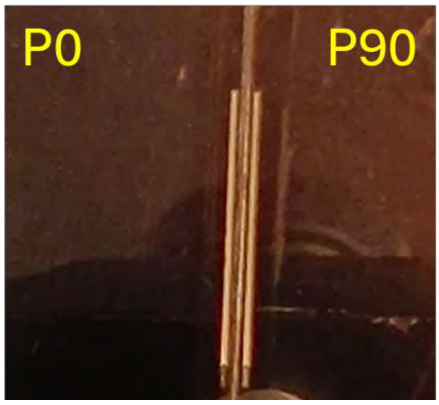

Fig. 2: Doble rendija en la que cada una de las rendijas tiene asociada un polarizador lineal orientados ortogonalmente, a 0° (P0) y 90° (P90).

Para analizar el dispositivo es necesario conocer la dependencia de la fase observada en la figura de interferencias en función del ángulo de rotación del elemento bajo prueba. Al girar el retardador, la figura interferencial se desplaza lateralmente. Este desplazamiento puede asociarse con un desfase producido en la luz que ha atravesado una rendija respecto a la de la otra mediante la ecuación

$$\phi = \frac{2\pi\Delta x}{P}, \qquad (1)$$

donde P es el periodo del patrón interferencial y Δx es el desplazamiento del patrón. Este desfase se puede relacionar con el acimut, θ, y la retardancia, Δ, como

$$tan\phi = \frac{-sin\Delta cos2\theta}{cos\Delta cos^2 2\theta + sin^2 2\theta}. \qquad (2)$$

Entonces, se puede caracterizar el retardador mediante la medición de ϕ para varios valores de θ y ajustando los valores obtenidos a la Ec. (2), o determinando los ángulos de giro en que ϕ es máxima y mínima, como se ilustra abajo en la Fig. 3.

Se ha evaluado la fiabilidad de este método de forma numérica, mediante el módulo Py-Pol [11], frente a tolerancias del montaje y desviaciones de los elementos polarizadores con respecto a su comportamiento ideal.

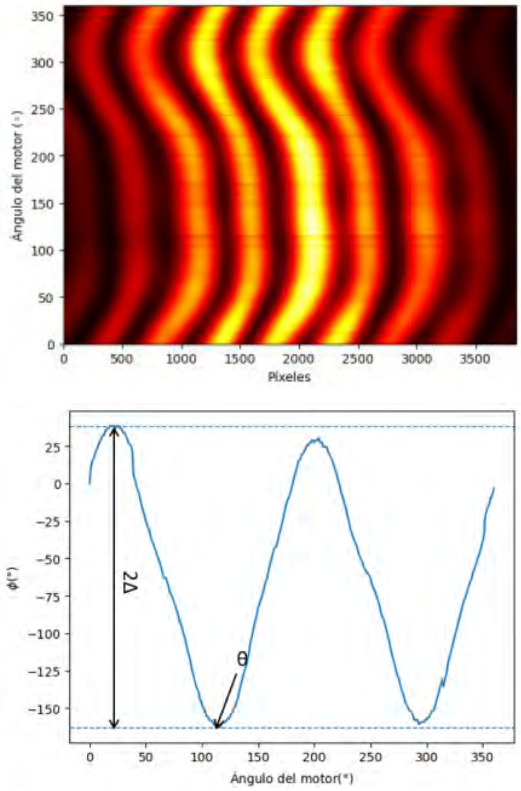

Fig. 3: Arriba: Mapa en falso color de las franjas de interferencia medidas con la cámara. Cada fila de la imagen corresponde con la suma en Y de la intensidad para un ángulo de giro de R diferente. Abajo: Variación de la fase interferencial en función del ángulo de rotación calculada a partir del movimiento del patrón en la dimensión X. A partir de estos datos se pueden obtener los valores de retardancia y de acimut, como se indica en la imagen.

3.- Resultados

Operacionalmente, el método propuesto requiere el registro de las franjas de interferencias producidas por la doble rendija conforme se rota el retardador que se desea caracterizar.

En el mapa representado arriba en la Fig. 3, se muestra la distribución de intensidad en el campo interferencial conforme se va rotando el retardador para uno de los retardadores estudiados. Es decir, cada línea de esta imagen corresponde a una posición angular del retardador en su montura. La gráfica de arriba de la figura 3 muestra la variación de la intensidad en función del ángulo de rotación. En la gráfica de abajo de la Fig. 3 se muestra la fase global observada mediante el interferómetro en función del acimut del retardador que se desea evaluar. A la vez, esta figura muestra la relación entre esta dependencia con los valores de retardancia y de acimut que se desea conocer. Todos estos datos corresponden a una lámina de cuarto de onda optimizada para una longitud de onda de 405 nm, que al medir en 635 nm resulta tener una retardancia de 210º.

4.- Conclusiones

En esta contribución se muestra un procedimiento robusto y, a la vez, sencillo para conocer la retardancia y el acimut de un retardador. El método proporciona valores coincidentes con los obtenidos mediante otros métodos bien aceptados y con las especificaciones comerciales del dispositivo medido. La ventaja de este método es que no es necesario emplear retardadores calibrados previamente, ni sistemas de luz policromática, y el montaje experimental es relativamente sencillo.

Agradecimientos: Este trabajo ha sido realizado gracias a los siguientes proyectos: "DISCREPO" PDC2023-145843.I00; "MINIMET" CPP2023-011006 del Ministerio de Economía y Competitividad, Unión Europea - Fondo Europeo del Desarrollo Regional; y al proyecto "VDOEST", referencia PID2022-138071OB-I00 del Plan Nacional de Investigación, Ministerio de Ciencia e Innovación. Joaquín Andrés-Porras y Ángela Soria-Garcia agradecen la financiación de sus contratos predoctorales de la UCM y del Banco Santander.

Referencias

[1] José J. GIL, Razvigor OSSIKOVSKI, *"Polarized light and the Mueller matrix approach"* (CRC press, 2022).

[2] K. SHAIK "*Spectral filters for laser communications*", (The Telecommunications and Data Acquisition Progress Report TDA PR 1991: 42-106).

[3] Giovanni Decot GALGANO, André Bohomoletz HENRIQUES, "*Determining the fast axis of a wave plate*", (Proceedings do ENFMC, 2006).

[4] Ming-Horng CHIU, Cheng-Der CHEN, Der-Chin SU, "*Method for determining the fast axis and phase retardation of a wave plate*" (JOSA A, 1996, vol. 13, no 9, p. 1924-1929).

[5] Guohua LI, Jizhong LI, Yi LI, "Determination of the fast axis with an infrared spectrometer for quartz and mica waveplates" (Applied optics, 1990, vol. 29, no 13, p. 1870-1871).

[6] Archana SHAH, Pallavi GHALSASI, "*Use of interference colours to distinguish between fast and slow axes of a quarter wave plate*", (European Journal od Physics, 2019, vol. 40, no 6, p. 065301).

[7] Petre Catalin LOGOFATU, "*Simple method for determining the fast axis of a waveplate*", (Optical Engineering, 2002, vol. 41, no 12, p. 3316-3318).

[8] J. del HOYO et al. "Interferometric method for simultaneous characterization of retardance and fast axis of a retarder" (Optics and Laser in Engineering, 2024, vol 179, p. 108262).

[9] J. del HOYO et al. "Dispositivo optoelectrónico para determinar de forma simultánea la retardancia absoluta y el ángulo de ghiro de un retardador óptico", OEPM 2024, P# 2936683.

[10] Armando GONZÁLEZ-GARCÍA, "Dispositivo optoelectrónico basado el interferómetro de Young para caracterizar un retardador óptico". Memoria de Trabajo de Fin de Máster. UCM (2024)

[11] Jesús DEL HOYO, Luis Miguel SANCHEZ-BREA, Ángela SORIA-GARCIA, "*Open source library for polarimetric calculations py_pol*", (Computational Optics 2021 SPIE, 2021. p. 12-20)

Fotónica integrada

IMB-CNM Silicon Nitride Platform for Integrated Photonics

Marçal Blasco-Solvas, Joaquín Hernández-Betanzos, Jad Sabek, Carlos Domínguez-Horna, and Joaquín Faneca

Instituto de Microelectrónica de Barcelona, IMB-CNM (CSIC), Campus UAB, 08193 Barcelona, Spain

Contact: Joaquín Faneca (joaquin.faneca@imb-cnm.csic.es).

ABSTRACT:

Silicon nitride-based photonic integrated circuits (PICs) are a well-established platform that enable applications beyond the limitations of silicon-on-insulator-based PICs. This paper presents the latest advancements in the IMB-CNM (CSIC) silicon nitride platform for integrated photonics, including the development of building blocks in the visible spectrum, studies on refractive index and auto-fluorescence, and the integration of CMOS-compatible silicon nitride modulators in the C-band using crystalline and amorphous silicon. Additionally, the Multi-Project Wafer (MPW) services and dedicated runs offered by IMB-CNM to fabless companies are discussed.

Key words: Photonic integrated circuits, silicon nitride, visible range, photoluminescence, refractive index, semiconductor fabrication, clean room, CMOS compatible, modulator, multi-project wafer.

1. Introduction

Silicon nitride (SiN) is emerging as an alternative material for photonic integrated circuits (PICs), expanding the capabilities of silicon-on-insulator (SOI), one of the leading technology platforms for PICs. With its broad transparency window—ranging from the visible to the mid-infrared spectrum—along with low optical losses and the absence of two-photon absorption at telecommunication wavelengths, SiN serves as an ideal complement to silicon, enabling applications requiring visible light operation or high-power nonlinear functionalities, while still supporting telecommunication wavelengths, where it may be preferred over SOI for certain applications.

Furthermore, SiN is fully compatible with Complementary Metal-Oxide Semiconductor (CMOS) fabrication processes, facilitating cost-effective and large-scale manufacturing. Also, its refractive index contrast with silica (2 vs 1.5), is lower than that of silicon (3.5 vs 1.5), making SiN more tolerant to fabrication errors [1]. Another interesting property of SiN that is not present in SOI is the manufacturing flexibility. SiN can be deposited by Low Pressure Chemical Vapor Deposition (LPCVD) and by Plasma-Enhanced Chemical Vapor Deposition (PECVD), allowing to combine SiN with other photonic structures [2]. This gives SiN multilayer stacking capabilities, while SOI typically requires wafer bonding for similar stacking, which involves precise alignment and additional processing steps [3]. As a result, SiN multilayer stacking provides greater process flexibility, potentially lower fabrication costs, and easier integration with standard semiconductor manufacturing techniques, while enabling higher component density through vertical integration.

In this work, we present the IMB-CNM SiN photonics platform advancements comprising visible-range passive building blocks, the tuneability of the refractive index and photoluminescence (PL) of the material, and CMOS-compatible SiN optical modulators;

following with a section regarding the multi-project wafer (MPW) services offered by this platform and finally concluding with a section that explains the future objectives and prospects.

2. Visible range integrated photonics

One of the most interesting properties of SiN is its broad transparency window, which encompasses the whole visible range of the spectrum. This, together with other properties mentioned in the introduction, gives SiN the potential to become the leading PICs technology platform for applications that require visible light, such as biosensing and spectroscopy, opto-genetics, quantum computing, metrology, underwater communications, light sources, imaging or display technologies. Because of that, one of the objectives of the SiN photonic platform of IMB-CNM is to develop a full process design kit (PDK) in the visible range of the spectrum, to enable designers from fabless companies and research centers to exploit the characteristics of this well-studied material, the same way it has been doing it for years with telecommunications wavelengths [4].

So far, at the IMB-CNM SiN platform various building blocks in the visible range of the spectrum have been designed and tested, including waveguides, bent waveguides, multi-mode interferometers (MMIs) and grating couplers [5]. These components have been designed and fabricated for purple, blue, green and red wavelengths (405, 480, 520 and 633 nm, respectively), some of them shown in fig. 1 [6].

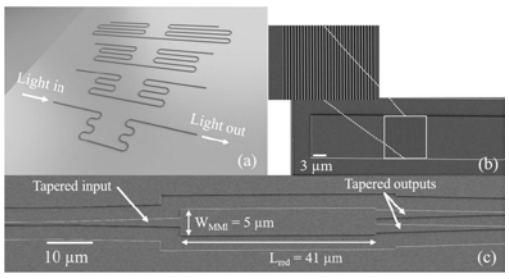

Fig. 1 (a) Schematic of waveguides of different lengths and scanning electron microscope images of (b) a grating coupler and (c) an MMI.

Measurements of the losses have been performed for wavelengths of 633 nm, see table I, reaching state-of-the-art losses while maintaining a high confinement factor of 90.5%, allowing high integration density.

Table 1 Optical performance of the SiN building blocks operating at 633 nm.

Component	***Losses***
Waveguide	*3.6 ± 0.2 dB/cm*
Bend	*0.20 ± 0.03 dB*
Grating Coupler	*11.7 ± 0.6dB*
MMI	*0.20 ± 0.04 dB*

3. Silicon nitride tuneability

When working with visible wavelengths, SiN can exhibit auto-fluorescence, an unwanted effect that may interfere with the propagating signal. A notable characteristic of SiN is its tuneability, including the ability to modify its auto-fluorescence properties. By adjusting the precursor gases during deposition and applying different thermal annealing processes, it is possible to achieve a range of refractive indices and PL responses. [7].

3.1. Photoluminescence

Two different ratios between the precursor gases, dichlorosilane (DCS) and ammonia (NH3), were studied in the platform, one for stoichiometric SiN (SSN), with a ratio DCS/NH3 of 0.33, and one for silicon-rich SiN (SRN) with a ratio of 3.6. Furthermore, different thermal annealing processes were applied, including both conventional furnace annealing and rapid thermal annealing (RTA) at 950ºC and 1100ºC. Additionally, the effect of the annealing atmosphere was studied by performing the treatments in nitrogen and argon. In fig. 2 the highest and lowest PL responses obtained in each atmosphere, 2.a for the SSN and 2.b for the SRN, are shown. The results obtained show that a considerable PL reduction of 95% for SSN can be achieved with a RTA of 30 s performed at 1100ºC in argon atmosphere. Depending on the signal wavelength, another approach to minimize interference with auto-fluorescence is the use

of SRN, where the PL peak is red-shifted between 140 and 190 nm compared to SSN.

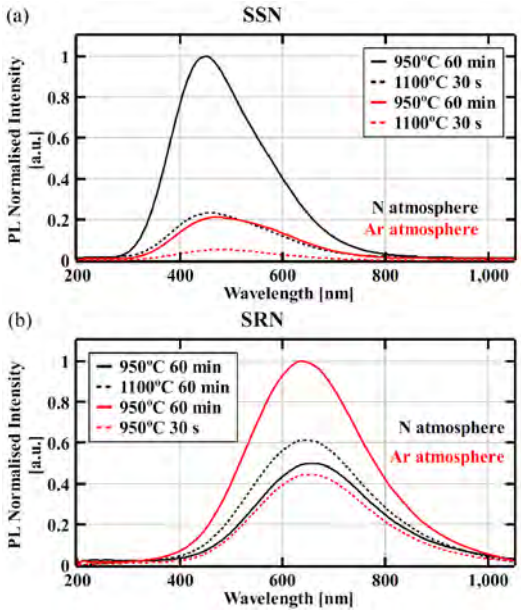

Fig. 2 Comparison between the highest and lowest PL response for nitrogen and argon atmosphere annealing for (a) SSN and (b) SRN.

This shift is also accompanied by an increase in the refractive index increase of up to a 7%, as explained in the following section.

3.2. Refractive index

The variation in deposition conditions and subsequent thermal annealing processes not only affects the PL response of the material but also changes its refractive index. Table 2 shows the values achieved by each treatment. This refractive index tuneability also enables the possibility to obtain, for example, multilayer stacking circuits with different material properties.

To show its potential, an asymmetrical vertical directional coupler between an SRN and an SSN waveguide has been designed and simulations show a coupling length of 9.8 μm, with a coupling power of 95.8%. A schematic of the component is shown in fig. 3. This would allow to change light from one layer to another, taking advantage of the properties of each one individually.

Table 2 Refractive index values at 633 nm of SiNx films as deposited, and for two different annealing processes using different atmospheres.

Annealing process	*Losses*	*N.A.**	*950ºC 60 min*	*1100ºC 30 s*
As deposited	*SSN*	*2.035*	*...*	*...*
	SRN	*2.206*	*...*	*...*
N atmosphere	*SSN*	*...*	*2.079*	*2.086*
	SRN	*...*	*2.229*	*2.2075*
Ar atmosphere	*SSN*	*...*	*2.089*	*2.100*
	SRN	*...*	*2.190*	*2.208*

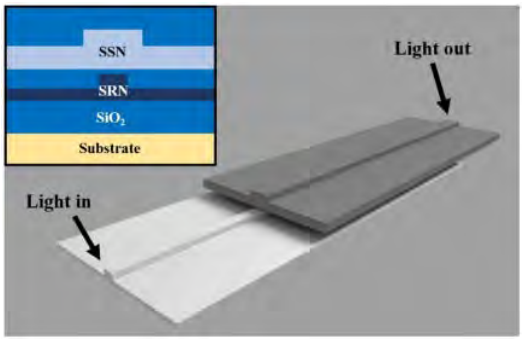

Fig. 3 3D schematic of the designed vertical coupler, with the cross-section inset.

4. CMOS compatible SiN modulators

The dielectric nature of SiN inhibits the direct modulation of its refractive index. Therefore, external indirect methods are required to achieve changes in this property. To address this limitation, a thin amorphous (a-Si) or crystalline (c-Si) silicon p-n junction positioned either on top or beneath the SiN structure to enable active modulation in the C-band (1550 nm). The main proposal for active tuning of the optical signal is to accumulate or deplete charge carriers in the p-n junction in order to modify the refractive index, taking advantage of the carrier plasma dispersion effect. At the same time, the effective refractive index (n_{eff}) of the Si/SiN waveguide (WG) system is altered, which means that the mode of the propagated wave exhibits different n_{eff} as a function of the charge carrier excess due to the applied bias voltage. Fig. 4 shows a schematic of the device.

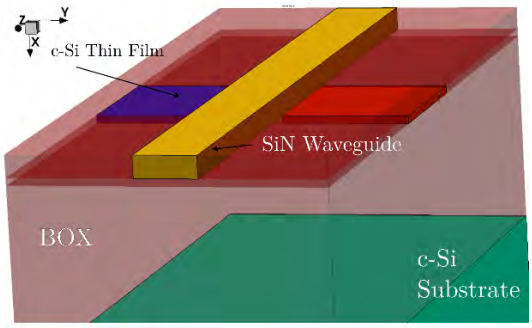

Fig. 4 3D schematic of the designed lateral p-n junction under the SiN waveguide.

The fabrication starts from a SOI wafer with a 50 nm thick c-Si layer. The process involves etching all the Si except for the area of the modulator. Afterward, the implantation occurs, followed by the deposition of a SiO_2 layer on top, which is then planarized to the level of the c-Si modulator. The initial approach involves using a symmetrical c-Si junction, with the p-region and n-region each having a width of 500 nm. The metallurgical junction is at the WG center. The p-doped side has a boron concentration of 10^{18} cm^{-3}, and the n-doped side has a phosphorus concentration of 10^{17} cm^{-3}. In the next step, 300 nm of SiN are deposited using LPCVD, and the structures are patterned by etching. Finally, a 2 µm SiO_2 capping layer is deposited to protect the device. Final SiO_2 cladding etching is required to reach the contacts. Transversal cut of the modulator can be seen in the fig. 5.

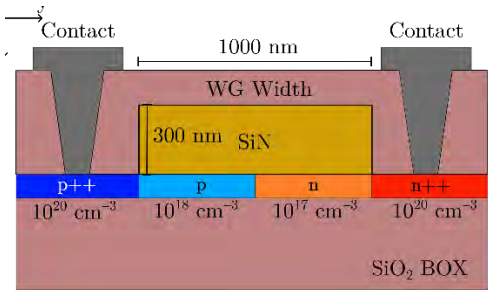

Fig. 5 Transversal cut of the designed lateral p-n junction beneath the SiN waveguide.

According to the electrical results of the lateral p-n junction with acceptor and donor concentrations of 10^{18} cm^{-3} and 10^{17} cm^{-3}, respectively, achieving a depletion width of 1 µm, covering the whole WG width, requires a high reverse voltage bias, which can lead to device breakdown. To increase the Δn_{eff} and reduce the footprint of the modulator, more free carriers are required. For the symmetrical p-n junction, a forward bias near the high injection condition is proposed to increase the carrier density in the c-Si film, thereby overcoming the breakdown voltage issue associated with reverse bias. Fig. 6 displays the value of n_{eff} for different voltages ranging from 0V to V_F = 1V.

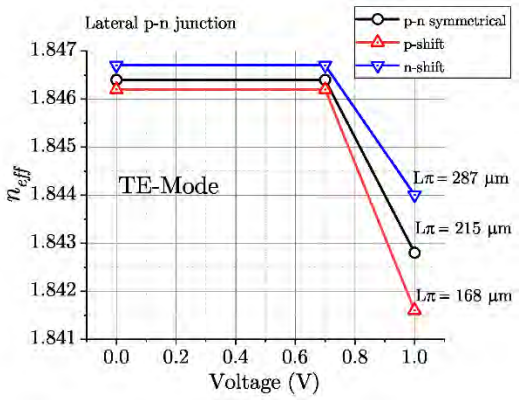

Fig. 6 Effective refractive index for the TE mode for different lateral p-n junctions under forward bias.

Table 3 Comparison of CMOS compatible SiN-based optical modulator performance using crystalline silicon, detailing modulator length, power consumption and insertion losses.

Modulator	*Lπ (µm)*	*Pc (mW)*	*IL (dB)*
p-n symmetrical	*215*	*16.95*	*3.0*
p-shift	*168*	*13.24*	*3.2*
n-shift	*287*	*22.62*	*2.2*

For 1V and transversal electric mode (TE), three different configurations can be found: a symmetrical p-n junction, a p-n junction with the n-region covering the width of the WG and the p-region positioned on one side away from the WG (n-shift), and swapping the positions of the n-region and p-region, (p-shift). Table 3 shows the comparison of the performance of these different lateral p-n junction modulators including the modulator length to achieve a π phase-shift (L_π), power consumption (P_c) and

insertion losses (IL). A more detailed analysis, design, and operation of these devices can be found in [8].

5. IMB-CNM silicon nitride services

In this framework, the latest advancements and future prospects of the IMB-CNM open-access photonic foundry, based on CMOS-compatible silicon nitride technology, are presented and analyzed. The access models enabled by generic integration and process design kits (PDKs) are outlined, along with a discussion of the available technical features and tools. There are two different approaches: the multi-project wafer (MPW) approach and the dedicated run approach.

5.1. Multi-project wafer

The MPW approach enables cost-sharing by allowing multiple customers to fabricate their PICs within the same batch or wafer run. By distributing costs across different users, this method significantly reduces expenses, as customers only pay for the specific area of the chip they utilize. This strategy is particularly suitable for research institutions, universities, and companies looking to develop prototypes and optimize processes at an industrial level, with the goal of eventually transferring the technology to full-scale production.

The large-scale fabrication of 100/150 mm wafers using IMB-CNM technology further enhances cost efficiency, as seen in fig.7.

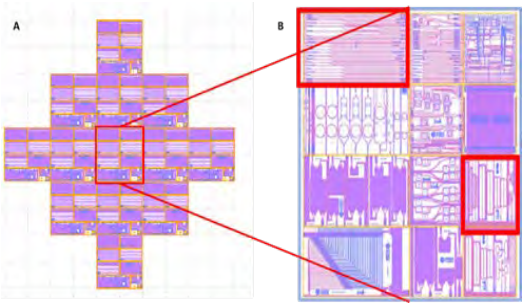

Fig. 7 Scheme representing the PICs layout during the MPW: (a) shows an example of a final wafer layout with all the chips and (b) a single chip layout with the dices of different partners.

Furthermore, the MPW approach takes advantage of an open foundry with well-defined processes, eliminating the need for individual fabrication facilities and shortening design cycles. Collaborating with a design house which offers a library aligned with the MPW foundry for wavelengths of 1310 nm and 1550 nm, further optimizes the process by minimizing design iterations and avoiding licensing fees. This approach offers an efficient solution for streamlining photonic integration and manufacturing.

5.2. Dedicated process approach

The dedicated run approach offers a fully customized wafer fabrication process for a single customer, providing maximum flexibility in design, process modifications, and production volume. This method is particularly suitable for those requiring tailored PICs beyond the constraints of shared MPW runs.

Although it demands a larger investment, multiple design software licenses, and specialized expertise in integrated optics, it offers significant advantages. Customers can fully customize materials, process steps, and device architectures to meet specific performance requirements. Additionally, the approach allows for greater control over fabrication parameters, enabling the development of innovative designs and proprietary technologies. The flexible fabrication line ensures adaptability to evolving needs, making it an ideal solution for those transitioning from prototyping to pilot production while maintaining full ownership of their designs.

5.3. Fabrication process overview

From a technological perspective, the PIC fabrication process begins with a silicon wafer, where a 2.5 µm silicon oxide layer is formed through thermal oxidation. This is followed by the definition of shallow and deep waveguides, achieved using LPCVD of a 300 nm Si_3N_4 layer, stepper photolithography, and 150/300 nm dry etching.

To ensure protection, a 2 µm cladding layer is deposited using PECVD of SiO_2. Selective area trench definition is performed using stepper photolithography and SiO_2 dry and/or wet etching. These trenches can be engineered to expose the silicon nitride waveguide, enabling further processing or device

integration. Finally, thermo-heaters can be integrated through metal deposition on top of the SiO_2 cladding, enabling the implementation of passive dynamic devices within the PICs. The technological process is illustrated in fig.8.

Fig. 8 The different technological steps and basic structures.

6. Future work, trends and prospects

The number of silicon nitride-based applications in the visible range is expected to grow in the coming years. To maintain its mission of supporting industry and innovation, IMB-CNM will continue advancing its silicon nitride photonic platform, finalizing a complete PDK optimized for the visible range, which will be available to fabless companies and research centers. A key focus will be the development of CMOS-compatible silicon nitride optical modulators, enabling efficient signal processing and integration with existing semiconductor technologies. Additionally, IMB-CNM will focus on tuning silicon nitride's optical properties to enhance its use in nonlinear and quantum applications, expanding its role in next-generation photonic technologies. IMB-CNM will also further develop its MPW program in silicon nitride photonic integrated circuits, providing a robust platform for cost-effective prototyping. By actively participating in European pilot lines and competence centers under the Chips Joint Undertaking, IMB-CNM aims to enhance access to cutting-edge photonic technologies. These efforts position IMB-CNM at the forefront of silicon nitride photonics innovation, reinforcing its leadership in PICs.

***Acknowledgements*:** We would like to acknowledge Iñigo Artundo and David Domenech from VLC Photonics for their constant support and advice. This research was funded by the funding agency MCIN/AEI/10.13039/501100011033 and by the European Union "NextGenerationEU"/PRTR under the projects: TED2021-132584B-C22, PLEC2022-009381, FJC2020-042823-I, RYC2023-043256-I and CEX2023-001397-M.

References

[1] Roel BAETS, Ananth Z. SUBRAMANIAN, *et al.*, *"Silicon Photonics: silicon nitride versus silicon-on-insulator"*, in Proceedings of Optical Fiber Communications Conference and Exhibition (OFC), 2016.

[2] Pascual MUÑOZ, Gloria MICÓ, *et al.*, *"Silicon Nitride Photonic Integration Platform for Visible, Near-Infrared and Mid-Infrared Applications"* , Sensors, 17, 2088, 2017

[3] Martin EIBELHUBER, Thorsten MATTHIAS, *et al.*, *"Advanced bonding techniques for photonic integrated circuits"*, in Proceedings of CS Mantech Conference, 2014

[4] IMB-CNM (CSIC) Silicon Nitride Photonic Integration Platform, https://www.imb-cnm.csic.es/en/micro-and-nanofabrication-clean-room/silicon-nitride-photonic-integration-platform

[5] Marçal BLASCO-SOLVAS, Berta FERNÁNDEZ-VIOR, *et al.*, *"Silicon Nitride Building Blocks in the Visible Range of the Spectrum"*, Journal of Lightwave Technology, 42, 17, 6019-6027, 2024.

[6] Joaquín FANECA-RUEDAS, Jad SABEK, *et al.*, *"Basic building blocks development for a SiN platform in the visible range"*, in Proceedings of IEEE 17th International Conference on Group IV Photonics, 2021.

[7] Marçal BLASCO, Samuel DACUNHA, *et al.*, *"Silicon nitride stoichiometry tuning for visible photonic integrated components"*, Applied Physics Letters, 124, 22, 221104, 2024.

[8] Joaquín HERNÁNDEZ-BETANZOS, Marçal BLASCO-SOLVAS, *et al.*, *"Advancements in CMOS-Compatible Silicon Nitride Optical Modulators via Thin-Film Crystalline or Amorphous Silicon p-n Junctions"*, Photonics, 11(8), 762, 2024.

Simulador eficiente de antenas ópticas integradas con radiación en ángulos arbitrarios

Elio Godoy-Lorite [(1)], Laureano Moreno-Pozas [(1)], Robert Halir [(1)], Alejandro Ortega-Moñux [(1)], J.Gonzalo Wangüemert-Pérez [(1)], Iñigo Molina-Fernández [(1)]

1. Telecommunication Research Institute (TELMA), Universidad de Málaga, Louis Pasteur 35, 29010 Málaga, Spain.

Contact: Elio Godoy-Lorite (eliogl@ic.uma.es).

ABSTRACT

The increasing interest in free-space optical communications (FSOC) and Light Detection and Ranging (LiDAR), requires gratings capable of emitting highly collimated beams, with Rayleigh distances in the order of centimeters or even meters. This requires the design of weak-strength gratings, which radiate little amount of power per unit length. In addition, dynamic beam steering is essential for these applications, enabling efficient environmental scanning and tracking of moving objects. This work aims to develop an accurate and efficient simulation tool to accelerate the design of weak-strength gratings, and study the effect of feeding light with arbitrary angles into the antenna. Comparison with results obtained with a full-vectorial 3D FDTD simulator, shows very good agreement with the advantage of decreasing simulation times by up to a factor of $\times 514$.

Key words: Integrated Photonics, Silicon Photonics, grating coupler, metamaterial, simulator, pertubative method, steering, small divergence, FSO, antenna.

1.- Introducción

La fotónica del silicio se posiciona como una de las soluciones más prometedoras para abordar las limitaciones de la microelectrónica tradicional en términos de velocidad y consumo energético [1]. Existen una multitud de aplicaciones en fotónica del silicio, incluyendo el biosensado [2], las comunicaciones cuánticas [3], las comunicaciones en espacio libre [4] o el LiDAR [5]. Uno de los elementos clave en cualquiera de estas aplicaciones, son las rejillas de difracción, que funcionan como antenas ópticas integradas. Estas rejillas permiten hacer de interfaz entre el chip y una fibra o el chip y el espacio libre.

Cuando se diseñan para proyectar haces en espacio libre, las antenas suelen ser de baja fuerza de radiación para conseguir haces cuya distancia de Rayleigh supere los centímetros [6], esto se traduce en anchos de haz por debajo del grado [7].

En este contexto, explorar estructuras periódicas que presenten perturbaciones débiles, ya sea por la profundidad de grabado o por el contraste de los materiales empleados, está cobrando interés en la literatura para realizar antenas de baja fuerza de radiación. [7].

Para facilitar el diseño de estas antenas, en un trabajo previo [8] se presentó un simulador electromagnético de estructuras periódicas en las que la dirección de propagación coincide con la dirección de la periodicidad. Este simulador se basaba en el método perturbacional (MP) propuesto en [9], y demostró dar resultados excelentes [8]. En el trabajo aquí presentado se presenta una versión mejorada del simulador previo. En particular, este simulador permite evaluar las características de radiación de la antena

cuando ésta es alimentada con incidencia oblicua. Esto tiene aplicaciones para evaluar el funcionamiento de antenas escaneables que controlen la dirección de apuntamiento en función del ángulo de alimentación. El trabajo se apoya en la teoría general planteada en [10], y aquí es adaptada para poder seguir empleando el método perturbacional. El resto de secciones de este trabajo se han organizado del siguiente modo. En la Sección 2 se plantea la teoría necesaria para el desarrollo del simulador, y en la Sección 3 se comparan los resultados y los tiempos de cómputo con un simulador 3D-Full Vectorial FDTD. Se demuestra que los resultados conseguidos con este simulador son precisos, ya que el error relativo de varias métricas de la antena está por debajo del 2%. Además, se consiguen reducir los tiempos de simulación hasta ×514.

En este trabajo, se sigue la siguiente notación: los vectores unitarios se denotan como $\hat{a}$, mientras que se utiliza $\vec{b}$ para denotar vectores no unitarios, los vectores columna se denotan como $\bar{c}$ o $\bar{C}$, y $\bar{\bar{D}}$ para las matrices.

2.- El método perturbacional para excitación oblicua

Este trabajo puede considerarse la continuación natural del trabajo previo presentado en [8]. En este trabajo se presentó un análisis modal de estructuras periódicas cuya perturbación es débil. Los modos de estas estructuras periódicas, denominados modos Floquet-Bloch (FB) [11, 12], son también periódicos. Mediante análisis perturbacional, ya que la estructura considerada en [8] presenta una perturbación débil debida al grabado parcial del núcleo, cada armónico del modo puede determinarse resolviendo un problema de líneas de transmisión independiente. Cada línea representa una capa dieléctrica de la estructura, que depende del orden del armónico y de su polarización. En [8], solo se consideró el análisis modal de los modos Floquet cuya propagación se realiza en el eje x de la Figura 1 (a), es decir, los modos determinados tienen una frecuencia espacial nula en dirección y.

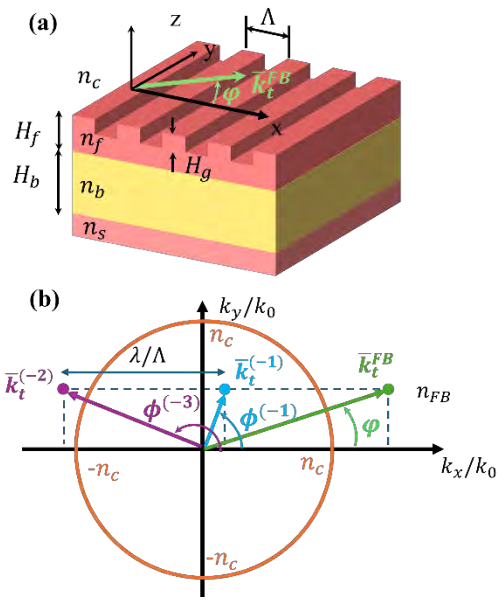

Fig. 1. (a) Rejilla de difracción con excitación oblicua. El índice de refracción de las capas, así como su altura, se suponen arbitrarios. (b) Proyección en el plano XY del diagrama k de la cubierta cuando el modo se propaga con un ángulo φ respecto a x. Los vectores están representados en el dominio de la frecuencia espacial, k_x, k_y.

En este trabajo, se extiende este análisis perturbacional para modos FB que puedan propagarse con ángulos arbitrarios en el plano del chip (plano *XY* en la Figura 1(a)), es decir, con un ángulo φ con respecto al eje x. Esto hace que la polarización del campo no pueda considerarse TE o TM pura, y por tanto no sea posible resolver cada armónico de forma independiente, mediante la resonancia transversal de una estructura de líneas de transmisión en serie.

Al considerar modos que pudieran propagarse de forma oblicua por la estructura, sus armónicos van a presentar una frecuencia espacial en dirección y distinta de cero, tal y como se observa en la Figura 1(b). En esta figura se representan los vectores de onda de cada uno de los armónicos proyectados en el plano del chip, $\vec{k}_t^{(n)}$, donde $n = 0, -1, \ldots$ representa el orden del armónico. Se comprueba que la constante de fase de todos los armónicos en el eje y, k_y, es la misma, cumpliendo las condiciones de contorno de la estructura periódica.

No obstante, como la estructura presenta una periodicidad en la dirección x, cada armónico tendrá una frecuencia espacial distinta en la dirección x, k_x, según la ecuación siguiente:

$$\vec{k}_t^{(n)} = k_{t,x}^{FB}\hat{x} - n\frac{2\pi}{\Lambda}\hat{x} + k_{t,y}^{FB}\hat{y}, \qquad (1)$$

donde Λ es el periodo de la estructura, y $\vec{k}_t^{FB} = k_{t,x}^{FB}\hat{x} + k_{t,y}^{FB}\hat{y}$ es el vector de onda del modo. A partir de (1), es posible calcular los ángulos de radiación en esféricas de cada armónico como [13]

$$\begin{aligned}\phi^{(n)} &= \operatorname{asin}\left(\frac{k_{t,y}^{n}}{|\vec{k}_t^{(n)}|}\right)\\ \theta^{(n)} &= \operatorname{asin}\left(\frac{|\vec{k}_t^{(n)}|}{k_0 n_c}\right)\end{aligned}, \qquad (2)$$

donde $\phi^{(n)}$ es, según la Figura 1(b), el ángulo de cada armónico con el eje x. $\theta^{(n)}$ es el ángulo que forma cada armónico con respecto al eje z, k_0 es el número de onda en el vacío, y n_c es el índice de refracción de la cubierta.

Para poder realizar el análisis modal, se ha de aplicar la condición de resonancia transversal en el eje z. Para ello se va a descomponer el operador nabla, $\vec{\nabla}$, y los campos electromagnéticos en la componente perpendicular al plano del chip (componente z) y en las componentes paralelas al plano del chip, denominadas componentes transversales, es decir:

$$\begin{cases}\vec{\nabla} = \vec{\nabla}_t + \vec{\nabla}_z\\ \vec{\mathrm{E}} = \vec{\mathrm{E}}_t + \vec{\mathrm{E}}_z\\ \vec{H} = \vec{H}_t + \vec{H}_z\end{cases}. \qquad (3)$$

Introduciendo esta descomposición en las ecuaciones de Maxwell, y tras una serie de manipulaciones matemáticas, se llega al sistema de ecuaciones diferenciales siguiente:

$$\begin{aligned}\frac{\partial \bar{E}_t^{(n)}}{\partial z} &= -j\bar{\bar{Z}}^{(n)}\bar{H}_t^{(n)} + \bar{\rho}^{(n)}\\ \frac{\partial \bar{H}_t^{(n)}}{\partial z} &= -j\bar{\bar{Y}}^{(n)}\bar{E}_t^{(n)} + \bar{\xi}^{(n)}\end{aligned}. \qquad (4)$$

En (4), las componentes de los campos están acopladas por el efecto de la matriz

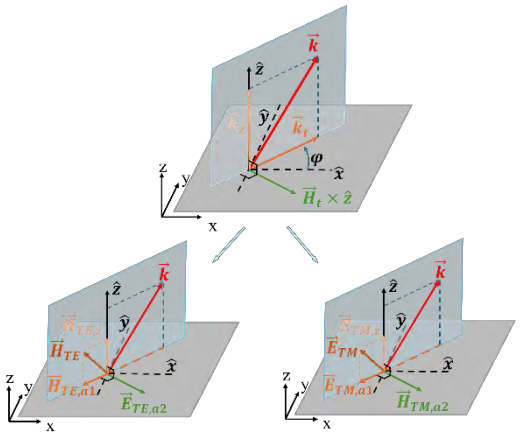

Fig. 2. Cambio de base para una onda genérica polarizada que se propaga con un ángulo φ con respecto al eje x.

impedancia $\bar{\bar{Z}}^{(n)}$ y admitancia $\bar{\bar{Y}}^{(n)}$, que son matrices 2x2, donde n es el orden del armónico n-ésimo. Los vectores columna $\bar{\rho}^{(n)}$ y $\bar{\xi}^{(n)}$ contienen la información de la perturbación, producida por la estructura periódica.

Para poder desacoplar las componentes de los campos, es necesario expresar los campos electromagnéticos en una base ortogonal donde sí sea posible distinguir entre polarización TE y TM pura.

Gráficamente, se puede explicar a partir de la Figura 2, donde se ilustra el cambio de base para un caso genérico de una onda propagándose con un cierto ángulo φ con respecto al eje x. Claramente, si se trabaja con la base canónica $\boldsymbol{\mathcal{B}} = \{\hat{x}, \hat{y}, \hat{z}\}$, no es posible separar en polarización TE y TM un campo polarizado de forma arbitraria. No obstante, eligiendo la siguiente base

$$\boldsymbol{\mathcal{M}} = \{\hat{k}_t, \hat{k}_t \times \hat{z}, \hat{z}\} = \{\hat{a}_1, \hat{a}_2, \hat{z}\}, \qquad (5)$$

cualquier campo se puede expresar como combinación lineal de la polarización TE y TM.

Esta idea se traduce matemáticamente en diagonalizar las matrices impedancia y admitancia en (3). Así, la matriz impedancia se expresa como

$$\bar{\bar{Z}}^{(n)} = \bar{\bar{A}}^{(n)}\bar{\bar{Z}}_D^{(n)}\bar{\bar{A}}^{(n)^{-1}}, \qquad (6)$$

siendo $\bar{\bar{A}}^{(n)}$ la matriz de cambio de base para el armónico n-ésimo. La matriz $\bar{\bar{Z}}_D^{(n)}$ es una matriz diagonal con los autovalores de la matriz $\bar{\bar{Z}}^{(n)}$, los cuales contienen la información de las impedancias de cada uno de los modos. Dado que $\bar{\bar{Z}}^{(n)} = \left(\bar{\bar{Y}}^{(n)}\right)^{-1}$, ambas matrices se pueden diagonalizar con el mismo juego de autovectores. Los autovalores de la matriz admitancia se calculan entonces haciendo el inverso de cada uno de los autovalores de la matriz impedancia.

Al aplicar este cambio de base a la ecuación (4), se puede demostrar que, mediante los cambios de variable de la Tabla I, el problema se reduce a un problema de líneas de transmisión matricial diagonal 2x2 donde cada onda de tensión (y de corriente) está desacoplada del resto, y se puede tratar de forma independiente. Así, el sistema de la ecuación (4) se reduce a las ecuaciones del telegrafista siguientes:

$$\frac{\partial \bar{V}^{(n)}}{\partial z} = -j\bar{\bar{Z}}_D^{(n)}\bar{I}^{(n)} + \bar{v}^{(n)} \qquad \frac{\partial \bar{I}^{(n)}}{\partial z} = -j\bar{\bar{Y}}_D^{(n)}\bar{V}^{(n)} + \bar{\imath}^{(n)} \quad , \qquad (7)$$

siendo $\bar{V}^{(n)}$ e $\bar{I}^{(n)}$ vectores columna con las ondas de tensión y corriente de cada modo, y $\bar{v}^{(n)}$ e $\bar{\imath}^{(n)}$ vectores columna con las fuentes independientes de tensión y corriente que modelan la perturbación periódica. Esto permite tratar cada armónico del modo Floquet en una base diferente, y propagar cada polarización de forma independiente. Deshaciendo el cambio de base y el cambio de variable de la Tabla I, el modo FB total soportado por la estructura se podrá obtener sumando la aportación de cada uno de estos armónicos, de la siguiente forma:

$$\vec{E}_{FB} = \left(\sum_n \vec{\psi}^{(n)}(z)\, e^{-j\vec{k}_t^{(n)}\cdot\vec{r}}\right) e^{-\alpha \hat{k}_{FB}\cdot\vec{r}}, \qquad (8)$$

donde $\vec{\psi}^{(n)}(z)$ es el perfil del armónico concreto, $\hat{k}_{FB}$ es la dirección de propagación del modo FB y α la constante de atenuación.

Tabla I. Relaciones entre las ondas de tensión y corriente y los campos electromagnéticos. Expresiones de las fuentes de tensión y de corriente y de las impedancias en función de la polarización.

TE	TM
$H_{a1}^{(n)} = -I^{(n)}$	$E_{a1}^{(n)} = V^{(n)}$
$E_{a2}^{(n)} = V^{(n)}$	$H_{a2}^{(n)} = I^{(n)}$
$H_z^{(n)} = \frac{k_t^{(n)}}{\omega\mu} V^{(n)}$	$E_z^{(n)} = -\frac{k_t^{(n)}}{\omega\epsilon_0\epsilon_h} I^{(n)}$
$v^{(n)} = 0$	$v^{(n)} = -j\frac{\epsilon^{(n)} k_t^{(n)}}{\omega\epsilon_0\epsilon_h^2} I^{(0)}$
$i^{(n)} = -j\omega\epsilon_0\epsilon^{(n)} V^{(0)}$	$i^{(n)} = -j\omega\epsilon_0\epsilon^{(n)} V^{(0)}$
$Z = \frac{\omega\mu}{k_z^{(n)}}$	$Z = \frac{k_z^{(n)}}{\omega\epsilon_0\epsilon_h}$

3.- Resultados de simulación

En esta sección se va a verificar el funcionamiento del simulador desarrollado comparándolo con el método de diferencias finitas FDTD 3D-Full Vectorial del simulador comercial Lumerical. Para ello, se va a simular una rejilla de difracción en plataforma SOI estándar con grabado parcial de H_g =30 nm, cuyas dimensiones son: $H_f = 220$ nm, $H_b = 2$ µm y cubierta de 2.2 µm de altura. El índice de refracción de cada capa es: $n_f = n_s = 3.476$ y $n_b = n_c = 1.444$. El periodo es $\Lambda = 1.6$ µm, el ciclo de trabajo del 50%, y el armónico en radiación es, en este caso, el tercero $n = -3$. La comparación se va a realizar tanto en términos de tiempos de cómputo como en similitud de resultados. Para ello, se van a distinguir dos casos: excitación normal a la rejilla de difracción, $\varphi = 0^o$, y excitación oblicua, $\varphi = 8^o$.

En la Figura 3(a) se muestra la potencia radiada por la rejilla de difracción con excitación normal. Se comprueba que el decaimiento exponencial, correspondiente al término $e^{-\alpha\hat{k}_{FB}\cdot\vec{r}}$ de la ecuación (8), es de 3.1 Np/mm con el método perturbacional (MP) y de 3.11 Np/mm con FDTD, obteniendo un error relativo del 0.32%. El diagrama de radiación obtenido con el MP se ilustra en la Figura 3(b), comprobándose que la dirección de radiación también tiene

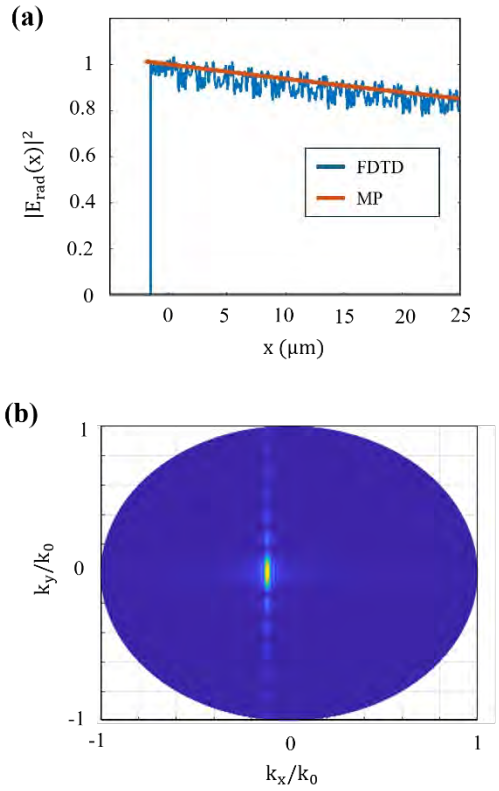

Fig. 3. Figuras para excitación normal, $\varphi = 0^o$. (a) Comparación con FDTD de la potencia radiada. El mallado espacial FDTD ha sido de 5nm. (b) Diagrama de radiación obtenido con el MP.

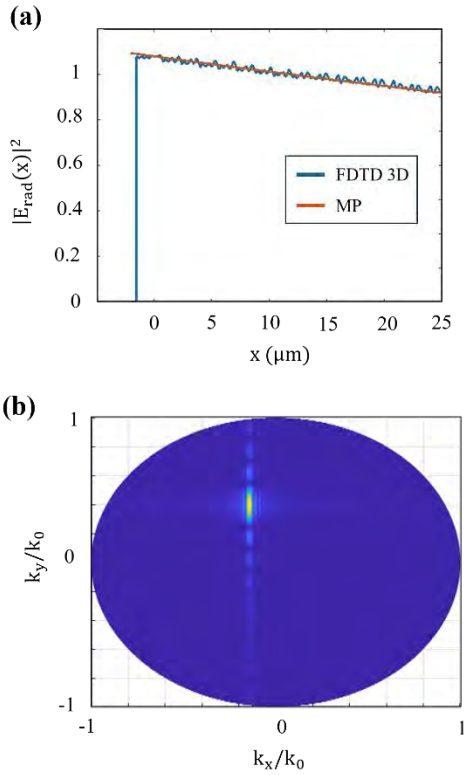

Fig. 4. Figuras para excitación oblicua, $\varphi = 8^o$. (a) Comparación con FDTD 3D de la potencia radiada. El mallado en FDTD 3D en los tres ejes espaciales ha sido de 10nm. (b) Diagrama de radiación obtenido con el MP.

$\phi^{(-3)} = 0^o$. En la Tabla II se muestra la diferencia de tiempos de simulación entre FDTD y el simulador basado en el MP, consiguiendo una ganancia de $\times 11$. Es importante notar que para este caso, la simulación FDTD no es 3D, pues al excitar con $\varphi = 0$, la estructura puede simularse con una anchura infinitesimal. Por otro lado, tal y como se recoge en la Tabla III, los resultados de simulación entre ambos simuladores presentan un error relativo máximo del 1.67%, para el caso del ángulo de radiación $\theta^{(-3)}$.

En la Figura 4 se han presentado los resultados de simulación correspondientes a la incidencia oblicua. Al igual que en el caso anterior, la potencia radiada por unidad de longitud de la Figura 4(a) coincide. Por otro lado, en la Figura 4(b) se tiene el diagrama de radiación, centrado en un ángulo $\phi^{(-3)} = 24.5^o$, que coincide con el resultado de la ecuación (2). La diferencia entre este ángulo y el de excitación se puede explicar a partir de la Figura 1(b), donde cada armónico presenta un ángulo en el chip diferente. En este caso, la diferencia de tiempos de simulación recogida en la Tabla II es mucho mayor, consiguiendo una reducción de $\times 514$. Esto se debe a que, al excitar de forma oblicua, la simulación FDTD ha de ser 3D, con una guía de cierta anchura para poder propagar oblicuamente. Esto supone un gran avance a la hora del diseño eficiente de estructuras de este tipo, ya que se reduce enormemente el tiempo necesario para ello, asegurando además que los resultados que se consiguen son precisos, tal y como se muestra en la Tabla III, donde el error relativo máximo asociado en este caso a la eficiencia de radiación, es de 1.47%.

4.- Conclusiones

En este trabajo se ha desarrollado un simulador electromagnético de rejillas de difracción para excitación con ángulos arbitrarios basado en el método perturbacional. Este simulador permite el

Tabla II. Comparativa de los tiempos de simulación entre el MP y FDTD 3D para excitación normal y excitación oblicua. (*) En este caso la simulación FDTD 3D presenta un ancho infinitesimal.

φ	MP (Este trabajo)	FDTD 3D	Reducción
0º	5 s	12min 10s (*)	$\times 11^{(*)}$
8º	65 s	9h 17min	$\times 514$

Tabla III. Comparativa de los resultados obtenidos con el MP y con FDTD 3D para excitación normal y excitación oblicua. (*) En este caso la simulación FDTD 3D presenta un ancho infinitesimal.

	MP (Este trabajo)	FDTD 3D	φ
$\alpha\left(\frac{\mathbf{Np}}{\mathbf{mm}}\right)$	3.1	3.11 (*)	0º
η %	57	57 (*)	
$\phi^{(-3)}$ (º)	0	0 (*)	
$\theta^{(-3)}$ (º)	-6.7	-6.8 (*)	
$\alpha\left(\frac{\mathbf{Np}}{\mathbf{mm}}\right)$	3.1	3.1	8º
η %	60	59	
$\phi^{(-3)}$ (º)	110	110	
$\theta^{(-3)}$ (º)	24.5	24.5	

análisis de estructuras dieléctricas con un número de capas arbitrario, de dimensiones y materiales genéricos. Esto ha permitido reducir los tiempos de cómputo hasta en $\times 514$ en comparación con un simulador vectorial FDTD 3D, sin comprometer la precisión de los resultados, ya que se encuentran errores relativos por debajo del 2%.

Agradecimientos: Este trabajo ha sido financiado por el Ministerio de Universidades, Ciencia e Innovación bajo el proyecto PID2022-139540OB-I00, el proyecto TED2021-130400BI00/AEI/10.13039/501100011033/ Unión Europea Next-GenerationEU/PRTR, el proyecto PDC2023-145833-I00, el proyecto PID2023-151178OB-I00, la cátedra PERTE-Chip bajo el proyecto TSI-069100-2023-0013 y la Universidad de Málaga.

Referencias

[1] Shekhar, S. et al. "Roadmapping the next generation of silicon photonics". *Nature Communications*, *15*(1), 751, 2024.

[2] A. Sánchez-Ramírez, et al., "Comparing dielectric and plasmonic waveguides in a Mach–Zehnder architecture with coherent readout for sensing applications," *Optics & Laser Technology*, 168, 109813, 2024.

[3] Alejandro Sánchez-Postigo, et al., "Engineering subwavelength grating photonic integrated structures for quantum applications," *Smart Photonic and Optoelectronic Integrated Circuits* 2024.

[4] A. Martinez, et al., "Self-adaptive integrated photonic receiver for turbulence compensation in free-space optical links," *Scientific Reports*, 14, 1, 20178, 2024.

[5] J. Chen, et al., "Coaxial transceiving LiDAR based on a silicon photonic optical phased array," *Optics Letters*, 49, 12, 3424-3427, 2024.

[6] C. Ropp et al., "Meta-grating outcouplers for optimized beam shaping in the visible," *Optics Express*, 29(10):14789–14798, 2021.

[7] P. Ginel-Moreno, et al., "Integrated metamaterial surface-emitting antenna for beam steering applications," *IEEE 17th International Conference Group IV Photonics (GFP),* 2021.

[8] Elio Godoy-Lorite, et al., "Simulador electromagnético eficiente para el diseño de rejillas de difracción débiles en guías dieléctricas," XXXIX *URSI*, 2024.

[9] T. Tamir and S.T. Peng. "Analysis and design of grating couplers". *Applied physics*, 14:235–254, 1977.

[10] S. Peng, "Rigorous formulation of scattering and guidance by dielectric grating waveguides: general case of oblique incidence," *Journal of the Optical Society of America A*, 6, 12, 1869-1883, 1989.

[11] G. Floquet, "Sur les équations différentielles linéaires à coefficients périodiques," *Annales scientifiques de l'École normale supérieure*, 12, 47-88, 1883.

[12] F. Bloch, "Über die Quantenmechanik der Elektronen in Kristallgittern," *Zeitschrift für Physik*, 52, 7, 555-600, 1929.

[13] Kim, S., et al. "Photonic waveguide to free-space Gaussian beam extreme mode converter". *Light: Science & Applications*, 7 (1), 72. 2018.

Next-generation photonic devices enabled by functional materials in silicon photonics

Jorge PARRA [1], Iñigo LÓPEZ MULET [1], Jorge CASO [1], Juan Francisco MORCILLO [1]
Pablo SANCHIS [1]

1. Nanophotonics Tecnhnology Center, Universitat Politècnica de València, Camino de Vera s/n, 46022 Valencia, Spain

Contact: Pablo SANCHIS (pabsanki@ntc.upv.es).

ABSTRACT:

The integration of phase-change materials (PCMs) and transparent conducting oxides (TCOs) into silicon photonics offers a promising route to achieve enhanced performance and enable the development of new devices and functionalities. Here, we present several hybrid devices that leverage the unique optoelectronic properties of these materials. A non-volatile photonic switch based on antimony selenide (Sb_2Se_3) is first demonstrated. Additionally, we highlight the use of indium tin oxide (ITO) as an energy-efficient heater for optical phase shifters. Novel optical activation functions using both PCMs and TCOs are also proposed for spiking neural networks. An all-optical activation function is achieved using vanadium dioxide (VO_2), showcasing a triangular-like response with sub-nanojoule activation energy. Furthermore, the capability to generate an electro-optical spiking response using hybrid ITO/Si devices is also demonstrated. These advancements underscore the potential of PCMs and TCOs in driving the development of next-generation PICs for applications in datacom, telecom, artificial intelligence, and beyond.

Key words: Integrated photonics, silicon photonics, phase-change materials, transparent conducting oxides, datacom, telecommunications, artificial intelligence

1.- Introduction

Silicon photonics is currently the most suitable platform for the development of large-scale photonic integrated circuits (PICs) [1]. The distinctive features are the high refractive index of silicon, allowing compact footprints and thereby the integration of many devices on a single chip, and the compatibility with the Complementary Metal-Oxide-Semiconductor (CMOS) processes employed in the microelectronics industry, which means that fabrication can be done on existing infrastructure with an affordable cost.

Nowadays, silicon PICs are used mainly in high-speed transceivers for optical interconnects in data centers and telecommunication networks [2]. However, the range of applications is expanding into many other fields, with photonic processors for telecom and artificial intelligence applications arising as one of the major areas of expansion [3]. As a result, the demand for new building blocks and higher performance is skyrocketing and becoming increasingly diverse [4].

In this context, integrating new materials into the silicon photonic platform is gaining increasing interest. Two important classes of materials with unique optoelectronic properties are phase-change materials (PCMs) [5] and transparent conducting oxides (TCOs) [6]. In this work, we summarize the main benefits of these materials and present several examples of hybrid devices based on their monolithic integration in silicon photonic structures.

2.- PCM/Si photonic devices

2.1.- Non-volatile photonic switch using Sb_2Se_3

Antimony selenide (Sb_2Se_3) belongs to the family of chalcogenide phase change materials (PCMs), which stand out for their ability to reversibly switch between their amorphous and crystalline states in a non-volatile way [7]. Hence, Sb_2Se_3 is regarded as a particularly promising material for energy-efficient reconfiguration applications with operation speeds in the nanosecond range. Additionally, Sb_2Se_3 is also highlighted for its negligible optical loss and large refractive index contrast (~0.7) at telecom wavelengths. Therefore, very compact devices can be built using hybrid Sb_2Se_3/silicon photonic structures [8].

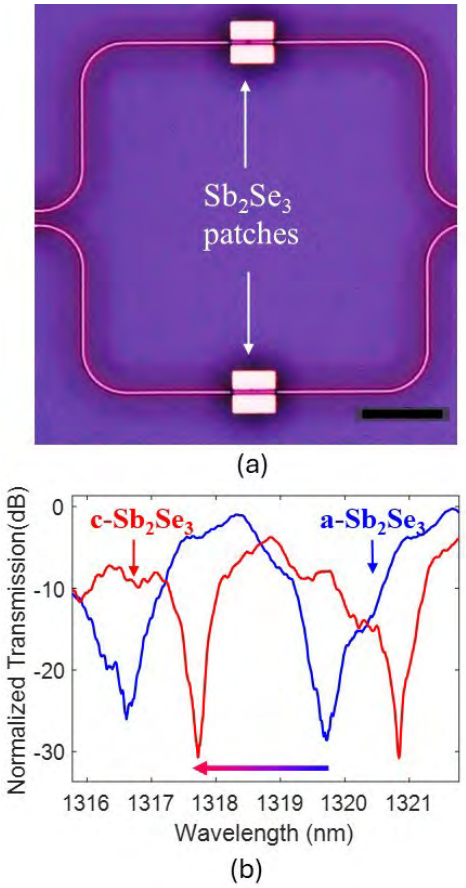

Fig. 1: (a) Microscope image of a symmetric MZI with 6-µm-long Sb_2Se_3 patches placed in both arms over the silicon waveguides. Scale bar is 10 µm long. (b) Wavelength shift produced in the MZI when changing Sb_2Se_3 from the amorphous state (blue line) to the crystalline state (red line).

Here, we propose a non-volatile photonic switch based on a 2×2 symmetric Mach Zender interferometer (MZI), as shown in Fig. 1(a). The active section is based on a hybrid waveguide that is composed of a 450 nm × 220 nm silicon (Si) waveguide with a 40 nm thick and a 6 µm long Sb_2Se_3 patch on top. The Sb_2Se_3 patch is fabricated by e-beam evaporation, followed by a lift-off process.

The Sb_2Se_3 patch is initially deposited in an amorphous state. The state of the Sb_2Se_3 patch was switched via optical pumping with a 639 nm laser. As a result, the MZI response is shifted as the Sb_2Se_3 is changed between the amorphous and crystalline states, as shown in Fig. 1(b) for the case of an asymmetric MZI. This phase transition results in a non-volatile optical phase shift of approximately 0.2π/µm.

2.2.- An optical activation function using VO_2

Achieving efficient nonlinearity remains a challenge for all-optical neural networks. PCMs also show a big potential in this field [9, 10]. Vanadium dioxide (VO_2) is a PCM that exhibits an abrupt and reversible optical loss variation when shifting from insulating to metallic state. The insulator-to-metal transition (IMT) can be provoked via heating and occurs close to room temperature (~65ºC) [11]. In this work, we demonstrate a hybrid VO_2/Si device with a 2-µm-long footprint designed to enable an all-optical activation function for photonic neural networks. Specifically, a triangular-like response is achieved with sub-nanojoule activation energy.

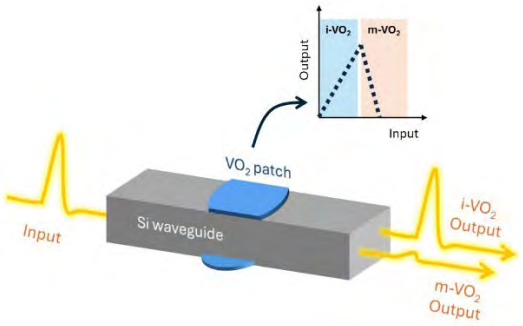

Fig. 2: Hybrid VO_2/Si device for enabling an all-optical activation function.

The proposed device is shown in Fig. 2 and consists of a 500 nm-wide and 220 nm-thick Si waveguide with a 40 nm-thick and 2 µm-diameter VO_2 patch grown on top by molecular beam epitaxy [12]. The device response was measured at 1550 nm, though its spectral response is demonstrated to extend across the telecom C-band. A nonlinear triangular response with an activation power of ~0.4 mW is attained, as depicted in Fig. 3.

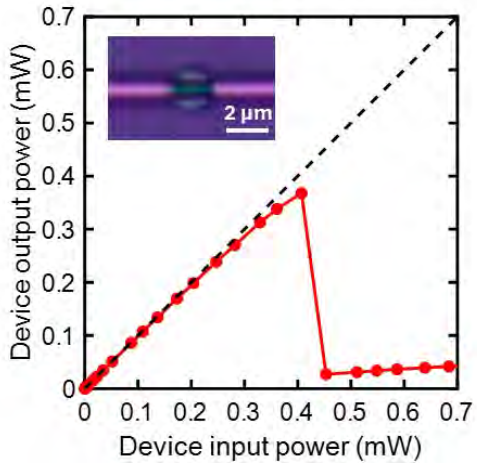

Fig 3: Triangle-like response triggered by the optical power of the input pulse. The inset shows a microscopic image of the fabricated device.

The temporal dynamics of the device were characterized by means of a pump-probe setup, using 1550 nm wavelength optical pulses with 50 ns duration as the pump, and a 1565 nm continuous wave signal as the probe. Energy values as low as ~100 pJ were sufficient to trigger the IMT. Also, fall and rise times below 30 ns and 100 ns, respectively, were measured.

3.- TCO/Si photonic devices

3.1.-Energy-efficient heaters using ITO

Typically, materials with large optical losses, such as metals, are employed as microheaters for silicon-based thermo-optic phase shifters. Consequently, the heater must be placed far from the waveguide, which could come at the expense of the phase shifter's performance [13]. Reducing the gap between the waveguide and the heater allows for the reduction of power consumption and increases the switching speed. Indium tin oxide (ITO) could be employed as a transparent heater in the near-infrared spectrum by tailoring its optical and electrical properties during the fabrication process. In such a way, the distance between the waveguide and the heater can be significantly reduced. We have demonstrated ultralow-loss, low-power, and fast Si phase shifters by using compact ITO microheaters [14]. Figure 4(a) shows the optical phase shifter consisting of a standard silicon waveguide with a 50-µm-long ITO heater, with a gap between the two of 320 nm. A power consumption of ~10 mW with a switching speed of 5.2 µs was experimentally demonstrated.

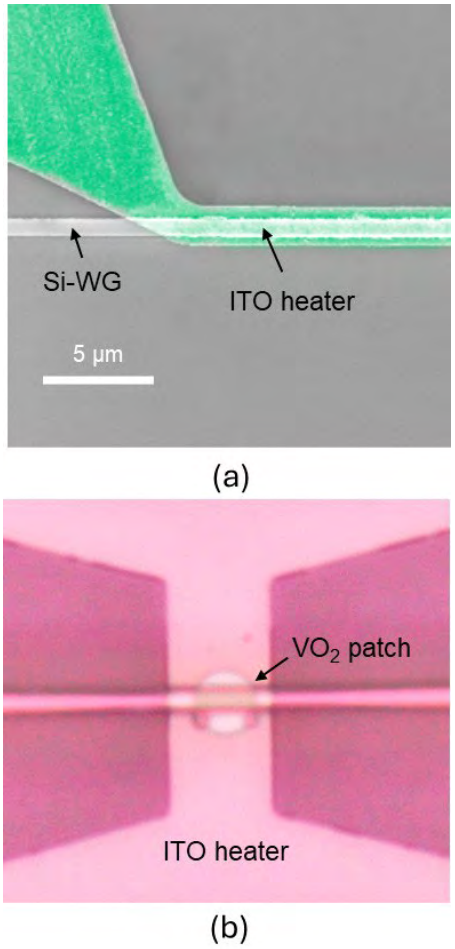

Fig. 4: (a) False-colored scanning electron image of an optical phase shifter consisting of a standard silicon waveguide with a 50-µm-long ITO heater. (b) Optical micrograph of a VO_2/Si waveguide with an ITO heater on top deposited at room temperature.

On the other hand, the thermal budget of a PIC can hinder the integration of certain materials prone to degradation with high process temperatures such as VO_2. By harnessing the fabrication parameters that can be played during ITO deposition, we have demonstrated the monolithic fabrication of VO_2/Si waveguides with ITO heaters on top deposited at room temperature by means of RF sputtering, as depicted in Fig. 4(b).

3.2.- An optical activation function using ITO

Optical activation functions may also be developed using TCOs with faster speeds than PCMs [15]. Furthermore, the optical properties of TCOs can be selectively tuned using a post-growth reactive laser annealing technique [16]. Here, we present our recent work towards the experimental demonstration of an electro-optical spiking response in a hybrid ITO/Si device.

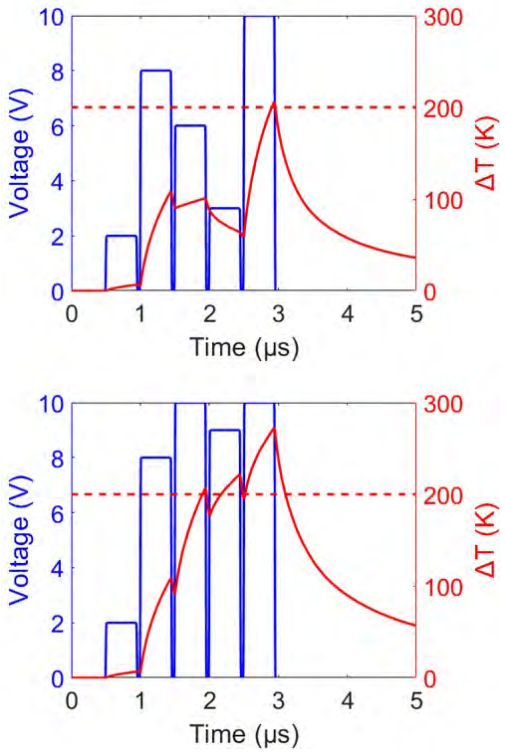

Fig. 5: Simulated temporal response of the ITO/Si device under an applied electrical signal (blue) consisting of a train of five pulses with different voltages. The simulated temperature variation (red) and activation threshold (dashed red) is shown.

The working principle is based on a reversible variation of both the real and imaginary parts of ITO's refractive index as a function of its internal temperature, which can be modulated by applying short electrical pulses.

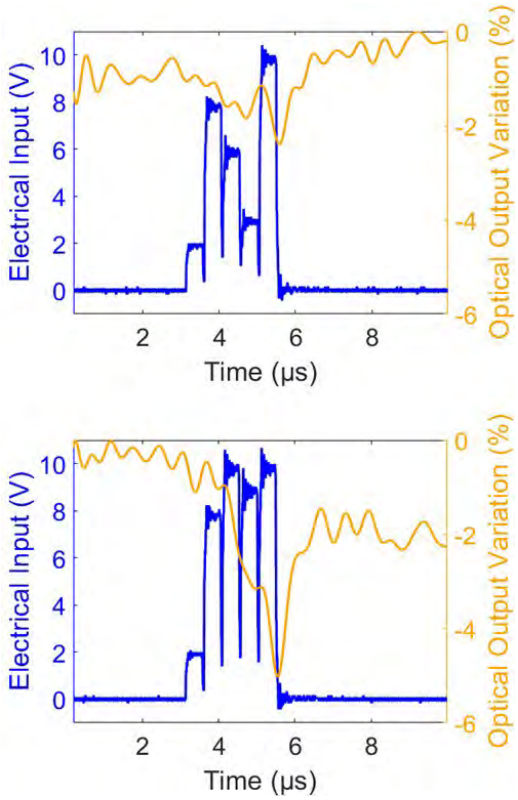

Fig. 6: Experimental temporal response of the ITO/Si device under an applied electrical signal.

Our device consists of an ITO microwire placed on top of a standard Si waveguide. When a train of electrical pulses is applied to the ITO microwire, its temperature increases due to Joule heating. This temperature change may affect the refractive index of the ITO layer.

The temporal response of the ITO/Si device was characterized by applying a train of five electrical pulses with varying voltages. Simulation and experimental results were obtained to analyze the behavior of the device. Depending on the temperature reached, as estimated by simulations and shown in Fig. 5, the experimental optical losses of the device may change notably, generating an optical spike at the output, as observed in Fig. 6.

4.- Conclusion

We have highlighted the potential of PCMs and TCOs for achieving enhanced performance, for example, serving as more energy-efficient heaters, as well as enabling the development of new photonic devices such as compact photonic switches with non-volatile behavior, and new functionalities like all-optical and electro-optical activation functions for spiking neural networks.

Both families of materials can be monolithically integrated into existing silicon photonics platforms, facilitating the development of large-scale photonic integrated circuits (PICs). Therefore, integrating functional materials into silicon photonics is expected to play a pivotal role in expanding the adoption of integrated photonics in arising sectors such as artificial intelligence, autonomous vehicles, and quantum computing.

Acknowledgements: We acknowledge funding from grants PID2022-137787OB-I00 and TED2021-132211B-I00, funded by MCIN/AEI/10.13039/501100011033, and grant CIPROM/2022/14, funded by the Generalitat Valenciana. J.Parra acknowledges Universitat Politècnica de València for grants PAID-10-23 and PAID-06-23.

References

[1] Sudip SHEKHAR et al., "*Roadmapping the next generation of silicon photonics*", *Nat. Commun*., 15:751, 1-15, 2024.

[2] Xuetong ZHOU et al., "*Silicon photonics for high-speed communications and photonic signal processing*", npj Nanophoton., 1, 1–14, 2024.

[3] Maksim MAKARENKO et al., "*Photonic optical accelerators: The future engine for the era of modern AI?*", APL Photonics, 8, 110902, 2023.

[4] Roel BAETS et al., "*Heterogeneous integration in silicon photonics: opportunities and challenges: opinion*", Opt. Mater. Express, 13, 3439–3444, 2023.

[5] Rui CHEN et al., "*Opportunities and Challenges for Large-Scale Phase-Change Material Integrated Electro-Photonics*", ACS Photonics, 9, 3181–3195, 2022.

[6] Alan X. WANG, Wei-Che HSU, "*Perspective on integrated photonic devices using transparent conductive oxides: Challenges and opportunities*", Applied Physics Letters, 124, 060503, 2024.

[7] Matthew DELANEY et al., "*A New Family of Ultralow Loss Reversible Phase-Change Materials for Photonic Integrated Circuits: Sb_2S_3 and Sb_2Se_3*" Adv. Funct. Mat., 30, 2002447, 2020.

[8] Jorge PARRA, Miro KOVYLINA, Amadeu GRIOL, Pablo SANCHIS, "*Nonvolatile reconfigurable polarization rotator at datacom wavelengths based on a Sb_2Se_3/Si waveguide*", Opt. Express, 32, 40581-40592, 2024.

[9] Jorge PARRA, Juan NAVARRO-ARENAS, Pablo SANCHIS, "*Sub-milliwatt threshold power and tunable-bias all-optical nonlinear activation function using vanadium dioxide for wavelength-division multiplexing photonic neural networks*", Scientific Reports, 15:5608, 1-11, 2025.

[10] Juan-Francisco MORCILLO, Pablo SANCHIS, Jorge PARRA, "*On-chip electro-optical spiking VO_2/Si device with an inhibitory leaky integrate-and-fire response*", Opt. Mat. Exp., 14, 2681-2693, 2024.

[11] Sebastian CUEFF et al., "VO_2 nanophotonics", APL Photonics 5, 110901, 2020.

[12] Bart VAN BILZEN et al., "*Production of VO2 thin films through post- deposition annealing of V_2O_3 and VO_x films*", Thin Solid Films, 591, 143–148, 2015.

[13] Jorge PARRA et al., "*Silicon thermo-optic phase shifters: a review of configurations and optimization strategies*", Adv. Phot. Nex., 3, 044001, 2024.

[14] Jorge PARRA, Juan HURTADO, Amadeu GRIOL, Pablo SANCHIS, "*Ultra-low loss hybrid ITO/Si thermo-optic phase shifter with optimized power consumption*", Opt. Express, 28, 9393–9404, 2020.

[15] Juan NAVARRO-ARENAS, Jorge PARRA, Pablo SANCHIS, "*Complex-valued trainable activation function hardware using a TCO/silicon modulator*", Opt. Mater. Express, 13, 2869–2881, 2023.

[16] Juan NAVARRO-ARENAS et al., "*Local Tuning of the Epsilon-Near-Zero Condition in Hybrid Silicon Waveguides Using Reactive Laser Annealing*", Adv. Phot. Res., 2400140, 1-7, 2025.

Prototyping of microstructures for photonic devices and glass interposers using powerful femtosecond laser source

Bogusz STĘPAK, Natalia GRUDZIEŃ, Rafał SMOLIN, Katarzyna PIETRUSIŃSKA, Yuriy STEPANENKO, Michał NEJBAUER, Juan Luis VADILLO

1. Fluence Technology, ul. Kolejowa 5/7, 01-217 Warszawa

Contact: Bogusz STĘPAK (bstepak@fluence.technology).

ABSTRACT:

Ultrafast lasers are the most powerful tool for both direct and chemical etching-assisted methods used to fabricate high-aspect-ratio structures with controllable shape in glass. Other applications useful in photonic and microfluidic device fabrication and integration include: glass welding, waveguide and grating writing, selective surface activation before metallization and others. This study highlights advancements in microfabrication using rear-side ablation and percussion drilling. We demonstrate the non-tapered holes with an optional tilt up to 50 deg. We obtained hole diameters of less than 50 µm with an aspect ratio of 1:24. The influence of pulse duration and pulse repetition rate on the depth of microholes fabricated via percussion drilling was investigated. Fast penetration of 1 mm thick fused silica is shown with smooth, shiny hole walls. The results were achieved using a laser source generating >200 µJ energy in a single pulse at a wavelength of 1030 nm (Jasper X0, Fluence Technology, Poland).

Key words: femtosecond laser, bottom-up, ablation, microstructure, hole drilling, through-glass via, microfabrication in glass, high-aspect ratio

1.- Introduction

One of the most powerful microfabrication methods in glass is selective laser etching (SLE), also known as laser-induced deep etching (LIDE) or femtosecond laser irradiation and chemical etching (FLICE). This two-step process involves fast laser modification using ultrashort pulses followed by chemical etching. However, environmental concerns related to the chemical part of the process, raised by some of the companies, indicate the need for alternative methods. Single-step fabrication of through-glass-vias (TGV) for glass interposers in advanced chip packaging is achievable using direct laser ablation techniques. One such method is rear-side ablation, commonly called the "bottom-up" approach [1]. This technique exploits the fact that the operational wavelength is nonlinearly absorbed by the material, with absorption occurring only in regions where the intensity threshold is exceeded. A key advantage of bottom-up processing is its ability to manufacture vias of almost any shape (similar to SLE). Nonlinear absorption allows for in-volume glass modification or ablation at the rear side, leaving the material above unaffected. The common problem is heating and modification of the glass above the ablation zone when using a high pulse repetition rate, which causes the jumping of ablation to the top surface before the intended volume is removed. The nonlinear

beam propagation also increases the difficulty of controlling the process. Obtaining an aspect ratio above 1:10 is challenging with this technique also due to the problem of clogging the hole by ablation products. In our research, we demonstrate the results of deep optimization of the laser parameters and scanning strategy, which led us to obtain repeatable results with high productivity. Our method enables the efficient and precise drilling of holes with diameters below 50 µm and an aspect ratio of 1:24.

Another possible method of a single-step process is top-down approach e.g. percussion drilling. However, this technique faces several challenges when using ultrashort pulses: the formation of conical shapes resulting in drilling saturation, low aspect ratio, radially distributed in-volume defects, heat-affected zone causing residual stress, and glass cracking. For these reasons, typically reported depth of drilled holes with repetitive single pulses do not exceed 300 µm regardless pulse energy, glass type or NA [2,3].

Femtosecond lasers are powerful tools for many other processes useful in photonic chip fabrication and integration such as glass welding, waveguide writing, writing of gratings, encapsulation of sensors, trimming, selective surface activation for metallization and others.

2.- Experimental

Processing of glass was performed using Fluence's Jasper X0 femtosecond fiber laser operating at an average power of 30 W at 1030 nm wavelength. In the percussion drilling experiments, the maximum pulse energy used was 250 µJ. The available pulse repetition rates range from single pulse up to 20 MHz. The laser generates a high-quality Gaussian beam with $M^2 < 1.15$ and very high temporal pulse contrast. The laser is operating in energy-stabilized mode providing a stable pulse energy at varying pulse repetition rates. This feature allows for advanced pulse-on-demand (advanced POD) functionality with minimized timing jitter. The pulse duration is tunable between 250 fs and 20 ps. In the experiment, the fundamental wavelength of 1030 nm was used. The beam diameter was adjusted before focusing by using an automated beam expander. The beam was deflected by an excelliSCAN$_{14}$ galvanometric scanner equipped with a telecentric objective. In the rear-side ablation experiments, the galvoscanner was positioned above the sample by using a precise linear stage (Fig. 1).

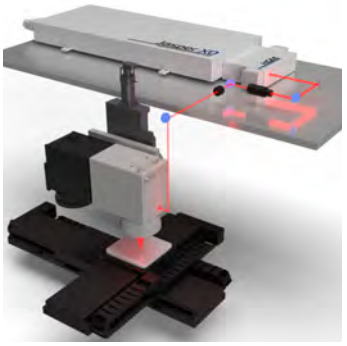

Fig. 1: Experimental setup in the Ultrafast Laser Application Laboratory at Fluence.

3.- Results

2.3.- Bottom-up glass processing

The investigation of rear-side ablation drilling resulted in through, taper-free holes. This method allows to form tilted vias with varying diameters larger than a spot size. Figure 3 presents 46 µm holes in 1.1 mm thick BK7 glass with an aspect ratio of 1:24. Drilling time varies depending on the hole size, glass type, and thickness. For instance, it takes 15 seconds to drill one 45 µm diameter hole presented in Fig. 3 (1.1 mm glass thickness). When drilling in 0.5 mm thick EXG, such hole fabrication takes 4 seconds (Fig. 2). However, it is worth noting that 90% of drilling time is spent on the movement of the vertical positioning stage between layers. The pitch between holes may be reduced to a value smaller than the diameter without the quality and speed decrease. Drilling using the bottom-up method creates no cracks or significant chipping at the inlet and outlet of the holes.

Fig. 2: Image taken with camera during the bottom-up drilling in 0.5 mm EXG glass. The hole diameter is 60 µm.

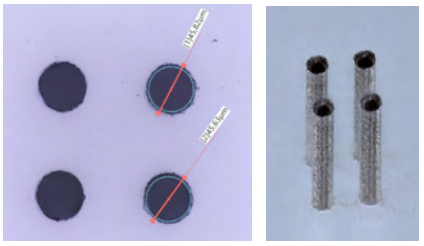

Fig. 3: TGVs in 1.1 mm thick Schott BK7 glass drilled using bottom-up method: 2x2 matrix with 46 µm diameter. Aspect ratio: 1:24.

The holes were drilled by changing the focal plane position several times during the process. The time needed for positioning of the galvoscanner mounted on a linear stage in our setup is much longer than the time required for the ablation. As we calculated, the time when the scanner is operating is lower than 500 ms for the hole diameter of 70 µm and 500 µm thick substrate. Therefore, rear-side drilling is both flexible and fast while giving repeatable and well-controlled geometries. The record aspect ratio obtained with this method is 1:32, which translates to a 34 µm hole diameter in 1.1 mm BK7. However, this method requires a microscope objective, which increases the processing time.

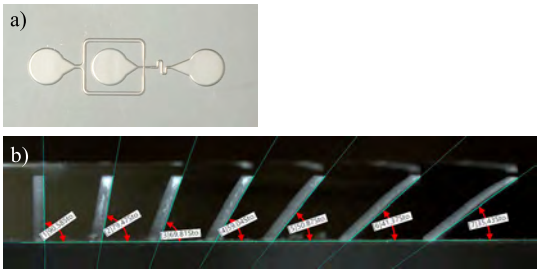

Fig. 4: a) The example of microfluidic device (3.5 x 1.5 mm) fabricated using bottom-up method; b) series of tilted vias in EXG glass with diameter of 125 µm.

2.4.- Top-down glass processing

A common problem in percussion drilling of glass with ultrashort pulses is a conical shape, causing drilling saturation and defects in the volume surrounding holes. After optimization of focusing conditions, we were able to achieve depth of holes exceeding 400 µm with reduced conicity using only 800 pulses. It may be concluded that light is reflected multiple times, as in a waveguide. For this reason, deep drilling can be obtained without moving the focal plane during the process. The sufficient pulse energy helps to drill deeper holes. The results presented here were obtained with a single pulse energy of 250 µJ.

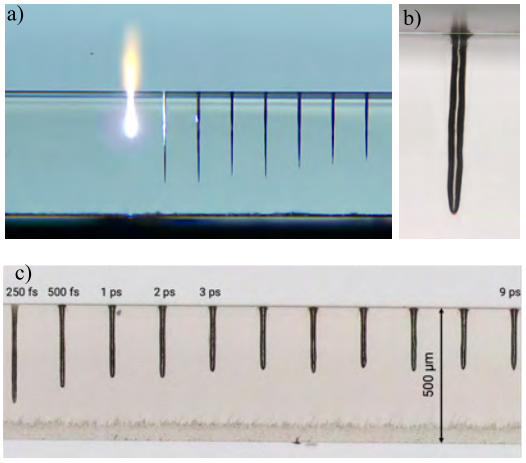

Fig. 5: a) Image taken with camera during the top-down percussion drilling in 1.1 mm BK7 glass. The hole diameter is ~20 µm; b) high quality walls after drilling in EXG glass; c) A series of holes drilled using a constant number of pulses 800 at different pulse duration between 250 fs and 9 ps. The applied pulse repetition rate was 10 kHz and 80 ms processing time per hole. Substrate: 0.5 mm thick Eagle XG glass.

In Fig. 5c we show a series of holes drilled with a constant number of pulses and varying pulse duration between 250 fs and 9 ps. As can be seen, the shorter the pulse, the deeper the hole. Significant differences in drilling depth can be observed below 1 ps, and even below 500 fs which is a surprising result. In glass drilling, the pulse duration is one of the most important parameters. The holes drilled using 250 fs pulses are 1.7 times deeper than

those drilled with $\tau > 3$ ps. The depth increase between 500 fs and 250 fs is around 25%. Detailed measurements are presented in Fig. 6.

Moreover, we observed a higher risk of cracking when using picosecond pulses. Increasing the pulse repetition rate may increase the depth of the hole due to heat accumulation.

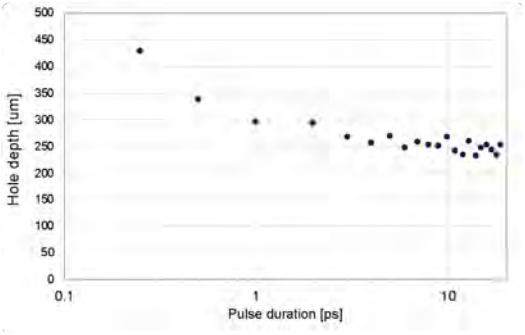

Fig. 6: The graph presents the measured hole depth as a function of pulse duration for 800 pulses per hole at 10 kHz. Substrate: Eagle XG glass.

Eventually, we investigated through hole drilling which is crucial for TGV application. When a hole opening starts to be created, the plasma can evacuate at the rear side. As a result, the end part of the hole is getting conical and the number of pulses required to make the opening wider may be even higher than that used for main drilling. The obtained wall quality is very high with no signs of cracking (Fig. 7).

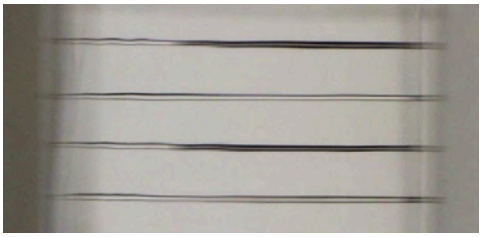

Fig. 7: Through holes in 1.0 mm thick fused silica drilled by percussion drilling within 20 ms per hole.

4.- Conclusion

We report on femtosecond laser drilling in glasses widely used in the electronics industry. The bottom-up approach results in taper-free holes with controllable tilt angles relative to the glass surface. Diameters may vary from less than 50 µm up to hundreds of micrometers in glass with a thickness of around 1 mm, resulting in a high aspect ratio of 1:24. This method provides well-controlled geometry of vias, making it useful in prototyping. The percussion drilling method achieves drilling times of tens of milliseconds per hole, providing shiny walls and reduced conicity. We demonstrated TGV fabrication in a 0.5 mm thick glass substrate and 950 µm-deep blind holes in borosilicate glass. Pulse duration plays a crucial role in obtaining the maximal depth. Drilling with repetitive single pulses revealed significant potential for fast fabrication of TGVs. Obtained drilling speeds and quality are comparable to results obtained using GHz burst.

Acknowledgements: The project is co-financed by the European Union through the European Regional Development Fund.

References

[1] Mackevičiūtė, M., Dudutis, J. and Gečys, P., "Fast and efficient bottom-up cutting of soda-lime glass using GHz bursts of short laser pulses," Opt. Laser Eng. 183, 108490 (2024). https://doi.org/10.1016/j.optlaseng.2024.108490

[2] Balage, P., Lopez, J., Guilberteau, T., Lafargue, M., Bonamis, G., Hönninger, C. and Manek-Hönninger, I., "Through glass via drilling using GHz-bursts of femtosecond pulses: challenges and implementation," J. Laser Micro/Nanoeng. (submitted) (2024).

[3] Ren, G., Sun, H., Nakagawa, K., Sugita, N. and Ito, Y., "Crackless high-aspect-ratio processing of a silica glass with a temporally shaped ultrafast laser," Opt. Lett. 49(9), 2321-2324 (2024). https://doi.org/10.1364/OL.522052

Simplified Polarization Independent Integrated Coherent Receiver for Passive Optical Networks

Natalia HERGUEDAS [(1)], Jorge CIUDAD-REAL [(1)], David IZQUIERDO [(1)], Pascual SEVILLANO [(1)], Ignacio GARCÉS [(1)]

1. Grupo de Tecnologías Fotónicas (GTF), Instituto de Investigación en Ingeniería de Aragón (I3A), Universidad de Zaragoza, C/ Mariano Esquillor Edificio I+D+i, Zaragoza.

Contact: Natalia HERGUEDAS (nherguedas@unizar.es).

ABSTRACT:

In this work, we present a polarization-independent integrated heterodyne coherent receiver fabricated using InP technology for coherent passive optical networks (PONs). The characterization of the integrated polarization beam splitter (PBS) reveals deviations from ideal polarization separation due to manufacturing imperfections, significantly impacting overall receiver performance. While the PBS allows thermal tuning, it does not provide an operating point that achieves a satisfactory polarization separation. To evaluate the receiver performance, a 2 Gb/s 4QAM signal has been used to analyse the bit error rate (BER) and error vector magnitude (EVM) for two polarization states aligned with the main propagation axes in the photonic integrated circuit. The results indicate that, despite the incomplete polarization separation, the receiver successfully recovers signals with BER values of 10^{-2} in these two orthogonal states of polarization. Although further optimization of polarization management and development of new DPS corrections will be essential to enhance system performance, the proposed architecture has been validated.

Key words: integrated photonics, coherent receiver, passive optical networks, photonic integrated circuits, fibre optical communications.

1.- Introduction

Passive optical networks (PONs) represent without doubt the most relevant infrastructure of today's access communications. Both wired and mobile networks rely on fast and reliable optical fibre links installed in our cities using this point to multipoint architecture [1]. Actual PON standards provide 10 Gb/s downstream links to a relatively high number of users. However, the increasing demand for higher bandwidth, number of users and link distances is pushing the need of higher optical power budgets for these PONs. Particularly, the next PON standards will support 50 or 100 Gb/s downstream links, which are not expected to be provisioned by Intensity Modulation / Direct Detection (IM/DD) standard links because receiver sensitivities decrease with increasing bandwidths, and chromatic dispersion (CD) issues may arise [2]. For these data bit rates, coherent receivers are being considered as an attractive solution since their sensitivities are much higher than those of direct detection receivers at the same bitrate. In addition, links based on coherent receivers can handle better the CD problems that may be encountered when transmitting high bit-rate signals over several tens of km of single-mode optical fibres. However, coherent receivers, which are being used extensively for backbone and metro point-to-point links, also present fundamental problems for access networks, namely, the complexity of 90º hybrids, the extra cost that the local oscillator (LO) laser and other components imply in the Optical Network Unit (ONU) at the user's end, and the dependence of the receiver on the polarization

of the incoming signal, which has to beat with the fixed polarization state of the LO.

In this work, we present a simplified integrated coherent transceiver fabricated on InP technology, where we try to address these problems. On the one hand, most of the ONU components are integrated in one Photonic Integrated Circuit (PIC), resulting in a cost-effective solution, and InP technology also enables the integration of the LO laser in the PIC in the near future. On the other hand, we include a Glance-like receiver architecture [3] that achieves polarization independent signal reception. Although this scheme has been successfully validated in previous works [4], polarization management in integrated optics is a challenging task that may compromise the polarization independence of the receiver.

2.- Integrated coherent Receiver

2.1.- Glance-based design and theory

Our polarization-independent heterodyne coherent receiver, depicted in Fig. 1, is based on the polarization-insensitive coherent receiver architecture proposed by Glance [3]. The optical front end of the receiver comprises a polarization-maintaining (PM) coupler, a polarization beam splitter (PBS), and two photodetectors (PDs). The local oscillator (LO) polarization state is set at a fixed angle of 45° relative to the PBS axis, and its wavelength is shifted from the received signal central wavelength. Although this architecture incurs a sensitivity penalty of 3 dB compared to conventional polarization-controlled heterodyne receivers, it provides polarization insensitivity for DPSK modulation through the straightforward addition of the detected signals. In our previous implementations, the system not only provides polarization-insensitive detection [4], but also enables recovery of polarization-multiplexed (PolMux) signals when employing more sophisticated digital processing algorithms [5].

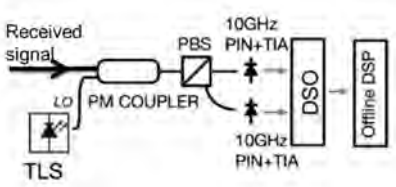

Fig. 1: Schematic of the polarization-independent receiver.

2.2.- PIC Design

Using the previously described receiver architecture, we designed and fabricated a photonic integrated circuit (PIC) implementing a complete transceiver scheme, whose schematic is shown in Fig. 2.

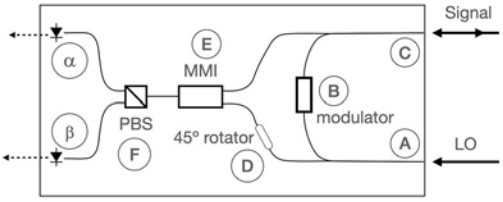

Fig. 2: Schematic of the transceiver integrated into the PIC.

The main function of the transceiver PIC is the Glance-based coherent receiver. It manages the local oscillator that enters through port A, passes through a 45° polarization rotator (D), and then reaches a multimode interferometer (MMI, E), where it is coupled with the received signal that enters through port C. The MMI output is directed to the PBS (F), which, theoretically, separates polarizations TE and TM, each of which is sent to a different photodiode (α and β).

The PIC also includes an electro-absorption modulator (EAM, B), that serves as a first step in the implementation of a transmitter. For this purpose, part of the LO light feeds the EAM and exit through port C.

For the PIC fabrication we chose the multi-project wafer (MPW) service of the Heinrich-Hertz-Institut (HHI), and we utilised their process design kit (PDK) building blocks. A photo of the manufactured PIC is shown in Fig. 3.

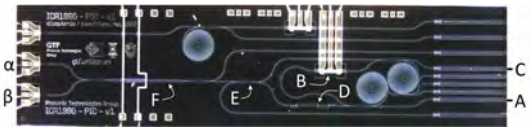

Fig. 3: Photograph of the manufactured PIC.

The most relevant device for the polarization insensitiveness of our receiver is the PBS, therefore its structure and operation basis is key for our receiver performance.

3.- Integrated PBS characterization

The integrated PBS is an HHI building block and it is based on a Mach–Zehnder interferometer (MZI) [6]. Each of the MZI arms has a heater that allows the tuning of the PBS operating point. When a current is applied to the heater, the waveguide heats up, changing the effective refractive indexes and modifying the PBS polarization separation characteristics.

Initial tests on the PIC revealed that the PBS does not separate correctly the TE and TM polarizations; instead, each output contains a linear combination of both. This effect may be caused by an error in the MZI waveguide widths during the PIC manufacturing process, and it may be corrected by thermal tuning of the PBS, as previously explained. However, as will be shown later, this approach is not always effective.

The PBS response to TE and TM polarizations as a function of the heater current is shown in Fig. 4. Negative heater currents correspond to heating the lower arm of the PBS, while positive currents correspond to heating the upper arm. It can be observed that the injected current, and therefore the temperature difference between arms, has a noticeable impact on the operation of the PBS. It can be also observed that the two outputs present complementary optical powers, in the sense that a minimum of one polarization in one given output corresponds to a maximum of this polarization in the other output. Finally, it can be also seen that TM polarization always presents a lower value than the TE one.

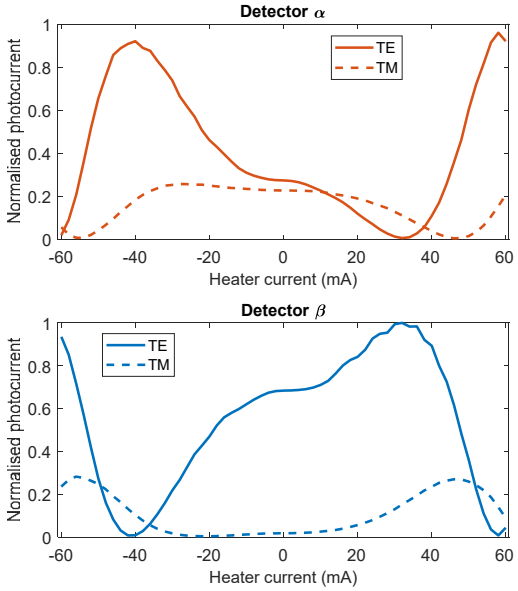

Fig. 4: Normalised detected photocurrents in each photodetector (α and β) when light is coupled into a specific polarization (TE or TM).

In order to study and optimise the operating point of the PBS, we introduce the Polarization Extinction Ratio (PER) for each detector as the figure of merit:

$$PER_\alpha = \frac{P_\alpha^{TE}}{P_\alpha^{TM}} \ , \qquad (1)$$

$$PER_\beta = \frac{P_\beta^{TE}}{P_\beta^{TM}} \ , \qquad (2)$$

where P_i^j represents the received power in detector i when light is coupled with polarization j. Fig. 5 shows the PER in each photodetector as a function of the heater current. As can be seen, the peaks of both PER curves do not occur at the same heater current. This discrepancy makes it impossible to find an operation point (or single current) that fully separates the polarizations. Therefore, it would be necessary to implement additional Digital Signal Processing (DSP) corrections to fully compensate the manufacturing errors.

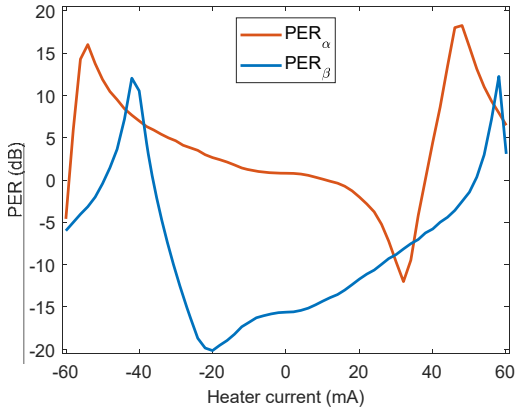

Fig. 5: PER in each photodetector as a function of the current in the PBS heater.

The PBS optimal operating point would be where both photodetectors have the highest PER. In this sense, the best operating point would be at -40 mA where both PER are above 6 dB. However, as it has been mentioned, in this operating point the detected signals at PD β are very low, and its limited Signal-to-Noise Ratio, SNR, could compromise the receiver performance. For this reason, we choose to operate at 0 mA, as PD β receives only one polarization, while PD α receives both, but at sufficiently high levels.

4.- Measurement and Results

To validate the integrated receiver, we have tested it with a 2 Gb/s 4QAM (Quadrature Amplitude Modulation) signal with two different states of polarization (SOP). These SOPs are aligned with the two main propagation axes and polarization in the PIC, namely TE and TM. These measurements are a preliminary evaluation of the receiver and the PBS operation, and they should be completed with more exhaustive measurements to fully check the independent polarization behaviour of the integrated receiver.

4.1. – Experimental setup

The experimental setup, shown in Fig. 6, uses an 80 GSa/s Arbitrary Waveform Generator (AWG) to generate the electrical signals that drive each arm of an IQ modulator. A 2 Gb/s bitstream is encoded with a 4QAM scheme and filtered using CAP pulse shaping filters to reduce the used optical bandwidth.

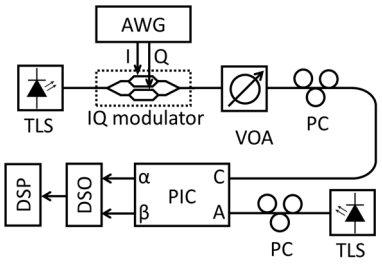

Fig. 6: Experimental setup for the integrated receiver evaluation.

The IQ modulator modulates a 1550 nm light from a Tuneable Laser Source (TLS), which is then passed through a Variable Optical Attenuator (VOA) to adjust its power. Finally, a Polarization Controller (PC) is used to adjust the SOP of the received signal entering the PIC.

The LO, in turn, is generated by other TLS shifted 0.020 nm (~2.5 GHz) from the central wavelength of the received signal and whose SOP is aligned with one of the axes of the PIC using a PC placed before the PIC.

The two photocurrents of the detectors, α and β, are digitalised by a 20 GHz Digital Storage Oscilloscope (DSO) and digitally processed offline. The Digital Signal Processing (DSP) includes a Phase-Locked Loop (PLL) to down-convert the heterodyne detected signals to baseband, CAP matched filtering and IQ symbol sampling. Then the IQ sampled symbols are equalised by a decision feedback equaliser (DFE) and decoded to compute EVM and BER for each photodiode independently.

In this preliminary evaluation the signals coming from the two photodiodes are independently processed, but in a real scenario they should be combined adequately in order to obtain a fully polarization-independent receiver.

4.2. – Results

The received symbol constellations for TE and TM polarizations at each photodetector can be seen in Fig. 7. These results, obtained for a received power of -7.30 dBm, are aligned with expectations based on Fig. 4. In detector α, both polarizations present close power levels, resulting in similar symbol dispersions and comparable EVM values. In

contrast, the detected current in detector β for the TE polarization is significantly higher than in α, enabling much better symbol differentiation and leading to a lower EVM. However, for TM the current in β is weak, causing a poor SNR and preventing symbol differentiation in the constellation.

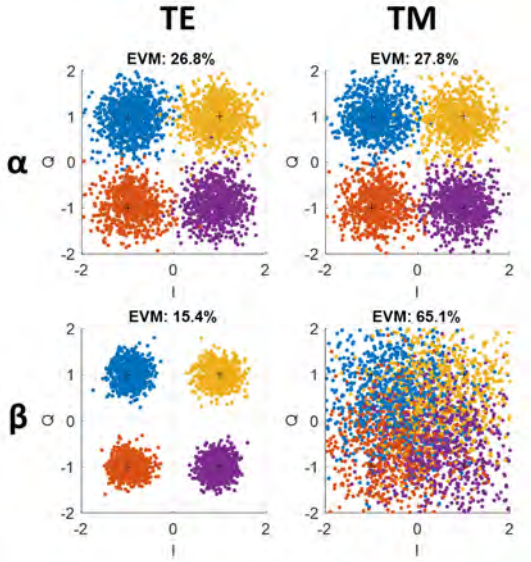

Fig. 7: Constellations obtained in each photodetector (α and β) when light is coupled into a specific polarization (TE or TM).

Fig. 8 presents the BER and EVM sensitivity curves for TE and TM polarizations as a function of the received optical power at the PIC input. As expected, the TE and TM polarizations in detector α (orange lines) behave similarly, whereas TE in detector β (solid blue line) shows significantly better results for both BER and EVM, while TM in β (dashed blue line) has much worse values. This is consistent with the levels shown in Fig. 4 and constellations in Fig. 7.

It is worth noting that we analyse BER and EVM in each detector separately rather than jointly, as this is a preliminary step before combining by DSP both polarizations in a single measurement.

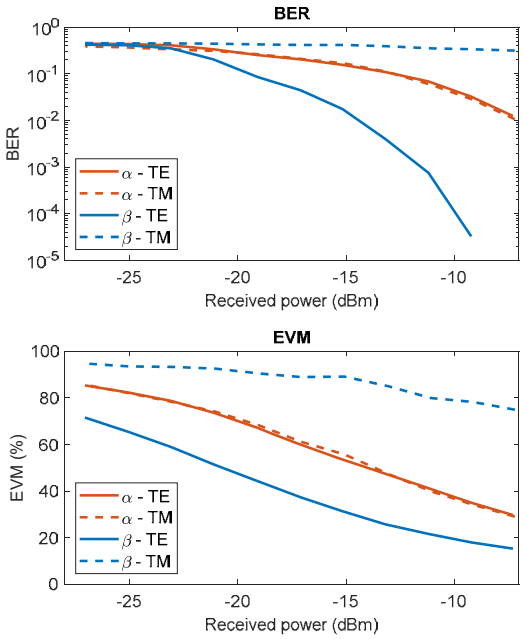

Fig. 8: BER and EVM sensitivity curves for each photodetector (α and β) and polarization (TE or TM).

5.- Conclusions

In this work we have designed and fabricated an integrated coherent transceiver using InP technology for PONs. The evaluation of the Photonic Integrated Circuit (PIC) has revealed that the PBS included to achieve a polarization independence is unable to fully split orthogonal polarizations, and thus it does not meet the design specifications entirely. Although some thermal tuning of the response of the PBS is possible, there is not an operating point that achieves a good polarization separation of the signal with PER values comparable to those obtained in fibre-based polarization splitting devices. This may be due to tolerances and imperfections in the PIC fabrication process.

However, it has been demonstrated that, even in a non-optimal scenario, the proposed architecture for the coherent detection scheme is functional. Indeed, the system is capable of recovering signals for the orthogonal polarization states TE and TM. BER values for a 2 Gb/s 4QAM transmission signal are in the range of 10^{-2} for -7.3 dBm received optical power of the signal at the PIC input.

To ensure the insensitivity of the device to the SOP of the received signal, a linear combination of the signals detected by both photodetectors may be conducted. This approach can be implemented by using a DSP algorithm able to compensate for the PBS polarization separation curves.

Acknowledgements: This work was supported by the Gobierno de Aragón (T20_23R), the Agencia Estatal de Investigación MICIU/AEI/10.13039/501100011033 (PID2020-114916RB-I00), the Agencia Estatal de Investigación MICIU/AEI/10.13039/501100011033 and FEDER, UE (PID2023-148342OB-I00), and the Agencia Estatal de Investigación MICIU/AEI/10.13039/501100011033 and European Union NextGenerationEU/PRTR (PDC2023-145803-I00).

References

[1] W. Hu and Y. Zhu, "100G and Beyond for PON and Short Reach Optical Networks," in 2023 Optical Fiber Communications Conference and Exhibition (OFC), pp. 1–43, 2023.

[2] Y. Zhu, L. Yi, B. Yang, X. Huang, J. S. Wey, Z. Ma, and W. Hu, "Comparative study of cost-effective coherent and direct detection schemes for 100 Gb/s/λ PON," Journal of Optical Communications and Networking, vol. 12, no. 9, pp. D36–D47, 2020.

[3] B. Glance, "Polarization independent coherent optical receiver," Journal of Lightwave Technology, vol. 5, no. 2, pp. 274–276, 1987.

[4] M. Barrio, D. Izquierdo, J. A. Altabás, and I. Garcés, "50 Gb/s Transmission using OSSB-MultiCAP Modulation and a Polarization Independent Coherent Receiver For Next-Generation Passive Optical Access Networks," Journal of Lightwave Technology, vol. 39, no. 18, pp. 5722–5729, 2021.

[5] D. Izquierdo, M. Barrio, P. Sevillano, J. A. Altabas, and I. Garces, "100 Gb/s/λ polarization multiplexing PON downlink based on simplified heterodyne coherent reception," Journal of Optical Communications and Networking, vol. 16, no. 12, pp. 1241–1248, 2024.

[6] D. Pérez-Galacho et al., "Integrated Polarization Beam Splitter for 100/400 GE Polarization Multiplexed Coherent Optical Communications," in Journal of Lightwave Technology, vol. 32, no. 3, pp. 361-368, 2014.

Dual-comb generator based on a monolithically integrated InP Photonic Integrated Circuit

Pablo LÓPEZ-QUEROL[(1)], Clara QUEVEDO-GALÁN[(1)], José Manuel G. TIJERO[(1)], Ignacio ESQUIVIAS[(1)], and Antonio PÉREZ-SERRANO[(1)]

1. CEMDATIC-ETSI Telecomunicación, Universidad Politécnica de Madrid, 28040 Madrid, Spain

Contact: Pablo LÓPEZ-QUEROL (pablo.lquerol@upm.es).

ABSTRACT:

We present a high-resolution dual-comb generator monolithically integrated into a Photonic Integrated Circuit (PIC) based on an open-access indium phosphide platform. The system consists of two gain-switched semiconductor ring lasers operating under common optical injection, ensuring mutual coherence and no perturbation of the emission of the injecting laser. Dual-comb generation and detection is demonstrated, enabling efficient down-conversion of broadband optical spectra into a low-bandwidth RF signal, facilitating high-resolution measurements with simple electronics. These results pave the way for compact, fast, and high-resolution dual-comb systems applicable to spectroscopy, distance measurement, and optical metrology.

Key words: Optical Frequency Combs, Dual-comb spectroscopy, Photonic Integrated Circuits

1.- Introducción

Los peines de frecuencia óptica (*Optical Frequency Combs,* OFCs) han revolucionado la fotónica en los últimos 20 años, impulsando avances en campos tan diversos como la espectroscopía molecular [1], la medida de distancias [2], las telecomunicaciones [3], los relojes atómicos [4] y la generación de señales [5]. Un OFC es una señal pulsada coherente cuyo espectro está compuesto por un conjunto de tonos de frecuencia distribuidos uniformemente con un espaciamiento determinado por la frecuencia de repetición f_R, abarcando un ancho de banda espectral $\Delta\upsilon$.

Existen diversas técnicas para generar OFCs. Los láseres de bloqueo de modo (*Mode-Locking Lasers,* MLLs) [6] y los resonadores de microanillo (*Microring Resonators,* MRRs) [7] permiten generar peines con un gran ancho de banda y un gran número de tonos. Sin embargo, la frecuencia de repetición está determinada por la longitud de la cavidad. Por otro lado, la generación de peines de frecuencia a través de la técnica de conmutación de ganancia (*Gain-Switching,* GS) [8] permite configurar la frecuencia de repetición de manera flexible en un rango que va desde unos pocos MHz hasta decenas de GHz, simplemente cambiando la frecuencia de la señal de modulación aplicada. No obstante, es importante destacar que estos últimos tienen un ancho de banda limitado en comparación con sus contrapartes de MLL o MRR pero permiten implementar generadores de OFCs de manera sencilla y eficiente. Además, se necesita de inyección óptica externa para dotar de coherencia a los pulsos consecutivos producidos por la conmutación de ganancia del láser y dar lugar a un OFC.

La interferometría de peine dual (*Dual-comb interferometry*) [1] es una técnica avanzada de medida que cuenta con una amplia variedad de aplicaciones, entre ellas la espectroscopía. Se basa en la medida del patrón de

interferencia generado por la interacción de dos OFCs que son mutuamente coherentes, pero con frecuencias de repetición ligeramente diferentes, f_{R1} y f_{R2}, donde $f_{R1} = f_{R2} + \delta f$. La interferencia de ambos peines en un fotodetector da lugar a un interferograma, cuya frecuencia de repetición se encuentra en el rango de radiofrecuencia (RF). La transformada de Fourier de este interferograma da lugar a un peine de frecuencias RF que consiste en una versión comprimida del espectro óptico original. El factor de compresión (CF) viene dado por $CF = f_{R1}/\delta f$. De esta forma, un ancho de banda óptico $\Delta\upsilon$ queda comprimido en un ancho de banda eléctrico $\Delta\upsilon$ / CF, lo que permite realizar medidas espectroscópicas de alta resolución con electrónica de bajo ancho de banda. La resolución de la medida viene dada por la frecuencia de repetición de los peines.

En este trabajo presentamos un sistema de peine dual o dual-comb para espectroscopía en un Circuito Integrado Fotónico (PIC) monolíticamente integrado basado en una plataforma de integración genérica de Fosfuro de Indio (InP). El diseño se basa en los bloques básicos (BBs) estándar de la librería de componentes del fabricante. La fabricación se lleva a cabo en una oblea multiproyecto, lo que permite ahorrar costes.

2.- Diseño y esquema del Circuito Fotónico Integrado

La Fig. 1 muestra una fotografía del PIC fabricado junto con su esquema. Para la generación de los dos OFCs, se emplea la técnica de GS con dos láseres de anillo de semiconductor (*Semiconductor Ring Lasers,* SRLs). El bloqueo por inyección óptica común en los dos SRLs proporciona coherencia mutua entre los dos peines. Para esto, como láser inyector se utiliza un láser SG-DBR integrado o un láser externo sintonizable de ancho de línea estrecho inyectado a través de una de las entradas del PIC.

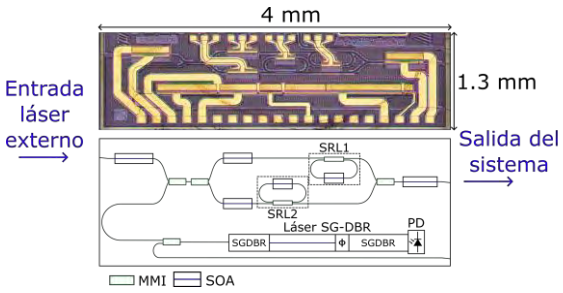

Fig. 1: Fotografía del dispositivo fabricado y esquema del PIC.

Puesto que la implementación del esquema de inyección óptica en PICs se ve limitada por la falta de aisladores ópticos en plataformas de integración genéricas [9], se propone el uso de SRLs, que presentan una alta unidireccionalidad en su emisión cuando se inyectan ópticamente [10]. De esta forma se evita que el láser maestro se vea afectado por la emisión de los láseres esclavos. Además, para controlar la potencia de inyección, se emplean dos amplificadores ópticos de semiconductore (SOAs) dispuestos antes de los SRLs y dos SOAs en las entradas/salidas del chip para amplificar la señal óptica.

3.- Resultados experimentales

Como señal de GS se utilizan dos trenes de pulsos eléctricos [11] con frecuencias $f_{R1} =$ 500 MHz y $f_{R2} =$ 500.1 MHz, siendo el factor de compresión $CF =$ 5,000. Como fuente de inyección óptica común, se emplea el láser sintonizable externo. Además, se ha investigado la generación de OFCs utilizando el láser SG-DBR integrado; sin embargo, los peines obtenidos presentan un menor ancho de banda y una mayor anchura de línea en sus tonos.

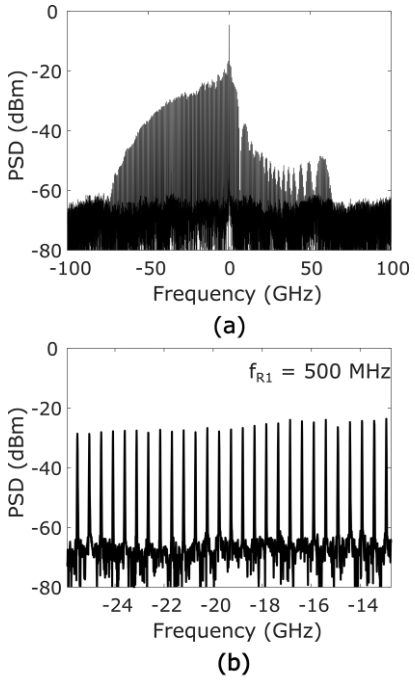

Fig. 2: (a) OFC generado en el SRL1 a una frecuencia de repetición de f_{R1} = 500 MHz y (b) vista ampliada donde se pueden distinguir los tonos del peine.

La Fig. 2 (a) muestra el peine generado en el SRL1 con f_{R1}, cuya vista ampliada en una región del espectro se muestra en la Fig. 2 (b), donde se pueden apreciar claramente los distintos tonos del peine. Para mejorar la representación, el eje de frecuencias se ha centrado en 0 GHz, correspondiente a la frecuencia óptica de inyección del láser externo. El ancho de banda del peine es de aproximadamente 30 GHz a 10 dB del tono de mayor potencia, excluyendo la inyección. Simultáneamente, en el SRL2 se genera otro peine con características similares a f_{R2}. No se observa ninguna perturbación mutua entre ambos anillos cuando están generando los OFCs. A través de la salida del sistema, ambos peines se detectan en un fotodetector, dando lugar a los resultados mostrados en la Fig. 3.

La Fig. 3(b) muestra el peine RF obtenido aplicando la Transformada Rápida de Fourier (FFT) un interferograma de 200 µs, del que se muestra una traza en la Fig. 3(a). Los espectros de RF medidos consisten en armónicos individuales separados por 100 kHz, lo que corresponde a δf. El ancho de banda óptico de los peines, queda comprimido de manera efectiva en un ancho de banda eléctrico de 6 MHz, lo que permite realizar medidas con electrónica de bajo ancho de banda.

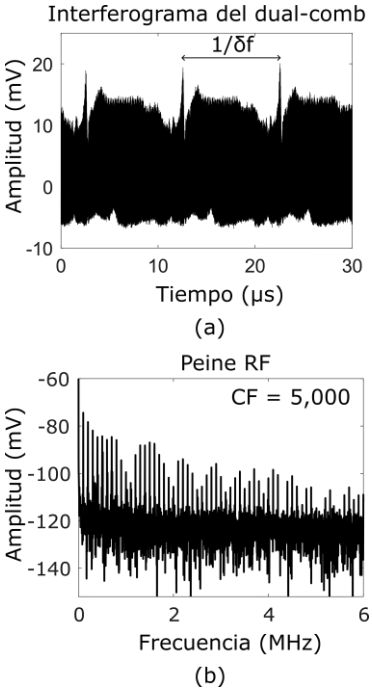

Fig. 3: (a) Medida del interferograma resultante del batido de los dos peines en el fotodetector y (b) su FFT, que muestra el peine de RF que mapea el espectro óptico en un bajo ancho de banda eléctrico.

4.- Conclusión

En este trabajo presentamos un interferómetro de peine dual de alta resolución, monolíticamente integrado en un PIC. El PIC está basado en BBs estándar de una plataforma de acceso abierto basada en InP, y ha sido fabricado en una oblea multiproyecto. Hasta donde alcanza nuestro conocimiento, este trabajo constituye una demostración de un interferómetro de peine dual en un PIC monolítico. Aunque estudios previos han demostrado la integración monolítica de fuentes de peine dual [12], no se había reportado hasta ahora la detección del batido de estos peines y la conversión a bajas frecuencias. Este avance permite abrir nuevas líneas de investigación orientadas al desarrollo de sistemas de peine dual integrados, compactos, rápidos y de alta resolución, que pueden utilizarse en

numerosas aplicaciones como la espectroscopía o la medida de distancias.

Acknowledgements: This work was funded by the grants TED2021-131957B-100 and PID2021-1234590B-C21 funded by Ministerio de Ciencia e Innovación (Spain), MCIN/AEI/10.13039/501100011033 and by the European Union NextGenerationEU/PRTR and ERDF ‘‘A way of making Europe’’.

References

[1] N. Picqué and T. W. Hänsch, “*Frequency comb spectroscopy*,” Nat. Photonics, 13, 146–157, 2019.

[2] Z. Zhu and G. Wu, “*Dual-comb ranging*,” Engineering 4, 772–778, 2018.

[3] P. Marin-Palomo, J. N. Kemal, P. Trocha, et al., “*Comb-based WDM transmission at 10 Tbit/s using a DC-driven quantum-dash mode-locked laser diode*,” Opt. Express 27, 31110–31129, 2019.

[4] T. Udem, R. Holzwarth, and T. W. Hänsch, “*Optical frequency metrology*,” Nature, 416, 233–237, 2022.

[5] V. Torres-Company and A. M. Weiner, “*Optical frequency comb technology for ultra-broadband radio-frequency photonics*,” Laser & Photonics Rev. 8, 368–393, 2014.

[6] W. Wei, J. Chen, J. Huang, et al., “*Advances of semiconductor mode-locked laser for optical frequency comb generation*,” National Sci. Open 1, 20220026, 2022.

[7] A. L. Gaeta, M. Lipson, and T. J. Kippenberg, “*Photonic-chip-based frequency combs*,” Nat. Photonics 13, 158–169, 2019.

[8] P. M. Anandarajah, K. Shi, J. O’Carroll, et al., “*Phase shift keyed systems based on a gain switched laser transmitter*,” Opt. Express 17, 12668–12677, 2009.

[9] M. P. Vaughan, I. Henning, M. J. Adams, et al., “*Mutual optical injection in coupled dbr laser pairs*,” Opt. Express 17, 2033–2041, 2009.

[10] L. Chrostowski and W. Shi, “*Monolithic injection-locked high-speed semiconductor ring lasers*,” J. Light. Technol. 26, 3355–3362, 2008.

[11] A. Rosado, A. Pérez-Serrano, J. M. G. Tijero, et al., “*Enhanced optical frequency comb generation by pulsed gain-switching of optically injected semiconductor lasers*,” Opt. Express 27, 9155–9163, 2019.

[12] J. K. Alexander, L. Caro, M. Dernaika, et al., "*Integrated dual optical frequency comb source*," Opt. Express 28, 16900-16906, 2020.

Design of a Monolithically Integrated Photonic Microwave Phase Shifter

Gonzalo SOLDEVILLA, Pablo LÓPEZ-QUEROL, José Manuel G. TIJERO, Ignacio ESQUIVIAS and Antonio PÉREZ-SERRANO

CEMDATIC, E.T.S.I. Telecomunicación, Universidad Politécnica de Madrid, 28040 Madrid, Spain.

Contact: Gonzalo SOLDEVILLA (gonzalo.soldevilla@upm.es).

ABSTRACT:

In this contribution we report on the design of a photonic-based microwave phase shifter with four independent outputs that could be used in a beamforming network of phased array antennas operating in the bands X and Ku. We show its operation principle and simulations of its performance when using input RF signals with single or multiple frequencies. Here, we report on the design of an Indium Phosphide photonic integrated circuit that will be fabricated through a multi-project wafer run.

Key words: Microwave Photonics, Photonic Integrated Circuits, RF Phase Shifters, Phased Array Antennas, Beamforming Network, Optical Frequency Shifter.

1.- Introduction

Phased Array Antennas (PAAs) are extensively used in radar and radiofrequency communication systems due to their ability to generate a directive beam that can be dynamically steered based on an input control signal. Compared to other alternatives, they offer superior precision in controlling and shaping the radiation pattern, along with the advantage of reducing sidelobes [1].

A PAA is composed of 3 main parts: the RF source/detector, the antennas and a beamforming network. The beamforming network is the key element of PAA. It is composed of several independent paths connecting the antennas and the RF source/detector. The transmission characteristics of each path indicate the direction of radiation of the PAA. These characteristics can be changed using control elements which feed every antenna of the array. These control elements can be of two types: based on phase shifters or True Time Delay (TTD) elements.

TTD control elements correspond to weights in the array factor which have an exponential dependence with a linear phase relationship with frequency [1]. Considering this dependence the group delay can be demonstrated to be independent of the frequency. The use of these control elements provides a stationary pointing direction for all frequencies avoiding dispersion and preserving the shape of the signal. On the other hand, beam steering using tuneable phase shifters shows a peak at a direction which depends on the frequency. This produces an undesired effect, called beam squint phenomenon, which causes the beam to point out at different directions as the frequency varies [1]. This phenomenon can limit the operational bandwidth, which is also influenced by other parameters of the array, such as the number of antennas and their spacing.

Phase shifters used in beamforming networks can be implemented using Microwave Photonics due to its capability to translate optical phase shifts into RF phase shifts [2]. This technique helps overcome limitations of electronic circuits in phase shifting

implementation. Notably, it offers improved features such as immunity to electromagnetic interferences, broader bandwidth, increased signal purity, better linearity and faster response time [2,3].

There are several approaches for implementing Microwave Photonic RF Phase Shifters such as the use of a dual parallel Mach-Zehnder modulator (DPMZM) [4], the use of a DPMZM with an optical band-pass filter [5,6], which can be implemented using a circulator and a Fiber Bragg Grating (FBG) [7], and the use of Stimulated Brillouin Scattering (SBS) [8]. However, the most promising approach consists of the implementation of these phase shifters in Photonic Integrated Circuits (PICs). PICs provide increased stability, reduced size and weight, and the possibility of using low operating power [2, 3].

Various groups have developed distinct implementations using PICs based on multiple technologies such as Silicon on Insulator (SOI) [2,9,10,11,12], polymer [13] and Silicon Nitride (Si_3N_4 TriPleX) [14], implementing different techniques to achieve phase shifting. For example, some contributions include an optical deinterleaver filter (ODF) in the PIC [2,9], while some rely on Microring resonators (MRRs) to achieve phase shift [10,11,14] and others use a SBS based module for the same purpose [12].

In this contribution we propose a monolithically integrated RF Phase Shifter suitable for controlling beam steering in a PAA operating in the radar bands X and Ku, spanning from 8 GHz to 18 GHz. The Phase Shifter will be developed in an Indium Phosphide (InP) PIC, which has the advantage of including active and passive elements, in particular, lasers, fast modulators, and photodiodes which are needed for the design.

Our phase shifter is based on an IQ modulator which acts as a frequency shifter and different paths consisting of Electro-Optic Phase Modulators (EOPMs) which introduce independent phase shifts in the resulting RF signal. The signal coming out of the IQ modulator beats with the signal coming out of the EOPM corresponding to each path in a Photodetector (PD) which allows the obtention of the phase shifted RF signals.

This document is organized as follows. In Section 2, we explain the design of the RF phase shifter and its working principles. Later, in Section 3 we detail the simulation model, whose results are present in Section 4. Finally, we summarize the conclusions in Section 5.

2.- Design and mathematical description

The schematic of the microwave phase shifter is shown in Fig. 1.

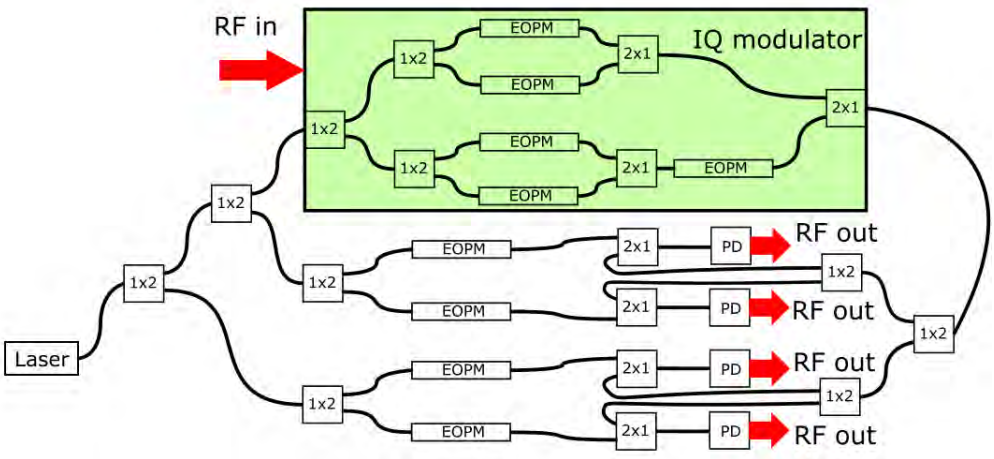

Fig. 1: Schematic of the proposed microwave phase shifter.

The system is based on a single-mode laser that produces a CW output that is divided between different paths. A part of this light is directed to a frequency shifter, which is realized using an IQ modulator. This modulator consists of a Mach-Zehnder Interferometer (MZI) which contains a Mach-Zehnder Modulator (MZM) in the upper branch and a MZM followed by a EOPM in the lower one. Each MZM is itself formed by a 1x2 coupler which leads to two arms, in both of which there is an EOPM, and a 2x1 coupler where both arms end. The input RF signal is introduced in the IQ modulator, with RF signals in quadrature driving each MZM.

In addition to the IQ modulator, the light from the laser is directed to four paths. At each path, an EOPM introduces a phase shift in the laser signal and a 2x1 coupler is used to join the signal coming from the EOPM to the signal coming from the IQ modulator. Finally, these signals beat in a PD. The electrical signals coming out of the PDs constitute the 4 RF signal outputs.

Both MZMs in the IQ modulator are driven in Push-Pull mode, with a DC and a RF signal, while the EOPMs in the IQ modulator and the four paths are driven by just a DC signal. The DC signal introduced in both MZMs bias it at a transmission minimum to achieve carrier suppression. In the simplest case, the RF signal introduced in the upper MZM consists of a cosine at frequency ω_{RF} and the one introduced in the lower MZM consists of a sine at the same frequency. Finally, the EOPM is driven to introduce a phase difference of $\pi/2$ so that both branches are in quadrature.

In this way the IQ modulator behaves as a frequency shifter providing a carrier-suppressed single-sideband (CS-SSB) signal [15] which is given by:

$$E_{IQ} = \frac{2}{\sqrt{2}} E_0 J_1\left(\frac{\pi A}{2V_\pi}\right) e^{j(\omega_c+\omega_{RF})t}, \quad (1)$$

Where A is the amplitude of the RF signal, ω_{RF} is its frequency, V_π defines the difference between maximum and minimum transmission operation points of the MZM, J_1 is the 1st order Bessel function, E_0 is the amplitude of the electric field coming from the laser, which is proportional to $\sqrt{P_0}$, being P_0 the input power of the laser, and ω_c is the carrier frequency of the laser signal.

The CS-SSB signal generated at the output of the IQ-Modulator is sent to every path of the beamforming network. The signal coming from the laser is also sent to every path where it is phase shifted by a EOPM driven by a DC voltage. The signal obtained as the output of the i-EOPM is given by

$$E_{shift} = E_0 e^{j(\omega_c t+\phi_i)}, \quad (2)$$

where Φ_i is the phase shift introduced by the i-EOPM.

The phase shifted and the frequency shifted signals beat at the PD corresponding to each path. At the output of each PD there is a RF signal, given by

$$\begin{aligned} E_{out} &= \left|E_{IQ} + E_{shift}\right|^2 = \\ &= |E_0|^2 \left(1 + 2{J_1}^2\left(\frac{\pi A}{2V_\pi}\right)\right. \\ &\left. + 2\sqrt{2}J_1\left(\frac{\pi A}{2V_\pi}\right)\cos(\omega_{RF}t - \phi_i)\right), \end{aligned} \quad (3)$$

whose frequency corresponds to the one selected for the RF signals driving the MZMs of the IQ-modulator. This output signal is also phase shifted from the original RF signal by a value corresponding to the phase shift introduced by the EOPM of each path. Thus, the phase shift introduced in each path can be controlled by selecting the DC signal that drives the corresponding EOPM. It can also be deduced that the power of both the DC component and the component in ω_{RF} depend on the power of the input laser and the modulation depth.

3.- Simulation model

The simulations have been carried out in VPIphotonics Design Suite Simulation Software and the schematic used for the simulation, which emulates the design in Fig. 1, is shown in Fig. 2.

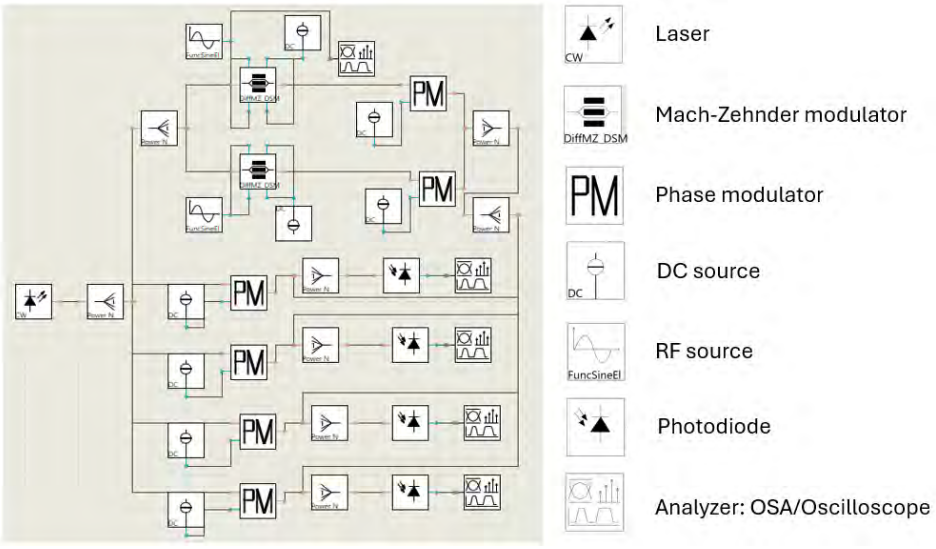

Fig. 2: Schematic used for simulation.

In this schematic, we used splitters and combiners instead of 1x2 or 2x1 couplers for simplicity as they provide basically the same results. These splitters divide the input power into the different channels so that each channel receives P_{in}/N, being N the number of output channels, while the combiners receive N input channels being the output power the addition of the power of every input channel divided by N.

Regarding the parameters of the different elements, the laser has an output CW power of 10 mW, a central frequency of 193.1 THz and a 10 MHz linewidth. The MZM has a value of V_π of 4 V and an insertion loss of 3 dB, while the Phase Modulator (PM) allows to select an arbitrary phase shift. Finally, the PD has a responsivity of 1 A/W, a thermal noise of 10^{-11} A/$\sqrt{Hz}$ and includes shot noise.

4.- Simulation results

The first simulations were made taking a single-frequency input RF signal. The default RF frequency in our simulations is 10 GHz and the default RF amplitude is 2 V.

Initially, we checked that the RF output power grows linearly with the laser power, as expected. We also observed that the RF output power is significantly lower than the RF input power, which is caused by losses in the MZMs composing the IQ modulator and losses caused by the power splitters. As a numerical example, the value of G_{RF}, which is obtained as the rate between the RF output and input powers, for a laser power of 10 dBm, is -40.8 dB.

Different simulations were made studying the RF output signal of one of the paths for different phase shifts in the EOPM of the corresponding path. The results of these simulations are shown in Fig. 3.

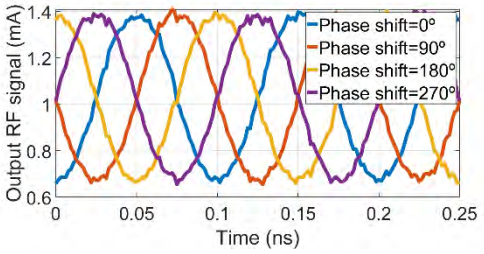

Fig. 3: Comparison of the output RF signals introducing different phase shifts.

The output signal is phase shifted by a value equal to the phase shift introduced by the EOPM, as expected, according to Eq. (3). Furthermore, the amplitude of the output signal is independent of the phase shift that is introduced to the path. The noise that affects the output signal is mainly caused by the shot noise in the PD which has not been filtered.

We also show in Fig. 4 the spectrum of one of the output RF signals shown in Fig. 3.

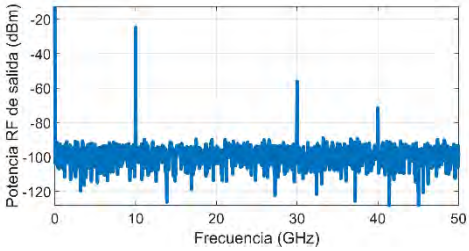

Fig. 4: Spectrum of one of the output RF signals.

In addition to the DC component and the component at the frequency of the input RF signal, other spurious harmonics appear. The main one is the 3rd harmonic, in this case located at 30 GHz. The harmonics coming from signals in the radar X and Ku bands will lay outside the bands and they can, therefore, be electrically filtered.

Subsequently, we selected a different phase shift (PS) for the EOPM corresponding to each one of the four paths and we made a simulation in which the output signal from each path was plotted. The results of this simulation are shown in Fig. 5.

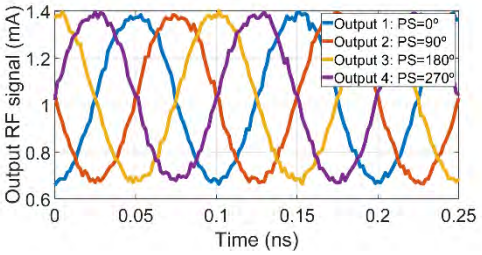

Fig. 5: Comparison of RF signals from the different outputs.

The behaviour of the different RF signal outputs is the same as the one obtained taking different phase shifts for one of the paths. Therefore, it can be confirmed that the design allows the performance of four independent RF phase shifts simultaneously.

After evaluating the performance of our RF phase shifter with a single-frequency RF signal as input, we also wanted to examine the behavior of the system when multiple frequencies are introduced. We introduced two RF signal inputs simultaneously with frequencies of 10 and 18 GHz. The output RF signal from each path is shown in Fig. 6 (a) and the spectrum corresponding to the output of the first path is shown in panel (b).

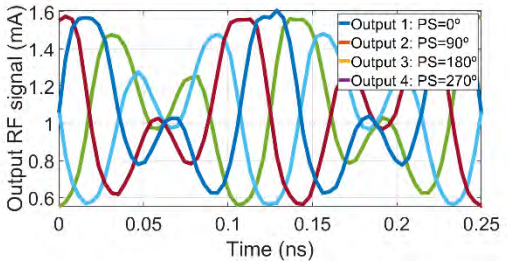

(a)

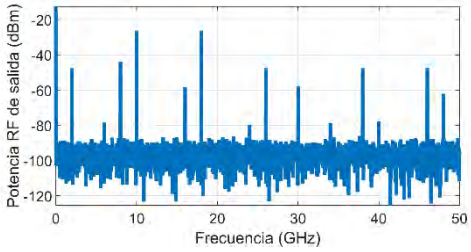

(b)

Fig. 6. (a): Comparison of the output RF signals of the different paths (b): Spectrum of one of the output RF signals.

As shown in Fig.6 (a), the output RF signal from each path contains the same frequencies as the input signal and is phase shifted with respect to it by a value equal to the phase shift introduced by the EOPM of the corresponding path. The amplitude of the RF output signal is independent of the introduced phase shift. On the other hand, in the spectrum we can see spurious signals coming from intermodulation terms in the working band which reduce the maximum RF input power that can be used to achieve a spurious-free output.

5.- Conclusion

In this contribution we reported the design of a photonic-based RF phase shifter for the X and Ku radar bands. We have shown its operation principle and its usefulness for single-frequency RF input signals. Nevertheless, this work is still in progress. We will evaluate additional design parameters that have not yet been analyzed, such as the spurious-free dynamic range when multiple frequencies are introduced in the RF phase shifter. We will design the PIC layout containing the RF phase shifter that will be

sent to an InP foundry for fabrication in a multi-project wafer. Finally, we will experimentally characterize the fabricated PIC to verify its consistency with the simulated results.

Acknowledgements: This work has been supported by the Secretaría de Estado de Telecomunicaciones e Infraestructuras Digitales, Ministerio para la Transformación Digital y de la Función Pública, funded by NextGenerationEU, in the context of the Programme for the creation of Chip University-Business Chairs, Project TSI 069100-2023-0016, Chip Chair UPM-INDRA (CAUPIME).

References

[1] Jianping YAO, José CAPMANY, Ming LEE, *"Microwave Photonics"* (John Wiley & Sons, 2024).

[2] Claudio PORZI et al., *"Photonic Integrated Microwave Phase Shifter up to the mm-Wave Band With Fast Response Time in Silicon-on-Insulator Technology"*, Journal of Lightwave Technology, vol. 36, no. 19, pp. 4494-4500, 2018.

[3] Francesco AMATO et al., "*Photonic integrated circuits for ultra-fast steering in phased-array antennas*", in Proceedings of International Conference on Space Optics — ICSO, 2019.

[4] Erwin H. W. CHAN et al., "*Photonic RF Phase Shifter Based on Optical Carrier and RF Modulation Sidebands Amplitude and Phase Control*", Journal of Lightwave Technology, vol. 30, no. 23, pp. 3672-3678, 2012.

[5] Jianguo SHEN et al., "*A photonic rf phase shifter based on a dual-parallel mach–zehnder modulator and an optical filter*", Applied physics express, vol. 5, no. 7, 072502, 2012.

[6] Yunxin WANG et al., "*All-optical microwave photonic downconverter with tunable phase shift*", IEEE Photonics Journal, vol. 9, no. 6, pp. 1–8, 2017.

[7] Tianwei JIANG et al., "*Photonic downconversion with tunable wideband phase shift*", Opt Lett., vol. 41, no. 11, 2016.

[8] Alayn LOAYSSA et al., "*Broad-Band RF photonic phase shifter based on stimulated Brillouin scattering and single-sideband modulation*", Photonics Technology Letters, vol. 18, no. 1, pp. 208-210, 2006.

[9] Giovanni SERAFINO et al., *"A Photonic Beamforming Network Based on Phase Shifters for Microwave Wide-Band Applications"*, in Proceedings of 21st International Conference on Transparent Optical Networks (ICTON), pp. 1-4, 2019.

[10] Minhao PU et al., *"Widely tunable microwave phase shifter based on silicon-on-insulator dual-microring resonator"*, Opt. Express, vol. 18, no. 6, pp. 6172-6182, 2010.

[11] Giovanni SERAFINO et al., *"Design and characterization of a photonic integrated circuit for beam forming in 5G wireless networks",* in Proceedings of International Topical Meeting on Microwave Photonics (MWP), pp. 1-4, 2017.

[12] Luke MCKAY et al., *"Broadband Brillouin Phase Shifter Utilizing RF Interference: Experimental Demonstration and Theoretical Analysis",* Journal of Lightwave Technology, vol. 38, no. 14, pp. 3624-3636, 2020

[13] Sang-Shin LEE et al., *"Demonstration of a photonically controlled RF phase shifter",* IEEE Microwave and Guided Wave Letters, vol. 9, no. 9, pp. 357-359, 1999

[14] Gaojian LIU et al., *"Linearized integrated microwave photonic circuit for filtering and phase shifting",* APL Photonics, vol. 8, no.5, 051303, 2023

[15] Silvia DEL RÍO-MARTÍN, *"Development of a radiofrequency phase shifter based on photonic components",* M.S. Thesis, Universidad Politécnica de Madrid, 2023.

Development of Silicon Nitride Photonic Integrated Circuits: Fully in-house Fabrication and Optical Characterization

Giuseppe Libero BUFI [(1)], Christian Camilo CANO-VASQUEZ [(1)], Louw Roel van der ZON [(1)], Adrián FERNÁNDEZ [(1)], Rubén ALEMANY [(1)], César ALMINYANA [(1)] Isabelle RODRIGUEZ [(2)], Gloria MICÓ [(1)], Pascual MUÑOZ [(1)] and Daniel PASTOR [(1)]

1. UPVfab – Photonics Research Labs – iTEAM Research Institute, Universitat Politècnica de València, c/ Camino de Vera s/n, 46021 Valencia, Spain.
2. Instituto de Tecnología Química (UPV-CSIC), Universitat Politècnica de València, Consejo Superior de Investigaciones Científicas, Av. Los Naranjos s/n, 46022 Valencia, Spain

Contact: Giuseppe Libero BUFI (giuseppelibero.bufi@upv.es).

ABSTRACT:

We report the development of a purely-passive silicon nitride (SiN) photonic integrated circuit platform, fabricated entirely in house within the UPVfab cleanroom facility. The process flow includes thermal oxidation, LPCVD SiN deposition, UV lithography, and ICP-RIE etching. A 300 nm-thick stoichiometric SiN layer was deposited on 3 µm of thermally grown oxide, and patterned into basic photonic building blocks, including straight waveguides, Mach-Zehnder interferometers, and ring resonators. Optical characterization confirms successful light guiding, functional interference behavior, and resonant responses consistent with design, demonstrating the maturity of the in-house platform and validating its potential for future photonic integration.

Key words: Photonics, PIC, SiN, fabrication, optical characterization

1.- Introduction

Integrated photonics is becoming a key technology for addressing the growing demands of data processing, communication, and sensing in emerging fields such as artificial intelligence and quantum computing [1-2].

Among the various material platforms, silicon nitride (SiN) stands out due to its ultra-low losses, wide transparency range, and full compatibility with CMOS fabrication processes, making it an ideal choice for scalable and high-performance photonic devices [3].

In this work, we present the fabrication of a purely-passive SiN-based photonic integrated platform for near-infrared (NIR) applications, and its optical characterization of three fundamental building blocks: straight waveguide, Mach-Zehnder interferometer (MZI) and ring resonators.

The front-end manufacturing process flow was carried out entirely in house within the micro-fabrication pilot line cleanroom facility UPVfab, contributing to ongoing efforts toward the development of a dedicated photonic foundry.

2.- Fabrication

2.1.- Overview

In SiN integrated photonic platforms, a waveguide core thickness below 400 nm is typically employed, resulting in a moderate index contrast that enables broad applicability across various designs and use cases [3]. In this work, we take as reference the 300 nm-thick SiN platform reported in [4], which is well-suited for operation in the NIR range. A 300 nm thickness is commonly

adopted by several foundries, including IMB-CNM and Cornerstone, due to its versatility and fabrication compatibility.

Although the waveguide core thickness may vary within the sub-400 nm regime, the standard fabrication process flow remains largely consistent across platforms, typically consisting of the following steps: thermal oxidation for buried oxide (BOX) formation, SiN core deposition, lithographic patterning and pattern transfer through etching, and final encapsulation with a cladding layer.

Fig. 1 shows the schematic cross-section of the 300 nm SiN PIC fabricated in this work. The current development includes all process steps up to etching. The cladding layer was not included in this fabrication run, as the deposition process is currently undergoing qualification within our cleanroom facility.

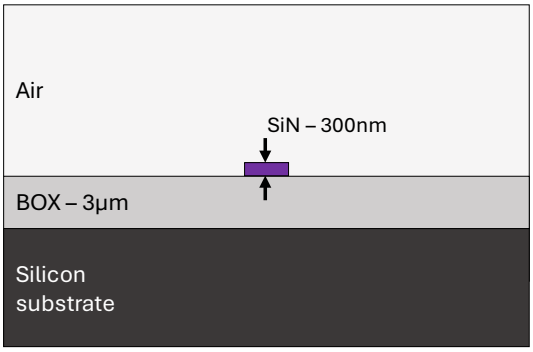

Fig. 1: Schematic cross-section of the SiN photonic technology presented in this work.

Nonetheless, the fabricated devices exhibit proper optical functionality and are suitable for characterization, as presented in Section 3. This provides valuable feedback on the current state of our fabrication capabilities.

Single-side polished, <100> oriented, 150 mm phosphorous doped 675 µm thick silicon wafers with a resistivity of 10-20 Ω·cm were used for this study.

2.2.- Buried oxide formation

A silica layer provides optical isolation by confining light within the SiN core and preventing leakage into the silicon substrate. High-quality BOX can be obtained through thermal oxidation of silicon, with typical thicknesses in the range of 2-3 µm. In this work, a target thickness of 3 µm was selected. To achieve this within a reasonable timeframe (<20 h), wet oxidation was employed, given its higher growth rate in the diffusion-limited regime.

The process was performed in a TEMPRESS oxidation furnace at 1100 °C and atmospheric pressure using pyrogenic wet oxidation. Water vapor is generated by burning hydrogen (H_2) in oxygen (O_2) gas within an external chamber connected to the furnace tube, with flow rates of 9.0 slm and 6.0 slm, respectively.

Oxidation time was determined using the Deal-Grove model [5], based on prior calibration of the system for <100> silicon wafers. The measured linear rate constant (B/A) was 5.88 µm/h, and the parabolic rate constant (B) was 0.48 µm^2/h, resulting in a required oxidation time of approximately 19.27 h to grow 3 µm of SiO_2.

To ensure process control, the oxidation was divided into multiple sub-steps, with intermediate thickness measurements. Fig. 2 shows the measured oxide thickness as a function of oxidation time, in excellent agreement with the Deal-Grove prediction.

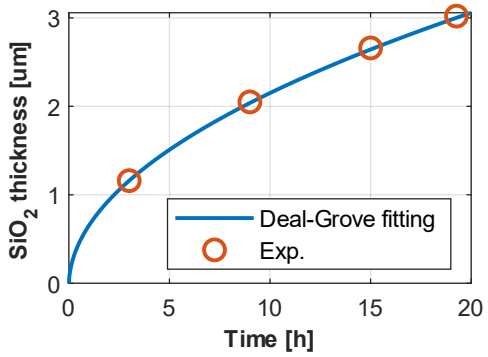

Fig. 2: SiO_2 thickness vs. oxidation time at 1100 °C on <100> P-doped Si wafers. Dots show experimental data; the solid line is the Deal–Grove fit with B/A=5.88 µm/h, and B=0.48 µm^2/h.

The grown oxide was characterized using spectroscopic ellipsometry with a Horiba Uvisel Plus over the 320-1650 nm wavelength range, at a fixed incidence angle of 70°. A Cauchy dispersion model was used to extract film thickness and optical constants, yielding a refractive index of 1.45 at 1550 nm for the SiO_2 layer.

2.3.- SiN deposition

The deposition of the SiN layer represents a critical step in the photonic platform fabrication process, as it directly influences the optical performance and mechanical stability of the final devices.

For this work, the SiN layer was deposited using low-pressure chemical vapor deposition (LPCVD) in the TEMPRESS furnace with hot-wall, 5 zones resistance-heated, horizontal, fused silica tube design.

LPCVD operates in a surface reaction-controlled regime, where the deposition rate is governed by the surface reaction kinetics rather than by gas diffusion. As a result, maintaining constant wafer loading and uniform gas flow is essential to achieving high uniformity in thickness and refractive index across the wafer batch.

The 300 nm deposition was carried out at a temperature of 810 °C and a pressure of 250 mTorr, using dichlorosilane (DCS) and ammonia (NH_3) as precursor gases, with flow rates of 60 sccm and 180 sccm, respectively.

The process followed a previously qualified recipe, with a deposition rate of 28.3 Å/min. A total deposition time of 106 minutes was used to achieve the target 300 nm thickness on top of the SiO_2 BOX.

Spectroscopic ellipsometry measurements yielded a final film thickness of 313 nm, with a point-to-point non-uniformity of 2.4% across the wafer. The extracted refractive index at 1550 nm was 1.96, in close agreement with the expected value for stoichiometric silicon nitride (≈2.00) [6].

2.4.- Lithography

The nitride layer has been patterned using UV lithography with a mask aligner (EVG 620NT) and positive-tone photoresist (PR) (AZ® MiR™ 701 Series). A mask aligner is a cost-effective tool allowing photoresist patterning resolutions down to 0.5 µm. Since the required minimal feature size (MFS) for all photonic structures in this platform is 1 µm or bigger, a mask aligner is more than adequate. Furthermore, the lithography process can be transferred to low-cost, high-volume CMOS manufacturing using a commercial scanner or stepper. The structures can also be created using electron beam lithography, which is useful for developing test structures or when higher resolutions are required [7].

For enhancing the PR adhesion Hexamethyldisilane (HMDS) was applied to the substrate and cured at 120 °C. The PR was spin coated to a thickness of 1 µm, the edge bead removed and followed by a Soft Bake of 90 s at 90 °C at a vacuum-contact hotplate.

The resist was exposed using a mask aligner emitting a 110 mJ dose at a wavelength of 365 nm. The mask was in contact with the resist using vacuum contact. To mitigate standing wave effects, a post exposure bake of 90 s, 110 °C was performed at a vacuum-contact hotplate directly afterwards.

For developing the PR in a controlled and repeatable manner, puddle developing was performed in an automated tool. The photoresist was in contact with the developer (AZ® 726MIF) for 48 s.

Using the described lithography process it was possible to achieve a minimum feature size down to 0.7 µm. A top view of several test patterns is shown in Fig. 3.

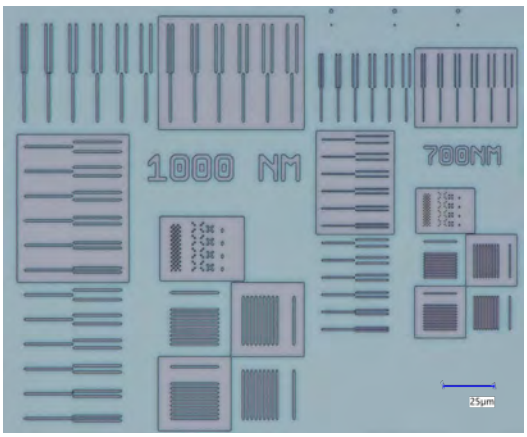

Fig. 3: Microscope picture of the patterned PR. The structures on the left have a linewidth of 1 µm, on the right the linewidth is 0.7 µm. The spacing of the forks starts at the linewidth and increases with 0.5 µm to determine any over etch.

2.5.- Etching

The transfer of the photoresist pattern onto the SiN layer was carried out via dry etching.

Unlike wet etching, which is -generally speaking- inherently isotropic and results in rounded sidewalls, dry etching enables vertical sidewalls and improved pattern fidelity. Fluorine-based chemistries are typically used for dry-etching of silicon-based materials such as Si, SiO_2, and SiN, where the volatile byproduct SiF_4 is formed in the plasma phase [8].

In this work, inductively coupled plasma reactive ion etching (ICP-RIE) Nordiko chamber was employed to etch the SiN layer. Such systems allow independent control of the plasma density (via ICP power) and ion energy (via RF substrate bias), enabling fine tuning of the process between physical (ion-driven, anisotropic) and chemical (reactive, isotropic) etching regimes. This flexibility is key for optimizing etch rate, selectivity, and sidewall quality.

After a process optimization, a suitable recipe for SiN etching was identified. The final process was performed at a chamber pressure of 50 mTorr, using a gas mixture of 40 sccm CF_4 and 5 sccm O_2. The ICP and substrate powers were set to 200 W and 30 W, respectively. Under these conditions, the process achieved a SiN etch rate of 43 nm/min, with an etch selectivity of 0.6 relative to the PR mask and 2.6 with respect to the underlying SiO_2.

Considering these parameters, the SiN layer was etched for 6 minutes. Fig. 5 presents a cross-section of the resulting waveguide, showing a well-defined etched profile. The final structure exhibits a sidewall slope of approximately 71°, along with visible sidewall roughness and surface irregularities.

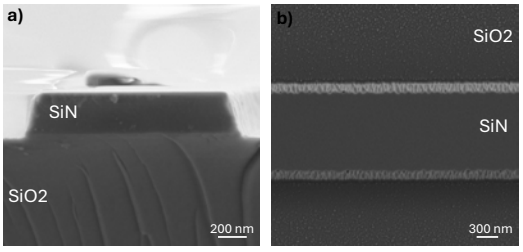

Fig. 4: a) SEM cross-sectional image and b) top-view image of the resulting waveguide structure after the ICP-RIE etching.

Ongoing analysis suggests that the dielectric screen of the ICP system's window may be sputtered by the fluorine-based plasma, subsequently redepositing onto the wafer surface and contributing to micro-masking effects and sidewall degradation. Additionally, the lithographic process plays a critical role in determining the final sidewall profile: any deviation from verticality in the resist pattern is directly transferred to the SiN layer during etching. Further improvements to both chamber conditions and lithographic patterning are currently under evaluation to enhance etch quality.

3.- Characterization

3.1.- Photonic structures

3.3.1. Optical Input/Output: Grating Couplers

Photonic characterization of the fabricated circuits prior to wafer dicing is desirable. For this reason, vertical coupling structures such as grating couplers (GCs) are employed. Based on the MFS achievable with the lithography process, grating couplers were designed for light coupling to the wafer. The final design was implemented at each input and output port of the photonic structures to facilitate optical access during characterization. Microscope images of the implemented GSs are shown in Fig. 5 b) and c).

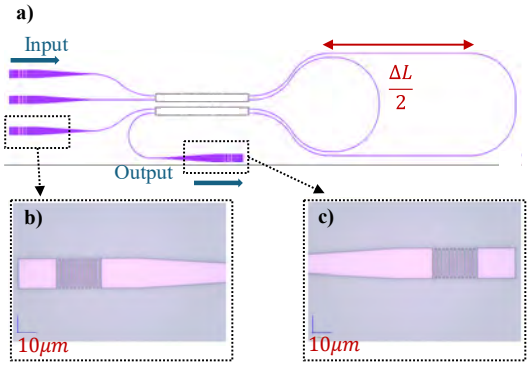

Fig. 5: a) Layout of the fabricated unbalanced Mach-Zehnder interferometer with input and output grating couplers. b) and c) Microscope images of the fabricated grating couplers.

3.3.2. Unbalanced Mach-Zehnder Interferometer

An unbalanced MZI fabricated in silicon nitride using the process described in

Section 2 is implemented. A pair of 2×2 50:50 multimode interference couplers (MMIs) from the CNM-VLC PDK is used to split and recombine the optical signal between the two arms of the interferometer. The optical path length difference (ΔL=605 µm) is introduced by extending the straight sections of the upper arm, located on the right side of the layout due to the figure orientation. This structure is connected to input and output grating couplers for vertical coupling. With this configuration (shown in Fig. 5 a)), it is possible to launch light using either bare single fibers or tailored fiber arrays.

3.3.3. Ring resonators

Three ring resonators were fabricated using the MMIs with coupling ratios available in the VLC-CNM PDK (K=50:50; 15:85; 85:15). The designs were based on the three geometric parameters defined in Fig. 6: bend radius (R=100 µm), horizontal (SSx=675.84 µm) and vertical (SSy=10 µm) straight section lengths. These parameters determine the total optical path length of the resonator and influence the free spectral range (FSR). All three rings will have the same total optical path length (L=2000 µm) and hence, the same FSR (approximately 607 pm).

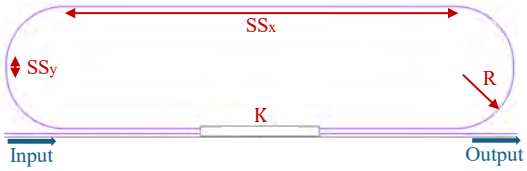

Fig. 6: Layout of the fabricated Ring Resonators. R: radius of the bends, K: coupling relationship, SSy: straight section y-axis, SSx: straight section x-axis.

3.2.- Setup

Fig. 7 shows the experimental setup used for the optical characterization of silicon nitride photonic integrated circuits at the wafer level. A broadband amplified spontaneous emission (ASE) source (FiberLabs ASE-FL7015, C+L band) is used to illuminate the devices. Light is coupled into and out of the photonic circuits via vertically aligned cleaved standard single-mode fibers positioned using a 3-axis motorized stage.

The output signal is collected by an optical spectrum analyzer (Thorlabs OSA205C), which records the spectral response of the device under test. Instrumentation is controlled via a MATLAB-based interface that manages data acquisition and facilitates post-processing of the collected spectra.

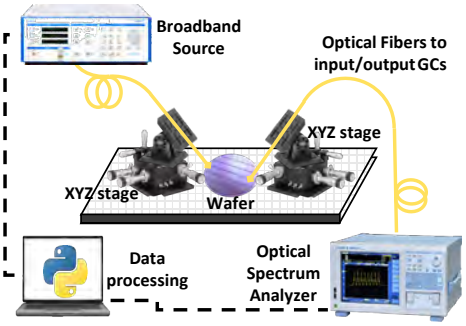

Fig. 7: Wafer-level optical characterization setup using a broadband ASE source and vertical fiber coupling. A 3-axis stage aligns cleaved fibers to the chip, and an OSA collects the output for post-processed spectral analysis.

3.3.- Measurement results

3.3.1. Unbalanced Mach-Zehnder Interferometer

Fig. 8 displays the normalized transmission spectrum of the unbalanced MZI fabricated in silicon nitride. The device response shows a periodic interference pattern with a measured FSR of approximately 1.983 nm. The measured extinction ratio is close to 20 dB. This performance suggests that the MMI couplers splitting ratio is close to 50:50, given the optical path length difference between arms (ΔL=605 µm) and the expected propagation losses (2-3 dB/cm).

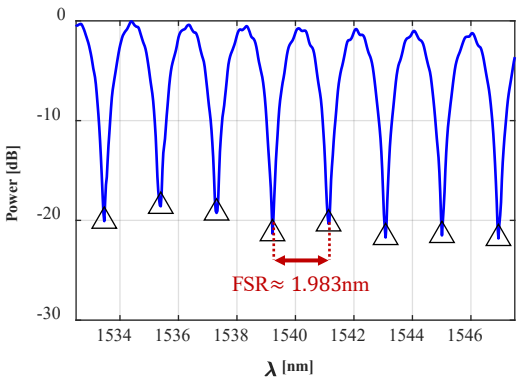

Fig. 8: Transmission spectrum of the fabricated unbalanced Mach-Zehnder interferometer with a measured FSR of approximately 1.983 nm and extinction ratio close to 20 dB.

3.3.2. Ring resonators

Fig. 9 presents the measured transmission spectra for the in-house fabricated silicon nitride ring resonators. Each trace corresponds to a MMI coupler with different power splitting ratio: 50:50 (blue), 85:15 (red), and 15:85 (green). The resonance depths vary significantly depending on the MMI coupling ratio, which is consistent with the change in coupling conditions associated with each power splitting configuration.

All designs exhibit periodic resonances with the same FSR, as expected from their identical optical path lengths (L=2000 µm). However, the measured FSR of approximately 0.618 nm differs slightly from the expected value of 0.607 nm. This deviation could be attributed to variations in the group index of the fabricated devices. Using the measured FSR, the actual group index can be estimated from the relation $n_g = \lambda^2 / FSR \cdot L$, yielding $n_g \approx 1.945$.

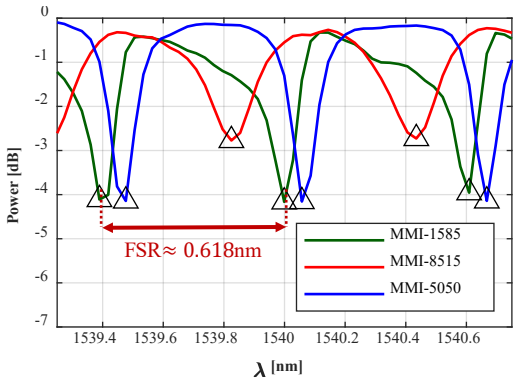

Fig. 9: Normalized transmission spectra of ring resonators implemented with MMI couplers of varying splitting ratios: MMI-1585 (green), MMI-8515 (red), and MMI-5050 (blue). The measured FSR is approximately 0.618 nm.

4.- Conclusion

The fabrication and optical characterization of SiN photonic integrated circuits were successfully carried out using a fully in-house front-end process. The experimental results obtained from ring resonators and MZIs confirm the functionality of the fabricated structures and show good agreement with the expected FSR and interference patterns. These outcomes validate the capability of the current UPVfab platform to realize standard SiN photonic components. Ongoing efforts are focused on further characterization to quantify propagation losses and effective refractive indexes, as well as on improving process steps such as etching and lithography to enhance sidewall quality and overall device performance. This work lays the groundwork for the continued development of a dedicated photonic foundry infrastructure.

Acknowledgements:
The authors received support through projects TED2021-132584B-C21, PID2022-139447NB-I00, PDC2023-145798-I00, TSI-069100-2023-0002, COMCUANTICA/001-002, and GL. Bufi PhD grant PID2019-110877GB-I00.

References

[1] S. SHEKHAR et al., *Roadmapping the next generation of silicon photonics,* Nat Commun, 15, 751, 2024.

[2] S. NING et al., *Photonic-Electronic Integrated Circuits for High-Performance Computing and AI Accelerators*, Journal of Lightwave Technology, vol. 42, no. 22, pp. 7834-7859, 2024.

[3] K. A. BUZAVEROV et al., *Silicon Nitride Integrated Photonics from Visible to Mid-Infrared Spectra*, Laser Photonics Rev, 18, 2400508, 2024.

[4] P. MUÑOZ et al., *Silicon Nitride Photonic Integration Platforms for Visible, Near-Infrared and Mid-Infrared Applications*, Sensors, 17, 2088, 2017.

[5] B. E. DEAL, A. S. GROVE, *General Relationship for the Thermal Oxidation of Silicon*, J. Appl. Phys, 36 (12), 3770–3778, 1965.

[6] K. LUKE et al., *Broadband mid-infrared frequency comb generation in a Si3N4 microresonator*, Opt. Lett., vol. 40, pp. 4823-4826, 2015.

[7] E. SHARMA et al., *A. Evolution in Lithography Techniques: Microlithography to Nanolithography.* Nanomaterials (Basel). 2022 Aug 11;12(16):2754

[8] P. E. RILEY et al., *Comparison of etch rates of silicon nitride, silicon dioxide, and polycrystalline silicon upon O2 dilution of CF4 plasmas*, J. Vac. Sci. Technol. B, 7 (6): 1352–1356, 1989.

Large-scale Silicon Photonics antenna for next-generation integrated FSO transceivers

José LOZANO ARGÜESO [(1)], Pablo GINEL MORENO [(1)], Alejandro ORTEGA MOÑUX[(2)]

1. AGPhotonics, S.L., Edf. Bioinnovación UMA, C. Severo Ochoa, 34, 29590 Málaga, Spain.
2. Telecommunication Research Institute (TELMA), Universidad de Málaga, E.T.S. Ingeniería de Telecomunicación, Bulevar Louis Pasteur 35, 29010 Málaga, Spain

Contact: José Lozano Argüeso (jose@ag-photonics.com).

ABSTRACT:

Mobile networks and internet data traffic are experiencing unprecedented growth, prompting the need for novel solutions that address the limitations of conventional telecommunications infrastructures. We report the design of an integrated optical antenna operating in the C band on a Silicon Photonics platform. The proposed antenna features a large footprint of 1.5 × 1.1 mm², achieving uniform beam divergences of 0.08° in both dimensions (θ, Φ), with a pointing angle of ~37° at 1550 nm and a scanning efficiency of 0.14°/nm. Furthermore, the design demonstrates a high tolerance to fabrication errors, maintaining stable radiation characteristics even with dimensional variations of up to ±50 nm. These advancements underscore the potential of our integrated optical antenna for next-generation Free Space Optical Communications.

Key words: Silicon Photonics, Integrated Optics, Free-Space Optics, Optical Wireless Communications, Integrated Optical Antenna

1.- Introduction

The growing demand for data in both mobile networks and the internet presents two critical challenges: i) current telecommunications infrastructure is expected to face traffic loads approximately 20 times greater than today's levels by the end of the decade, and ii) processing such high volumes of information will drive up power consumption in existing communication devices. Consequently, there is a pressing need to upgrade these networks by integrating new technologies that can mitigate these issues.

In this context, today's wireless communications predominantly rely on RF (Radio Frequency) links, which offer data rates on the order of hundreds of Mbps—significantly lower than the hundreds of Gbps to Tbps achievable with optical fiber. This performance gap has spurred a paradigm shift toward Optical Wireless Communications (OWC), also known as Free Space Optical Communications (FSOC/FSO). These systems promise point-to-point wireless links capable of supporting Gbps data rates, while providing a low-power, highly directive optical solution that is inherently difficult to intercept [1 - 4].

Nonetheless, current transceiver designs for OWC, which are based on discrete optical components, face significant challenges in terms of size, weight, and power consumption (SWaP). These issues are especially critical in applications such as non-terrestrial networks (NTNs), where systems are deployed on unmanned aerial vehicles (UAVs, HAPs, planes) or even in space (e.g., satellites and cubesats)[5].

In this context, integrated photonics offers a compelling solution by enabling the generation, routing, modulation, processing,

and detection of optical signals via photonic integrated circuits (PICs), analogous to electronic integrated circuits (ICs). Silicon Photonics (SiPh) has attracted significant attention from both academia and industry due to its scalability, CMOS compatibility with standard microelectronic fabrication processes, and the significant reductions in SWaP and cost it enables [6]. As a result, SiPh-based FSO systems can deliver high-speed, secure, and energy-efficient communication links while maintaining a compact footprint suitable for a wide range of applications [7,8].

In response to these challenges, this work addresses them by designing a novel type of integrated optical antenna operating in the C band for the TE polarization. The proposed solution not only enables the creation of large radiating apertures but also facilitates the emission of highly collimated beams, all while remaining fully compatible with commercial silicon photonics fabrication processes (Section 2).

The antenna is designed with a footprint of 1.5 × 1.1 mm², as shown in Fig. 1, deliberately chosen to ensure that the beam divergence is equal in both dimensions, as discussed in the Results section. This tailored aspect ratio yields an exceptional beam divergence of 0.08º × 0.08º, which results in a high directivity of 70 dBi. Additionally, by scanning the wavelength, the radiation angle (θ_{rad}) can be finely tuned with a scanning efficiency of 0.14º/nm. Moreover, by combining thermal scanning in the feeder to control the Φ angle with wavelength tuning to adjust the θ_{rad} angle, full 2D beam steering can be achieved using a single control element.

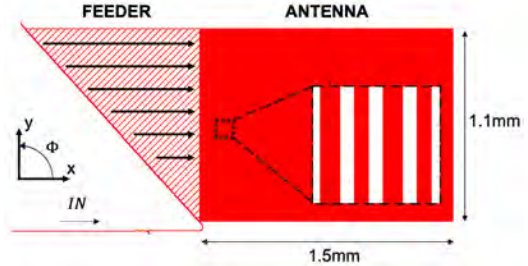

Fig. 1 GDS layout of the designed system. The red rectangle represents the proposed antenna, while the striped triangle corresponds to the feeding device with an exponential feeding profile adapted from [9]. The inset provides a zoomed-in top view of the periodic structure.

2.- Integrated large-aperture optical antenna design in Silicon Photonics

The antenna has been designed on a commercial Silicon Photonics platform with a silicon ($n_{si} \approx 3.45$) thickness of 220 nm and a etch depth 150 nm. The entire structure is surrounded by silicon dioxide ($n_{SiO2} \approx 1.45$), with a substrate thickness of 3 µm and a cladding layer of 3 µm. Additionally, a minimum feature size (MFS) of 140 nm has been considered to ensure compatibility with DUV standard fabrication processes of the foundry.

2.1.- Antenna topology

The topology of the proposed optical antenna is shown in Fig. 2. It consists of a periodic structure with a period Λ_{rad}, where each unit cell is divided into two equal sections of length Λ_{semi}. Each section comprises three regions: (i) a silicon region with a height of 150 nm and a length $b_j/2=(1-DC_j)\cdot\Lambda_{semi}$, (ii) a silicon region with a height of 220 nm and a length $a_j = DC_j\cdot \Lambda_{semi}$, and (iii) a third region identical to the first one.

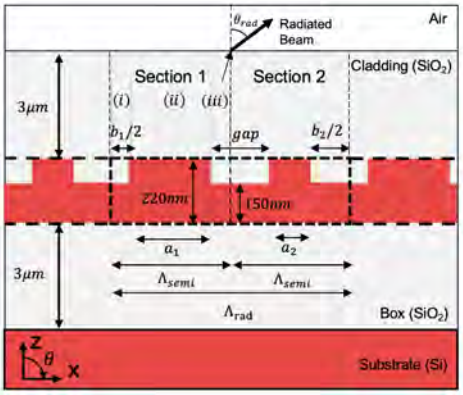

Fig. 2 Schematic of the antenna periodicity in SOI, viewed from the side, with the relevant parameters needed to fully define the structure.

Therefore, the gap between 220 nm regions is defined as $\text{gap} = (b_1 + b_2)/2$.

2.2.- Operating principle

The main idea is to transform a periodic non-radiating structure with a period of Λ_{semi}, into a weakly radiative structure by introducing a small perturbation to that periodicity. For example, consider a simple periodic structure

with a duty cycle DC=0.5 and a period Λ_{semi}=370nm, which does not radiate. We can modify this structure so that it consists of two concatenated sections that are very similar but have a period of $\Lambda_{rad}=2\Lambda_{semi}$=740nm. The first section would have a duty cycle $DC_1=0.5+\delta$ and the second section would have $DC_2=0.5-\delta$, where δ is the perturbation. This slight change in the duty cycle between the two sections introduces weak radiation, allowing the structure to become weakly radiative while still maintaining its overall periodicity.

The grating equation is given by:

$$n_F \sin(\theta_m) = n_{B,m} = n_{eff} + \frac{\lambda}{\Lambda_{rad}} m \quad (1)$$

Where n_F is the far field index, in this case air, θ_m is the angle of radiation in air for a given order m, $n_{B,m}$ is the Bloch index for a m-order, n_{eff} is the effective refractive index of the mode propagating in the grating, λ is the wavelength, 1550 nm in our case, and Λ_{rad} is the pitch of the complete structure.

As shown in Equation (1), the radiation angle exhibits a predictable dependence on wavelength, a phenomenon confirmed through the wavelength scanning simulation presented in the results section.

The required radiation strengths (α) to achieve efficient field radiation in large-scale apertures range between 1 mm^{-1} and 2 mm^{-1}. This is due to the exponential decay characteristic of a non-apodized antenna grating, following the relation $P_{wg}(z)=\exp(-2\alpha z)$, where the total radiated power is given by $P_{rad}= 1-\exp(-2\alpha L)$.

2.3.- Design workflow

We have chosen to work with the diffraction order m=-1, which means that, from this point forward, we will define the radiation angle as $\theta_{-1}=\theta_{rad}$.

The periodicity Λ_{rad} must be carefully selected to ensure that for the second diffraction order (m=-2), the condition $|n_{B,-2}| > n_{SiO2}$ is satisfied, and that it is sufficiently distant from the Bragg region so that the diffraction order remains unaffected, as illustrated in Fig. 3. This precise design choice not only prevents unwanted second-order radiation from coupling into the silicon dioxide cladding but also mitigates undesirable reflections resulting from Bragg resonances.

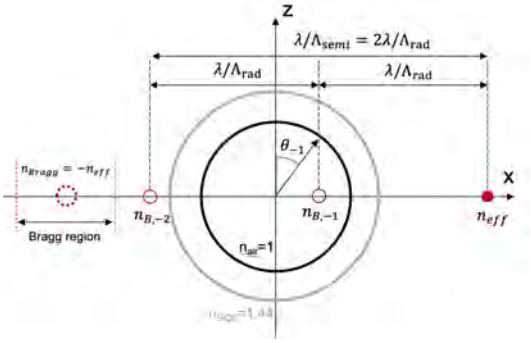

Fig. 3 The radiation phase-matching circle relevant to the analysis. The solid black line represents the radiation circle in air, while the gray line corresponds to that of SiO_2. A propagating wave within the grating, characterized by its effective index (n_{eff}), experiences a momentum shift induced by the grating periodicity, giving rise to diffraction orders (m = -1, m = -2, ...). The first diffraction order (m = -1) satisfies the phase-matching condition with air, radiating at a specific angle (θ_{-1}), whereas the second order (m = -2) lies between the Bragg region and the SiO_2 circle.

To ensure that the chosen design parameters are compatible with the requirements of commercial fabrication facilities with a Minimum Feature Size (MFS) of 140 nm and a gap (GAP) of 140 nm, we establish the following constraints:

a_1>MFS, a_2>MFS, gap>GAP

After selecting a pitch of Λ_{rad}=740nm, a simulation sweep was performed using the FEXEN software [10], and for time consuming reasons we didn't consider the substrate. The simulation explored variations in DC_1 and DC_2, yielding the radiation strength shown in Fig. 4(a) and the Bloch index (n_B) for each combination, as depicted in Fig. 4(b).

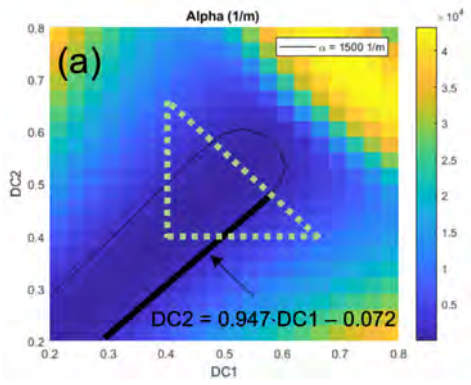

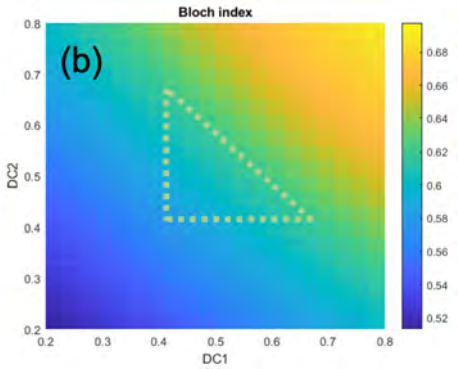

Fig. 4 Sweeps of DC_1 and DC_2 for (a) The radiation strength of the antenna [m^{-1}]. It can be observed that when $DC_1 = DC_2$, the radiation strength drops to zero. The black contour line highlights the regions where α=1500 m^{-1}. The dashed green triangle indicates the region with values suitable for commercial fabrication. (b) The Bloch index (n_B). We can observe that the Bloch index is positive for every combination, indicating forward radiation ($\theta_{rad}=sin^{-1}(n_B)$).

The black solid line shown in Fig. 4(a) indicates a linear relationship between both duty cycles, following the expression $DC_2 \approx 0.974 \cdot DC_1 - 0.072$, with a slope close to 1, which indicates that small variations in the design parameters will have minimal impact on the antenna's performance, thereby ensuring its robustness to manufacturing tolerances. This is due to the fact that a variation in widths (ΔW) causes a simultaneous increase or decrease in both DC1 and DC2, as it is shown in Fig. 5. After defining the design area, we repeat the simulation in a finer region while considering the effects of the substrate. This results in the following linear relationship for values near α=1500 m^{-1}: $DC_2 \approx 0.819 \cdot DC_1 - 0.05$. Finally, we select the values for our antenna and improve the reflections at the input by adding an adaptation gap, as seen in Fig. 5, which reduce them from 1% to 0.02%

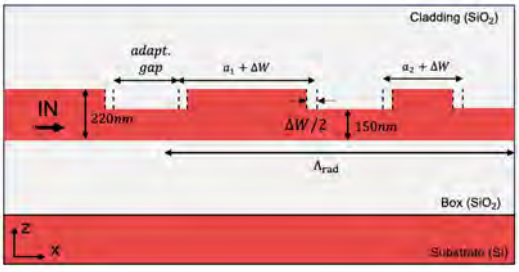

Fig. 5. Schematic of the antenna input section including the adaptation gap to minimize reflections and the definition of fabrication tolerance errors. The 220 nm sections may experience an increase in width due to fabrication tolerances. We define the total width increment of a block as ΔW, with an expansion of $\Delta W/2$ on each side.

Table 1: The first two rows represent the designed values, while the last two rows contain the parameters obtained from simulator.

Λ_{rad}	DC_1	DC_2	adapt. gap
740nm	0.63	0.46	168nm
α	n_{eff}	n_B	$\theta_{rad}(air)$
1.5mm^{-1}	2.68	0.59	36.7°

Therefore, with an α of 1500 m^{-1} and a propagation distance of 1.5 mm at a wavelength of 1550 nm, the radiated power reaches 98.8%. To continue, a tolerance analysis was performed on the structure's widths, ensuring that the 220nm regions are defined as in Fig. 5.

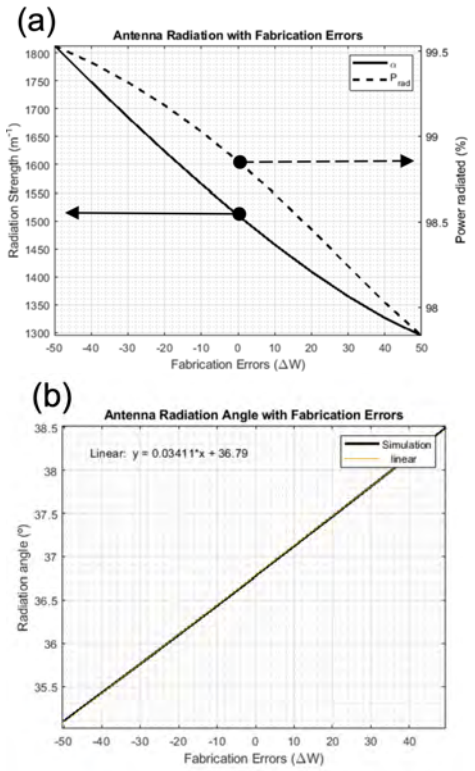

Fig. 6 Sweep in fabrication errors: a) Radiation strength on the left axis and radiated power percentage for a 1.5 mm antenna. (b) Angle of radiation (θ_{rad}).

The results clearly demonstrate that the designed structure is highly tolerant to significant fabrication errors (ΔW=±50nm)

in terms of radiation strength, as shown in Fig. 6 (a). The radiation strength varies from 1800 to 1300 m^{-1}, meaning that the total radiated power remains remarkably stable, staying between 99.5% and 98% for an antenna length of 1.5mm. While the radiation angle experiences a variation of ±1.75°, this deviation remains within an acceptable range for practical applications.

Additionally, a wavelength sweep from 1550 nm to 1600 nm was performed, revealing a scanning efficiency of 0.14°/nm. Furthermore, it was confirmed that during this wavelength sweep, the radiation strength remains relatively stable, with total radiated power varying only slightly from 99% to 97%.

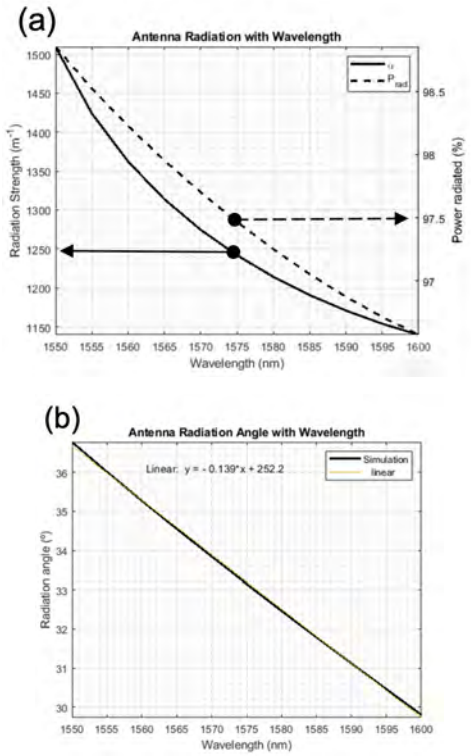

Fig. 7 Sweep in wavelength: a) Radiation strength on the left axis and radiated power percentage for a 1.5 mm antenna. (b) Angle of radiation(θ_{rad}).

Ultimately, we validated the radiation properties of the antenna for the nominal case through an FDTD simulation using the commercial software Tidy3D, obtaining results highly consistent with those previously discussed.

4.- Results

Finally, the designed antenna is fed by a lateral light deflector [9], as shown in Fig. 1. The lateral deflector has been adapted to ensure compatibility with the chosen platform. In addition, the antenna dimensions have been carefully chosen to compensate for the obliquity factor; since the beam radiates at an angle away from the normal, it broadens according to $FWHM_{\theta_{rad}} = FWHM_{0°}/\cos(\theta_{rad})$, where FWHM is the full width half maximum angle.

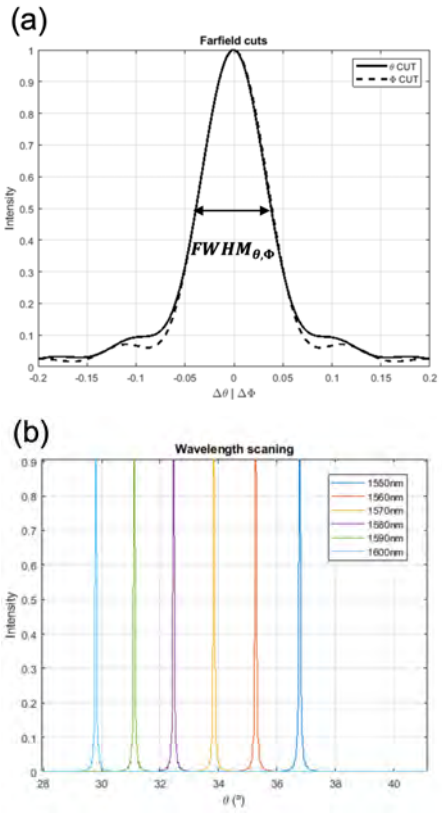

Fig. 8 Final results of the radiated beam: (a) Simulated radiation pattern for the designed antenna device in Fig. 1, exhibiting beam divergences of $FWHM_{\theta,\Phi}$ =0.08° in both dimensions, where $\Delta\theta = \theta - \theta_{rad}$ and $\Delta\Phi = \Phi$, being Φ the angle perpendicular to θ ; and (b) radiation patterns of the antenna for wavelengths of 1550 nm, 1560 nm, 1570 nm, 1580 nm, 1590 nm, and 1600 nm.

The main characteristics of the designed antenna include a beam divergence of 0.08° × 0.08°, which results in a directivity of 70dBi, with a pointing angle of 36.77° at 1550 nm. Additionally, it achieves a scanning efficiency of 0.14°/nm. Moreover, due to the exponential feeding and the exponential radiation profile

in the antenna, which result in a 2D Lorentzian radiation pattern, the device does not exhibit sidelobes. The design shows a directionality of approximately 0.22, which could be further improved by employing TM polarization or by adjusting the BOX height.

5.- Conclusion

In summary, this work has demonstrated the successful design of a novel integrated optical antenna operating in the C band. The proposed solution effectively enables the creation of large radiating apertures and the emission of highly collimated beams, both critical for advanced FSO systems. Notably, the design remains fully compatible with commercial silicon photonics fabrication processes, ensuring ease of integration and scalability.

The antenna exhibits robust performance, showing high tolerance to fabrication errors while maintaining stable radiation properties. Moreover, the structure's ability to produce highly collimated beams directly contributes to enhanced directivity and overall system performance. By leveraging the advantages of Silicon-on-Insulator (SOI) technology and standard CMOS-compatible processes, the proposed design not only reduces SWaP but also enables cost-effective mass production, significantly enhancing scalability.

Overall, these advancements position the developed optical antenna as a promising candidate for next-generation, high-speed, and energy-efficient optical communication systems. Future work will focus on further refining the design parameters and exploring advanced beam steering techniques to fully exploit the potential of silicon photonics in FSO applications. Additionally, the antenna has been sent for fabrication, and experimental measurements of the results will be conducted in the coming months.

Acknowledgements: Proyecto subvencionado por el CDTI y apoyado por el Ministerio de Ciencia e Innovación en el Marco del Programa Misiones de Ciencia e Innovación vinculadas al PERTE de Microelectrónica y Semiconductores del año 2023 (00166003/MIG-20231008).

References

[1] T. Ismail, E. Leitgeb, y T. Plank, «Free Space Optic and mmWave Communications: Technologies, Challenges and Applications», *IEICE Trans. Commun.*, vol. E99.B, n.º 6, pp. 1243-1254, 2016,

[2] A. Trichili, M. A. Cox, B. S. Ooi, y M.-S. Alouini, «Roadmap to free space optics», *J. Opt. Soc. Am. B*, vol. 37, n.º 11, p. A184, nov. 2020,

[3] H.-B. Jeon *et al.*, «Free-Space Optical Communications for 6G Wireless Networks: Challenges, Opportunities, and Prototype Validation», *IEEE Commun. Mag.*, vol. 61, n.º 4, pp. 116-121, abr. 2023,

[4] A. Jahid, M. H. Alsharif, y T. J. Hall, «A contemporary survey on free space optical communication: Potentials, technical challenges, recent advances and research direction», *J. Netw. Comput. Appl.*, vol. 200, p. 103311, abr. 2022,

[5] A. Gupta, D. Dhawan, y N. Gupta, «Review on UAV-based FSO links: recent advances, challenges, and performance metrics», *Opt. Eng.*, vol. 63, n.º 04, oct. 2023, Accedido: 29 de abril de 2024. [En línea].

[6] S. Y. Siew *et al.*, «Review of Silicon Photonics Technology and Platform Development», *J. Light. Technol.*, vol. 39, n.º 13, pp. 4374-4389, jul. 2021,

[7] Y. Guo, Y. Guo, C. Li, H. Zhang, X. Zhou, y L. Zhang, «Integrated Optical Phased Arrays for Beam Forming and Steering», *Appl. Sci.*, vol. 11, n.º 9, p. 4017, abr. 2021,

[8] J. He, T. Dong, y Y. Xu, «Review of Photonic Integrated Optical Phased Arrays for Space Optical Communication», *IEEE Access*, vol. 8, pp. 188284-188298, 2020,

[9] A. Hadij-ElHouati *et al.*, «High-efficiency conversion from waveguide mode to an on-chip beam using a metamaterial engineered Bragg deflector», *Opt. Lett.*, vol. 46, n.º 10, p. 2409, may 2021,

[10] Photonics&RF Research Lab, Universidad de Málaga, *FEXEN: Fourier EXpansion ENviroment*. (2024).

Biofotónica

Portable multispectral fundus camera: a pilot study

Marina BOU-MARIN [1], Meritxell VILASECA [1] and Francisco J. BURGOS-FERNÁNDEZ [1]

1. Centre for Sensors, Instruments and Systems Development, Universitat Politècnica de Catalunya, Rambla Sant Nebridi 10, Terrassa 08222 (Barcelona), Spain

Contact: Marina BOU-MARIN (marina.bou@upc.edu).

ABSTRACT:

In ophthalmology, traditional color-based cameras are commonly used for eye fundus examination but lack spectral resolution, which may cause certain alterations to go unnoticed. To address this issue, multispectral imaging systems have been developed. These systems capture images across multiple spectral bands, from the visible (VIS) to the near-infrared (NIR), providing more detailed information about fundus structures. This study presents a prototype towards a portable multispectral fundus camera that captures images in the 470–850 nm spectral range, offering both high spatial and spectral resolution. The camera consists of a modified PanOptic™ ophthalmoscope with fiber-coupled LEDs and a monochrome CMOS camera, all controlled with a software developed in Matlab. Reflectance values are extracted from fundus structures, and a contrast parameter is used for their discrimination. Results show that the prototype is able to obtain spectral images in the VIS and NIR, and quantitative spectral data can be extracted from the fundus images.

Key words: biophotonics, multispectral imaging, reflectance, near-infrared, fundus, retina, choroid.

1.- Introduction

In the field of ophthalmology, visualizing the ocular fundus is a key aspect for diagnosing fundus pathologies. Fundus cameras, equipped with color sensors are widely used for fundus imaging as they provide fast and accurate information [1]. These devices typically include digital cameras that capture color images through three channels (R, G, and B), resulting in a very limited spectral resolution [2]. However, due to the phenomenon of metamerism, structures with different spectral properties may be perceived as having the same color, i.e., they can be perceived as healthy even they are abnormal or simply go undetected.

To overcome this limitation, multispectral (MS) imaging systems have recently been introduced for fundus analysis, allowing image acquisition across more than three spectral bands in the visible (VIS) range, and even in the near-infrared (NIR). This approach has proven to be highly valuable for diagnosis, since fundus reflectance strongly depends on the chemical composition of biological tissues, particularly the retina, enabling better differentiation between healthy and diseased structures [3]. Additionally, NIR light penetrates deeper into the fundus layers due to its reduced absorption, allowing the visualization of subretinal lesions, the choroid and its blood vessels [4].

Several studies have determined the spectral properties of eye's structures [3], [5]. One of the most important layers in the eye fundus is the retinal pigment epithelium (RPE), with high melanin concentration absorbing strongly in the UV and blue ranges, and whose spectral absorption decreases with increasing wavelength [6]. Short wavelengths in the VIS facilitate the observation of the most superficial retinal structures, such as the optic disc, which is full of nerve fibers that show

maximum reflectance between 460 and 560 nm [7]. Wavelengths between 500 nm and 700 nm allow the study of the vascular layers of the retina, thus being able to differentiate arteries and veins (oxygenated and deoxygenated blood). Around 600 nm, the difference in absorption between oxygenated and deoxygenated blood is maximized so that veins and arteries can be easily discriminated. Beyond 700 nm, oxygenated blood increases its spectral absorption while at the same time melanin absorption decreases, thus obtaining a higher contrast between the fundus and the choroidal vessels [8].

Until now, multispectral fundus cameras have been bulky, expensive, and designed for tabletop use. In this work, we developed a prototype towards a portable multispectral fundus camera capable of capturing images within the 470–850 nm spectral range, offering high spatial and spectral resolution. A preliminary study was conducted on human eyes. The acquired spectral images were processed to extract the reflectance values of different fundus structures, enabling the detection of alterations associated with fundus diseases.

2.- Methods and materials

2.1.- Portable multispectral fundus camera

The developed prototype features a PanOptic™ ophthalmoscope (Hill-Rom Holdings, Inc.), which permits to illuminate the eye fundus and collect the reflected light (Fig. 1 A). A set of six fiber-coupled LEDs with peak wavelengths between 470 nm and 855 nm (Thorlabs, Inc.) are coupled to the PanOptic™ ophthalmoscope through a custom-made optical fiber with seven inputs and one output to illuminate the eye fundus sequentially (AMS Technologies AG) (Fig. 1 B). A 12-bit CMOS monochromatic camera UI-1480SE-M-GL (Imaging Development Systems GmbH) with an 8-mm objective lens is attached to the ophthalmoscope in order to capture the light reflected by the eye fundus. Additionally, the prototype includes two NIR LEDs (one for each eye) with emission at 830 nm as fixation targets to ensure the proper position of the patient's eye. Sliders are also included in order to precisely align the prototype with the eye.

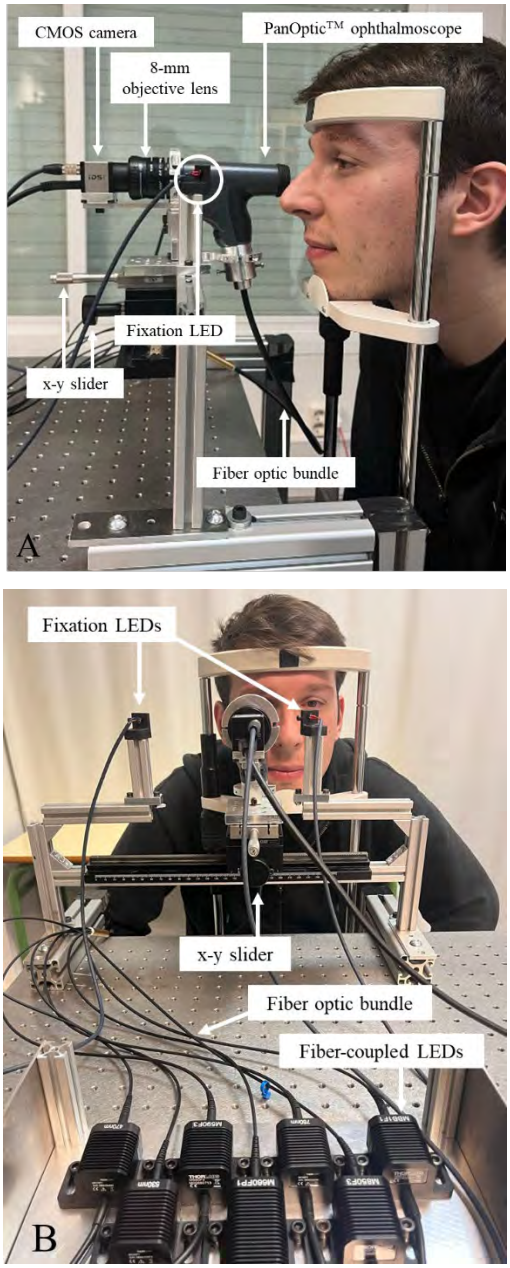

Fig. 1: Portable multispectral fundus camera. A) Lateral view; B) Frontal view.

A customized software was implemented in Matlab R2022b to control the LEDs, the camera, and to ensure their synchronization when obtaining the sequence of multispectral images. In this regard, the time span of the acquisition must be as short as possible to avoid artifacts due to eye movements and blinking. Time optimization for each wavelength was performed by using an

artificial eye OEMI-7 (Ocular Instruments Inc.). Considering the brighter structure in the retina of this artificial eye, i.e., the optic disk, the acquisition time and the emission of the LEDs were adjusted to obtain images with the maximum dynamic range but avoiding saturation. This was done according to the UNE-EN ISO 10940 and UNE-EN ISO 15004-2: 2007 safety standards [9], [10]. By doing so, each image is acquired in 158.729 ms, and accounting for the computing time between acquisitions, a full multispectral image sequence lasts 1 second. Fig. 2 shows the normalized spectral emission of the LEDs. Table 1 shows their optical characteristics and the output power, measured with the power meter PM100D (Thorlabs GmbH), within the limits of the safety rules, used in order to obtain sufficient signal from the eye fundus.

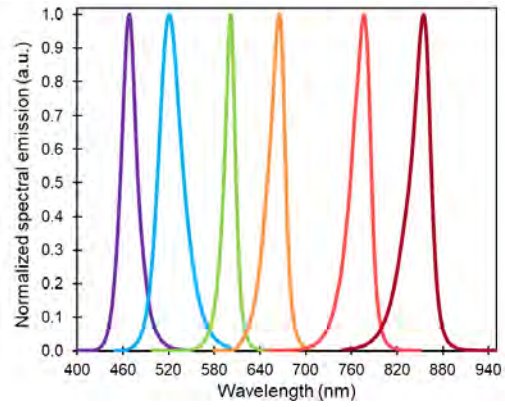

Fig. 2: Normalized spectral emission of the LEDs.

Table 1: Optical characteristics of the LEDs: peak wavelength (λ_p), Full Width at Half Maximum (FWHM) and output power.*

LED reference	***λ_p (nm)***	***FWHM (nm)***	***Output power* (mW)***
M470F3	*470*	*20*	*253.5*
M530F2	*520*	*30*	*119.5*
M590F3	*600*	*16*	*84.23*
M660FP1	*660*	*18*	*117.8*
M780F2	*770*	*28*	*107.3*
M850F3	*855*	*30*	*217.6*

*The output power corresponds to the maximum value below the limits established by the safety standards UNE-EN ISO 10940 and UNE-EN ISO 15004-2: 2007.

2.2.- Image processing

In addition to the fundus images, background and dark images of an absorptive black sheet were captured for each patient, to compensate for internal reflections from the system, with the LEDs turned on and off, respectively. For calibration and to retrieve reflectance data, images of a calibrated white standard (BN-R98-SQC, Gigahertz-Optik GmbH) were also acquired to compensate for the spectral response of the system, which varies across spectral bands due to differences in the quantum efficiency of the camera and the output power of the LEDs; Equation 1 describes how this was performed, where $I_C(\lambda)$, $I(\lambda)$, $I_B(\lambda)$, $I_D(\lambda)$, and $I_W(\lambda)$ correspond to the digital levels of the corrected, non-corrected, background, dark, and white reference images, respectively; R_W is the calibration factor given by the white standard's manufacturer. All images were captured using exactly the same parameters for the LEDs emission and the camera acquisition. Fig. 3 shows an example of the four images acquired for each spectral band.

$$I_C(\lambda) = R_W(\lambda)\frac{\left(I(\lambda) - I_D(\lambda)\right) - \left(I_B(\lambda) - I_D(\lambda)\right)}{\left(I_W(\lambda) - I_D(\lambda)\right)} \quad (1)$$

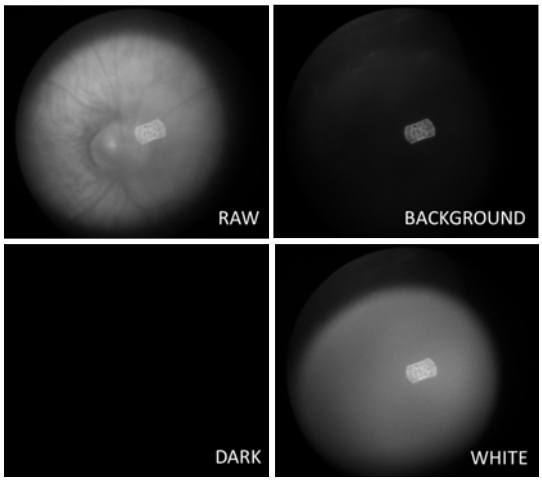

Fig. 3: Raw fundus, background, dark and white standard images for one spectral band (770 nm).

Images were processed to eliminate internal reflections of the system and shadows by subtracting dark and background images from the fundus and white images. Then, reflectance values could be extracted by

compensating the spectral response of the system with the white reference.

2.3.- Evaluation of fundus structures

In this study, reflectance values were retrieved for three different structures from the eye fundus: the optic disc, veins and arteries. To better compare them, the global contrast, $GC(\lambda)$ [3], was calculated for each channel computing the ratio between the reflectance of the structure under study - computed as the mean of the points selected over it -, $R(\lambda)$, and the mean reflectance of the entire fundus image, $R_{FOV}(\lambda)$, as shown in Eq. (2).

$$GC(\lambda) = \frac{R(\lambda)}{R_{FOV}(\lambda)} \quad (2)$$

3.- Results

Fig. 4 shows a full multispectral fundus image sequence of a healthy eye obtained with the prototype after the image processing.

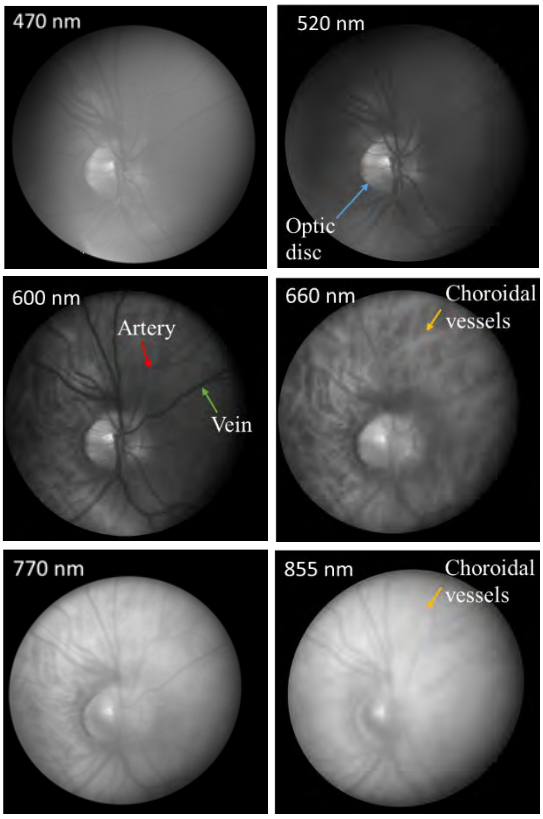

Fig. 4: Complete sequence of spectral images of a healthy eye acquired with the multispectral fundus camera.

As can be seen, the optic disc has a higher reflectance in the VIS range compared with the rest of the fundus. This property can be detected when analyzing its global contrast; see Fig. 5, where the optic disc curve remains above one in all the VIS range, indicating a higher reflectance at these wavelengths. In the NIR range, its reflectance decreases. Regarding blood vessels, wavelengths around 600 nm allow the differentiation between arteries and veins, since oxygenated blood has less absorption, so that arteries look brighter [6].

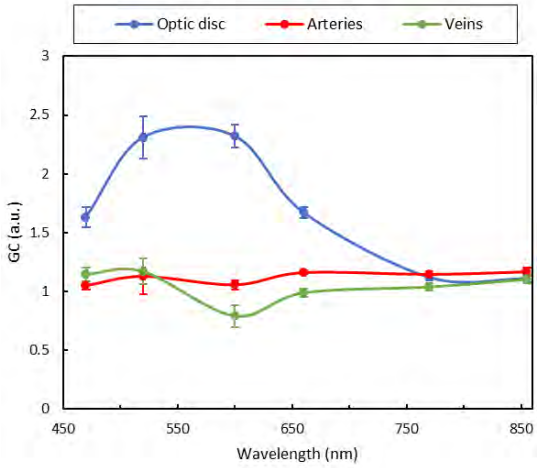

Fig. 5: Mean ± standard error of the global contrast (GC) of the optic disc, veins and arteries in the spectral range evaluated.

3.- Conclusions and ongoing work

This pilot study has demonstrated the feasibility of performing multispectral imaging and retrieving quantitative data by means of a simplified, portable version of a fundus camera. Additionally, a second variant of the prototype based on the RGB camera of a smartphone and a broadband LED is being built; the PanOptic™ ophthalmoscope will be also used as the optical system. Once this second system is fully developed, a clinical study will be carried out on healthy and diseased fundus. The goal is to compare and complement the information provided by the two approaches as well as their ease of use and implementation.

Acknowledgements: This publication is part of the project PID2023-147541OB-I00, funded by MCIU /AEI /10.13039/501100011033 and by FEDER, UE. The first author gratefully acknowledges the Universitat Politècnica de Catalunya and Banco Santander for the financial support of her predoctoral grant FPI-UPC.

References

[1] N. Panwar *et al.*, 'Fundus Photography in the 21st Century—A Review of Recent Technological Advances and Their Implications for Worldwide Healthcare', *Telemed. E-Health*, vol. 22, no. 3, Art. no. 3, 2016, doi: 10.1089/tmj.2015.0068.

[2] I. B. Styles, A. Calcagni, E. Claridge, F. Orihuela-Espina, and J. M. Gibson, 'Quantitative analysis of multi-spectral fundus images', *Med. Image Anal.*, vol. 10, no. 4, Art. no. 4, 2006, doi: 10.1016/j.media.2006.05.007.

[3] F. J. Burgos-Fernández *et al.*, 'Reflectance evaluation of eye fundus structures with a visible and near-infrared multispectral camera', *Biomed. Opt. Express*, vol. 13, no. 6, Art. no. 6, 2022, doi: 10.1364/BOE.457412.

[4] T. Alterini, F. Díaz-Doutón, F. J. Burgos-Fernández, L. González, C. Mateo, and M. Vilaseca, 'Fast visible and extended near-infrared multispectral fundus camera', *J. Biomed. Opt.*, vol. 24, no. 09, Art. no. 09, 2019, doi: 10.1117/1.JBO.24.9.096007.

[5] T. Berendschot, 'Fundus reflectance—historical and present ideas', *Prog. Retin. Eye Res.*, vol. 22, no. 2, Art. no. 2, 2003, doi: 10.1016/S1350-9462(02)00060-5.

[6] F. C. Delori and K. P. Pflibsen, 'Spectral reflectance of the human ocular fundus', *Appl. Opt.*, vol. 28, no. 6, Art. no. 6, 1989, doi: 10.1364/AO.28.001061.

[7] K. T. and K. M. A. Cernosek P., 'Nerve Fiber Layer Defects Imaging in Glaucoma', in *The Mystery of Glaucoma*, T. Kubena, Ed., InTech, 2011. doi: 10.5772/21020.

[8] D. Toslak *et al.*, 'Portable ultra-widefield fundus camera for multispectral imaging of the retina and choroid', *Biomed. Opt. Express*, vol. 11, no. 11, pp. 6281–6292, Nov. 2020, doi: 10.1364/BOE.406299.

[9] 'ISO 10940:2010, Ophthalmic instruments—fundus cameras. International Organization for Standardization'. 2010.

[10] *UNE-EN ISO 15004-2:2007: Instrumentos oftálmicos : requisitos fundamentales y métodos de ensayo : (ISO 15004-2:2007).. Protección frente a los daños ocasionados por la luz*. AENOR, 2007.

Inteligencia artificial y fotónica

Machine Learning Approach to Find the Optimal Window for LIPSS Formation in Femtosecond Laser Processing

Aitor LARRRAÑAGA-JAIO[1,2], Iñigo RAMON-CONDE[1,2], Aldara PAN CABO[1,2], Isabel AYERDI OLAIZOLA[1,2], Santiago M OLAIZOLA[1,2], Ainara RODRÍGUEZ[1,2]

1. CEIT-Basque Research and Technology Alliance (BRTA), Manuel Lardizabal 15, 20018 Donostia/San Sebastián, Spain.
2. Universidad de Navarra, Tecnun, Manuel Lardizabal 13, 20018 Donostia/San Sebastián, Spain.

Contact: Ainara Rodríguez (airodriguez@ceit.es).

Abstract:
Femtosecond-laser-induced surface modification is extremely sensitive to processing parameters, where delicate energy deposition dynamics and non-linear effects determine the outcome. Generally, insufficient energy deposition leads to nanobubble formation, while excessive energy deposition causes ablation, leaving only a narrow optimal parameter window for laser-induced surface structure (LIPSS) generation. This study presents a machine learning framework aimed at delineating these regimes by classifying surface outcomes into three distinct classes: Nanobubbles, LIPSS, and Ablation. Using extensive experimental data, features from both fundamental parameters (e.g., power, scanning speed, frequency) and derived metrics (e.g., fluence, overlap, cumulative dose) were engineered. Several machine learning models were evaluated and was found that the ensemble methods, particularly XGBoost and Random Forest, best capture the delicate balance required for LIPSS formation. Notably, the best-performing model achieved an accuracy of 97%.

Key words: Femtosecond laser, Surface-texturing, Machine learning, LIPPS, Nanostructures.

1 Introduction

Laser surface engineering has emerged as a leading technique in advanced manufacturing and materials science. Among the various processes, laser-induced periodic surface structures (LIPSS) are of particular importance, as they enable precise modification of surface textures and properties. LIPSS occur on a wide range of solid materials upon exposure to intense linearly polarized coherent electromagnetic radiation [1]. LIPSS can enhance material performance across a wide range of applications, from biocompatible biomedical implants to robust aerospace components — imparting the desired optical, mechanical, and chemical characteristics [2, 3].

This work is focused on exploiting machine learning to predict and distinguish the laser parameters that lead to successful LIPSS formation. Given the inherent nonlinearity of femtosecond laser processing, the conventional trial-and-error approach is both time-consuming and resource-intensive, requiring extensive operator expertise [4]. Using an extensive experimental dataset, combinations of processing parameters that result in LIPSS are identified.

The prediction of LIPSS formation represents a significant advance over traditional statistical analyses previously applied [5]. By integrating machine learning models trained on extensive experimental data, this work enables a more efficient exploration of the parameter space in femtosecond laser processing. This not only accelerates the development cycle for laser-engineered surfaces, but also helps conserve valuable materials, reduce costs, and save time.

2 Methodology

2.1 Dataset description and Experimental conditions

The experimental data were obtained by processing various substrates with a laser in a clean room environment, where the ambient temperature was maintained at 21ºC and the relative humidity at 50% to minimize external variations. Laser processing was carried out using an Amplitude Satsuma HP pulsed laser with a central wavelength of 1030 nm and with pulse durations of 280 femtoseconds.

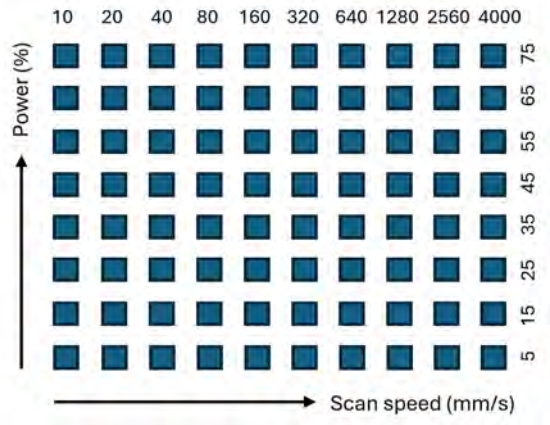

Figure 1: Distribution of hatched squares in the designed parameter-matrix for the stainless steel substrate. The power values are expressed as a percentage relative to the maximum power output of the laser source.

A substrate-adjusted power vs. scan speed parameter matrix was employed during the experimental campaign to assess the effects of multiple laser and scanner settings on surface phenomena. In each element of the matrix, a hatched square with 0.05 mm of hatch pitch was processed (see example Figure 1). In addition to those variations, these matrixes were repeated by varying the following parameters:

- Beam polarization: 4 linear polarization settings (0º, 45º, 90º, and 135º).
- Pulse repetition rate: 4 distinct output frequency settings (50, 125, 250, and 500 kHz).
- Substrate materials: 4 materials, including Copper (Cu), Stainless Steel (AISI 304), Aluminium (Al), and Titanium (TiAl6V4).

Each combination of parameters was applied to the substrates, and the resulting surface modifications were imaged using Scanning Electron Microscopy (SEM) to enable consistent classification into one of three categories: Ablation, LIPSS, or Nanobubbles (Figure 2).

In addition to recording the fundamental process parameters, several derived variables were calculated and introduced to the models to better characterize the laser–surface interactions and feature engineer the models:

- Pulse Energy (E): Defined as the ratio of laser power (P) to the pulse-picker frequency (f):

$$E = P/f, \tag{1}$$

  where the pulse-picker frequency was set constant to $f = 500$ kHz.

- Fluence (F): Represents the energy density per pulse, and it is calculated by dividing the pulse energy (E) by the spot area:

$$F = E/\pi \cdot r^2, \tag{2}$$

  where $r = 15$ μm is the radius of the laser spot at the focal point.

- Number of Pulses (ϕ): Indicates the number of overlapping pulses and is determined using the beam diameter ($2 \cdot r$), the pulse repetition rate (ν), and the scanning speed (v):

$$\phi = (2 \cdot r \cdot \nu)/v. \tag{3}$$

- Dose (D): Represents the accumulated energy density, and it is obtained by multiplying the fluence with the number of pulses:

$$D = F \cdot \phi. \tag{4}$$

Previous works demonstrated the significant influence of these parameters, such as the laser fluence [6] and the number of overlapping pulses [7] on LIPSS generation. LIPSS formation is generally attributed to a Coulomb

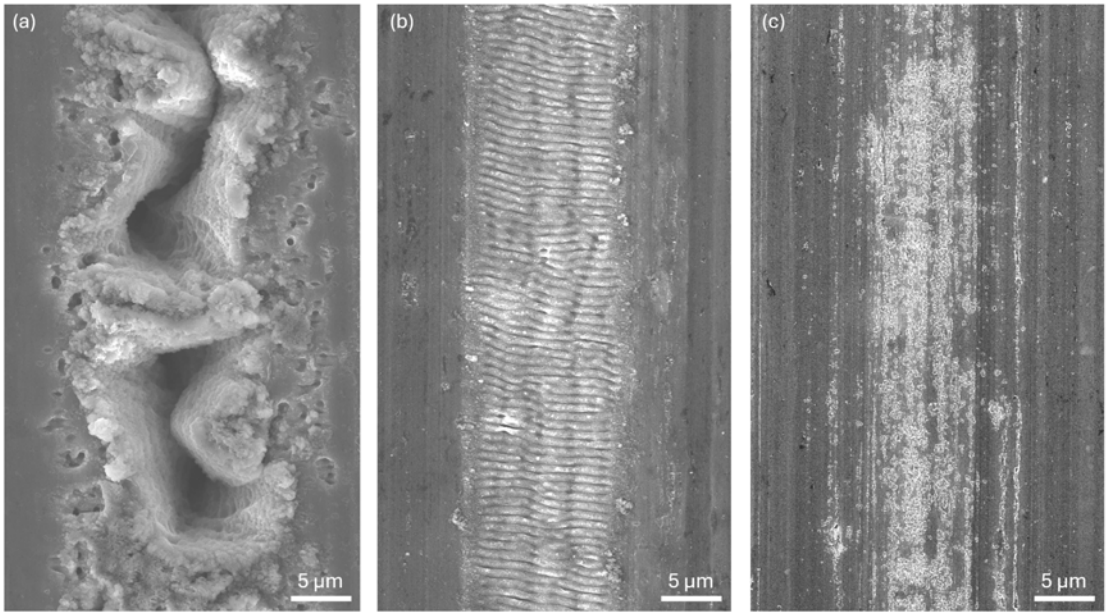

Figure 2: SEM images of different results assignment examples in an aluminium substrate: (a) Ablation, (b) LIPSS, and (c) Nanobubbles.

explosion triggered by surface two-plasmon resonance [4] within a specific range of laser fluence. In this regime, there exists a lower threshold below which, the energy is insufficient to overcome the material's bonding energy, and an upper threshold above which direct laser ablation occurs [8], leading to significant structural damage. Furthermore, as the number of overlapping pulses increases—due to longer scanning times—the cumulative effect lowers the fluence required for effective LIPSS generation. For this reason, the cumulative dose becomes also an important parameter in LIPSS generation.

2.2 Data Preprocessing

Reliable classification requires a comprehensive data preprocessing pipeline. Categorical features (e.g., substrate type and polarization orientation) are one-hot encoded to preserve non-ordinal relationships. Numerical features—including power, scanning speed, pulse repetition frequency, and the derived variables (Equations 1-4)—are standardized using the Standard Scaler to ensure that differences in scale do not bias the models. The target variable is label encoded, mapping Ablation, LIPSS, and Nanobubbles to unique numerical labels.

2.3 Models and algorithms

In this study, the following machine learning models are evaluated:

- Decision Tree (DT): Uses a tree-like structure where internal nodes represent decisions on input features and leaves represent class labels. It recursively partitions the dataset to form simple, interpretable decision boundaries.
- Random Forest (RF): An ensemble method that builds multiple independent decision trees and aggregates their predictions to enhance overall robustness and reduce the risk of overfitting.
- Support Vector Machine (SVM): Finds the optimal hyperplane that separates classes by maximizing the margin between different classes. It uses kernel functions to manage non-linearly separable data and outputs probability estimates.
- Linear Discriminant Analysis (LDA): Projects the data onto a lower-dimensional

space with enhanced class separability by maximizing the ratio of between-class variance to within-class variance under the assumption of normally distributed classes.

- eXtreme Gradient Boosting (XGBoost): An advanced gradient boosting algorithm that builds an ensemble of decision trees sequentially. Each new tree is trained to correct errors from previous trees, and built-in regularization techniques help prevent overfitting.
- Artificial Neural Network (ANN): Comprises interconnected nodes (neurons) organized in layers to learn complex, non-linear relationships between inputs and outputs through iterative training.

Hyperparameters are carefully tuned with Bayesian optimization algorithms to ensure the best performance across different models.

2.4 Performance evaluation

The complete parameter space—comprising power, scanning speed, polarization, frequency, and material—was used to collect a comprehensive set of experiments. The dataset was split into training (80%) and testing (20%) sets via stratified sampling to preserve class balance. The testing set was predicted with all the models and evaluated with different metrics:

- Accuracy: The fraction of total predictions that are correct (i.e., true positives and true negatives). While it gives an overall performance measure, it may be misleading with imbalanced classes.
- Precision: The ratio of true positives to the total predicted positives for a given class, indicating the correctness of positive predictions.
- Recall: The proportion of actual positives correctly identified by the model, reflecting its ability to detect a specific class.
- F1-Score: The harmonic mean of precision and recall, providing a single measure that balances both metrics, especially useful in cases of uneven class distribution.
- Receiver Operating Characteristic - Area Under the Curve (ROC-AUC): Plots the true positive rate against the false positive rate and measures the area below the curve. It indicates the overall ability of the model to distinguish between classes, with 1.0 denoting perfect classification and 0.5 corresponding to random guessing.

Each of these metrics provides a unique perspective on the model's performance, helping to evaluate not only its overall accuracy but also its effectiveness in correctly identifying each class—especially in scenarios where a single metric might not provide a complete representation.

3 Results

Figure 3 shows the ROC curves for each model evaluated. These curves illustrate the trade-offs between the true positive and false positive rates across different classification thresholds, providing a clear depiction of each model's diagnostic ability.

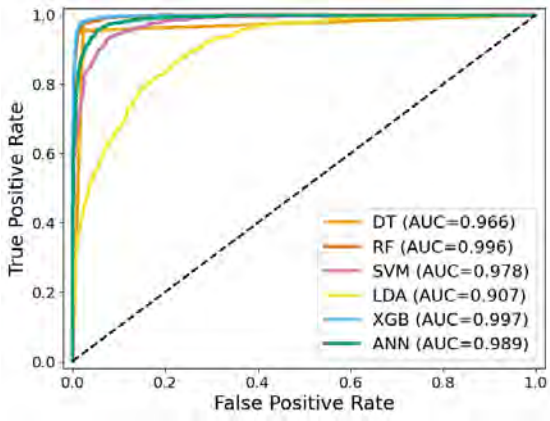

Figure 3: Micro-Averaged ROC curves for each model evaluated.

To provide a comprehensive overview of the model performance, Table 1 displays exact metrics for each evaluated model. In addition, the radar chart in Figure 4 offers a visual comparison of these metrics across models,

Model	Accuracy	Precision	Recall	F1-Score	ROC-AUC
Decision Tree	0.955	0.954	0.955	0.954	0.966
Random Forest	0.966	0.965	0.964	0.964	0.996
Support Vector Machine	0.894	0.899	0.886	0.889	0.978
Linear Discriminant Analysis	0.742	0.749	0.736	0.738	0.907
XGBoost	**0.970**	**0.969**	**0.968**	**0.968**	**0.997**
Artificial Neural Network	0.926	0.925	0.919	0.921	0.989

Table 1: Summary of detailed performance metrics of the evaluated models on the dataset. The best performing metrics are highlighted in **bold**.

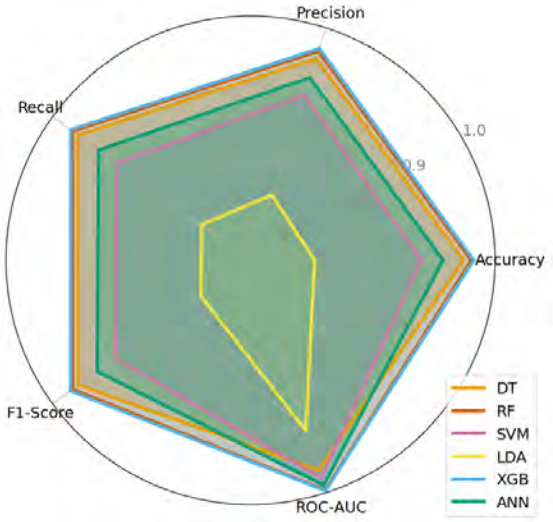

Figure 4: Radar Chart comparing models based on accuracy, precision, recall, F1-score, and ROC-AUC.

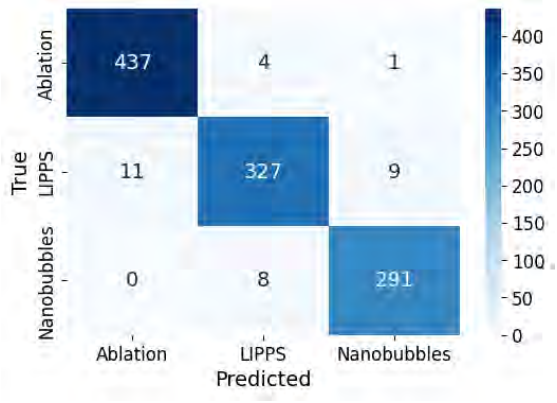

Figure 5: Confusion matrix for the XGBoost classifier.

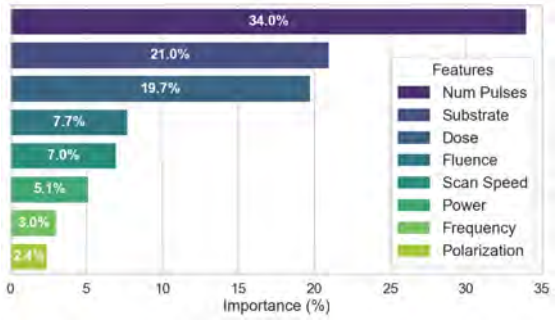

Figure 6: Feature importances for the XGBoost classifier.

facilitating an at-a-glance evaluation of their strengths and trade-offs.

XGBoost classifier demonstrated the highest overall performance according to the metrics in Table 1, closely followed by the random forest. Figure 5 shows the confusion matrix for the best performing model, highlighting its class-specific performance and misclassification rates.

In Figure 6, the relative importance of various parameters for classification is displayed. Notably, the number of pulses and the dose rank very high, indicating that the cumulative effects, capturing how energy is delivered to the material, are critical for determining the resulting surface modification, in agreement with the findings in [9]. The substrate type also shows high importance, underscoring its significant role in the laser–material interaction. Although other parameters such as fluence, scanning speed, power, and frequency exert a non-negligible influence, they are largely embedded in the number of pulses and dose (see Equations 3 and 4). This redundancy may cause these raw features to contribute less independently to the predictive power. Additionally, the linear polarization direction exhibits a low correlation with the resulting

surface structure, as expected; polarization primarily affects the orientation of LIPSS rather than their formation.

4 Conclusion and Future Work

This study demonstrates that machine learning can effectively predict and classify laser-induced surface phenomena by identifying the narrow processing window for LIPSS formation. By extracting features from both fundamental parameters (e.g., power, scanning speed, pulse frequency) and derived variables (e.g., fluence, overlapping pulses, cumulative dose), the multi-class classification approach distinguished among nanobubble formation, LIPSS, and ablation. Notably, ensemble methods—especially the XGBoost classifier—achieved an accuracy of 97% and a ROC-AUC of 0.997, underscoring the potential of these techniques in process control.

The results also highlight the critical role of cumulative parameters in driving LIPSS formation. However, certain limitations should be noted: the hatch pitch was held constant, and variations in the experimental setup or environment may influence the process in ways not captured by the current dataset. These factors might affect the generalizability of the model in different settings.

Future work will focus on expanding the dataset through automated data collection to encompass a broader range of experimental conditions, refining protocols, and integrating deep neural network architectures alongside real-time adaptive learning. Such improvements are expected to facilitate not only classification but also the prediction of detailed LIPSS characteristics, thereby enhancing laser process control in industrial applications.

Acknowledgements

This work is part of Laser4surf and Susaan projects. Laser4surf received funding from the European Union's Horizon research and innovation programme under grant agreement N° 768636. Susaan has received funding from the European Union's Horizon 2020 research and innovation programme under grant agreement N°101057988.

References

[1] H. M. van Driel, J. E. Sipe, and J. F. Young, "Laser-induced periodic surface structure on solids: A universal phenomenon," *Phys. Rev. Lett.*, vol. 49, pp. 1955–1958, Dec 1982.

[2] J. Bonse, S. V. Kirner, and J. Krüger, "Laser-induced periodic surface structures (lipss)," *Handbook of laser micro-and nano-engineering*, pp. 1–59, 2020.

[3] A. Vorobyev and C. Guo, "Multifunctional surfaces produced by femtosecond laser pulses," *Journal of Applied Physics*, vol. 117, no. 3, 2015. Cited by: 397; All Open Access, Bronze Open Access, Green Open Access.

[4] H.-Y. Song, S.-B. Liu, H. Liu, Y. Wang, T. Chen, and X.-M. Dong, "Subwavelength topological structures resulting from surface two-plasmon resonance by femtosecond laser exposure solid surface," *Optics Express*, vol. 24, no. 11, pp. 12151–12165, 2016.

[5] B. Wang, P. Wang, J. Song, Y. C. Lam, H. Song, Y. Wang, and S. Liu, "A hybrid machine learning approach to determine the optimal processing window in femtosecond laser-induced periodic nanostructures," *Journal of Materials Processing Technology*, vol. 308, p. 117716, 2022.

[6] G. Schnell, U. Duenow, and H. Seitz, "Effect of laser pulse overlap and scanning line overlap on femtosecond laser-structured ti6al4v surfaces," *Materials*, vol. 13, no. 4, p. 969, 2020.

[7] D. S. Milovanović, B. Gaković, C. Radu, M. Zamfirescu, B. Radak, S. Petrović, Z. R. Miladinović, and I. N. Mihailescu, "Femtosecond laser surface patterning of steel and titanium alloy," *Physica Scripta*, vol. 2014, no. T162, p. 014017, 2014.

[8] E. G. Gamaly, A. V. Rode, B. Luther-Davies, and V. T. Tikhonchuk, "Ablation of solids by femtosecond lasers: Ablation mechanism and ablation thresholds for metals and dielectrics," *Physics of plasmas*, vol. 9, no. 3, pp. 949–957, 2002.

[9] M. Ye, J. Sun, Z. Chen, W. Tao, Y. Lian, and Z. Yang, "Controlling the morphologies of femtosecond laser-induced periodic surface structure on silicon by combining deep learning with energy deposition model," *Materials & Design*, vol. 242, p. 113021, 2024.

Addressing ROS 2 Limitations for Dependable Multimodal Sensing Applications

Jokin AROZAMENA-RODRÍGUEZ[(1) (2)], Santiago ROYO[(2)], Jorge PARRA[(1)], Maider ZAMALLOA[(1)]

1. Ikerlan Technology Research Centre, P.◦ J.M. Arizmendiarrieta 2, Arrasate-Mondragon, 20500, Basque Country, Spain
2. Centre for Sensors, Instruments and Systems Development (CD6), Universitat Politècnica de Catalunya - BarcelonaTech (UPC), Rambla Sant Nebridi 10, Terrassa, 08222, Spain

Contact: Jokin Arozamena-Rodríguez (jarozamena@ikerlan.es).

ABSTRACT:

Multimodal sensing applications integrate multiple optoelectronic sensors and their corresponding data processing algorithms. To do so, they rely on an underlying software layer, known as middleware, that handles communication and interoperability among the different components. The Robot Operating System 2 (ROS 2) has become a standard middleware for developing such applications. However, ROS 2's non-deterministic execution, lack of real-time guarantees, and limited fault tolerance hinder its implementation for dependable industrial applications. This communication overviews the advantages and limitations of ROS 2 for multimodal sensing applications and proposes a novel synchronous, sequential execution model with a centralized system database to overcome its limitations. The aim is to implement such execution model in a multimodal railway obstacle detection system that combines a LiDAR with thermal and RGB cameras.

Key words: Multimodal sensing, ROS 2, Dependability, Sensor data processing

1.- Introduction

The combination of multiple sensors and sensing technologies, known as multimodal sensing, has become a standard approach in developing robust perception applications for robotics and autonomous vehicles [1]. These applications integrate various optoelectronic sensors (such as camera, LiDAR, and radar) with software components that process their data into higher-level information. These multimodal strategies rely on an underlying software layer that effectively handles communication and interoperation between the various components that make up their architectures [2]. Such software layer is commonly referred to as *middleware*.

To avoid the need for developing a custom middleware for each specific application, modern approaches leverage multi-purpose hardware-agnostic middleware frameworks. These frameworks allow developers to abstract low-level functionalities like scheduling, execution, and communication from high-level application specific code [2]. In this context, the Robot Operating System (ROS), particularly its latest iteration, ROS 2, has emerged as the most widely adopted alternative in both research and industry [3]. ROS 2 serves as an open-source middleware that facilitates integration between optoelectronic sensors and data processing algorithms in highly modular and scalable manner. However, these attributes alone are often insufficient for industrial applications.

In industrial environments, failures during operation can lead to severe consequences, including human injury or damage to valuable infrastructure. Therefore, for industrial multimodal sensing applications ensuring the

correct operation of the middleware becomes crucial [4]. The ability of a system to provide guarantees that minimize the probability of failure is known as dependability. Although ROS 2 is widely used in multimodal sensing applications, the existing literature highlights several dependability limitations [5], [6], [7]. In this communication we aim to overview the state-of-the-art ROS 2 middleware for developing dependable multimodal sensing applications and present our proposed approach to address its limitations. The long-term goal is to achieve a dependable middleware for a multimodal railway obstacle detection application that combines a LiDAR with thermal and RGB cameras.

2.- Overview of ROS 2 for multimodal sensing applications

2.1.- Advantages of ROS 2

ROS 2 has become one the most popular middleware frameworks to develop multimodal sensing applications. This rise in popularity is due to the following advantages:

A. High modularity, scalability, and reusability. ROS 2's allows developers to build their applications as a decentralized system of nodes that execute tasks and communicate with each other without a single point of failure. This modularity makes it possible to add, modify, and deploy sensor processing tasks with ease. This also allows the reusability of existing nodes across applications without performing a complete system redesign, which reduces development times and costs.

B. High sensor integration and compatibility. The ROS 2 ecosystem includes a vast library of plug-and-play drivers for many camera, LiDAR, and radar sensors in the market. This simplifies the sensor integration process, allowing developers to focus on higher-level functionalities rather than low-level hardware manipulation. Additionally, ROS 2 includes multiple standardized message interfaces for sensor data, which enable seamless exchange of information among data processing pipelines and ensures compatibility. ROS 2 also provides an Interface Definition Language (IDL) that allows developers to easily define and integrate custom message interfaces.

C. Integration with perception tools and libraries. ROS 2 natively supports widely used perception libraries such as OpenCV [8] and PCL (Point Cloud Library) [9], enabling advanced processing of visual and spatial data. ROS 2 also provides built-in message synchronization tools to properly manage multiple sensor inputs. This facilitates the development of sophisticated multimodal sensing algorithms, including object detection, segmentation, and sensor fusion techniques.

D. Advanced sensor simulation tools. ROS 2 offers native compatibility with powerful simulation environments such as Gazebo and Isaac Sim, allowing developers to test and validate sensor configurations in realistic virtual environments before deploying them in real-world applications. These tools help reduce development time, optimize sensor placement, and enhance reliability.

E. Extensive community and high accessibility. ROS 2 benefits from a large and active community of developers and researchers who contribute to its continuous improvement. The ecosystem includes a vast repository of pre-built packages and third-party tools that simplifies the developing process, reducing the time and expertise required to integrate sensors into larger applications. Moreover, the extensive documentation and tutorials further lower the barrier to entry for new users.

2.2.- Limitations of ROS 2

While ROS 2 offers numerous advantages for multimodal sensing systems, it also comes with certain dependability limitations that developers must consider. Among these drawbacks we highlight the following:

A. Non-deterministic execution. To maximize flexibility and modularity, ROS 2 employs an asynchronous and concurrent execution model. However, this design choice introduces significant non-determinism in execution order [5]. Specifically, ROS 2 does not provide explicit control over the scheduling of processes, making it difficult to

establish predictable sensor data processing pipelines. The default round-robin scheduling strategy can lead to priority inversion, where low-priority tasks may block the execution of high-priority ones. These factors make it impossible to enforce a strict execution sequence.

B. Lack of real-time guarantees. Although ROS 2 was designed to address the real-time shortcomings of ROS 1, it still struggles to meet strict temporal requirements. Priority inversion and message saturation can cause unpredictable delays [5], making it difficult to maintain low-latency sensor processing. Additionally, ROS 2 lacks native compatibility with real-time operating systems (RTOS) [6]. This results in the use of commercial OS, whose operation introduces unwanted system scheduling and memory access interruptions.

C. Insufficient fault tolerance features. Dependability in multimodal sensing systems requires robust fault tolerance mechanisms, but ROS 2 built-in capabilities in this regard are very limited [7]. There are no native redundancy mechanisms, meaning that sensor failures can easily propagate through the system without fallback solutions. Neither does ROS 2 provide voting mechanisms or other robust architecture features. While some built-in monitoring and diagnostic tools exist, they are not comprehensive enough and do not include automated failure recovery strategies.

D. Unrobust memory management. Memory management in ROS 2 remains a significant challenge, particularly in long-running sensor applications where stability is crucial. ROS 2 lacks robust memory pre-allocation strategies, leading to unpredictable dynamic memory allocation during execution [7]. This can cause latency spikes when new memory is requested, page faults, and other memory related failures.

3.- Addressing ROS 2 limitations

We propose a new ROS2-based execution model to address the limitations discussed earlier. Using a multimodal sensing pipeline as an example, we first describe the standard ROS 2 execution model, then introduce our proposed model, highlighting its differences and improvements.

3.1.- ROS 2 execution model

Figure 1 shows an example of a multimodal sensing execution pipeline following the ROS 2 execution model. In this one, optoelectronic sensors act as external input data sources which are then processed by a sequence of software tasks, which in ROS 2 are referred to as *callbacks*, following an execution pipeline designed by the user. In this example callbacks communicate with each other following ROS 2's base Publisher-Subscriber model. As shown in Figure 1, the ROS 2 execution model follows a distributed architecture (i.e. combines multiple processing units potentially connected across

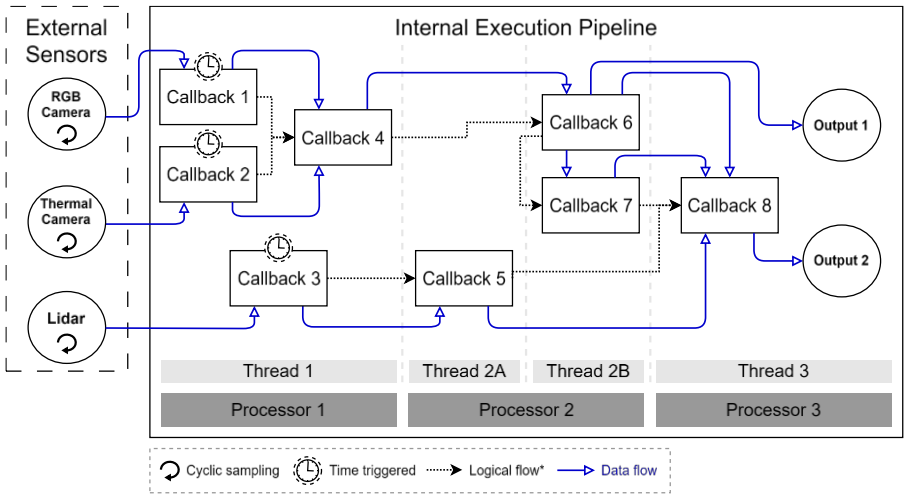

Fig. 1: Multimodal sensing pipeline example following ROS 2 execution model. (*)The dotted arrows indicate the logical callback sequence, which ROS 2's asynchronous execution may not follow in order.

a network) and allows for multi-threading execution. Most importantly, the execution of callbacks occurs asynchronously, triggered by non-sequential timer and communication events.

Following the execution logically, the multimodal sensing pipeline begins with time-triggered callbacks, responsible for calling the sensor drivers, pulling their sensed data, and publishing them in the corresponding ROS 2 message interfaces. The rest of callbacks are executed based on the availability of new messages from previous callbacks which they are subscribed to. The data communication in ROS 2 is peer-to-peer, where callbacks directly transfer data between them without the need of intermediaries.

From the example pipeline, one can observe that in ROS 2 different logical callback sequences can be executed concurrently. For example, the callbacks responsible of processing point cloud data may intercalate with those corresponding to image data. A logical sequence of callbacks receives the name of *chain*. Figure 2 shows the three different chains identified in the example. Another aspect to point out is that in ROS 2 there can be multiple outputs published at different points of the chains.

This concurrency of callback chains is one of the main causes of ROS 2 non-determinism. Moreover, other works [5] have observed that chains can often negatively interfere with each other (e.g., priority inversion) and create unacceptable delays that hinder real-time compliance.

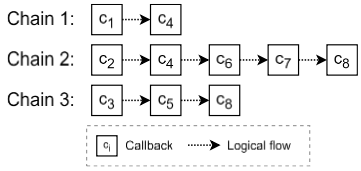

Fig. 2: Chains in the ROS 2 execution pipeline example. This assumes c_2's data being the critical event that advances c_4 to c_6.

3.2.- New ROS2-based execution model proposal

To address the limitations of ROS 2, we propose to develop a new ROS2-based synchronous and sequential execution model. Figure 3 shows the same pipeline example of the previous section under the new proposed execution model. It contains three new custom components.

Both the Input Manager and Output Manager handle pulling and pushing information, respectively, from external devices or systems. Their purpose is to limit these external interactions into explicitly defined steps of the pipeline to avoid uncontrolled interferences in the rest of the chain. In the new example, the Input Manager replaces callbacks 1,2 & 3 as they essentially fulfill the same purpose. The Cyclic Timer component starts the execution of the pipeline, which in the ROS 2 model is handled by timer-triggered callbacks. Again, the purpose is to concentrate this timer behavior into a single

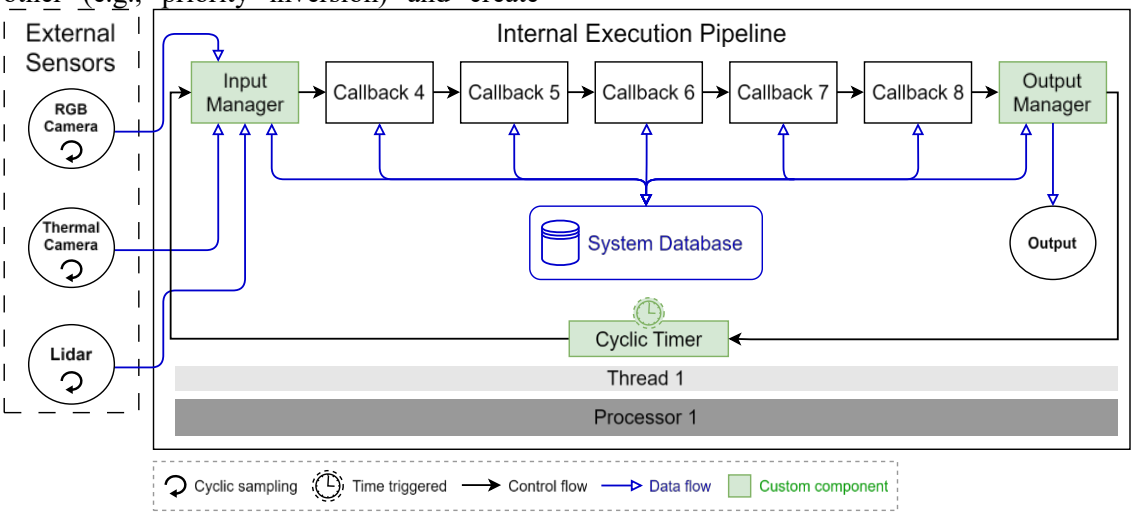

Fig. 3: New proposed execution and data flow model visualized using previous example.

well-defined and controllable component. This approach also allows to define an explicit and constant cycle time for the execution of the chain, gaining more real-time behavior.

In the proposed model, all three of these new components are mandatory for every chain. The idea is for users to configure them to adapt their custom use-cases. With these new considerations, one can appreciate that the new pipeline of the system is reduced to one synchronous and sequential chain, visualized in Figure 4. This significantly increases the determinism of the system.

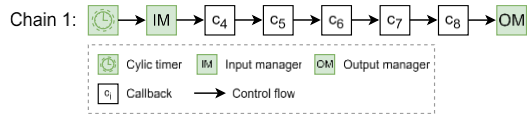

Fig. 4: Single deterministic chain in the proposed execution model example.

Other significant new feature of the proposed model is its centralized communication architecture. Here, all system components transfer data through a global System Database. This concentration of information about all internal components of the system allows for the implementation of comprehensive monitoring and diagnostic techniques that can significantly increase the robustness of the application.

Furthermore, the proposed model reduces the architecture of the system to a single threaded execution hosted by a single processor. This is not a permanent choice but an initial simplified approach to avoid potential sources of variability from trying to control and synchronize multiple threads and processors. Thus, a strategy where different callback chains are parallelized in different processors and later synchronized remains a possible future implementation.

Finally, the proposed model aims to maintain compatibility with ROS 2 interfaces, allowing developers to seamlessly transition their ROS 2-based applications into the new deterministic execution framework. This approach enables developers to leverage ROS 2's flexibility and ease of prototyping, while ensuring that the final application meets industrial-grade requirements.

3.3.- Potential challenges

The execution model presented above will most likely introduce certain challenges that must be carefully considered. Among these drawbacks we find:

A. Slow processing times. Replacing ROS 2's asynchronous, concurrent execution model with a synchronous and sequential pipeline will impact processing speed. In ROS 2, concurrently run tasks can leverage multi-core processors to handle multiple sensor streams in parallel. In contrast, a strictly sequential execution model where each sensor data processing step must wait for the completion of the previous one loses that performance boost. This may hinder the ability to meet the application's time requirements.

B. Higher data flow overhead. The introduction of a centralized system database requires to continuously manage, store, and retrieve data from and to the database, introducing frequent queries and updates, increasing data traffic, and adding extra computational burden. Moreover, having multiple components access the same memory requires more detailed and complex memory access and isolation strategies.

C. Loss of ROS 2 features. The transition from ROS 2's decentralized architecture to a synchronous, centralized execution model may come at the cost of certain built-in ROS 2 functionalities. For example, ROS 2 allows developers to dynamically add or remove sensors at runtime without disrupting the system, a capability that is incompatible with the new proposed model. Furthermore, built-in ROS 2 tools, such as *rviz2* for visualization, may no longer be supported in the new execution model.

4.- Future application: Railway obstacle detection

This work is conducted in the context of developing a multimodal railway obstacle detection system. Its objective is to automate the identification of potentially hazardous objects on railway tracks and their surroundings to enhance the autonomy and safety of railway systems. The system is based

on the L3CAM multimodal sensing unit [10], which integrates a LiDAR, an RGB camera, and a thermal camera.

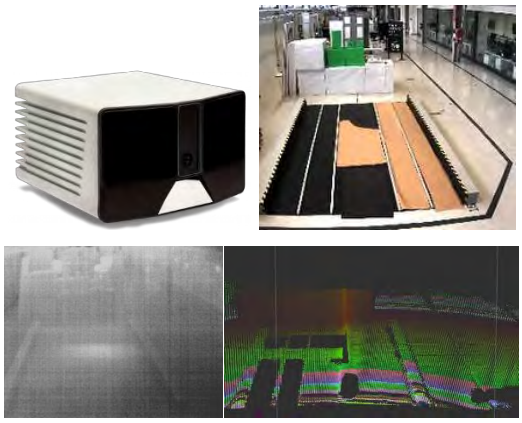

Fig. 1: Top-left: L3CAM multimodal sensing unit [10]. *Top-right, bottom-left, & bottom-right: RGB image, thermal image, and point cloud of scaled railway model, respectively.*

The goal is to implement the middleware techniques discussed in this work within the data processing pipeline of the L3CAM. This includes handling point clouds, thermal images, and RGB images, as well as their corresponding data fusion, to achieve a predictable and robust industrial-grade perception application.

5.- Conclusion

In this work we have reviewed the use of the widely adopted ROS 2 middleware for optoelectronic multimodal sensing systems, outlining both its advantages and limitations. Among its limitation we highlight dependability related including a non-deterministic execution pipeline and the absence of robust fault tolerance mechanisms. To address these challenges, we have proposed a new execution model that implements a synchronous and sequential execution model along with a centralized system database. The proposed execution model aims to achieve deterministic and highly monitorable sensor processing pipelines. Still these modifications will introduce some drawbacks that must be properly handled.

Acknowledgements: This work was developed within the MEDUSA project's framework: "Red tecnológica de ingeniería aplicada al desarrollo de soluciones inteligentes para conducción autónoma centrada en la persona (CER-20231011), Red de Excelencia CERVERA" funded by the "Ministerio de Ciencia, Innovación y Universidades de España" via "Centro para el Desarrollo Tecnológico y la Innovación E.P.E. (CDTI) (Spain)", supported by the European Union's Recovery and Resilience Facility (RRF).

References

[1] De Jong YEONG, Gustavo VELASCO-HERNAN-DEZ, John BARRY, and Joseph WALSH, *"Sensor and Sensor Fusion Technology in Autonomous Vehicles: A Review"*, Sensors, 21, 6, 2140, 2021.

[2] Henrik ANDREASSON, Giorgio GRISETTI, Todor STOYANOV, and Alberto PRETTO, "*Software Architectures for Mobile Robots*", Encyclopedia of Robotics, 1–11, 2024.

[3] Steve MACENSKI *et al.*, *"Robot Operating System 2: Design, Architecture, and Uses In The Wild"*, *Science Robotics*, 7, 66, eabm6074, 2022.

[4] Yuxiao ZHANG, Alexander CARBALLO, Hanting YANG, and Kazuya TAKEDA, *"Perception and sensing for autonomous vehicles under adverse weather conditions: A survey"*, ISPRS Journal of Photogrammetry and Remote Sensing, vol. 196, pp. 146–177, 2023.

[5] Songran LIU *et al.*, *"RTeX: An Efficient and Timing-Predictable Multithreaded Executor for ROS 2"*, IEEE Transactions on Computer-Aided Design of Integrated Circuits and Systems, vol. 43, no. 9, pp. 2578–2591, 2024.

[6] Kaiwalya BELSARE *et al.*, *"Micro-ROS"*, Robot Operating System (ROS), vol. 1051, pp. 3–55. 2023.

[7] Austin PROBE *et al.*, *"Space ROS: An Open-Source Framework for Space Robotics and Flight Software"*, AIAA SCITECH 2023 Forum, 2023.

[8] Gary BRADSKI, *"The OpenCV Library"*, Dr. Dobb's Journal of Software Tools, 2000.

[9] Radu B. RUSU and Steve COUSINS, *"3D is here: Point Cloud Library (PCL)"*, IEEE International Conference on Robotics and Automation (ICRA), 2011.

[10] Beamagine: LiDAR Imaging L3CAM, https://beamagine.com/meet-l3cam/

Multimodal data acquisition prototype for autonomous driving in adverse weather conditions

Gerard DeMAS-GIMÉNEZ[(1)], Adrià SUBIRANA[(1)], Pablo GARCÍA-GÓMEZ[(2)], Eduardo BERNAL[(1)], Jordi RIU[(2)], Josep Ramon CASAS[(3)], Santiago ROYO[(1,2)]

1. Centre de Desenvolupament de Sensors, Instrumentació i Sistemes (CD6-UPC), Universitat Politècnica de Catalunya, 08222 Terrassa, Spain.
2. Beamagine S.L. Carrer de Bellesguard 16, 08755 Castellbisbal, Spain
3. Image Processing Group, TSC Department, Universitat Politècnica de Catalunya (UPC), 08034 Barcelona, Spain.

Contact: Gerard DeMAS-GIMÉNEZ (gerard.de.mas@upc.edu).

ABSTRACT:

Autonomous driving has made significant progress in recent years, but adverse weather conditions still remain a major challenge for perception and decision-making algorithms. This work presents a multimodal data acquisition prototype designed to enhance autonomous vehicle perception in challenging environments such as fog, heavy rain, and snow. The system is mounted on a Dacia Duster and features a diverse sensor suite including visible, Short-Wave Infra-Red, thermal, and polarimetric cameras with a solid-state LiDAR and automotive radars. The whole system is calibrated with dedicated calibration boards developed on purpose to enable data fusion across all modalities. Initial results demonstrate the effectiveness of our approach, showing that critical environmental features can be detected reliably across various weather conditions. Future work includes the release of a fully annotated multimodal dataset to support further research in adverse weather perception.

Keywords: autonomous driving, multimodal imaging, data fusion, LiDAR, SWIR, thermal imaging, artificial intelligence, data set, adverse weather conditions

1.- Introduction

Autonomous driving has emerged as one of the most transformative areas in modern transportation, promising to redefine mobility and enhance road safety. The development of autonomous vehicles (AVs) relies on advanced sensing and perception systems that allow the vehicle to understand its environment in real-time. As the demand for safer, more efficient transportation grows, the autonomous driving industry has become a highly competitive sector, attracting significant investments and leading to diverse approaches in vehicle design, data acquisition, and perception technologies. Companies across the world are developing different strategies to address the unique challenges of autonomous navigation, from environmental perception to decision-making and control to get an edge over their competitors.

A crucial element in these advancements is the data acquisition systems employed by AVs, as they are in charge to feed the machine learning models that power autonomous driving. While some companies focus on integrating multiple sensor modalities, others have opted for more specialized approaches, focusing on specific data types to optimize performance.

One clear example of a specialized approach is Tesla, Inc.'s vision-centered approach. Their sensor suite consists on having multiple cameras to get a 360º field of view (FOV)

around the vehicle. Tesla, Inc.'s "Autopilot" system detects objects and estimates depth with only images and sophisticated neural networks. While this system maintains reduced costs, as visible cameras are generally cheaper than other sensors like Light Detection And Ranging (LiDAR), it compromises safety and robustness in certain environmental conditions where visible cameras might fail, like fog or low light.

In contrast, companies like Waymo, LLC. have embraced a multimodal approach, integrating LiDAR, radar, and visible cameras to enhance perception accuracy and robustness. For instance, low-light scenarios will not present as much problems with this configuration as LiDAR and radars, being active sensors, do not rely on external illumination. However, low-visibility scenarios such as fog, heavy rain, and snow will still compromise the safety of the ride.

While rare in some environments, these adverse weather conditions present a big problem to tackle in order to obtain full autonomous driving, not to mention countries where such conditions are frequent.

This paper explores the development of a multimodal autonomous driving prototype designed to produce a rich dataset for research and development of novel autonomous driving perception algorithms under adverse weather conditions. By integrating unconventional sensors, such as thermal and polarimetric cameras or solid-state LiDAR, alongside more traditional modalities like radar and visible cameras, the prototype aims to create a more diverse and accurate dataset for testing and enhancing autonomous driving systems. Through the careful collection and fusion calibration of such multimodal data, this approach has the potential to offer new insights into the performance and reliability of autonomous systems under any weather condition.

2.- State-of-the-art Data sets for autonomous driving

2.1 KITTI

The KITTI[1] dataset is one of the most widely known benchmarks in autonomous vehicle research. It is considered the pioneer of modern autonomous driving datasets as it was the first to include 3D laser scanner and 3D annotations in real live scenarios. They equipped a Volkswagen Passat (B6) with: two color and two grayscale visible cameras with a big horizontal FOV, a 64-beam spinning LiDAR with a maximum range of 100m, and a GPS/IMU localization system. The set up has been calibrated to enable data fusion. The data set includes good-weather, urban scenes.

2.2 Waymo Open

Released in 2019, Waymo-Open[2] is Google's approach to autonomous driving. Waymo-Open is presented as the largest and most diverse autonomous driving dataset. Figure 1 shows the sensor layout and coordinate system of Waymo's data acquisition prototype. Their prototype counts with: five rotating LiDAR sensors, five high resolution pinhole cameras. The sensors are precisely calibrated and synchronized to enable data fusion and capture the vehicle's surrounding environment. The data is captured at different times and in different weather conditions, even though sunny scenes are the most common and visibility is always clear, mostly in urban scenes.

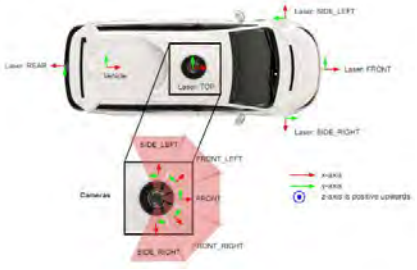

Fig.1: Waymo's data acquisition prototype for Waymo Open[2].

2.3 NuScenes

Introduced by Motional in 2019, nuScenes[3] it is largely considered the reference dataset for autonomous driving. The data was collected in Boston (USA) and Singapore, offering challenging scenes with complex traffic dynamics and dense urban structures. The data is collected at different times of the day (day and night) and weather conditions (sun, light rain, and clouds). However, there is no sign of adverse weather conditions such as heavy rain, fog, or snow. NuScenes uses an extensive sensor suite mounted on a Renault

Zoe custom data acquisition prototype as shown in Fig 2. The vehicle is equipped with: six RGB visible cameras that cover 360º of FOV, one 32 beam spinning LiDAR, five frequency modulated continuous wave (FMCW) radars, and one GPS/IMU system for localization. All sensors are synchronized and calibrated to enable data fusion.

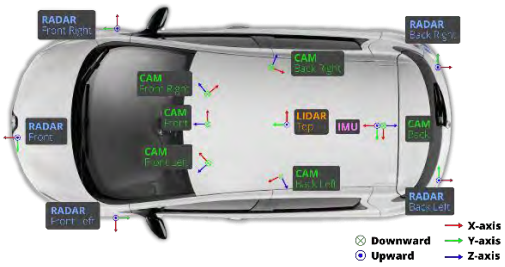

Fig. 2: NuScenes'[3] data acquisition prototype.

2.4 Seeing Through Fog (STF)

Previous data sets only focus in good environmental conditions. Even nuScenes'[3] and Waymo's[2] rainy scenes have fairly good visibility. As a result, existing autonomous systems perform well under normal imaging conditions but fail under adverse weather due to the bias toward clear scenes. Mercedes-Benz alongside Ulm and Princeton universities tackled the issue presenting the first multimodal data set under adverse weather conditions [4]. To overcome the challenges of adverse weather conditions, they presented a sensor suit sensible to the visible, mm-wave, Near Infra-Red (NIR), and Far Infra-Red (FIR) band. They used: two visible stereo cameras, a gated NIR camera, a FMCW radar, a 64-beam spinning LiDAR, a thermal camera, and an IMU. The data set includes urban and highway scenes of northern Europe.

3.- Design and Sensor Suite

As we have just seen, there is no publicly available data set except for STF[4] that has a wide range of sensors and is tested under harsh environmental conditions. Therefore, this work intends to fill the gap in the literature by proposing developing a design for robust multimodal autonomous driving under adverse weather conditions that complements the work done by STF[4]. Our proposed sensor suite can be found in Fig 3.

We equipped a Dacia Duster with the following sensors: three RGB high-resolution visible cameras, one short-wave infra-red (SWIR) camera, one thermal camera, one polarimetric camera, two radars, one solid-state LiDAR, and a GNSS/INS system.

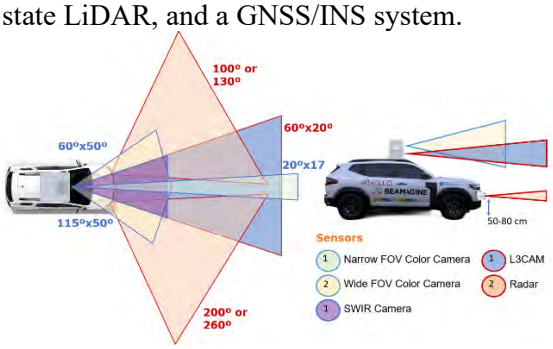

Fig. 3: Design of the developed data acquisition prototype.

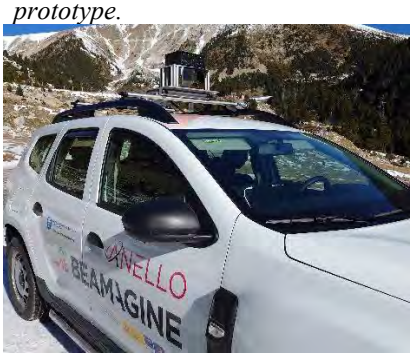

Fig. 4: Cameras and LiDAR assembled on the vehicle.

The RGB cameras are all Allied Vision Alvium G1-319c. Two of them have a wide FOV of 60º by 50º that give a combined 115º of horizontal FOV of the vehicle. They have part of their FOVs overlapped to enable stereo imaging, if desired. The other RGB camera has a narrow FOV of 20º by 17º that focuses on small far objects in the frontal direction of the car. The SWIR camera is a Basler Ace 2X a2A640-240gmSWIR sensible in the range from 400nm to 1700nm. This region has a remarkable penetration through turbid media such as fog or smoke. The camera is able to see the lights of cars in dense fog environments before than visible cameras. Both radars are Smartmicro sensor UMRR-96 Type 153 Automotive, they operate in the range of 76-81GHz and have a nominal range of up to 120m with 130º of FOV. This model aims at short to medium range and very wide horizontal angular coverage, providing short, medium- and long-range modes. It is almost

unaffected by bad weather. The thermal camera is a Seek Thermal C304SP that operates in the range from 7.8µm to 1400µm with a FOV of 56º x 42º. The polarimetric camera is a LUCID Vision Labs Phoenix™ PHX050S1-QC. This camera gives RGB information as well as linear polarization intensity for 0º, 45º, 90º, and 135º. The last two cameras come together with a solid-state MEMS LiDAR with 60º by 40º of FOV produced by Beamagine S.L. in a multimodal sensor suite called L3CAM. Solid state LiDARs have more resolution and range than their spinning counterparts. However, they cannot have a 360º of horizontal FOV. Thanks to this sensor we can also study how a higher point cloud resolution affects feature extraction and detection in state-of-the-art 3D object detection neural networks. Additionally, the prototype also counts with an Anello EVK, a GNSS unit used for localization and odometry.

Table 1: Failure mode comparison of our prototype.

	Sun	Night	Rain	Snow	Fog
LIDAR	✓	✓	~	~	~
RADAR	✓	✓	✓	✓	✓
RGB	✓	✗	~	~	✗
POL	✓	✗	~	~	~
LWIR	~	✓	~	~	✗
SWIR	✓	~	✓	✓	✓

While our system has considerably more imaging modes than other data acquisition prototypes, our FOV is restricted to just the frontal part of the vehicle. Nevertheless, there is a FOV of 60º by 20º where all modalities overlap. This gives the system a lot of redundancy and robustness against adverse weather conditions. For example, if the prototype is driving in low-light conditions, the visible, polarimetric, and SWIR camera will not produce good data, yet, we can still use the thermal camera combined with radars and the solid-state LiDAR to identify the environment well enough. Table 1 shows a comparison of the performance of each sensor in our sensor suite. It can be seen that there is always at least a 2D sensor and a 3D sensor in good performance regime independently of the weather condition.

4.- Data Fusion

In order to fully exploit the advantages of our multimodal configuration we have to be able to perform data fusion among the imaging modes. Data fusion requires two key components to be implemented: temporal synchronization and spatial registration.

For temporal synchronization, we let each sensor record data at their maximum frame rate and temporally pair the data with our main sensor, the solid-state LiDAR, via best effort synchronization. With that strategy, we achieve temporal differences of less than 50ms between every sensor with respect to the main sensor per frame. The solid-state LiDAR used has a frame rate of 7Hz.

On the other hand, spatial registration has been carried out using [5]. Common reference features have to be found in every mode with the solid-state LiDAR. This is not trivial as each sensor has its own sensitivity range and they may not share it with other sensors in the system. Therefore, we designed two different calibration boards. One for visible, thermal, and LiDAR calibration and another for visible, radar, and LiDAR calibration.

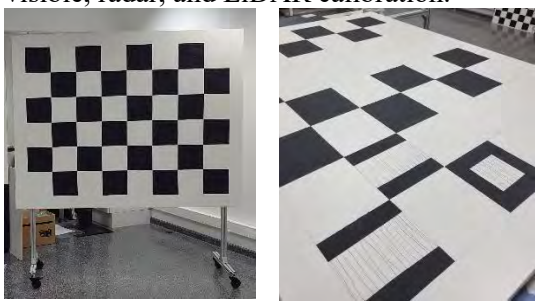

Fig. 5: Visible, thermal, LiDAR calibration board. Left: complete board. Right: nichrome wire under the absorbing tape.

The visible-thermal-LiDAR calibration board (Fig.5) consists of a 5 by 7 squarred checkerboard. Each square is made of a tape that greatly absorbs 1064nm light, so no returns from the LiDAR are obtained from them. Behind the tape, there is a nicrom wire that greatly heats up when current passes through it, making the squares visible for the thermal camera. The intersection between the squares can be obtained through classical

image processing algorithms. The later board cannot be used to calibrate the radars as the metallic wire used to detect the pattern with the thermal camera interferes with the radar waves. As a result, another board was designed adapting the previous calibration board ideas of [6]. This time, we generate a similar, smaller pattern with the same absorbing tape to be able to detect the board with both, visible cameras and the LiDAR. The board is made of Styrofoam, which is invisible for radar waves. Behind the board a metallic retroreflector is placed to force a high-intensity return from the radar. The board can be seen in Fig. 6.

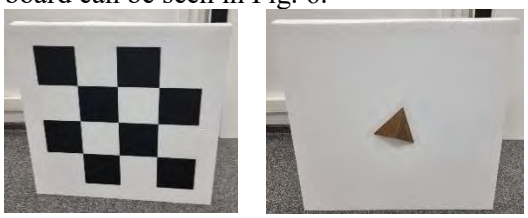

Fig.6: Visible, radar, LiDAR calibration board. Left: frontal part of the board. Right: rear, where the retroreflector is placed.

By taking multiple captures of each board independently we can obtain the intrinsic and extrinsic parameters for every sensor, registering the different imaging modes.

5.- Results

Once the prototype was finally assembled and all sensors were calibrated, we drove it around different environments in search of diverse weather conditions. We also tested how data fusion was consistent even with high dynamic scenes. In Fig. 7 a point cloud projected onto an image can be seen. We can see how the points coincide with the shapes of the objects on the image.

Fig. 7: LiDAR point cloud projected onto an RGB image in a dynamic scene.

Figures 8-10 show captured samples under different weather scenarios. A mosaic of six images is presented. The top row consists of the wide left, narrow, and wide right images respectively. Below, thermal, polarimetric, and SWIR. After that a bird-eye-view of the LiDAR point cloud is presented. Fig. 8 consists on an urban scene with clear vision. Every sensor performs well under these conditions. Differently, Fig. 9 shows a road scene with dense fog. It can be seen how visible cameras are really affected by the condensed water in front of them. The thermal camera also yields poor data as infra-red light is greatly absorbed by water. LiDAR detectivity drops significantly, however, a traffic light visible on the narrow image can still be detected at a high distance. SWIR, on the other hand, still presents a well-defined image with good detectivity of the van's frontal lights. Finally, Fig. 10 presents an urban scene while snowing. Again, visible cameras struggle to produce good results, while the SWIR and the thermal cameras can still operate properly. Especially the thermal camera detecting pedestrians, as they are way hotter than the rest of the snowy environment.

Fig. 8: Urban sample with good visibility.

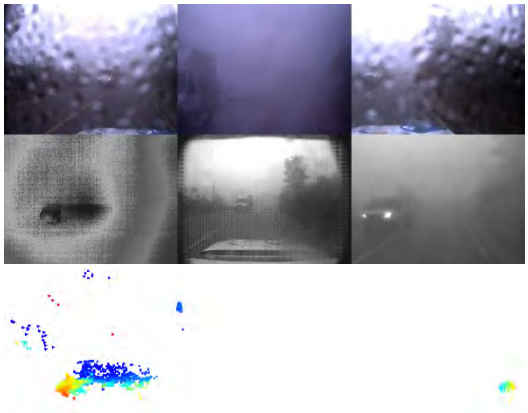

Fig. 9: Road sample with dense fog.

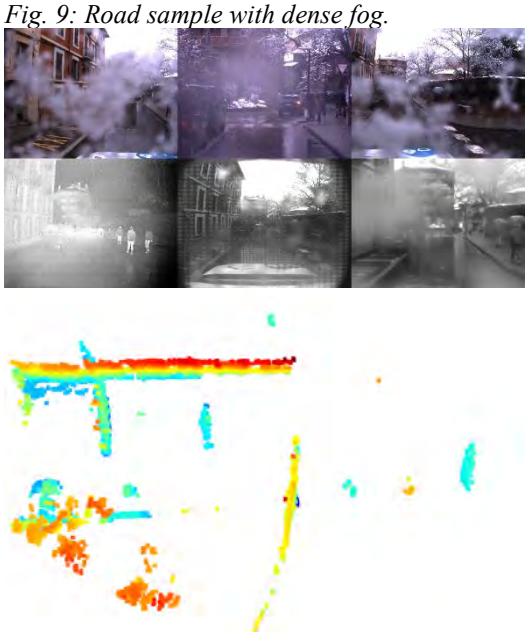

Fig. 10: Urban sample while snowing.

6.- Conclusions and future work

A multimodal data acquisition prototype specially designed to be able to explore perception under adverse weather conditions has been developed and described. Furthermore, two novel multimodal extrinsic calibration boards have been developed to enable data fusion across all sensors. Results show that relevant features from the environment can be obtained regardless of the weather conditions, and that each sensor presents failure modes. As future work, a multimodal annotated data set is currently under development and is expected to be publicly published later this year.

Acknowledgements: This work has been sponsored by the Spanish Ministry of Science through projects TED2021-132338B-I00 and PID2023-152427OB-I00 and by the European commission through project GA-101139941. This work is part of a Ph.D. thesis with grant number 2023 FI-1 00229 co-funded by the European Union.

References

[1] Andreas GEIGER, Phillip LENZ, Raquel URTASUN, *"Are we ready for autonomous driving? The KITTI vision benchmark suite"*, in Proceedings of 2012 IEEE Conference on Computer Vision and Pattern Recognition, pp. 3354-3361, 2012.

[2] Pei SUN, Henrik KRETZSCHMAR, Xerxes DOTIWALLA, Aurélien CHOUARD, Vijaysai PATNAIK, Paul TSUI, *"Scalability in Perception for Autonomous Driving: Waymo Open Dataset"* in Proceedings of 2020 IEEE/CVF Conference on Computer Vision and Pattern Recognition, pp. 2443-2451, 2020.

[3] Holger CAESAR, Varun BANKITI, Alex H. LANG, Sourabh VORA, Venice Erin LIONG, Qiang XU, *"nuScenes: A Multimodal Dataset for Autonomous Driving"*, in Proceedings of 2020 IEEE/CVF Conference on Computer Vision and Pattern Recognition, pp. 11618-11628, 2020.

[4] Mario BIJELIC, Tobias GRUBER, Fahim MANNAN, Florian KRAUS, Werner RITTER, Klaus DIETMAYER, "*Seeing Through Fog Without Seeing Fog: Deep Multimodal Sensor Fusion in Unseen Adverse Weather"* in Proceedings of 2020 IEEE/CVF Conference on Computer Vision and Pattern Recognition, pp. 11679-11689, 2020.

[5] Pablo GARCÍA-GÓMEZ, Santiago ROYO, Noel RODRIGO, Josep R. CASAS, "*Geometric Model and Calibration Method for a Solid-State LiDAR*", Sensors, 20, 10, 2898, 2020.

[6] Joris DOMHOF, Julian F.P. KOOIJ, Dariu M. GAVRILA, "*An Extrinsic Calibration Tool for Radar, Camera, and LiDAR*" in Proceedings of 2019 International Conference on Robotics and Automation pp. 8107-8113, 2019.

Plastics Sorting Using Terahertz Frequencies and Machine Learning

Daniel MORENO-PARIS [(1)], David HERNANDEZ-GUERRERO[(1)], Aldo MORENO-OYERVIDES[(1)], Pedro MARTÍN-MATEOS[(1)], Oscar Elías BONILLA-MANRIQUE [(1)]

1. Electronics Technology Department, Universidad Carlos III de Madrid, Leganes, 28911 Madrid, Spain.

Contact: Daniel MORENO-PARIS (danmoren@pa.uc3m.es).

ABSTRACT:

This paper presents an investigation on the use of terahertz (THz) spectroscopy combined with machine learning (ML) algorithms for the nondestructive characterization and classification of plastics, including challenging materials with different colour, composition and thickness characteristics. Twelve different types of plastics were analyzed by measuring their spectral transmission in the low THz band (100-600 GHz). The acquired data were processed to extract relevant features, which were then used to train ML models capable of accurately distinguishing between plastic types. The results demonstrate the feasibility of this methodology for improving material identification techniques, crucial for recycling and industrial applications. The ability of the THz technique to overcome the limitations of infrared-based methods when analyzing black and multilayer plastics is highlighted. Dimensionality reduction by PCA and especially Savitzky-Golay filtering were shown to be useful in optimizing sorting performance.

Key words: Terahertz Spectroscopy, Machine Learning, Plastic Classification, Recycling, Material Identification, Non Destructive.

1.- Introduction

The growing production and inadequate disposal of plastics pose significant environmental challenges, with global usage expected to nearly double by 2050 [1]. Efficient recycling depends heavily on accurate plastic identification and classification, yet current methods—ranging from manual sorting and visual inspection to direct approaches based on physical properties and indirect techniques such as NIR, MIR, and XRF spectroscopy—still present limitations [2]. These include issues with complex materials such as black or multilayer plastics, low precision, or the use of ionizing radiation [3]. While automated and AI-based systems have significantly improved sorting efficiency and accuracy, non-destructive and reliable identification remains a pressing need [4]. In this context, terahertz (THz) spectroscopy is emerging as a promising alternative, offering specific spectral fingerprints for a wide range of materials and enabling precise identification without damaging the samples [5]. This study investigates the use of THz spectroscopy combined with machine learning to classify twelve types of plastics, aiming to enhance material identification for recycling and industrial applications.

2.- Materials and Methods

2.1.- Experimental setup

A custom terahertz (THz) spectroscopy system was developed to analyze the transmission properties of plastic samples in

the 100–600 GHz range. The setup includes three main components as shown in Figure 1: (A) THz generation is produced by the beat frequency of two 1550 nm semiconductor lasers, converted via a photoconductive antenna; (B) plastic samples, shaped into square laminates, were mounted using a magnetized holder for consistent alignment; (C) a Schottky receiver detected transmitted signals, which were acquired from both high-gain (HG) and low-gain (LG) channels.

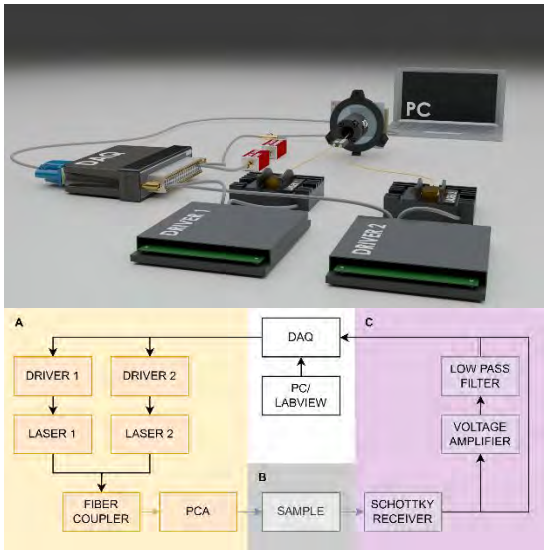

Fig. 1: THz spectroscopy system 3D schematic. A) THz Generation; B) Sample; C) THz Receiver.

2.2.- Data acquisition and processing

For data acquisition, the THz spectroscopy system was used to measure transmission across 12 different plastic types, detailed in Table 1, (identified with an alphabetic label), within the 100–600 GHz frequency range, using 10 GHz steps. Each frequency sweep accounted for laser stabilization times, which varied from 45 seconds at lower frequencies (100–200 GHz) to 20 seconds at higher frequencies (210–600 GHz). Data portions where the lasers were not completely stabilized were excluded, yielding 12 seconds of stable measurements per frequency point. Measurements were performed on 5 independent samples per plastic type over five different days, resulting in a dataset of 60 full frequency sweeps. At each frequency, approximately 1.200 readings are collected (≈100 readings per second for 12 seconds), considering that a sweep is performed over 51 frequencies, a total of about 61.200 points per sample is obtained. For each of the 12 plastics, 5 samples are measured, giving a total of about 306.000 data points per plastic type. The raw data included the transmission frequencies values, high-gain (HG) and low-gain (LG) channels signal values. The dataset is divided into training, validation and test. For the test set, the data from 1 of the 5 samples of each plastic is taken randomly (20% of the total), in order to avoid using data points from the same sweep (with the same ambient conditions) in the training data. The data from the remaining 4 sweeps of each plastic (80% of the total) is divided into 80% training and 20% validation.

Table 1: Plastic samples and assigned identification labels.

Plastic	***Characteristics***	***Label***
PE + EVOH	*Translucent*	*A*
PE + EVOH (Admer AT1707E)	*Translucent*	*B*
ABS + PC	*White*	*C*
ABS	*Black*	*D*
Ecovio + PVOH	*Translucent*	*E*
PP + EVOH (0.3mm)	*Translucent 0.3 mm*	*F*
Ecovio + PVOH + PHB	*Transparent*	*G*
PP + EVOH (0.7mm)	*Transparent 0.07 mm*	*H*
PS	*Translucent*	*I*
LDPE	*Transparent*	*J*
PVC	*White*	*L*
PET	*Transparent*	*O*

2.3.- Feature Extraction and Classification

The feature extraction techniques used in this study aim to isolate the most relevant information for plastic classification. Data

were segmented using time windows (preferably 0.1 seconds), and for each window, the mean and standard deviation of the high-gain (HG) and low-gain (LG) channel signals were calculated. These four values were then organized as input variables linked to each frequency measurement within the frequency range of interest. This process generated multiple input features per frequency, enabling machine learning models to differentiate plastic types based on their characteristic spectral responses. The primary goal was to reduce noise from individual measurements and structure the data for improved classification performance.

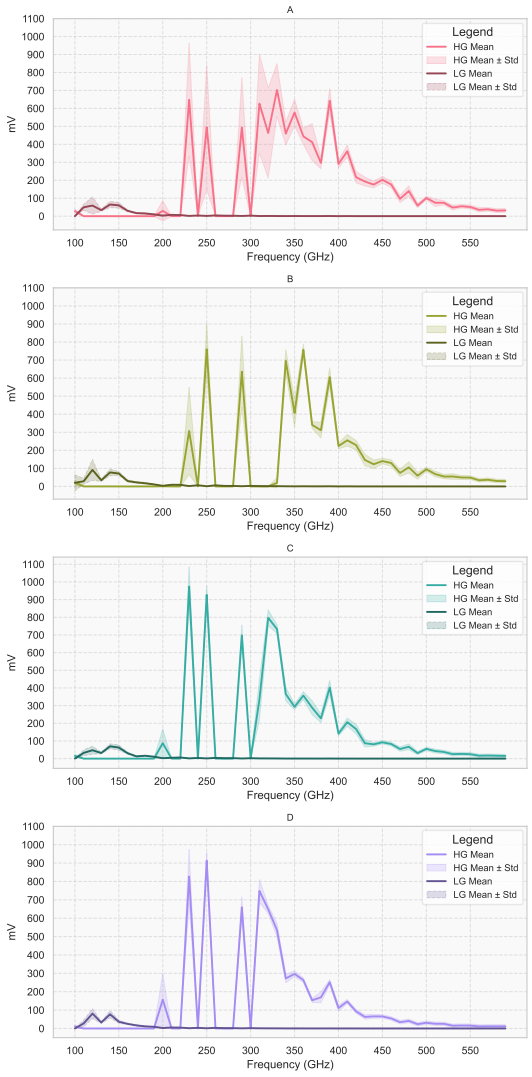

Fig. 2: Transmission gain spectra for both channels (HG and LG) with standard deviations of the analysed plastics with labels A, B, C and D.

Several machine learning techniques were employed for classification, including Random Forest (RF), Gradient Boosting (GB), Naive Bayes (NB), Logistic Regression (LR), and Support Vector Machines (SVM). To enhance model performance and reduce the effects of high dimensionality and noise, dimensionality reduction and filtering methods were applied. Principal Component Analysis (PCA) was used to retain the most significant variance, while the Savitzky-Golay (SG) filter smoothed the data without losing critical features. Feature selection strategies were also implemented, leveraging model-specific importance metrics, such as feature importance (RF, GB), coefficient magnitude (LR), and permutation importance (NB, SVM).

Table 2: Best-performing algorithms and preprocessing (SG with window size and polynomial order and PCA with percentage of total variance retained) for different sizes of frequency sub-groups.

Freqs.	***Preproc.***	***Algorithm***	***Accuracy***
50	*SG 3,2*	*GB*	*66.3%*
20	*SG 3,2*	*NB*	*87.7%*
10	*SG 5,3*	*NB*	*88.0%*
5	*SG 5,3*	*NB*	*85.8%*
3	*PCA 0.95*	*RF*	*81.0%*
1	*SG 3,2*	*RF*	*58.2%*

3.- Results

The results demonstrate the effectiveness of THz spectroscopy combined with machine learning for the classification of 12 relevant plastic types. Distinct spectral transmission signatures were observed for each plastic in the 100–600 GHz range, particularly above 300 GHz in the high-gain (HG) channel. Although the low-gain (LG) channel also provided useful information, it was less discriminative. Notably, the analysis showed that acceptable classification performance could be achieved using only three selected

frequencies, as shown in Figure 3, enabling the potential development of real-time classification systems based on fixed-frequency THz sources.

Classification performance metrics, summarized in Table 2, highlight the impact of preprocessing methods (SG filtering, PCA) and classification algorithms. For example, an accuracy of 88.0% was achieved using SG and Naïve Bayes with 10 frequencies, as shown in Table 1, while PCA with only three components and Random Forest yielded 81.0% accuracy. However, some limitations were found in distinguishing plastics with very similar spectral features (e.g., E vs. G and H vs. J). The approach proved especially effective for black plastics and multilayer samples (Figures 3 and 6), which are typically challenging for near-infrared spectroscopy.

The study suggests that incorporating environmental data (humidity, temperature) and expanding the dataset would enhance model robustness and generalizability. Overall, the results confirm the feasibility of a fast, non-destructive, and accurate classification system for diverse plastic materials using THz spectroscopy and machine learning.

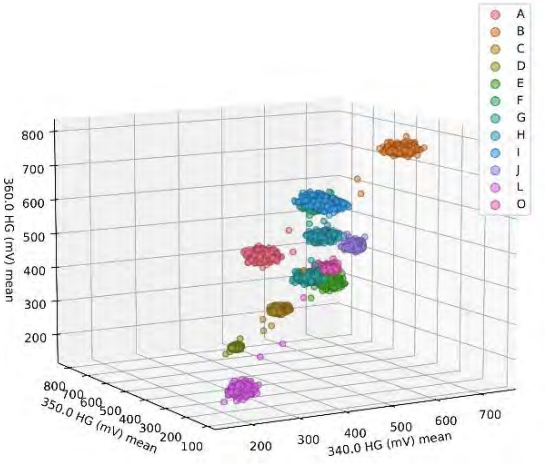

Fig. 3: 3D plot of HG mean (0.1s windows) for every plastic for 340, 350 and 360 GHz frequencies.

4.- Conclusion

This study highlights the potential of combining Terahertz (THz) spectroscopy with machine learning algorithms for the automated classification of plastics, including challenging materials such as black and multilayer plastics. By leveraging the distinct spectral transmission properties of plastics in the low-THz range (100–600 GHz), the proposed methodology demonstrated strong performance across 12 plastic types. Dimensionality reduction (PCA) and data smoothing (Savitzky-Golay filtering) proved effective in enhancing classification accuracy, and promising results were achieved even when using only three selected frequencies. This suggests the feasibility of real-time classification systems based on fixed-frequency THz sources. While some limitations remain, such as the difficulty in separating materials with similar spectral fingerprints, the approach shows considerable promise. Future improvements, including environmental data acquisition and expanded datasets, could further enhance model robustness. Overall, the integration of THz spectroscopy and machine learning offers a fast, non-destructive, and accurate solution for advanced plastic sorting in industrial and recycling applications.

Acknowledgements: This work was supported by the regional project "Aplicación de Inteligencia Artificial para el análisis de combustiones en tiempo real (IA_aCTRl-CM-UC3M)", funded by the Comunidad de Madrid. It was also partially supported by the national project PIC-PAPER (ref. PDC2023-145875-I00), funded by the Spanish Ministry of Science, Innovation and Universities.

References

[1] Monika DOKL, Anja COPOT, Damjan KRAJNC, Yee VAN FAN, Annamaria VUJANOVIĆ, Kathleen B. AVISO, Raymond R. TAN, Zdravko KRAVANJA, Lidija ČUČEK, *"Global projections of plastic use, end-of-life fate and potential changes in consumption, reduction, recycling and replacement with bioplastics to 2050"*, Sustainable Production and Consumption, vol. 51, pp. 498–518, 2024.

[2] Narinder SINGH, David HUI, Rupinder SINGH, I.P.S. AHUJA, Luciano FEO, Francesco FRATERNALI, *"Recycling of plastic solid waste: A state of art review and future applications"*, Composites Part B: Engineering, vol. 115, pp. 409–422, 2017.

[3] Biswajit RUJ, Vivek PANDEY, Priyajit JASH, V.K. SRIVASTAVA, *"Sorting of plastic waste for effective recycling"*, International Journal of Applied Science and Engineering Research, vol. 4, no. 4, pp. 564–571, 2015.

[4] Berny CARRERA, Victor L. PIÑOL, Judit B. MATA, Kwanho KIM, *"A machine learning based classification models for plastic recycling using different wavelength range spectrums", Journal of Cleaner Production*, vol. 374, p. 133883, 2022.

[5] R. SAFIAN, Galia GHAZI, Nafiseh MOHAMMADIAN, *"Review of photomixing continuous-wave terahertz systems and current application trends in terahertz domain"*, Optical Engineering, vol. 58, pp. 110901–110901, 2019.

Optoelectrónica en energía renovable

Capa antirreflejante en el rango visible basada en nanopartículas metálicas embebidas en un fotopolímero. Aplicación a células solares de película delgada

Óscar ESTEBAN [(1)], Sirona VALDUEZA-FELIP [(1)], Fernando B. NARANJO [(1)]

1. Grupo de Ingeniería Fotónica, Universidad de Alcalá, Escuela Politécnica Superior, 28805 Alcalá de Henares.
Unidad Asociada Instituto de Óptica-CSIC, Tecnologías Fotónicas y de Sensores

Contacto: Óscar ESTEBAN (oscar.esteban@uah.es).

ABSTRACT:

We present a low-cost method to implement a single-layer antireflective coating (ARC) including metallic nanoparticles embedded into a polymer matrix. The metamaterial is formed by a 1% in weight of Aluminium nanoparticles (NPs) randomly dispersed into a transparent UV curable photopolymer matrix that can be deposited on different substrates, which extends its application not only to solar cells but also to the protective glass covers. Our results show an average reflectance reduction up to 50% in the whole VIS spectral range when the substrate is a soda-lime glass slide. The deposition method, based on the doctor-blade technique, is simple and inexpensive, since does not require clean-room nor vacuum equipment, being able to roll out the ARC layer even on already existing devices. The developed ARC was also deposited on top of a fully operative InN on Si thin-film solar cell, pointing to a relative 9.0% increment in the conversion efficiency.

Key words: Antireflective coating, metamaterial, metallic nanoparticles, thin-film solar cell, III-nitride

1.- Introducción

La tecnología fotovoltaica se ha revelado como una alternativa prometedora para satisfacer la demanda mundial de energía y mitigar al mismo tiempo los efectos del cambio climático. Aunque existen dispositivos fotovoltaicos que alcanzan altas eficiencias de conversión [1], sigue siendo necesario reducir el coste por watio generado para ser competitivos con las fuentes de energía tradicionales para conseguir una verdadera transición energética. Una vía hacia este objetivo es el uso de las células solares basadas en película delgada, que no sólo reducen la cantidad de material necesario para fabricar las capas constituyentes de la célula, sino que también reducen los residuos y la energía requerida en el proceso de fabricación y permiten su integración en dispositivos autónomos [2]. Sin embargo, este tipo de célula solar presenta menos eficiencia que las convencionales debido al reducido espesor de la capa activa, que por un lado reduce la probabilidad de absorción de los fotones incidentes y por otro aumenta las pérdidas de Fresnel en la superficie frontal debido al elevado contraste del índice de refracción con el medio incidente [3]. Para minimizar estas pérdidas por reflexión, es habitual utilizar revestimientos antirreflejantes (ARC) para ajustar el índice de refracción y lograr la mayor transmitancia posible en la superficie de entrada del dispositivo. [4].

Una revisión exhaustiva de las diferentes opciones de recubrimientos antirreflejantes demuestra que pueden conseguirse reflectancias muy bajas, pero con altos costes de procesado y con tolerancias muy estrictas.

En este contexto, dado que la industria fotovoltaica es muy sensible a costes, la idoneidad de un ARC depende en gran medida de la relación entre la mejora de la eficiencia y los gastos generales de proceso de recubrimiento. Además, una baja reflectancia en un gran ancho de banda espectral suele implicar estructuras multicapa [5], que requiere un riguroso control del índice de refracción y espesor de cada capa.

En este trabajo, presentamos el desarrollo de un ARC monocapa mediante el embebido de nanopartículas metálicas distribuidas de manera aleatoria en una matriz polimérica. Es eficiente en el rango visible, donde la luz solar es más intensa. Tanto las nanopartículas como el polímero son comerciales, y la técnica de depósito por *doctor-blade* es sencilla, económica, bien adaptada a recubrimientos a gran escala, y que además es óptima para crear películas relativamente gruesas a partir de una solución viscosa. Además, es fácilmente escalable a la producción en masa [6] sin necesidad de utilizar una sala blanca o un equipo de depósito en vacío.

2.- Fabricación y depósito de ARC

Como ya se ha mencionado, el ARC propuesto se basa en nanopartículas metálicas distribuidas aleatoriamente en una matriz de fotopolímero. Estas NPs son de Aluminio (Al-NPs), un material de bajo coste, abundancia natural y fácil procesado. Además de sus buenas propiedades de *scattering* y la posibilidad de generar resonancias plasmónicas en el rango espectral VIS-NIR. Una ventaja adicional es la posibilidad de obtener directamente dichas NPs en formato de polvo.

Mediante la técnica *doctor-blade*, se deposita de sobre un sustrato el metamaterial formado por las Al-NPs y el fotopolímero. Para ello, hay que tener en cuenta varios parámetros. El primero es la viscosidad del material de recubrimiento, que debe tener el valor y la consistencia adecuados para garantizar una aplicación uniforme. La velocidad y la presión de aplicación estarán relacionadas con el grosor de la película depositada. En nuestro caso, se ha aplicado una velocidad constante de unos 3 cm/s a una presión también constante. El espesor de la película depositada está fijado por el de la cinta adhesiva utilizada para sujetar el sustrato sobre una superficie plana, y se ha estimado en ~50 µm. Este valor se ha mantenido constante en todas las muestras fabricadas sobre portaobjetos de vidrio, y es el límite de nuestro dispositivo experimental.

El fotopolímero elegido es un adhesivo óptico (NOA61). La selección específica de NOA61 (adquirido a Thorlabs) procede de su transparencia óptica en el rango VIS-NIR, sus buenas propiedades de adhesión, su reducida merma y su resistencia a la radiación UV. Además, una vez curado puede soportar temperaturas de hasta 260ºC cuando se deposita sobre un sustrato.

Las Al-NPs utilizadas en este trabajo tienen un tamaño de 110 nm. La elección principal proviene de la mejora de la eficiencia de la célula solar cuando se utilizan Al-NPs de tamaño 90 nm [7]. Además, existen dos razones adicionales para dicha selección. Una es que el tamaño esté en el orden de magnitud de las longitudes de onda de interés. La otra es que no deben ser tan grandes como para causar efectos de sombra, ni tan pequeñas como para dificultar la ruptura de agregados. Entre los tamaños disponibles en el mercado, los que más se acercan a cumplir estos requisitos son los de 110 nm.

Su concentración en el ARC debe ser lo suficientemente baja como para evitar la interacción entre ellas, lo que ocasionaría efectos multipolares que suponen un gran aumento de la reflectancia en la región espectral de interés [3]. Así, en este estudio se ha elegido una concentración de alrededor del 1% en peso en el fotopolímero, lo que significa añadir 0,025gr de Al-NPs por mililitro de fotopolímero. Estos valores son constantes para todas las muestras fabricadas.

La viscosidad de NOA61 a 25ºC oscila entre 300 y 450 cps, que es demasiado elevada como para permitir una aplicación uniforme. Así, su valor se reduce mezclándolo con metanol (viscosidad 1,1 cps) en una fracción de volumen del 74-26% respectivamente. Con esto, se alcanza una viscosidad media inferior

a 100 cps. Sin embargo, el metanol es útil no sólo para reducir la viscosidad, sino también para dispersar eficazmente las Al-NPs que se van a embeber en el fotopolímero. En efecto, el formato en polvo de las NPs conlleva la presencia de grandes agregados que deben deshacerse antes de añadirlas a la mezcla precursora del ARC. Para ello se sigue un procedimiento específico consistente en mezclar NPs y metanol 50ºC y 300 rpm durante 30' en un agitador magnético cuidando de mantener la concentración en peso deseada. A continuación, la mezcla resultante se somete a tratamiento de ultrasonidos durante 20', y se eliminan los agregados más grandes utilizando un filtro con un tamaño de poro de 50 µm. Esta mezcla se añade al fotopolímero para obtener el metamaterial.

Una vez preparada la mezcla, se dispone una porción en un extremo de un sustrato de vidrio, previamente limpiado con isopropanol y secado con N_2. A continuación se distribuye de manera uniforme con una varilla de vidrio en el montaje *doctor-blade* y se cura con UV durante 5'. Dado que el metanol se evapora tras la deposición, sólo queda en la superficie el fotopolímero con las NPs incrustadas.

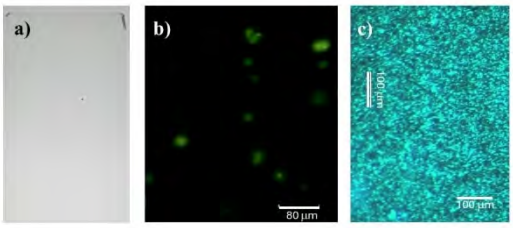

Fig. 1 a) Vista del portaobjetos recubierto con el ARC fabricado con la mezcla precursora después de la agitación termomecánica, sonicación y filtrado de agregados para obtener la suspensión coloidal de Al-NPs en el soporte. b) Imagen óptica de la muestra recubierta mostrando la baja densidad de agregados en el ARC. c) Imagen óptica del sustrato recubierto sin calentar, agitar y someter a tratamiento de US la mezcla precursora.

Las muestras resultantes son como las presentadas en la Fig. 1, donde se observa un portaobjetos de vidrio transparente con el ARC en la Figura 1a. Un zoom de una pequeña área de la ARC obtenido con un microscopio óptico (resolución espacial ~ 2 µm) muestra una baja densidad de agregados en la Figura 1b, muy inferior a la obtenida cuando la mezcla se obtiene por simple agitación mecánica para dispersar las Al-NPs en metanol. En este caso, se observa un aspecto turbio a simple vista y con una imagen de microscopio como la presentada en la figura 1c.

3.- Caracterización del ARC

Sobre las muestras fabricadas siguiendo el procedimiento anterior, se midieron su reflectancia y transmitancia en incidencia normal para obtener su respuesta operando como ARC.

Fig. 2 Esquema del montaje experimental. Como luz incidente se emplea el haz colimado procedente de una lámpara halógena. La reflectancia y la transmitancia espectrales se miden con un espectrómetro CCD.

El montaje experimental utilizado para evaluar el rendimiento espectral de las muestras se representa en la Fig. 2. La iluminación de la muestra se realiza con una lámpara halógena (AVALight-D(H)-S) conectada a una fibra bifurcada (200 µm de diámetro) unida a una lente colimadora en su extremo. La luz reflejada es recogida por la misma lente y se registra con un espectrómetro CCD (StellarNet Blue-Wave). El rango espectral de interés se limita al VIS (400-750 nm), donde se espera el máximo de energía solar AM1.5. El tiempo de integración se fija en 300 ms.

Para las medidas de transmitancia se modificó ligeramente el montaje añadiendo una fibra óptica de polímero (1 mm de diámetro) en la parte posterior de la muestra. En este caso se utilizó un tiempo de integración de 1 s.

El análisis de todas las medidas se realizó en relación con las obtenidas en un sustrato sin ARC. Para representar cuantitativamente la mejora en reflectancia y transmitancia de cualquier muestra recubierta con el ARC desarrollado, se calculó la diferencia relativa en ambas magnitudes de interés. De este modo, se definen dos funciones de mérito (FoM) diferentes:

$$\Delta R[\%] = \frac{R_{ARC} - R_{ref}}{R_{ref}} \times 100; \qquad (1)$$

$$\Delta T[\%] = \frac{T_{ARC} - T_{ref}}{T_{ref}} \times 100; \qquad (2)$$

para la reflectancia (1) y la transmitancia (2), respectivamente. Aquí, R_{ARC} y T_{ARC} son la reflectancia y la transmitancia medidas de la muestra recubierta con el ARC depositado, mientras que R_{ref} y T_{ref} son los valores de referencia medidos en la muestra sin ningún recubrimiento. Por tanto, una mejora por efecto del ARC significaría obtener valores negativos de la ecuación (1), $\Delta R<0$. Mientras que se buscan valores positivos de la ecuación (2), $\Delta T>0$.

3.1.- Al-NPs embebidas en fotopolímero como recubrimiento AR sobre sustrato de vidrio

En la Fig. 3 se representan los resultados obtenidos sobre la muestra de la figura 1b. Como puede observarse en la figura, la reflectancia, en línea sólida azul, disminuye un promedio del 50% en todo el rango espectral. Y se observa un pico estrecho a 660 nm en la reflectancia, compatible con el *backscattering* Mie para Al-NPs en un medio de las características del NOA61.

Sin embargo, esta resonancia no aparece en la transmitancia representada en la misma figura en línea sólida roja. En este caso se observa una mejora global ligeramente superior al 5% en todo el rango espectral. Este valor es comparable al reportado en la bibliografía, pero con una única capa y mediante un método de depósito simple y directo.

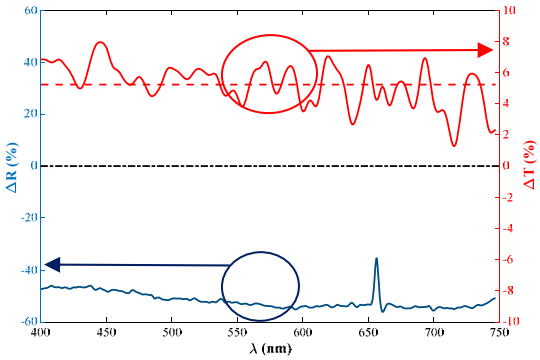

Fig. 3 En línea sólida azul se representa la mejora espectral en la reflectancia relativa de la muestra de vidrio recubierta con un ARC (eje izquierdo), con un promedio de ~50%. Se observa claramente un estrecho pico de resonancia a 660 nm. En línea sólida roja (eje derecho), se representa la mejora espectral relativa de la transmitancia de alrededor del 5% (trazada en línea discontinua roja) La referencia sin cambios se ha incluido como línea negra discontinua.

3.2.- Al-NPs operando como capa AR sobre células solares de película delgada

El objetivo final es aplicar las capas AR fabricadas en dispositivos fotovoltaicos. Con el fin de evaluar el rendimiento de la capa AR en una célula solar real, se depositó en una unión *n-p* formada por una película delgada de 176 nm de nitruro de indio (InN) crecida sobre un sustrato de Silicio con orientación cristalográfica (100) mediante pulverización catódica (*sputtering*) de radiofrecuencia a 550ºC [8]. Con el fin de proteger la superficie del InN, se aplicaron únicamente las Al-NPs de 110 nm de diámetro sin utilizar el fotopolímero como matriz de fijación.

La única FoM disponible cuando se utiliza una estructura semiconductora que absorbe en el rango VIS es el incremento relativo de reflectancia, representado en la Fig. 4. La reducción de reflectancia sigue una tendencia similar a la de la Fig. 3, obteniendo una mejora promedio de ~24%, principalmente en el rango de longitudes de onda más cortas.

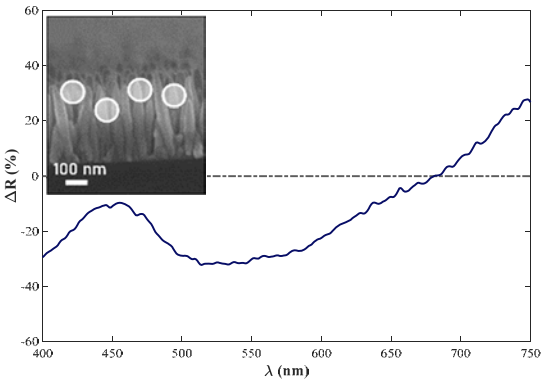

Fig. 4 Reflectancia espectral relativa medida cuando las Al-NPs están distribuidas aleatoriamente en la superficie de la estructura nanocolumnar semiconductora n-p mostrada en la imagen. Los círculos corresponderían a Al-NPs de 110 nm de diámetro. En este caso, R_{ref} es la reflectancia de la capa del nitruro sobre Si sin NPs. Se observa una reducción promedio de la reflectancia de aproximadamente un 24%.

Dicha estructura se procesó como dispositivo añadiendo contactos óhmicos superiores e inferiores de 120 nm de Al, tal y como se muestra en la Fig. 5, y se caracterizó mediante curvas de densidad de corriente-tensión (J-V) utilizando una estación de 2 puntas acoplada a una unidad de medidor de fuente e iluminándola bajo 1 sol (1 kW/m2) de luz estándar (simulador solar VeraSol clase AAA) con un espectro AM1.5G. Las curvas J-V medidas del dispositivo con y sin el recubrimiento AR se muestran en la misma Figura 5.

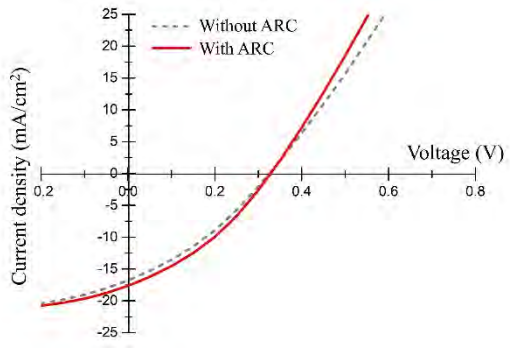

Fig. 5 Curvas J-V de un dispositivo de capa delgada de InN sobre Si con y sin revestimiento AR, mostrando el aumento de la J_{SC}.

La densidad de corriente de cortocircuito (J_{sc}) a través del dispositivo aumenta de 16.80 a 17.41 mA/cm^2 gracias a la incorporación de la capa AR, lo que apunta a un aumento relativo del 3.63%, que concuerda con la reducción de la reflectancia media ponderada proporcionada por dicha capa. La reducción de la reflectancia conduce a un aumento directo de la cantidad de luz transmitida a la célula, aumentando proporcionalmente su fotocorriente, J_{sc}, generada.

El factor de llenado (FF) y el voltaje en circuito abierto (V_{OC}) también aumentaron proporcionalmente, mostrando aumentos del 3.97% y el 3.12%, respectivamente. Sin embargo, el aumento del V_{OC} está dentro del error de medida, por lo que el aumento general de la eficiencia puede no deberse a la mejora del V_{OC}. En cambio, el aumento de la eficiencia del 0.16%, sí que puede atribuirse a los aumentos de J_{sc} y FF. En particular, se observa una mejora de la eficiencia de 1.78% al 1.94%, lo que representa un aumento relativo del 9.0%. Lo que valida el uso de Al-NPs en recubrimientos antirreflejantes para el incremento de eficiencia de células solares de película delgada.

4.- Conclusiones

En este trabajo, se ha demostrado la fabricación de un revestimiento monocapa antirreflejante mediante una técnica sencilla y de bajo coste. Su rendimiento ha sido satisfactorio cuando se ha aplicado a una célula solar de película delgada. El recubrimiento se basa en un metamaterial consistente en un fotopolímero con nanopartículas de aluminio de 110 nm de diámetro distribuidas aleatoriamente. Las Al-NPs son comercializadas en formato polvo, lo que significa que no es necesario ningún procedimiento de síntesis durante el proceso de fabricación.

La dispersión efectiva de las Al-NPs en el interior del metamaterial se consigue mediante un procedimiento termomecánico. A partir de la mezcla precursora, se depositó una capa de ~50 µm de espesor, el mínimo obtenible con nuestra configuración, utilizando la técnica de *doctor-blade*, que es fácil de implementar para la producción en masa.

El recubrimiento desarrollado reduce la reflectancia ~50% en todo el rango VIS,

aunque muestra un estrecho máximo local a 660 nm debido al *backscattering* Mie de Al-NPs aisladas en un medio como es el NOA61. Sin embargo, esta reducción no se refleja en un aumento de la transmitancia, que muestra un aumento relativo del ~5%, ya que la absorción parásita en las Al-NPs se mantiene. Con este incremento, la transmitancia de un portaobjetos de vidrio alcanza un valor superior al 96%.

Las capas AR desarrolladas han sido aplicadas en la superficie de un dispositivo fotovoltaico real, mostrando una reducción significativa de la reflectancia, incluso siendo la superficie del dispositivo ya texturizada debido a su propia morfología. El rendimiento fotovoltaico de la célula solar de capa delgada con la capa AR se midió bajo iluminación estándar con un espectro AM1.5G, mostrando una mejora de sus parámetros fotovoltaicos, lo que lleva a un incremento relativo de la eficiencia de un 9%.

Agradecimientos: Este trabajo ha sido parcialmente financiado por el proyecto GRISA (CM/JIN/2021–021) y el proyecto PTUAH24/016, financiado por la Universidad de Alcalá.

Referencias

[1] Martin A. GREEN, Ewan D. DUNLOP, Masahiro YOSHITA, Nikos KOPIDAKIS, Karsten BOTHE, Gerald SIEFER, Xiaojing HAO, "*Solar cell efficiency tables (version 62)*", Progress in Photovoltaics: Research and Applications 31, 651-663, 2023. https://doi.org/10.1002/pip.3726

[2] Mahmoud H. ELSHORBAGY, Kamal ABDEL-HADY, Hala KAMAL, Javier ALDA, "*Broadband anti-reflection coating using dielectric Si3N4 nanostructures. Application to amorphous-Si-H solar cells*", Optics Communications, 390, 130-136, 2017. https://doi.org/10.1016/j.optcom.2016.12.062

[3] Pablo A. SÁNCHEZ, Óscar ESTEBAN, Mahmoud H. ELSHORBAGY, Alexander CUADRADO, Javier ALDA, "*Effective index model as a reliable tool for the design of nanostructured thin-film solar cells*", Scientific Reports 13, 6227, 2023. https://doi.org/10.1038/s41598-023-33085-3

[4] Ji CHUNXUE, Liu WEN, Bao YIDI, Chen XIAOLING, Yang GUIQIANG, Wei BO, Yang FUHUA, Wang XIAODONG, "*Recent Applications of Antireflection Coatings in Solar Cells*", Photonics 9, 906, 2022. https://doi.org/10.3390/photonics9120906

[5] Adam M. LAW, Luksa KUJOVIC, Mustafa TOGAY, Rachael C. GREENHALGH, Luis C. INFANTE-ORTEGA, Xiaolei LIU, "*A Broadband Multilayer Antireflection Coating for Thin Film CdSeTe/CdTe Solar Cells*", IEEE Journal Photovoltaics 14, 305-309, 2024. https://doi.org/10.1109/JPHOTOV.2023.3341586

[6] Janghoon PARK, Keehyun SHIN, Changwoo LEE, "*Optimized design for anti-reflection coating process in roll-to-roll slot-die coating system*", Robotics and Computer-Integrated Manufacturing 30, 432-441, 2014, https://doi.org/10.1016/j.rcim.2014.02.001

[7] Abolfazl JANGJOY, Hamid BAHADOR, Hamid HEIDARZADEH, "*A Comparative Study of a Novel Anti-reflective Layer to Improve the Performance of a Thin-Film GaAs Solar Cell by Embedding Plasmonic Nanoparticles*", Plasmonics 16, 395-401, 2021. https://doi.org/10.1007/s11468-020-01297-2

[8] Rodrigo BLASCO, Sirona VALDUEZA-FELIP, Daniel MONTERO, Michael SUN, Javier OLEA, Fernando B. NARANJO, "*Low-to-Mid Al Content (x = 0–0.56) AlxIn1−xN Layers Deposited on Si(100) by Radio-Frequency Sputtering*", Physica Status Solidi (b) 257, 1900575, 2020. https://doi.org/10.1002/pssb.201900575

Comparación teórica de concentradores solares luminiscentes con distintas geometrías

Jagoba BARATA [1], Jon ARRUE [2], Joseba ZUBIA [2], M. Asunción ILLARRAMENDI [1]

1. Departamento de Física Aplicada, Escuela de Ingeniería de Bilbao, Universidad del País Vasco (UPV/EHU), Plaza Ingeniero Torres Quevedo 1, 48013, Bilbao, España.
2. Departamento de Ingeniería de Comunicaciones, Escuela de Ingeniería de Bilbao, Universidad del País Vasco (UPV/EHU), Plaza Ingeniero Torres Quevedo 1, 48013, Bilbao, España.

Contacto: Jagoba BARATA (jagoba.barata@ehu.eus).

ABSTRACT:

In this work, a theoretical study of luminescent solar concentrators based on two different geometries, namely elliptical cylinders and half cylinders, has been carried out by means of a Monte-Carlo ray-tracing technique. The dye Lumogen F Red 305, uniformly distributed in the cross-section of each geometry with the same number of molecules, has been employed. Through a comparative analysis of the average wavelength and of the typical figures of merit in the field of luminescent solar concentrators, such as the external photon efficiency and the concentration factor, this work clarifies how to improve the performance of these devices by optimising the geometry.

Key words: Luminescent solar concentrators, Solar energy, Monte Carlo, ray tracing, polymer optical fibre, Lumogen F Red 305

1.- Introducción

Los concentradores solares luminiscentes (CSLs) se empezaron a desarrollar en la década de los 70 con el objetivo de reducir el coste de la energía eléctrica generada por las células fotovoltaicas solares [1]. Estos dispositivos fotónicos consisten en materiales luminiscentes que absorben la luz solar y la reemiten a través del material huésped, típicamente una guía de ondas hecha con polímeros, tales como el poli (metil metacrilato) (PMMA). Parte de dicha luz se guía hasta los extremos, donde se colocan las células solares. Debido a que el área de los extremos es menor que el área iluminada, la superficie de las células empleadas se reduce y, por ende, se aminoran los costes. Asimismo, el material huésped suele ser económico, rebajando más el precio. Además, los CSLs no solo absorben la luz solar directa, sino también la difusa, por lo que no necesitan un sistema de seguimiento del sol. Esta ventaja hace a los CSLs adecuados en entornos donde el espacio es limitado, como los espacios urbanos [2-3].

Una de las geometrías utilizadas en los CSLs es la cilíndrica, que presenta una serie de ventajas frente a la ortoédrica, como poder obtener hasta 1.9 veces más concentración de la luz, según diversos trabajos teóricos, o la posibilidad de conectar los CSLs fácilmente a fibras ópticas transparentes, permitiendo colocar la célula solar en una ubicación más adecuada, entre otras [4].

Aprovechando el grado de libertad que ofrece cambiar la geometría, en este trabajo se compararán CSLs basados en geometrías semicilíndricas, tanto con su parte plana iluminada directamente como no, y geometrías cilíndricas elípticas con diferentes excentricidades, con la finalidad de esclarecer cuál es la óptima, ver Fig. 1. En el caso del cilindro elíptico, uno de sus semiejes estará horizontal cuando la luz solar incide verticalmente. Los resultados se obtendrán

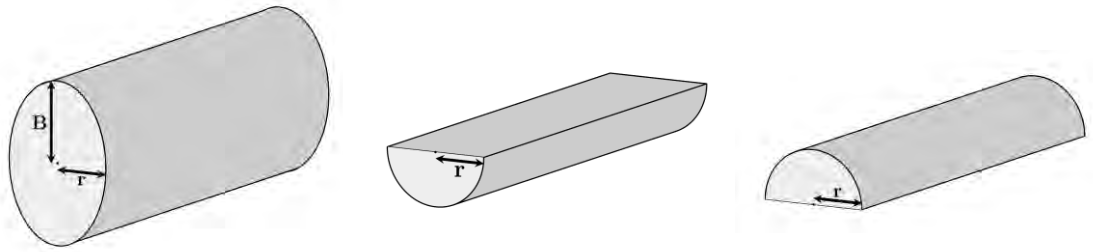

(a) (b) (c)

Fig. 1: Diferentes geometrías analizadas en este trabajo: (a) Geometría cilindro-elíptica; (b) semicilindro con la parte plana completamente iluminada y (c) semicilindro con la parte curva completamente iluminada.

teóricamente aplicando simulaciones de Monte-Carlo mediante la técnica de trazado de rayos que hemos utilizado previamente en otro trabajo [5]. Entre las geometrías analizadas en este estudio, tanto la geometría cilíndrica como la cilindro-elíptica achatada son aquellas geometrías que concentran más la luz solar cuando la longitud de los concentradores es suficientemente larga.

2.- Fundamentos teóricos

Con la finalidad de realizar una comparación adecuada, es conveniente que tanto el área iluminada como el número de moléculas luminiscentes sean iguales en todas las geometrías. Para cumplir el primer requisito, se necesita que el radio del semicilindro y el semieje horizontal sean iguales. El segundo requisito se satisface variando la concentración de las moléculas en las distintas geometrías. Para ello, se tomará como referencia la concentración *N* de la geometría del cilindro elíptico cuando su excentricidad es 0 (cilindro circular). Teniendo en cuenta esto, las concentraciones para las geometrías cilindro-elípticas y semicilíndricas son, respectivamente:

$$N_{cilindro-elíptico} = \frac{r}{B} N_{cilindro} \qquad (1)$$

$$N_{semicilindro} = 2N_{cilindro} \qquad (2)$$

siendo $N_{cilindro-elíptico}$ la concentración en las geometrías cilindro-elípticas, r el radio de la geometría cilíndrica, $N_{cilindro}$ la concentración empleada en el cilindro, B el semieje vertical, y $N_{semicilindro}$ la concentración en los semicilindros.

Por otra parte, el rendimiento de un CSL se cuantifica a través de la eficiencia fotónica externa, definida como el cociente entre el número de fotones por segundo que salen de los extremos del CSL y el número de fotones por segundo que llegan al CSL, esto es:

$$\eta_{ext} = \frac{\Phi_{out}}{\Phi_{\odot}} = \eta_{abs} \times \eta_{int} \qquad (3)$$

Además, η_{ext} se puede describir como el producto de la eficiencia de absorción y la eficiencia fotónica interna. Esta última puede interpretarse como la eficiencia de guiado del CSL y es independiente tanto de la anchura del espectro de absorción como de la fuente utilizada. Otro parámetro importante en el ámbito de los CSLs es el factor de concentración, definido como:

$$C = \eta_{ext} G \qquad (4)$$

donde G es la ganancia geométrica, es decir, el cociente entre el área iluminada y el área de los extremos. Un factor de concentración mayor que 1 implica que la irradiancia en la salida es mayor que la irradiancia solar incidente.

Todas las geometrías estarán dopadas uniformemente con el colorante Lumogen F Red 305 (LR) de la compañía BASF con una concentración de 500 ppm en la geometría cilíndrica. Las concentraciones para las demás geometrías se obtendrán mediante (1) y (2). Asimismo, se impondrá que, en caso de no haber dopante, el coeficiente de atenuación sea el conseguido para el PMMA en el visible, aproximadamente 0.02 m^{-1}. Con dopante, hay un incremento en dicho valor que se supondrá

que es proporcional a la concentración. En total, se tiene que el valor total, incluido el incremento por dopante para 500 ppm, es 4.6 m^{-1} para la geometría cilíndrica. Este valor se midió experimentalmente aplicando la técnica no destructiva de iluminación lateral fluorescente. La longitud iluminada en las distintas geometrías, que denominaremos z_e, variará entre 2.5 cm y 30 cm. Por otra parte, B variará entre 0.15 mm y 2 mm en las geometrías cilindro-elípticas. Igualmente, tanto semieje horizontal como el radio de los semicilindros tendrán un valor de 0.5 mm. Estos parámetros se utilizarán en las simulaciones de trazado de rayos de Monte Carlo. En total, se lanzarán 105000 fotones por cada centímetro de longitud en cada CSL dentro de un rango espectral comprendido entre 360 nm y 850 nm, intervalo en el cual se encuentran tanto el espectro de absorción como el de emisión del colorante LR.

3.- Resultados y discusión

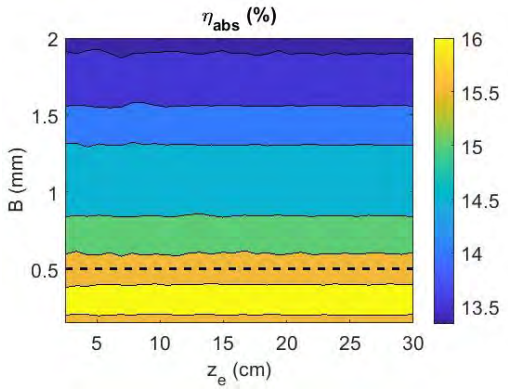

Fig. 2: η_{abs} en función de z_e y del semieje B para las geometrías cilindro elípticas. La línea discontinua corresponde al caso del cilindro.

En la Fig. 2 se muestra la eficiencia de absorción en función tanto de z_e como del semieje B. Se puede observar como η_{abs} permanece constante para distintas z_e si B lo es. Por otra parte, en el caso de mantener z_e constante, se contempla como, a medida que B disminuye, la eficiencia de absorción aumenta hasta que $B \approx 0.3$ mm. Cabe señalar que la mayor eficiencia no se obtiene cuando $B = 0.5$ mm, es decir, en el caso de un cilindro.

En la Fig. 3 se muestra la eficiencia de absorción en función de la longitud iluminada para los semicilindros. Al igual que en la Fig. 2, ésta permanece constante para distintas longitudes iluminadas. Como era de esperar, la geometría que proporciona una mayor eficiencia de absorción es aquella en la que la parte plana permanece iluminada por el sol. Esto es debido a las menores pérdidas por reflexión de luz solar en esta geometría respecto aquellas que tienen la parte curva iluminada.

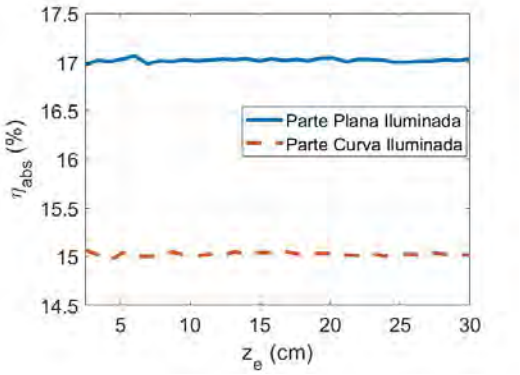

Fig. 3: η_{abs} en función de z_e para las geometrías semicilíndricas.

En la Fig. 4 se muestra η_{int} en función de la longitud iluminada y del semieje B para las geometrías cilindro-elípticas. En general, este parámetro decrece a medida que la longitud iluminada crece. La atenuación del material huésped y las perdidas por el cono de escape son las principales causas de este comportamiento. Este último efecto se debe a fotones emitidos en ángulos con la normal a la superficie menores que el ángulo crítico, provocando que la luz emitida salga del CSL.

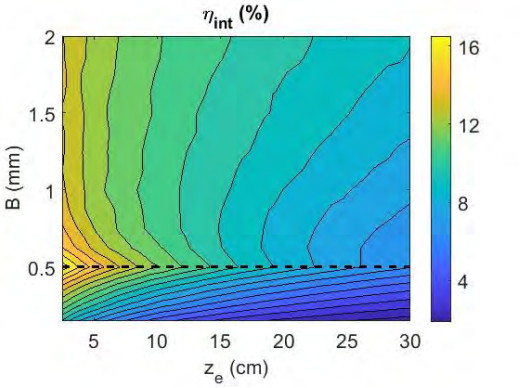

Fig. 4: η_{int} en función de z_e y del semieje B para las geometrías cilindro-elípticas. La línea discontinua corresponde al caso del cilindro.

Asimismo, el comportamiento de η_{int} al disminuir el semieje vertical es creciente con z_e pequeñas hasta llegar a un valor máximo en $B = 0.5$ mm (cilindro circular). A partir de este valor, η_{int} decrece progresivamente. Estas tendencias se deben a que las pérdidas del cono de escape, que son las predominantes en el guiado en este caso, disminuyen mientras η_{int} crece. En el máximo de η_{int} las perdidas por cono de escape son mínimas, y son máximas en el mínimo, como se puede apreciar en la Fig. 5 para pequeñas z_e. No obstante, a medida que se alargan las geometrías, el efecto de la atenuación del material huésped cobra suma importancia, provocando que aquellas geometrías con poca atenuación posean una η_{int} mayor, es decir, aquellas con B grandes.

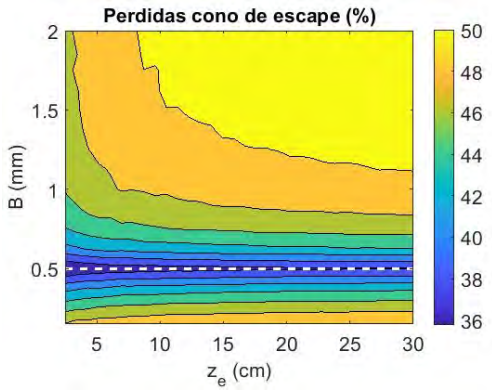

Fig. 5: Pérdidas por cono de escape en función de z_e y el semieje B para las geometrías cilindro-elípticas. La línea discontinua corresponde al caso del cilindro.

En la Fig. 6 se muestra η_{int} en función de z_e de las dos geometrías semicilíndricas. Como era de esperar, ambas geometrías poseen los mismos valores de η_{int}, puesto que, como ya se especificó con anterioridad, η_{int} trata la eficiencia de propagación, y, como ambas geometrías son simétricas, η_{int} debe ser el mismo. Igualmente a lo que ocurría en la Fig. 4, η_{int} decrece con z_e. En cuanto a los valores numéricos, éstos son menores que los de las geometrías cilindro-elípticas de la Fig. 4, es decir, las eficiencias de propagación de los semicilindros son menores que las de las geometrías cilindro-elípticas.

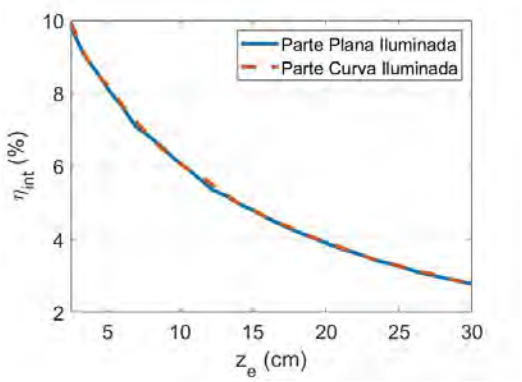

Fig. 6: η_{int} en función de z_e para las geometrías semicilíndricas.

En la Fig. 7 se muestra η_{ext} en función de z_e y del semieje B para la geometría cilindro-elíptica. Como se puede observar, el comportamiento con z_e es el mismo que el de η_{int}, puesto que la eficiencia de absorción era constante con z_e. Es interesante observar que, a pesar de que algunas geometrías tengan una η_{abs} mayor, η_{int} acaba siendo la que determina qué geometría posee una η_{ext} mayor, a saber, la geometría cilíndrica para longitudes cortas donde el efecto de la atenuación es despreciable y son las perdidas por cono de escape las predominantes, y aquellas geometrías cilindro-elípticas con B grandes para longitudes largas, donde el efecto de la atenuación predomina.

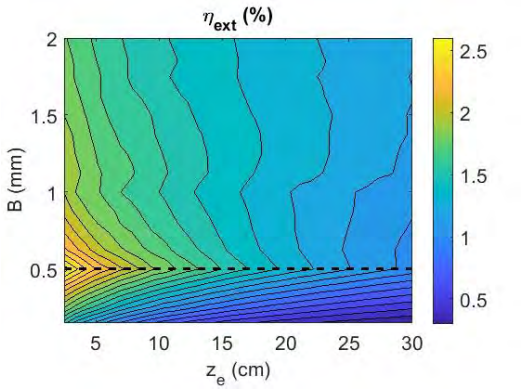

Fig. 7: η_{ext} en función de z_e y del semieje B para las geometrías cilindro-elípticas. La línea discontinua corresponde al caso del cilindro.

En la Fig. 8 se muestra el comportamiento de η_{ext} para los casos de los semicilindros. Se puede observar cómo el mayor η_{ext} se da para aquella geometría con la parte plana iluminada. Este resultado era esperable, debido a que η_{int} era la misma para ambas

geometrías. Similarmente, la geometría con la parte plana iluminada tenía una mayor eficiencia de absorción, por consiguiente, η_{ext} resulta ser mayor.

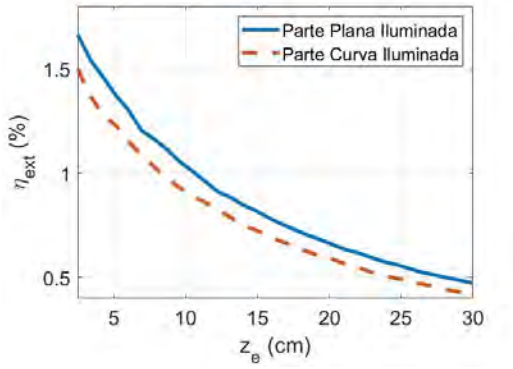

Fig. 8: η_{ext} en función de z_e para las geometrías semicilíndricas.

Si se comparan las η_{ext} entre las geometrías cilindro-elípticas y las semicilíndricas, se observa que los valores para los semicilindros son menores, siendo la de menor valor aquella con la parte plana sin iluminar directamente. Como resultado de este primer análisis, la geometría con un mayor valor de η_{ext} entre todas las analizadas es la correspondiente al cilindro para longitudes cortas, y para las largas los mejores son los cilindros elípticos con semieje B grande.

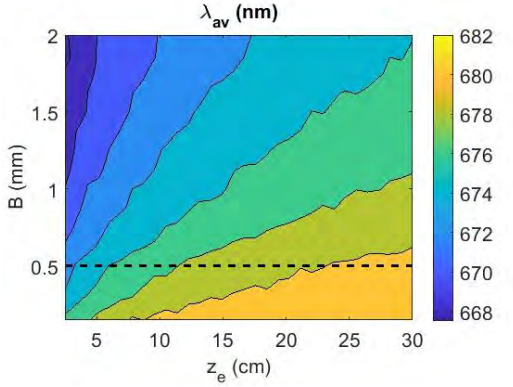

Fig. 9: λ_{av} en función de z_e y del semieje B para las geometrías cilindro-elípticas. La línea discontinua corresponde al caso del cilindro.

Una de las características más importantes de los CSLs es dónde está centrado su espectro de salida, con el fin de que este espectro coincida adecuadamente con la responsividad de las células solares. En la Fig. 9 se muestra la longitud de onda media del espectro de salida, denominada λ_{av}, para las geometrías cilindro-elípticas. En general, λ_{av} se enrojece a medida que se alargan las distintas geometrías. Este fenómeno guarda relación con el incremento de las reabsorciones: véase como aumentaban las pérdidas por cono de escape al aumentar z_e (ver Fig. 5). Asimismo, existe un corrimiento hacia el rojo a medida que B se vuelve más pequeño, siendo este valor ≈7 nm para todas las z_e en comparación con geometrías con $B = 2$ mm. En cuanto a los semicilindros, λ_{av} muestra el mismo comportamiento con z_e. Además, el valor numérico de λ_{av} es aproximadamente la misma que con las geometrías cilindro-elípticas con un semieje $B \approx 0.3$ mm.

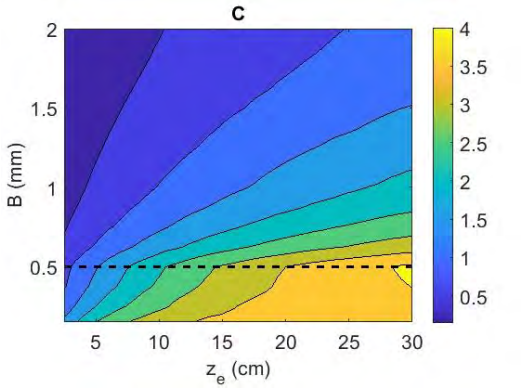

Fig. 10: C en función de z_e y del semieje B para las geometrías cilindro-elípticas. La línea discontinua corresponde al caso del cilindro.

En la Fig. 10 se muestra el comportamiento de C en función tanto de z_e como del semieje B. En esta ocasión, a pesar de que η_{ext} disminuía con z_e (ver Fig. 7), C aumenta con z_e de forma saturada. El motivo radica en que la ganancia geométrica compensa notablemente la disminución en η_{ext}. El efecto de la saturación se debe a la atenuación del material huesped. Otra fenómeno interesante en estas geometrías es el análisis en función del semieje B manteniendo z_e constante. Se observa cómo C aumenta a medida que dicho semieje va disminuyendo, en z_e cortas, siendo el aumento significativamente mayor a partir de $B \approx 1$ mm. Cabe destacar que, a pesar de que el máximo en η_{ext} para z_e largas ocurra en B grandes, C toma un máximo en geometrías cilíndricas y cilindro-elípticas un poco achatadas.

Por otra parte, en la Fig. 11 se representa C en función de z_e para los semicilindros. Al igual que en el caso anterior, C crece de forma

saturada con z_e debido a la atenuación del material huésped. Como era de esperar, la geometría en la que la parte plana está iluminada presenta una mayor C, ya que, la eficiencia de absorción es mayor.

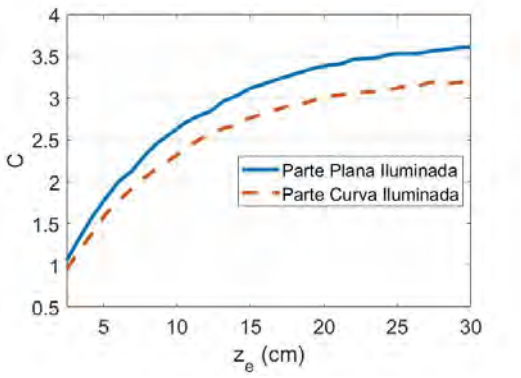

Fig. 11: C en función de z_e para las geometrías semicilíndricas.

Si se compara C para las geometrías analizadas en este trabajo, se obtiene que los semicilindros poseen una C más grande que los cilindros elípticos, exceptuando aquellas geometrías con B más pequeñas que 0.25 mm en distancias cortas, y aquellas con B más pequeñas que 0.5 mm en distancias largas.

4.- Conclusiones

En este trabajo se han analizado teóricamente concentradores solares luminiscentes de diferentes geometrías dopados con el colorante Lumogen F Red 305, empleando simulaciones de Monte Carlo con la técnica de trazado de rayos. La comparación entre las distintas geometrías se ha realizado evaluando la eficiencia fotónica externa, la eficiencia de absorción, la eficiencia fotónica interna, la longitud de onda media y el factor de concentración.

Se ha obtenido que la geometría con mejor eficiencia fotónica interna es la geometría cilíndrica en longitudes iluminadas cortas y las cilindro-elípticas con gran semieje vertical en longitudes largas, mientras que aquella geometría con una mayor eficiencia de absorción es la semicilíndrica con la parte plana iluminada directamente. Se ha visto cómo las longitudes de onda medias se corren hacía el rojo tanto con la elongación como con el achatamiento de las geometrías cilindro-elípticas, pero son parecidas a las obtenidas en los semicilindros. Por otra parte, las geometrías con mejor eficiencia fotónica externa corresponden a aquellas con mejor eficiencia fotónica interna. No obstante, las geometrías semicilíndricas, concretamente aquella con la parte plana iluminada, son las que obtienen el factor de concentración más grande en longitudes cortas de iluminación, junto al cilindro elíptico más achatado. Para largas longitudes de iluminación, la mejor geometría es la cilíndrica o la cilíndrico-elíptica algo achatada. Además, presentan un mayor desplazamiento del espectro de emisión hacia el rojo, favoreciendo el solapamiento con la responsividad de las células PV.

Agradecimientos: Este trabajo ha sido financiado con las ayudas I+D+i/PID2021-122505OBC31, PID2024-155582OB-C31 and TED2021-129959B-C21, financiados por MCIN/AEI/10.13039/501100011033, "ERDF A way of making Europe", y "European Union Next Generation EU/PRTR". Igualmente, este trabajo ha sido apoyado por la ayuda No. IT11452-22 y financiado por el Gobierno Vasco, por ELKARTEK 2023 (µ4Smart-KK-2023/00016 y Ekohegaz II-KK-2023/00051), por ELKARTEK 2025 (Smart- SmartµS and Newhegaz) y por la UPV/EHU Translight.

Referencias

[1] W.H. WEBER, John LAMBE, *"Luminescent greenhouse collector for solar radiation"*, Appl. Opt., 15, 10, 2299-2300, 1976.

[2] Ioannis PAPAKONSTANTINOU *et al.*, *"The Hidden Potential of Luminescent Solar Concentrators"*, Adv. Energy Mater., 11, 3, 2002883, 2021.

[3] Jean RONCALI, *"Luminescent Solar Collectors : Quo Vadis?"*, Adv. Energy. Mater., 10, 36, 2001907, 2020.

[4] K.R. MCINTOSH *et al.*, *"Theoretical comparison of cylindrical and square-planar luminescent solar concentrators"*, 88, 2, 285-290, 2007.

[5] Jon ARRUE *et al.*, *"Design of more efficient luminescent solar concentrators by using peripherally dye-doped stacked optical fibers"*, Opt. Express, 31, 15, 23990-24004, 2023.

Impacto del espesor de la capa de nitruro en la eficiencia fotovoltaica de heterouniones AlInN/a-Si/Si(100)

Sirona VALDUEZA-FELIP [(1)], Michael SUN [(1)], Miriam CADENAS [(1)], Sofía FIGUEROA [(1)], Fernando B. NARANJO [(1)]

1. Grupo de Ingeniería Fotónica, Universidad de Alcalá, Escuela Politécnica Superior, 28805 Alcalá de Henares.
Unidad Asociada Instituto de Óptica-CSIC, Tecnologías Fotónicas y de Sensores

Contacto: Sirona VALDUEZA-FELIP (sirona.valduezafelip@uah.es).

ABSTRACT:

Here, we present the optimization of the III-nitride layer thickness of solar cells based on *n*-AlInN on *p*-Si(100) heterojunctions with an amorphous Si (a-Si) buffer layer of 15 nm. Particularly, we study the influence of different AlInN thickness, ranging from 80 to 330 nm, on the structural and optical properties of the material, and also their device quality operating as solar cell. The AlInN and a-Si layers were deposited by RF and DC sputtering, respectively. Samples were then processed into ~1-cm^2 devices and electrically characterized in the dark and under one-sun standard AM1.5G illumination. The optimum thickness was found to be 130 nm, achieving maximum photovoltaic parameters (V_{OC} = 0.35 V, J_{SC} = 18.5 mA/cm^2, FF = 37.1%) thanks to the improved dark electrical diode characteristics (reduced R_S and J_0, and enhanced R_{SH}). This leads to a conversion efficiency of 2.4%, value that could be doubled by optimizing the upper electrical contact.

Key words: III-nitride semiconductors, radio-frequency sputtering, AlInN, silicon, solar cells, PN heterojunction, amorphous silicon buffer layer

1.- Introducción

La búsqueda de células solares eficientes, económicas y duraderas ha impulsado la investigación y el desarrollo de distintos materiales semiconductores y sus posibles combinaciones. Entre ellos, el nitruro de aluminio e indio (AlInN) es un candidato prometedor debido a sus ventajosas propiedades electrónicas y ópticas, como su alto coeficiente de absorción [1]. La integración del AlInN con sustratos de silicio (Si) se beneficia de la banda prohibida directa del AlInN, al mismo tiempo que utiliza la tecnología del silicio, bien establecida y rentable, y abundante en la Tierra.

La energía de banda prohibida del ternario AlInN es sintonizable desde el infrarrojo (0.7 eV para el InN) hasta el ultravioleta (6.2 eV para el AlN), dependiendo del contenido de Al. Dicha variabilidad es una ventaja para optimizar la eficiencia de la célula solar basada en Si, ya que ajustando la composición de Al, es posible alinear la banda prohibida del AlInN con el espectro óptimo de absorción de la radiación solar, mejorando así la eficiencia de conversión fotovoltaica del dispositivo. Además, los materiales nitruros poseen una excelente estabilidad térmica y química, haciéndolos resistentes a entornos hostiles, como el espacio estelar [1].

El AlInN ha sido sintetizado utilizando diversas técnicas de fabricación, como la deposición química metal-orgánica en fase vapor (MOCVD) [2], la epitaxia de haces

moleculares (MBE) [3] y la pulverización catódica (*sputtering*) reactiva. El *sputtering* reactivo puede dividirse en dos tipos: el que utiliza la combinación de gases de argón y nitrógeno para la deposición del material [4-6], y el que utiliza sólo nitrógeno [7-9]. En nuestro grupo de investigación, empleamos este último método ya que mejora la calidad cristalina de las capas depositadas, a costa de reducir su velocidad de depósito.

El contenido de Al en la capa de AlInN, que afecta a la energía de la banda prohibida del material, a la estructura cristalina y a las características eléctricas generales, influye decisivamente en el rendimiento de estas células solares de heterounión. De facto, nuestro grupo de investigación ha demostrado recientemente que el contenido de Al óptimo para células solares de AlInN sobre Si(100) se encuentra entorno al 20-35% [10].

Por otro lado, las propiedades y la calidad de la interfaz entre la capa de AlInN y el sustrato son cruciales para el buen funcionamiento de dispositivos electrónicos verticales. Sin embargo, el desajuste inherente del parámetro de red cristalina entre el (Al)InN y el Si (-35% para el InN y -43% para el AlN) presenta retos importantes, como la elevada densidad de defectos que se puede crear en la capa de nitruro, y en la intercara, debido a la tensión residual generada. La incorporación de una capa amortiguadora (*buffer*) de silicio amorfo (a-Si) entre el nitruro y el Si desempeña un papel fundamental para mitigar dicho desajuste de red y minimizar los defectos generados en la interfaz, y reducir por tanto las pérdidas por recombinación del dispositivo. Recientemente, nuestro grupo de investigación ha demostrado el efecto positivo y la importancia de introducir una capa *buffer* de a-Si con efecto pasivante en células solares de nanocolumnas de InN sobre Si(100), siendo el espesor óptimo de dicha capa *buffer* de 15 nm [11].

Otro parámetro importante en el diseño de una célula solar es el espesor de la capa ventana, siendo en nuestro caso la capa de AlInN. Tal y como presenta Blasco *et. al.*, las mejores prestaciones se obtienen en capas finas de alta calidad en las que se produzca una reducida absorción de la luz en el material [12], pudiendo alcanzar así más favorablemente la intercara de la unión, donde se encuentra la región de carga espacial y el campo eléctrico presente separe las cargas que puedan alcanzar los contactos. Sin embargo, también hay que tener en cuenta el espesor mínimo crítico de la capa, a partir del cual se obtienen capas con la calidad y propiedades adecuadas para obtener dispositivos que funcionen correctamente. Es por ello que para encontrar ese punto intermedio, en este trabajo se estudia la influencia del espesor de la capa de nitruro en la heterounión AlInN/a-Si/Si(100), con el objetivo de mejorar el rendimiento fotovoltaico de dichos dispositivos.

2.- Medidas experimentales

Las estructuras se fabricaron mediante pulverización catódica reactiva por RF, sobre substratos de Si(100) dopado tipo p de 375 µm de espesor (resistividad ~1-10 Ω·cm). Los detalles del sistema de depósito se pueden encontrar en [11]. Primeramente, se depositó una capa *buffer* de Si de 15 nm de espesor a 550 ºC y 30 W (DC) 13]. Dichas condiciones dan lugar a capas de Si amorfas y compactas. Después, se depositaron las capas de AlInN en atmósfera de N_2 puro con un flujo de 14 sccm y una presión de 0.47 Pa. La temperatura de substrato se fijó a 550 ºC y la potencia de RF aplicadas a los blancos de In/Al fueron de 30/125 W. Las capas de AlInN crecidas bajo estas condiciones muestran un alto dopaje tipo n ($n\sim10^{20}$-10^{21} cm^{-3}) [14]. El tiempo de depósito se varió para dar lugar a diferentes espesores nominales de AlInN (80, 130, 230 y 330 nm), correspondientes a las muestras E80, E130, E230 y E330 de este estudio.

La orientación cristalina y la mosaicidad de las capas se evaluó mediante difracción de rayos X de alta resolución (HRXRD). Se realizaron medidas de transmisión óptica en muestras crecidas simultáneamente sobre zafiro para evaluar su energía de *gap*.

A continuación, se procesaron dispositivos con un área activa de ~0.7 cm^2, utilizando máscaras sólidas para los contactos delantero y trasero, formados por ~120 nm de Al depositado por *sputtering* DC a temperatura

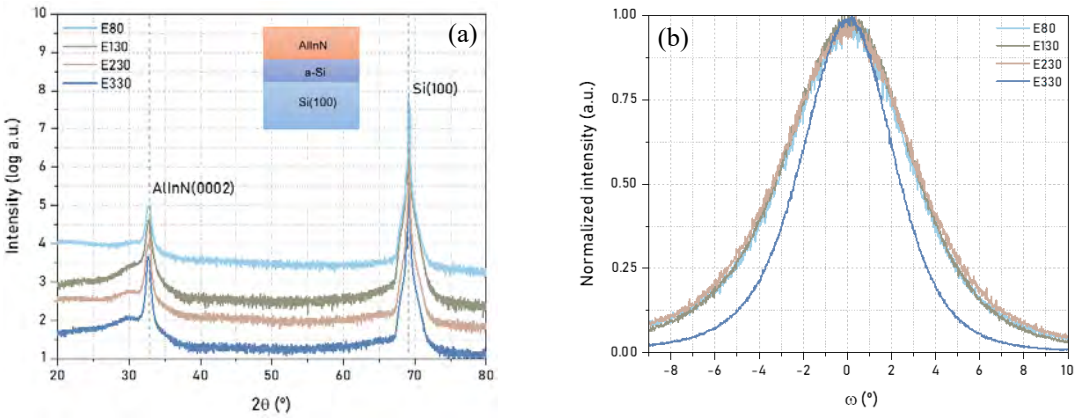

Fig. 1: (a) Espectros HRXRD de las muestras con diferente espesor de AlInN. Inset: Esquema de la estructura estudiada. (b) Curvas rocking de las muestras con diferente espesor de AlInN.

ambiente a 100 W y 75 W, respectivamente. Bajo estas condiciones, las resistividades de los contacto superior e inferior, medidas mediante el método de línea de transmisión, son 3.5 $\Omega \cdot cm^2$ y 2.6 $\Omega \cdot cm^2$, respectivamente. Los dispositivos se caracterizaron mediante curvas de corriente-voltaje utilizando una estación de dos puntas acoplada a una unidad de fuente-medida en condiciones de oscuridad y bajo un sol (1 kW/m^2) de iluminación AM1.5G.

3.- Resultados y discusión

3.1.- Caracterización estructural

Para estudiar la calidad estructural de las capas de AlInN/a-Si se realizaron medidas de difracción de rayos X de alta resolución (HRXRD) en muestras crecidas sobre Si(100). El resultado de los difractogramas $2\theta/\omega$ se muestra en las Figura 1(a). Las medidas muestran una estructura wurtzita orientada a lo largo del eje *c* para todas las muestras, arrojando un contenido de Al de 0.32 ±0.01 independientemente del espesor de la capa. Por otro lado, la anchura a media altura (FWHM) de la *rocking curve* de (0002) del AlInN, mostrado en la Figura 1(b), es similar para las muestras con menor espesor (80-230 nm), entorno a (6.7±0.2)º reduciéndose a 5.0º para la muestra con mayor espesor (330 nm), lo que indica que la mosaicidad del AlInN se reduce para espesores mayores o iguales a 330 nm.

3.2.- Caracterización óptica

Las propiedades ópticas de las capas se estudiaron mediante medidas de transmitancia a temperatura ambiente realizadas en las capas depositadas simultáneamente sobre zafiro. En la Figura 2(a) se muestran los espectros de transmitancia de todas las muestras estudiadas. La absorción de las capas puede deducirse de los espectros de transmitancia siguiendo la relación $\alpha(E) \propto -ln(T)$, sin considerar las pérdidas ópticas por dispersión y reflexión. A partir del ajuste lineal del coeficiente de absorción al cuadrado α^2 frente a la energía, podemos deducir la energía de *gap* aparente de las muestras de ~2.2 eV (563 nm) para un espesor de 80 nm, y de ~2.1 eV (590 nm) para espesores mayores, lo que concuerda con la alta concentración de portadores residuales esperada para ese contenido de Al [10] y el efecto Burstein-Moss [15].

3.3.- Caracterización eléctrica de dispositivos de InN sobre Si(100) con capa *buffer*

La Figura 3 muestra las medidas de densidad de corriente-voltaje (J-V) de los dispositivos AlInN/a-Si/Si(100) en función del espesor de la capa de AlInN (a) en oscuridad y (b) bajo un sol de iluminación AM1.5G. En la parte interior de la Figura 3(a) se muestra una fotografía superior de una célula solar de nitruro real, donde se muestra el contacto superior con tres dedos metálicos.

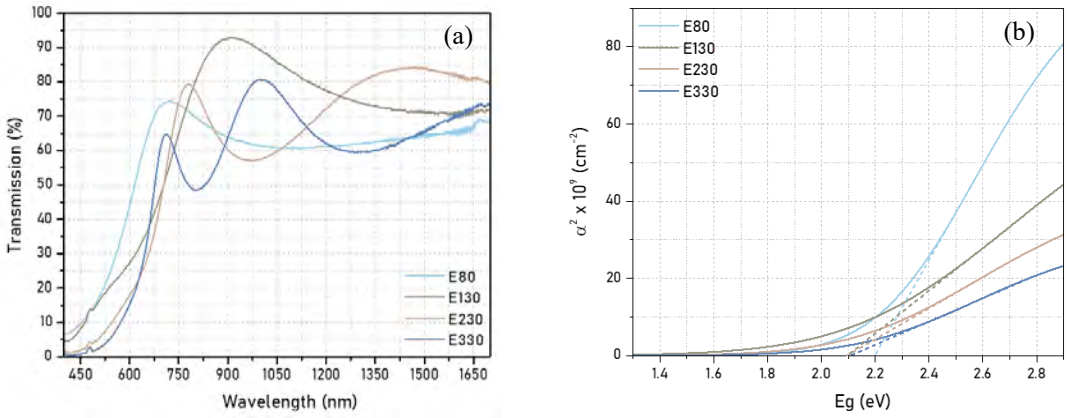

Fig. 2: (a) Espectro de transmisión de las muestras con diferente espesor de AlInN. (b) Coeficiente de absorción al cuadrado α^2 frente a la energía, extraído de la aproximación sigmoidal de las muestras depositadas sobre zafiro. Nota: la energía de la banda prohibida se ha estimado utilizando el espesor nominal de las capas.

Las curvas J-V en oscuridad se analizaron utilizando el modelo de un diodo para extraer las resistencias serie y paralela (R_S, R_{SH}), la densidad de corriente inversa de saturación (J_0) y el factor de idealidad (η); mientras que las curvas J-V iluminadas permitieron evaluar las características fotovoltaicas de los dispositivos en términos de voltaje de circuito abierto (V_{OC}), densidad de corriente de cortocircuito (J_{SC}), factor de forma (FF) y eficiencia (ver Tabla 1).

La resistencia serie en una célula solar tiene dos causas principales: el movimiento de la corriente de portadores a través del dispositivo y las resistencias de los contactos superior e inferior, los cuales en nuestro caso son iguales en todas las muestras estudiadas. Por otro lado, la resistencia paralela es un indicador de la calidad de la intercara de la heterounión, siendo mejor cuanto más alta sea. Una resistencia paralelo baja suele causar pérdidas de potencia en el dispositivo al proporcionar una vía de corriente alternativa para la corriente fotogenerada, reduciendo la densidad de corriente que fluye a través de la unión y también el voltaje en circuito abierto de la célula solar.

En nuestro caso, se observa como la resistencia serie aumenta ligeramente y la resistencia paralela disminuye en mayor medida al aumentar el espesor de la capa de AlInN de 130 nm a 330 nm. Esta tendencia de empeoramiento con el espesor también se observa en la corriente inversa de saturación, y en menor medida en el factor de idealidad, y puede ser debido al aumento de la resistencia de la capa con el espesor de la misma. Además, dispositivos con capas de AlInN más finas (80 nm) muestran un empeoramiento en todos sus parámetros en oscuridad, debido quizás a que la calidad de la capa no sea todavía lo suficiente buena como para generar una buena unión con el silicio.

El análisis de las curvas J-V en iluminación revela un máximo de la V_{OC} de 0.35 V, de la J_{SC} de 18.5 mA/cm^2, el FF de 37.1% para la muestra con 130 nm de AlInN, arrojando una máxima eficiencia de la serie de 2.4%. Estas mejoras en los parámetros del dispositivo E130 se debe a las características en oscuridad anteriormente mencionadas. Dada nuestra experiencia previa, dicho valor de eficiencia podría ser duplicado con la optimización del contacto superior de Al, depositándolo en RF en vez de en DC [10].

Tabla 1: Resumen de las propiedades eléctricas de los dispositivos AlInN/a-Si/Si(100).

Muestra	R_S ($\Omega \cdot cm^2$)	R_{SH} ($k\Omega \cdot cm^2$)	J_0 ($\mu A/cm^2$)	η	V_{OC} (V)	J_{SC} (mA/cm^2)	FF (%)	Eff. (%)
E80	*7.3*	*1.2*	*5.5*	*1.8*	*0.30*	*18.5*	*33.0*	*1.8*
E130	*6.6*	*58.0*	*0.2*	*1.4*	*0.35*	*18.5*	*37.1*	*2.4*
E230	*6.8*	*15.3*	*0.9*	*1.4*	*0.30*	*19.0*	*34.7*	*2.0*
E330	*7.9*	*0.88*	*9.1*	*1.9*	*0.30*	*15.7*	*29.8*	*1.4*

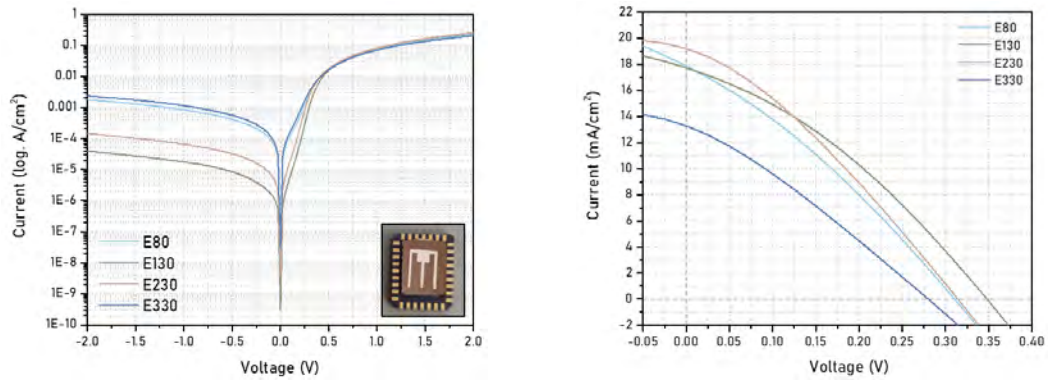

Fig. 3. (a) Curvas absolutas de densidad de corriente-tensión de los dispositivos con diferente espesor de AlInN en oscuridad. Inset: fotografía de una célula solar de nitruro III real. (b) Curvas de densidad de corriente-voltaje de los dispositivos con diferente espesor de AlInN bajo iluminación de 1 sol AM1.5G.

4.- Conclusiones

En este trabajo presentamos la influencia del espesor de la capa de nitruro en células solares de heterounión AlInN/a-Si/Si(100), para espesores nominales de 80, 130, 230 y 330 nm. Las medidas de difracción de rayos X nos indican que el contenido de Al de la aleación es prácticamente insensible con el espesor, resultando en torno a un 32% para todas las muestras bajo estudio. Así mismo, la energía de banda prohibida se mantiene en 2.1-2.2 eV, en concordancia con la alta concentración de portadores presente en dichas muestras en el orden de 10^{20} cm^{-3}. Las medidas eléctricas realizadas en los dispositivos procesados arrojan que el espesor óptimo de capa de AlInN es de 130 nm, alcanzando los mayores parámetros fotovoltaicos (V_{OC} = 0.35 V, J_{SC} = 18.5 mA/cm^2, FF = 37.1%) gracias a la mejora de las características eléctricas en oscuridad del dispositivo (reducción de R_S y J_0, y mejora de R_{SH}). Esto conduce a una eficiencia de conversión del 2.4%, valor que podría llegar a duplicarse con la optimización del contacto eléctrico superior.

Agradecimientos: Este trabajo ha sido financiado por el proyecto RELY (MICIU/ AEI/ 10.13039/ 501100011033 Next Generation EU/ PRTR) con ref. PDC2023-145888-I00, y el proyecto GRAFENIT de la Universidad de Alcalá (PIUAH24/IA-053).

Referencias

[1] J. D. Cañón-Bermúdez, L. F. Mulcué-Nieto, *"Indium aluminum nitride: A review on growth, properties, and applications in photovoltaic solar cells"*, Heliyon, 10, 2024.

[2] D. V. Dinh, N. Hu, Y. Honda, H. Amano, M. Pristovsek, *"Indium incorporation and optical properties of polar, semipolar and nonpolar InAlN"*, Semicond. Sci. Technol., 35, 035004, 2019.

[3] A. G. Bhuiyan, S. Islam, A. Hashimoto, *"Molecular beam epitaxy of InAlN alloys in the whole compositional range"*, AIP Advances, 10, 015053, 2020.

[4] W. Song, T. Li, L. Zhang, W. Zhu, L. Wang, *"Influence of growth parameters on microstructures and electrical properties of InxAl1-xN thin films using sputtering"*, Journal of Alloys and Compounds, 885, 160977, 2021.

[5] W. Lv, L. Shen, J. Liu, J. Chen, L. Wi, D. Qi, G. Zhang, X. Li, *"Mechanical properties of single-phase AlInN films across the compositional range (0 < x < 0.7) grown by radio-frequency magnetron sputtering"*, Applied Surface Science, 504, 144335, 2019.

[6] J. Chen, D. Qi, X. Li, J. Song, L. Shen, *"Optical and electrical properties of Al1-xInxN films with wide middle-composition range by RF sputtering"*, Applied Physics A 128, 142, 2022.

[7] S. Valdueza-Felip, A. Núñez-Cascajero, R. Blasco, D. Montero, L. Grenet, M. de la Mata, S. Fernández, L. R.-D. Marcos, S. I. Molina, J. Olea, *"Influence of the AlN interlayer thickness on the photovoltaic*

properties of in-rich AlInN on Si heterojunctions deposited by RF sputtering", AIP Advamnces 8, 115315, 2018.

[8] R. Blasco, S. Valdueza-Felip, D. Montero, M. Sun, J. Olea, F. B. Naranjo, *"Low-to-Mid Al content (x = 0–0.56) AlxIn1-xN layers deposited on Si(100) by radio-frequency sputtering*", Phys. Status Solidi, 257, 1900575, 2020.

[9] M. Sun, R. Blasco, J. Nwodo, M. de la Mata, S. I. Molina, A. Ajay, E. Monroy, S. Valdueza-Felip and F. B. Naranjo, *"Comparison of the material quality of AlxIn1-xN (x-0-0.50) films deposited on Si(100) and Si(111) at low temperature by reactive RF sputtering",* Materials, 15, 7373, 2020.

[10] M. Sun, R. G. Cornejo, M. de la Mata, S. I. Molina, B. Damilano, S. Valdueza-Felip, F. B. Naranjo, *"Enhancing solar cell efficiency of $Al_xIn_{1-x}N$/Si heterojunctions using an a-Si buffer: a study of material, interface and device properties"*, Submitted to Surfaces and Interfaces, 2025

[11] M. Sun, R. Gómez, B. Damilano, J. M. Asensi, F. B. Naranjo, S. Valdueza-Felip, *"InN nanowire solar cells on Si with amorphous Si interlayer deposited by sputtering"*, Materials Science in Semiconductor Proc., 176, 108321, 2024.

[12] R. Blasco, F. B. Naranjo, S. Valdueza-Felip, *"Design of AlInN on silicon heterojunctions grown by sputtering for solar devices"*, Current Applied Physics, 20, 1244, 2020.

[13] M. Sun, S. Valdueza-Felip, F. B. Naranjo, *"Amorphous silicon films and nanocolumns deposited on sapphire and GaN by DC sputtering"*, Phys. Status Solidi B, 2200578, 2023.

[14] S. Valdueza-Felip, R. Blasco, J. Olea, A. Díaz-Lobo, A. F. Braña, F. B. Naranjo, *"AlxIn1-xN on Si(100) solar cells (x = 0-0.56) deposited by RF sputtering"*, Materials, 13, 2336, 2020.

[15] H. He, Y. Cao, R. Fu, W. Guo, Z. Huang, M. Wang, C. Huang, J. Huang, H. Wang, *Band gap energy and bowing parameter of In-rich InAlN films grown by magnetron sputtering"*, Applied Surface Science, 256, 1812, 2010.

Medida de flujo solar concentrado en simulador solar basado en fibra óptica y fotodiodo

Manuel JEREZ [(1)], Alejandro CARBALLAR [(1)], Ricardo CONCEIÇÃO [(2)], José GONZÁLEZ-AGUILAR [(2)], Xabier RÁNDEZ [(3)], Olaia ITOIZ [(3)]

1. Departamento de Ingeniería Electrónica – E.T.S. de Ingeniería – Universidad de Sevilla; C/ Camino de los Descubrimientos, s/n, 41092 Sevilla, España.
2. Unidad de Procesos de Alta Temperatura, IMDEA Energía, Av. Ramón de La Sagra, 3, 28935 Móstoles, Madrid, España
3. Departamento de Energía Solar Térmica y Almacenamiento Térmico, CENER, C/ Ciudad de la Innovación nº7, 31651 Sarriguren, Navarra, España.

Contact: Manuel JEREZ (mjerez@us.es).

ABSTRACT:

Extreme operating conditions encountered in solar receivers of Concentrated Solar Thermal (CST) power plants, such as elevated temperatures, high solar fluxes, and thermal cycling, present substantial challenges for conventional sensors. Optical fibers present a viable alternative for solar flux measurement in these harsh environments; however, their long-term performance and degradation mechanisms necessitate comprehensive investigation and characterization. This study presents two tests performed using high-flux solar simulators to explore the capabilities of optical fibers for measuring concentrated solar flux in an environment at temperatures exceeding 500 °C and fluxes above 1.1 MW/m². Various fibers were tested and then analyzed using Scanning Electron Microscopy (SEM) to evaluate their structural integrity and material degradation. The results highlight significant coating deterioration, fiber retraction, and thermal-induced stress effects, all of which adversely affect measurement accuracy and reliability.

Keywords: Concentrated Solar Power, Thermal Solar Energy, Radiometer, Solar Simulator, Fiber-optic Sensors.

1.- Introducción

Los sensores de fibra óptica han revolucionado la monitorización en entornos extremos debido a su resistencia a la interferencia electromagnética, su diseño ligero y su durabilidad. Dentro de los sensores ópticos, las redes de difracción de Bragg en fibra (FBG) son la tecnología de sensado óptico más utilizada, permitiendo la detección precisa de cambios en temperatura o presión en industrias que van desde la ingeniería civil hasta la extracción de petróleo [1].

A medida que el mercado energético global completa su transición hacia las energías renovables, las plantas de energía solar térmica de concentración (CSP/CST) presentan grandes desafíos, sobre todo en la monitorización de los procesos que intervienen desde la focalización de los rayos de luz hasta la transformación en calor [2]. Los sistemas CSP requieren tecnologías de detección avanzadas que proporcionen mediciones en tiempo real con alta precisión en condiciones extremas, como radiación intensa, temperaturas de hasta 1000 °C y gradientes térmicos superiores a 500 °C [3]. En este contexto, las fibras ópticas emergen como una alternativa a los dispositivos de medición tradicionales, los cuales no logran

proporcionar datos precisos. El uso de fibras ópticas como captadores de radiación solar ha sido ampliamente investigado en los últimos años y en [4] se demostró su capacidad para proporcionar mediciones precisas de la irradiancia normal directa (DNI) en un sistema basado en fotodiodo de silicio y un algoritmo de calibración.

La adopción de sensores de fibra óptica como captadores de radiación solar en los receptores CSP mejoraría el mantenimiento predictivo y la eficiencia al proporcionar mediciones en tiempo real y la distribución del flujo concentrado en la superficie. Sin embargo, su implementación a gran escala en plantas CSP requiere una validación rigurosa para evaluar su rendimiento bajo temperaturas extremas, esfuerzos mecánicos y exposición prolongada a radiación concentrada. En este trabajo se presenta la prueba de concepto de un dispositivo para la medición de flujo solar concentrado en receptores solares basado en el uso de una fibra óptica de alta temperatura y fotodiodo semiconductor. Los ensayos de laboratorio han sido realizados en simuladores solares de alto flujo con lámpara de xenón (HFSS) y la evaluación del daño en las fibras ópticas expuestas a la alta radiación mediante su inspección en un microscopio electrónico de barrido (SEM).

2.- Montaje experimental

2.1.- Fibras ópticas para alta temperatura

A pesar de que las fibras ópticas, que tradicionalmente se encuentran fabricadas en óxido de silicio, tienen estabilidad térmica hasta aproximadamente 1200 ºC, las fibras ópticas comerciales vienen encapsuladas en materiales plásticos que limitan su funcionamiento hasta no más allá de los 100 ºC. Para aplicaciones como la de este trabajo, donde se persigue alcanzar temperaturas extremas, es necesario el uso de un encapsulado especial para garantizar la protección de la fibra hasta 1000 ºC. Además, para aplicaciones con aún mayores exigencias térmicas, las fibras ópticas de zafiro permiten alcanzar temperaturas superiores a los 2000 ºC.

Para la presente aplicación de medida de flujo solar concentrado, los diseños de fibra óptica para alta temperatura se realizaron en colaboración con la empresa Engionic (Berlín, Alemania). La Fig. 1a muestra la estructura de la fibra óptica diseñada, así como el detalle (utilizando un SEM) de la punta expuesta a la radiación; en la Fig. 1b. Atendiendo a ambas, se observa que a la fibra óptica, con su núcleo y cubierta, se le añade un recubrimiento de oro o poliamida de alta temperatura. Este conjunto se introduce dentro de un capilar de acero, y entre ambas un relleno de alúmina que busca aislar la fibra óptica del calentamiento sufrido por el acero. Esta configuración preserva la integridad estructural de todo el dispositivo, manteniendo el tamaño reducido que se busca para interferir lo menos posible con el receptor CSP.

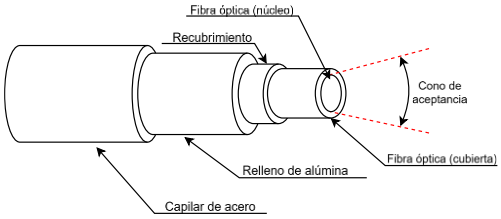

(a)

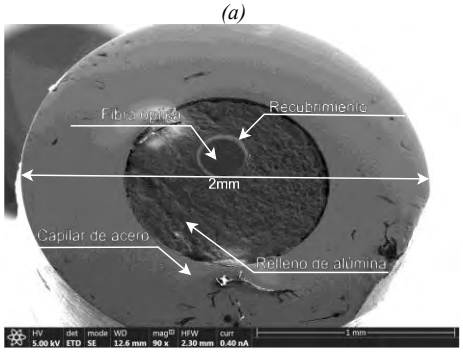

(b)

Figura 1. (a) Esquema de la estructura de diseño de la fibra óptica de alta temperatura y (b) imagen de detalle de la punta de la fibra óptica de alta temperatura obtenida por microscopía SEM.

De acuerdo con las especificaciones del fabricante, las fibras ópticas recibidas mantienen un rendimiento estable hasta los 700 °C y pueden soportar picos de temperatura de hasta 1000 °C, que, a pesar de no cumplir con los requisitos de la aplicación prevista, resultan adecuados para el experimento de prueba de concepto en el simulador solar.

2.2.- Montaje en el simulador solar de alto flujo

Para el presente trabajo, la primera prueba de concepto fue realizada en el simulador solar de alto flujo KIRAN-42 localizado en IMDEA Energía (Móstoles, Madrid) y la segunda en el HFSS que se encuentra en Centro Nacional de Energías Renovables - CENER (Sarriguren, Spain).

KIRAN42 utiliza siete lámparas de xenón dispuestas de forma elipsoidal, permitiendo alcanzar una densidad de flujo pico de 3.6 MW/m^2; aunque en los experimentos sólo una de ellas fue empleada. Enfrentado al simulador, una mesa de posicionamiento en tres ejes permite realizar el montaje que se detalla más adelante. Además, el ensayo incluye un radiómetro Gardon de referencia con el que comparar las medidas realizadas por el dispositivo basado en fibra óptica. El control del sistema se realiza externamente, permitiendo manejar las lámparas, la mesa de pruebas, la cámara CCD y los sistemas de refrigeración. Durante los experimentos, las fibras ópticas se expusieron a la radiación utilizando una placa de Inconel con conectores estancos a través de los cuales pasaba la fibra, como se muestra en la Fig. 2a, asegurando que el extremo de la fibra estuviera correctamente orientado hacia la fuente de luz. Esta placa estaba cubierta por una plancha de alúmina que solo dejaba expuesta una pequeña sección para que la fibra recibiera la radiación.

Por otro lado, el simulador solar de CENER cuenta con una lámpara de xenón que se encuentra dentro de una cámara, como se muestra en la Fig. 2b. Este simulador posibilita niveles de potencia ajustables y cuenta con un espejo elipsoidal que enfoca la luz emitida, permitiendo variar el flujo solar desde aproximadamente 180 kW/m² hasta 1.1 MW/m² en el punto focal. El montaje realizado fue similar al realizado en IMDEA, con una placa de acero colocada sobre una mesa posicionadora a través de la cual se hacía pasar la fibra. La placa estaba cubierta con lana cerámica para protegerla de las altas temperaturas. En este caso, un termopar se colocó junto al conector de la fibra para medir la temperatura en la parte trasera del acero.

(a)

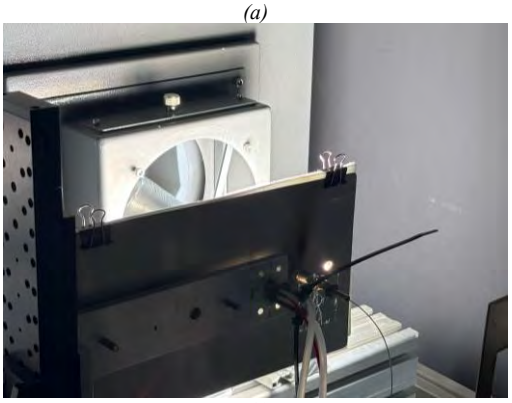

(b)

Figura 2. (a) Montaje del extremo de la fibra expuesta a la radiación en el simulador solar de IMDEA Energía y (b) detalle de la parte posterior del montaje en el simulador solar de CENER.

3.- Resultados

Los resultados obtenidos en las dos campañas de ensayos en simulador solar avalan el uso de la configuración propuesta como válida para la medida de flujo concentrado. Estas pruebas de concepto han permitido identificar algunos problemas deben ser atajados antes de realizar el diseño final que será instalado en los receptores CSP. Entre todas las fibras, aquellas con mayores diámetros, de 200 µm, son las que han obtenido mejores resultados de medida; siendo son los que se reportan a continuación.

La primera observación que debe hacerse está relacionada con los valores de medida obtenidos, que quedan lejos de la medida realizada por el radiómetro comercial instalado en ambos experimentos. En la Fig.

3a, correspondiente a los experimentos realizados en IMDEA Energía, se observan valores de flujo máximos ligeramente superiores a 190 kW/m^2 y 170 kW/m^2 en las fibras con recubrimiento de oro y poliamida, respectivamente. Este valor se encuentra lejos del arrojado por el Gardon en ese momento, que era en torno a 330 kW/m^2. El mismo fenómeno fue observado en el simulador solar de CENER, como se muestra en la Fig. 3b. En este caso, se muestra la evolución en la medida comparando los valores arrojados por el Gardon y la fibra, donde se comparan la medidas arrojadas por los dos instrumentos colocándolos en el foco de forma alterna en tres posiciones distintas de potencia. En este caso, se observa que el flujo medido por la fibra es en todos los casos de aproximadamente la mitad de la medida proporcionada por el Gardon.

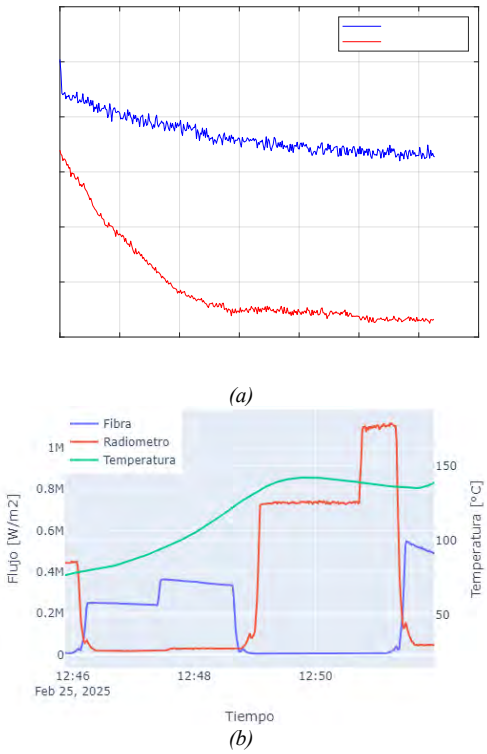

Figura 3. (a) Medida de flujo concentrado con fibras con recubrimiento de oro y poliamida en IMDEA Energía y (b) medida de flujo concentrado con fibra óptica y recubrimiento de poliamida en CENER.

Esta discrepancia en las medidas de flujo óptico entre el radiómetro Gardon y el radiómetro basado en fibra óptica tiene varias causas. El motivo fundamental está relacionado con los ángulos de incidencia de la luz. En el caso de las fibras ópticas, la apertura numérica de 0.22 define un campo de visión de 24º, suficiente para acoplar la luz en el simulador solar de IMDEA, pero no en el de CENER, donde más del 35% de los rayos dirigidos por la lámpara tienen mayor apertura de la marcada por el cono de aceptación de la fibra y, por tanto, no pueden ser capturados por la fibra, lo que explica la diferencia tan grande con el Gardon en este caso. Por otro lado, la fibra atenúa todos los rayos que no inciden perpendicularmente en la fibra debido a la función penumbra que impone la característica de apertura numérica, lo cual contribuye también a esa diferencia entre las dos medidas de flujo.

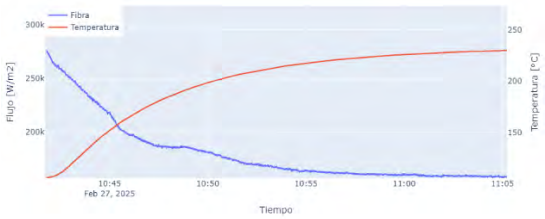

Figura 4. Medida de flujo concentrado en función de la temperatura utilizando fibra con recubrimiento de poliamida.

Además de este hecho, en la Fig. 4 se observa el otro gran problema que debe ser solucionado, que tiene que ver con la dependencia de la temperatura, que también se intuye en la Fig. 3, sobre todo en el caso de la fibra de poliamida. En este caso, se compara el flujo medido por la fibra óptica en el simulador solar de CENER con la medida de temperatura del termopar colocado detrás de la placa de acero; y resulta evidente que cuando la temperatura aumenta, la medida disminuye hasta que se alcanza el régimen permanente en ambas magnitudes.

Después de realizar ambas campañas de medidas, algunas de las fibras puestas a prueba fueron llevadas a un SEM con el objetivo de evaluar el daño sufrido por las mismas, lo cual se muestra en la Fig. 5.

En primer lugar, en la Fig. 5a, se observa una fibra con 200 µm de diámetro de núcleo y recubrimiento de poliamida. En este caso, la observación más significativa es que la fibra

óptica se ha retraído de la superficie estructural circundante, en contraste con la Fig. 1b, donde la fibra se mostraba en línea con el resto del capilar. Además de este hecho, se observa un espacio vacío entre el núcleo de la fibra y el relleno de alúmina, lo que indica la pérdida o degradación del recubrimiento de poliamida. En dicha Fig. 5a también se muestran grietas en la alúmina que actúa como aislante, las cuales no deberían afectar al funcionamiento del sistema en tanto que este material sólo cumple la función de aislar térmicamente la fibra del resto del capilar.

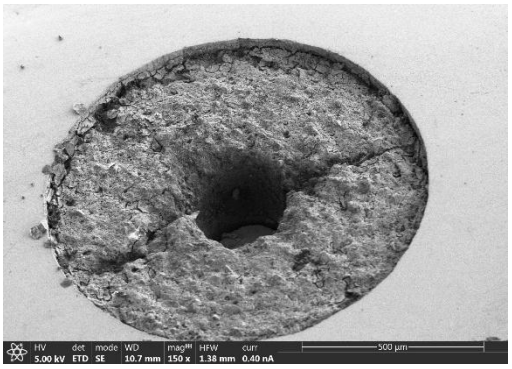

(a)

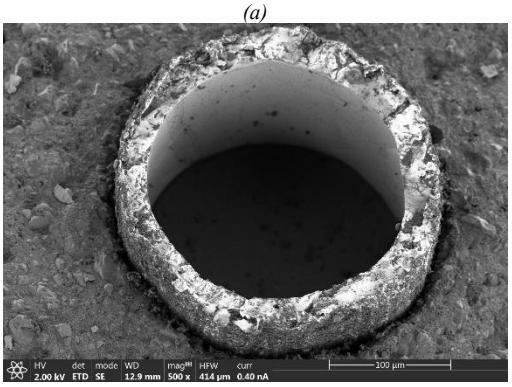

(b)

Figura 5. Detalle de las puntas de las fibras ópticas observada con microscopía SEM tras su exposición a alta radiación: (a) fibra de 200 µm de diámetro de núcleo y recubrimiento de poliamida y (b) fibra de 200 µm de diámetro de núcleo y recubrimiento de oro.

Por otro lado, se muestra en la Fig. 5b una fibra del mismo tamaño, pero con recubrimiento de oro. La principal característica distintiva con respecto a la fibra analizada previamente es la integridad estructural del recubrimiento, que mantiene su cohesión en contraste con la degradación observada en los especímenes recubiertos de poliamida. Además, el recubrimiento de oro presenta un mayor grosor en comparación con los espacios vacíos observados en muestras anteriores, donde ocurrió la degradación del recubrimiento. En este caso, la fibra también se encuentra retraída respecto del resto de la estructura, con el recubrimiento de oro elevado respecto del relleno de alúmina. En ambas fibras, este fenómeno contribuye también a la pérdida de parte de la radiación incidente en la fibra óptica, afectando a la medida de flujo óptico, en tanto que se produce un efecto de túnel que ensombrece a la fibra y no permite capturar los rayos provenientes dentro su cono de aceptación completo.

4.- Conclusiones

En este trabajo, una prueba de concepto para evaluar el potencial de un montaje basado en fibra óptica y fotodiodo para medir flujo solar concentrado en receptores de CSP ha sido llevada a cabo. Distintas fibras se han puesto a prueba, alcanzando en dichos ensayos flujos superiores a 300 kW/m^2 y 550 kW/m^2, respectivamente; con temperaturas de operación superiores a 500 ºC en la punta de la fibra. Aunque los resultados confirman la viabilidad de medir el flujo solar concentrado, aún quedan desafíos antes de alcanzar el objetivo de poder medir flujo solar concentrado de hasta 1.5 MW/m². Entre ellos, se destaca la necesidad de ampliar el campo de visión de la fibra, actualmente limitado por la apertura numérica, para captar toda la radiación solar proveniente del campo de helióstatos, así como desarrollar estrategias para el montaje de las fibras en los receptores que reduzcan la conducción térmica y disminuyan la temperatura soportada por la punta de la fibra.

Tras la campaña de experimentos, se realizaron análisis con el SEM de los extremos de las fibras ópticas expuestas a la radiación, revelando modificaciones estructurales en su configuración. Se observaron grietas en el relleno de alúmina dentro del capilar metálico, que no deberían afectar las mediciones al ser solo un aislante térmico. En cuanto a los materiales que componen la fibra de alta temperatura, los ensayos confirmaron que la poliamida se

volatiliza en las temperaturas de trabajo; mientras que el oro, aun siendo mejor opción dada la estabilidad térmica en las medidas, requiere garantizar que no se supere su temperatura de fusión de 1064 ºC. Asimismo, se detectaron desplazamientos en las fibras ópticas dentro del capilar metálico, en forma de retracción, lo que podría haber contribuido a pérdidas de potencia por efectos de sombreado en el núcleo de estas.

Actualmente, se trabajar en el desarrollo de estrategias para proteger la punta de la fibra de las condiciones extremas de operación que influyen en su degradación, al mismo tiempo que se busca reducir la sensibilidad térmica de la medida de flujo óptico.

Acknowledgements: This research was developed within the scope of the projects CATION, TED2021- 132190BC22 funded by MCIN/AEI/10.130339/501100011033 and, as appropriate, by "European Union Next Generation/PRTR", and funded by CHLOE, Grant PID2021-125786OB-C22 funded by MCIN/AEI/10.130339/501100011033.
Lastly, the ASTERIx-CAESar project has received funding from the European Union's Horizon Europe research and innovation program under grant agreement Nº 101122231.

References

[1] S.N. Khonina et al., "Optical fiber sensors: Working principle, applications and limitations", Adv. Photonics Res. 2022, 3, 2100371 (July 2022). https://doi.org/10.1002/adpr.202100371.

[2] N. Jelley et al., "Concentrated solar power: Recent developments and future challenges", Proc. Inst. Mech. Eng. Part A, 229(7), pp. 693-713 (February 2019). https://doi.org/10.1177/0957650914566895.

[3] Y.-L. He et al., "He, Y.-L.; Wang, K.; Qiu, Y.; Du, B.-C.; Liang, Q.; Du, S. Review of the solar flux distribution in concentrated solar power: Non-uniform features, challenges, and solutions", Appl. Therm. Eng., 149, pp. 448-474 (February 2019). https://doi.org/10.1016/j.applthermaleng.2018.12.006.

[4] A. Carballar et al., "Measuring DNI With a New Radiometer Based on an Optical Fiber and Photodiode", Sensors vol. 24, pp. 3674 (June 2024). https://doi.org/10.3390/s24113674.

Using Semiconductor Photodiodes as Detector Element for Solar Radiation Measurements

Manuel JEREZ [(1)], Alejandro CARBALLAR [(1)], Joaquín GRANADO [(1)]

1. Electronic Engineering Department, Universidad de Sevilla (E.T.S. de Ingeniería), C/ Camino de los Descubrimientos s/n, 41092 – Sevilla, Spain

Contact: Manuel JEREZ (mjerez@us.es).

ABSTRACT:

An innovative pyrheliometer configuration utilizing optical fiber for solar radiation capture requires a detector element for the optical power measurements. In this sense, three distinct photodiodes—two silicon-based and one indium gallium arsenide (InGaAs)— are evaluated. Specifications of each photodetector are analyzed, including their spectral response, response time, and thermal characteristics, as well as the desired specifications for the application, also compared with a thermopile. The characteristics of semiconductor photodiodes are shown to be more appropriate for the application compared to thermopiles, which are conventionally utilized in radiometric instrumentation. Experimental results compare the three photodiodes against a commercial pyrheliometer, demonstrating that the system's behavior changes substantially depending on the type of photodetector employed. Among the three photodiodes investigated, one of the silicon-made devices exhibits performance most closely aligned with the commercial pyrheliometer, suggesting its potential as an optimal detection element in this novel proposal for radiometric measurements.

Key words: Photodetector, thermopile, photodiode, pyrheliometer, radiometer, solar irradiance, optical fiber, spectral response.

1.- Introduction

The intensity of solar radiation across Earth's surface is subject to several factors, including geographic location, time of day, and weather conditions. Measuring solar irradiance is critical for many applications, particularly in photovoltaic (PV) and concentrating solar power (CSP) plants, as it helps to optimize the efficiency of electricity generation. Solar irradiance can be categorized into three: Direct Normal Irradiance (DNI), originating from a small solid angle centered on the solar disk; Direct Horizontal Irradiance (DHI), corresponding to the scattered beams due to meteorological phenomena; and Global Horizontal Irradiance (GHI), which adds up both [1].

As defined by the International Organization for Standardization (ISO), the pyrheliometer is the most common instrument for the measurement of the DNI, while pyranometers are, in general, used for the measurement of DHI and GHI, although they can also act as a device for measurements of direct irradiance [2]. In both cases, the solar radiation captured needs to be converted into an electrical signal to be processed digitally, allowing to analyze and determine the value of the incident solar radiation. Generally, two options are available for this process: a thermopile in conjunction with a surface that absorbs light and converts it into heat, or a semiconductor photodiode, which transforms incident light into electric current [3].

In this work, four different photodetectors are discussed as detecting elements for solar

radiation, presenting results from the use of three photodiodes. In section two, the experimental assembly is showcased. In section three, the application requirements and photodetectors compared are introduced. In section four the results are shared; and in section five the conclusions and future work are presented.

2.- System Description

The proposed optical fiber-based pyrheliometer has been already presented by the authors in [4,5], describing all the details on the configuration and the choice of the optical fibers used for the DNI measurements. Regarding the calibration algorithm, which is also introduced in literature, the aforementioned articles only consider one silicon-based photodiode for the measurements, while in this case 3 photodetectors are compared (two Si-based photodiode and one InGaAs-based photodiode); which means different data used as input for the algorithm (corresponding to each response spectrum of the different photodiodes) and resulting in different values of the correction factor, which will be mentioned later in this article. The photodetectors analyzed in this work are all commercialized by THORLABS. Specifically, these include silicon photodiodes S140C and S150C, representing volumetric and compact types, respectively, and the volumetric InGaAs photodiode is model S144C.

Table 1: Summary of technical specifications considered for the current application for 4 THORLABS photodetectors.

Device	***Sensitivity***	***Response time***
Silicon S140C	*1nW*	*<1*µs
Silicon S150C	*10pW*	*<1*µs
InGaAs S144C	*1nW*	*<1*µs
Thermopile S401C	*1µW*	*1.1s*

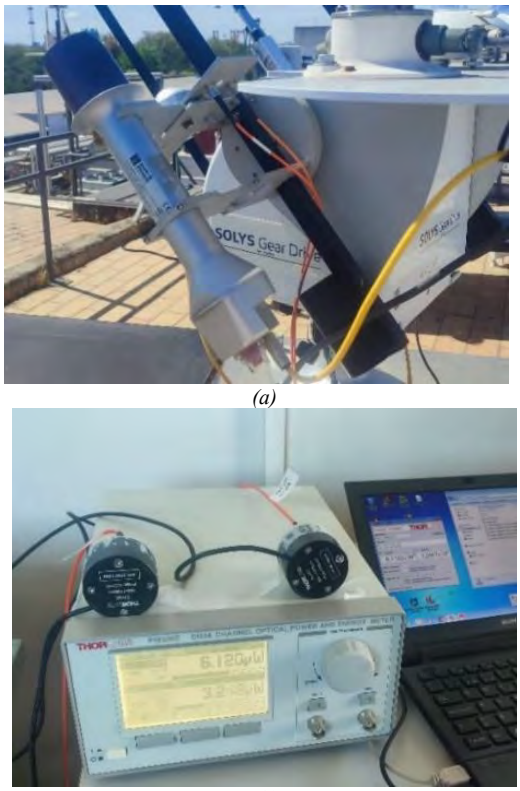

(a)

(b)

Figure 1. (a) Mounting of the fibers onto the solar tracker and placed next to a commercial pyrheliometer and (b) photodiodes THORLABS S140C and S144C, optical power monitor THORLABS PM320E and power tracing software.

For the evaluation of the photodetectors, two optical fibers have been mounted next to a commercial KIPP & ZONEN CHP1 pyrheliometer (to validate the DNI measurements). The optical fibers were mounted on the KIPP & ZONEN SOLYS Gear Drive solar tracker to ensure consistent tracking of the sun throughout the day; while the other tips were taken to an indoor laboratory, to prevent the effects of temperature in the measurement, and connected to the different photodetectors, which were linked to the optical power monitor (OPM) THORLABS PM320E. The measured optical power, after processing through the calibration algorithm, provides accurate DNI measurements, aligning closely to conventional pyrheliometer results, allowing to compare the behavior of the different photodetector devices. Fig. 1a displays the fibers and commercial

pyrheliometer mounted onto the solar tracker, while Fig. 1b showcases two of the photodiodes along with OPM and computer software.

3.- Application Requirements and Specifications

The photodetector represents a critical component in the proposed optical fiber-based pyrheliometer design, being responsible for transforming captured radiation into electrical energy to generate an optical power measurement. While any photodetector could theoretically fulfil this function, certain desirable parameters in the device specifications are essential to ensure fast, accurate and precise solar radiation measurement.

Sensitivity and response time are critical parameters in performance. Optimal sensitivity, characterized by low power, enhances the detection of minor irradiance variations, while a fast response time is essential for real-time detection. Semiconductor photodiodes outperform thermopiles in both aspects, enabling faster response and higher sensitivity across specific electromagnetic spectrum ranges. In contrast, thermopiles rely on slower heat transfer processes and are characterized by longer response times and diminished sensitivity at certain wavelengths. The third fundamental parameter to consider is the spectral response or responsivity of the photodetector, which determines the device's response across different wavelengths of the electromagnetic spectrum. In our application, it is desirable for this response to cover most of the solar spectrum, ranging from 300 nm to 4000 nm [1], and to remain as flat as possible. In this regard, thermopiles exhibit superior performance. As previously mentioned, thermopiles operate based on heat transfer processes, resulting in a flat response curve. Initial analysis suggests that thermopiles should theoretically be the optimal devices for this application, given their implementation in traditional pyrheliometers. However, constraints imposed by the requirements of the current application preclude this conclusion. Given the technical specifications on the thermopile, and taking into account its low value of sensitivity, the thermopile is discarded as an option to act as photodetector in the proposed radiometer configuration, as it needs to be able to detect small variations in solar radiation captured by small-sized optical fibers. In this sense, the optical power value captured by the 105µm core diameter fiber when measuring 900W/m^2 is around 6µW. Considering that sensitivity in thermopile is 1µW, small changes and low irradiance values will never be tracked by this type of photodetector. The necessity of semiconductor photodiodes for the purpose of this application therefore imposes the implementation of a calibration algorithm to compensate the effects of the limited and irregular photodiode sensitivity, as documented in [4,5].

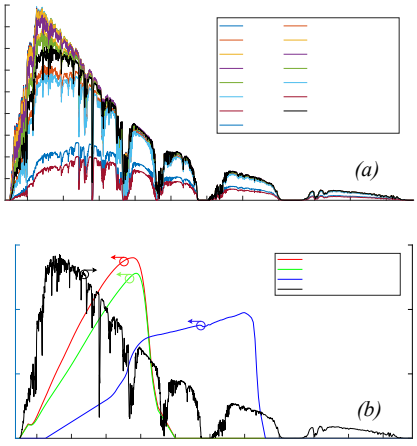

Figure 2. (a) Spectral irradiance evolution measured in Seville, Spain over 28th June 2019, compared against ASTM 1.5 G173-03 Reference Spectra. (b) Spectral response of the semiconductor photodiodes [8] analyzed against the reference solar spectrum [7]. The spectral response of photodiode S150C has been scaled for the purpose of the illustration.

An important consideration is that the solar spectrum is neither constant throughout the day nor across different locations. The angle of solar light incidence on the surface, and the atmospheric path length, which depends on the season, fundamentally alter the solar light spectrum received at sea level. The most substantial spectral modifications occur predominantly during dawn and dusk. Additionally, meteorological phenomena

contribute to further spectral variations [6,7]. Fig. 2a illustrates the previously mentioned phenomenon, depicting the evolution of the solar spectrum received in Seville, Spain, over 28th June 2019, compared with the ASTM 1.5 G173-03 Reference Spectra [8]. It is crucial to consider this aspect, as in the case of semiconductor photodiodes, the current generation at the output is intrinsically linked to the device's characteristic spectrum, with varying sensitivity across different wavelengths. These wavelength sensitivities can be predominant depending on the time of day or season.

As was mentioned earlier, the main advantages of the semiconductor photodiodes are the extremely low values of the response time, which is lower than 1µs for all of them, and the sensitivity, which is 10pW for the silicon S150C photodiode and 1nW for both volumetric devices. In Table 1, a summary of these parameters is displayed, as well as the specifications of thermopile S401C, where it is clear the great difference between both types of photodetectors when considering these parameters.

In contrast, photodiodes have their main weakness in the spectral irradiance specification, which is limited and changes throughout the entire range, as shown in Fig. 2b. This characteristic complicates irradiance value calculations, introducing the necessity of the calibration algorithm. In the mentioned figure, it can be seen how the InGaAs photodiode exhibits sensitivity in a higher spectral region, resulting in elevated power measurements when wavelength ranges starting from 1100 nm dominate the received power—a condition predominantly occurring during dawn and dusk. Due to the nature of the optical power meter, working with this type of photodiodes requires selecting a calibration wavelength within the detector's operating range. Consequently, the calibration factor used is not unique for each photodiode but varies depending on the selected wavelength. In this case, the chosen calibration wavelengths were 635 nm for the S140C, 1050 nm for the S144C, and 950 nm for the S150C, resulting in calibration factors of 1.3, 2.98, and 2.34, respectively.

4.- Results for DNI measurements

The first results for DNI measurements, presented in Fig. 3a are for measurements during the same day with two different photodiodes (silicon S140C and InGaAs S144C) using fiber FG105LVA, compared against a commercial pyrheliometer, it is clear that the behavior of both photodiodes is similar during the central hours of the day, where the irradiance values after being processed are similar to those from the commercial device, proving great sensitivity and similar response times to the pyrheliometer, keeping relative errors below 5% from 10:30h to 19:00h. This error is due to the tolerance in core diameter manufacturing tolerance, which is around 3%; as well as influenced by the use a model and not real spectral irradiance, and both could be enhanced by a refinement in the calibration.

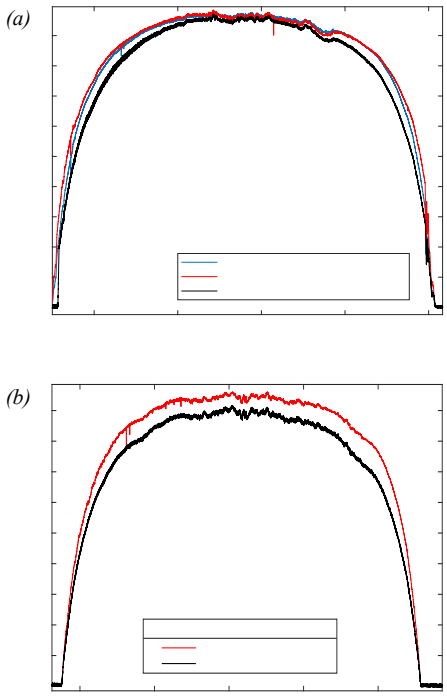

Figure 3. DNI measurement using as optical collector an optical fiber with 105µm core-diameter and: (a) silicon S140C and InGaAs S144C photodiodes and (b) silicon S150C photodiode, in all cases compared against a commercial pyrheliometer.

If the analysis is focused on the greatest divergencies seen on the comparison, they happen mainly at dawn and dusk, where the spectral irradiance suffers most variations against the model used in the calibration algorithm. If examined with further detail, the values from the InGaAs photodiode are higher than the silicon photodiode also at these times, while this did not happen at central hours of day. As shown in Fig. 2b, the responsivity of the InGaAs photodetector covers higher wavelengths in the spectrum, having more influence of these components at sunrise and sunset.

Lastly, Fig. 3b demonstrates that the performance of the S150C photodiode is analogous to previously discussed photodiodes. However, the divergence between the curve generated by this device and the commercial pyrheliometer is more pronounced, although the relative error consistently remains below 10%, which could be due to fiber misalignment, manufacturing tolerance or a divergence between theoretical and real photodiode response curves. This phenomenon is consistently observed across all measurements conducted with this fiber and detector, so it could potentially be mitigated by refining the calibration algorithm. This could be done in several ways, but current work focuses on changing the spectra used as a reference for the calibration factor computing depending on different conditions, such as time of day and season of the year; given its variability depending on those factors, as shown in Fig 2a. Besides, the use of a photodiode that is less sensitive to changes in spectrum could be beneficial, reducing the influence of these changes. In this sense, the InGaAs photodiode S144C has a flatter response, and covers a side of the spectrum with less changes along the day, potentially being the best option.

5.- Conclusions

In this work, various photodetectors were analyzed as solar radiation detectors in a new optical fiber-based pyrheliometer configuration. The study encompassed two stages: an initial phase examining the specifications of different employed devices and assessing their suitability for the intended application, followed by a second phase where the photodetectors were tested in a novel radiometer setup previously demonstrated. Among the options considered, semiconductor photodiodes exhibited superior performance leveraging their sensitivity and response time capabilities while overcoming spectral response curve limitations through the calibration algorithm employed; compared to the thermopile, which was considered an invalid option for this application due to its low sensitivity and response time. Among the evaluated photodiodes, the two volumetric models demonstrated the most promising performance, generating results comparable to those of a conventional pyrheliometer. Although both behave similarly, the silicon photodiode gave more accurate results, whereas the InGaAs photodiode behaved worse at the start and end of the day.

Acknowledgements: This research was developed within the scope of the projects CATION, TED2021- 132190BC22 funded by MCIN/AEI/10.130339/501100011033 and, as appropriate, by "European Union Next Generation/PRTR", and funded by CHLOE, Grant PID2021-125786OB-C22 funded by MCIN/AEI/10.130339/501100011033.
Lastly, the ASTERIx-CAESar project has received funding from the European Union's Horizon Europe research and innovation program under grant agreement Nº 101122231. The authors would like to thank the Group of Thermodynamics and Renewable Energy from the University of Seville. The information about the group can be found at https://gter.es/.

References

[1] P. Blanc et al., "Direct normal irradiance related definitions and applications: The Circumsolar Issue", Solar Energy vol. 110, pp. 561-577 (December 2014). https://doi.org/10.1016/j.solener.2014.10.001

[2] "Solar energy - Specification and classification of instruments for measuring hemispherical solar and direct solar radiation", ISO 9060:2018, International

Organization for Standardization, 2018 (rev. 2024).

[3] M. A. Martínez, "A New and Inexpensive Pyranometer for the Visible Spectral Range", Sensors vol. 9, pp. 4615-4634 (June 2009). https://doi.org/10.3390/s90604615

[4] R. Rodríguez-Garrido et al. "Pirheliómetro basado en fibra óptica y fotodiodo semiconductor", 13ª Reunión Española de Optoelectrónica, OPTOEL'23. Sevilla, España. (2023)

[5] A. Carballar et al., "Measuring DNI With a New Radiometer Based on an Optical Fiber and Photodiode", Sensors vol. 24, pp. 3674 (June 2024); https://doi.org/10.3390/s24113674.

[6] C.A. Gueymard et al., "Cloud and albedo enhancement impacts on solar irradiance using high frequency measurements from thermopile and photodiode radiometers. Part 1: Impacts on global horizontal irradiance", Solar Energy vol. 153, pp. 755-765 (September 2017); https://doi.org/10.1063/5.0007550

[7] J. L. Lean et al., "How Does the Sun's Spectrum Vary?", Journal of Climate, vol. 25, no. 7, pp. 2555-2560 (April 2012); https://doi.org/10.1175/JCLI-D-11-00571.1

[8] ASTM G173-03(2020); Standard Tables for Reference Solar Spectral Irradiances: Direct Normal and Hemispherical on 37◦ Tilted Surface. ASTM: West Conshohocken, PA, USA, 2020. Available online: https://www.astm.org/g0173-03r20.html (accessed on 28th November 2024)

Fotónica cuántica y no lineal

Efficient frequency down-conversion of quantum-dot-compatible single photons enabled by molecular modulation

Arturo MENA [(1)], Pau ARCOS [(1)], Joseba ZUBIA [(1, 2)], David NOVOA [(1, 2, 3)]

1. Department of Communications Engineering, University of the Basque Country (UPV/EHU), Torres Quevedo 1, 48013 Bilbao, Spain.
2. EHU Quantum Center, University of the Basque Country (UPV/EHU), 48013 Bilbao, Spain.
3. IKERBASQUE, Basque Foundation for Science, Plaza Euskadi 5, 48009 Bilbao, Spain.

Contact: Arturo MENA (arturo.mena@ehu.eus).

ABSTRACT:

We study the frequency transduction of single photons with wavelengths compatible with quantum dot technology. Highly efficient frequency downshifts of 125 THz are achieved by means of molecular modulation in an anti-resonant hollow-core fibre filled with hydrogen gas. This technique harnesses the Raman coherence waves generated by a synchronized pump beam to surpass the Raman threshold and down-convert arbitrary signals of any intensity after prior calibration of the phase matching in the fibre-gas device. The results of this work might facilitate the integration of quantum dot emitters with quantum memory systems, fostering advances in quantum communication and information processing technologies.

Key words: Quantum frequency conversion, hollow-core fibres, Raman scattering, molecular modulation.

1.- Introduction

Quantum light sources are an essential cornerstone of modern quantum technologies. Particularly, they are a fundamental component in the paradigm of hybrid quantum communication networks [1, 2, 3]. These networks depend on the capacity to encode information in the quantum states of photons, to transmit this information, for instance, over fibre-based transmission lines or through free space, and to store it as long as it deems suitable [1, 4]. Consequently, the necessity to integrate devices that operate within distinct spectral domains arises. This prompted the development of a wide variety of frequency transducers for quantum light in order to overcome this operational gap [5].

Most recently, gas-filled anti-resonant hollow-core fibres (ARFs) have emerged as promising candidates for tunable and highly efficient frequency conversion while preserving non-classical correlations [6]. This is achieved by means of molecular modulation, enabled by pre-excited Raman coherence waves generated by stimulated Raman scattering in the gaseous medium.

This technique allows for the subsequent conversion of phase-matched signals of arbitrary intensity without threshold, modifying their frequency by the corresponding Raman shift [6, 7]. In this situation, the phase-matching conditions are largely adjustable through engineering of the dispersion in the fibre-gas system, e.g. by modifying the fibre geometry or the properties of the gaseous medium [8]. In addition to this, owing to the low-loss, tight modal confinement achieved in the hollow core of ARFs, parasitic effects such as Rayleigh scattering can be avoided and the system presents a high damage threshold [9, 10],

allowing the access to a wider spectral domain and the use of suitable pump pulse energies.

In this work, we analyse the capabilities of molecular modulation in ARFs filled with hydrogen gas to down-shift the frequency of quantum-dot-compatible single photons and reach quantum memory wavelengths as a way to bridge these technologies through fibre-based solutions.

2.- Framework

2.1.- Frequency conversion based on molecular modulation

The concept of Raman coherence wave can be explained as a collective synchronized vibrational motion of the gas molecules filling the ARF, as is represented in Fig. 1.

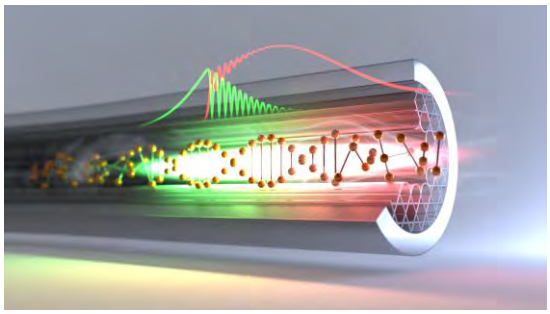

Fig. 1: Artistic depiction of the generation of vibrational molecular coherence by the beating of a pump beam (in green) and its down-shifted Stokes frequency component (in red) generated by SRS. The gas molecules filling the core of an ARF are represented along the propagation axis schematically.

This type of vibrational coherence is induced by the beating of the pump pulse and its down-shifted Stokes frequency component generated by SRS [11].

If there is no previous coherence present in the molecular system, the power of the pump beam needs to be above a minimum threshold to be able to initiate the stimulated generation of a Stokes signal. However, in the case in which a coherence wave has already been generated, a subsequent mixing signal can experience inelastic scattering without threshold provided phase-matching conditions are met. That is, by prior preparation of a coherence wave in the molecular system, the frequency of a mixing signal of arbitrarily low intensity down to the single-photon limit, can be down-shifted or up-shifted with high efficiency given adequate fulfilment of the following conditions [6, 7]:

$$\Omega_R - (\omega_M - \omega_D) = 0, \qquad (1)$$

$$\Delta\beta - (\beta_M - \beta_D) = 0, \qquad (2)$$

where Ω_R is the Raman shift, $\omega_{M(D)}$ and $\beta_{M(D)}$ are the frequency and propagation constant of the mixing (down-shifted) signal and $\Delta\beta = \beta_P - \beta_S$ is the propagation constant of the coherence wave given by the propagation constants β_P and β_S of the pump and Stokes frequencies. With this, the desired transition for frequency transduction can be targeted by modifying the parameters governing the dispersion of the gas-filled fibre, such as the size of the hollow core, the thickness of the walls in the microstructure, the gas pressure or the molecular species chosen for filling the fibre.

2.3.- Numerical modelling

In the scope of this work, we particularly focus on the transduction of a 580 nm (~517 THz) mixing photon to the down-shifted wavelength of 765 nm (~392 THz), separated by the ~125 THz Raman shift of the Q(1) vibrational transition of molecular hydrogen at room temperature.

To simulate the interaction dynamics in the hydrogen-filled ARF system, we use the semiclassical Maxwell-Bloch formalism for SRS [11] with 7 Raman sidebands (including the pump) together with an additional set of equations for the frequency sidebands of the mixing signal. The dispersion of the fibre is modelled using the resonance-free capillary model [12, 13].

3.- Results

Here we present the results of the analysis performed on an available ARF. For these simulations, we considered a gaussian pump pulse with a duration of 1.8 ns, a wavelength of 515 nm and an energy of 2 μJ. The pump pulse energy was optimized to obtain the maximum efficiency for a clean transduction

of the 580 nm mixing photon to the down-converted wavelength of 765 nm.

The dispersion of the gas-filled ARF was studied to determine the adequate pressure in which the phase-matching conditions are satisfied. This is done with the support of Fig. 2(a), where the dependence of the phase mismatch on the hydrogen gas pressure is shown. The dephasing $\vartheta_{AS} = 2\beta_P - \beta_S - \beta_{AS}$ represents the phase mismatch between the pump-Stokes coherence wave and the pump-anti-Stokes coherence wave. When $\vartheta_{AS} = 0$ at $P \approx 9$ bar, the rate of phonon creation induced by the pump-Stokes scattering process is balanced by the phonon annihilation rate from the pump-anti-Stokes process. This results in the suppression of the Raman gain during the pumping stage, preventing the effective generation of coherence and the subsequent conversion process of mixing-frequency single photons. In addition to this, the dephasings $\vartheta_U = (\beta_P - \beta_S) - (\beta_U - \beta_M)$ and $\vartheta_D = (\beta_P - \beta_S) - (\beta_M - \beta_D)$ represent the phase mismatch of the mixing and up-converted or down-converted photons with the coherence wave induced by the pump and Stokes fields. When one of these two dephasings is equally zero, the corresponding frequency conversion process is enhanced. An inset has been included in Fig. 2(a) to show how these dephasings and the coherence wave can be represented graphically over a dispersion diagram. In the inset, the dispersion is subtracted with the linear contribution $\beta_{ref} = \beta(\omega_{ref})\omega/\omega_{ref}$, where ω is the frequency and ω_{ref} a reference frequency value, to showcase the nonlinear dispersion component.

We find that $\vartheta_U = 0$ at $P \approx 11$ bar, which corresponds to the case of perfect phase matching for frequency up-conversion, and that $\vartheta_D = 0$ at $P \approx 19$ bar for frequency down-conversion. This analysis matches the simulation results shown in Fig. 2(b), where the output mixing, up-converted and down-converted average photon numbers are shown for a fibre length of 2.5 m. These values are normalized by the mixing photon number at the input.

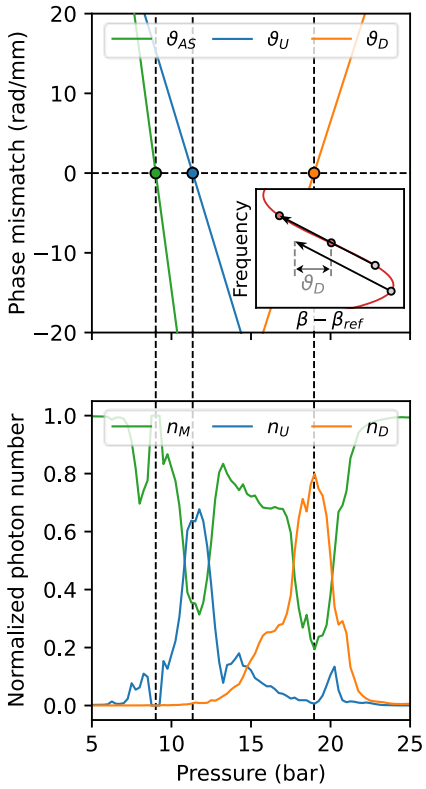

Fig. 2: (a) Pressure dependence of the dephasings corresponding to the Stokes and anti-Stokes fields (ϑ_{AS}) and frequency up-conversion (ϑ_U) and down-conversion (ϑ_D). An inset is included to illustrate ϑ_D and the coherence wave vector C_w (black arrows) generated by the pump and Stokes frequencies over an example of dispersion diagram with arbitrary units. (b) Normalized average photon numbers at the output of a 2.5 m-long fibre. Here, n_M, n_U and n_D denote the average mixing, up-converted and down-converted photon numbers. Vertical black dashed lines are included to highlight the relationship between (a) and (b).

Focusing on the propagation dynamics in the phase-matched down-conversion case at $P = 19$ bar, we find an increasing conversion efficiency of ~ 80% as shown in Fig. 3. We observe no significant dynamics until molecular coherence is developed after approximately 50 cm of propagation. Once coherence is developed in the system, a drastic population exchange begins between the mixing and down-converted signals, resulting in a generally smooth and efficient evolution.

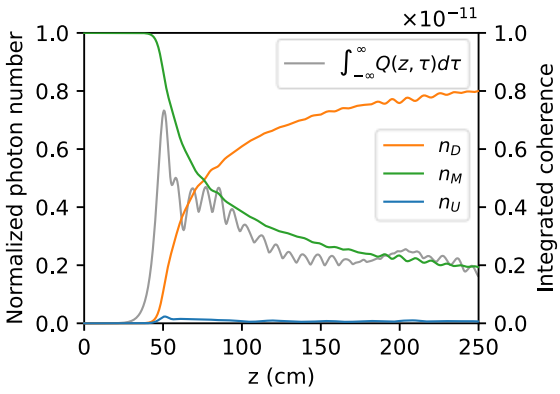

Fig. 3: Normalized mixing (n_M), down-converted (n_D) and up-converted (n_U) photon numbers and integrated coherence wave amplitude as a function of the propagation distance z.

4.- Conclusion

We have studied the frequency transduction of single photons from a quantum-dot-compatible wavelength of 580 nm to a down-converted wavelength of 765 nm in the operativity range of quantum memories via molecular modulation enabled by SRS in a hydrogen-filled ARF. By means of a comprehensive physical analysis of the gas-fibre system, we found the optimal parameters for this process, predicting down-conversion efficiencies of 80%. The future experimental demonstration of this phenomenology might pave the way to novel, highly-efficient quantum transducers compatible with existing optical fibre networks.

Acknowledgements: This work was supported by the grants PID2021-123131NA-I00, PID2021-122505OBC31, PRE2022-102843 and TED2021-129959B-C21, funded by MICIU/AEI/10.13039/501100011033, by "ERDF a way of making Europe", by the "European Union NextGenerationEU/PRTR" and "ESF+", and the Gobierno Vasco/Eusko Jaurlaritza (IT1452-22), ELKARTEK (μ4Smart-KK-2023/00016 and Ekohegaz II-KK-2023/00051), and the "Translight" initiative of UPV/EHU, and the IKUR Strategy of the Department of Education of the Basque Government through the grant IKUR_IKA_23/03. PA acknowledges support from the Basque Government grant for predoctoral researchers, Ref. PREGV23/47.

References

[1] H. J. KIMBLE, *"The quantum internet"*, Nature, 453, 7198, 1023-1030, 2008.

[2] Y. ARAKAWA, M. J. HOLMES, *"Progress in quantum-dot single photon sources for quantum information technologies: A broad spectrum overview"*, Appl. Phys. Rev., 7, 2, 021309, 2020.

[3] J. ZHANG, Y. KIVSHAR, *"Quantum metaphotonics: Recent advances and perspective"*, APL Quantum, 1, 2, 020902, 2024.

[4] K. HESHAMI, D. G. ENGLAND, P. C. HUMPHREYS, P. J. BUSTARD, V. M. ACOSTA, J. NUNN, B. J. SUSSMAN, *"Quantum memories: emerging applications and recent advances"*, J. Mod. Opt., 63, 20, 2005-2028, 2016.

[5] N. LAUK, N. SINCLAIR, S. BARZANJEH, J. P. COVEY, M. SAFFMAN, M. SPIROPULU, C. SIMON, *"Perspectives on quantum transduction"*, Quantum Sci. Technol., 5, 2, 020501, 2020.

[6] R. TYUMENEV, J. HAMMER, N. Y. JOLY, P. S. J. RUSSELL, D. NOVOA, *"Tunable and state-preserving frequency conversion of single photons in hydrogen"*, Science, 376, 6593, 621-624, 2022.

[7] S. T. BAUERSCHMIDT, D. NOVOA, B. M. TRABOLD, A. ABDOLVAND, P. St. J. RUSSELL, *"Supercontinuum up-conversion via molecular modulation in gas-filled hollow-core PCF"*, Opt. Express, 22, 17, 20566-20573, 2014.

[8] S. T. BAUERSCHMIDT, D. NOVOA, A. ABDOLVAND, P. St. J. RUSSELL, *"Broadband-tunable LP_{01} mode frequency shifting by Raman coherence waves in a H_2-filled hollow-core photonic crystal fiber"*, Optica, 2, 6, 536-539, 2015.

[9] S. GAO, Y. WANG, W. DING, Y. HONG, P. Wang, *"Conquering the Rayleigh Scattering Limit of Silica Glass Fiber at Visible Wavelengths with a Hollow-Core Fiber Approach"*, Laser Photonics Rev., 14, 1, 1900241, 2020.

[10] E. N. FOKOUA, S. A. MOUSAVI, G. T. JASION, D. J. RICHARDSON, F. POLETTI, *"Loss in hollow-core optical fibers:*

mechanisms, scaling rules, and limits", Adv. Opt. Photonics, 15, 1, 1-85, 2023.

[11] P. ARCOS, A. MENA, M. SÁNCHEZ-HERNÁNDEZ, E. ARROSPIDE, G. ALDABALDETREKU, M. A. ILLARRAMENDI, J. ZUBIA, D. NOVOA, *"Narrowband stimulated Raman scattering and molecular modulation in anti-resonant hollow-core fibres",* EPL, 147, 45001, 2024.

[12] E. A. J. MARCATILI, R. A. SCHMELTZER, *"Hollow metallic and dielectric waveguides for long distance optical transmission and lasers"*, Bell System Technical Journal, 43, 4, 1783-1809, 1964.

[13] M. A. FINGER, N. Y. JOLY, T. WEISS, AND P. ST.J. RUSSELL, *"Accuracy of the capillary approximation for gas-filled kagomé-style photonic crystal fibers"*, Opt. Lett., 39, 4, 821-824, 2014.

Deep ultraviolet source via cooperative Raman combs in gas-filled hollow-core fibres

Pau ARCOS [(1)], Joseba ZUBIA [(1,2)], David NOVOA [(1,2,3)]

1. Department of Communications Engineering, University of the Basque Country (UPV/EHU), Torres Quevedo 1, 48013 Bilbao, Spain.
2. EHU Quantum Center, University of the Basque Country (UPV/EHU), 48013 Bilbao, Spain.
3. IKERBASQUE, Basque Foundation for Science, Plaza Euskadi 5, 48009 Bilbao, Spain.

Contact: Pau ARCOS (pau.arcos@ehu.eus).

ABSTRACT:

Narrowband deep ultraviolet (DUV) light holds significant potential for applications in chemistry and biology. However, most existing DUV sources are neither compact nor user-friendly, limiting their accessibility and practicality. To address this challenge, we present a platform based on a bichromatic pump and stimulated Raman scattering in hydrogen-filled hollow-core fibres. This approach generates a coherent synchronous molecular motion in the gas, which, combined with precise dispersion engineering and meticulous control over the fibre attenuation landscape, enables a synergistic interaction between two distinct Raman combs whose spectral coverage extends deep into the ultraviolet region. This compact, robust and efficient system constitutes a promising solution to the limitations of traditional DUV sources, paving the way for a broader adoption of this technology in scientific research and industrial applications.

Key words: deep ultraviolet, photonic crystal fibre, Raman scattering, frequency conversion, dual pumping

1.- Introduction

Harnessing narrowband deep ultraviolet (DUV) light has aided progress in fields such as biochemistry by enabling access to the electronic outer-shell transitions in biomolecules [1]. While techniques like high-harmonic generation in solid-state systems can produce DUV light, it requires stringent operational conditions such as precise phase matching, and high pump intensities. Additionally, the nonlinear crystals required for room-temperature DUV generation are challenging to fabricate in large sizes, which limits the maximum energy attainable in the DUV laser system [2]. Despite significant progress, these systems are not largely frequency-tunable, and their performance is severely hampered by strong material dispersion in the UV and complex operational requirements, reducing their practicality.

In contrast, gas-filled anti-resonant fibers (ARFs) offer a compelling alternative by avoiding these limitations. These fibres feature broadband guidance from the mid-infrared to the vacuum ultraviolet, long light-matter interaction lengths and tight modal confinement, as well as pressure-tunable dispersion [3]. Interestingly, ultrafast self-compression and dispersive wave emission in gas-filled hollow capillaries and ARFs enable coverage of the DUV and vacuum ultraviolet spectral domains [4]. However, current implementations typically produce broadband spectra with low spectral power density at specific target wavelengths, limiting their utility for certain applications. Furthermore, they require ultrafast pump lasers, which are often bulky, sensitive to environmental conditions and complex, making the setup not easily portable and user-friendly.

By leveraging Raman-based frequency conversion in gas-filled ARFs, it is possible to achieve intense, narrowband DUV emission while maintaining a compact and portable architecture [5,6], thereby addressing the critical gaps left by other existing approaches.

In this work, we study a system composed of a hydrogen-filled ARF pumped simultaneously by two spectrally separated laser pulses. The bichromatic pumping configuration generates two distinct optical phonons with different spatial phases, enabling the simultaneous emission of two Raman combs alongside with their cooperative interaction. Remarkably, this hybrid Raman comb can in principle extend further into the DUV than any of the individual combs themselves. By precisely controlling the fibre dispersion, our design ensures pure intramodal interactions, restricting the observed nonlinear dynamics to the fundamental core mode while keeping the device robust and compact.

2.- Physics of fibre-based stimulated Raman scattering

Stimulated Raman scattering (SRS) in gas-filled ARFs occurs when an intense pump pulse interacts with the gas molecules confined in the fibre core. During this nonlinear inelastic scattering process, the photons transfer a part of their energy to excite molecular vibrations. The energy difference corresponds to the Raman transition frequency Ω_R, a unique value for each Raman-active molecular transition (for hydrogen gas, the first vibrational frequency shift is ~125 THz). As a result, the pump pulse is down-shifted in frequency, generating Stokes light at longer wavelengths. The pump-to-Stokes transition simultaneously triggers an optical phonon wave of synchronized molecular vibrations across the gas medium [7]. Within its lifetime, this molecular coherence wave can be used to up-shift the frequency of the pump pulse (or an arbitrary signal) by Ω_R to the anti-Stokes band, provided that the propagation constant of the optical phonon is equal to that of the pump-to-anti-Stokes (or signal-to-idler) transition.

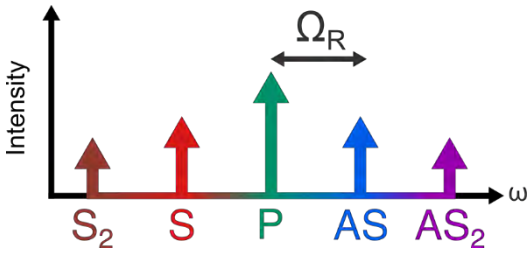

Fig. 1: Sketch of a Raman comb. The color-coding illustrates the frequency shift. The bands represented are the pump (P), Stokes (S), anti-Stokes (AS), 2nd Stokes (S_2) and 2nd anti-Stokes (AS_2).

Gas-filled ARF is an excellent platform for efficient SRS, because it increases the scattering probability through tight light-matter confinement in the small hollow channel, and permits adjustment of the phase-matching conditions through adjustment of the dispersion profile. This is achieved by precisely balancing the contributions of the gas (normal dispersion) and the geometry (anomalous dispersion) of the hollow-core fibre. In absence of loss-inducing resonances with the cladding structure, the frequency-dependent modal propagation constants can be calculated as $\beta = \sqrt{k_0^2 n^2 - u_0^2/a^2}$, where k_0 is the vacuum wavenumber, n is the refractive index of the filling gas, u_0 is the first zero of the 0^{th}-order Bessel function of the first kind and a is the effective core radius [8]. In this work, we engineer the dispersion curve to facilitate the generation of a hybrid Raman comb involving high-order anti-Stokes bands reaching to the DUV (Fig. 1).

3.- Numerical modelling

To fully capture the complex nonlinear interplay between the excited optical phonons, a dispersion analysis alone proves insufficient. We therefore employed a set of coupled Maxwell-Bloch equations [6,7] to model the dynamics of the full dual-Raman-comb system. This framework accounts for 4 anti-Stokes and 4 Stokes sidebands per comb, including their combined interactions and phonons across both frequency-shifted branches.

4.- Results and discussion

To find an optimal scenario for the observation if this phenomenology, we consider a 35 µm-core ARF filled with 15 bar of H_2. This fibre is simultaneously pumped by a 1.8 ns-long pump pulse at 1030 nm and its second harmonic at 515 nm. For simplicity, we restrict our analysis to intramodal interactions, assuming that all signals propagate in the fundamental LP_{01}-like core mode of the ARF.

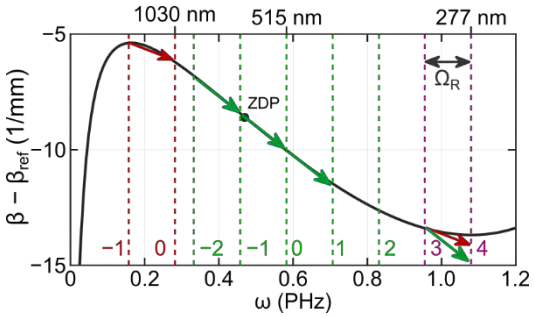

Fig. 2: Dispersion diagram (propagation constant vs. frequency). Each vertical dashed line marks a Raman band, and the optical phonons are represented by color-coded arrows. To bring out the subtle nonlinear dispersion component, we subtract a linear function of frequency β_{ref} to the propagation constants. The zero-dispersion point is marked as ZDP. For simplicity, we disregard the effect of resonances between the core mode and modes localized in the cladding walls.

Figure 2 illustrates the characteristic S-shaped dispersion profile of the system. The pump bands are explicitly labelled (1030 nm and 515 nm), whereas the sidebands are indexed by an integer m that follows the relation: $\omega_m = \omega_0 + \mathrm{m} \cdot \Omega_R$. The two distinct Raman combs are colour-coded (1030 nm: red and 515 nm: green). The arrows (i.e., graphical representations of the optical phonons) connecting the dispersion curve to the sidebands indicate phase-matched transitions that are likely to be efficient. In the same spirit, unmatched bands indicate significant phase mismatch, leading to sub-optimal conversion. In practical terms, the current example is chosen to minimize the overall dephasing and therefore maximize the frequency up-conversion processes.

To validate our concept, we numerically simulated the individual and combined Raman combs to compare their spectral densities at shorter wavelengths. Our results show that the hybrid dual-comb generated in the H_2-filled ARF pumped by two pulses of energies 40 µJ (515 mn) and 25 µJ (near-infrared), exhibits much higher spectral power in the 4th anti-Stokes sideband of the green comb (277.5 nm) than the single comb generated by the 515 nm pump pulse alone (see Fig. 3). Remarkably, this 1000-fold enhancement is achieved using only 50 cm of fibre length, highlighting the influence of the cooperative phonon-mediated nonlinearity.

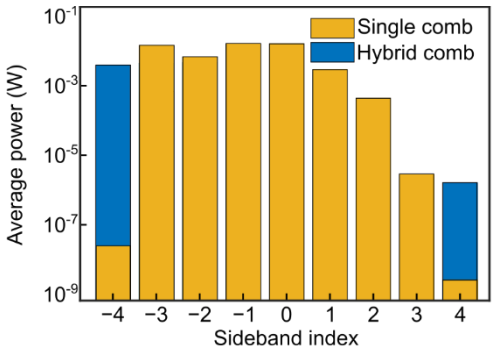

Fig. 3: Histogram representation of the power output of the hybrid Raman comb (logarithmic scale). The blue columns represent the single comb of the 515 nm pump, and the yellow columns represent the 515 nm bands in the hybrid Raman comb. The 4th anti-Stokes band is enhanced by 3 orders of magnitude using bichromatic pumping.

These results demonstrate that dual-Raman-comb systems can achieve higher spectral intensities in the UV spectrum compared to single-comb configurations. Importantly, the selected pump wavelengths (1030 nm + 2nd harmonic 515 nm) were chosen for their practical advantages. They are experimentally accessible with standard laser systems and require minimal optical architecture for generation. This combination of high efficiency, compactness and cost-effective design, sets our platform as a viable solution for scalable UV light sources.

5.- Conclusions and outlook

In this work, we have demonstrated that bichromatic pumping in gas-filled hollow-core fibres generates a hybrid Raman comb with higher spectral density in the UV compared to a single comb. By using two common and accessible wavelengths (515 nm and 1030 nm), we achieved efficient up-conversion to the DUV compatible with a compact arrangement. Our results might pave the way to novel fibre-based UV light sources with unprecedented performance.

Acknowledgements: This work was supported by the grants PID2021-123131NA-I00, PID2021-122505OB-C31, PRE2022-102843 and TED2021-129959B-C21, funded by MICIU/AEI/10.13039/501100011033, by "ERDF a way of making Europe", by the "European Union NextGenerationEU/PRTR" and "ESF+", and the Gobierno Vasco/Eusko Jaurlaritza (IT1452-22), ELKARTEK (μ4Smart-KK-2023/00016 and Ekohegaz II-KK-2023/00051), and the "Translight" initiative of UPV/EHU, and the IKUR Strategy of the Department of Education of the Basque Government through the grant IKUR_IKA_23/03.

References

[1] M. T. NEVES-PETERSEN, G. P. GAJULA, S. B. PETERSEN, *"UV light effects on proteins: from photochemistry to nanomedicine"*, in Molecular Photochemistry, S. Saha ed., IntechOpen, 2012.

[2] Y. SHI, Z. CUI, M. SUN et *al.*, *"Deep-UV laser source base on $\chi^{(2)}$ optical frequency conversion and $\chi^{(3)}$ stimulated Raman scattering"*, Opt. Lett., **50,** 1136-1139, 2025.

[3] P. St. J. RUSSELL, P. HÖLTZER, W. CHANG *et al.*, *"Hollow-core photonic crystal fibres for gas-based nonlinear optics",* Nat. Photonics, **8**, 278-286, 2014.

[4] J. C. TRAVERS, T.F. GRIGOROVA, C. BRAHMS *et al., "High-energy pulse self-compression and ultraviolet generation through soliton dynamics in hollow capillary fibres",* Nat. Photonics, **13,** 547-554 (2019).

[5] M. K. MRIDHA, D. NOVOA, P. HOSSEINI *et al., "Thresholdless deep and vacuum ultraviolet Raman frequency conversion in hydrogen-filled photonic crystal fiber",* Optica, **6,** 731-734 (2019).

[6] R. TYUMENEV, P. St. J. RUSSELL, D. NOVOA, *"Narrowband Vacuum Ultraviolet Light via Cooperative RamanScattering in Dual-Pumped Gas-Filled Photonic Crystal Fiber",* ACS Photonics, **7**, 1989-1993, 2020.

[7] P. ARCOS, A. MENA, M. SÁNCHEZ-HERNÁNDEZ *et al.*, "*Narrowband stimulated Raman scattering and molecular modulation in anti-resonant hollow-core fibres*," EPL, **147**, 45001, 2024.

[8] F. MELLI, L. ROSA, K. VASKO *et al.*, "*Analytical Framework for Mode-Coupling in Hollow-Core Inhibted-Coupling Fibers*," J. Light. Technol., in press, 2025.

Ultrafast Bright Squeezed Vacuum Light Source

María SÁNCHEZ-HERNÁNDEZ [1], Miriam LAZO [2], Arturo MENA [1], Tasio GONZÁLEZ-RAYA [3, 4], Mikel SANZ [2, 3, 4, 5], Joseba ZUBIA [1, 4], David NOVOA [1, 4, 5]

1. Department of Communications Engineering, University of the Basque Country (UPV/EHU), Torres Quevedo 1, 48013 Bilbao, Spain.
2. Department of Physical Chemistry, University of the Basque Country (UPV/EHU), Apartado 644, 48080 Bilbao, Spain.
3. Basque Centre for Applied Mathematics (BCAM), Alameda de Mazarredo 14, 48009 Bilbao, Spain.
4. EHU Quantum Centre, University of the Basque Country (UPV/EHU), 48013 Bilbao, Spain.
5. IKERBASQUE, Basque Foundation for Science, Plaza Euskadi 5, 48009 Bilbao, Spain.

Contact: María SÁNCHEZ-HERNÁNDEZ (maria.sanchezh@ehu.eus).

ABSTRACT:

Bright squeezed vacuum is a macroscopic quantum light state with smaller fluctuations than the vacuum in one of the field quadratures. These states can be generated via parametric down-conversion in nonlinear crystals. Once generated, understanding their interactions with matter, particularly at ultrafast time scales, is of utmost importance, for example, for replicating or transferring its quantum properties to other spectral regimes via nonlinear processes. Here we summarize our current efforts towards an ultrafast bright squeezed vacuum source operating in the near-infrared and with a pulse duration of hundreds of femtoseconds. We also explore theoretically a viable strategy for the spectral down-conversion of this source via quantum-enhanced stimulated Raman scattering inside hollow-core anti-resonant fibres. Our results might open new paths for quantum advantage in fields such as spectroscopy, microscopy and metrology.

Key words: Bright squeezed vacuum, ultrafast quantum optics, stimulated Raman scattering, hollow-core anti-resonant fibres.

1.- Introduction

Quantum states of light have become of great interest over the last decades. Among others, squeezed states present fluctuations below those of the vacuum for one of the field quadrature operators (Fig. 1(a)) [1]. When these states originate from vacuum noise, these vacuum fluctuations are called squeezed vacuum (Fig. 1(b)). Interestingly, the quantum properties of squeezed vacuum are maintained even if the number of photons is macroscopically large, giving rise to the so-called bright squeezed vacuum (BSV). Recent experimental work has achieved squeezed macroscopic states up to 10^{13} photons [2].

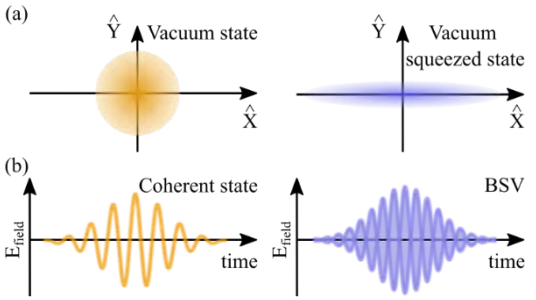

Fig. 1: (a) Phase diagrams for vacuum (yellow) and squeezed vacuum (blue) states. The former presents the same uncertainty for both quadratures, while for the latter the $\hat{Y}$ quadrature is squeezed. (b) Field representation for a coherent state with amplitude fluctuations around a non-zero mean value (yellow) and vacuum fluctuations with zero amplitude mean value (blue).

Squeezing can enhance the signal-to-noise ratio, and bright states are easily tailorable, so BSV constitute a powerful tool in several fields, such as quantum illumination protocols [3], optical imaging [4], measurement of gravitational waves [5], or spectroscopy [6].

One of the ways of achieving BSV light is via parametric down-conversion (PDC), a second-order nonlinear phenomenon where two photons, customarily called signal and idler, are generated from a single pump photon of higher energy. For that to be possible, energy and momentum must be conserved during the nonlinear interaction, a situation that can happen both in collinear or non-collinear geometries. This will in turn give rise to either spot-shaped or ring-shaped transversal profiles for signal and idler [7].

On the other hand, the Hamiltonian describing this kind of process has the form of a squeezing operator, which means that signal and idler outputs will always be squeezed. The parametric gain that quantifies the increase in the mean photon number, is also called squeezing parameter since it provides direct information about the reduction in the fluctuations of a given quadrature [7]. Thus, the brighter the source is, the more squeezed it becomes. The parametric gain depends on both pump and nonlinear medium properties, such as beam radius, electric field amplitude, nonlinear susceptibility or crystal length. For lower values of the gain, the process is called spontaneous PDC, leading to two-photon states or entangled photon pairs. However, if the parameter increases above unity, the generation rate is enhanced: photons produced at the beginning of the nonlinear medium seed the generation towards the end. Therefore, the generation rate and the number of produced photons increase exponentially along the nonlinear medium, allowing for a bright state.

Numerous studies of BSV generation have been reported employing picosecond-long pump pulses [8]. However, accessing the femtosecond regime is particularly attractive since it enables access to strong nonlinear interactions between BSV and matter [2, 9]. This new scenario poses many fundamental questions, such as, for example, how the quantum properties of the source can be transferred unaltered to other spectral domains in a controllable manner. In this regard, phenomena such as stimulated Raman scattering (SRS) in gases can be used for frequency down-conversion of quantum light. In Raman scattering, pump photons are scattered off in a molecular ensemble and excite molecules from the ground state to a vibrational excited state, emitting Stokes photons; or vice versa, emitting anti-Stokes photons [10]. On the other hand, anti-resonant hollow-core optical fibres constitute a promising candidate for pumping molecular gases with quantum light in a confined geometry. Typical guidance windows can extend from the ultraviolet to the mid-infrared, and their high damage threshold allows guided peak intensities up to 1 PW/cm^2 [11], making them an excellent platform for nonlinear photonics.

Here we summarize our current efforts towards an ultrafast BSV source operating in the near-infrared and with a pulse duration of hundreds of femtoseconds for quantum-enhanced light-matter interactions. We discuss how judicious adjustment of the set-up parameters allow for tuning several source properties, such as spectrum, spatial mode or squeezing. In addition, as an example of such quantum-enhanced interactions, we present our ongoing theoretical work on using this BSV source as a pump for stimulated Raman scattering in anti-resonant hollow core fibres.

2.- Bright squeezed vacuum generation

For the generation of BSV via PDC, a pump beam is focused into a 2-mm-thick β-barium borate (BBO) crystal (Fig. 2). The pump is an ultrafast laser emitting linearly-polarized pulses of ~200 fs FWHM duration and up to 1 mJ energy, centred at 515 nm. The repetition rate of the system is adjustable up to 10 kHz.

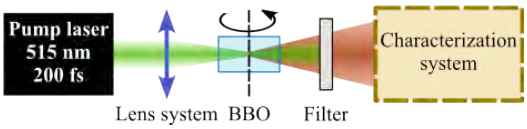

Fig. 2: Experimental set-up for the generation of ultrafast bright squeezed vacuum. The arrow above the BBO crystal indicates the possibility of tilting it for tuning the emission properties.

A two-lens arrangement permits control over the waist size and Rayleigh length of the propagating beam irradiating the BBO crystal. With all these tuning knobs, high values of the parametric gain and, consequently, high photon numbers and squeezing, can be achieved. After the nonlinear interaction in the crystal, the pump is filtered out so that the BSV emission can be unambiguously detected and characterized.

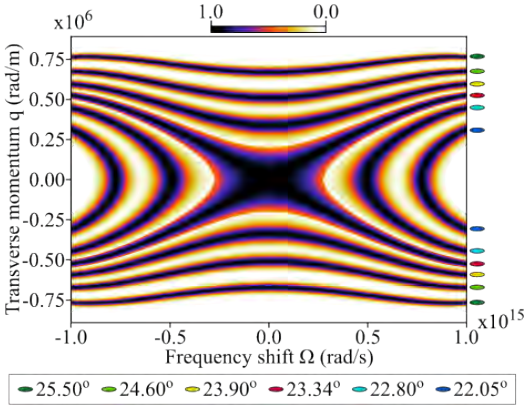

Fig. 3: Theoretical PDC spectra for different crystal orientations. Frequency shift is measured with respect to the degenerate 1030 nm wavelength. Spectra are displayed by changing the angle between the pump wavevector and the optical axes. The corresponding angles are represented by color-coded ellipses at the right edge of the plot.

The crystal is cut for type I degenerate PDC at 515 nm. Tilting the crystal modifies the angle between the pump wavevector and the optical axis in the crystal, thus changing the extraordinary refractive index in the pump propagation and its wavevector. This leads to modification of the phase-matching conditions, so that they are fulfilled for different signal-idler frequency pairs if the angle decreases, or for non-collinear geometry otherwise. Therefore, the spatio-spectral characteristics of the generated BSV can be largely controlled by simple adjustment of the crystal rotation (Fig. 3). Energy conservation forces the signal and idler frequency pairs to be symmetrically shifted a given frequency Ω around the degenerate signal at 1030 nm. On the other hand, the ring aperture in non-collinear cases can be represented by the transverse component of the wavevector q, since phase matching only depends on signal and idler wavevector orientations given a frequency pair and its corresponding refractive index for a fixed angle with the optical axis.

3.- BSV as pump source for SRS

The behaviour and space-time evolution of a classical field driving SRS inside a gas-filled hollow-core anti-resonant fibre can be described using a semiclassical Hamiltonian [12]. However, when dealing with non-classical states of light such as BSV, it is desirable to obtain a full quantum model to describe the interaction.

3.1.- Quantum Hamiltonian for SRS inside hollow-core anti-resonant fibres

The following quantum Hamiltonian was recently used to describe SRS inside hollow-core anti-resonant fibres along the propagation direction z [13]:

$$H = \hbar\Omega_{\mathrm{R}} J_z + \hbar\omega_P a_P^\dagger a_P + \hbar\omega_S a_S^\dagger a_S + \hbar G e^{(i\Delta\beta z)} a_P a_S^\dagger J^+ + \hbar G^* e^{(-i\Delta\beta z)} a_P^\dagger a_S J^-. \quad (1)$$

Here, molecules are described as two-level systems and collectively modelled as a spin system of size equal to the number of molecules inside the fibre. The spin operators (J_z, J^+, J^-) act on such global state, while the ladder operators act on the pump mode $(\mathrm{a_P}, \mathrm{a_P^\dagger})$, and on the Stokes mode $(a_S, a_S^\dagger)$.

The first term in Eq. (1), $\hbar\Omega_{\mathrm{R}} J_z + \hbar\omega_P a_P^\dagger a_P + \hbar\omega_S a_S^\dagger a_S$, corresponds to the self-energies of the molecules (with Ω_{R} as the frequency of the first vibrational level), the pump photons (with frequency ω_P) and the Stokes Photons (with frequency ω_S), respectively. The remaining terms describe the Raman interaction itself, accounting for the process where a pump photon is absorbed, generating one global molecular excitation and the emission of a frequency shifted Stokes photon, and the inverse process. These interaction terms depend on the parameter G, which is the coupling strength between the two photon modes and the molecules, and the dispersion of the fibre, modelled through the modal propagation constants β.

3.2.- BSV states as pump fields

The initial state of the system can be written as $S_P|0\rangle_P|i\rangle_S|I\rangle_M$, where $|i\rangle_S$ is the state of the Stokes photons, and $|I\rangle_M$ is the state of the molecules. The initial state of the pump photons, $S_P|0\rangle_P$ represents a BSV state, where S_P is the squeezing operator acting on the vacuum state. In order to obtain the final states of the pump, the Stokes photons and the molecules, the propagator for this Hamiltonian, $\exp\{(-i(t/\hbar)H\})$, has to be applied to the initial state. Due to the light-molecules coupling in the Hamiltonian, obtaining the final state of the system is not a trivial task and it is necessary to make several approximations to gain insight on the behaviour of the system.

The squeezing operator can be considered to induce a transformation on the pump ladder operators [1], giving a transformed Hamiltonian, $S_P^{\dagger}\mathrm{H}S_P$, easier to manipulate. By making this approximation, the operators acting on the pump mode are globally coupled to those acting on the Stokes mode and the molecules, which remain coupled through operators of different type. Since the system is initially in the low molecular excitation regime, a Holstein-Primakoff transformation [14] enables the mapping of the molecular spin ladder operators into ladder operators as the Stokes-type ones $(b, b^{\dagger})$, as shown in Eq. (2).

$$S^{\dagger}\,\mathrm{HS} \approx \hbar|G|\cosh(r)\sqrt{N}\left(a_P - a_P^{\dagger}\right)\mathrm{x}$$

$$\mathrm{x}\left(a_S b e^{-i(\phi+\Delta\beta z)} - a_S^{\dagger} b^{\dagger} e^{i(\phi+\Delta\beta z)}\right) \quad (2)$$

where r represents the squeezing parameter. With this Hamiltonian, the time evolution equations for the Stokes operators (Heisenberg picture) will only depend linearly on the molecule operators and on $(a_P - a_P^{\dagger})$. This frame would lead to expressions for the state evolution in the initial times and, after additional approximations, the evolution of the state as time goes on.

4.- Conclusions

Bright squeezed vacuum is a powerful tool for many applications of lightwave quantum technologies. To unlock its full potential, it is essential to develop tailorable sources of BSV and understand their interactions with matter in various scenarios. This work proposes an experimental set-up for the generation of a tuneable and gain-controllable ultrafast BSV source operating in the femtosecond regime. In addition, we theoretically explore a viable route to the spectral translation of such quantum light source using SRS in hollow-core anti-resonant fibres. Our preliminary results indicate that this challenge can be tackled using an approximated Hamiltonian where molecules and Stokes photons are coupled among them and globally to the pump mode. The practical implementation of these results might enable new paths to quantum advantage in fields such as spectroscopy, microscopy and metrology.

Acknowledgements: This work has been supported by HORIZONCL4-2022-QUANTUM01-SGA project 101113946 OpenSuperQ-Plus100 of the EU Flagship on Quantum Technologies, the Spanish Ramón y Cajal Grant RYC-2020-030503-I, project Grants No. PID2021-123131NA-I00, PID2021-125823NA-I00, PID2021-122505OB-C31 and TED2021-129959B-C21, funded by MICIU/AEI/10.13039/501100011033 and by "ERDF a way of making Europe", by "ERDF Invest in your Future", by the "European Union NextGenerationEU/PRTR" and "ESF+". We also acknowledge support from the Spanish Ministry of Economic Affairs and Digital Transformation through the QUANTUM ENIA project call –Quantum Spain, and by the EU through the Recovery, Transformation and Resilience Plan–NextGenerationEU within the framework of the Digital Spain 2026 Agenda, as well as from the Basque Government through Grants No. IT1455-22 and IT1470-22 and ELKARTEK (µ4Smart-KK2023/00016, Ekohegaz II-KK-2023/00051, and KUBIT KK-2024/00105), and from the IKUR Strategy under the collaboration agreement between Ikerbasque and BCAM on behalf of the Department of Education of the Basque Government and the grant IKUR IKA 23/04. MS-H and ML acknowledge support from the predoctoral grant "Formación de Profesorado

Universitario" FPU22/01451 and FPU23/02350, respectively, from the Spanish Ministry of Science, Innovation and Universities (MICIU).

References

[1] R. LOUDON, P. L. KNIGHT, *"Squeezed Light"*, Journal of Modern Optics, 34, 6-7, 709-759, 1987.

[2] A. RASPUTNYI, Z. CHEN, M. BIRK, O. COHEN, I. KAMINER, M. KRÜGER, D. SELETSKIY, M. CHEKHOVA, F. TANI, *"High-harmonic generation by a bright squeezed vacuum"*, Nature Physics, 20, 1960-1965, 2024.

[3] G. MASADA, *"Two-mode squeezed light source for quantum illumination and quantum imaging"*, in Proceedings of SPIE Quantum Communications and Quantum Imaging XIII, 961503, 2015.

[4] G. BRIDA, M. GENOVESE, I. R. BERCHERA, *"Experimental realization of sub-shot-noise quantum imaging",* Nature Photonics, 4, 227-230, 2010.

[5] M. TSE, H. YU, N. KIJBUNCHOO, A. FERNANDEZ-GALIANA, P. DUPEJ, L. BARSOTTI, C. D. BLAIR, D. D. BROWN, S. E. DWYER, *"Quantum-Enhanced Advanced LIGO Detectors in the Era of Gravitational-Wave Astronomy"*, Physical Review Letters, 123, 231107, 2019.

[6] P. CUTIPA, M. V. CHEKHOVA, *"Bright squeezed vacuum for two-photon spectroscopy: simultaneously high resolution in time and frequency, space and wavevector"*, Optics Letters, 47, 465-468, 2022.

[7] D. N. KLYSHKO, *"Photons Nonlinear Optics"* (Routledge, 1988).

[8] A. M. PÉREZ, T. SH. ISKHAKOV, P. SHARAPOVA, S. LEMIEUX, O. V. TIKHONOVA, M. V. CHEKHOVA, G. LEUCHS, *"Bright squeezed-vacuum source with 1.1 spatial mode"*, Optics Letters, 39, 2403-2406, 2014.

[9] M. E. TZUR, O. COHEN, *"Motion of charged particles in bright squeezed vacuum"*, Light: Science & Applications, 13, 41, 2024

[10] V. V. YAKOVLEV, G. I. PETROV, H. F. ZHANG, G. D. NOOJIN, M. L. DENTRON, R. J. THOMAS, M. O. SCULLY, *"Stimulated Raman scattering: old physics, new applications"*, Journal of Modern Optics, 56, 18-19, 1979-1973, 2009.

[11] C. WEI, J. WEIBLEN, C. R. MENYUK, J. HU, "*Negative curvature fibers*", Advances in Optics and Photonics, 9, 3, 504-561, 2017.

[12] M. G. RAYMER, I.A. WALMSLEY, *"III. The quantum coherence properties of stimulated Raman scattering",* Progress in Optics, 28, 181-270, 1990.

[13] T. GONZALEZ-RAYA, A. MENA, M. LAZO, L. LEGGIO, D. NOVOA, M. SANZ, *"Entanglement transfer during quantum frequency conversion in gas-filled hollow-core fibers"*, APL Photonics, *in press*, 2025.

[14] H. PRIMAKOFF, T. HOLSTEIN, "*Many-Body Interactions in Atomic and Nuclear Systems*", Physical Review, 55, 1218, 1939.

Towards a broadband measurement of waveguide dispersion curves

Marc P. SAFONT [(1)], Enrique SILVESTRE [(1,2)], Antonio DÍEZ [(1,3)], Martina DELGADO-PINAR [(1,3)], Miguel V. ANDRÉS [(1,3)], David CASTELLÓ-LURBE [(1,3)].

1. Institut de Ciència dels Materials (ICMUV), Universitat de València, Catedràtic José Beltrán 2, 46980 Paterna, València, Spain.
2. Departament d'Òptica i Optometria i Ciències de la Visió, Universitat de València, Dr. Moliner 50, 46100, Burjassot, València, Spain.
3. Departament de Física Aplicada i Electromagnetisme, Universitat de València, Dr. Moliner 50, 46100, Burjassot, València, Spain.

Contact: Marc P. SAFONT (marc.perez@uv.es).

ABSTRACT:

The dynamics of light pulses inside waveguides is often governed by the generalized nonlinear Schrödinger equation (GNLSE), where the interplay between nonlinear and dispersive effects determines the behavior of the electromagnetic field. Thus, knowledge about the nonlinear coefficient and the group-velocity dispersion curve is crucial to help understand and predict the evolution of pulses along the system. The use of a GNLSE conservation law allows a direct measurement of the ratio between the group-velocity dispersion parameter and the nonlinear coefficient. We propose and numerically validate a broadband technique to measure higher order dispersion coefficients obtaining good agreement over more than 200 THz.

Key words: nonlinearities, Kerr effect, chromatic dispersion, supercontinuum, pulses, waveguides.

1.- Introduction

Waveguides are key components in contemporary photonics, allowing light confinement and therefore enhancing light-matter interaction, that permit the study of nonlinear effects when the intensity of the electromagnetic field is sufficient. The most used tool to model the propagation of light pulses through a waveguide in the monomode regime is the GNLSE [1]

$$\partial_z \tilde{A}(z,\Omega) = i\beta_{\mathrm{p}}(\Omega)\tilde{A}(z,\Omega) + i\gamma_0 F[|A(z,T)|^2 A(z,T)], \quad (1)$$

$$\tilde{A}(z,\Omega) = F[A(z,T)], \quad (2)$$

where $A(z,T)$ represents the slowly varying envelope of the optical pulse, $\tilde{A}(z,\Omega)$ its Fourier transform, z is the propagation direction, T is the time expressed in the reference frame of the pulse and $\Omega = \omega - \omega_0$ is the frequency relative to the central frequency of the pulse. This partial differential equation involves the nonlinear coefficient, γ_0, which quantifies the strength of the nonlinear interaction and accounts for the Kerr effect, and the dispersion curve, $\beta_{\mathrm{p}}(\Omega)$. Both are determined by the transverse section of the waveguide. This function admits a Taylor decomposition

$$\beta_{\mathrm{p}}(\Omega) = \sum_{n=2}^{N} \frac{\beta_n}{n!}\Omega^n, \quad (3)$$

where β_n is the n-th order of dispersion. At high input powers the phenomenon of supercontinuum generation (SCG) is possible. Starting from a narrowband laser, the output of the waveguide reveals a bandwidth that can

span even hundreds of THz as a consequence of the interplay between nonlinearities and dispersion. Moreover, dispersion impacts on the phase-matching conditions for any nonlinear process occurring in the waveguide. Consequently, the form of the output spectrum is strongly conditioned by the shape of the dispersion curve.

Usual techniques for measuring waveguides dispersion are based on interferometric setups, such as a Michelson-type configuration. The phase difference between each arm of the interferometer results in an interferogram of maxima and minima, registered in an optical spectrum analyzer (OSA). This phase encodes the waveguide dispersion. There are several ways to extract the dispersion coefficients from this measurement, such as differential measurement from the position of the maxima and minima, direct fitting of the interferogram function or extraction of the phase. However, these strategies involve polynomial fittings to address higher order dispersion [2, 3]. Ref. [2] reports a measurement up to the fourth order dispersion by means of a direct fitting of the interferogram, which results in good experiment-to-theory agreement for β_2 and β_3 but large discrepancies when extracting β_4. Ref. [3] describes a direct phase extraction method implemented in an analogous setup, allowing a precise measurement of second and third-order dispersion.

Some differences can be argued with respect to our approach. Interferometric techniques require short fiber lengths, while our method can be implemented with virtually no limitations due to fiber length. Additionally, broadband sources are required to extract information of higher order dispersion through an interferometric setup. Exploiting SCG, our technique does not need to pump directly over a broad spectral range. The intuitive idea underlying our proposal is to take advantage of the print left by the dispersion curve on the output supercontinuum spectrum to measure it. Moreover, the fact that different physical observables are linked to each dispersion term can be considered an advantage compared to interferometric methods, in which a single observable is linked to the entire dispersion curve, since it is this fact at its core that makes it necessary to use polynomial fittings. This requirement increases the error from the original data, an issue that becomes limiting if one goes several iterations beyond a first derivative, which would be needed when addressing higher order dispersion terms [4].

2.- Working principles

Starting from Eq. (1) it is possible to derive a conservation law of the GNLSE following Ref. [5],

$$\frac{\mathrm{d}}{\mathrm{d}z}\left(\frac{\gamma_0\int_{-\infty}^{\infty}|A(z,T)|^4\mathrm{d}T}{2\int_{-\infty}^{\infty}|A(z,T)|^2\mathrm{d}T} + \frac{\int_{-\infty}^{\infty}\beta_\mathrm{p}(\Omega)\left|\tilde{A}(z,\Omega)\right|^2\mathrm{d}\Omega}{\int_{-\infty}^{\infty}\left|\tilde{A}(z,\Omega)\right|^2\mathrm{d}\Omega}\right)=0. \tag{4}$$

The quantities involved in the conservation law can be reinterpreted as experimentally accessible pulse characteristics [6]:

$$\rho(z)=\frac{\int_{-\infty}^{\infty}|A(z,T)|^4\mathrm{d}T}{2\int_{-\infty}^{\infty}|A(z,T)|^2\mathrm{d}T},$$
$$\mu_n=\frac{\int_{-\infty}^{\infty}\Omega^n\left|\tilde{A}(z,\Omega)\right|^2\mathrm{d}\Omega}{\int_{-\infty}^{\infty}\left|\tilde{A}(z,\Omega)\right|^2\mathrm{d}\Omega}, \tag{5}$$

where $\rho(z)$ is proportional to the pulse autocorrelation at zero time delay, and therefore can be measured with the use of an autocorrelator, and μ_n is n-th spectral moment, which needs an OSA in order to be determined for any n. Accordingly, the experimental setup, which is sketched in Fig. 1, can be considered relatively simple. Integrating over the length of the waveguide, L, the conservation law can be expressed in terms of path independent quantities,

$$\Delta\rho+\sum_{n=2}^{N}\frac{\beta_n}{n!\,\gamma_0}\Delta\mu_n=0, \tag{6}$$

where $\Delta X = X(L)-X(0)$ have been defined. Since input power is an experimentally controllable parameter, it allows generating the set of points that are contained in the

hyperplane defined by Eq. (6) and the subsequent fitting provides information about the slopes (the $\beta_n/n!\,\gamma_0$ coefficients).

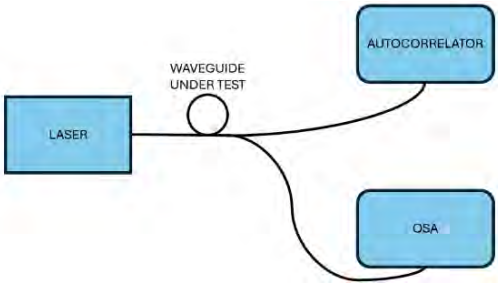

Fig. 1: Experimental setup scheme.

The results reported in Ref. [6] constituted the first experimental proof-of-concept of the method in the case $N = 2$, i.e., considering a flat dispersion curve. It is worth emphasizing that although we generalize the conservation law with the aim of proposing a broadband measurement, i.e., including higher order dispersion, not only the experimental setup does not change at all, but the measurements do not vary either. That is due to the fact that only the spectrum is needed to compute any spectral moment (μ_n).

Eq. (6) provides us a fit to an N dimensional hyperplane. In order to infer N, i.e., which is the highest order dispersion term needed to describe the relevant dispersion curve, we will make use of statistical parameters provided by the multiple linear fit. The fit also associates an error (σ) to each parameter, which can thus become compatible with zero. The quantity that quantifies this issue is the p-value, which is directly calculated from σ [7]. Following the 5σ limit as it is done in other physical scenarios [8], the upper limit for the p-value is stated in 10^{-5}. If the p-value obtained by the fit is higher than this limit, the parameter will be compatible with zero and therefore will not be needed for describing the dispersion curve. Conversely, if it is lower, we will take it into account.

The propagation in a nonlinear media by means of the GNLSE will be simulated using software owned by the Laboratory of Fiber Optics (LFO) based on a Runge-Kutta (RK) method and employing fast Fourier transforms (FFT). RK algorithms allow solving first degree partial differential equations of the form $\mathrm{d}A/\mathrm{d}z = H[z]$, while FFT are applied to evaluate the Fourier transforms in $H[z]$, see Eq. (1), efficiently.

We will add a 5 % random error in $\Delta\rho$ to account for the experimental uncertainty of the power measurements demanded to determine ρ. Note that this error is not due to any approximation involved in the conservation law, and consequently Eq. (6), which is an exact property of GNLSE. The errors affecting the spectral moments can be safely neglected. Moreover, despite large losses occur when coupling light into a chip, the power uncertainty remains below 5 % [9,10].

3.- Results

3.1.- Broadband measurement

The numerical proof-of-concept of our method will be performed simulating the silicon nitride chip of Ref. [11], where 1.4 octaves coherent SCG is experimentally demonstrate pumping at 1µm. As in the experiment, 92 fs long Gaussian pulses will be employed in our simulations. The dispersion curve associated to the 8 mm long silicon nitride chip of transverse dimensions 690×900 nm is shown in Fig. 2. Knowing the nonlinear coefficient from the reference, $\gamma_0 = 3\,\mathrm{W^{-1}m^{-1}}$, here we will apply our new methodology to numerically measure the full dispersion curve pumping at $\lambda_0 = 1030$ nm ($\nu_0 = 292$ THz). Input peak powers span up to 530 W.

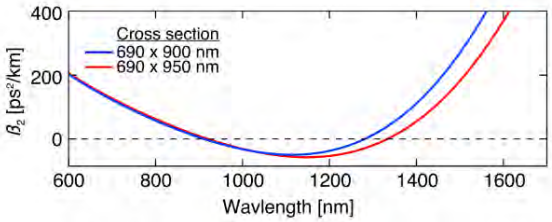

Fig. 2: $\beta_2(\Omega) = \frac{d^2}{d\Omega^2}\beta_\mathrm{p}(\Omega)$ as a function of the wavelength for the silicon nitride chip, extracted from Ref. [11]. The 690×900 nm case is addressed in this work.

Following the methodology as disclosed in the previous section, the p-values obtained for each parameter as a function of the space dimension leads to conclude that the optimal

dimension is $N = 6$, as it minimizes the largest number of p-values. This is in correspondance with the sampled dispersion curve used for the simulations, which we described as $\beta_{\mathrm{p}}(\Omega) = \sum_{n=2}^{N=6} \frac{\beta_n}{n!}\Omega^n$. The results from the numerical simulation of the experiment are shown in Table 1. We can state that the results are excellent, since the relative error given by the fit in the right column remains around 5 %, namely, similar to the Δρ error. Note that this fact represents a remarkable improvement with respect to techniques demanding polynomial fittings. A fair check between the obtained values and the actual parameters can be done by comparing their corresponding dispersion curves, which is done in Fig. 3. Superimposing the highest power output spectrum with the dispersion curve highlights the idea that the dispersion profile is encoded in the broadened spectra.

Table 1: Results of the fit pumping at 1030 nm. Comparison between the simulated value and the nominal one (fitted from Fig. 2) can be extracted from this table.

Coefficient	***Nominal Value***	***Result***	***Error***
β_2/γ_0	-1.22×10^{-2} W ps^2	$(-1.22 \pm 0.02) \times 10^{-2}$ W ps^2	1 %
β_3/γ_0	4.28×10^{-5} W ps^3	$(4.43 \pm 0.24) \times 10^{-5}$ W ps^3	5 %
β_4/γ_0	1.50×10^{-7} W ps^4	$(1.51 \pm 0.10) \times 10^{-7}$ W ps^4	6 %
β_5/γ_0	-1.23×10^{-9} W ps^5	$(-1.27 \pm 0.07) \times 10^{-9}$ W ps^5	6 %
β_6/γ_0	8.83×10^{-12} W ps^6	$(8.81 \pm 0.36) \times 10^{-12}$ W ps^6	4 %

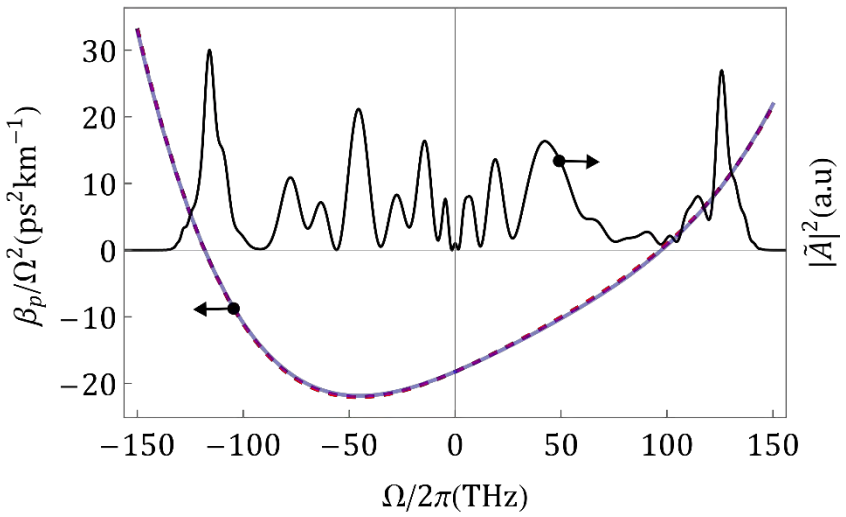

Fig. 3: Comparison between the dispersion curves using our approach (red dashed) and from Fig. 2. The output spectrum at the highest peak power considered in this measurement (black) is superimposed.

4.- Conclusion

This work constitutes numerical basis supporting the feasibility of a novel technique enabling the challenging measurement of higher order dispersion, generalizing the method presented in Ref. [6]. For the first time, the phenomenon of SCG is proposed for determining the dispersion over broad spectral ranges, based on a conservation law of GNLSE, as well as a methodology relying on statistical parameters to optimally handle the quantities associated with the fit. The

numerical measurement achieves accuracy comparable to the error included in the simulated quantities, in contrast to traditional interferometric techniques, supporting the viability of the method and paving the way for its experimental demonstration.

Acknowledgements: This work has been funded by Ministerio de Ciencia, Innovación y Universidades (PID2023-146725OB-I00, María Zambrano Fellowship ZA21-053, TED2021-130200B-I00, CNS2023-145717); European Commission (H2020-MSCA-RISE-2019 872049, María Zambrano Fellowship ZA21-053); Generalitat Valenciana (CIPROM/2022/030).

References

[1] Grovind P. AGRAWAL, *"Nonlinear Fiber Optics"* (Optics and Photonics. Academic Press, 1995).

[2] F. LEO, U. DAVE, S. KEYVANINIA, B. KUYKEN and G. ROELKENS, "*Measurement and tuning of the chromatic dispersion of a silicon photonic wire around the half band gap spectral region*", Optics Letters, 39, 711-714, 2014.

[3] Giorgio M. PONZO, Marco N. PETROVICH, Xian FENG, Peter HORAK, Francesco POLETTI, Periklis PETROPOULOS, and David J. RICHARDSON, "*Fast and broadband fiber dispersion measurement with dense wavelength sampling*", Optics Express, 22, 943-953, 2014.

[4] J. FOX, "*Applied Regression Analysis and Generalized Linear Models*" (Sage Publications, 2015).

[5] David CASTELLÓ-LURBE, Pedro ANDRÉS, and Enrique SILVESTRE, "*Dispersion-to-spectrum mapping in nonlinear fibers based on optical wave-breaking*", Optics Express, 21, 28550-28558, 2013.

[6] David CASTELLÓ-LURBE, Antonio CARRASCOSA, Enrique SILVESTRE, Antonio DÍEZ, Jurgen VAN ERPS, Nathalie VERMEULEN, and Miguel V. ANDRÉS, "*Measurement of the soliton number in guiding media through continuum generation*", Optics Letters, 45, 4432-4435, 2020.

[7] G. COWAN, "*Statistical data analysis*" (Oxford University Press, 1998).

[8] G. COWAN, K. CRANMER, E. GROSS and O. VITELLS, "*Asymptotic formulae for likelihood-based tests of new physics*", Eur. Phys. J., 71, 1554-1572, 2011.

[9] Y. A. VLASOV and S. J. MCNAB, "*Losses in single-mode silicon-on-insulator strip waveguides and bends*", Optics Express, 12, 1622-1631 (2004).

[10] J. VAN ERPS, T. CIUK, I. PASTERNAK, A. KRAJEWSKA, W. STRUPINSKI, S. VAN PUT, G. VAN STEENBERGE, K. BAERT, H. TERRYN, H. THIENPONT and N. VERMEULEN, "*Laser ablation - and plasma etching - based patterning of graphene on silicon-on-insulator waveguides*", Optics Express, 23, 26639-26650, 2015

[11] A. R. JOHNSON, A. S. MAYER, A. KLENNER, K. LUKE, E. S. LAMB, M. R. E. LAMONT, C. JOSHI, Y. OKAWACHI, F. W. WISE, M. LIPSON, U. KELLER and A. L. GAETA, "*Octave-spanning coherent supercontinuum generation in a silicon nitride waveguide*", Optics Letters, 40, 5117-5120, 2015.

Intracavity upconversion of images in the SWIR pumped by a passively V^{3+}:YAG Q-Switched Nd^{3+}:YVO_4 laser at 1342 nm

Adrián J. TORREGROSA [1], María Luisa RICO [2], Haroldo MAESTRE [1], Miguel CUENCA [1] Juan CAPMANY [1]

1. Instituto de Investigación en Ingeniería de Elche, I3E, Universidad Miguel Hernández, Av. de la Universidad s/n, 03202 Elche, (Alicante).
2. Depto. de Tecnología Informática y Computación, Universidad de Alicante, Ctra. San Vicente s/n, 03690 San Vicente del Raspeig, Alicante.

Contact: Adrián J. TORREGROSA (ajtorregrosa@umh.es).

ABSTRACT:

We present a short wave infrared (SWIR) image wavelength converter based on a passive Q-switched Nd^{3+}:YVO_4 solid-state laser at 1342 nm by a V^{3+}:YAG saturable absorber. Inside the laser cavity, the image upconversion takes place in a KTP nonlinear crystal by sum frequency mixing between the SWIR image and the laser oscillation through birefringent phase matching. The identification of an optimal cut of the KTP crystal allows extending the upconversion over a wide spectral range (1300 nm - 1850 nm) for visualization by Si-based CMOS/CCD cameras. An intracavity lenses configuration acting as a beam expander helps keeping the laser beam size fixed inside the Nd^{3+}:YVO_4 crystal for efficient Q-Switching while fitting it to the KTP cross-section for resolution improvement. Given the tradeoff between efficiency and resolution, intracavity intensity levels achieved, in the order of kW/cm^2, allow compensating efficiency provided by such broad beam sizes inside the nonlinear crystal.

Key words: Image upconversion, infrared imaging, nonlinear optics, solid state lasers.

1.- Introduction

La visualización de imágenes y de video en tiempo real en la región espectral del infrarrojo corto o SWIR (1100 nm -2500 nm) es especialmente útil en un amplio abanico de aplicaciones en campos tan diversos como en biomedicina, medioambiente, seguridad y defensa, industria, arte o en el ámbito agroalimentario. En la actualidad existen sensores de imagen IR de tipo array de plano focal o FPA (Focal plane array), basados en InGaAs, InSb o HgCdTe, pero el estado de la tecnología impide ofrecer simultáneamente buenas prestaciones en términos de resolución, contraste (relación señal a ruido) y velocidad, requiriendo en la mayoría de casos sistemas de enfriado para reducir el nivel de ruido a temperatura ambiente. Como consecuencia, las cámaras resultantes son más voluminosas y complejas de manejar. Sin embargo, la tecnología de sensores de tipo FPA basados en silicio reúne todas estas características simultáneamente dando lugar a cámaras más simples, compactas y de bajo coste. Mediante la conversión no lineal de longitud de onda es posible trasladar la información a la región del gap de silicio [1, 2] para aprovechar las prestaciones que ofrecen los sensores de tipo CMOS/CCD.

En este trabajo se propone un sistema convertidor de longitud de onda de imágenes en la región SWIR basado en un láser de estado sólido de Nd^{3+}:YVO_4 con emisión a 1342 nm en régimen pulsado mediante Q-Switch pasivo con absorbente saturable V^{3+}:YAG. En el interior de la cavidad láser tendrán lugar los procesos de mezcla de suma

de frecuencias (SFM, sum frequency mixing) entre las imágenes SWIR y la oscilación láser en un cristal no lineal de KTP. De este modo, la eficiencia de los procesos puede beneficiarse de las elevadas intensidades que se alcanzan intracavidad.

La identificación de un corte específico del cristal de KTP y su orientación óptima permite explotar los procesos de mezcla de interés mediante ajuste de fase birrefringente (BPM) abarcando una amplia región espectral comprendida entre 1300 nm - 1850 nm para su visualización mediante cámaras de CMOS/CCD en la región 660 nm - 770 nm. El sistema propuesto adopta un esquema típico de procesador óptico 4*f* [2]. A diferencia de los sistemas propuestos hasta la fecha, la cavidad láser cuenta además con una disposición de lentes intracavidad en una configuración de expansor de haz que permite adaptar el tamaño del haz en el cristal no lineal y en el cristal láser. El ajuste del haz a la sección del cristal no lineal (radio superior al mm) permite mejorar significativamente la PSF del sistema, y por ende, su resolución. Al mismo tiempo, en el interior del cristal láser se obtiene un tamaño uniforme y constante con el fin de alcanzar un solape espacial óptimo con el haz de bombeo a 808 nm, y mejorar así la eficiencia de la oscilación láser.

2.- Conversión de imagen por SFM.

Los procesos de conversión de longitud de onda de imagen explorados en este trabajo se centran en procesos de SFM mediante BPM en cristales no biaxiales. La imagen que resulta de la iluminación del objeto o de la escena deseados en la región SWIR a la longitud de onda $\lambda_{IR,}$ interacciona en el medio no lineal con la emisión de un láser que actúa como bombeo del proceso a la longitud de onda λ_p. El proceso de mezcla tiene lugar en el interior de la cavidad del láser de bombeo donde se alcanzan elevadas intensidades que permiten conseguir conversiones más eficientes (como se aprecia más adelante en (1)). De este modo, la imagen original se traslada fielmente a la longitud de onda convertida, $\lambda_c^{-1} = \lambda_p^{-1} + \lambda_{IR}^{-1}$ para su detección con sensores de imagen de silicio.

El proceso de conversión se produce en condiciones ideales de no extinción de la potencia de la onda de bombeo y considerando la interacción entre ondas planas e infinitas. La eficiencia relativa del proceso, η, definida como la relación entre la potencia asociada a la imagen convertida, P_c, con respecto a la de la imagen original, P_{IR}, viene dada por [3]:

$$\eta = \frac{8\pi^2 {d_{ef}}^2 L^2 I_P}{\varepsilon_0 c n_{IR} n_P n_C {\lambda_c}^2} \frac{sin^2(\Delta kL/2)}{(\Delta kL/2)^2} \qquad (1)$$

donde d_{ef} es el coeficiente no lineal efectivo del cristal no lineal, $n_{i,}$ es el índice de refracción para las ondas de bombeo (i=p), imagen IR (i=IR) y convertida (i=c), respectivamente. L es la longitud de la interacción, I_p es la intensidad de la onda de bombeo, ε_0 es la permitividad dieléctrica en el vacio, y c es la velocidad de la luz en el vacio. El valor del índice de refracción, n_i=$n_{,}^{p}$ (λ, θ, ϕ) depende de la longitud de onda a través de las expresiones de Sellmeier, de la dirección de propagación definida por el corte del cristal (ángulos θ y ϕ) y de la birrefringencia del cristal, recogida a través de las componentes de polarización ordinara (p=$pol.o$), y extraordinaria, (p=$pol.e$). El desajuste de fase, $\Delta k = \Delta k(\lambda, \theta, \phi)$, queda determinado por los vectores de onda de las ondas interactuantes, $k_i = 2\pi n_i/\lambda_i$, de forma que:

$$\Delta k = k_{IR} + k_p - k_c \qquad (2)$$

Dadas las características dispersivas y no lineales, así como la disponibilidad de cristales en volumen (o tipo *bulk*) de sección amplia que no comprometan la resolución por apertura, y también por su accesibilidad comercial a precios muy competitivos, se decide emplear un cristal no lineal de titanilfosfato de potasio ($KTiOPO_4$) o KTP, crecido por flujo de solución de alta temperatura (KTP tipo F).

La búsqueda del corte óptimo del cristal de KTP se realiza en los planos principales XZ e YZ (ϕ=0º, ϕ=90º, respectivamente), por lo que el objetivo se centra en encontrar el ángulo θ que defina la dirección de propagación (considerando que los procesos son cuasi

colineales) y el estado de polarización de las ondas interactuantes para alcanzar la condición de ajuste de fase (Δk=0) por BPM. Mediante la implementación de un algoritmo en MATLAB, que contempla el comportamiento dispersivo mediante las ecuaciones de Sellmeier [4] y el valor del coeficiente no lineal [5], se buscan aquellos cortes (ángulos θ) en los planos principales que minimicen el desajuste de fase (*phase mismatch*) de los vectores de onda interactuantes sobre el mayor rango espectral, es decir, que proporcionen $\partial\Delta k/\partial\lambda_{IR} \approx 0$.

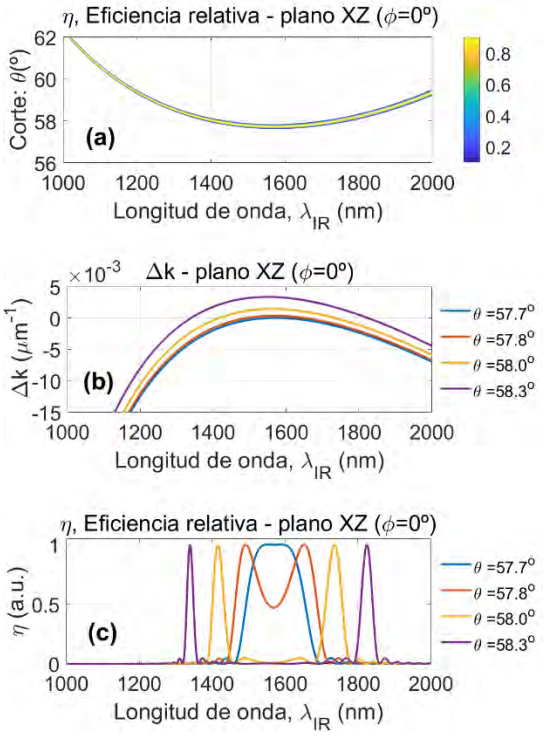

Fig. 1: Características del proceso de SFM en el plano XZ (ϕ=0º) de un cristal de KTP de longitud L=8 mm y con bombeo a 1342 nm: (a) Eficiencia de conversión para distintos cortes en θ. (b) Desajuste de fase Δk. (c) Eficiencia de conversión relativa.

La expresión del coeficiente no lineal efectivo en cristales de KTP para procesos de SFM mediante BPM de tipo II se reduce a: $d_{ef}=d_{31}\times sen(\theta)$ en el plano principal YZ, siendo d_{31} = 2.2 pm/V, *y* $d_{ef}=d_{32}\times sen(\theta)$ en el plano principal XZ, con d_{32} = 3.7 pm/V [5]. Se decide explorar en este último plano para alcanzar eficiencias de conversión más elevadas. El algoritmo proporciona como corte óptimo el centrado en las proximidades de $\theta\approx$60º, ϕ=0º, como se muestra en la Fig. 1, donde se obtiene una amplia banda de conversión en la región SWIR (entre 1300 nm y 1850 nm), y en la que el coeficiente no lineal efectivo se mantiene prácticamente constante $d_{ef}=3.14\pm0.01$ *pm/V*. En la Fig. 1.a se representa la eficiencia de conversion en función de la longitud de onda de iluminación en las proximidades del ángulo de corte $\theta\approx$60º contenido en el plano XZ. Asimismo, en la Fig.1.b, se muestra el comportamiento del desajuste de fase Δk sobre la región de interés, y de forma más clara, a través de la eficiencia de conversión relativa en la Fig.1.c para distintos ángulos en las proximidades del óptimo. Ello permite, mediante un ligero ajuste del cristal ($\Delta\theta=\pm$0.5º) en su plano XZ, obtener una amplia banda espectral de conversión comprendida entre 1300 nm y 1850 nm.

3.- Montaje experimental

En la Fig. 2.a. se muestra el sistema convertidor propuesto. Está basado en un láser de estado sólido de Nd^{3+}:YVO_4 siguiendo una disposición lineal doblada en ángulo recto mediante la utilización de un beam splitter polarizante (PBS). Esta configuración facilitará el acoplo de la imagen IR por polarización al interior de la cavidad donde tendrá lugar la conversión al visible con la oscilación láser a 1342 nm mediante SFM. El cristal de Nd^{3+}:YVO_4, que presenta una concentración de Nd^{3+} de 1% at, se bombea con un diodo laser a 808 nm con una potencia de hasta 5 W. El cristal láser está cortado según el eje cristalográfico *a* y se orienta para proporcionar oscilación láser linealmente polarizada paralela a la polarización vertical o *s* (perpendicular al plano de la figura), que a su vez coincidirá con la polarización ordinaria del cristal KTP. El láser opera en régimen pulsado mediante Q-Switch pasivo (PQS) con un absorbente saturable (AS) de V^{3+}:YAG con una transmitancia inicial del 96 %. La cavidad láser queda deliminada por el espejo plano depositado sobre la cara de entrada del cristal

láser (HR a 1342 nm y HT a 808 nm en su cara exterior) y el espejo de salida (OC) que es plano-cóncavo (HR a 1342 nm con un radio de curvatura de 3 m). A través del PBS, que presenta una transmitancia del 98,12% para la poloralización paralela al plano de la figura *(pol. p)*, se acopla la imagen al interior de la cavidad con polarización ortogonal a la oscilación láser para realizar la conversión en el KTP mediante BPM de tipo II, de manera que: 1550 nm (*pol. e*) + 1342nm (*pol .o*) → 719 nm (*pol. o*), como se muestra esquemáticamente en la Fig.2.b. El cristal KTP empleado presenta un corte (θ=60º, ϕ=0º), 5×5 mm^2 de sección 8 mm de longitud. Mediante pequeño ajuste en su plano XZ permitirá ajustar el proceso deseado, como se muestra en la Fig.1.a.

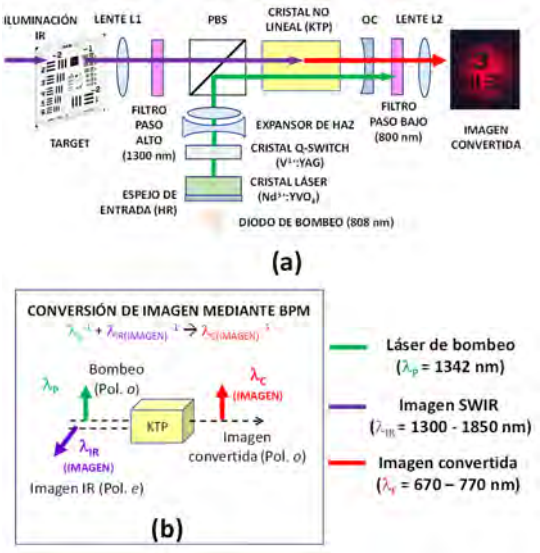

Fig. 2: (a) Esquema experimental del sistema convertidor de imagen. (b) Detalle del proceso de SFM mediante BPM de tipo II.

La inclusión del expansor de haz busca mantener el modo láser con un perfil gaussiano colimado en el cristal láser y en el absorbente saturable. Está formado por una lente de focal negativa de 6 mm y una lente de focal positiva de 50 mm en una configuración de telescopio. Ambas lentes tienen un recubrimiento AR a 1342 nm para minimizar las pérdidas intracavidad. Se estima que el haz presenta un diámetro de ~100 µm, para reducir el umbral de oscilación y aumentar la eficiencia del láser pulsado [4]. También ayuda a minimizar el efecto térmico proporcionando un rendimiento con altos niveles de potencia intracavidad. El modo láser también presenta un perfil colimado a lo largo del cristal no lineal de ~1 mm de diámetro. Para evaluar la conversión de imagen, se ilumina un test de resolución USAF-1951 con una fuente ASE centrada en 1550 nm en onda continua con una potencia total de ~100 mW.

En la Fig. 3 se muestran los espectros de la onda de bombeo a 1342 nm y el de la imagen resultante de la iluminación con fuente ASE centrada a 1550 nm tomados a la salida del convertidor. Cabe señalar que el espectro ASE presenta *pol. e* (componente contenida en el plano de la figura) como resultado de su paso a través del PBS.

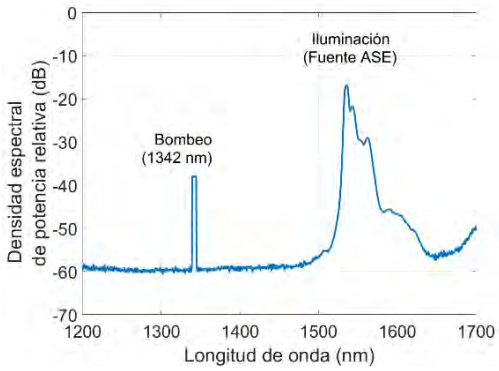

Fig. 3: Espectros del láser de bombeo y de la fuente de ilumnación (ASE) empleada en los procesos de conversión obtenidos por SFM.

Respecto al sistema óptico de formación de imágenes, sigue una configuración de procesador de Fourier 4*f* formado por dos lentes, L1 y L2, con focales de 50 y 75 mm, respectivamente. Ambas se encuentran alineadas con el brazo donde tiene lugar la conversión de imagen. El test de resolución se ubica en el plano focal del objeto de L1, y tras el proceso de conversión forma la imagen sobre el sensor ubicado en el plano focal de imagen de L2. Entre medias, el cristal de KTP se encuentra ubicado en el plano de Fourier del sistema óptico, lugar donde se hacen coincidir los focos de ambas lentes.

4.- Resultados

El láser convertidor con emisión a 1342 nm se bombea con un diodo láser a 808 nm con una potencia máxima de 5 W. El láser en régimen pulsado presenta un umbral 2.1 W. El comportamiento temporal en modo pulsado se muestra en la Fig. 4, donde se representa la duración del pulso y la frecuencia de repetición en función de la potencia de bombeo. A modo de ejemplo, la Fig.4.b y la Fig. 4.c representan las trazas temporales de los pulsos, presentando una duración de 400 ns (FWHM) y una frecuencia de repetición de 110 kHz cuando el láser es bombeado con 3.5 W de potencia.

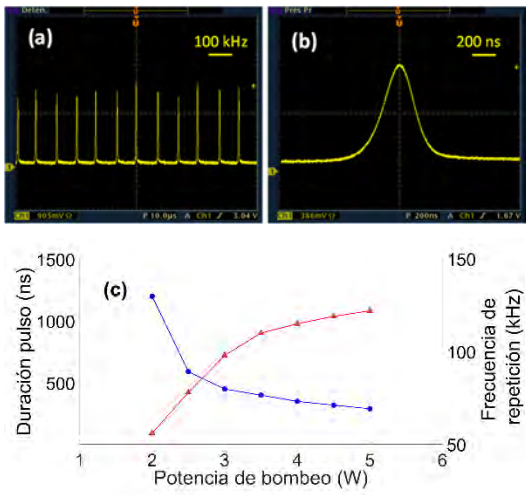

Fig. 4: (a) Comportamiento temporal del láser a 1342 nm con la potencia de bombeo. (b) Duración de pulso y (c) Frecuencia de repetición para 3.5 W de potencia de bombeo.

La operación en régimen pulsado persigue compensar mediante elevadas potencias de pico la reducción de eficiencia de conversión asociada al tamaño del haz cuando se desea incrementar la PSF del sistema. Cuando se desplaza el expansor de haz, el tamaño del modo en el interior del cristal láser se mantiene constante con la distancia y se estima un radio de unos 100 µm. Inicialmente el expansor se encuentra situado a 7 mm del espejo de entrada. Cuando se desplaza a lo largo de 10 mm, el tamaño del modo láser varía de forma lineal desde 0.8 mm hasta 1.2 mm en el interior del cristal no lineal.

Para determinar los niveles de potencia intracavidad se toma como referencia los niveles obtenidos a través de las caras de salida del PBS. La razón se debe a la disponibilidad de valores de tranmitancia más precisos (PBS103 de Thorlabs que presenta una transmitancia del 0,12% para *pol. s*) que los que se dispone para el espejo de salida. De este modo, para un bombeo de 5 W se obtiene a la salida del PBS un nivel de potencia media de 30 mW, siendo la duración de los pulsos de 290 ns y la frecuencia de repetición de 120 kHz. Cuando el expansor se situa a 12 mm del espejo de entrada, el tamaño del haz láser presenta un radio próximo a 1 mm. De esta manera, la intensidad de la onda de bombeo empleada en el proceso de conversión alcanza niveles próximos a los 23 kW/cm^2.

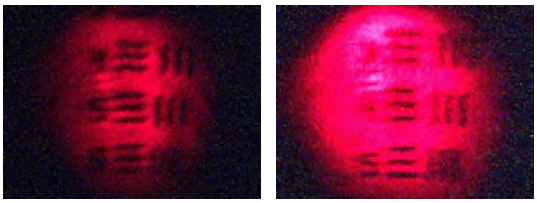

Fig. 5: Ejemplos de conversión de imagen a 671 nm y 719 nm con: (a) iluminación láser a 1342 nm, (b) fuente ASE centrada en 1550 nm.

Las figuras 5.a y 5.b recogen las imágenes capturadas por convertidas por el sistema propuesto, empleando un sensor CMOS (Onsemi MT9P031). Para ello, se iluminan previamente los motivos situados en torno al elemento 4 del grupo 3 (11,3 lp/mm) del test de resolución USAF-1951. La captura de las imagenes se realiza cuando láser convertidor se bombea con una potencia de 3.5 W (condiciones de las Figs. 4.a. y 4.b.). En la Fig.5.a. se muestra la conversión al segundo armónico (671 nm) cuando se emplea como iluminación la propia emisión láser, siguiendo una configuración como la empleada en [7]. Para la misma posición del cristal, la Fig. 5.b recoge la conversión mediante SFM (719 nm) cuando se emplea como iluminación una fuente ASE centrada en 1550 nm con un nivel de potencia de 100 mW. Para una adecuada visualización, la captura requiere el filtrado previo del segundo armónico. En la figura se aprecia que los niveles de potencia de

iluminación empleados conducen a la saturación del sensor. Dadas las características de coherencia de la fuente ASE y la aceptacia espectral del sistema, se consigue un mayor campo de visión respecto al obtenido mediante iluminación láser, como ya se ha demostrado previamente [8].

Por último y como referencia, la operación en modo pulsado del láser a una frecuencia de 100 kHz permitiría la integración de 100 imágenes convertidas por cada 1 ms de tiempo de exposición de la cámara. En cámaras convencionales, que operan a velocidades de 50 fotogramas/s (20 ms), se conseguirían integrar hasta 2000 imágenes por fotograma. De este modo, a pesar de que la eficiencia de conversión del sistema se presume baja, los niveles de intensidad intracavidad alcanzados (~kW/cm^2) permiten sobrepasar fácilmente el umbral de saturación del sensor.

5.- Conclusión

La identificación de cortes específicos en cristales no lineales en volumen, de tipo KTP, con gran disponibilidad comercial a un coste reducido, permite la implementación de sistemas convertidores de longitud de onda de imagen que cubren amplias regiones espectrales de una manera más sencilla y económica que los basados en cristales ferroeléctricos con microestructura de dominios. Respecto a estos últimos, también la disponibilidad de cristales con amplia sección evita limitaciones de resolución por efecto de apertura en las configuraciones 4*f*. El enfoque planteado en este trabajo permite además su aplicación en futuros trabajos centrados en la determinación de cortes que proporcionen amplias aceptancias angulares para la mejora de la resolución y del campo de visión cuando se emplea iluminación láser a longitudes de onda específicas. Por último, la implementación de una configuración basada en un expansor de haz intracavidad permite controlar el tamaño del haz láser en el medio no lineal hasta alcanzar valores compatibles con su sección transversal a la vez que posibilita adaptar su tamaño en el cristal láser y al absorbente saturable para obtener emisión láser eficiente en régimen pulsado mediante Q-Switch pasivo. De esta forma se consigue mejorar la resolución del sistema mediante el aumento de la PSF (apertura suave) a la vez que se compensa la eficiencia de conversión mediante intensidades del orden de kW/cm^2. Su incorporación en arquitecturas planteadas con anterioridad [7] pretende sentar las bases para la consecución de sistemas convertidores de imagen más simples y compactos, con buenas prestaciones en términos de resolución y eficiencia para el desarrollo de sistemas portátiles y versátiles para aplicaciones que requieran cubrir la región espectral del SWIR.

Agradecimientos: Agencia Estatal de Investigacion y FEDER (European Union Next Generation EU/PRTR), a través del proyecto PID2020-117658RB-I00 MICIU/AEI/10.13039/501100011033 y a la Generalitat Valenciana, a través del proyecto CIAICO/2021/326.

Referencias

[1] J. E. MIDWINTER, "*Parametric infrared image converters*" IEEE Journal of Quantum Electronics, 4(11), 716-720 (1968).

[2] C. PEDERSEN, E. KARAMEHMEDOVIC, J. S. DAM, P. TIDEMAND-LICHTENBERG, "*Enhanced 2D-image upconversion using solid-state lasers*", Optics Express, 17(23), 20885-20890 (2009).

[3] R. L. SUTHERLAND, "*Handbook of Nonlinear Optics*" (Marcel Dekker, 2003).

[4] K. KATO, E. TAKAOKA, "*Sellmeier and thermo-optic dispersion formulas for KTP*", Applied Optics, 41(24), 5040-5044 (2002).

[5] D. N. NIKOGOSYAN, "*Nonlinear Optical Crystals*" (Springer, 2005).

[6] J. J. DEGNAN, "*Optimization of passively Q-switched lasers*", IEEE Journal of Quantum Electronics, 31(11), 1890-1901(1995).

[7] A. J. TORREGROSA, H. MAESTRE, M. L. RICO, J. CAPMANY, "*Compact self-illuminated image upconversion system based on intracavity second-harmonic generation*" Optics Letters, 43(20), 5050-5053 (2018).

[8] A. J. TORREGROSA, H. MAESTRE, J. CAPMANY, "*Intra-cavity upconversion to 631 nm of images illuminated by an eye-safe ASE source at 1550 nm,*" Optics Letters, 40(22), 5315-5318 (2015).

Towards improved performance of an Yb:KGW laser-based intracavity image upconverter

Adrián J. TORREGROSA[(1)], María Luisa RICO[(2)], Juan CAPMANY[(1)], Miguel CUENCA[(1)], Angela E. ORTEGA[(1)], Carlos R. FERNÁNDEZ-POUSA[(1)] and Haroldo MAESTRE[(1)]

1. Engineering Research Institute of Elche-I3E, Universidad Miguel Hernandez de Elche, Avda. de la Universidad s/n, 03202 Elche (Alicante), Spain.
2. Computer Science Department, Universidad de Alicante, Ctra. San Vicente s/n, 03690 San Vicente del Raspeig (Alicante), Spain

Contact: Haroldo MAESTRE (hmaestre@umh.es).

ABSTRACT:

This paper presents an Yb:KGW laser-based intracavity image upconverter designed to enhance mid-IR imaging. Traditional mid-IR imaging faces limitations in sensor efficiency, resolution, and cost. Our approach uses IR to visible frequency shift imaging with non-linear Sum-Frequency Mixing (SFM) processes for real-time imaging using Si-based CMOS detectors. Key improvements include the use of a CPLN crystal for increased spectral and angular acceptance, broad SFM pump beams for high spatial resolution, and q-switched intracavity conversion to boost intensity and compensate for efficiency reduction tradeoffs. Additionally, we demonstrate that asymmetric laser modes within the cavity enhance image resolution. Results show successful real-time upconversion of mid-IR images to NIR. These characteristics pave the way for future high-performance mid-IR image upconverters and applications.

Key words: Image upconversion, Infrared imaging, Nonlinear optics, Solid-state lasers

1.- Introduction

Imaging in the mid and far infrared lacks image sensor arrays with high efficiency, high resolution and number of pixels, high speed and low cost [1]. Although imaging techniques in these bands have a wide range of applications, the lack of high-performance image sensors limits their widespread use. Infrared (IR) to visible frequency shift imaging is presented as an alternative, a technique that allows real-time imaging using conventional detectors (Si-based CMOS) with mature technology and high resolution and efficiency in potentially any spectral region [2].

This optical frequency upconversion technique is mostly based on non-linear Sum Frequency Mixing (SFM) processes. In SFM processes for imaging, an intense wave around 1 μm (SFM pump) is mixed with a wave in the mid-IR and a new wave is generated with a wavelength in the near infrared (NIR) that falls within the silicon absorption band (SFM or upconverted wave). The frequency shift can be applied to complete real-time images and is typically performed using a 4f imaging system with a non-linear optical crystal in the Fourier plane [3].

The IR image, thus, enters the 4f system and, after passing through the first lens, the spatial information is transformed into frequency information in the Fourier plane. This is where the non-linear crystal is located and where the image mixes with the SFM pump. The intensity of the SFM pump determines the efficiency of the IR to NIR frequency shift and, depending on the beam size of the SFM pump, it allows the conversion (equivalent to

transmission in a conventional 4f) of more or less infrared spatial frequencies to the NIR, where the new image, after passing through the second lens, is detected by high performance sensors. As it can be inferred, there is a trade-off here between the conversion efficiency and the resolution of the upconverter. These two characteristics are inversely related, as a very narrow SFM pump mode allows high optical intensity but avoids conversion of high spatial frequencies, and vice versa. Conversely, the properties of the nonlinear crystal dictate the nonlinear coefficient and phase matching, which in turn influence conversion efficiency, the range of wavelengths that can be converted, and the angular acceptance of the input image (field-of-view). One of the most commonly used non-linear crystals is $LiNbO_3$ with a periodically polarized domain structure (PPLN) due to its ferroelectric nature. Although these crystals have high efficiency, their wavelength and angular acceptances are narrow. To enhance these parameters, $LiNbO_3$ crystals with a chirped domain structure (CPLN) can be employed to significantly boost the angular and spectral acceptances, though at the expense of efficiency [4].

The aforementioned crystals have a typical thickness of 1 mm due to the manufacturing process, which also limits the achievable SFM pump beam diameter to <1mm and so the maximum spatial resolution, particularly in intracavity upconversion. This limitation does not occur in the direction perpendicular to the thickness. In this sense, it may be advantageous to use a wide SFM pumping mode in the dimension where the crystal does not represent a size constraint, and to transfer the improved resolution to the two spatial directions by rotating the sample and with targeted reconstruction software. This has been recently demonstrated in an external cavity configuration [5].

In this work, we combine a number of techniques to create an image converter by optimizing the key parameters of these systems in a single device, as outlines below:

1- Use of a CPLN crystal to increase the spectral (hyperspectral capability) and angular (field-of-view) acceptance of the converter.
2- Broad beam size of the SFM pump for high spatial resolution.
3- Q-switched intracavity conversion to boost the intensity of SFM pump and to compensate for the efficiency reduction due to the use of a broad beam.
4- The implementation of an asymmetrical SFM pumping mode is intended to address the limitations imposed by size constraints.

2.- Experimental setup of the upconverter

We present in Fig. 1 the experimental implementation of the intracavity image upconverter. The setting comprises a four mirror z-folded laser cavity. All mirrors (M1, M2, M3 and M4) are flat mirrors with highly reflective (HR) coatings at 1040 nm. In addition, M1 is antireflection (AR) coated at 981 nm and M4 is AR coated at 4 µm, respectively. The laser cavity has a total length (M1 to M4) of 150 mm. Since all cavity mirrors are flat, a 100 mm intracavity lens (ICL) is inserted to make the cavity stable. When ICL is around one focal length from M1 it provides an intracavity laser mode which focuses to a waist of 50 µm radius near M1, and becomes a collimated beam between ICL and M4 with a radius of ~500 µm. This configuration is adequate for good laser efficiency in the Yb:KGW crystal and good resolution in the non-linear crystal.

The laser crystal is placed near M1 and is a 3 mm x 3 mm cross sectional area, 4 mm long, N_g-cut Yb:KGW doped 3% at., which generates laser emission around 1040 nm in N_p-polarization. The Yb:KGW is pumped with a fiber-coupled (NA=0.22, 105 µm core) 981 nm laser diode (LD). The Yb:KGW laser can be operated in either CW or passively qswitched regimes. For passively q-switched operation, a Cr:YAG saturable absorber (SA), AR coated at 1040 nm and with an initial transmission T_0=90%, is inserted near M2. The non-linear crystal, where the upconversion takes place, is placed in the M3-M4 cavity arm. The nonlinear crystal is a CPLN crystal for broadband mid-IR

upconversion with a wide field-of-view and it is AR coated at the wavelengths of interest. The CPLN crystal is, simultaneously, placed at the Fourier plane of a 4f-system, with L1 and L2 imaging lenses. The CPLN has a linearly chirped poling period ranging from 19-24 μm, which means that mid-IR wavelengths from 2-4.5 μm can be phase-matched and upconverted with a field-of-view as wide as 30º.

The 4 μm radiation from a quantum-cascade laser (QCL) is collimated, transmitted through an USAF 1951 target for image formation and focused into the CPLN by means of L1. The mid-IR image and the intracavity SFM pump are mixed in the CPLN, taking advantage of the high intracavity 1040 nm intensity (CW or pulsed), which results in a high frequency conversion efficiency. Consequently, the mid-IR image is shifted to a new image of 825 nm which can be detected with a silicon CCD/CMOS high-sensitivity and high-resolution camera after propagation through L2.

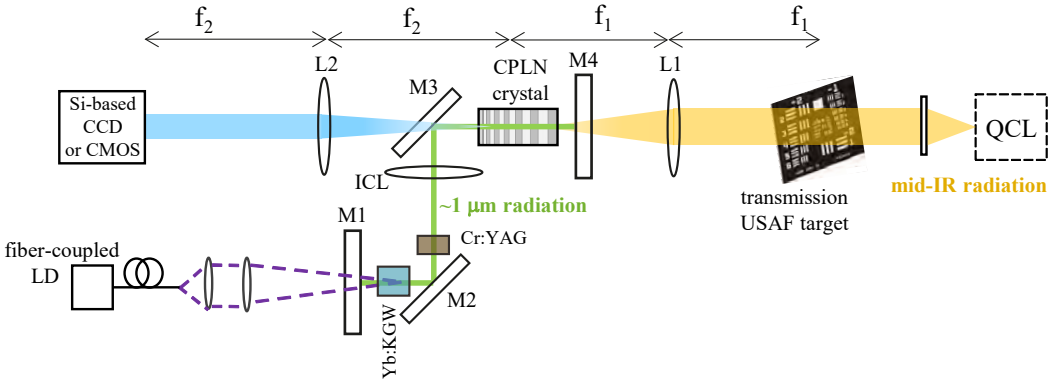

Fig. 1: Experimental setting of the proposed mid-IR image upconverter.

3.- Experimental results

Preliminary data on the converter characteristics are presented below. This section focuses on showing the conversion of mid-IR images to NIR, the intracavity q-switched operation to achieve high conversion efficiencies and the improvement of the converted image resolution by using asymmetric laser modes within the cavity.

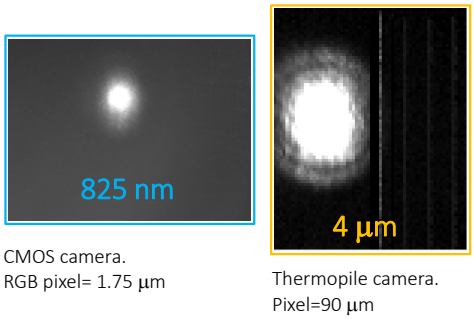

Fig. 2: Upconversion of the QCL laser transverse profile from mid-IR to the NIR.

3.1.- Intracavity mid-IR image upconversion

The intracavity power at 1040 nm in the Yb:KGW laser allows the image to be shifted from 4 μm to 825 nm and by SFG in the CPLN and detected by the Si camera. This conversion takes place in real time (as many frames/s as the CCD/CMOS camera allows) and, by operating in the Fourier plane of the 4f system, all the pixels are converted simultaneously without the need for spatial scanning techniques (raster scanning, etc...).

For comparison, the QCL laser mode image obtained directly on a pyroelectric array sensor and the NIR converted image detected with a Si-based CMOS camera are presented (Fig. 2). The frame colour of the images corresponds to the colours of the different optical bands depicted in Fig. 1. Despite the conversion being associated with a reduction in image size of the order of ρ, this factor can be compensated by the magnification of $\frac{\lambda_{up}}{\lambda_{IR}} \sim 5$ of the 4f system. Fig. 3 demonstrates the conversion of a USAF 1951 image (group

1, elements 5 and 6) from 4 µm to 825 nm and its visualization on a CMOS camera, as well as the magnification of the conversion by varying the ratio of f1 to f2 of the 4f system.

The portrayed uconversions were performed in CW regime and the conversion was appreciable from the moment the QCL laser emission threshold was reached. Alternatively, in CW, for a pump diode power at 981 nm absorbed of 5 W, approximately 60 W of intracavity power is achieved at 1040 nm.

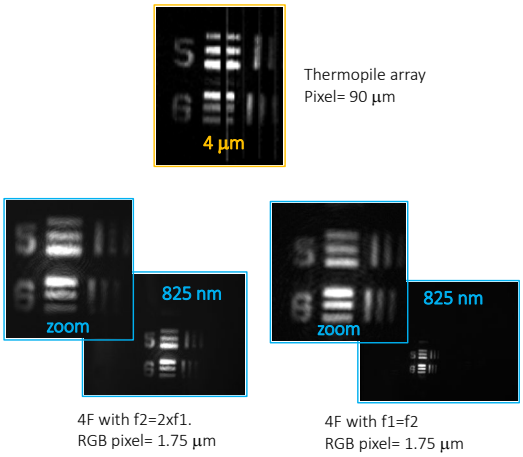

Fig. 3: Upconversion of mid-IR USAF 1951 images (group 1, elements 5 and 6) wavelength shifted to 825 nm for different remagnification ratios of the 4f system.

3.2.- Intracavity q-switched operation

In addition to continuous wave operation, the converter can be used in q-switched mode by inserting a Cr:YAG SA in the laser cavity. This configuration enables the attainment of pulsed emission within the pumping cavity of the SFM, with peak powers that reach of 100 kW, pulses with durations ranging from 20 to 30 ns, and repetition frequencies spanning from 8 to 20 kHz.

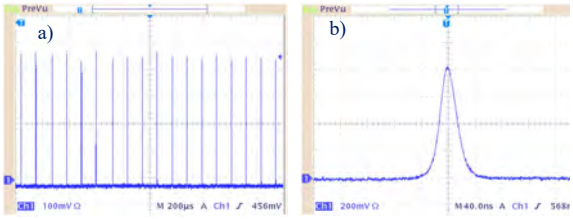

Fig. 4: a) Pulse train and b) single pulse waveforms of the passively q-switched laser for 5W of absorbed pump inside the Yb:KGW crystal.

Fig. 4 illustrates the temporal trace of q-switched regime for a 5 W absorbed pumping in the laser crystal. Fig. 4.a shows the qswitch pulse train with a repetition frequency of 9 kHz. Fig. 4.b shows the waveform of the generated pulses with a width of 25 ns (FWHM) measured at the output of M4 and corresponds to a peak intracavity power of 50 kW.

3.3.- Resolution enhancement with asymmetric SFM pump

The shape and size of the intacavity laser mode (1040 nm, SFM pump) act as a soft-aperture in the Fourier plane of the upconverter, allowing the transmission (or conversion) of a larger or smaller number of spatial frequencies of the infrared illumination. The physical aperture represented by the CPLN crystal (1 mm (vertical) x 3 mm (horizontal)) imposes limitations, primarily in the vertical direction, on the maximum attainable mode size and, consequently, on the resolution. When taking into account the thermal lens in the Yb:KGW crystal (for 5 W absorbed at 981 nm) and when properly adjusting the cavity size, and the position of the ICL (Fig. 1), the laser mode can be oscillated with a diameter close to 2.5 mm at the CPLN crystal position.

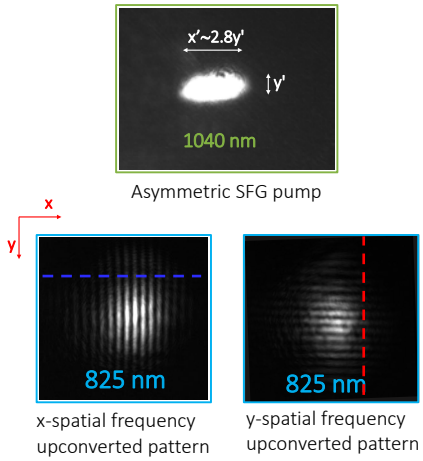

Fig. 5: Asymmetric SFM pump profile and upconversion of x-oriented and y-oriented patterns.

In this configuration, with the CPLN crystal inside the cavity, an aperture effect is observed in the vertical direction, resulting in an asymmetric laser mode where the horizontal width is approximately three times the vertical width. This configuration enables the enhancement of image resolution for spatial frequencies aligned with the widest axis of the pumping mode (y-axis). As illustrated in Fig. 5, the asymmetric intracavity laser mode at 1040 nm facilitates a higher resolution conversion for a given spatial frequency when oriented horizontally with respect to the vertical orientation. A mid-IR (4 µm) pattern with a single period of 0.4 mm, oriented in both *x* and *y* axes, is upconverted to 825 nm. The enhancement in resolution is clearly observable in the upconversion for the *x* axis orientation.

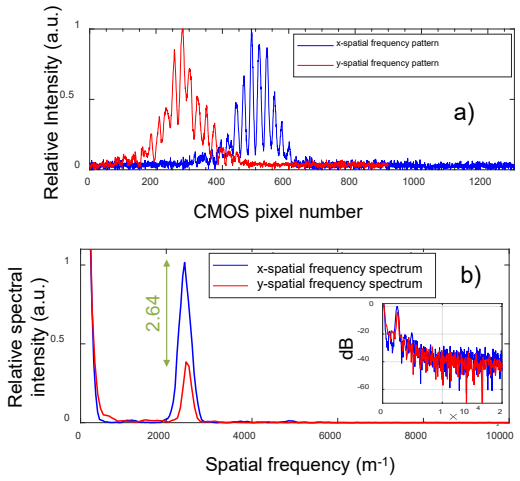

Fig. 6: a) Lines of pixels and b) FFT spatial frequency spectrum of x-oriented and y-oriented patterns.

The dashed lines (blue and red) represent a single line of pixels of the upconverted image in either horizontal (red) or vertical (blue) pattern orientation. These were extracted from image areas where their corresponding pixels were not saturated, and their information is analyzed in Fig. 6. Fig. 6 a) displays the normalized intensity versus pixel number of the analyzed line for both horizontal (blue) and vertical (red) orientation. It is evident from this figure that for the x-oriented pattern a better image contrast is obtained than for the y-orientation due to a smaller aperture effect in the x-orientation, where the SFM pumping mode is wider. From Fig. 6.a, in Fig. 6.b. we obtained, by FFT, the spectrum of spatial frequencies present in the converted image when the pattern is oriented in both x and y directions. In this representation (Fig. 6.b) the horizontal axis has been rescaled to represent the spatial frequency of the mid-IR image, instead of the NIR converted one, which is not the same due to the angular reduction of the conversion process. The figure illustrates the squared amplitude of the spatial frequencies of the 4 µm image pattern within the spatial frequency spectrum of the converted image upon orientation. The periodicity of this pattern is 0.4 mm, corresponding to a spatial frequency of 2500 m^{-1}. For this spatial frequency, the intensity of the pattern frequency in the spectrum for the x-orientation is 2.64 times higher than for the y-orientation, which roughly corresponds to x-axis and y-axis gaussian apertures with a ratio of widths 1/e of 2.8 (Fig. 5).

4.- Conclusion

This work demonstrates significant advancements in mid-IR imaging through the development of an Yb:KGW laser-based image upconverter. By integrating a CPLN crystal, broad SFM pump beams, and q-switched intracavity conversion, we have achieved enhanced spectral and angular acceptance, high spatial resolution, and improved conversion efficiency. The experimental results confirm the successful real-time upconversion of mid-IR images to NIR. The use of asymmetric laser modes within the cavity further enhances image resolution, particularly for spatial frequencies aligned with the widest axis of the pump mode. These improvements address the limitations of traditional mid-IR imaging systems, offering a high-performance solution that can be applied in various fields requiring advanced imaging capabilities. Future work will focus on optimizing these parameters further and exploring additional applications of this technology.

Acknowledgements: This work has received financial support from Agencia Estatal de Investigación (Grant PID2020-117658RBQ1

I00, MICIU/AEI/10.13039/501100011033); European Regional Development Fund; Conselleria de Innovación, Universidades, Ciencia y Sociedad Digital, Generalitat Valenciana (Grant CIAICO/2021/326).

References

[1] J. Dam, P. Tidemand-Lichtenberg, and C. Pedersen, "Room-temperature mid-infrared single-photon spectral imaging," Nature Photon 6, 788–793 (2012).

[2] A. Barh, P. J. Rodrigo, L. Meng, C. Pedersen, and P. Tidemand-Lichtenberg, "Parametric upconversion imaging and its applications," Adv. Opt. Photon. 11, 952-1019 (2019).

[3] C. Pedersen, E. Karamehmedović, J. Dam, and P. Tidemand-Lichtenberg, "Enhanced 2D-image upconversion using solid-state lasers," Opt. Express 17, 20885-20890 (2009).

[4] K. Huang, J. Fang, M. Yan, et al. "Wide-field mid-infrared single-photon upconversion imaging," Nat Commun 13, 1077 (2022).

[5] T. Zheng, Z. Wei, K. Huang, M. Yu, J. Fang, Z. Wen, J. Zhang, and H. Zeng, "Mid-infrared Fourier ptychographic upconversion imaging," Optica 11, 1716-1724 (2024).

Impact of nonlinearity multifrequency dispersion on instabilities cancelation

Miguel A. BOSCH [(1)], Enrique SILVESTRE [(1,2)], Martina DELGADO-PINAR [(1,3)], Antonio DÍEZ [(1,3)], Miguel V. ANDRÉS [(1,3)] and David CASTELLÓ-LURBE [(1,3)]

1. Institut Universitari de Ciències dels Materials (ICMUV), Universitat de València, Catedrático Agustín Escardino 9, Paterna 46980, Spain.
2. Departament d'Òptica i Optometria i Ciències de la Visió, Universitat de València, Dr. Moliner 50, Burjassot 46100, Spain.
3. Departamento de Física Aplicada i Electromagnetisme, Universitat de València, Dr. Moliner 50, Burjassot 46100, Spain.

Contact: Miguel A. Bosch (miguel.bosch@uv.es).

ABSTRACT:

In the modeling of propagation of optical pulses, the multifrequency character of nonlinearities is usually omitted, leading to the use of the well-known generalized nonlinear Schrödinger equation. However, in recent years, arguments have been put forward suggesting that such a multifrequency dispersion could have a significant impact on pulse dynamics, opening new frontiers in the field of nonlinear optics. This paper explores analytically how the dependence of nonlinearities on multiple frequencies affects, in particular, the process of modulation instability. Remarkably, scenarios where modulation instability should arise according to the generalized nonlinear Schrödinger equation become stable when the full nonlinearity multifrequency dispersion is taken into account.

Key words: nonlinear optics, modulation instability, coherence, multifrequency dispersion,

1.- Introduction

One of the key properties that gives nonlinear optics its complexity is the interaction of multiple frequencies, where different frequencies interact to create new ones. In the propagation of optical pulses through waveguides, when we deal with dispersive nonlinearities, the study of dynamics becomes a computationally demanding problem [1,2]. Traditionally, this issue has been addressed by omitting the multifrequency nature of nonlinearities dispersion. This leads to the generalized nonlinear Schrödinger equation (GNLSE) [3], which allows the study of optical pulse propagation with a manageable computational cost. Although this approximation works for a wide range of cases, when nonlinear dispersion is present, the GNLSE has some fundamental limitations, such as the lack of energy conservation or photon number conservation [4].

In recent years, some works have shown how nonlinearities dispersion can give rise to new phenomena [5-6]. A clear example of this was reported in Ref. [5], where it was theoretically demonstrated that a dispersive nonlinear coefficient could cancel the modulation instability (MI) in the anomalous dispersion regime, scenario that had been considered forbidden before. The growing interest in the use of dispersive nonlinearities has recently motivated the derivation of the so-called multifrequency nonlinear Schrödinger

equation (MFNLSE) [7], which rigorously incorporates the nonlinearities multifrequency dependence maintaining the computational advantages of the GNLSE. Moreover, the MFNLSE conserves the pulse energy and number of photons. Accordingly, the MFNLSE offers the opportunity to study, even analytically, the impact of multifrequency nonlinearities on pulse propagation.

The present work evaluates how the multifrequency character of the nonlinearities impacts on the stability of the system. A linear stability analysis has been carried out to obtain the gain of the MI process under the MFNLSE and to deduce the conditions that allow its cancelation. Finally, numerical simulations of the MFNLSE and GNLSE have been performed to verify the analytical expressions and compare both theories.

2.- Modulation instability cancelation

Our starting point is the MFNLSE [7],

$$\frac{\partial \psi}{\partial z} = -\frac{\alpha}{2}\psi + i\hat{\beta}_{\mathrm{p}}\psi + i\hat{\eta}\psi^{*}\hat{\Gamma}_{\mathrm{K}}\psi^{2}\,, \quad (1)$$

where $\psi(z,t)$ is the normalized field envelope, α represents the waveguide losses, $\hat{\beta}_{\mathrm{p}} = \mathcal{F}^{-1}\beta_{\mathrm{p}}(\Omega)\mathcal{F}$ refers to the linear operator that accounts for the group velocity dispersion and $\mathcal{F}$ describes the Fourier transform computed at the relative frequency $\Omega = \omega - \omega_0$, where ω_0 denotes the pump center frequency. Importantly, the multi-frequency nonlinearity dispersion results in a splitting of the usual nonlinear operator $\hat{\gamma} = \mathcal{F}^{-1}\gamma(\Omega)\mathcal{F}$, where $\gamma(\Omega)$ denotes the nonlinear coefficient, into two operators. On the one hand, $\hat{\eta} = \mathcal{F}^{-1}\eta(\Omega)\mathcal{F}$ conveys the truly single-frequency dispersion. On the other hand, $\hat{\Gamma}_{\mathrm{K}} = \mathcal{F}^{-1}\Gamma\left(\frac{\Omega}{2}\right)\mathcal{F}$ is responsible for incorporating the multifrequency dependence. We refer the reader to Ref. [7] for more details about these coefficients.

Our study will focus on the simplest case that takes into account the dispersion of nonlinearities, as well as the new multi-frequency dependence: $\beta_{\mathrm{p}}(\Omega) = \frac{\beta_2}{2}\Omega^2$, $\eta(\Omega) = \eta_0 + \eta_1\Omega$ and $\Gamma(\Omega) = \Gamma_0 + \Gamma_1\Omega$, where $\{\beta_2, \eta_0, \eta_1, \Gamma_0, \Gamma_1\}$ are the parameters of the Taylor's expansion around ω_0 of $\beta_{\mathrm{p}}(\Omega)$, $\eta(\Omega)$ and $\Gamma(\Omega)$, respectively.

Along the lines of the stability analysis to study MI under the GNLSE [3], we derive here the following expression for the maximum gain of MI under the Eq. 1,

$$g_{\mathrm{MI}}(P_{\mathrm{p}}) = -\mathrm{sign}(\beta_{2\mathrm{eff}})2\,\eta_0\Gamma_0 P_{\mathrm{p}} - 2P_{\mathrm{p}}^2\frac{\eta_1^2\Gamma_0^2}{|\beta_{2\mathrm{eff}}|}\,, \quad (2)$$

where P_{p} is the power of the pump and we have introduced an effective group velocity dispersion coefficient $\beta_{2\mathrm{eff}} \equiv \beta_2 + 2\eta_1\Gamma_1 P_{\mathrm{p}}$. To understand Eq. 2, we plot it employing the set of parameter values included in Table 1. It is important to notice that the orders of magnitude of the nonlinear coefficients used have been chosen so that notable discrepancies between the MFNLSE and GNLSE will arise, as it will become apparent later.

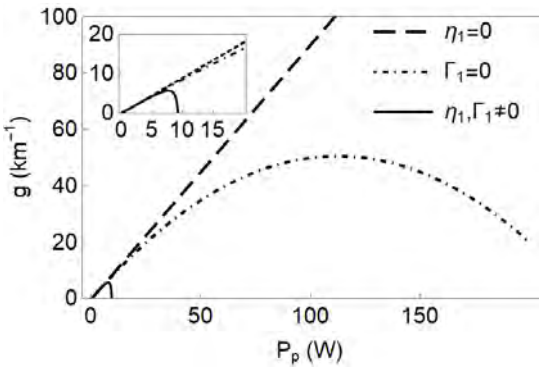

Fig. 1. MI gain as a function of pump power for $\eta_1 = 0$ *(dashed line),* $\Gamma_1 = 0$ *(dash-dotted line) and* $\eta_1, \Gamma_1 \neq 0$ *(solid line).*

Table 1. Waveguide parameters used in the simulations.

$\beta_2 = -5\ \mathrm{ps^2\ km^{-1}}$
$\alpha = 6 \times 10^{-3}\ \mathrm{m^{-1}}$
$\eta_0 = 9 \times 10^{6}\ \mathrm{m^{-1}}$
$\Gamma_0 = 5 \times 10^{-11}\ \mathrm{W^{-1}}$
$\eta_1 = 2 \times 10^{6}\ \mathrm{ps\ m^{-1}}$
$\Gamma_{1\mathrm{th}} = 1.23 \times 10^{-10}\ \mathrm{ps\ W^{-1}}$

In view of Fig. 1, the dispersion in the $\eta(\Omega)$ modifies the shape of the gain function (differences between the dashed and dash-dotted lines). This feature guarantees the existence of a maximum in the gain function, $g_{\mathrm{MI,max}}$, which makes it possible to have a stability condition, $g_{\mathrm{MI,max}} \leq \alpha$, where the MI process is suppressed regardless of the pump power used. This scenario is similar to the known result for GNLSE demonstrated in Ref. [5]. Then, the dispersion in $\Gamma(\Omega)$ reduces the value of $g_{\mathrm{MI,max}}$, thus further facilitating the stabilization of the system.

To obtain $g_{\mathrm{MI,max}}$, we maximize Eq. 2 as a function of the pump power and recast the stability condition in terms of the waveguide parameters,

$$\Gamma_1 \geq \Gamma_{1\mathrm{th}} = \Gamma_0 \frac{|\beta_2|}{\alpha}\left(\frac{\eta_0}{\eta_1} - \sqrt{2\frac{\alpha}{|\beta_2|}}\right), \quad (3)$$

where $\{\eta_0, \eta_1, \Gamma_0, \Gamma_1\}$ have been assumed to be positive. Based on Eq. 3, MI can be suppressed in the anomalous dispersion regime provided Γ_1 is above certain threshold. It is worth emphasizing that if Eq. 3 is fulfilled, no instabilities are expected regardless of the input pump power and duration.

3.- Numerical simulations

To test the stability condition, numerical simulations of Eq. 1 have been performed for cases where Eq. 3 is satisfied and cases where it is not. To carry out this numerical study, Γ_1 has been taken as the control parameter and the values of the parameters $\{\alpha, \beta_2, \eta_0, \eta_1, \Gamma_0\}$ have been set as indicated in Table 1. In addition, 100 ps and 150 W pulses propagated along 250 m have been used. Finally, a noise background at -80 dB has also been added.

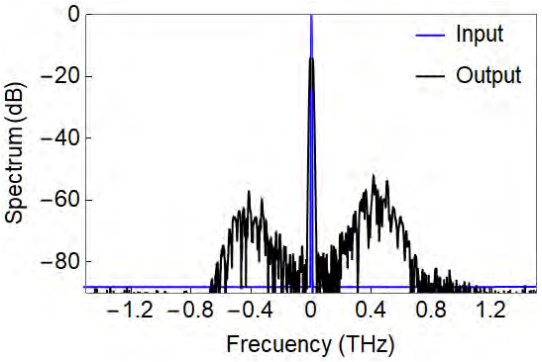

Fig. 2. Output spectrum predicted by the MFNLSE when $\Gamma_1 = 0 < \Gamma_{1\mathrm{th}}$.

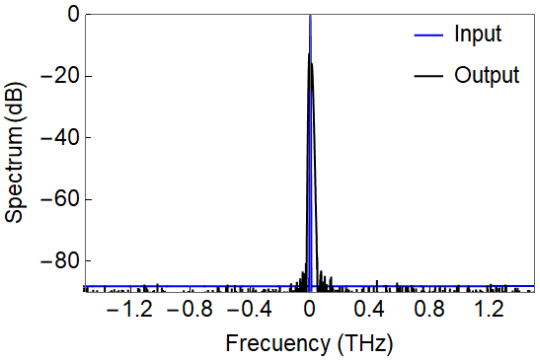

Fig. 3. Output spectrum predicted by the MFNLSE when $\Gamma_1 = 1.3 \times 10^{-10}\ \mathrm{ps\ W^{-1}} > \Gamma_{1\mathrm{th}}$.

Fig. 2 and Fig. 3 show the output spectra for the case where $\Gamma_1 < \Gamma_{1\mathrm{th}}$ (Fig. 2) and for the case where $\Gamma_1 > \Gamma_{1\mathrm{th}}$ (Fig. 3). If $\Gamma_1 < \Gamma_{1\mathrm{th}}$, amplification of the bands of the spectrum characteristic of the MI process is seen [3,8,9]. In sharp contrast, when the stability condition is fulfilled, $\Gamma_1 > \Gamma_{1\mathrm{th}}$, the MI bands disappear and amplification does not occur, as predicted by our theoretical model.

Since Fig. 2 and Fig. 3 have numerically validated our Eq. 3, to further confirm that the instabilities cancellation is due to the multifrequency nature of the nonlinearities, we have also simulated the case in Fig. 3 assuming a single-frequency nonlinearity

dispersion, i.e., modeling the nonlinear term as $\gamma_{\text{eff}}(\Omega)\mathcal{F}[|\psi|^2\psi]$, where $\gamma_{\text{eff}}(\Omega) \equiv \eta(\Omega)\Gamma(\Omega)$, similarly to the GNLSE, instead of $\eta(\Omega)\mathcal{F}\left[\psi^*\mathcal{F}^{-1}\Gamma\left(\frac{\Omega}{2}\right)\mathcal{F}\psi^2\right]$, as done in the MFNLSE. Showing a clear amplification of the background noise, Fig. 4 demonstrates that the nonlinearity dependence on multiple frequencies plays a key role in stabilizing the pulse propagation studied in this work. In other words, the GNLSE could not explain the scenario illustrated by Fig. 3.

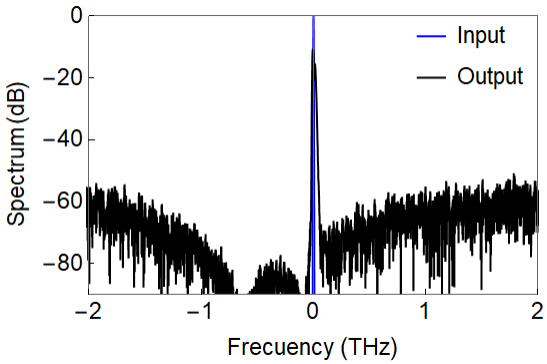

Fig. 4. Output spectrum corresponding to the case in Fig. 3 but predicted by the GNLSE instead of the MFNLSE.

4.- Conclusion

In this work we have studied modulation instability under the multifrequency nonlinear Schrödinger equation to explore the effects of the multifrequency dispersion of nonlinearities. On this basis, we have derived and validated by means of simulations an analytical condition enabling the suppression of instabilities at any power in the anomalous group-velocity dispersion regime. Importantly, we have also demonstrated numerically how the common assumption that nonlinearities depend on a single frequency fails to account for such a stabilization.

Acknowledgements: This work has been funded by Ministerio de Ciencia, Innovación y Universidades (CNS2023-145717, PID2023-146725OB-I00, María Zambrano Fellowship ZA21-053); Generalitat Valenciana (CIPROM/2022/30); European Commission (H2020-MSCA-RISE-2019-872049, María Zambrano Fellowship ZA21-053).

References

[1] J. LAEGSGAARD, *"Mode profile dispersion in the generalized nonlinear Schrödinger equation."* Opt. Express 15, 16110-16123, 2007.

[2] Truong X. TRAN and Fabio BIANCALANA, "*An accurate envelope equation for light propagation in photonic nanowires: new nonlinear effects*," Opt. Express 17, 17934-17949, 2009.

[3] Govind P. AGRAWAL, "*Nonlinear fiber optics"*, Academic Press, 4th edition, 2007.

[4] J. BONETTI, N. LINALE, A. D. SÁNCHEZ, S. M. HERNANDEZ, P. I. FIERENS, and D. F. GROSZ, "*Modified nonlinear Schrödinger equation for frequency-dependent nonlinear profiles of arbitrary sign",* J. Opt. Soc. Am. B 36, 3139-3144, 2019.

[5] David CASTELLÓ-LURBE, "*Breaking fundamental noise limitations to supercontinuum generation.*", Opt. Lett. 47, 6, 1299-1302, 2022.

[6] J. BONETTI, N. LINALE, A. D. SÁNCHEZ, S. M. HERNANDEZ, P. I. FIERENS, and D. F. GROSZ, "*Modulation instability in waveguides with an arbitrary frequency-dependent nonlinear coefficient*," Opt. Lett. 45, 2498-2501, 2020.

[7] David CASTELLÓ-LURBE, Enrique SILVESTRE and Miguel V. ANDRÉS, "*Multifrequency nonlinear Schrödinger equation"*, Opt. Lett. 49, 16, 4713-4716, 2024.

[8] A.V. GORBACH, X. ZHAO, and D.V. SKRYABIN, "*Dispersion of nonlinearity and modulation instability in sub-wavelength semiconductor waveguides",* Opt. Express. 19, 9345-9351, 2011.

[9] Yuanjiang XIANG, Shuangchun WEN, Xiaoyu DAI, Zhixiang TANG, Wenhua SU, and Dianyuan FAN, "*Modulation instability induced by nonlinear dispersion in nonlinear metamaterials",* J. Opt. Soc. Am. B. 24, 3058-3063, 2007.

TERRASSA · OPTOEL · DEL 2 AL 4 DE JULIO DE 2025 ·